



Universiteit
Leiden
The Netherlands

The chemistry of planet-forming disks: a story from inner to outer disk

Temmink, M.

Citation

Temmink, M. (2026, June 5). *The chemistry of planet-forming disks: a story from inner to outer disk*. Retrieved from <https://hdl.handle.net/1887/4304669>

Version: Publisher's Version

License: [Licence agreement concerning inclusion of doctoral thesis in the Institutional Repository of the University of Leiden](#)

Downloaded from: <https://hdl.handle.net/1887/4304669>

Note: To cite this publication please use the final published version (if applicable).

The chemistry of planet-forming disks

A story from inner to outer disk

Proefschrift

ter verkrijging van
de graad van doctor aan de Universiteit Leiden,
op gezag van rector magnificus prof. dr. S. de Rijcke,
volgens besluit van het college voor promoties
te verdedigen op vrijdag 5 juni 2026
klokke 10:00 uur
door

Milou Temmink

geboren te Olst, Nederland
in 1999

Promotores:

Prof. dr. E.F. van Dishoeck

Prof. dr. M.R. Hogerheijde Universiteit Leiden
Universiteit van Amsterdam

Co-promotor:

Dr. N. van der Marel

Promotiecommissie:

Prof. dr. I.A.G. Snellen

Prof. dr. B.R. Brandl

Prof. dr. E.A. Bergin University of Michigan, USA

Dr. M. Benisty Max-Planck Institute for Astronomy, Germany

Dr. K. Zhang University of Wisconsin-Madison, USA

ISBN: 978-94-6496-564-3

Printed by: Gildeprint

Cover design: Milou Temmink

It will (get worse), but then it will get better.
Then it will get worse again. Then better.
This is life, and I will not lie by saying every day will be sunshine.
But there will be sunshine again, and that is a very different thing to say.
That is truth.

- *Wit (Rhythm of War)*

Table of contents

1	Introduction	1
1.1	Star- and planet-formation	1
1.2	Planet-forming disks	3
1.2.1	Disk constituents	3
1.2.1.1	Dust and ice	3
1.2.1.2	Gas	5
1.2.2	Disk evolution	7
1.2.2.1	Viscous evolution	8
1.2.2.2	MHD disk wind	8
1.2.2.3	Accretion, accretion outbursts, and (late) infall	9
1.2.2.4	(Photoevaporative) disk winds	10
1.2.2.5	Planet formation and radial drift	10
1.2.3	Disk observations	12
1.2.3.1	Near-infrared	12
1.2.3.2	Mid-infrared	13
1.2.3.3	Far-infrared and (sub-)millimetre	13
1.2.4	Disk substructures	14
1.2.4.1	Rings and gaps	15
1.2.4.2	Rings and cavities	15
1.2.4.3	Asymmetries	16
1.2.4.4	Spiral arms	17
1.2.4.5	Shadows and misalignments	18
1.2.4.6	Substructures and radial drift	19
1.3	Astrochemistry	20
1.3.1	Energy levels and transitions	20
1.3.1.1	Ro-vibrational transitions	21
1.3.2	Excitation analysis	22
1.3.3	Chemical processes	24
1.3.3.1	Gas-phase chemistry	24
1.3.3.2	Grain-surface chemistry	26
1.4	This thesis	26
1.4.1	Future prospects	30

PART I	Chemical and physical structure of the inner disk	31
2	MINDS: The DR Tau disk I. Combining JWST-MIRI data with high-resolution CO spectra to characterise the hot gas	33
2.1	Introduction	36
2.2	Observations	38
2.2.1	JWST-MIRI observations	38
2.2.2	Continuum subtraction	39
2.2.3	High-resolution CO observations	40
2.3	Analysis	41
2.3.1	LTE slab models	41
2.3.2	CO line profiles and rotational diagrams	42
2.4	Results	44
2.4.1	JWST spectrum and detected molecules	44
2.4.1.1	$^{12}\text{CO}_2$	45
2.4.1.2	HCN & C_2H_2	45
2.4.2	CO analysis	46
2.4.2.1	^{12}CO as seen by JWST-MIRI	46
2.4.2.2	iSHELL CO line profiles and rotational diagrams	48
2.4.2.3	Optical depth: ^{12}CO and ^{13}CO	51
2.4.2.4	Estimated emitting radii of CO	52
2.4.2.5	LTE versus non-LTE	53
2.4.2.6	Implication for JWST-MIRI analysis	54
2.4.2.7	JWST-MIRI line profile: Pseudo-Voigt versus Gaussian	56
2.5	Discussion	57
2.5.1	CO excitation temperature as probed by JWST-MIRI	57
2.5.2	Emitting region of CO	57
2.5.3	Comparing the emitting properties of CO with the other molecules	58
2.6	Conclusions & summary	59
	Appendices	61
2.A	Continuum subtraction	61
2.B	Uncertainties for the JWST-MIRI subbands	61
2.C	χ^2 -maps of CO_2 , HCN, and C_2H_2	64
2.D	Complementary CO ro-vibrational observations	65
2.D.1	Line information and integrated fluxes	65
2.D.2	Full iSHELL model	68
2.D.3	χ^2 -maps of the CO rotational diagrams	69
2.D.4	Optical depth of ^{12}CO	70
2.D.5	LTE versus non-LTE	70
2.D.6	Convolution iSHELL to JWST-MIRI resolution	71
2.D.6.1	Gaussian line profile	72
3	MINDS: The DR Tau disk II. Probing the hot and cold H₂O reservoirs in the JWST-MIRI spectrum	73

3.1	Introduction	75
3.2	Observations	76
3.3	Analysis and results	78
3.3.1	Single H ₂ O LTE slab models	79
3.3.2	Cold and warm H ₂ O reservoirs: large disk template	82
3.3.2.1	Identifying unblended lines	82
3.3.2.2	Large disk template: CI Tau	83
3.3.3	Cold and warm H ₂ O reservoirs: multi-component slab models	84
3.3.3.1	Radial temperature gradient	86
3.3.3.2	Radial and vertical temperature gradient: no shielding	86
3.3.3.3	Radial and vertical temperature gradient: accounting for spatial shielding	88
3.3.4	Line pair ratios	88
3.3.5	Searching for H ₂ ¹⁸ O	91
3.3.6	Other emission features	92
3.3.6.1	OH	93
3.3.6.2	Atomic and molecular hydrogen	93
3.3.6.3	Non-detections	94
3.4	Discussion	96
3.4.1	The need for H ₂ O line overlap	96
3.4.2	The need for a radial temperature gradient	96
3.4.3	The importance of radial drift	98
3.4.4	CO versus H ₂ O	98
3.5	Conclusions and summary	99
	Appendices	102
3.A	Uncertainties for the JWST-MIRI subbands	102
3.B	H ₂ O slab models across the wavelength regions	103
3.B.1	Without line overlap	103
3.B.2	With line overlap	105
3.C	Selected, isolated H ₂ O transitions	107
3.D	Two versus three component fits	108
3.E	Multi-component corner plots	109
3.F	H ₂ ¹⁸ O over 17.0-27.5 μ m	113
3.G	Searching for other molecular species	113
3.G.1	Atomic and molecular hydrogen	113
3.G.2	Simple molecules	115
3.G.3	Hydrocarbons	117
4	MINDS: Water reservoirs of compact planet-forming dust disks A diversity of H₂O distribution	119
4.1	Introduction	121
4.2	Sample and observations	123
4.2.1	Sample	123
4.2.2	Observations and data reduction	124
4.3	Methodology	126

4.3.1	Rotational H ₂ O spectrum: Parametric analysis	127
4.3.2	Rotational H ₂ O spectrum: Multiple components	130
4.3.3	Line flux ratios	130
4.4	Results	131
4.4.1	Parametric analysis	131
4.4.2	Multiple component analysis	133
4.4.3	Line flux ratios	134
4.5	Discussion	134
4.5.1	Profile types and H ₂ O reservoirs	135
4.5.2	Role of sub-structures	137
4.5.3	Profile implications	138
4.5.4	Line width comparison	140
4.5.5	Comparisons with previous analyses	140
4.5.6	Other molecular species	143
4.6	Conclusions and summary	144
	Appendices	146
4.A	Velocity shifted slab models	146
4.B	S/N on the continuum and uncertainties for the observations . . .	147
4.C	Slab model fit regions	147
4.D	Fit results	148
4.E	Other molecular species	159
4.E.1	Molecules per source	159
4.E.2	Tentative detection of CH ₄ in CY Tau	160
4.F	Integrated line fluxes	161
4.G	Profile comparison	161
 PART II Substructures in the outer disk		167
5	MINDS: The influence of outer dust disk structure on the volatile delivery to the inner disk	169
5.1	Introduction	171
5.2	ALMA observations	171
5.3	Visibility fitting	172
5.4	Characterising the millimetre continuum emission	176
5.5	Comparison with previous works	178
5.6	Identified structures, snowlines, and proposed scenarios	181
5.7	Concluding remarks	182
 PART III Outer disk chemistry		183
6	Characterising the molecular line emission in the asymmetric Oph-IRS 48 Temperatures, timescales, and sub-thermal excitation	185
6.1	Introduction	188

6.2	Data	189
6.3	Methods	191
6.3.1	Identifying detected transitions	191
6.3.2	Integrated intensity and rotational diagram analysis	192
6.4	Results	192
6.4.1	SO ₂	193
6.4.2	CH ₃ OH	194
6.4.3	H ₂ CO	194
6.5	Discussion	196
6.5.1	Sub-thermal excitation	196
6.5.2	Temperature and vertical structure	199
6.5.2.1	Temperature structure	199
6.5.2.2	Vertical structure	200
6.5.3	Optical depth and emission structure	202
6.5.3.1	Optical depth	202
6.5.3.2	Continuum affecting the line emission	205
6.5.4	Future observations	206
6.6	Timescales: Vertical mixing, desorption, and photodissociation	206
6.6.1	Methodology	206
6.6.2	Timescale comparisons	209
6.7	Conclusions and summary	210
	Appendices	214
6.A	SO ₂ , CH ₃ OH, and H ₂ CO transitions	214
6.B	Line profiles	216
6.C	H ₂ CO line ratios	218
6.D	Observations-to-model ratios and uncertainty maps	219
6.E	H ₂ CO moment-0 maps	220
6.F	Observed transitions per pixel	221
6.G	Channel maps	222
6.H	Timescale figures	223
7	The asymmetric carbon-rich chemistry of the planet-forming disk of HD 142527 triggered by late infall	225
7.1	Introduction	227
7.2	Observations and self-calibration	229
7.3	Molecular emission	231
7.3.1	Detected molecular species and azimuthal distributions	231
7.4	Analysis and discussion	232
7.4.1	Inclination and position angle	232
7.4.2	Brightness temperature	232
7.4.3	Molecular asymmetries and structures	233
7.4.3.1	Enhanced surface density: C ¹⁷ O and HCO ⁺	233
7.4.3.2	Spirals or late infall: H ₂ CO, C ₂ H, and CN	235
7.4.3.3	H ₂ CO formation timescale delay	238
7.4.3.4	Azimuthal or vertical variations: CS	239
7.4.3.5	A potential shock: SO	240

7.4.4	Origins of the spirals and dust trap	241
7.4.5	Future work and studies	241
7.5	Summary	242
	Appendices	245
7.A	Observational details	245
7.B	Self-calibration: S/N -ratios	245
7.C	Molecular species: detections and non-detections	246
7.C.1	Weak and/or tentative detections	247
7.C.2	Non-detections	247
7.D	Continuum brightness temperature	251
7.E	H_2CO channel maps	251
7.F	Tracing the ^{12}CO spiral arms	251
7.G	Deprojected maps: C_2H and H_2CO	254
	Bibliography	254
	Nederlandse samenvatting	279
	Publications	287
	Curriculum Vitae	295
	Acknowledgements	297

Chapter 1

Introduction

Questions that captivate many astronomers are "Where does life form?" and "Could there be life elsewhere in the Universe?" Presently, over 6,000 exoplanets have been discovered and, statistically speaking, it is expected that every star hosts at least one planet, making it nearly unthinkable that life has only ever thrived on Earth. To answer these questions and to determine whether the Earth is a unique case, we need to understand planets, the regions in which they form and how they evolve. Disks around young, newly-formed stars play a crucial role in answering these questions, as they are the cradles of planets and set their (chemical) composition.

With every passing day, our understanding of planet-forming disks grows, in part due to the active development of new telescopes and instruments. The field of planet-forming disks and the adjacent field of astrochemistry have undergone rapid developments over this past decade through new observations and insights from telescopes such as the Atacama Large Millimeter/submillimeter Array (ALMA; Wootten & Thompson 2009) and the *James Webb* Space Telescope (JWST; Rigby et al. 2023). This thesis uses these telescopes to make the next step in the investigation of the chemical composition of planet-forming disks.

1.1 Star- and planet-formation

To study planet-forming disks, one needs to understand the different phases of star- and planet-formation (see Shu et al. 1987, McKee & Ostriker 2007, Luhman 2012, and Tobin & Sheehan 2024 for elaborate reviews). The processes occur in molecular clouds, and the phases range from the initial collapse of dense cores to the formation of a disk, and, finally, a planetary system (see Figure 1).

Molecular clouds. Clouds are dense structures in the interstellar medium (ISM) that consist mainly of gas (99% of the mass) and a small fraction of silicate and carbonaceous dust grains (Draine 2003). The process of star-formation happens in the dense molecular clouds ($n_{\text{H}} > 10^3 \text{ cm}^{-3}$) that have low temperatures (Öberg

& Bergin 2021) and, as the name suggests, are mainly made up of molecules (see panel a of Figure 1).

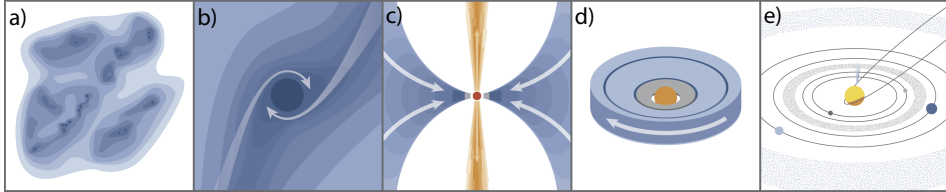


Figure 1.1: Different phases of star- and planet formation. Panel a) displays the molecular cloud with dense cores indicated by the dark blue regions. Panel b) marks the collapse of such a cloud core. Panel c) highlights the protostellar phase, indicating the accretion process, the formation of the disk, and outflowing material. Panel d) displays the planet-forming disks, and Panel e) shows the final stage, the remnant planetary system. This figure has been adopted from Öberg & Bergin (2021).

Pre-stellar cores. The molecular clouds consist of even denser regions ($n_{\text{H}} \sim 10^4$ – 10^5 cm^{-3}), known as pre-stellar cores, with temperatures of $\sim 10 \text{ K}$ (see Bergin & Tafalla 2007 for a review). Once the inward gravitational force of the core overcomes the outward (turbulent, magnetic, and thermal) pressure, the dense core collapses and a young protostar forms at its centre (see panel b of Figure 1).

Protostars. The stage of a young protostar is characterised by accretion, disk formation, and outflows and jets (see panel c of Figure 1). As the young star is still surrounded by material from its parent cloud, also known as the protostellar envelope, it can directly accrete this material to gain more mass. At the same time, a disk is formed around the young protostar to conserve the angular momentum of the system (Cassen & Moosman 1981). This also acts as a funnel, allowing the young protostar to accrete even more material. The protostellar outflows and jets act, on the other hand, as a means of removing angular momentum. This stage lasts for about a million years and ends once the envelope has dispersed.

Planet-forming disks. Once the protostellar envelope is dispersed, the young star, still surrounded by a disk, becomes visible. This stage is known as the planet-forming disk stage (see panel d of Figure 1) and is the topic of this thesis. During this phase, the star is still accreting mass from the disk, but planets are also actively forming (Williams & Cieza 2011). Although the onset of planet formation may already start in the earlier phases (Harsono et al. 2018; Tychoniec et al. 2020), the planets will be actively accreting material from the disk (both dust and gas), in turn shaping the disk’s evolution.

Observationally, young stellar objects are divided into different classes. The most deeply embedded protostars are denoted as Class 0 objects, whereas the less embedded young protostars are denoted as Class I objects. Pre-main sequence stars surrounded by planet-forming disks, the topic of this thesis, are known as Class II objects. A final class, the Class III objects, are young stars which are surrounded by very little dust. These systems mark the final stage between a planet-forming disk and a full planetary system, such as the Solar System. Aside

from the different classes based on the star-formation stage, planet-forming disks themselves are subdivided into categories based on the mass and/or spectral type of their host stars. The lowest mass stars ($M_* \leq 0.2 M_\odot$) are known as Very Low Mass Stars (VLMSs) and are empirically considered to be objects with spectral types equal to or later than M5 (Pinilla 2022), while the heavier stars ($1.5 M_\odot \leq M_* \leq 10 M_\odot$) with spectral types of F, A, and B are known as Herbig stars (Herbig 1960; Brittain et al. 2023). Stars with masses in between these limits and, therefore, have a similar mass as the Sun, are known as T-Tauri stars. The disks around each of these stars are thus known as VLMS disks, T-Tauri disks, and Herbig disks.

Planet-forming disks are, from a chemical point of view, also extremely interesting objects. Since they are a critical stage in between the cold molecular clouds and the emerging planetary systems, understanding the chemical composition and the ongoing chemical processes in disks is of key importance. One question that needs to be answered: is the chemistry in planet-forming disks a result of inheritance of the earlier phases, or has a chemical reset taken place following the formation of the protostar and heating up of the environment and the disk?

Planetary systems. Once the disk is dispersed (after ~ 1 -10 million years; Mamajek 2009), through a combination of accretion and (photoevaporative) winds (Alexander et al. 2006a,b; Ercolano & Pascucci 2017; Pascucci et al. 2023), the final stage of star- and planet-formation is marked by a remnant planetary system (see panel e of Figure 1), consisting of planets and larger planetesimals. These systems can still evolve due to interactions and collisions between the different bodies (see, for example, Wyatt 2018) and the evolution of the star itself.

1.2 Planet-forming disks

1.2.1 Disk constituents

Planet-forming disks consist of dust grains, gaseous molecules, and icy mantles coating the dust grains. Each of these constituents has its own distinct signatures, yet all three are inherently connected through both physical and chemical processes. Figure 1.2 displays a schematic overview of a planet-forming disk, highlighting key processes and observable signatures.

1.2.1.1 Dust and ice

Following their parent clouds, planet-forming disks consist of only a small percentage ($\sim 1\%$ by mass) of solid dust particles. These particles range from small micron-sized particles, which are well coupled to the gas particles, to larger millimetre-sized grains that have settled to the midplane and even larger, kilometre-sized planetesimals. Since the solid particles set the initial composition of rocky terrestrial planets and the cores of giant planets, understanding their chemical makeup is of great importance.

A dust grain itself is mainly composed of silicate material (Colangeli et al. 2003; Henning 2010). Throughout the ISM, the silicates are mainly amorphous

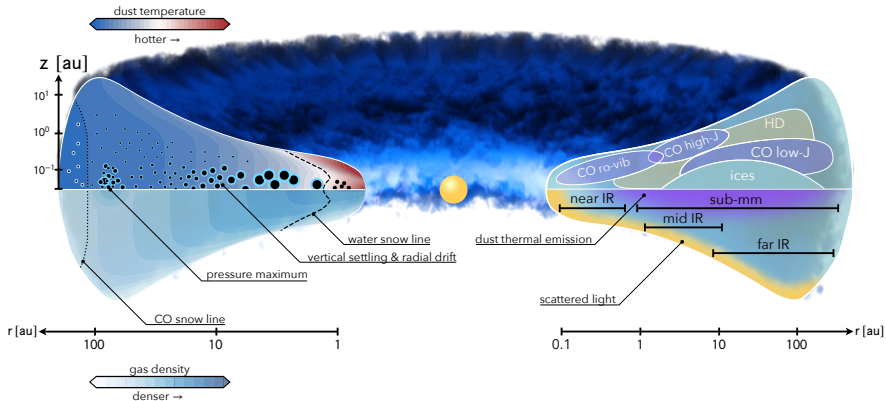


Figure 1.2: Schematic overview of a planet-forming disk. The left side of the image indicates the changing temperature (top) and density (bottom) structures across the disk. The right side of the cartoon displays the expected emitting regions of simple molecules (top) and the emitting wavelength range of different parts of the disk (bottom). This figure has been adopted from Miotello et al. (2023).

(i.e., the atoms are distributed in a disordered, random structure), whereas the presence of crystalline silicates (i.e., the atoms are distributed in an ordered, repeating structure) has been confirmed in disks (see, for example, Waelkens et al. 1996; Bouwman et al. 2001; Juhász et al. 2010). Crystalline silicates yield crucial information on the thermal history of the dust, as their formation may follow from either gas-phase condensation or thermal annealing of the amorphous grains (see, for example, Fabian et al. 2000). Infrared spectroscopy is of crucial importance for inferring the composition of the solid particles. Previous observations of the Infrared Space Observatory (ISO) and the *Spitzer* Space Telescopes (see, also, Malfait et al. 1998; Olofsson et al. 2009; Watson et al. 2009) and, more recently, JWST (Jang et al. 2024), have revealed that disks contain features of olivine ($\text{Mg}_{2x}\text{Fe}_{2-2x}\text{SiO}_4$, where $0 \leq x \leq 1$), pyroxene ($\text{Mg}_x\text{Fe}_{1-x}\text{SiO}_3$, where $0 \leq x \leq 1$), forsterite (Mg_2SiO_4), and enstatite (MgSiO_3).

If a dust grain finds itself beyond the snowline - the boundary region in the disks where a molecule is for 50% in the gas and is for 50% frozen-out on the dust grains - it will be coated by an icy mantle. In reality, the snowline is a 2D structure, often referred to as a snow surface, following the temperature distribution in the disks, which decreases vertically downwards and radially outwards (see Figure 1.2). Since molecules have different binding energies, E_{bind} , molecules with lower binding energies, i.e. apolar ices, such as CO and N_2 ($E_{\text{bind}} \lesssim 1000$ K; Bisschop et al. 2006), will freeze out at lower temperatures compared to those with higher binding energies (Boogert et al. 2015), i.e. polar ices, such as H_2O and CH_3OH ($E_{\text{bind}} \gtrsim 5600$ K; Penteado et al. 2017).

Similar to the dust grains themselves, direct observations of the ices yield information on the thermal history of an astronomical body. Heating can crystallise the ices, but also cause segregation - the separation of mixed ices - which yield unique ice features, such as the double-peaked CO₂ ice-band at 15 μm (Ehrenfreund et al. 1997; Gerakines et al. 1999; Pontoppidan et al. 2008b). Furthermore, infrared spectroscopy plays an important role in directly observing and disentangling the composition of the ices. However, the analysis of ice observations in planet-forming disks is not as straightforward. Due to scattering, a photon may have traversed different regions of a disk with different optical depths and, therefore, the observations need to be modelled in great detail (Sturm et al. 2023c,b,a).

1.2.1.2 Gas

Planet-forming disks are thought to be mainly comprised of gas, with a general mass fraction of $\sim 99\%$. The bulk of the gas is molecular hydrogen (H₂); however, the lack of a permanent dipole makes it hard to observe. With the first rotational excited state having a high upper level energy of $E_{\text{up}} > 500$ K, the emission will be faint in the cold outer regions of the disk. The concepts of energy levels and transitions are explained in Section 1.3.1. Ro-vibrational transitions of H₂ with JWST now yield information on the hot, inner regions of the disks or extended emission that traces, for example, a wind/outflow. Therefore, other molecular species are needed to infer information on the bulk of the gas residing in disks. One such molecule is hydrogen deuteride (HD), of which only a few observations exist and the currently operating telescopes and instruments are not sensitive to its emission. Observations of the *Herschel* Space Observatory have allowed the detection of HD in the disks of TW Hydrae (Bergin et al. 2013), DM Aurigae, and GM Aurigae (McClure et al. 2016). Even though the interpretation of the observations is not without caveats and requires detailed modelling (Trapman et al. 2017; Kama et al. 2020; Calahan et al. 2021), the observations have allowed for constraints on the gas masses of these disks. Observations with the future space-based mission PRobe far-Infrared Mission for Astrophysics (PRIMA; Glenn et al. 2025), or the balloon-mission Planetary Origins and Evolution Multispectral Monochromator (POEMM; Stacey & POEMM Science Team 2025), may lead to more detections of HD in disks.

Carbon monoxide (CO), on the other hand, is a molecule that can be readily observed in disks. With an upper level energy of $E_{\text{up}} \sim 5$ K, the fundamental $J=1-0$ rotational transition is a prime target for observations with, for example, ALMA. However, CO cannot be directly used as a proxy to estimate the total number of H₂ molecules and, therefore, the gas mass. This is mainly due to optical depth effects and uncertainties in the fractional abundance of CO with respect to H₂. Studies have shown that the fractional abundance can decrease from a value of $\sim 10^{-4}$ to a value of 10^{-5} or 10^{-6} (see, for example, Zhang et al. 2021). Unless the fractional abundance is precisely known for a disk, the estimated mass may be off by a (few) order(s) of magnitude. Nonetheless, CO plays a crucial role in the analysis of planet-forming disks. Multiple studies have shown that observations of CO can be used to trace the disk's temperature structure (Law et al. 2021;

Leemker et al. 2022), to investigate its vertical extent (see, for example, Law et al. 2021; Paneque-Carreño et al. 2023), as well may be used to search for kinematical signatures from hidden planetary candidates (Perez et al. 2015; Pinte et al. 2019; Izquierdo et al. 2022).

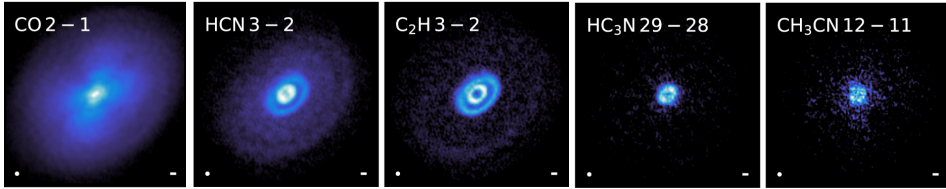


Figure 1.3: Various molecular species observed in the disk of HD 163296 with ALMA. This figure has been adapted from Öberg et al. (2021).

Aside from CO, a wide variety of other molecular species, both simple and complex, have been observed in planet-forming disks. Observations with ALMA have revealed that many molecular species, tracing different chemical processes, can be detected in the colder outer regions (see Figure 1.3). For example, ethynyl radical (C_2H), cyanide radical (CN), and hydrogen cyanide (HCN) have all been related to UV-driven chemistry (Jansen et al. 1995; Sternberg & Dalgarno 1995), while C_2H is also a direct tracer of the important elemental carbon-to-oxygen ratio (C/O-ratio) tracer (Bergin et al. 2016; Kama et al. 2016; Miotello et al. 2019). Similarly, the ratio of carbon monosulfide (CS) and sulfur monoxide (SO) can also be taken as a proxy for the C/O-ratio (Le Gal et al. 2021). SO, together with sulfur dioxide (SO_2) and other species, is also thought to be a tracer of (weak) shocks (see, for example, van Gelder et al. 2021; Booth et al. 2023). The molecular ions of formylium (HCO^+) and diazenylium (N_2H^+) are direct tracers of ionisation in the disk (Kastner et al. 1997; Öberg et al. 2011; Cleeves et al. 2015). HCO^+ can also be a direct tracer of X-ray flares from the host star (Waggoner & Cleeves 2022). N_2H^+ , on the other hand, can directly trace the freeze-out and chemical transformation of CO (Qi et al. 2013; van 't Hoff et al. 2017), since its gas-phase formation is most efficient in the regions of the disk where CO is depleted and, therefore, may play a crucial role in determining the disk's gas mass (Trapman et al. 2022b). Deuterated formylium (DCO^+) and formaldehyde (H_2CO) are thought to trace cold chemistry (Öberg et al. 2010), since DCO^+ - similar to N_2H^+ - forms most efficiently in the gas around the CO snowline. H_2CO , on the other hand, can form efficiently in the gas (Fockenberg & Preses 2002; Atkinson et al. 2006), but it can also form efficiently on the icy dust grains through the hydrogenation of CO (Watanabe & Kouchi 2002; Fuchs et al. 2009; Santos et al. 2022). Upon further hydrogenation of H_2CO on the grains, methanol (CH_3OH), the simplest complex organic molecule (COM, a molecule with at least six atoms of which at least one is carbon; Herbst & van Dishoeck 2009) may form. Thus far, CH_3OH and other COMs, such as methyl formate (CH_3OCHO) and dimethyl ether (CH_3OCH_3), have mainly been found in the disks around young Herbig stars (van der Marel et al. 2021a; Brunken et al. 2022; Yamato et al. 2024a;

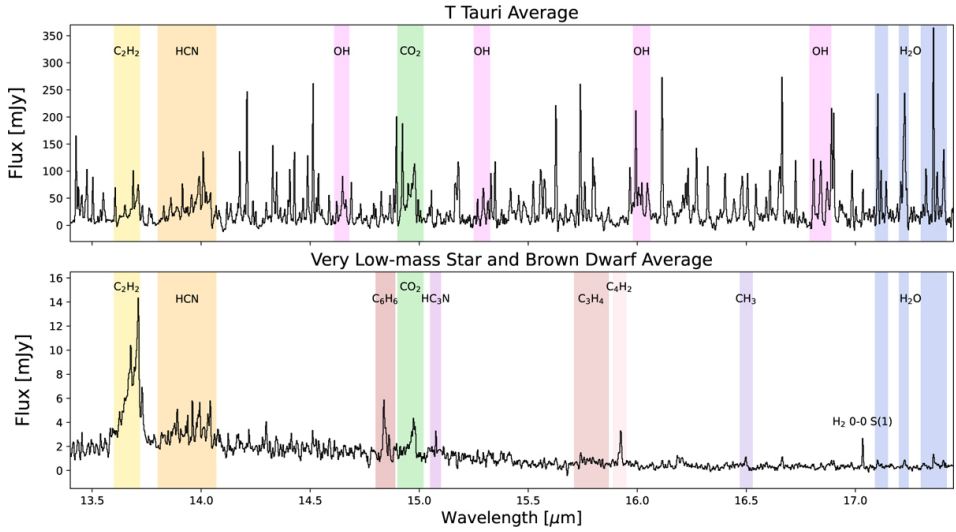


Figure 1.4: Averaged mid-infrared spectrum of a sample of T-Tauri disks (top) and VLMS disks (bottom). Detected molecular species are highlighted by the coloured areas. This figure has been adopted from Grant et al. (2025).

Booth et al. 2024a, 2025). As these disks are often too warm for CO to be directly frozen out, in situ formation of species like CH_3OH is unlikely, and the molecules are thought to be inherited from the earlier phases, as also evidenced by their association with icy dust traps.

Observations of *Spitzer* (Pontoppidan et al. 2010; Carr & Najita 2011) and, more recently, JWST reveal crucial information on the chemical composition of the hot, inner regions of planet-forming disks. In particular, the Medium Resolution Spectrometer (MRS; Wells et al. 2015) mode of the Mid-InfraRed Instrument (MIRI; Rieke et al. 2015) now provides the unique opportunity to study those inner regions with high sensitivity and resolution. The data reveal that the spectra of many T-Tauri disks are dominated by species like water (H_2O), hydroxyl radical (OH), carbon dioxide (CO_2), HCN, and acetylene (C_2H_2 ; see, for example, Grant et al. 2023b; Gasman et al. 2023; Temmink et al. 2024b,a, 2025b). This is in stark contrast to their lower-mass counterparts, as the spectra of VLMS disks are dominated by large hydrocarbons (Tabone et al. 2023; Arabhavi et al. 2024), such as ethylene (C_2H_4), ethane (C_2H_6), and even benzene (C_6H_6). The large contrast is displayed in Figure 1.4, where the average JWST spectra of a sample of T-Tauri disks and VLMS disks are presented (Grant et al. 2025).

1.2.2 Disk evolution

Planet-forming disks are not static objects, but they evolve. Crucial for the evolution of the disk is the distribution and conservation of angular momentum. Two leading hypotheses allow for the redistribution of angular momentum: viscous evolution (Shakura & Sunyaev 1973; Lynden-Bell & Pringle 1974) and magneto-

hydrodynamic (MHD) disk winds (Blandford & Payne 1982; Lesur et al. 2013). While both processes may be operating at the same time, it is thought that viscous evolution dominates during the early evolution of the disks, while MHD winds take over at a later stage (Trapman et al. 2022a). However, the main driver behind the evolution of planet-forming disks is still heavily debated (see, for example, Manara et al. 2023 and Pascucci et al. 2023). Other than the redistribution of angular momentum, processes such as accretion and accretion outbursts, planet formation and radial drift, and (photoevaporative) disk winds also play roles in the evolution of disks.

1.2.2.1 Viscous evolution

The viscous evolution model is based on the notion that the rotation velocity of a disk is not constant. Instead, according to Kepler’s law, it decreases with the square of the radial distance with respect to the host star. Therefore, the inner regions of the disk rotate faster than the outer regions. If one considers two adjacent rings of gas, the one closer to the host star will rotate faster, and this creates a shearing force between the two bands. This friction causes angular momentum transfer between the two bands, where the inner band loses angular momentum and slows down, while the outer one gains angular momentum and speeds up. As a result, the inner band will move closer to the host star and may be accreted, while the outer band moves radially outward, effectively spreading the disk out over a larger distance (Shakura & Sunyaev 1973; Lynden-Bell & Pringle 1974; Pringle 1981).

The efficiency of this viscous spreading is set by the viscosity of the disk itself, which can be parametrised as (Shakura & Sunyaev 1973),

$$\nu = \alpha c_s H. \quad (1.1)$$

Here, c_s is the sound speed, while H denotes the scale height of the disk. α is the dimensionless viscosity parameter whose value is heavily debated. While it was generally thought that a high viscosity value of $\alpha=10^{-2}$ is needed to explain the observations (Hartmann et al. 1998; Armitage 2015), more recent works suggest that a lower value of $\alpha \sim 10^{-3}$ - 10^{-4} is more consistent with observations (see, for example, Flaherty et al. 2015; Trapman et al. 2020).

1.2.2.2 MHD disk wind

While the viscous evolution model suggests that the disk’s radius increases with time, the MHD disk wind model suggests, instead, that the disk shrinks with time. The model relies on gas in the inner regions to be ionised, such that the gas, together with a large amount of angular momentum, can be removed through a disk wind following interactions with the magnetic field of the disk (see Lesur et al. 2023 for a recent review). Upon removal of the angular momentum, various modelling works have shown that this can yield efficient accretion onto the host star (Béthune et al. 2017; Zhu & Stone 2018; Tabone et al. 2022).

1.2.2.3 Accretion, accretion outbursts, and (late) infall

Both the viscous disk model and the MHD disk wind model show that accretion of disk material by the host star is inherent to the evolution of a disk. The accretion rate is not constant over the disk lifetime and can be paired with short-lived accretion (out)bursts that last a few hours or extreme events that last up to decades, but are much rarer (see Fischer et al. 2023 for a recent review). Both events can change the chemical composition of the disk over time, with the extreme events likely having a longer-lasting effect.

The short-lived events can be subdivided into three categories (Fischer et al. 2023): Routine Variability, Burst, and Outburst. During the first two events, the brightness of the star increases by a few magnitudes (up to a factor 10) and these last for a few hours to a week, whereas during an Outburst the brightness increases by several magnitudes (factors of >10) and lasts from months up to decades. As the brightness increases, the disk heats up, and this directly impacts the chemistry. As a result, snowlines are pushed further outwards, and molecules may sublimate - undergo a phase transition from solid to gas - from the icy grains. Smith et al. (2025) showed that the outbursting history of the system of EX Lup (Aspin et al. 2010) has pushed the H_2O snowline further out and increased the abundance of H_2O in the inner regions of the disk near the snowline. It is further expected that even Routine Variability can have this effect, where the snowlines are regularly pushed further out, and the emission can (temporarily) be enhanced due to sublimation.

A more extreme case is the system of V883 Ori, which underwent an extreme outbursting event that increased its luminosity to approximately $\sim 1000 L_{\odot}$ (Leemker et al. 2021). This outburst has revealed the emission of H_2O and its isotopologues (HDO and D_2O) in the cold outer regions (~ 80 au) of the disk (Tobin et al. 2023; Leemker et al. 2025). The observations show that the isotope ratios, $\text{HDO}/\text{H}_2\text{O}$ and $\text{D}_2\text{O}/\text{H}_2\text{O}$, are consistent with those found for the earlier protostellar phases and in comets of the Solar System. This suggests that the H_2O -ice in the cold outer disks is inherited from the earlier phases and that disks, therefore, play a crucial role in linking the chemical content of a planetary system with that of the ISM (Visser et al. 2009; Tobin et al. 2023). While H_2O plays a crucial role in linking the composition of ices across the different phases, the gas-phase reservoirs of other species, such as H_2CO , CH_3OH , and other COMs, are also enhanced by sublimation following an accretion outburst (see, for example, van 't Hoff et al. 2018; Lee et al. 2019; Yamato et al. 2024b; Calahan et al. 2024).

While accretion is often considered with respect to the host star, the disk itself may still accrete material from the immediate environment or the remnant envelope. In particular, streamers or late infalling material may replenish the disk with fresh material that can have a (local) effect on the chemical composition or (weakly) shock the disk, liberating ices from the grains (see, for example, Garufi et al. 2022). Existing observations reveal large-scale structures, extending up to thousands of au, in the disks of, for example, GM Aur (Huang et al. 2021) and SU Aur (Akiyama et al. 2019), in which the infalling material of SU Aur can even be traced by small dust grains (see Figure 1.5; Ginski et al. 2021).

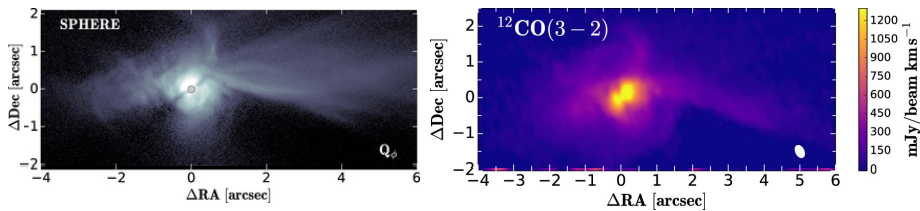


Figure 1.5: Late infalling material in the disk of SU Aur. The left image shows the extended visible in the small dust grains, while the right image displays those seen in the CO gas emission. This figure has been adapted from Ginski et al. (2021).

1.2.2.4 (Photoevaporative) disk winds

As opposed to accretion processes, where the disk gains mass, it may also lose mass through (photoevaporative) disk winds. One type of disk wind has previously been discussed, the MHD disk wind (see Section 1.2.2.2). The other type of wind that drastically changes the evolution of the disk in its later and may even lead to its dispersal is a photoevaporative (PE) wind (see Pascucci et al. 2023 for a recent review). Opposed to MHD winds, PE winds are thermally driven by EUV, FUV or X-ray radiation and do not affect the angular momentum transport within disks. A PE wind consists of gas that is heated up enough by the radiation such that its thermal energy exceeds the gravitational field of the host star.

Slow disk winds launched from the inner regions of disks, either driven by MHD or photoevaporation, can also be observed. Such winds have been proposed to explain the single-peaked line profiles of ro-vibrational CO observations (see, for example, Bast et al. 2011; Pontoppidan et al. 2011; Brown et al. 2013; Banzatti et al. 2022), although the precise origins of these winds are still under discussion. JWST observations of extended H_2 now also reveal the spatially resolved emission of disk winds (Arulanantham et al. 2024; Schwarz et al. 2025), also in the earlier Class I phase (e.g., Tychoniec et al. 2024).

1.2.2.5 Planet formation and radial drift

Even though planet formation is expected to already start in the earlier stages of star formation (Harsono et al. 2018; Tychoniec et al. 2020), the detection of protoplanets in the systems of PDS 70 (Keppler et al. 2018; Müller et al. 2018; Haffert et al. 2019) and WISPIT 2 (van Capelleveen et al. 2025) reveal that they directly impact the evolution of disks.

Planet formation follows from the evolution and coagulation of the dust grains (see Drażkowska et al. 2023 for a recent review). The evolution or growth of dust grains is the result of direct interactions with the gas particles. Because small (micron-sized) dust grains are coupled to the gas, they are located throughout the entire disk. Collisions between and efficient sticking of individual dust grains allow them to grow to millimetre-sizes (see, for example, Blum & Wurm 2008; Brauer et al. 2008; Birnstiel et al. 2010). Upon growing in size, the dust grains decouple from the gas. Gravitational effects cause the dust grains to settle to the

midplane, but the growth itself may be impeded as bouncing and fragmentation effects become important (Dubrulle et al. 1995; Duchêne et al. 2003; Villenave et al. 2020). An additional effect that impedes the growth of dust grains is radial drift. As the dust grains are decoupled from the gas, they move on Keplerian orbits, whereas the gas particles orbit with sub-Keplerian velocities. This velocity difference causes the dust grains to feel an aerodynamic drag force that causes the grains to lose angular momentum and move radially inward towards the host star.

Due to the radial decrease of temperature and density (see Figure 1.2), the disk has a negative pressure gradient (Drażkowska et al. 2023). With particles tending to move rapidly towards the host star, so-called pressure traps (localised pressure maxima; Pinilla et al. 2012b,a) may help overcome the growth barrier imposed by radial drift. Such pressure traps may be caused by embedded (planetary and (sub)stellar) companions in the disk (Pinilla et al. 2012a), hydrodynamical processes (such as the Rossby wave instability (RWI) and the vertical shear instability (VSI); Urpin & Brandenburg 1998; Lovelace et al. 1999; Li et al. 2000) and gravitational instability (Rice et al. 2004), and magnetohydrodynamic processes (such as zonal flows and dead zones; Gammie 1996; Hawley 2001; Johansen et al. 2009). Bae et al. (2023) contains a recent review on all these processes and their inner workings, which are beyond the scope of this thesis. As these pressure traps effectively create a pile-up of dust particles, the dust-to-gas ratio will locally increase, and this yields a favourable location of planetesimal formation, for example, through the streaming instability (Youdin & Goodman 2005; Drażkowska et al. 2016).

Aside from dust traps, snowlines - and, in particular, the H_2O snowline - may also yield favourable conditions for planetesimal formation. A pile-up of material near the snowline can also be caused by the cold-finger effect (Cuzzi & Zahnle 2004), where gaseous H_2O molecules inside the snowline are diffused radially outwards beyond the snowline and freeze out on the dust grains (Stevenson & Lunine 1988).

As soon as planetesimals have formed, the formation of planets may continue through one of two paradigms: planetesimal accretion or pebble accretion, see Drażkowska et al. (2023) for a recent review on both scenarios. Planetesimal accretion relies on the assumption that all bodies are planetesimals (sizes of $\gtrsim 10$ kilometre) and that only the gravitational interactions between these bodies matter (Wetherill & Stewart 1989; Lissauer 1993; Kokubo & Ida 1996). As opposed to planetesimal accretion, pebble accretion is the addition of small dust grains to an already present larger body or planetary embryo (Johansen & Lacerda 2010; Ormel & Klahr 2010; Johansen & Lambrechts 2017). Additional differences between the two paradigms are their effective radial distances. Whereas planetesimal accretion only works in the immediate environment of the planetesimal, pebble accretion works over a larger area following the inward drift of the smaller pebbles (Ormel & Klahr 2010; Lambrechts & Johansen 2012). Furthermore, the efficiency of pebble drift depends on the mass of the planetary embryo and requires a large pebble reservoir (Guillot et al. 2014). As soon as the embryo hits the so-called pebble isolation mass - the mass where an embryo can open a gap in the disk and, as a result, a pressure maximum is generated exterior to the gap - pebble accretion

is halted (Lambrechts et al. 2014; Bitsch et al. 2018; Ataiee et al. 2018). The efficiency of planetesimal accretion, however, depends on the density of planetesimals in the region, and the efficiency of planetesimal accretion drops off quickly with the mass of the forming planet (see, for example, Kokubo & Ida 2002).

Once the planetary embryo is massive enough, either through planetesimal or pebble accretion, it may accrete gas from the surrounding disk, forming an atmosphere (or envelope) (Ikoma & Kobayashi 2025). With increasing mass of the embryo, the efficiency of gas accretion grows as well. If the mass of the embryo exceeds the critical mass - the mass where the total solid mass and envelope mass become equal - gas accretion continues through a runaway process and a gas giant planet forms (see, for example, Pollack et al. 1996). If the embryo never meets the critical mass, the resulting planets are more terrestrial-like and are dominated by solid material with a tiny atmosphere.

1.2.3 Disk observations

Due to both the dust constituents (dust and gas) and the changing thermal and density structure, observations at different wavelengths are sensitive to different components and regions of the disk (see the right side of Figure 1.2). Figure 1.6 shows an example of different types of observations for the disk of TW Hya (Andrews 2020), displaying the variations in morphology and radial extent of the small micrometre-sized dust grains, the millimetre-sized dust grains, and the CO gas emission. Observations spanning the near-infrared, mid-infrared, far-infrared, and (sub)-millimetre wavelengths are of particular interest for this thesis.

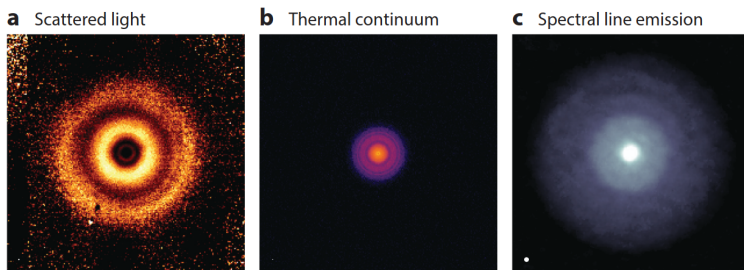


Figure 1.6: Different faces of the disk around TW Hya. The left panel shows the scattered light from the micrometre-sized dust grains, while the middle panel shows the thermal continuum emitted by the millimetre-sized dust grains. The right-most panel displays the extent of the gas disk. This figure has been adopted from Andrews (2020).

1.2.3.1 Near-infrared

Observations at wavelengths probing the near-infrared (NIR, $\lambda \sim 1\text{-}2.5 \mu\text{m}$) regime trace the inner-most regions of planet-forming disks ($\lesssim 1$ au). Furthermore, the NIR wavelengths are sensitive to the light scattered by the small dust grains at the disk's surface layer (see left panel of Figure 1.6) and, therefore, also provide

insights into the distribution of these small dust grains throughout the disk. While scattered light observations are not the focus of this thesis (see Benisty et al. 2023 for a recent review on the observations and techniques), they reveal key information on a disk’s structure and configuration, which are highlighted in Section 1.2.4.

1.2.3.2 Mid-infrared

The IR wavelength regime is subdivided into different bands, of which the *L*- ($\lambda \sim 3.5 \mu\text{m}$; Glass 1999) and *M*-band ($\lambda \sim 4.5 \mu\text{m}$; Glass 1999) are most interesting for tracing the chemical conditions in a disk. With high spectral resolution, spectroscopic instruments on ground-based observatories like the CRyogenic high-resolution InfraRed Echelle Spectrograph (CRIRES, $R \sim 80,000$; Kaeufl et al. 2004; Dorn et al. 2014, 2023) on the Very Large Telescope (VLT), iSHELL ($R \sim 80,000$; Rayner et al. 2016, 2022) on NASA’s Infrared Telescope Facility (NASA-IRTF), and NIRSPEC on Keck II ($R \sim 25,000$; McLean et al. 1998), yield observations of ro-vibrational transitions of molecular species, such as CO, OH, H₂O, CO₂, HCN, methane (CH₄), and, C₂H₂ (see, for example, Mandell et al. 2012). In the not-too-distant future, the Mid-infrared ELT Imager and Spectrograph (METIS) on the Extremely Large Telescope (ELT) will yield additional observations of these regions and molecules with unprecedented sensitivity and resolution ($R \sim 100,000$; Brandl et al. 2021).

While *L*- and *M*-band observations can be carried out from the ground, larger wavelengths need to be observed from space due to the Earth’s atmosphere being opaque, mainly due to H₂O vapour, at these wavelengths. Space-based MIR observations have a rich history due to the wealth of information that was gathered with the ISO (1995-1998; Kessler et al. 1996) and the *Spitzer* Space Telescope (2003-2020; Werner et al. 2004). Recently, mid-infrared observations and, in particular, mid-infrared spectroscopy have been reinvigorated with the launch of JWST. With improved sensitivity, spatial resolution and spectral resolution ($R > 1500-3000$ compared to *Spitzer*’s $R \sim 90$; Houck et al. 2004), JWST’s MIRI instrument is crucial in revealing the chemical composition of the inner (≤ 10 au) of planet-forming disks (see Figure 1.4). Chapters 2, 3, and 4 of this thesis make use of JWST-MIRI observations as part of the Guaranteed Time Observations (GTO) Miri Mid-Infrared Disk Survey (MINDS, PI: T. Henning; Kamp et al. 2023; Henning et al. 2024) collaboration. As discussed in Section 1.2.1.2, these observations cover transitions of H₂O, CO₂, HCN, C₂H₂, and more. Additionally, the Near-InfraRed Spectrographa (NIRSpec; Jakobsen et al. 2022) instrument onboard JWST can be used to cover molecular transitions in the 2.5-5 μm wavelength range, although many nearby planet-forming disks exceed its brightness limit and saturate the detector.

1.2.3.3 Far-infrared and (sub-)millimetre

At even longer wavelengths, instruments observing in the far-infrared (FIR) and (sub-)millimetre regimes probe the outer regions of planet-forming disks ($\gtrsim 10$ au). Since the decommissioning of the *Herschel* Space Telescope (2009-2013; Pilbratt et al. 2010), now over a decade ago, no telescope or instrument probing the FIR

wavelength regime exists. However, this may change with the proposed observatories of PRIMA and POEMM.

While there is a lack of FIR instruments, (sub-)millimetre astronomy is thriving. Not only due to the high sensitivity and resolution of ALMA, but also that of the Northern Extended Millimeter Array (NOEMA) and the Submillimeter Array (SMA; Ho et al. 2004). The power of (sub-)millimetre astronomy can be found in the use of interferometric techniques offering much higher spatial resolution. By combining the observations of multiple individual antennas, the dust and gas in planet-forming disks can be spatially resolved, yielding unique insights into their distributions and structures. ALMA has a total of 66 antennas (50 12-metre in an extended configuration and 4 12-metre and 12 7-metre antennas in a compact configuration) that form effective telescope diameters from 150 metres to a total of 16 kilometres. As the ALMA antennas have different receiver bands, the maximum achievable spatial resolution depends on the observing wavelength and the maximum baseline between the different antennas. In the most extended configuration in ALMA Band 10 (0.3-0.4 millimetre or frequencies of 787-950 GHz), ALMA can reach spatial resolution down to 5 milliarcseconds (0.005"). For a planet-forming disk at 140 parsecs (see, for example, Kenyon et al. 1994), the approximate distance to the Taurus star-forming region, this allows details to be discernible at scales of 0.7 au, corresponding to the orbit of Venus. However, at these short wavelengths (or high frequencies), the Earth's atmosphere nearly becomes opaque to (sub-)millimetre radiation and, therefore, low atmospheric water vapour levels are required for successful observations. Aside from high spatial resolution capabilities, ALMA also allows for high spectral resolution observations. With a maximum resolution of 0.01 km s⁻¹ (or 10 m s⁻¹), the dynamics of the gas can be studied in great detail.

1.2.4 Disk substructures

The first high spatial resolution image of a planet-forming disk taken by ALMA revolutionised our vision of these systems. The image revealed that the dust disk around the young star HL Tau was not smooth but consisted of multiple rings and gaps (ALMA Partnership et al. 2015). With ALMA, many of these substructures have been found, ranging from these gapped disks to disks with large cavities and even asymmetric features (van der Marel et al. 2013; Casassus et al. 2013). While substructures in the millimetre dust continuum generally gain the most attention, similar structures can also be found in the scattered light and gas emission (see Andrews 2020; Bae et al. 2023; Benisty et al. 2023 for recent reviews). Crucially, a disk can contain multiple types of substructures, and the structures do not have to match between the different types of observations (i.e., a disk can physically look different in the millimetre continuum emission and scattered light; see, for example, Figure 1.6).

1.2.4.1 Rings and gaps

The type of substructure that is most commonly found is that of rings and gaps, similar to the disk of HL Tau. The system of HL Tau is rather unique, given its high multiplicity of rings (a total of 7 have been identified; ALMA Partnership et al. 2015). While multi-ring systems are not uncommon, a large sample of disks only seems to contain a single ring. It must be noted, however, that the majority of disks have not been observed with the highest spatial resolution and, therefore, rings and other substructures may currently be hidden from our view.

One of the leading theories for the formation of (multiple) rings and gaps are (planetary) companions embedded in the disks. In this scenario, the companion directly carves a gap in the disk (i.e., accreting all the dust grains on their orbit), which yields a pressure bump at the outer boundary of the gap (Pinilla et al. 2012b,a). The properties of the gap (that is, its width and depth) depend on the mass of the companion, in addition to the viscosity of the disk and temperature (see van der Marel & Pinilla 2023 for a recent view). It is, however, not well understood whether the number of observed gaps directly translates to the number of (planetary) companions in the system. It has been shown, for example, that a companion can open multiple gaps due to migration (Bae et al. 2017; Dong et al. 2017; Wafflard-Fernandez & Baruteau 2020).

1.2.4.2 Rings and cavities

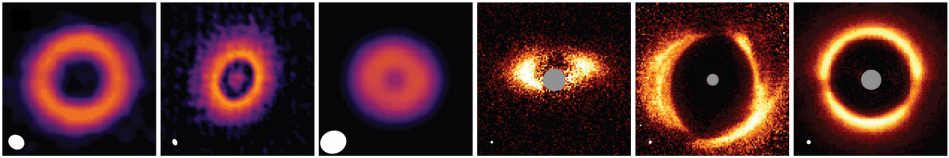


Figure 1.7: Disks with large inner cavities. The first three images are of the millimetre dust continuum, whereas the latter three are taken in scattered light. From left to right: RXJ1604.3-2130, DM Tau, DoAr 44, Oph-IRS 48, HD 142527, and RXJ1604.3-2130. This figure has been adapted from Andrews (2020).

Aside from multiple rings and gaps, depleted cavities are also commonly observed substructures (see Figure 1.7). Such systems, which lack strong dust emission from their inner regions, are known as so-called transition disks (Espaillat et al. 2014; van der Marel 2023) and were originally identified through their spectral energy distributions (SEDs; Strom et al. 1989; Skrutskie et al. 1990). Their SEDs lack an excess of NIR and MIR emission, which are otherwise an indication of the presence dust grains in the inner region. Similar to the origins of rings and gaps, the most popular theory for the depleted cavities is (planetary) companions. A famous example is the PDS 70 system, where two known planetary companions can be found in the cavity (Keppler et al. 2018; Müller et al. 2018; Haffert et al. 2019). Other than companions, photoevaporative winds (Hollenbach et al. 1994; Alexander et al. 2006a,b; Espaillat et al. 2014) and the edges of dead zones may also yield large cavities (see, for example, Regály et al. 2012).

While these cavities are devoid of dust grains, gas may still be present. Gas inside the cavity was first indirectly inferred through signatures of accretion (Najita et al. 2007). In addition, detailed analysis of the CO ro-vibrational transitions showed that the cavity in the gas could be smaller than the one in the dust (Pontoppidan et al. 2008a; Brittain et al. 2009; Salyk et al. 2009). Spatially resolved images with ALMA now directly reveal the presence of gas inside the cavities (see, for example, Bruderer et al. 2014; Pérez et al. 2014; van der Marel et al. 2016b). Whether gas can be found in the cavity or not depends on its formation. If the cavity is due to a photoevaporative wind, it is expected that the cavity is fully depleted of both dust and gas. Similarly, a massive companion, such as a gas giant planet, carving a gap in the dust is expected to also carve a gap in the gas, the depth of which is again dependent on the companion’s mass and the disk’s viscosity. A dead zone, on the other hand, is not expected to result in a change in the gas surface density (van der Marel et al. 2016b).

1.2.4.3 Asymmetries

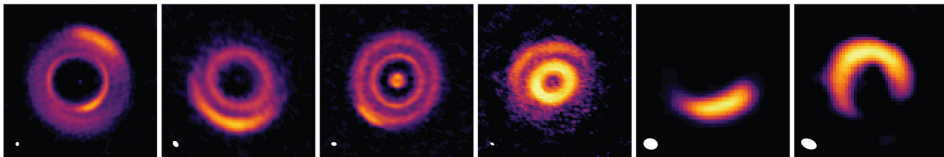


Figure 1.8: Disks with observed asymmetric features in the millimetre dust continuum. From left to right: MWC 758, HD 135344B, HD 143006, V1247 Ori, Oph-IRS 48, HD 142527. This figure has been adapted from Andrews (2020).

Asymmetric features, also described as arcs or crescents, are much rarer compared to rings, cavities and gaps (Andrews 2020; Bae et al. 2023). They can, however, be found in a variety of scenarios. The most extreme of which is a partial ring, an arc-like structure, around a cavity. Additional asymmetries are arc-like structures in ringed systems (Marino et al. 2015a; van der Marel et al. 2016a; Kraus et al. 2017) or arc-like structures inside a cavity (Isella et al. 2018; Long et al. 2022). Figure 1.8 provides a few examples of planet-forming disks with asymmetries.

One of the leading theories for asymmetric features is vortices. Various hydrodynamic instabilities can lead to vortices, which include the RWI. In particular, an anticyclonic vortex is thought to have a pressure maximum at its centre (Lovelace & Romanova 2014), which effectively can trap the dust in these arc-like features. An anticyclonic vortex can decay after many orbits (Godon & Livio 1999; Rometsch et al. 2021), (re-)distributing the material in a ring-like morphology. The RWI can be generated by a (planetary) companion, at the inner edge of a dead zone, or by late infalling material (see Bae et al. 2023 for a recent review). The last scenario has recently gotten more observational traction with the suggestion that late infalling material may be the cause of the observed asymmetries in the disks of HD 34700A (Stadler et al. 2026) and HD 142527 (see Chapter 7 of this thesis).

The gas emission of an asymmetric disk is also of great interest. In particular, azimuthally asymmetric disks are thought to be a perfect laboratory for studying the direct connection between the dust and gas composition. The case the Oph-IRS 48 disk, the most asymmetric disk known to date (van der Marel et al. 2013), is a great example. The molecular emission of Oph-IRS 48 (second to last disk in Figure 1.8), which ranges from simple molecules (such as NO, SO and SO₂) to complex molecules (such as CH₃OH and CH₃OCH₃), is found to be more or less co-spatial with the millimetre continuum emission (Booth et al. 2021a, 2024b; van der Marel et al. 2021a; Brunken et al. 2022; Leemker et al. 2023). This suggests strongly that the dust trap is an ice trap and the molecular emission becomes visible due to sublimation of the ices following efficient radial and vertical transport of the icy dust grains to elevated layers near the inner edge of the dust trap. However, interpreting the data became more complex by the realisation that processes like photodissociation can efficiently destroy the molecules in these layers. Furthermore, the photodissociation products may actually be used in the gas-phase formation of different species, yielding distinct reservoirs of molecules that either sublimate from the grains or were formed directly in the gas (Temmink et al. 2025a; see Chapter 6 of this thesis).

Another example is the asymmetric disk of HD 142527 (Fujiwara et al. 2006; Ohashi 2008; Casassus et al. 2013; the last disk in Figure 1.8). As opposed to Oph-IRS 48, the gas emission in HD 142527 is not co-spatial with the dust trap. Instead, the emission peaks on the opposite side of the disk (van der Plas et al. 2014; Temmink et al. 2023). The discovery of spiral arms in the gas emission of CN, C₂H, and H₂CO, suggests that the molecular is unrelated to the dust, but are, instead, thought to be the result of late-infalling material (see Chapter 7 in this thesis).

1.2.4.4 Spiral arms

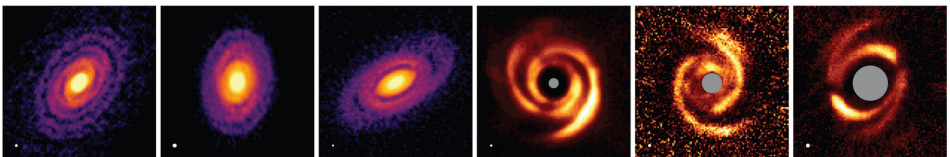


Figure 1.9: Disks with observed spiral arms. The first three images are of the millimetre dust continuum, whereas the latter three are taken in scattered light. From left to right: IM Lup, WaOph 6, Elias 27, HD 135344B, MWC 758, and HD 100453. This figure has been adapted from Andrews (2020).

Spiral arms are predominantly observed in the scattered light, in contrast to other substructures (see, Benisty et al. 2023, for a recent view). Only a handful of disks have confirmed detection of spiral arms in the millimetre continuum emission (see, for example, Huang et al. 2018a), but they are more common in the CO gas emission (Christiaens et al. 2014; Teague et al. 2019; Wölfer et al. 2023). Various explanations exist for the origin of spiral arms in planet-forming disks.

These range from density perturbation caused by embedded (planetary) companions (Kley 1999) or gravitational instability (Rice et al. 2004), to interactions with the surrounding material, such as a remnant cloud envelope or late infalling material (Lesur et al. 2015; Kuznetsova et al. 2022). Additionally, interactions (or fly-bys) between the stars of a wide-separation binary (Mayama et al. 2020; Ménard et al. 2020) and shadows (Montesinos et al. 2016; Zhang et al. 2025) may also launch spiral-like features in a disk.

Aside from seeing spiral arms in the CO gas emission, the role of spirals in setting the observable chemistry is not well known. One way spirals can affect the chemistry is through (weak) shocks. The detection of SO, a well known shock tracer, has been attributed to shocks induced by spirals arms in the disks of AB Aur (Speedie et al. 2025), CQ Tau, and MWC 758 (Zagaria et al. 2025). Recently, spiral-like features were seen in the emission of H₂CO, C₂H, and CN (see Chapter 7 of this thesis). These features are thought to be the result of infalling material that replenish the disk with fresh material and, therefore, allows for the gas-phase formation of these molecules.

1.2.4.5 Shadows and misalignments

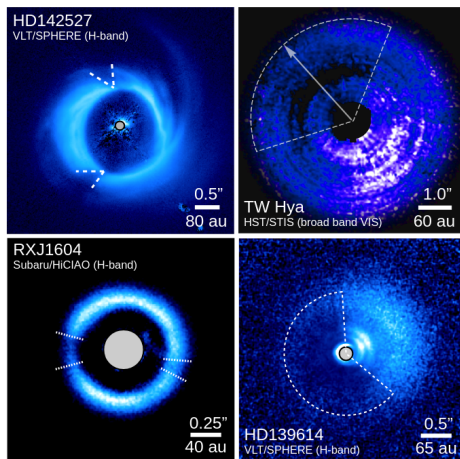


Figure 1.10: Shadows in the scattered light images of four disks. The left two disks have shadows confined to small azimuthal increments, whereas the right two disks show broad shadows. This figure has been adapted from Benisty et al. (2023).

Shadows are another feature that is predominantly observed in the scattered light. Shadows are dips in a disk’s brightness profile at confined azimuthal angles (see Figure 1.10; Benisty et al. 2023). The observed shadows are divided into two categories: the first category contains disks with narrow shadows spanning small azimuthal increments, while the second category consists of disks with shadows spanning a wide azimuthal increment (up to half the disk’s azimuthal extent).

The appearance of shadows is often linked with a misaligned inner disk, that

is, the inner disk is inclined with respect to the planet of the outer disk. The misalignment causes part of the starlight to be blocked, effectively casting a shadow at the outer regions (Marino et al. 2015b). A larger misalignment is thought to yield the narrow shadows, while a smaller misalignment will yield the broader shadows. The misalignment is often considered to be the result of a dynamical perturbation by a close-in companion. For a handful of disks, this theory of a misaligned inner disk has been confirmed to be the cause of the shadows (Benisty et al. 2018; Bohn et al. 2022).

Other than dynamical perturbations, shadows may also be caused by interactions with late infalling material (SU Aur; Ginski et al. 2021) or material surrounding a binary system, such as is the case for GG Tau A (Krist et al. 2002; Itoh et al. 2014; Keppler et al. 2020). Additional explanations for shadows in disks without misalignments can be found in irregular or lifted dust clumps either through magnetospheric accretion or disk winds (Pinilla et al. 2018; Rich et al. 2019).

1.2.4.6 Substructures and radial drift

The observed substructures, especially those in the millimetre dust continuum, are thought to be mainly the result of pressure traps (see Section 1.2.2.5). These structures may, therefore, prevent radial drift and facilitate the formation of planetesimals and larger bodies (see, Birnstiel 2024, for a recent review). If radial drift is impeded by substructures, not only may this facilitate planet formation, but it may also impact the observable chemistry. Radial drift, after all, will bring ices from the outer regions into the inner parts of disks where they may sublimate and enrich the gas.

With many important snowlines (i.e., those of H_2O and CO_2) being located in the inner few au of the disks, close to the host star, the importance of radial drift and substructures has regained attention with the launch of JWST. In particular, Banzatti et al. (2020) proposed a simple scenario where the H_2O reservoir in the inner regions of small disks ($R_{\text{dust}} \leq 60$ au) is enhanced due to efficient radial drift and subsequent sublimation of the H_2O -ice, whereas that in larger disks ($R_{\text{dust}} > 60$ au) with structures is not enhanced as the drifting grains are trapped in the structures. For disks with large cavities, the H_2O reservoir was expected to be depleted. Recent works have now shown that this scenario is much more complex, as disks with large cavities can have H_2O in their inner regions (Perotti et al. 2023; Schwarz et al. 2024; Mallaney et al. 2026) and not every small disk is enhanced in the H_2O reservoir (Temmink et al. 2025b; see Chapter 4 of this thesis).

Models that can test the efficiency of gaps in stopping the drift, for example, by including gaps with different depths and widths, further complicate this story. It has been shown that the effect of H_2O -enhancement in the inner regions is only temporary, up to a few million years, when gaps are considered (Kalyaan et al. 2021, 2023). The enhancement can be prolonged if small grains are considered or if the gaps are less deep and, therefore, more susceptible (or leaky) to grains passing through (Pinilla et al. 2024; Mah et al. 2024). Additionally, the radial location of

the gap matters a lot (Kalyaan et al. 2023; Sellek et al. 2025). If a gap is located closer to the host star, the influence of a gap halting the drift will be greater than if the gap were located further out. Finally, models that study the effect of dust optical depth have also shown that the enhancement of the gas reservoirs following radial may not be visible at all, as drifting particles also enhance the dust density in the inner regions (Sellek et al. 2025; Houge et al. 2025).

The relation between substructures, radial drift, and the molecular composition, is, therefore, rather complex. From an observational point of view, many aspects require further study. For example, the models have shown that gaps located at closer radial distances are more important for impeding drift. Detecting structures at these distances requires high spatial resolution observations with, for example, ALMA, and special super-resolution techniques to hunt for substructures at smaller scales than can be resolved directly from the images (see, for example, Tazzari et al. 2016, 2017; Jennings et al. 2022a). Additionally, the efficiency of radial drift has not been studied for a large number of disks. Trapman et al. (2019) proposed a scenario where the ratio between the gas and dust disk sizes ($R_{\text{gas}}/R_{\text{dust}}$) can be used as an estimate for the efficiency of radial drift. If this ratio is larger than 4, the disk is expected to undergo very efficient radial drift, explaining the smaller size of the dust disk. A great example is the small disk of CX Tau, where Facchini et al. (2019) reported a value of $R_{\text{gas}}/R_{\text{dust}} > 5$. While observations of the gas and dust exist for a large number of disks, this ratio has not been estimated for many of them. The importance of radial drift and substructures on the observable chemistry can be further explored by continuing to hunt for substructures in disks (in particular, those at smaller radial distances) and combining this with the estimated ratios of the gas disk and dust disk sizes.

1.3 Astrochemistry

Astrochemistry is the field of study that combines astronomy and chemistry by studying (either through observations, theory, or experiments) the abundances of elements and ongoing chemical reactions in space (see Tielens 2013; van Dishoeck 2014 for recent reviews). Observationally, molecules can be directly studied in emission, where a photon is emitted following the energetic transition from a higher state to lower state. Conversely, molecules can also absorb light by undergoing such a transition from a lower to a higher state. Throughout the remainder of this chapter, we only focus on the emission of light.

1.3.1 Energy levels and transitions

Molecules have three distinct types of energy levels: electronic, vibrational, and rotational (Figure 1.11, see Tennyson 2019; Tielens 2021 for extensive overviews of energy levels and spectroscopy). The energy levels are structured, where a single electronic energy level is subdivided into various vibrational levels, and each vibrational level is subdivided into many rotational states. For levels closer together (i.e., rotational levels), less energy is required for a transition to happen compared

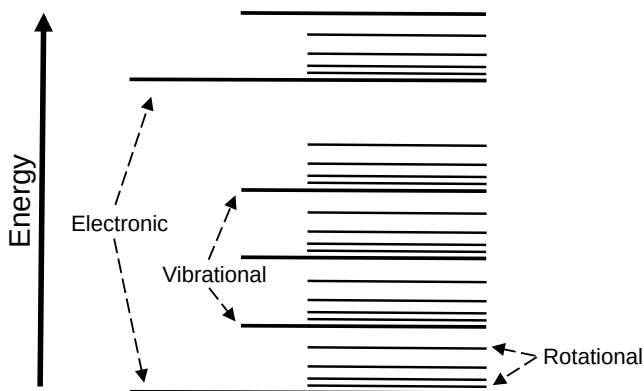


Figure 1.11: Schematic of the different energy levels.

to levels that are separated by a larger distance (i.e., vibrational and electronic levels). As the difference between energy levels (ΔE) is directly connected to the wavelength of a photon (λ), $\Delta E = hc/\lambda = h\nu$, the different levels emit or absorb at different wavelengths. The electronic transitions involve photons that emit at optical wavelengths, whereas those following from vibrational and rotational transitions emit at, respectively, infrared and (sub-)millimetre or radio wavelengths. In equation for the energy levels, h denotes the Planck constant, c the speed of light, and ν is the frequency of the light emitted by a photon. As electronic transitions are not part of this thesis, we focus on the vibrational and rotational transitions in the remainder of this section. In planet-forming disks, a molecule is generally collisionally excited from the ground (i.e., the state with the lowest energy) to a higher energetic state, where the collisional partner is mainly H_2 , before it cascades back down to the ground state by emitting a photon.

1.3.1.1 Ro-vibrational transitions

During a transition between vibrational levels, the rotational level may also change, resulting in so-called ro-vibrational transitions. The change in a rotational level is denoted by the quantum number ΔJ , and can have values of $\Delta J=0, \pm 1$. For linear molecules with a degenerate bending mode where all three values of ΔJ are allowed (such as CO_2 , HCN , and C_2H_2), the ro-vibrational spectrum has a distinct layout: as vibrational transitions with no change in the rotational level have similar energy differences, photons with very similar wavelengths are emitted. This yields a very broad spectrum in the feature that is known as the *Q*-branch. If $\Delta J=-1$, the transition happens between energy states that are closer together in energy space and, therefore, ΔE is smaller. This, therefore, yields distinct transitions (also known as the *P*-branch) to the right of the *Q*-branch when plotted as a function of wavelength. Conversely, transitions with $\Delta J=+1$ yield distinct transitions (also known as the *R*-branch) to the left of the *Q*-branch. For diatomic molecules (such as CO), the *Q*-branch transitions are forbidden, yielding a spectrum consisting

of only the *P*- and *R*-branches. An asymmetric top molecule, such as H_2O , has a very irregular spectrum due to additional ortho and para states with different rotational levels. Simulated spectra of each of these molecules are displayed in Figure 1.12 to highlight the differences.

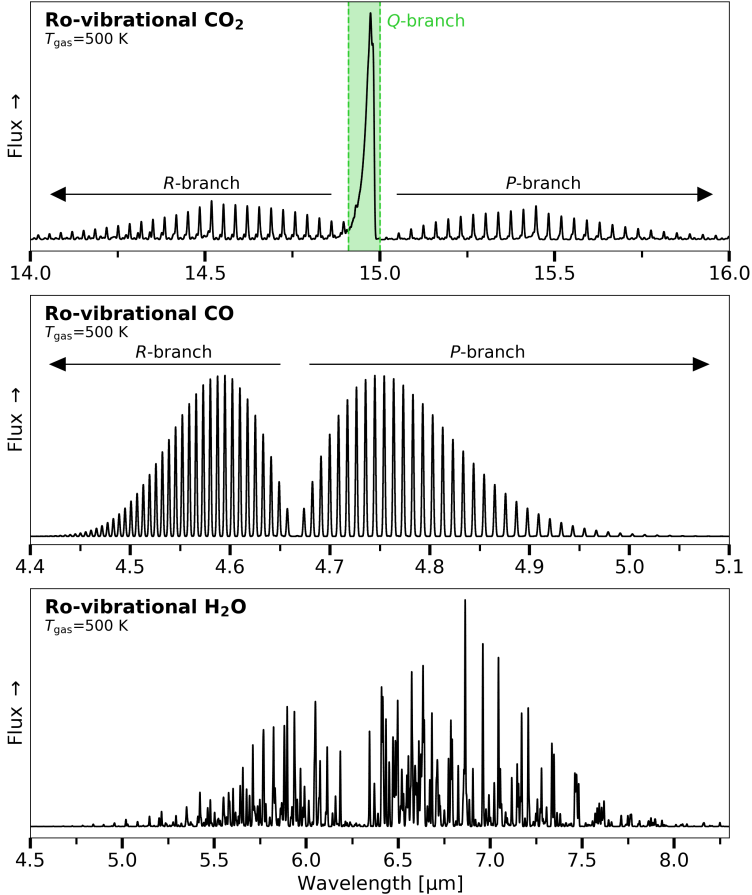


Figure 1.12: Simulated, optically thin ro-vibrational spectra of CO_2 (top panel), CO (middle panel), and H_2O (bottom panel) at $T_{\text{gas}} = 500$ K. The *Q*-, *P*- and *R*-branches of CO_2 and the *P*- and *R*-branches of CO are indicated.

1.3.2 Excitation analysis

The spectra provide direct information on the properties of the gas. The intensity of each line is, after all, directly related to the column density of the molecular species ($I \propto N$). The ease of the analysis depends on whether the molecular excitation is in local thermal equilibrium (LTE) or not. In the case of LTE, the density of the gas is sufficiently high such that it exceeds the critical density, and

the level populations can be described by a single excitation temperature (T_{ex}), their distributions are proportional to $n_i \propto \exp(-E_i/k_{\text{B}}T_{\text{ex}})$. Here, E_i is the upper level energy of the i -th transition.

One aspect that complicates an excitation analysis is the notion of optical depth. Optical depth (τ) is a measure of the transparency of a material to light. If the molecular gas is optically thin ($\tau \ll 1$), the emission of these species throughout the entirety of an astronomical object (i.e., a cloud or a disk) can be observed. However, once the emission becomes optically thick ($\tau \geq 1$), the emission will not be able to penetrate the optically thick gas, and only part of the molecular column can be observed. If the optical depth is known, a correction factor ($1 - \exp(-\tau)$) to the column density can be applied during an excitation analysis, but precise estimations of the optical depth are hard to obtain. Optically thick emission can, however, be extremely useful if one is interested in the temperature of a gaseous medium. In this case, the brightness temperature provides a direct estimate of the kinetic temperature (T_{kin}) of the gas.

Furthermore, it is not only the optical depth of the gas that needs to be taken into account when inferring the column density of a molecular species. The optical depth of the dust, which is wavelength dependent, matters as well, especially at NIR and MIR wavelengths, as the smaller micrometre-sized dust grains are distributed throughout the entire disk. Once the dust becomes optically thick ($\tau_{\text{dust}} \geq 1$) at a certain wavelength, it will absorb emission originating from deeper inside the disk.

In the case of non-LTE emission, the analysis of the molecular emission requires full radiative transfer calculations (see, for example, van der Tak et al. 2007) and extensive knowledge of the collisional rate coefficient of the molecule with a collisional partner (often H_2). An example is given by the sub-thermal excitation in the low-density regions of planet-forming disks, such as their surface layers. For CH_3OH , simulations at low densities ($n_{\text{gas}} \sim 10^7 \text{ cm}^{-3}$) found excitation temperature significantly below the kinetic temperature of the gas (i.e., $T_{\text{ex}} \neq T_{\text{kin}}$; Johnstone et al. 2003). Upon increasing the density of the gas ($n_{\text{gas}} \sim 10^9 \text{ cm}^{-3}$), the excitation temperature nearly matched the kinetic temperature ($T_{\text{ex}} \sim T_{\text{kin}}$), implying that the emission had thermalised and, therefore, LTE could be assumed.

Aside from low-density environments, non-LTE excitation can also be due to IR or UV pumping and prompt emission following the formation of the molecule. Both of these processes can be very important for JWST observations. The emission of SO_2 at $7 \mu\text{m}$ in the protostar NGC 1333 IRAS 2A has been attributed to IR pumping (van Gelder et al. 2024), where the absorbance of IR photons leads to increased populations of higher energy levels than can be expected from collisional excitation alone (Bruderer et al. 2015; Bosman et al. 2017). Prompt emission occurs when a molecule ends up in a higher excited state following, for example, the photodissociation of its parent species (Tabone et al. 2021). For disks, this can be very important for the emission of OH, since it is the photodissociation product of H_2O (Carr & Najita 2014; Tabone et al. 2024).

1.3.3 Chemical processes

As described before, the important constituents of the stages of star- and planet formation (and, therefore, planet-forming disks) are the gas, the dust grains, and the icy mantles coating the grains. Important processes that regulate the observable chemistry are, therefore, subdivided into gas-phase reactions and processes occurring on the surfaces of grains or in the ices (see Figure 1.13). Öberg & Bergin (2021) and van't Hoff & Bergner (2026) contain recent reviews on the ongoing chemical processes in disks.

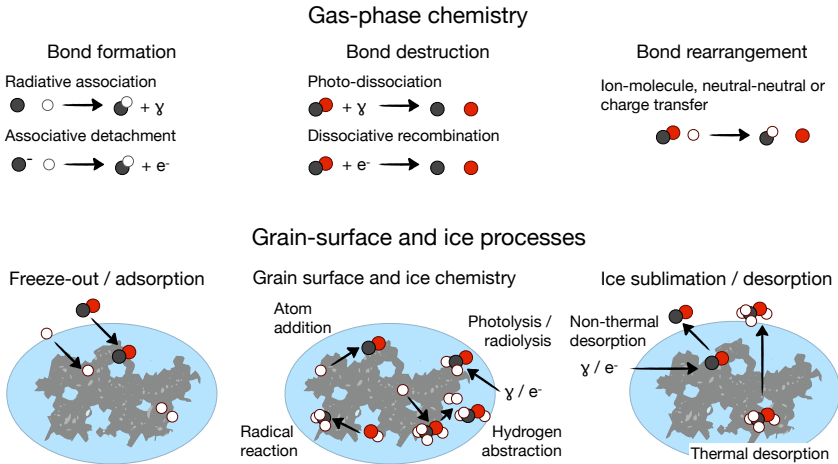


Figure 1.13: Overview of the ongoing chemical processes in the ISM and planet-forming disks. The gas-phase processes are shown on the top, whereas the bottom is dedicated to grain-surface and ice processes. This figure has been adapted from Öberg & Bergin (2021).

1.3.3.1 Gas-phase chemistry

The conditions (i.e., low densities and temperatures) in planet-forming disks are generally not suited for three-body reactions. Instead, the chemistry is driven by two-body reactions. These reactions involve bond formation (radiative association and associative detachment), bond destruction (photodissociation and dissociative recombination), and bond rearrangement (ion-molecule, neutral-neutral, and charge transfer) processes. Only within the innermost regions of disks, where the densities ($n_{\text{gas}} \gtrsim 10^{12} \text{ cm}^{-3}$) and temperatures ($T > 100 \text{ K}$) are high, three-body processes may become important (see, for example, van't Hoff & Bergner 2026). As three-body processes are beyond the scope of this thesis, the remainder of this section focuses on two-body processes.

Bond formation. Out of the two gas-phase bond formation processes, radiative association is considered to be the most important. However, due to the radiative stabilisation of the molecule through vibrational transitions taking much

longer than collisional timescales, the likelihood of such reactions taking place is small. Therefore, radiative association is most efficient and important for reactions involving reactants that are very abundant, such as atomic and molecular hydrogen (H and H₂; Herbst & Klemperer 1973). Compared to radiative association, associative detachment is much rarer as the reactions involve anions (negatively charged ions, like OH⁻; Millar et al. 2007).

Bond destruction. The destruction of a molecule through the absorption of a photon is known as photodissociation (see Heays et al. 2017 for an overview). While the majority of molecules are directly destroyed if the energy of the photon is higher than the covalent bond strengths, generally requiring ultraviolet (UV, or higher) energies, molecules like H₂ and CO dissociate through the absorbance of specific lines (that is at specific wavelengths or frequencies; Stecher & Williams 1967; Abgrall et al. 1992). The molecule is, in that case, in an excited state from which it can move into a dissociated state (also known as predissociation and works for CO; van Dishoeck & Black 1988) or dissociate through spontaneous decay (H₂). As the photodissociation of H₂ and CO involves specific lines, self-shielding effects can become very important in halting the destruction. Self-shielding occurs when the gas becomes optically thick against the incident radiation and, therefore, deeper layers are effectively shielded against photodissociation.

UV-photodissociation is inherently linked with photon-dominated regions (PDRs; Tielens & Hollenbach 1985), regions that are subject to immense UV-irradiation from nearby (massive) stars. A well-known example is the Orion Bar south of the Trapezium Cluster. The surface layers of planet-forming disks can, effectively, also be considered to be PDRs, as these regions are directly subject to irradiation from the host star (van Dishoeck 2006; Bergin et al. 2007). The structure of a PDR is simple: closest to the radiation source, the majority elements are in ionised atomic states (i.e., C⁺). Deeper into the PDR (or disk surface layer), the atoms will be in a neutral state, and even deeper, the elements can be bound up in molecules.

Through collisions with electrons, ions may also be destroyed in favour of forming two neutral molecules or an atom and a molecule. As a result of dissociative recombination, both smaller (i.e., HCO⁺+e⁻ → HCO; Herbst & Klemperer 1973) and larger molecules can form (i.e., CH₃CNH⁺+e⁻ → CH₃CN+H; van't Hoff & Bergner 2026).

Bond rearrangement. Of the gas-phase bond rearrangement processes, ion-neutral reactions dominate the gas-phase chemistry in planet-forming disks. As ions are required for these processes, a source of ionisation is required. Within disks, ionisation occurs through UV irradiation, X-rays, cosmic rays, and radionuclides (Glassgold et al. 1997; Walsh et al. 2012; Eistrup et al. 2016). For ion-molecule reactions, H₃⁺ plays a crucial role. H₃⁺ forms after an ionisation event of H₂, and its density is found to be largely constant. Therefore, the gas-phase chemical timescale is largely influenced and set by H₃⁺. Well-known examples are the formation of HCO⁺ (H₃⁺+CO → HCO⁺+H₂; Herbst & Klemperer 1973) and H₂D⁺ (H₃⁺+HD → H₂D⁺ + H₂; Watson 1976), a molecule driving the deuteration of other species.

While neutral-neutral and charge transfer reactions are less dominant, they still

can play a crucial role in setting the abundance of certain species. An example of neutral-neutral reactions is related to the formation of H_2O and CO_2 through reactions with OH (respectively, $\text{H}_2 + \text{OH} \rightarrow \text{H}_2\text{O} + \text{H}$ and $\text{CO} + \text{OH} \rightarrow \text{CO}_2 + \text{H}$; Charnley 1997; van Dishoeck et al. 2013; Bosman et al. 2022b). In the hot inner regions of disks ($T > 200$ K) the gas-phase formation of H_2O dominates over the gas-phase formation of CO_2 . In the colder regions ($T < 200$ K), it is the formation of CO_2 that is more efficient.

1.3.3.2 Grain-surface chemistry

While grain-surface chemistry is not the direct focus of this thesis, ices are extremely important for the chemistry of planet-forming disks. Through freeze-out and sublimation processes, grains directly affect the observable chemistry by either depleting the molecular reservoir (freeze-out) or enhancing it (sublimation). Within disks, this is all regulated by snowlines. The release of a molecule from the grain inside its snowline following, for example, radial drift is known as a thermal desorption process, but various non-thermal processes also occur. These processes include photodesorption, chemical desorption, and shocks (see Cuppen et al. 2024 for a recent review). A well-known example of non-thermal desorption in a disk is the detection of CH_3OH in the disk of TW Hya (Walsh et al. 2016; Ilee et al. 2026).

Whereas freeze-out and sublimation directly affect the observed molecular reservoirs, it is the processes that happen on the grains themselves that are of crucial importance in the formation of molecular species. Their initial formation is dominated by the addition of atomic hydrogen (Hasegawa et al. 1992). This process has been very important in the formation of H_2 (Gould & Salpeter 1963; Wakelam et al. 2017), H_2O (hydrogenation of atomic oxygen; Tielens & Hagen 1982), and species like H_2CO and CH_3OH (hydrogenation of CO; Watanabe & Kouchi 2002; Fuchs et al. 2009; Santos et al. 2022). Grain-surface processes can also lead to the formation of more complex species, involving radicals following photodissociation or hydrogen abstraction events.

Crucial for the efficiency of grain-surface chemistry is the notion that grain-surface reactions are effectively three-body processes, which is in stark contrast with the gas-phase processes. Here, the grains are the third body and act as catalysers by absorbing the energy released by bond formation.

1.4 This thesis

With the recent launch of JWST and the ongoing studies with ALMA, the chemistry in both the inner (< 10 au) and outer (> 10 au) regions of planet-forming disks can be studied in great detail. Constraining the chemical composition in both regions is crucial for our understanding of the chemical evolution of these systems, and, in particular, the composition of the emerging planets. Radial drift and substructures play a key role in this regard, as they can directly influence the observable chemistry. This thesis focuses, therefore, on the chemical compositions in both regions and investigates the role of both drift and structure in setting the

chemistry. Subsequently, the thesis is subdivided into three parts: the first part (Chapters 2, 3, and 4) focuses on the inner disk physical structure and chemistry using new data from the JWST/MIRI through the MINDS collaboration, the second part (Chapter 5) focuses on high-resolution ALMA observations to hunt for substructures in the outer disk, and the third and final part (Chapters 6 and 7) focuses on the outer disk chemistry. A summary of each of the chapters and the main conclusions is provided below.

Chapter 2. *MINDS: The DR Tau disk. I. Combining JWST-MIRI data with high-resolution CO spectra to characterise the hot gas*

This chapter focuses on the JWST spectrum of the IR bright disk of DR Tau, revealing strong emission signatures of CO, H₂O (the focus of Chapter 3), OH, CO₂, HCN, and C₂H₂. High spectral resolution, ground-based observations of IRTF-iSHELL and VLT-CRIRES were used to analyse the excitation conditions of CO, which were also able to describe the MIRI observations. This suggests that the ground-based and JWST observations can be used in tandem to explore the conditions in the inner regions. Based on derived temperatures and emitting areas, the emission structure of the disk was revealed: CO emits from the hot, innermost regions of the disk, even from inside the dust sublimation radius. HCN and C₂H₂ are expected to emit from a deeper layer in the disk, whereas CO₂ emits from even deeper or further out. Additionally, the CO observations suggests that the inner disk may be misaligned with respect to the outer disk.

Chapter 3. *MINDS: The DR Tau disk. II. Probing the hot and cold H₂O reservoirs in the JWST-MIRI spectrum*

The H₂O emission observed with JWST-MIRI/MRS can be subdivided into the ro-vibrational transitions emitting at the shorter wavelengths (<10 μm) and the pure rotational transitions at longer wavelengths (>10 μm). The emission traces a radial gradient in the disk, where the temperature decreases with wavelength, while the emitting radius increases. Three different reservoirs can be distinguished using the pure rotational H₂O transitions: hot ($T \sim 800$ K), warm ($T \sim 470$ K), and cold ($T \sim 180$ K). The cold component may be enhanced by drifting icy pebbles crossing the snowline, however, this could not be confirmed. Crucially, a comparison between the derived abundances (i.e., the total number of molecules) of H₂O and CO ($\mathcal{N}_{\text{H}_2\text{O}}/\mathcal{N}_{\text{CO}} \sim 0.17$) suggests that the H₂O abundance may be slightly depleted.

Chapter 4. *MINDS: Water reservoirs of compact planet-forming dust disks: A diversity of H₂O distributions*

To investigate the potential role of radial drift in enhancing the gaseous cold H₂O reservoir, this chapter focuses on analysing the pure rotational transitions of a sample of 8 compact disks ($R_{\text{dust}} \lesssim 60$ au). By investigating the strengths of the different rotational H₂O reservoirs and deriving line ratios that trace their respective strengths, it was found that only two of the eight disks show strong cold H₂O emission. This reservoir may be enhanced due to radial drift in these two disks, but accretion variability could not be ruled out. Four of the other disks show

strong emission from all three components, but the cold reservoir is not enhanced. The spectra of the final two disks are dominated by other molecules (such as CO_2), and only show weak emission the rotational H_2O transitions. The weakness of the H_2O reservoirs may be the result of a (small) inner cavity.

The main results of Part 1 of this thesis, the chemical and physical structure of the inner disk, can be summarised as follows:

- High-resolution, ground-based observations of CO are crucial for deriving the excitation temperature, column density, and emitting radius. Additionally, they can be used to study potential misalignments between the inner and outer disk. (Chapter 2)
- The pure rotational H_2O transitions observed with JWST-MIRI/MRS can be attributed to three different reservoirs: hot, warm, and cold. The strengths of these reservoirs may reveal whether the H_2O is enhanced near the snow-line (following, for example, radial drift or accretion variability) or if the reservoirs are depleted (due to, for example, an inner cavity). (Chapter 3 and 4)
- Not all compact disks are enhanced in their cold H_2O reservoirs due to efficient radial drift. (Chapter 4)

Chapter 5. *MINDS: The influence of outer dust disk structure on the volatile delivery to the inner disk*

This chapter is part of Gasman et al. (2025). The main goal of this study was to investigate the influence of outer disk substructures on the volatile delivery by radial drift to the inner disk. Through a visibility fitting approach, archival high-resolution ALMA observations were analysed to hunt for substructures that could not be seen in the image plane. The found substructures include a small inner cavity in the disk of BP Tau. No direct connection between the inferred substructures and inner disk reservoirs - in particular, that of H_2O - could be established. As an example, a deep gap in the inner regions of Sz 98 was found, yet this disk also showed the strongest cold H_2O reservoir, suggesting that the gap may be leaky to gas and small dust grains.

The main results of Part 2, the outer disk structure, are as follows:

- ALMA visibility fitting techniques are a powerful tool to study substructures at small radial locations. A small sample of 8 disks reveals that substructures at distances of $\lesssim 15$ au may be a common occurrence. (Chapter 5)

Chapter 6. *Characterising the molecular line emission in the asymmetric Oph-IRS 48 dust trap: Temperatures, timescales, and sub-thermal excitation*

The Oph-IRS 48 disk is an interesting laboratory to study the role of its azimuthally asymmetric dust trap in setting the observable chemistry. Using the many observed transitions of SO_2 , H_2CO , and CH_3OH , the goal of this chapter was to constrain the excitation conditions at the location of the dust trap. No

thermal signatures of a vortex trapping the dust particles were found. Through a rotational diagram analysis, it was found that both CH_3OH and H_2CO are subthermally excited, pointing to them being located in the lower density upper layers of the disk. Conversely, SO_2 is seen to be thermally excited, which implies that its emission originates from a layer close to the midplane. The photodissociation timescales reveal that both CH_3OH and H_2CO must be rapidly dissociated ($\tau_{\text{pd}} < 1$ year). Crucially, the photodissociation products of CH_3OH (and H_2O and CH_4) are needed in the gas-phase formation of H_2CO , suggesting that two reservoirs of H_2CO may be present, which can also explain its somewhat larger azimuthal distribution: one reservoir due to the sublimation of ices, another due to efficient gas-phase formation.

Chapter 7. *The asymmetric carbon-rich chemistry of the planet-forming disk of HD 142527 triggered by late infall*

Using new ALMA observations in tandem with archival observations, this chapter focuses on the molecular asymmetries in the disk of HD 142527. The majority of the azimuthal asymmetries can be explained by late infall. The infalling material is thought to replenish the disk with fresh atomic carbon that locally enhances the C/O-ratio and causes the efficient gas-phase formation of hydrocarbons (such as C_2H), CN, and CS. Furthermore, the infalling material may also have triggered the instability that created the dust asymmetry and may be the cause of a co-spatial enhancement in the gas surface density.

The main results and conclusions of part 3, the chemical composition of the outer disk, can be summarised as follows:

- The emission of CH_3OH and H_2CO in the disk of Oph-IRS 48 originates from a small radial sliver near the inner edge of the dust trap and is subthermally excited due to the lower gas density of the emitting upper layer. The emission of SO_2 originates from a layer close to the midplane, based on its thermal excitation requiring a high density. (Chapter 6)
- The rapid photodissociation of CH_3OH , H_2O , and CH_4 in the elevated emitting layers of Op-IRS 48 may facilitate efficient gas-phase formation of H_2CO . (Chapter 6)
- The chemical composition in the outer disk of HD 142527 is not dominated by the large asymmetric dust trap or the shadows observed in scattered light due to the misaligned inner disk. Instead, it may be set by late infalling material. (Chapter 7)
- Observing molecules like CN, C_2H , and H_2CO in disks with spiral-like features may reveal unique insights into the role of infalling material in setting the outer disk composition. (Chapter 7)

1.4.1 Future prospects

The high sensitivity and resolution observations of JWST and ALMA now provide unique insights into the chemical composition from the inner to outer disk. To improve our understanding of the (chemical and physical) processes dominating the chemistry, future studies should focus on combining these observations. To study the chemistry across the full disks, we need to constrain both the physical and thermal structures within the disks. Both existing and future telescopes give us the means to achieve this, especially since the future of observationally studying planet-forming disks is bright.

The flawless launch of JWST has opened up the possibility of extending the mission from its original 10 years to 20 years. If no complications arise, the telescope will remain operational for over a decade, yielding ample time opportunity to continue studying the inner disk compositions. More observations of different environments, such as disks with high UV irradiation or disks in binary systems, may yield more insights into the curious differences between the C-rich inner disks of VLMS stars and the more O-rich T-Tauri disks. Furthermore, this allows for time-domain studies to take place, where re-observing a disk or making use of the introduced Long-Term Monitoring Initiative would allow for variability studies following, for example, variable accretion and/or accretion outbursts.

With ALMA already having been operational for over a decade, it has revolutionised our understanding of the outer disk chemistry. The doubling of the bandwidth during the upcoming ALMA Wideband Sensitivity Upgrade (WSU; Carpenter et al. 2023) will target many more molecular transitions in a single observation. This is of particular interest for observations of C_2H , as its transitions are not close in frequency space to commonly observed species, such as the CO isotopologues. Therefore, we will gain a lot more information on the chemical composition and elemental ratios of many disks in the not-too-distant future.

As the construction of the ELT is well underway, high-resolution and sensitivity observations with the integral field unit of METIS (Brandl et al. 2021) are on the horizon. METIS will not only achieve high spectral resolution ($R \sim 100,000$) that will be crucial for inferring the inner disk conditions and structures through the ro-vibrational CO transitions, but it also has a high spatial resolution ($\sim 0.03''$) that can directly reveal gas substructures in the bright Herbig disks. The observations also yield the opportunity to study the ro-vibrational bands of CO isotopologues, ^{13}CO and C^{18}O , and additional bands of H_2O , HCN, C_2H_2 , and CH_4 . By combining these data with JWST observations, the inner disk chemical abundances may be further constrained.

While there are presently no operational FIR telescopes, this may be changed in the near future by the potential missions POEMM and PRIMA. POEMM is a proposed balloon mission that would observe a subset of disks in a 20-day flight through the Antarctic skies. PRIMA is, on the other hand, one of the final candidates for an upcoming NASA probe mission and has many crucial science goals (see, for example, Banzatti et al. 2025a; Pontoppidan et al. 2025; Salyk & Gasman 2025): constrain the gas mass using HD, to further investigate the cold H_2O reservoir, and to hunt for emission of H_2 ^{18}O .

PART I

Chemical and physical
structure of the inner disk

Chapter 2

MINDS: The DR Tau disk

I. Combining JWST-MIRI data with high-resolution CO spectra to characterise the hot gas

M. Temmink, E. F. van Dishoeck, S. L. Grant, B. Tabone, D. Gasman, V. Christiaens, M. Samland, I. Argyriou, G. Perotti, M. Güdel, T. Henning, P.-O. Lagage, A. Abergel, O. Absil, D. Barrado, A. Caratti O Garatti, A. M. Glauser, I. Kamp, F. Lahuis, G. Olofsson, T. P. Ray, S. Scheithauer, B. Vandenbussche, L. B. F. M. Waters, A. M. Arabhavi, H. Jang, J. Kanwar, M. Morales-Calderón, D. Rodgers-Lee, J. Schreiber, K. Scwharz, L. Colina

A&A, 686, A117 (2024)

Abstract

Context. The MRS mode of the JWST-MIRI instrument has been shown to be a powerful tool to characterise the molecular gas emission of the inner region of planet-forming disks. Investigating their spectra allows us to infer the composition of the gas in these regions and, subsequently, the potential atmospheric composition of the forming planets. We present the JWST-MIRI observations of the compact T-Tauri disk, DR Tau, which are complemented by ground-based, high spectral resolution ($R \sim 60000$ - 90000) CO ro-vibrational observations.

Aims. The aim of this work is to investigate the power of extending the JWST-MIRI CO observations with complementary, high-resolution, ground-based observations acquired through the SpExoDisks database, as JWST-MIRI's spectral resolution ($R \sim 1500$ - 3500) is not sufficient to resolve complex CO line profiles. In addition, we aim to infer the excitation conditions of other molecular features present in the JWST-MIRI spectrum of DR Tau and link those with CO.

Methods. The archival complementary, high-resolution CO ro-vibrational observations were analysed with rotational diagrams. We extended these diagrams to the JWST-MIRI observations by binning and convolution with JWST-MIRI's pseudo-Voigt line profile. In parallel, local thermal equilibrium (LTE) 0D slab models were used to infer the excitation conditions of the detected molecular species.

Results. Various molecular species, including CO, CO₂, HCN, and C₂H₂, are detected in the JWST-MIRI spectrum of DR Tau, with H₂O being discussed in a subsequent paper. The high-resolution observations show evidence for two ¹²CO components: a broad component (full width at half maximum of FWHM \sim 33.5 km s⁻¹) tracing the Keplerian disk and a narrow component (FWHM \sim 11.6 km s⁻¹) tracing a slow disk wind. The rotational diagrams yield CO excitation temperatures of $T \geq 725$ K. Consistently lower excitation temperatures are found for the narrow component, suggesting that the slow disk wind is launched from a larger radial distance. In contrast to the ground-based observations, much higher excitation temperatures are found if only the high- J transitions probed by JWST-MIRI are considered in the rotational diagrams. Additional analysis of the ¹²CO line wings suggests a larger emitting area than inferred from the slab models, hinting at a misalignment between the inner ($i \sim 20^\circ$) and the outer disk ($i \sim 5^\circ$). Compared to CO, we retrieved lower excitation temperatures of $T \sim 325$ - 900 K for ¹²CO₂, HCN, and C₂H₂.

Conclusions. We show that complementary, high-resolution CO ro-vibrational observations are necessary to properly investigate the excitation conditions of the gas in the inner disk and they are required to interpret the spectrally unresolved JWST-MIRI CO observations. These additional observations, covering the lower- J transitions, are needed to put better constraints on the gas physical conditions and they allow for a proper treatment of the complex line profiles. A comparison with JWST-MIRI requires the use of pseudo-Voigt line profiles in the convolution rather than simple binning. The combined high-resolution CO and JWST-MIRI observations can then be used to characterise the emission, in addition to the physical and chemical conditions of the other molecules with respect to CO. The inferred

excitation temperatures suggest that CO originates from the highest atmospheric layers close to the host star, followed by HCN and C₂H₂ which emit, together with ¹³CO, from slightly deeper layers, whereas the CO₂ emission originates from even deeper inside or further out of the disk.

2.1 Introduction

The majority of the exoplanet population are thought to form in the inner regions (<10 au) of planet-forming disks (Morbidelli et al. 2012; Dawson & Johnson 2018). The chemical composition of these regions and, subsequently, the accreting planetary atmospheres are dictated by their high temperatures and densities, in addition to the location of the H_2O and CO_2 snowlines (e.g. Pontoppidan et al. 2014; Walsh et al. 2015; Öberg & Bergin 2021; Bosman et al. 2022b; Mollière et al. 2022). Snowlines are the radial distances that dictate what elements are for 50% present in the gas and that are locked-up in the icy mantles of dust grains for the other 50%.

Over the recent years, the Atacama Large Millimeter/submillimeter Array (ALMA) has allowed us to characterise the chemical composition of the gas, dust, and ice in the outer regions of planet-forming disks with an unprecedented sensitivity, as over 30 molecular species and 17 rare isotopologues have been detected (e.g. Booth et al. 2021b; van der Marel et al. 2021a; Brunken et al. 2022; Furuya et al. 2022; McGuire 2022; Öberg et al. 2023; Booth et al. 2024b). The composition of the inner planet-forming zone is, however, hard to probe with ALMA, as an angular resolution of a few milli-arcseconds is required to resolve structures at 1 au scales in the nearest star-forming regions. These resolutions can only be achieved in the most extended configurations (C-10 with baselines of 16.2 km) for the highest frequencies (602-720 GHz in Band 9 and 787-950 GHz in Band 10) and are sensitive to only the dust continuum (see, for example, Andrews et al. 2018).

Recently, the Medium Resolution Spectroscopy (MRS; Wells et al. 2015; Argyriou et al. 2023) mode of the Mid-InfraRed Instrument (MIRI; Rieke et al. 2015; Wright et al. 2015, 2023) aboard the *James Webb Space Telescope* (JWST; Rigby et al. 2023) has provided a new opportunity to study the inner planet-forming regions. Within its wide wavelength range (4.9 to 28.1 μm), a large ensemble of molecular species (including CO, CO_2 , and H_2O) are covered. As JWST-MIRI only covers the highest J -transitions of the P branch of CO (i.e. $J \geq 25$ for the ^{12}CO $v=1-0$ P branch) at a low spectral resolution ($R \sim 3500$) and many T-Tauri disks are too bright for the JWST Near Infrared Spectrograph (NIRSpec), complementary observations are required to fully investigate the excitation and kinematics of CO. These spectrally resolved observations can be obtained with ground-based telescopes, such as the upgraded Cryogenic IR Echelle Spectrometer (CRIRES+) at the Very Large Telescope (VLT), the iSHELL instrument at the NASA Infrared Telescope Facility (IRTF), and/or Keck-NIRSPEC (e.g. Salyk et al. 2011a; Brown et al. 2013; Banzatti et al. 2022; Grant et al. 2023a).

In this work, we present the JWST-MIRI observations of DR Tau, an actively accreting ($\dot{M} \simeq 2 \times 10^{-7} M_{\odot} \text{ yr}^{-1}$; Manara et al. 2023) T-Tauri star ($M \simeq 0.93 M_{\odot}$, $L \simeq 0.63 L_{\odot}$; Long et al. 2019) located at a distance of ~ 195 pc (Gaia Collaboration et al. 2018) in the Taurus star-forming region. In addition, we used complementary, high spectral resolution CO ro-vibrational observations to fully investigate the CO excitation properties.

The chemical composition of its inner disk has been revealed with instruments such as VLT-CRIRES and *Spitzer*. Available spectra show that lines originating

from the inner part of the DR Tau disk have one of the highest line-to-continuum ratio and that a wide variety of molecular species are present (CO, CO₂, OH, H₂O, HCN and C₂H₂; Bast et al. 2011; Mandell et al. 2012; Brown et al. 2013; Banzatti et al. 2020). As we subsequently show, these are all also detected with JWST-MIRI. Other works on high spectral-resolution, infrared observations have shown that the ¹²CO line profile can consist of two components: one narrow component related to a possible disk wind, while the other one is broad and the result of the disk’s Keplerian rotation (Bast et al. 2011; Brown et al. 2013; Banzatti et al. 2022). We revisit this analysis with recent high-resolution observations. As JWST-MIRI also observes part of the CO ro-vibrational ladder, it will be of interest to investigate how these observations of a limited number of high-*J* levels compare with the full range of *J*-levels covered from the ground, especially since the disk of DR Tau is too bright for JWST-NIRSpec observations. Additionally, we investigate how the emitting radius provided by LTE slab models to fit the CO rotational ladder compares with the expected inner and emitting radius of CO, which can be derived from optically thin and/or well resolved line profiles using Kepler’s law (Salyk et al. 2011a; Banzatti & Pontoppidan 2015; Banzatti et al. 2020).

The outer disk can, on the other hand, be investigated with millimetre instruments. ALMA observations have shown that the dust disk is very compact, with a 95% effective radius of $\sim 0.28''$ or ~ 54 au (Long et al. 2019). At the current resolution ($\sim 0.1''$) of the ALMA data, no dust substructures have been detected, however, visibility- and super-resolution fitting techniques suggest that the disk may be comprised of two rings in the outer disk (respectively at ~ 22 au and ~ 42.5 au; Jennings et al. 2020, 2022b; Zhang et al. 2023). Furthermore, Jennings et al. (2022b) note that the visibilities hint at underresolved structures at small spatial scales, which likely point towards a partially resolved inner disk. The structure of the innermost region of the disk can be characterised with instruments on the Very Large Telescope Interferometer (VLTI) and the GRAVITY instrument has, in particular, shown that the inner disk of DR Tau ($i \sim 18^\circ$; GRAVITY Collaboration et al. 2021) may be misaligned with respect to the outer disk ($i=5.4$; Long et al. 2019).

The compact size of the millimetre-sized dust disk and potential hints of substructures make DR Tau a very interesting target to explore the role of the inward drift of icy pebbles in enhancing the emission seen in the inner disk. H₂O will be of importance in investigating the significance of radial drift, as shown by Banzatti et al. (2020, 2023a). In addition, Braun et al. (2021) derive a gas disk radius of 246 au based on ALMA observations of ¹³CO and C¹⁸O. This yields a gas-to-dust disk radius ratio of ~ 4.6 . As noted by Trapman et al. (2019) a ratio of >4 is a clear sign of dust evolution and radial drift, suggesting that drift is very effective in the disk of DR Tau and that the molecular emission in the inner disk may be enhanced.

This paper is structured as follows: in Sections 7.2 and 4.3 we describe, respectively, the data acquisition, reduction, and analysis methods, while Section 2.4 contains our results. The discussions can be found in Section 7.4. Section 4.6 contains the conclusions and a small summary. Furthermore, the H₂O emission

observed in DR Tau are investigated and discussed together with OH and first limits on H₁ and H₂ in a separate paper (Temminck et al. 2024a). Any H₂O slab models displayed will be further explained in that paper.

2.2 Observations

In the following subsections we describe the used observations (JWST-MIRI in Section 2.2.1 and IRTF-iSHELL in Section 2.2.3) and data reduction techniques. Additionally, we introduce our continuum subtraction method in Section 2.2.2.

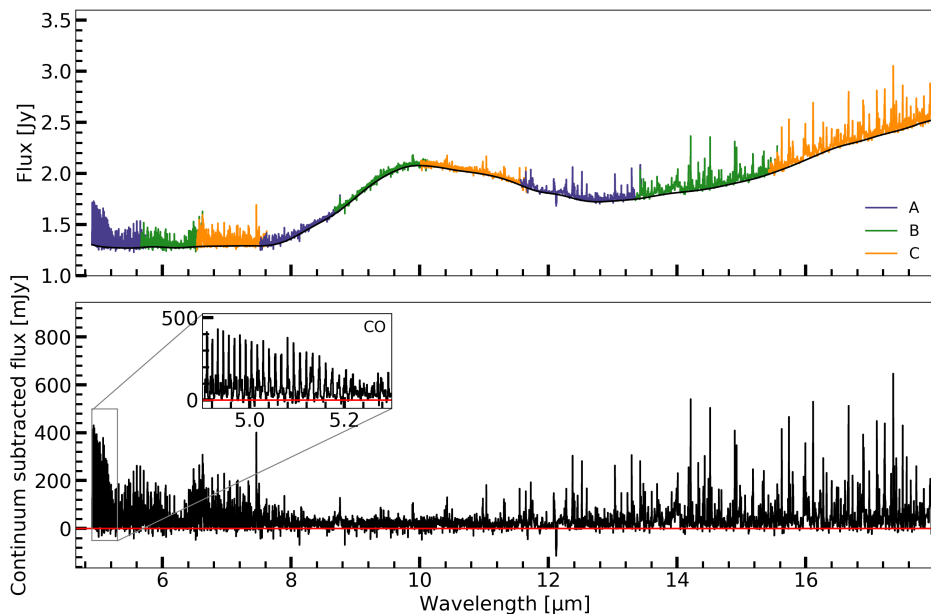


Figure 2.1: JWST-MIRI MRS spectrum of DR Tau over channels 1 through 3 (4.9-17.98 μm). The different wavelength ranges (subbands) of each MIRI channel are indicated in the top panel in blue (‘A’), green (‘B’), and orange (‘C’), respectively. The black line displays the estimated continuum. The bottom panel shows the continuum subtracted JWST-MIRI spectrum and contains a zoom-in on the CO transitions (4.9-5.3 μm). The red line in the bottom panel highlights the zero flux level.

2.2.1 JWST-MIRI observations

The MIRI/MRS observations of DR Tau have been taken as part of the MIRI mid-INfrared Disk Survey (MINDS; Henning et al. 2024) JWST Guaranteed Time Observations Program (PID: 1282, PI: T. Henning). The MRS mode involves 4 Integral Field Units: channel 1 (4.9-7.65 μm), channel 2 (7.51-11.71 μm), channel 3 (11.55-18.02 μm), and channel 4 (17.71-27.9 μm). As each channel consists of 3

wavelength subbands (respectively, A, B, and C), the MRS observations are comprised of a total of 12 wavelength bands. The data were taken in FASTR1 readout mode on March 4 2023, using a four-point dither pattern and a total on-source integration time of ~ 27.8 minutes.

A combination of the standard JWST pipeline (version 1.11.2, Bushouse et al. 2023a) and routines from the VIP package (Gomez Gonzalez et al. 2017; Christiaens et al. 2023), to compensate for known issues from the standard pipeline, have been used to reduce the data. Similar to the standard pipeline, the reduction pipeline is structured around the 3 main stages: Detector1, Spec2, and Spec3. We have skipped the background subtraction step in the Spec2 stage, and the outlier detection step in Spec3. The outlier detection step is known to introduce spurious artefacts in unresolved sources due to undersampling of the point-spread function (PSF). To compensate for the outlier detection, we have implemented the bad pixel correction routines from the VIP package. The bad pixels are identified through sigma-filtering and corrected through a Gaussian kernel. VIP-based routines have also been used for the centroiding of the central star. The frames of each spectral cube were aligned through an image cross-correlation algorithm, before a 2D Gaussian fit was used to identify the centroid location in the weighted mean image of the spectral cubes. These centroid locations are, subsequently, used for aperture photometry. We have extracted the spectrum by summing the signal in a 2.0 full-width half maximum (FWHM= $1.22 \lambda/D$, where $D \sim 6.5$ m is the diameter of the telescope) aperture centred on the source. To adjust for background emission, we have estimated the background from an annulus directly surrounding the aperture used for the aperture photometry. Aperture correction factors are used to account for the flux of the PSF outside the aperture and inside the annulus (Argyriou et al. 2023).

The calibrated JWST-MIRI spectrum of DR Tau over channels 1 through 3 is presented in Figure 3.1. The different MIRI subbands are displayed in different colours.

2.2.2 Continuum subtraction

Due to the line-richness of the DR Tau spectrum, we employed a different continuum subtraction method compared to Grant et al. (2023b) and Gasman et al. (2023). The method here relies on a baseline estimation using the PYBASELINES package (Erb 2022). Before estimating the baseline, we masked downward spikes, such that they cannot influence the estimate. The downward spikes were masked using the following method: the continuum level was roughly estimated using a Savitzky-Golay filter, consisting of window sizes of 100 data points and polynomials of order 3. Through an iterative process, we removed all emission lines which extended above 2σ of the standard deviation (STD) of the Savitzky-Golay filter. Once no emission lines remained, we subtracted the final Savitzky-Golay filter and considered all 3σ downward outliers from the residuals as downward spikes. These downward spikes were subsequently masked from the baseline estimation on the full spectrum. The baseline was estimated using the ‘Iterative Reweighted Spline Quantile Regression’ (IRSQR) method, which uses penalised splines and an iter-

ative reweighted least squares technique to apply quantile (using a value of 0.05) regression. Within the method, we have used cubic splines with knots every 75 points and differential matrices of order 3.

The estimated baseline and continuum-subtracted spectrum are displayed in the top and bottom panel of Figure 3.1, respectively. Appendix 2.A shows and explains the intermediate steps from the applied continuum subtraction method.

2.2.3 High-resolution CO observations

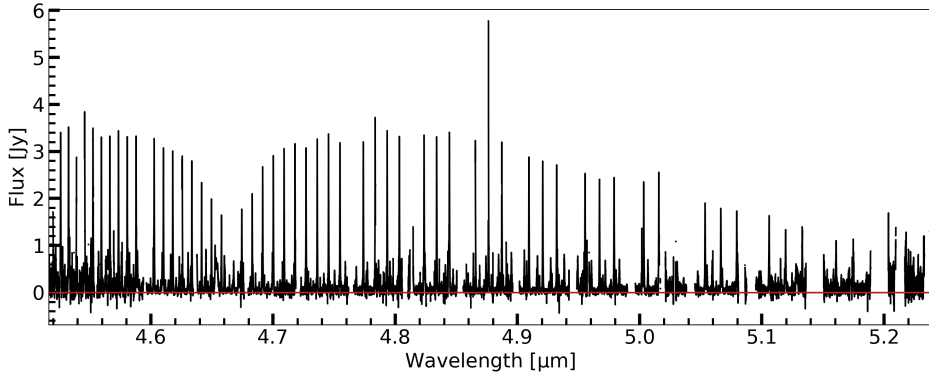


Figure 2.2: Continuum-subtracted iSHELL spectrum of DR Tau. The wavelength gaps visible in the spectrum have either not been observed, or were removed due to interference from telluric lines.

To complement the high- J levels of the CO P branch visible in the JWST spectrum at the shortest wavelengths ($<5.3 \mu\text{m}$), we have acquired high-resolution ($R \simeq 60000\text{-}92000$) IRTF-iSHELL (Rayner et al. 2016, 2022) data through SpExoDisks¹ (Wheeler et al. 2024). The iSHELL data were taken on January 23 2022 (see also Banzatti et al. 2022), were flux calibrated using the allWISE catalogue (WISE-W2: $\lambda=4.6 \mu\text{m}$, $F=1.91\pm 0.16 \text{ Jy}$; Wright et al. 2010; Cutri et al. 2013), and have been corrected for telluric features. As the allWISE flux calibration yields a small offset compared to the JWST-MIRI continuum, we have scaled the iSHELL observations by a factor ~ 0.71 , assuming that the flux at $\sim 5 \mu\text{m}$ is consistent across both observations. The required scaling may be the result of variability. However, as the iSHELL data were flux calibrated using WISE-W2 ($\lambda=4.6 \mu\text{m}$), JWST-NIRSpec observations are required to properly investigate variability. As DR Tau is too bright to observe with JWST-NIRSpec, this comparison cannot be made. The data extend over the wavelength range from approximately $\sim 4.516 \mu\text{m}$ to $\sim 5.239 \mu\text{m}$ and cover ro-vibrational transitions of ^{12}CO ($v=1\text{-}0$, $v=2\text{-}1$, and $v=3\text{-}2$) and ^{13}CO ($v=1\text{-}0$), several H_2O transitions, and the HI Pfund β ($\sim 4.655 \mu\text{m}$) and Humphreys ($\sim 4.675 \mu\text{m}$) lines. These data complement and extend upon the earlier VLT-CRIRES observations (at $R \simeq 100000$), see Bast et al.

¹SpExoDisks: <https://www.spexodisks.com/>

(2011), Brown et al. (2013), and Banzatti & Pontoppidan (2015).

Similar to the continuum subtraction method described in Section 2.2.2, we subtracted the baseline using the IRSQR-method. However, for the iSHELL data we did not mask any downward spikes, we used a quantile regression with a value of 0.10, and we placed the knots every 100 data points. The continuum-subtracted iSHELL data are presented in Figure 2.2. A comparison between the JWST-MIRI and iSHELL observations in the 4.9–5.1 μm region is displayed in Figure 2.3.

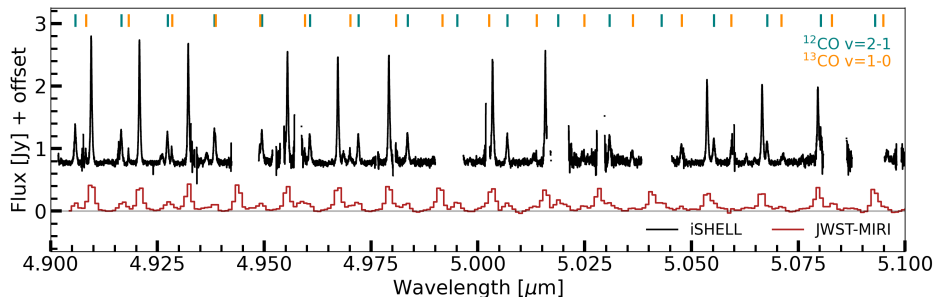


Figure 2.3: Comparison between the JWST-MIRI (red) and iSHELL (black) data within the wavelength region of 4.9–5.1 μm , to highlight the differences in flux and resolution. The iSHELL observations are offset by 0.75 Jy. The vertical lines at the top of the plot indicate the positions of the $^{12}\text{CO } v=2-1$ (teal) and $^{13}\text{CO } v=1-0$ (orange) transitions, to highlight the main contributors of the secondary CO emission peaks visible in this wavelength region.

2.3 Analysis

The following subsections provide an overview of the used techniques for obtaining the excitation properties. In Section 2.3.1 we describe our slab model retrieval process that has been used to characterise the emission from CO_2 , HCN, and C_2H_2 observed with JWST-MIRI. On the other hand, the techniques invoked for obtaining the CO line profiles and the rotational diagrams are described in Section 2.3.2.

2.3.1 LTE slab models

To extract information about the molecular features seen in the JWST-MIRI observations, we implement the same LTE slab model fitting procedure as described in Grant et al. (2023b); Gasman et al. (2023); Perotti et al. (2023), and Tabone et al. (2023). We have obtained the required spectroscopic data through the HITRAN database (Gordon et al. 2022). Our slab models assume Gaussian line profiles with a broadening of $\Delta V=4.7 \text{ km s}^{-1}$ ($\sigma=2 \text{ km s}^{-1}$), following Salyk et al. (2011b). In addition, we have accounted for the mutual shielding of adjacent lines in the Q branches of CO_2 , HCN, and C_2H_2 (see Tabone et al. 2023 for a description). We have convolved our CO_2 , HCN, and C_2H_2 models to a resolving power

of $\Delta\lambda/\lambda \sim 2500$. Finally, the SPECTRES package (Carnall 2017) was used to convolve the slab models to the JWST-MIRI wavelength grid.

The models consists of 3 free parameters that need to be varied to obtain the best fit to the molecular features: the column density N (in cm^{-2}), the gas temperature T (in K) and the emitting area πR_{em}^2 , which is parameterised by the emitting radius R_{em} (in au). We note that while the slab models are parameterised by a circular area, the observed emission may have a different emission morphology with an equivalent area. For example, the emission can originate from an annulus with an area equal to πR_{em}^2 .

To acquire the best combination of values for N , T , and R_{em} , we selected relatively isolated lines or regions of lines and used a reduced χ^2 analysis to fit the slab models to these lines:

$$\chi^2 = \frac{1}{N_{\text{obs}}} \sum_{i=1}^{N_{\text{obs}}} \frac{(F_{\text{obs},i} - F_{\text{mod},i})^2}{\sigma^2}. \quad (2.1)$$

Here, N_{obs} denotes the number of data points that were used for the fits, while F_{obs} and F_{mod} are, respectively, the observed and modelled continuum-subtracted fluxes. σ is the estimated noise. As opposed to Grant et al. (2023b) and Gasman et al. (2023), we have not estimated the noise from line-free regions, as those are not present in the extremely line-rich spectrum of DR Tau. Instead we base our values for σ on the median continuum flux level in each combination of channels and ranges, and divide this by the highly idealised signal-to-noise ratio (S/N) acquired through the JWST *Exposure Time Calculator* (ETC)². The median flux, obtained uncertainty and the estimate from the ETC for each subband can be found in Table 3.A.1. To account for the regions covering multiple subbands, we use a weighted average of the estimated uncertainties for each respective band. The adopted weights represent the number of data points used from each subband in the χ^2 -analysis and this yields a different value for σ for each molecule. We list the range of σ values for the molecules detected in Table 2.1. Our derived values for σ are higher than those found for GW Lup ($\sigma \sim 0.4$ mJy in Channel 3; Grant et al. 2023b) and Sz 98 ($\sigma \sim 1.8$ -9.6 mJy; Gasman et al. 2023), due to our adopted method. The confidence intervals for our fits are defined as $\chi_{\text{min}}^2 + 2.3$, $\chi_{\text{min}}^2 + 6.2$ and $\chi_{\text{min}}^2 + 11.8$ for 1σ , 2σ , and 3σ , respectively (Avni 1976; Press et al. 1992).

Throughout our χ^2 analysis we have used models based on the following grids for N , T and R_{em} : N ranged from 12 to 22 in \log_{10} -space, where we used a spacing of $\Delta(\log_{10}(N))=0.1$. For T , we have used a spacing of $\Delta T=25$ K and a range of $150 \leq T \leq 2500$ K. We note that R_{em} was allowed to vary between 0.01 au and 10 au, using steps of $\Delta R=0.02$ au.

2.3.2 CO line profiles and rotational diagrams

To obtain information about T , N , and R from the high-resolution ro-vibrational transitions of ^{12}CO and ^{13}CO we carried out a rotational diagram analysis on the integrated fluxes, following the method described in Appendix A of Banzatti

²ETC: <https://jwst.etc.stsci.edu/>

et al. (2012). We note that rotational diagram analyses and slab model fitting procedures are inherently the same, as long as the assumption of LTE is valid. We have assumed a Doppler broadening of $\delta V = 1 \text{ km s}^{-1}$. We note that using the same broadening as for the JWST-MIRI slab models ($\delta V = 4.7 \text{ km s}^{-1}$) in the rotational diagram analysis, the same excitation temperatures are inferred. However, the resulting column densities and emitting radii are found to be, respectively, higher and lower, while the total number of molecules is increased by less than 5%.

The required integrated fluxes have been obtained by, first, creating a weighted-averaged, normalised line profile, using the transitions that are unblended, not affected by telluric features, and have a high S/N -ratio. For the weighted average, we have used the errors on the flux as the weights. The line profile has been used to acquire one fixed value for the slight velocity offset (ΔV) from the heliocentric velocity ($\sim 27.6 \text{ km s}^{-1}$; Ardila et al. 2002) and for the FWHM.

For the ro-vibrational ladders of ^{12}CO ($v=1-0$, $v=2-1$, and $v=3-2$; see Section 2.4.2.2), we find that the line profile consists of two components: a narrow one, likely tracing an inner disk wind, and a broad one that traces the Keplerian rotation of the inner disk, as previously observed in Bast et al. (2011) and Brown et al. (2013). For these double components, we have used a double Gaussian line profile, whereas for the ^{13}CO $v=1-0$ transitions we have used a single Gaussian line profile. The line profiles were fitted using the python-package LMFIT (Newville et al. 2014). These line profiles have been used to obtain the integrated fluxes of a larger set of transitions, including lines that are partly blended with other transitions and/or have a lower S/N -ratio. For ^{12}CO $v=3-2$, no blended transitions are included, as we were unable to extract reasonable (compared with respect to the unblended lines) fluxes. The integrated fluxes have been acquired using the method described in Banzatti et al. (2012), based on the techniques provided in Pascucci et al. (2008); Najita et al. (2010) and Pontoppidan et al. (2010). In short, we invoke 1000 iterations of adding normally distributed noise to the observed flux. For each iteration, we determine the integrated flux and, subsequently, acquire a Gaussian distribution of measured line fluxes. We use the median of this distribution as the actual line flux and take the FWHM as the uncertainty.

To obtain information about both components, we carried out the rotational diagram analysis for all observed components separately. If the rotational diagrams consist of a straight line, the excitation temperature can be derived from the inverse of the slope of a fitted straight line, whereas the column density is given by the intercept. If the diagrams display curvature, which is an indication of optically thick emission (see Section 6.5.3.1), slab models must be used to properly derive the excitation conditions. Similarly as above, we have obtained the CO spectroscopic data from the HITRAN database. The best fitting values for T , N , and R_{em} have, similar to the slab-model fitting procedure, been acquired through a χ^2 -analysis, where σ in equation (4.7) now denotes the acquired error on the integrated flux. For the iSHELL data, we have used slightly different grids for the column density and temperature, but with the same step sizes: $14 \leq \log(N) \leq 22 \text{ cm}^{-2}$, $300 \leq T \leq 3000 \text{ K}$. For the emitting radius we adjusted both the grid and the stepsize into, respectively, $0.01 \leq R_{\text{em}} \leq 1 \text{ au}$ and $\Delta R_{\text{em}} = 0.001 \text{ au}$. We have used the same grid for the different isotopologues and vibrational transitions.

2.4 Results

We present the results of our analysis in the following subsections. In particular, we highlight the observed molecular species with JWST-MIRI (CO_2 , HCN, and C_2H_2) in Section 2.4.1 and we provide an extensive analysis of the CO emission in Section 2.4.2, including our results regarding the excitation conditions, the line profiles, the optical depth, and the emitting radius.

2.4.1 JWST spectrum and detected molecules

The JWST-MIRI spectrum of DR Tau presented in Figure 3.1 is very line-rich. Most of the visible lines correspond to H_2O transitions, which are analysed in (Temminck et al. 2024a). Here, we focus on the molecules, besides H_2O and OH, for which transitions are covered by JWST-MIRI. The bottom panel of Figure 3.1 also contains a zoom-in on the CO transitions ($J \geq 25$), highlighting the strong emission features.

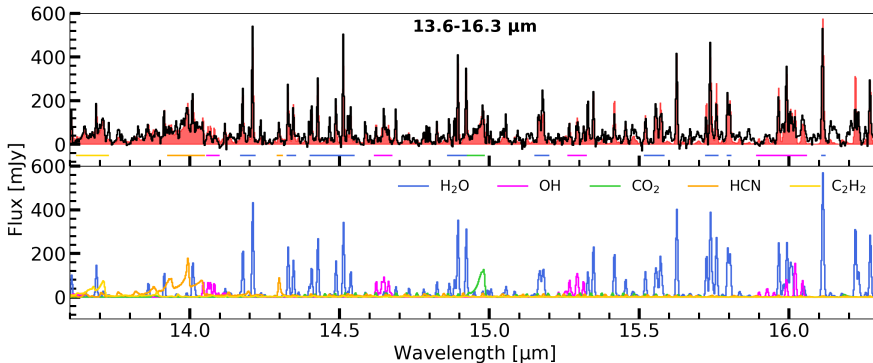


Figure 2.4: Best-fitting slab models of $^{12}\text{CO}_2$, HCN, and C_2H_2 in the 13.6-16.3 μm wavelength region. The top panel displays the continuum subtracted JWST spectrum in a specific region, while the full model spectrum is shown in red. In addition, the horizontal bars show for each molecule the spectral windows used in the χ^2 fits. The bottom panel shows the models for the individually detected molecules. The H_2O and OH slab models are shown for completeness. Their model properties are presented in (Temminck et al. 2024a)

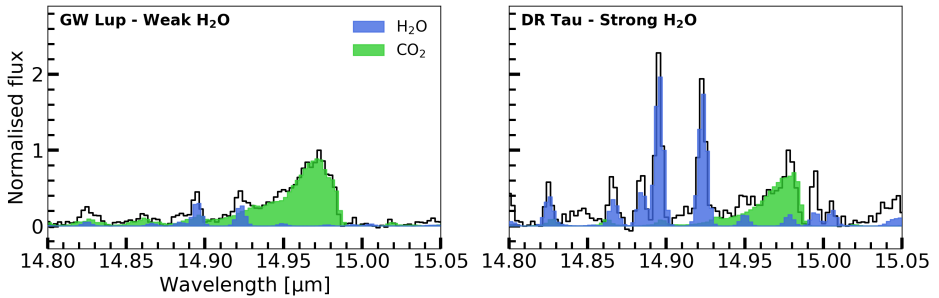
We detect emission from CO, CO_2 , HCN, and C_2H_2 . Table 2.1 displays the parameters of the best fitting slab models for CO_2 , HCN, and C_2H_2 . The uncertainties listed have been derived from the minimum and maximum value for each parameter that falls within the 1σ -confidence interval. We also list the total number of molecules (\mathcal{N}), which is well constrained for optically thin emission. The total number of molecules has been calculated by multiplying the column density with the emitting area: $\mathcal{N} = N \pi R_{\text{em}}^2$. The best fitting slab models are displayed in Figure 3.B.1, whereas the χ^2 -maps are shown in Figure 2.C.1.

Table 2.1: Parameters of the best-fitting slab models for the different molecules observed with JWST-MIRI.

Molecule	$\log_{10}(N)$ [cm^{-2}]	T [K]	R_{em} [au]	\mathcal{N}
13.6-16.3 μm ($\sigma=2.19$ - 2.23 mJy)				
$^{12}\text{CO}_2$	$17.4^{+0.7}_{-0.2}$	325^{+50}_{-100}	$0.53^{+0.36}_{-0.06}$	4.96×10^{43}
HCN	$14.7^{+2.1}_{-0.6}$	900^{+50}_{-50}	$4.83^{+4.96}_{-4.38}$	8.22×10^{42}
C_2H_2	$15.0^{+5.6}_{-1.7}$	775^{+150}_{-625}	$1.45^{+8.56}_{-1.32}$	1.48×10^{42}

2.4.1.1 $^{12}\text{CO}_2$

The Q branch of $^{12}\text{CO}_2$ is well detected in DR Tau, whereas individual P - and R branch, and the hot-bands are not strongly detected. Our fit only extends over the Q branch, which yields a column density of $N=10^{17.4} \text{ cm}^{-2}$, a gas temperature of $T=325$ K and an emitting radius of $R=0.53$ au. Compared to H_2O , our $^{12}\text{CO}_2$ Q branch is significantly weaker. This is similar to Sz 98 (Gasman et al. 2023) and EX Lup (Kóspál et al. 2023), but totally the opposite for GW Lup (Grant et al. 2023b) and PDS 70 (Perotti et al. 2023). The difference with GW Lup is also visualised in Figure 2.5, which displays a zoom-in on the normalised $^{12}\text{CO}_2$ Q branch. As opposed to GW Lup, we do not detect any emission signature from $^{13}\text{CO}_2$.

**Figure 2.5:** Zoom-in on the $^{12}\text{CO}_2$ Q branch (14.80-15.05 μm) of GW Lup (left; Grant et al. 2023b) and DR Tau (right). Both spectra have been scaled to a common distance of 150 pc and normalised to the peak of the $^{12}\text{CO}_2$ Q branch.

2.4.1.2 HCN & C_2H_2

Similar to GW Lup (Grant et al. 2023b), but contrarily to PDS 70 (Perotti et al. 2023), we detect HCN and C_2H_2 in the wavelength region of 13.6-16.3 μm . The HCN Q branch ($\sim 14 \mu\text{m}$) and hot-band ($\sim 14.3 \mu\text{m}$) are both strongly detected. The emission is likely optically thin, which causes the column densities and emitting radius to be degenerate (see also Figure 2.C.1). Nonetheless, our best-fitting slab model suggests a column density of $N=10^{14.7} \text{ cm}^{-2}$, a temperature of $T=900$

K, and an emitting radius of $R=4.83$ au.

The parameters of C_2H_2 ($\sim 13.7 \mu\text{m}$) are much less constrained compared to those of HCN. Similar to GW Lup, the inferred column density is on the border between optically thin and thick, which adds another degeneracy: for high column densities, there is a degeneracy between the column density and the gas temperature. For C_2H_2 we find a best-fitting column density of $N=10^{15.0} \text{ cm}^{-2}$, a temperature of $T=775$ K, and a emitting radius of $R=1.45$ au.

2.4.2 CO analysis

As the main focus of this paper is the CO emission and a comparison between the JWST-MIRI and IRTF-iSHELL observations, this following section presents the results of the extensive CO analysis.

2.4.2.1 ^{12}CO as seen by JWST-MIRI

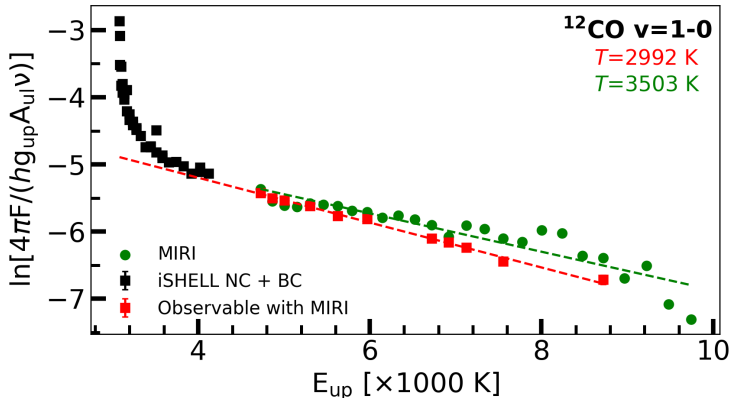


Figure 2.6: Rotational diagram of the ^{12}CO $v=1-0$ transitions. As JWST-MIRI is unable to distinguish between the narrow (NC) and broad (BC) components, their contributions have been added together. The black squares indicate the fluxes inferred from the iSHELL observations, while the ones marked denote the transitions that are also observable with JWST-MIRI. Errorbars on the iSHELL observations are plotted, however, these are too small with respect to the size of the squares. The circles in green are the integrated fluxes inferred from the JWST-MIRI observations using a pseudo-Voigt profile. The red, dashed line is a fit to the red points, used to derive what excitation temperature JWST-MIRI would probe as seen with the iSHELL observations ($T=2992\pm 40$ K). The green dashed line indicates the excitation temperature derived from these observations, $T=3503_{-269}^{+318}$ K.

For molecules, such as CO, with well identified individual ro-vibrational lines, the excitation is commonly analysed by plotting the integrated fluxes in a rotational diagram. Figure 2.6 shows in green the measured JWST-MIRI fluxes of ^{12}CO using a pseudo-Voigt profile (Labiano et al. 2021), assuming that the observable

flux originates in the $v=1-0$ lines, that is, we ignore any blending with the ^{12}CO $v=2-1$, $v=3-2$, and ^{13}CO $v=1-0$ transitions. Recall that JWST-MIRI only probes the transitions with the largest J values ($J \geq 25$) of the ^{12}CO P branch.

The temperature, T_{ex} , derived from such a rotational is given by the inverse of the slope, whereas the column density can be obtained from the intercept. For ^{12}CO , we acquire a temperature as high as $T_{\text{ex}}=3503_{-269}^{+318}$ K and a column density as low as $1.3 \times 10^{17} \text{ cm}^{-2}$ assuming an emitting area with a radius of 0.4 au (see Table 2.2). However, this simple analysis assumes that the line emission is optically thin. If the emission is optically thick, the inferred temperature can be much higher than the actual kinetic temperature. As demonstrated by, for example, Herczeg et al. (2011) (see their Appendix D) and Francis et al. (2024), optically thick line emission introduces a curvature at medium J values. This curvature causes the high- J transitions (probed by JWST-MIRI) to mimic much higher excitation temperatures than the kinetic one when only those transitions are fitted in a diagram.

We emphasise this point by including the integrated iSHELL fluxes of the ^{12}CO $v=1-0$ transitions in Figure 2.6, with the black and red squares obtained by taking the sum over the narrow and broad components. The red squares mark the transitions that are observable with JWST-MIRI and, as seen in the Figure, some small differences are visible in the measured fluxes with respect to JWST-MIRI, as we have not accounted for the blending of lines in the JWST-MIRI spectrum. As shown in Figure 2.D.5, many of the ^{12}CO $v=1-0$ transitions are blended with other lines, while only a handful are unblended, some of which are highlighted in Figure 2.D.5, whereas a few more can be found at longer wavelengths ($\geq 5.18 \mu\text{m}$). Such blending will be worse for sources with higher intrinsic line wings (e.g. sources with outflows or galaxies), where one may not be able to detect any unblended line at all.

The iSHELL fluxes clearly show a curvature in the rotational diagrams. For comparison, we fitted a straight line to the iSHELL integrated fluxes that cover the JWST-MIRI wavelength range (the red squares). The fit yields an excitation temperature of $T_{\text{ex}}=2992 \pm 40$ K. As will be demonstrated in Section 2.4.2.2 (see Table 2.2), the inferred temperatures are much lower when the iSHELL observations are fitted over the full range of J values with a LTE slab model that accounts for optical depth. This demonstrates the importance of having information on the fluxes of the lower- J lines.

As mentioned before, JWST-MIRI's resolution is not sufficient to distinguish between the two components present in the complex line profile of ^{12}CO . The total ^{12}CO line profile can, on the other hand, only be marginally resolved with JWST-MIRI. For unblended ^{12}CO $v=1-0$ transitions (see Section 2.4.2.6), we infer values for the FWHM in the range of $\sim 84-100 \text{ km s}^{-1}$, which are slightly larger than JWST-MIRI's velocity resolution of $\sim 80 \text{ km s}^{-1}$ (Labiano et al. 2021). The narrow component, tracing the disk wind, could potentially be observed with JWST-MIRI as extended emission. However, no extended emission is observed in the CO lines.

2.4.2.2 iSHELL CO line profiles and rotational diagrams

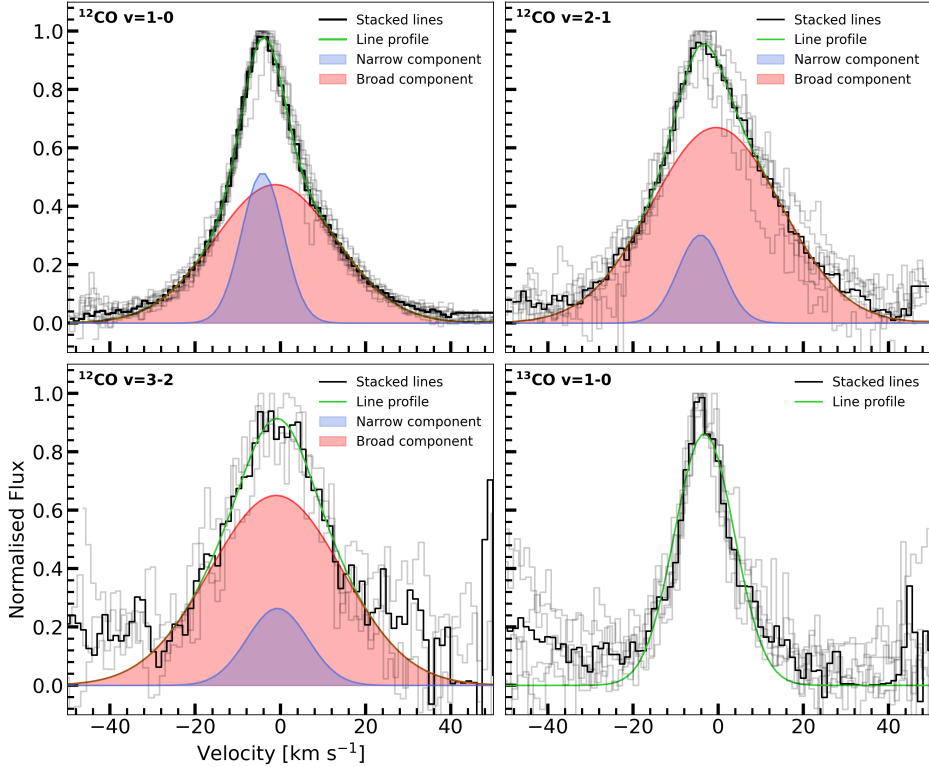


Figure 2.7: Fitted iSHELL line profiles for the $^{12}\text{CO } v=1-0$, $v=2-1$, $v=3-2$, and the $^{13}\text{CO } v=1-0$ transitions. The median line profile is shown in black, whereas the fitted line profile is shown in green. For the ^{12}CO transitions, we have indicated the narrow and broad components in, respectively, blue and red. The faint, grey line profiles visible in the background correspond to the individual line profiles used in creating the weighted-averaged, normalised line profile.

A proper analysis of the high-resolution, ground-based CO observations starts with a thorough analysis of the line profiles. The line profiles are displayed in Figure 2.7, whereas the acquired values for ΔV and the FWHM are listed in Table 2.2. The rotational diagrams themselves are displayed in Figure 2.8, while the best-fit parameters, for the broad and narrow components, are summarised, together with the values for the average FWHM and ΔV , in Table 2.2. The rotational diagrams (Figure 2.8) of the ^{12}CO vibrational ladders and $^{13}\text{CO } v=1-0$ transitions are presented separately. In addition, we separated out the narrow and broad components for ^{12}CO . For the broad component we find consistently higher integrated fluxes and excitation temperatures compared to those of the narrow one. All diagrams display an upward curvature at the lower end of the E_{up} range, suggesting optically thick emission. Optical depth is further discussed in Section

6.5.3.1. We do not list any uncertainties on the best fitting parameters (T and N), but they can be viewed in Figure 2.D.2. Models, based on the rotational diagrams, for the transitions of ^{12}CO $v=1-0$ (red), $v=2-1$ (blue), $v=3-2$ (green), and ^{13}CO $v=1-0$ (yellow) are displayed in Figure 2.D.1, while a zoom-in on the 4.68–4.72 μm region is shown in Figure 2.9, to provide a better view of how well the model fits the data.

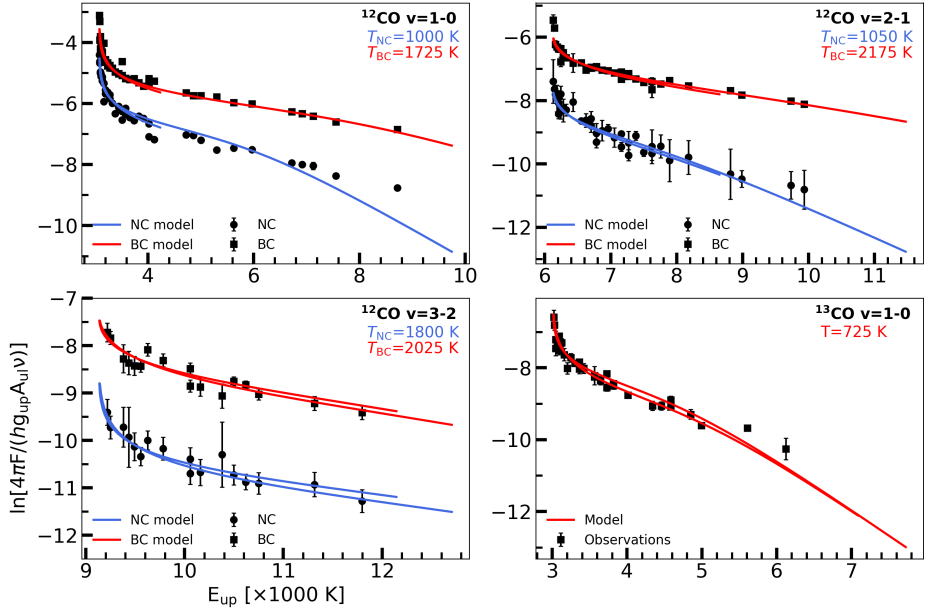


Figure 2.8: Rotational diagrams for ^{12}CO $v=1-0$ (top left), $v=2-1$ (top right), $v=3-2$ (bottom left), and ^{13}CO $v=1-0$ (bottom right). In each panel, the slab models are given by the solid line. For the ^{12}CO transitions, the narrow and broad components (NC and BC, respectively) are shown separately. The integrated fluxes for the narrow component are given by the dots, while those for the broad component are indicated by the squares. The two lines in each model correspond the R - and P branches.

We find column densities in the range of 1.6×10^{17} – 5.0×10^{18} cm^{-2} for the different transitions and temperatures of 725–2175 K. We find that the narrow components of the various ^{12}CO ro-vibrational transitions trace colder temperatures (respectively, 1000, 1050, and 1800 K) compared to the broad components (respectively, 1725, 2175, and 2025 K), confirming the different origins of the two components and suggesting that the broad component does trace the hot inner regions of the disk. For ^{13}CO we find a significantly lower temperature of 725 K, which is slightly higher than the value reported by Bast et al. (2011) and Brown et al. (2013) of $T=510$ – 570 K. However, both Bast et al. (2011) and Brown et al. (2013) used only transitions with $E_{\text{up}} \sim 3000$ – 4000 K, whereas our data include transitions with values of E_{up} up to ~ 6200 K.

Table 2.2: Best fit parameters acquired through the rotational diagram analysis for the iSHELL data.

Molecule	Vibr. Trans.	$\Delta V^{(\alpha)}$ [km s ⁻¹]	FWHM [km s ⁻¹]	N [cm ⁻²]	T [K]	R_{em} [au]	$\mathcal{N}^{(\beta)}$
¹² CO	v=1-0 (NC)	-4.2	11.6	3.2×10^{17}	1000	0.46	$>4.6 \times 10^{43}$
	v=1-0 (BC)	-1.2	33.5	6.3×10^{17}	1725	0.38	$>6.3 \times 10^{44}$
	v=2-1 (NC)	-4.1	12.5	7.9×10^{17}	1050	0.21	$>2.3 \times 10^{43}$
	v=2-1 (BC)	-0.5	35.8	5.0×10^{17}	2175	0.22	$>1.6 \times 10^{43}$
	v=3-2 (NC)	-0.7	16.9	5.0×10^{18}	1800	0.05	$>8.8 \times 10^{42}$
	v=3-2 (BC)	-1.0	36.6	1.6×10^{18}	2025	0.13	$>1.9 \times 10^{43}$
¹³ CO	v=1-0	-3.2	16.5	1.6×10^{17}	725	0.47	$>2.4 \times 10^{43}$
C ¹⁸ O	v=1-0	-4.2	10.3	2.0×10^{16}	975	0.23	7.4×10^{41}

Notes. (α): ΔV is the offset of the line centre with respect to the heliocentric velocity of DR Tau, ~ 27.6 km s⁻¹.

(β): As both ¹²CO and ¹³CO are found to be optically thick (see Section 6.5.3.1), the values listed for the total number of molecules must be treated as lower limits.

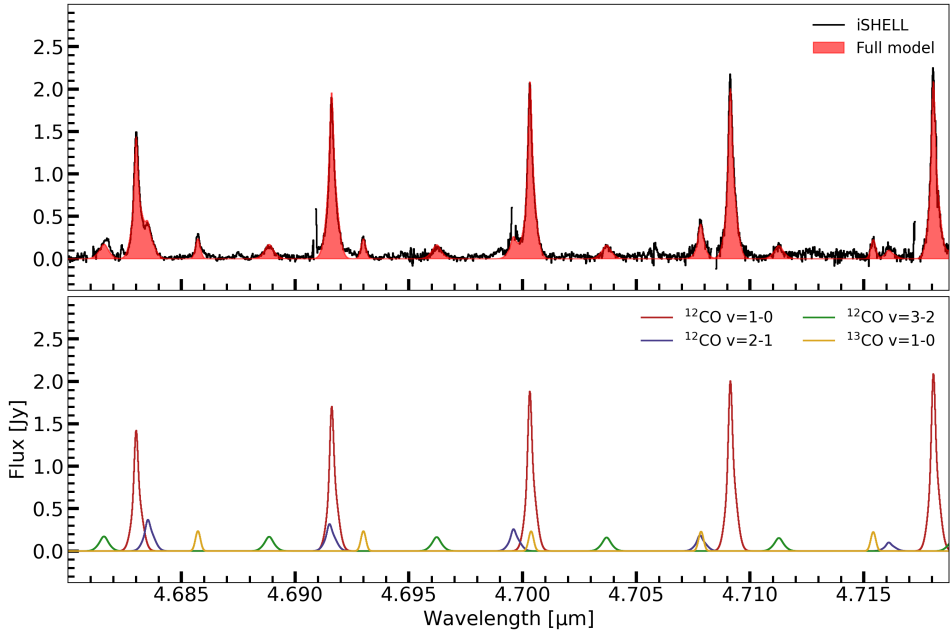


Figure 2.9: Zoom-in (4.68-4.72 μm) of the continuum-subtracted iSHELL spectrum of DR Tau with a model based on the best-fitting parameters obtained through the rotational diagram analysis. A full version can be found in Figure 2.D.1.

2.4.2.3 Optical depth: ^{12}CO and ^{13}CO

As previously found by Brown et al. (2013), the ^{12}CO emission of DR Tau is optically thick. Similarly as their Figure 11, Figure 2.D.3 displays the rotational diagrams of the ^{12}CO $v=1-0$, where we have combined the narrow and broad components, and ^{13}CO $v=1-0$ transitions together. In addition, we have multiplied the best fitting model of ^{13}CO by a factor of 68 to account for the isotopologue ratio as in the solar neighbourhood (Milam et al. 2005; $^{12}\text{C}/^{13}\text{C}=68\pm 15$). If ^{12}CO were optically thin, the scaled ^{13}CO model would have coincided with the ^{12}CO fluxes. However, we see that the scaled ^{13}CO lies above the ^{12}CO fluxes, confirming in a similar manner as Brown et al. (2013) that ^{12}CO is optically thick. Furthermore, ^{12}CO being optically thick is also confirmed by the shape of the line fluxes. As shown by Herczeg et al. (2011) (see their Figure D.1), for optically thin emission one would expect a straight line, whereas if the emission becomes optically thick the fluxes of the lines with higher upper level energies flatten off. Furthermore, as seen in Figure 2.D.3, the ^{13}CO $v=1-0$ model is also not completely a straight line, suggesting that the ^{13}CO is also (moderately) optically thick. However, as the ^{13}CO emission is less optically thick, a better lower limit on the total number of molecules can be obtained by multiplying the total number of molecules found for ^{13}CO by the isotopologue ratio of 68. This multiplication yields a total number of molecules of $\mathcal{N}_{\text{CO}} \simeq 1.6 \times 10^{45}$.

As the ^{13}CO emission is also (moderately) optically thick, rarer, less optically thick isotopologues are needed to infer the total amount of molecules. While C^{18}O is not detected in the iSHELL observations, the $v=1-0$ transitions are detected in the VLT-CRIRES data of Bast et al. (2011). For a description of the data, we refer to Bast et al. (2011) and Brown et al. (2013). We also scale the VLT-CRIRES data to match the JWST-MIRI flux at $\sim 5 \mu\text{m}$. Using the same approach as described in Section 2.2.3, we carry out a rotational diagram analysis for the C^{18}O $v=1-0$ transitions to obtain a better estimate for the total number of molecules.

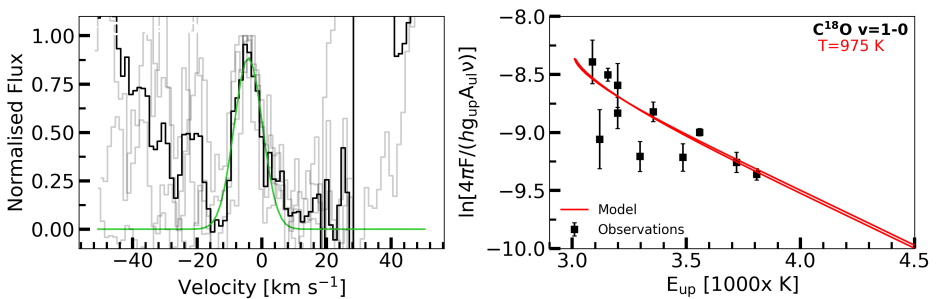


Figure 2.10: Inferred Gaussian line profile (left panel) and rotational diagram (right panel) for the C^{18}O $v=1-0$ transitions. The rotational diagram yields an excitation temperature of $T=975$ K.

First, for the C^{18}O line profile we find a velocity offset of $\Delta V = -4.2 \text{ km s}^{-1}$

with respect to DR Tau’s heliocentric velocity and a FWHM of 10.3 km s^{-1} . Second, the rotational diagram yields an excitation temperature of $T=975 \text{ K}$, a column density of $N=2.0 \times 10^{16} \text{ cm}^{-2}$, and an emitting radius of $R_{\text{em}}=0.23 \text{ au}$. The acquired line profile and rotational diagram are displayed in, respectively, the left and right panel of Figure 2.10. The χ^2 -map, visualising the uncertainties of the fit, is shown in the bottom right panel of Figure 2.D.2. The inferred excitation temperature for C^{18}O is found to be higher than that of ^{13}CO . However, the χ^2 -maps of C^{18}O show a large contour for the 1σ uncertainty, suggesting that the temperatures agree within the uncertainties. Finally, multiplying the column density by the corresponding emitting area yields a total number of molecules of $\mathcal{N}=7.4 \times 10^{41}$, which multiplied by the isotopologue ratio of $^{16}\text{O}/^{18}\text{O}=557 \pm 30$ (Wilson 1999) yields $\mathcal{N}_{\text{CO}}=4.1 \times 10^{44}$.

2.4.2.4 Estimated emitting radii of CO

Previous studies (e.g. Salyk et al. 2011a; Banzatti & Pontoppidan 2015; Banzatti et al. 2022) have shown that the emitting radius where the line flux peaks can be estimated from the line profiles using Kepler’s law, as the emission is broadened by the Keplerian rotation:

$$R = GM_* \left(\frac{\sin(i)}{\Delta v} \right)^2, \quad (2.2)$$

where i is the inclination and Δv is the line width, often taken to be equal to the half width at half maximum (HWHM). The inner emitting radius can, subsequently, also be estimated by taking Δv equal to the half width at 10% (HW10%; Banzatti et al. 2022). Both the HWHM and the HW10% have been derived from the averaged line profiles displayed in Figure 2.7, for simplicity we have taken the HWHM equal to half the FWHM listed in Table 2.2. Assuming the inclination of the inner disk of DR Tau to be equal to the inclination of the outer disk, we use $i=5.4^\circ$ (Long et al. 2019). Furthermore, as this method only applies to the lines broadened by the Keplerian rotation, we calculate the (inner) emitting radius only for the broad components of the different ^{12}CO line profiles and the ^{13}CO $v=1-0$ line profile. The calculated values are listed in Table 2.3.

All the calculated emitting radii (R_{CO}) differ significantly from those inferred through the rotational diagrams. One potential explanation for the differences can be found in the chosen value for the inclination. The used inclination has been derived from the continuum emission as probed by ALMA. However, inner disks can be misaligned with respect to the outer disk, for instance caused by perturbations induced by companions (see, for example, Bohn et al. 2022). By testing a wide variety of larger inclinations, we infer that inclinations of, respectively, 20.1° , 22.4° , 23.0° , and, 10.2° are required to match the corresponding emitting radii for the broad components of the various ^{12}CO vibrational transitions and the ^{13}CO $v=1-0$ transitions inferred from the rotational diagrams. This holds for the assumption that these emitting radii correspond to circular area enclosing the host star. As the high inferred excitation temperatures suggest that the emission of the broad component must originate from inside the dust sublimation radius, this assump-

Table 2.3: Derived (inner) emitting radii for the ro-vibrational transitions of ^{12}CO and ^{13}CO using an inclination of $i=5.4^\circ$.

Molecule	Vibr. Trans.	HWHM [km s $^{-1}$]	R_{CO} [au]
^{12}CO	v=1-0	16.8	0.03
	v=2-1	17.9	0.02
	v=3-2	18.3	0.02
^{13}CO	v=1-0	8.3	0.11
Molecule	Vibr. Trans.	HW10% [km s $^{-1}$]	$R_{\text{CO,in}}$ [au]
^{12}CO	v=1-0	29.5	0.01
	v=2-1	32.0	0.01
	v=3-2	32.7	0.01
^{13}CO	v=1-0	14.4	0.04

tion may be valid for DR Tau. Such a higher inferred inclination of the inner disk agrees with the value of $i_{\text{inner}} \sim 18_{-18}^{+10^\circ}$ derived by GRAVITY Collaboration et al. (2021) using VLTI-GRAVITY observations. It must be noted, however, that the uncertainties on this inclination also encompass the inclination of the outer disk ($i_{\text{outer}}=5.4_{-2.6}^{+2.1^\circ}$). Although this cannot yet be confirmed, the VLTI-GRAVITY observations and the CO line profiles both hint at a misalignment between the inner and outer disk.

2.4.2.5 LTE versus non-LTE

When using slab models or creating rotational diagrams, LTE is (almost) always assumed, but the question remains whether this is a valid assumption. A simple test to see if all ^{12}CO emission lines can be characterised by a single temperature can be carried out by using the ^{12}CO v=1-0 best-fit parameters for the v=2-1 transitions. If the v=1-0 parameters reproduce the observed v=2-1 fluxes, the emission can be considered in LTE. Otherwise, the vibrational excitation is in non-LTE and the various transitions need to be considered separately, as we have done for the high-resolution observations. The right panel of Figure 2.D.4 shows the model prediction of the ^{12}CO v=2-1 transitions using the best-fit parameters of the v=1-0 transitions (see Table 2.2). As can be seen, the model overpredicts the emission of the ^{12}CO v=2-1 transitions, confirming that the vibrational excitation is not in LTE. The various vibrational transitions thus need to be considered separately, while the rotational populations can still be in LTE.

Our findings are not surprising, considering the work by Bast et al. (2011). They find a higher vibrational temperature ($T \sim 1700$ K) for DR Tau, while only a temperature of $T \sim 500$ K for the rotational ^{13}CO lines. Higher vibrational temperatures are more commonly found for Herbig Ae/Be stars (e.g. Brittain et al. 2007 and van der Plas et al. 2015), which may be attributed to their higher UV fields and subsequent UV-pumping into the higher vibrational states. For

T-Tauri stars, UV-pumping into the higher vibrational states can be achieved through higher UV fluxes following accretion by the host star (Valenti et al. 2000). As DR Tau is known to be an actively accreting system, UV-pumping provides a possible explanation for the higher vibrational temperatures found by Bast et al. (2011).

2.4.2.6 Implication for JWST-MIRI analysis

While the LTE slab model of ^{12}CO fitted to the JWST-MIRI observations (see Table 2.1) roughly agrees with the excitation parameters found for the ^{12}CO $v=1-0$ broad component (see Table 2.2), these results must be treated with caution. As mentioned before, the JWST-MIRI observations do not have the spectral resolution to distinguish between the broad and narrow components observed for ^{12}CO and, as discussed in Section 2.4.2.5, the CO emission is not in LTE, suggesting that the observed emission cannot be described by a single temperature. In the following section, we explore how the slab models fitted to the rotational diagrams of the iSHELL observations can be used to describe the CO emission as observed by JWST-MIRI.

The main difference between the JWST-MIRI and iSHELL observations is the spectral resolution of JWST-MIRI, which does not allow one to distinguish between the narrow and broad components (this also holds for JWST-NIRSpec), as displayed in Figure 2.7. In addition, as mentioned before, the JWST-MIRI observations only cover the high- J transitions of the P branch. The excitation temperature as probed by JWST-MIRI would, subsequently, not only be affected by the combination of both components (likely approaching the weighted average of the two), but would also be biased to higher excitation temperatures following the inclusion of only transitions with high upper level energies. As discussed in Section 2.4.2.1 and displayed in Figure 2.6, a temperature of ~ 2992 K is acquired from the lines covered by JWST-MIRI, which is significantly higher than probed by the high-resolution iSHELL observations. Additionally, as shown in Figure 2.3, various transitions that are unblended in the iSHELL spectrum are blended in the JWST-MIRI one. Subsequently, it is harder to identify the contributions from the various (vibrational) transitions in JWST-MIRI's spectrum.

To be able to compare the CO emission observed with iSHELL and JWST-MIRI, and, more importantly, to show that we probe the same emission with both instruments, we bin our iSHELL model to JWST-MIRI's lower spectral resolution and convolve the binned model with JWST-MIRI's line profile. The binning was carried out using the python-package SPECTRES, whereas the convolution was implemented using ASTROPY and a kernel based on JWST-MIRI's line profile. As discussed in Labiano et al. (2021), JWST-MIRI's line profile is best described by a pseudo-Voigt profile, which is a weighted sum between a Gaussian and a Lorentzian profile (see Equation 2.3). In comparison, a normal Voigt profile is given by the convolution of a Gaussian and Lorentzian profile. To create the convolution kernel, we first identified the strongest, unblended ^{12}CO $v=1-0$ transitions in the JWST-MIRI spectrum. These lines are displayed in Figure 2.D.5. Subsequently, we created an average, normalised line emission profile, which is displayed

in Figure 2.D.6, by considering the 7 resolution elements enclosing the line peaks (blue shaded areas in Figure 2.D.5). Finally, we used LMFIT to fit a pseudo-Voigt profile to the averaged emission, which is also shown in Figure 2.D.6. The fitted pseudo-Voigt profile was, subsequently, adopted as our convolution kernel.

The used pseudo-Voigt profile is described by the following equation:

$$f(x; A, \mu, \sigma_f, \alpha) = \frac{(1 - \alpha)A}{\sigma_g \sqrt{2\pi}} e^{-(x-\mu)^2/2\sigma_g^2} + \frac{\alpha A}{\pi} \left[\frac{\sigma_f}{(x - \mu)^2 + \sigma_f^2} \right]. \quad (2.3)$$

Here, A denotes the amplitude, μ the centre of the line, σ_f describes the width, and α gives the weights. Furthermore, σ_g is defined as $\sigma_g = \sigma_f / \sqrt{2 \ln(2)}$. Table 2.4 gives the best fitting values and their confidence intervals for A , μ , σ_f , and α .

Figure 2.11 shows our results: the top panel shows the full CO model on

Table 2.4: Best-fitting values and the corresponding confidence intervals for the pseudo-Voigt profile used to characterise the JWST-MIRI line profile.

Parameter ⁽¹⁾	Value	Confidence interval
A	2.99	± 0.22
μ	2.84	± 0.06
σ_f	1.03	± 0.08
α	0.76	± 0.20

Notes. (1): the units of the listed parameters are all arbitrary, see also Figure 2.D.6.

top of the iSHELL observations, whereas the middle and bottom panel shows the model on top of the JWST-MIRI data after applying the binning and convolution, respectively. As clearly shown in the middle panel, solely binning the high-resolution model down to JWST-MIRI's resolution does not provide a good fit, as the peak flux is clearly overproduced. The subsequent convolution, on the other hand, yields a good description of the JWST-MIRI observations, as is shown in the bottom panel. To conclude, by binning a high-resolution model to JWST-MIRI's spectral resolution and by convolving the model with JWST-MIRI's line profile, we have shown that the high-resolution observations can be used as a good template for the JWST-MIRI observations and that a proper treatment of the line profile is crucial.

We note that, even after convolution, the model does not provide a perfect fit to the JWST-MIRI observations. The small residual differences are potentially related to uncertainties of the flux calibration of the iSHELL observations or the different sensitivities of the instruments. In addition, stellar variability at the 20% level cannot be excluded as an explanation. Nonetheless, we have shown and argue that the best way to characterise the CO lines observed with JWST-MIRI is to combine them with high spectral resolution observations of ground-based instruments, such as iSHELL or VLT-CRIRES(+), that are publicly available for many sources through SpExoDisks.

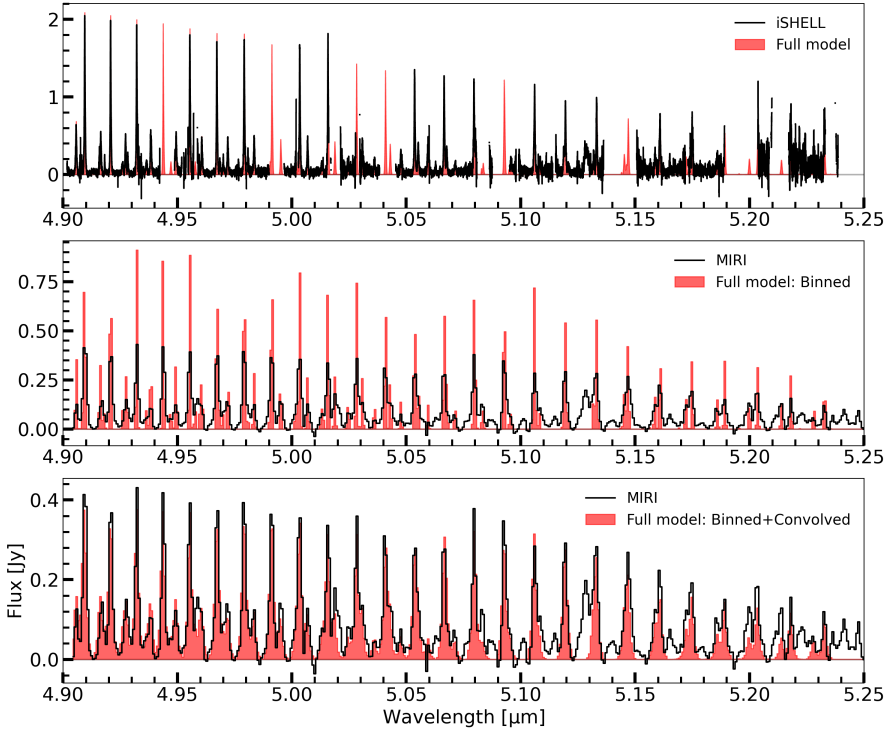


Figure 2.11: The top panel shows the continuum-subtracted iSHELL data (black) with the best-fitting model (red) based on the various slab model fits to the rotational diagrams over the 4.90-5.25 μm wavelength region. The middle panel shows the best fitting model binned to the JWST-MIRI resolution together with the JWST-MIRI observations, whereas the bottom panel shows the model convolved with the pseudo-Voigt profile shown in Figure 2.D.6.

2.4.2.7 JWST-MIRI line profile: Pseudo-Voigt versus Gaussian

As line profiles are often considered to be of pure Gaussian nature, we discuss in this subsection the different results one may acquire when treating JWST-MIRI's line profile as a Gaussian. When using a Gaussian line profile, we derive integrated fluxes that are 10% or less smaller than those acquired when using a pseudo-Voigt profile. Figure 2.D.7 compares the JWST-MIRI rotational diagrams when considering the different line profiles. A straight line fitted to the Gaussian integrated fluxes yields an excitation temperature of $T=3565^{+368}_{-305}$ K, which is slightly higher than the one ($T=3503^{+318}_{-269}$ K) probed when using a pseudo-Voigt profile. The temperatures do, however, agree well within the uncertainties.

In addition, we reproduce the analysis conducted in Section 2.4.2.6 for a Gaussian line profile, given by the first part of Equation 2.3 (setting $\alpha=0$). Figure 2.D.6 contains the fitted Gaussian line profile to the normalised, unblended ^{12}CO transitions, which is described by the following parameters: $A=2.40$, $\mu=2.85$, and

$\sigma_g=0.98$. The bottom panel of Figure 2.D.8 shows the convolution of the binned CO model with the Gaussian line profile. A close visual comparison between Figures 2.11 and 2.D.8 yields only small differences between the two convolutions: the main difference can, as expected, be found in the line wings of the convolved model. The Lorentzian contribution ensures that the pseudo-Voigt profile provides a better fit to the line wings compared to the Gaussian one. On the other hand, the Gaussian convolution can yield a model with slightly higher peak values, as less flux is distributed over the line wings.

Even though the Gaussian convolution yields similar results as the pseudo-Voigt one, the pseudo-Voigt profile, as found by Labiano et al. (2021), provides a significantly better description of the JWST-MIRI observations in subband 1A, as demonstrated by Figure 2.11. Depending on the application, a Gaussian profile may provide a sufficient fit to the observations, but one must take into consideration that the flux in the line wings will be underproduced.

An incorrect treatment of the line profile can also impact the analysis of the excitation conditions, as the underproduced line wings may result in an underestimation of the line fluxes. For example, the integral of the Gaussian line profile displayed in Figure 2.D.6 is $\sim 5\%$ lower than that of the Pseudo-Voigt line profile. Consequently, a rotational diagrams analysis can yield a lower value on the total column density and a different value for the excitation temperature, depending on how the slope is changed by these underestimated fluxes.

2.5 Discussion

2.5.1 CO excitation temperature as probed by JWST-MIRI

As shown in Figure 2.6, the excitation temperature derived when only considering the high- J transitions observed by JWST-MIRI, assuming optically thin emission, is significantly higher than that derived from a rotational diagram that includes also lower- J values. As discussed in Section 2.4.2.1, the higher excitation temperature follows from the fact that the ^{12}CO emission is optically thick. We emphasise the need for complementary observations when deriving the excitation properties of CO, either from space (e.g. with JWST-NIRSpec) or from the ground (e.g. with VLT-CRIRES(+), IRTF-iSHELL or Keck-NIRSPEC). If only space-based observations are used, we advise to treat the results with caution, since JWST-NIRSpec and JWST-MIRI do not have the spectral resolution to resolve the commonly observed, complex CO line profiles of planet-forming disks (see also Banzatti et al. 2022, 2023b).

2.5.2 Emitting region of CO

The high inferred excitation temperatures of $T \geq 1725$ K suggest that the broad component of the ^{12}CO emission must come from inside the dust sublimation radius ($T_{\text{dust}} \simeq 1500$ K) as also indicated in Figure 14 of Banzatti et al. (2022). Alternatively, the emission may originate from an elevated layer of the disk's atmosphere, where the gas temperature can be well above that of the dust. The

^{13}CO emission, on the other hand, should trace a deeper layer of the disk, as it is less optically thick compared to ^{12}CO , consistent with the lower probed excitation temperature. Depending on the flaring of the inner disks, the emission originating from these elevated emitting layers (as seen from the disk's midplane) could also explain the larger inclinations, or viewing angles, required for the emitting radii derived from the CO line profiles and slab models fitted to the rotational diagrams to match. Alternatively, a misalignment between the inner and outer disks, as hinted at by the VLTI-GRAVITY and ALMA observations, may also explain the required inclinations.

Thermo-chemical models have shown that the gas temperature in the inner regions of T-Tauri disks, in particular the elevated layers, can reach temperatures of ≥ 1000 K (Thi et al. 2013; Bruderer et al. 2015; Walsh et al. 2015; Woitke et al. 2018). These high temperatures further strengthen the notion that the CO emission must originate from the region inside of the dust sublimation radius and/or elevated layers of the disk.

2.5.3 Comparing the emitting properties of CO with the other molecules

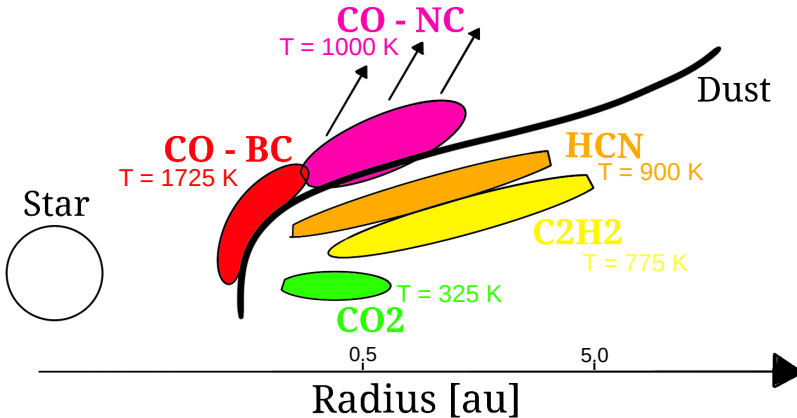


Figure 2.12: Cartoon visualising the expected emission regions, based on the slab models and interpreting the emitting radius as the disk radius, for our investigated molecules (CO, CO₂, HCN, and C₂H₂).

Compared with the other molecules studied here, CO₂, HCN, and C₂H₂, the excitation temperatures probed by CO are much higher. It must be noted that the temperatures inferred for CO₂, HCN, and C₂H₂ are similar to those in the other T-Tauri disks, GW Lup and Sz 98 (Grant et al. 2023b; Gasman et al. 2023). Models by Woitke et al. (2018) suggest that the emission likely originates from an onion-like structure, where CO has the highest emitting height and C₂H₂ the lowest. CO₂ and HCN originate from layers in between, with CO₂ originating from a slightly higher layer than HCN. Based on the derived excitation temperatures,

this is in partial disagreement with our slab modelling efforts, which suggest that the CO_2 emission should originate from either a deeper emitting layer or from a larger radial distance compared to that of HCN and C_2H_2 . The expected emission regions, based on our slab models, for the investigated molecules are visualised in Figure 2.12. Since the same findings hold for the disks around GW Lup and Sz 98, additional (thermo)chemical modelling work is necessary to explain the observations and to infer from which layers these molecules originate from.

2.6 Conclusions & summary

In this work we have investigated the JWST-MIRI observations of the disk around the young star DR Tau. In addition, we have used complementary, high resolution CO ro-vibrational observations to fully investigate the emission properties of CO. Below we summarise our main conclusions:

- We have confirmed the detections of CO, $^{12}\text{CO}_2$, HCN, and C_2H_2 with JWST-MIRI, all of which have been observed before with Spitzer and from the ground. With JWST-MIRI we are now able to better constrain the excitation conditions and find excitation conditions of $^{12}\text{CO}_2$, HCN, and C_2H_2 for DR Tau that are similar to those derived for GW Lup and Sz 98. The conditions suggest that HCN and C_2H_2 originate from a layer higher up in the disk's atmosphere than $^{12}\text{CO}_2$.
- Using high-resolution IRTF-iSHELL observations we have thoroughly analysed the CO emission properties using slab model fits to rotational diagrams. These observations cover various transitions of ^{12}CO $v=1-0$, $v=2-1$, and $v=3-2$, and ^{13}CO $v=1-0$. Similar to previous studies, we note that the ^{12}CO transitions are comprised of two components: a narrow and a broad component. The narrow part is linked to a potential inner disk wind, whereas the broad component is thought to arise from the Keplerian rotation of the disk. The high inferred temperatures (≥ 1725 K) for the broad component of the ^{12}CO transitions suggest that the emission likely originates from a high atmospheric layer and/or from inside the dust sublimation radius.
- In addition to the emitting radii inferred from the slab models, we have calculated the emitting radii based on the line profiles, which are found to be significantly smaller than those inferred from the rotational diagrams. To match the emitting radii, we require higher inclinations (or viewing angles if the emission comes from a flared elevated layer) of the inner disk of $i \sim 10\text{-}23^\circ$, suggesting, under the assumption that the inferred emitting radii correspond to a circular emitting area enclosing the host star, that the inner disk of DR Tau may be slightly misaligned with the respect to the outer disk ($i_{\text{outer}} \sim 5^\circ$).
- Based on the flux ratios and curvature visible in the rotational diagrams, we find that the ^{12}CO and ^{13}CO transitions are optically thick. Using C^{18}O transitions covered in VLT-CRIRES observations and applying the same

rotational diagram analysis, we have inferred a total number of molecules for CO in the inner disk (≤ 0.23 au) of DR Tau: $\mathcal{N}_{\text{CO}} \sim 4.1 \times 10^{44}$.

- Finally, we show that, to properly compare the JWST-MIRI and high-resolution, ground-based CO observations, one needs to bin the high-resolution model to JWST-MIRI’s spectral resolution and convolve the binned spectrum with a pseudo-Voigt profile.

With this work we emphasise that, although JWST-MIRI is a powerful instrument and is able to confidently detect the high- J transitions of CO, complementary, high-resolution observations are necessary to properly investigate the physical properties of the emitting gas. For DR Tau, the Keplerian CO emission must originate from inside the dust sublimation radius at temperatures of $T \geq 1725$ K, close to the host star. Other molecules, such as $^{12}\text{CO}_2$, HCN, and C_2H_2 are found to originate from farther out in the disk, with $^{12}\text{CO}_2$ likely originating from the deepest layer in the disk of DR Tau. In addition, the slow disk wind, as traced by the narrow component of ^{12}CO ($T \geq 1000$ K), is launched from a larger radial distance compared to the Keplerian emission.

Acknowledgements

The authors would like to thank Andrea Banzatti for the many very useful discussions.

This work is based on observations made with the NASA/ESA/CSA James Webb Space Telescope. The data were obtained from the Mikulski Archive for Space Telescopes at the Space Telescope Science Institute, which is operated by the Association of Universities for Research in Astronomy, Inc., under NASA contract NAS 5-03127 for JWST. These observations are associated with program #1282. The following National and International Funding Agencies funded and supported the MIRI development: NASA; ESA; Belgian Science Policy Office (BELSPO); Centre Nationale d’Etudes Spatiales (CNES); Danish National Space Centre; Deutsches Zentrum für Luft- und Raumfahrt (DLR); Enterprise Ireland; Ministerio De Economía y Competividad; Netherlands Research School for Astronomy (NOVA); Netherlands Organisation for Scientific Research (NWO); Science and Technology Facilities Council; Swiss Space Office; Swedish National Space Agency; and UK Space Agency.

This research used the SpExoDisks Database at www.spexodisks.com

M.T. and E.v.D. acknowledge support from the ERC grant 101019751 MOLD-ISK. E.v.D. acknowledges support from the Danish National Research Foundation through the Center of Excellence “InterCat” (DNRF150). B.T. is a Laureate of the Paris Region fellowship program, which is supported by the Ile-de-France Region and has received funding under the Horizon 2020 innovation framework program and Marie Skłodowska-Curie grant agreement No. 945298. D.G., V.C., I.A., A.O., and B.V. thank the Belgian Federal Science Policy Office (BELSPO) for the provision of financial support in the framework of the PRODEX Programme of the European Space Agency (ESA). V.C. and A.O. acknowledge fund-

ing from the Belgian F.R.S.-FNRS. G.P. gratefully acknowledges support from the Max Planck Society. T.H. and K.S. acknowledge support from the European Research Council under the Horizon 2020 Framework Program via the ERC Advanced Grant Origins 83 24 28. D.B. and M.MC have been funded by Spanish MCIN/AEI/10.13039/501100011033 grants PID2019-107061GB-C61 and No. MDM-2017-0737. A.C.G. acknowledges from PRIN-MUR 2022 20228JPA3A “The path to star and planet formation in the JWST era (PATH)” and by INAF-GoG 2022 “NIR-dark Accretion Outbursts in Massive Young stellar objects (NAOMY)” and Large Grant INAF 2022 “YSOs Outflows, Disks and Accretion: towards a global framework for the evolution of planet forming systems (YODA)”. I.K., A.M.A., and E.v.D. acknowledge support from grant TOP-1 614.001.751 from the Dutch Research Council (NWO). I.K. and J.K. acknowledge funding from H2020-MSCA-ITN-2019, grant no. 860470 (CHAMELEON). T.P.R acknowledges support from ERC grant 743029 EASY. L.C. acknowledges support by grant PIB2021-127718NB-I00, from the Spanish Ministry of Science and Innovation/State Agency of Research MCIN/AEI/10.13039/501100011033.

Appendix

2.A Continuum subtraction

This section provides the immediate steps of the continuum subtraction described in Section 2.2.2. The necessary images are shown in Figure 2.A.1. The top panel of this figure shows the final Savitzky-Golay filter (green) after all $>2\sigma$ emission lines (light grey) have been filtered, together with the line-filtered spectrum. The middle panel displays the residuals after subtracting the Savitzky-Golay filter from the line-filtered spectrum. The green lines indicate the $-3\times$ level of the STD of the residuals. All the red crosses indicate the data points that lie below the $-3\times$ STD lines and have, subsequently, been masked throughout the baseline estimation. Finally, the bottom panel shows the full JWST-MIRI spectrum, together with the estimated baseline, and the masked data points.

2.B Uncertainties for the JWST-MIRI subbands

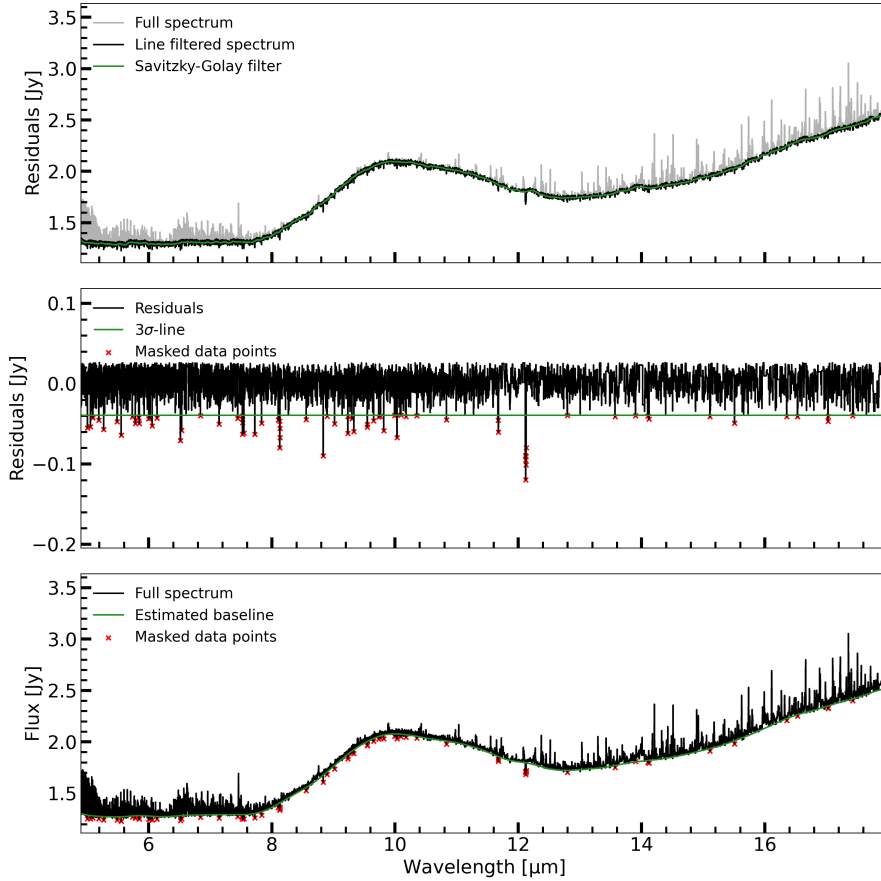


Figure 2.A.1: Intermediate steps of the continuum subtraction method described in Section 2.2.2. The top panel shows the final Savitzky-Golay filter (green) on the filtered line spectrum (black) and the filtered lines (light grey). The middle panel displays the residuals (black; line-filtered spectrum after subtracting the Savitzky-Golay filter), together with their $-3\times\text{STD}$ level (green), and the data points that fall below the $-3\times$ level (red crosses). The bottom panel shows the full JWST-MIRI spectrum (black) together with the estimated baseline (green) and the data points that have been masked throughout the estimation of the baseline (red crosses).

Table 2.B.1: Median continuum flux, estimated S/N from the ETC, and the acquired uncertainty σ for each subband.

Subband (μm)	Median flux [Jy]	ETC S/N	σ [mJy]
1A (4.90-5.74)	1.31	482.3	2.7
1B (5.66-6.63)	1.31	539.2	2.4
1C (6.53-7.65)	1.32	653.2	2.0
2A (7.51-8.77)	1.43	677.7	2.1
2B (8.67-10.13)	1.98	895.9	2.2
2C (10.02-11.70)	2.03	982.5	2.1
3A (11.55-13.47)	1.79	845.3	2.1
3B (13.34-15.57)	1.89	865.5	2.2
3C (15.41-17.98)	2.34	1030.3	2.3
4A (17.70-20.95)	2.74	425.0	6.4
4B (20.69-24.48)	2.85	246.3	11.6
4C (24.19-27.90)	2.69	76.6	35.2

2.C χ^2 -maps of CO₂, HCN, and C₂H₂

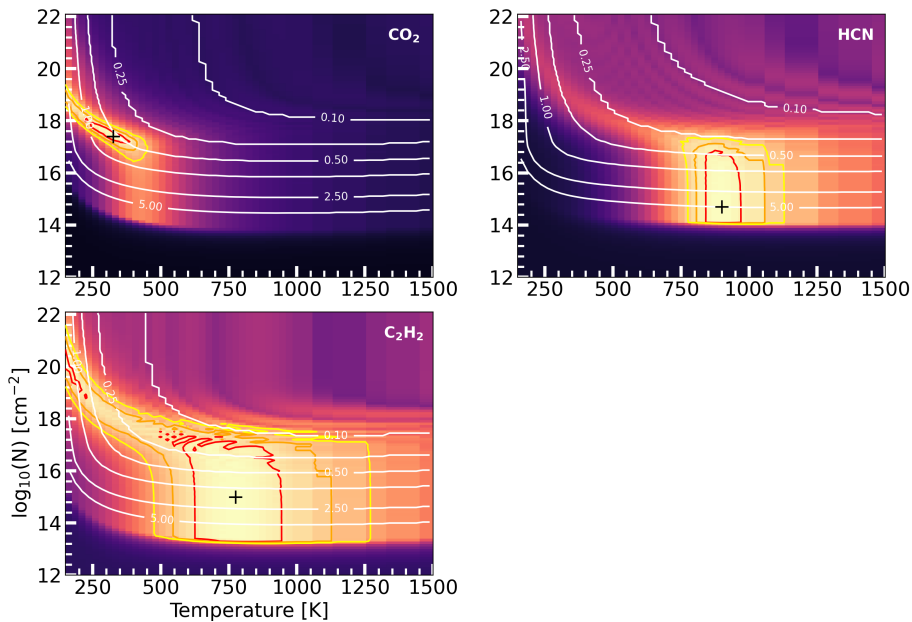


Figure 2.C.1: Normalised χ^2 maps (χ_{\min}^2/χ^2) for CO₂ (top left), HCN (top right), and C₂H₂ (bottom left). The dark plus indicates the best fitting parameters, while red, orange, and yellow contours indicate the 1 σ -, 2 σ -, and 3 σ -confidence intervals, respectively. The white contours indicate the emitting radii in au.

2.D Complementary CO ro-vibrational observations

2.D.1 Line information and integrated fluxes

Table 2.D.1: Information on the CO transitions used for the rotational diagrams and corresponding integrated fluxes.

Molecule	Rot. Trans.	Wavelength [μm]	E_{up} [K]	A_{ul} [s^{-1}]	g_{up}	Int. Flux ^(a)		Line prof. ^(b)	Blend ^(c)	
						Narrow comp. [$\text{erg s}^{-1} \text{cm}^{-2}$]	Broad comp.			
$^{12}\text{CO } v=1-0$	R-18	4.52589	4123.9	19.15	39	$1.98 \pm 0.05 \times 10^{-14}$	$1.34 \pm 0.03 \times 10^{-13}$	N	N	
	R-17	4.53237	4020.0	19.03	37	$2.04 \pm 0.05 \times 10^{-14}$	$1.38 \pm 0.03 \times 10^{-13}$	N	N	
	R-14	4.55236	3741.0	18.66	31	$2.84 \pm 0.17 \times 10^{-14}$	$1.12 \pm 0.04 \times 10^{-13}$	N	Y	
	R-13	4.55922	3658.9	18.52	29	$2.91 \pm 0.06 \times 10^{-14}$	$1.01 \pm 0.01 \times 10^{-13}$	N	Y	
	R-12	4.56617	3582.2	18.38	27	$3.00 \pm 0.09 \times 10^{-14}$	$9.77 \pm 0.17 \times 10^{-14}$	N	N	
	R-11	4.57323	3511.0	18.24	25	$2.99 \pm 0.06 \times 10^{-14}$	$9.75 \pm 0.20 \times 10^{-14}$	N	Y	
	R-10	4.58038	3445.3	18.08	23	$3.12 \pm 0.07 \times 10^{-14}$	$9.36 \pm 0.14 \times 10^{-14}$	N	N	
	R-9	4.58764	3385.1	17.91	21	$2.30 \pm 0.19 \times 10^{-14}$	$8.99 \pm 0.20 \times 10^{-14}$	N	Y	
	R-7	4.60244	3281.0	17.52	17	$3.00 \pm 0.07 \times 10^{-14}$	$8.86 \pm 0.12 \times 10^{-14}$	N	Y	
	R-6	4.61000	3237.1	17.28	15	$3.00 \pm 0.31 \times 10^{-14}$	$8.33 \pm 0.07 \times 10^{-14}$	N	Y	
	R-5	4.61766	3198.8	17.00	13	$2.92 \pm 0.06 \times 10^{-14}$	$7.86 \pm 0.12 \times 10^{-14}$	N	Y	
	R-4	4.62541	3165.9	16.65	11	$1.65 \pm 0.04 \times 10^{-14}$	$1.12 \pm 0.02 \times 10^{-13}$	N	N	
	R-3	4.63328	3138.5	16.20	9	$2.94 \pm 0.06 \times 10^{-14}$	$6.64 \pm 0.09 \times 10^{-14}$	Y	N	
	R-2	4.64124	3116.6	15.54	7	$2.39 \pm 0.04 \times 10^{-14}$	$5.88 \pm 0.07 \times 10^{-14}$	Y	N	
	R-1	4.64931	3100.1	14.42	5	$1.63 \pm 0.03 \times 10^{-14}$	$5.45 \pm 0.06 \times 10^{-14}$	Y	N	
	R-0	4.65749	3089.2	11.95	3	$1.13 \pm 0.04 \times 10^{-14}$	$4.43 \pm 0.06 \times 10^{-14}$	N	Y	
	P-1	4.67415	3083.7	35.46	1	$1.47 \pm 0.05 \times 10^{-14}$	$5.35 \pm 0.09 \times 10^{-14}$	N	N	
	P-2	4.68264	3089.2	23.51	3	$2.34 \pm 0.04 \times 10^{-14}$	$4.71 \pm 0.07 \times 10^{-14}$	N	Y	
	P-3	4.69124	3100.1	21.04	5	$2.46 \pm 0.04 \times 10^{-14}$	$5.27 \pm 0.16 \times 10^{-14}$	N	Y	
	P-4	4.69995	3116.6	19.92	7	$2.83 \pm 0.05 \times 10^{-14}$	$6.42 \pm 0.10 \times 10^{-14}$	N	Y	
	P-5	4.70877	3138.5	19.26	9	$3.03 \pm 0.05 \times 10^{-14}$	$7.26 \pm 0.09 \times 10^{-14}$	Y	N	
	P-6	4.71769	3165.9	18.80	11	$3.32 \pm 0.09 \times 10^{-14}$	$7.01 \pm 0.15 \times 10^{-14}$	Y	N	
	P-7	4.72673	3198.8	18.45	13	$2.75 \pm 0.08 \times 10^{-14}$	$7.73 \pm 0.13 \times 10^{-14}$	N	Y	
	P-8	4.73587	3237.1	18.17	15	$3.28 \pm 0.04 \times 10^{-14}$	$7.71 \pm 0.06 \times 10^{-14}$	Y	N	
	P-9	4.74513	3281.0	17.93	17	$3.35 \pm 0.07 \times 10^{-14}$	$8.10 \pm 0.10 \times 10^{-14}$	Y	N	
	P-10	4.75450	3330.3	17.71	19	$2.80 \pm 0.06 \times 10^{-14}$	$8.78 \pm 0.09 \times 10^{-14}$	N	Y	
	P-12	4.77358	3445.3	17.35	23	$2.98 \pm 0.06 \times 10^{-14}$	$8.70 \pm 0.08 \times 10^{-14}$	Y	N	
	P-13	4.78330	3511.0	17.19	25	$2.05 \pm 0.09 \times 10^{-14}$	$1.38 \pm 0.06 \times 10^{-13}$	N	N	
	P-14	4.79312	3582.2	17.03	27	$3.21 \pm 0.05 \times 10^{-14}$	$8.50 \pm 0.07 \times 10^{-14}$	N	N	
	P-17	4.82331	3828.5	16.61	33	$2.95 \pm 0.06 \times 10^{-14}$	$8.83 \pm 0.08 \times 10^{-14}$	N	Y	
	P-18	4.83361	3921.6	16.48	35	$2.85 \pm 0.06 \times 10^{-14}$	$8.26 \pm 0.22 \times 10^{-14}$	N	Y	
	P-19	4.84403	4020.0	16.35	37	$2.50 \pm 0.08 \times 10^{-14}$	$9.45 \pm 0.14 \times 10^{-14}$	N	Y	
	P-25	4.90912	4725.0	15.62	49	$2.19 \pm 0.04 \times 10^{-14}$	$8.66 \pm 0.07 \times 10^{-14}$	Y	N	
	P-26	4.92041	4861.5	15.50	51	$2.20 \pm 0.04 \times 10^{-14}$	$8.16 \pm 0.06 \times 10^{-14}$	Y	N	
	P-27	4.93182	5003.4	15.39	53	$1.94 \pm 0.07 \times 10^{-14}$	$8.36 \pm 0.12 \times 10^{-14}$	N	N	
	P-29	4.95504	5303.5	15.16	57	$1.48 \pm 0.10 \times 10^{-14}$	$8.50 \pm 0.16 \times 10^{-14}$	N	N	
	P-31	4.97878	5625.1	14.93	61	$1.65 \pm 0.07 \times 10^{-14}$	$7.38 \pm 0.16 \times 10^{-14}$	N	Y	
	P-33	5.00305	5968.2	14.71	65	$1.65 \pm 0.09 \times 10^{-14}$	$7.36 \pm 0.14 \times 10^{-14}$	N	N	
	P-37	5.05324	6718.9	14.28	73	$1.15 \pm 0.04 \times 10^{-14}$	$6.13 \pm 0.07 \times 10^{-14}$	N	N	
	P-38	5.06613	6920.0	14.17	75	$1.11 \pm 0.05 \times 10^{-14}$	$5.90 \pm 0.08 \times 10^{-14}$	N	N	
	P-39	5.07917	7126.4	14.06	77	$1.08 \pm 0.12 \times 10^{-14}$	$5.50 \pm 0.22 \times 10^{-14}$	N	Y	
	P-41	5.10568	7555.1	13.85	81	$8.02 \pm 0.58 \times 10^{-15}$	$4.73 \pm 0.11 \times 10^{-14}$	N	Y	
	P-46	5.17452	8719.7	13.32	91	$5.76 \pm 0.43 \times 10^{-15}$	$3.90 \pm 0.29 \times 10^{-14}$	N	Y	
	$^{12}\text{CO } v=2-1$	R-22	4.55692	7625.6	37.63	47	$3.86 \pm 0.83 \times 10^{-15}$	$2.91 \pm 0.72 \times 10^{-14}$	N	Y
		R-21	4.56309	7501.1	37.43	45	$3.85 \pm 0.52 \times 10^{-15}$	$3.47 \pm 0.09 \times 10^{-14}$	N	Y
		R-19	4.57573	7268.3	37.01	41	$3.12 \pm 0.54 \times 10^{-15}$	$4.13 \pm 0.11 \times 10^{-14}$	N	Y
R-18		4.58219	7159.9	36.79	39	$5.77 \pm 0.38 \times 10^{-15}$	$3.25 \pm 0.07 \times 10^{-14}$	N	Y	
R-17		4.58875	7057.0	36.57	37	$4.86 \pm 1.49 \times 10^{-15}$	$3.75 \pm 0.26 \times 10^{-14}$	N	N	
R-14		4.60902	6780.5	35.86	31	$3.46 \pm 0.63 \times 10^{-15}$	$3.62 \pm 0.12 \times 10^{-14}$	N	Y	
R-13		4.61598	6699.2	35.60	29	$5.34 \pm 1.10 \times 10^{-15}$	$3.29 \pm 0.18 \times 10^{-14}$	Y	N	
R-12		4.62303	6623.2	35.33	27	$5.86 \pm 1.25 \times 10^{-15}$	$2.86 \pm 0.22 \times 10^{-14}$	N	N	
R-11		4.63019	6552.7	35.05	25	$5.28 \pm 0.39 \times 10^{-15}$	$3.31 \pm 0.07 \times 10^{-14}$	N	Y	
R-9		4.64481	6427.9	34.43	21	$7.91 \pm 2.35 \times 10^{-15}$	$2.70 \pm 0.80 \times 10^{-14}$	N	N	
R-6		4.66750	6281.3	33.22	15	$4.41 \pm 0.37 \times 10^{-15}$	$2.30 \pm 0.06 \times 10^{-14}$	N	Y	
R-5		4.67528	6243.3	32.69	13	$5.93 \pm 1.45 \times 10^{-15}$	$1.63 \pm 0.25 \times 10^{-14}$	Y	N	
R-4		4.68315	6210.7	32.02	11	$2.60 \pm 0.37 \times 10^{-15}$	$2.07 \pm 0.07 \times 10^{-14}$	N	Y	
R-1		4.70742	6145.5	27.73	5	$2.25 \pm 0.66 \times 10^{-15}$	$1.54 \pm 0.12 \times 10^{-14}$	N	Y	
P-1		4.73265	6129.2	68.19	1	$1.40 \pm 0.96 \times 10^{-15}$	$9.67 \pm 1.64 \times 10^{-15}$	N	N	
P-4		4.75886	6161.8	38.31	7	$3.62 \pm 0.60 \times 10^{-15}$	$1.75 \pm 0.21 \times 10^{-14}$	N	Y	

Table 2.D.1: Continuation of Table 2.D.1

Molecule	Rot. Trans.	Wavelength	E_{up}	A_{ul}	g_{up}	Int. Flux ^(a)		Line prof. ^(b)	Blend ^(c)
						Narrow comp.	Broad comp.		
		[μm]	[K]	[s^{-1}]		[erg s^{-1}]	[cm^{-2}]		
	P-5	4.76782	6183.6	37.04	9	$3.96 \pm 1.66 \times 10^{-15}$	$2.02 \pm 0.33 \times 10^{-14}$	N	N
	P-6	4.77689	6210.7	36.15	11	$4.10 \pm 1.59 \times 10^{-15}$	$2.31 \pm 0.32 \times 10^{-14}$	N	N
	P-7	4.78608	6243.3	35.48	13	$3.96 \pm 1.31 \times 10^{-15}$	$2.64 \pm 0.22 \times 10^{-14}$	N	N
	P-8	4.79537	6281.3	34.94	15	$4.24 \pm 1.52 \times 10^{-15}$	$2.61 \pm 0.27 \times 10^{-14}$	N	N
	P-9	4.80479	6324.7	34.48	17	$4.80 \pm 0.90 \times 10^{-15}$	$2.51 \pm 0.20 \times 10^{-14}$	N	Y
	P-15	4.86370	6699.2	32.48	29	$5.79 \pm 1.32 \times 10^{-15}$	$2.95 \pm 0.23 \times 10^{-14}$	Y	N
	P-16	4.87394	6780.5	32.21	31	$3.86 \pm 1.19 \times 10^{-15}$	$3.17 \pm 0.22 \times 10^{-14}$	Y	N
	P-17	4.88429	6867.3	31.95	33	$4.44 \pm 1.44 \times 10^{-15}$	$2.99 \pm 0.25 \times 10^{-14}$	Y	N
	P-18	4.89477	6959.4	31.70	35	$4.92 \pm 0.68 \times 10^{-15}$	$3.07 \pm 0.15 \times 10^{-14}$	N	Y
	P-20	4.91609	7159.9	31.21	39	$3.04 \pm 0.42 \times 10^{-15}$	$3.23 \pm 0.07 \times 10^{-14}$	N	Y
	P-21	4.92694	7268.3	30.97	41	$3.62 \pm 1.29 \times 10^{-15}$	$2.92 \pm 0.23 \times 10^{-14}$	N	N
	P-22	4.93792	7382.0	30.73	43	$4.68 \pm 0.65 \times 10^{-15}$	$2.82 \pm 0.13 \times 10^{-14}$	N	Y
	P-24	4.96025	7625.6	30.27	47	$3.55 \pm 1.90 \times 10^{-15}$	$2.78 \pm 0.33 \times 10^{-14}$	N	N
	P-25	4.97161	7755.5	30.05	49	$3.70 \pm 1.36 \times 10^{-15}$	$2.65 \pm 0.22 \times 10^{-14}$	Y	N
	P-26	4.98310	7890.7	29.82	51	$2.44 \pm 1.61 \times 10^{-15}$	$3.04 \pm 0.27 \times 10^{-14}$	Y	N
	P-28	5.00647	8177.3	29.38	55	$2.85 \pm 1.51 \times 10^{-15}$	$2.72 \pm 0.25 \times 10^{-14}$	N	N
	P-32	5.05482	8814.6	28.52	63	$1.85 \pm 1.47 \times 10^{-15}$	$2.57 \pm 0.24 \times 10^{-14}$	N	N
	P-33	5.06725	8987.2	28.31	65	$1.62 \pm 0.43 \times 10^{-15}$	$2.29 \pm 0.07 \times 10^{-14}$	N	Y
	P-37	5.11838	9731.0	27.47	73	$1.43 \pm 0.62 \times 10^{-15}$	$2.05 \pm 0.12 \times 10^{-14}$	N	Y
	P-38	5.13151	9930.1	27.26	75	$1.27 \pm 0.78 \times 10^{-15}$	$1.89 \pm 0.14 \times 10^{-14}$	N	Y
¹² CO v=3-2	R-30	4.56764	11797.2	56.33	63	$1.55 \pm 0.38 \times 10^{-15}$	$1.00 \pm 0.14 \times 10^{-14}$	N	N
	R-27	4.58436	11315.7	55.55	57	$1.96 \pm 0.50 \times 10^{-15}$	$1.08 \pm 0.16 \times 10^{-14}$	N	N
	R-23	4.60800	10748.0	54.46	49	$1.68 \pm 0.38 \times 10^{-15}$	$1.10 \pm 0.13 \times 10^{-14}$	N	N
	R-22	4.61415	10619.3	54.17	47	$1.65 \pm 0.27 \times 10^{-15}$	$1.29 \pm 0.10 \times 10^{-14}$	N	N
	R-21	4.62041	10496.0	53.88	45	$1.82 \pm 0.38 \times 10^{-15}$	$1.31 \pm 0.12 \times 10^{-14}$	N	N
	R-20	4.62676	10378.0	53.59	43	$2.65 \pm 1.83 \times 10^{-15}$	$9.14 \pm 2.35 \times 10^{-15}$	Y	N
	R-18	4.63976	10157.9	52.97	39	$1.63 \pm 0.45 \times 10^{-15}$	$9.88 \pm 1.94 \times 10^{-15}$	Y	N
	R-17	4.64641	10055.9	52.66	37	$1.49 \pm 0.33 \times 10^{-15}$	$9.49 \pm 1.20 \times 10^{-15}$	N	N
	R-12	4.68118	9626.2	50.89	27	$2.11 \pm 0.42 \times 10^{-15}$	$1.43 \pm 0.19 \times 10^{-14}$	N	N
	R-11	4.68844	9556.3	50.49	25	$1.38 \pm 0.27 \times 10^{-15}$	$9.24 \pm 1.15 \times 10^{-15}$	Y	N
	R-10	4.69581	9491.8	50.06	23	$1.54 \pm 0.45 \times 10^{-15}$	$8.49 \pm 1.71 \times 10^{-15}$	N	N
	R-9	4.70328	9432.7	49.59	21	$1.70 \pm 1.07 \times 10^{-15}$	$8.16 \pm 2.01 \times 10^{-15}$	N	N
	R-8	4.71085	9378.9	49.08	19	$1.88 \pm 0.79 \times 10^{-15}$	$7.95 \pm 2.35 \times 10^{-15}$	N	N
	R-5	4.73421	9249.8	47.09	13	$1.22 \pm 0.29 \times 10^{-15}$	$8.07 \pm 1.09 \times 10^{-15}$	N	N
	P-6	4.83745	9217.5	52.11	11	$1.54 \pm 0.42 \times 10^{-15}$	$8.30 \pm 1.62 \times 10^{-15}$	N	N
	P-16	4.93614	9782.0	46.44	31	$1.76 \pm 0.43 \times 10^{-15}$	$1.13 \pm 0.15 \times 10^{-14}$	N	N
	P-19	4.96812	10055.9	45.34	37	$1.63 \pm 0.39 \times 10^{-15}$	$1.10 \pm 0.13 \times 10^{-14}$	N	N
¹³ CO v=1-0	R-30	4.55970	5607.8	18.60	126	-	$5.10 \pm 0.40 \times 10^{-15}$	N	Y
	R-26	4.58188	4992.5	18.25	110	-	$4.65 \pm 0.30 \times 10^{-15}$	N	Y
	R-23	4.59947	4585.4	17.97	98	-	$8.28 \pm 0.93 \times 10^{-15}$	N	N
	R-22	4.60551	4460.0	17.88	94	-	$6.71 \pm 0.78 \times 10^{-15}$	N	N
	R-21	4.61165	4339.9	17.78	90	-	$6.39 \pm 0.81 \times 10^{-15}$	Y	N
	R-18	4.63062	4010.5	17.48	78	-	$7.30 \pm 0.31 \times 10^{-15}$	N	Y
	R-16	4.64373	3817.0	17.26	70	-	$8.36 \pm 0.80 \times 10^{-15}$	Y	N
	R-15	4.65043	3728.0	17.15	66	-	$7.45 \pm 0.72 \times 10^{-15}$	Y	N
	R-13	4.66411	3565.8	16.91	58	-	$8.69 \pm 0.73 \times 10^{-15}$	N	N
	R-10	4.68535	3361.6	16.51	46	-	$1.01 \pm 0.08 \times 10^{-14}$	N	N
	R-9	4.69262	3304.0	16.36	42	-	$8.79 \pm 0.74 \times 10^{-15}$	Y	N
	R-7	4.70747	3204.4	16.01	34	-	$6.05 \pm 0.95 \times 10^{-15}$	N	Y
	R-6	4.71504	3162.5	15.79	30	-	$7.69 \pm 1.33 \times 10^{-15}$	N	N
	R-4	4.73047	3094.4	15.22	22	-	$6.12 \pm 0.77 \times 10^{-15}$	N	N
	R-3	4.73834	3068.2	14.81	18	-	$6.06 \pm 0.92 \times 10^{-15}$	N	N
	R-2	4.74631	3047.2	14.20	14	-	$4.87 \pm 1.18 \times 10^{-15}$	N	N
	P-2	4.78771	3021.0	21.50	6	-	$5.84 \pm 1.17 \times 10^{-15}$	N	N
	P-3	4.79630	3031.5	19.25	10	-	$7.03 \pm 0.99 \times 10^{-15}$	N	N
	P-4	4.80499	3047.2	18.23	14	-	$4.86 \pm 1.01 \times 10^{-15}$	N	Y
	P-6	4.82270	3094.4	17.20	22	-	$1.01 \pm 0.05 \times 10^{-14}$	N	Y
	P-7	4.83172	3125.8	16.89	26	-	$9.66 \pm 1.11 \times 10^{-15}$	Y	N
	P-10	4.85942	3251.6	16.22	38	-	$8.91 \pm 1.05 \times 10^{-15}$	N	N
	P-12	4.87844	3361.6	15.89	46	-	$7.67 \pm 1.00 \times 10^{-15}$	Y	N
	P-13	4.88812	3424.4	15.75	50	-	$8.40 \pm 1.15 \times 10^{-15}$	N	N
	P-15	4.90781	3565.8	15.47	58	-	$7.79 \pm 2.00 \times 10^{-15}$	N	N
	P-16	4.91783	3644.3	15.35	62	-	$7.16 \pm 0.82 \times 10^{-15}$	N	N
	P-17	4.92796	3728.0	15.23	66	-	$9.16 \pm 0.26 \times 10^{-15}$	N	Y
	P-18	4.93821	3817.0	15.11	70	-	$7.35 \pm 0.56 \times 10^{-15}$	N	Y
	P-25	5.01328	4585.4	14.34	98	-	$5.03 \pm 0.39 \times 10^{-15}$	N	Y
	P-27	5.03582	4851.7	14.13	106	-	$4.32 \pm 0.58 \times 10^{-15}$	N	Y
	P-35	5.13110	6123.2	13.33	138	-	$1.98 \pm 0.59 \times 10^{-15}$	N	Y

Table 2.D.1: Continuation of Table 2.D.1

Molecule	Rot. Trans.	Wavelength [μm]	E_{up} [K]	A_{ul} [s^{-1}]	g_{up}	Int. Flux ^(α)		Line prof. ^(β)	Blend ^(γ)
						Narrow comp.	Broad comp.		
						[$\text{erg s}^{-1} \text{cm}^{-2}$]			
$\text{C}^{18}\text{O } v=1-0$	R-12	4.68007	3485.0	16.66	27	-	$1.51 \pm 0.18 \times 10^{-15}$	Y	N
	R-10	4.69434	3354.6	16.39	23	-	$1.87 \pm 0.16 \times 10^{-15}$	N	N
	R-7	4.71646	3198.0	15.88	17	-	$1.68 \pm 0.32 \times 10^{-15}$	Y	N
	R-5	4.73170	3119.7	15.42	13	-	$7.80 \pm 1.98 \times 10^{-16}$	Y	N
	R-4	4.73947	3088.4	15.11	11	-	$1.26 \pm 0.24 \times 10^{-15}$	N	N
	P-8	4.84983	3156.3	16.51	15	-	$1.64 \pm 0.09 \times 10^{-15}$	N	Y
	P-9	4.85907	3198.0	16.29	17	-	$1.32 \pm 0.18 \times 10^{-15}$	N	N
	P-11	4.87786	3297.2	15.93	21	-	$1.09 \pm 0.14 \times 10^{-15}$	Y	N
	P-15	4.91678	3558.0	15.36	29	-	$1.77 \pm 0.06 \times 10^{-15}$	N	Y
	P-17	4.93692	3719.7	15.11	33	-	$1.52 \pm 0.13 \times 10^{-15}$	N	N
	P-18	4.94717	3808.3	15.00	35	-	$1.44 \pm 0.07 \times 10^{-15}$	N	Y

Notes. (α): for the ^{13}CO and $\text{C}^{18}\text{O } v=1-0$ transitions, we list the integrated flux of the single component under the column of the broad component, assuming that the observed emission originates from the Keplerian disk.

(β): this entry lists all the transitions that have been used in acquiring the median, normalised line profile (Y) and those that have only been used for the rotational diagram (N).

(γ): this entry lists all the transitions that are blended with other transitions.

2.D.2 Full iSHELL model

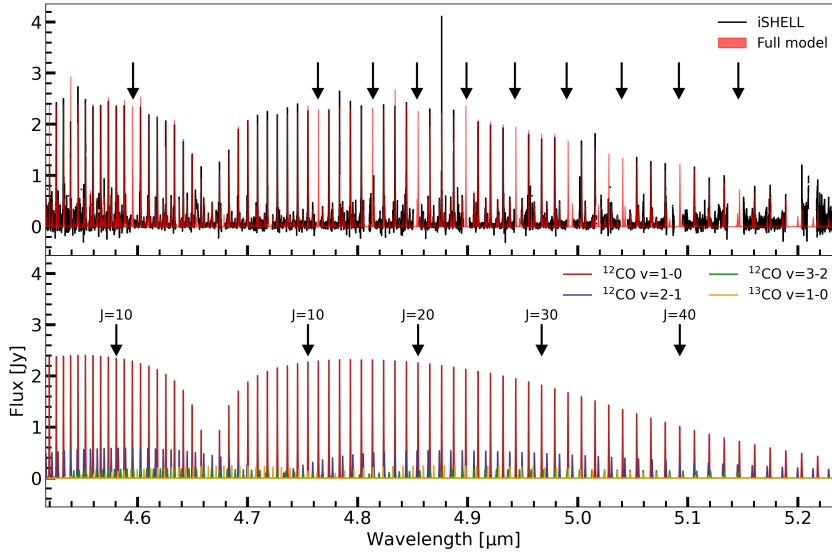


Figure 2.D.1: Continuum-subtracted iSHELL spectrum of DR Tau with a model based on the best-fitting parameters obtained through the rotational diagram analysis. The gaps visible (highlighted by the black arrows in the top panel) in the iSHELL spectrum correspond to removed telluric features. The top panel shows the full model, whereas the bottom panel shows the contribution of each band separately. For ^{12}CO , the narrow and broad component are shown together. In addition, in the bottom panel we highlight the ^{12}CO transitions which have an upper level J -value of 10, 20, 30, or 40.

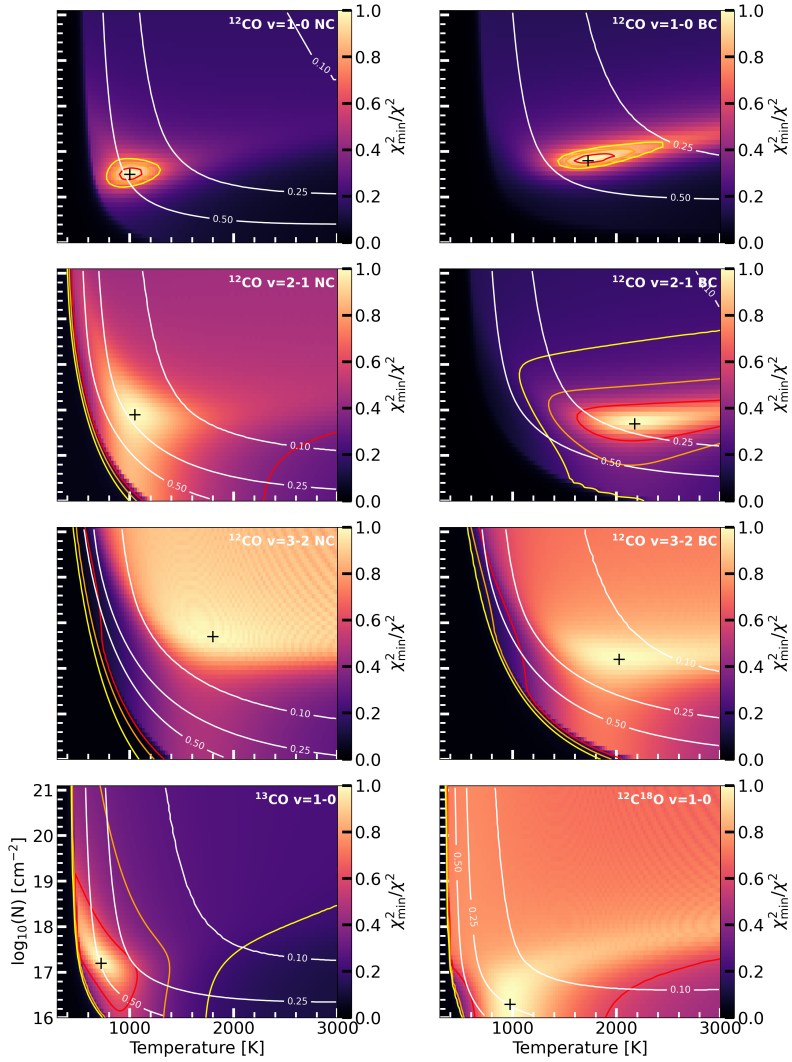
2.D.3 χ^2 -maps of the CO rotational diagrams

Figure 2.D.2: Similar as Figure 2.C.1, but for the iSHELL CO rotational diagrams. The top row shows those for the narrow (left) and broad (right) component of ^{12}CO $v=1-0$ transitions. Those for the ^{12}CO $v=2-1$ and $v=3-2$ transitions are shown on the second and third row, respectively, whereas the ones for the ^{13}CO and C^{18}O (using VLT-CRIRES data) are shown on the bottom row.

2.D.4 Optical depth of ^{12}CO

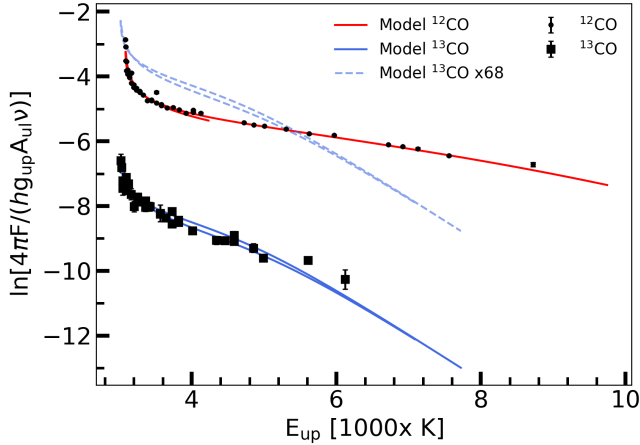


Figure 2.D.3: Rotational diagrams for ^{12}CO $v=1-0$ (dots) and ^{13}CO $v=1-0$ (squares). The dashed blue line indicates the model of ^{13}CO ($T=750$ K) multiplied by a factor of 68 to account for the isotopologue ratio. The fluxes shown for the ^{12}CO are a summation of the narrow ($T=1000$ K) and broad ($T=1725$ K) components.

2.D.5 LTE versus non-LTE

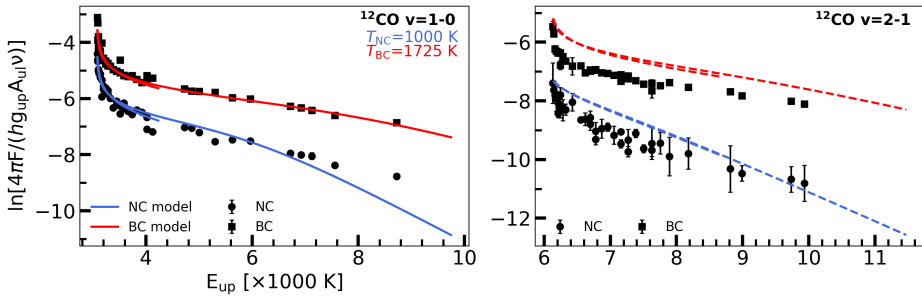


Figure 2.D.4: Comparison between the rotational diagrams of the ^{12}CO $v=1-0$ and $v=2-1$ transitions to test the assumption of LTE. The left panel shows the ^{12}CO $v=1-0$ rotational diagrams (see also Figure 2.8). The right panel shows the non-LTE test, where the ^{12}CO $v=2-1$ integrated fluxes are shown together with expected models based on the results of the ^{12}CO $v=1-0$ rotational diagrams. As the models overproduce the observed ^{12}CO $v=2-1$ fluxes, invalidating the assumption that the levels can be characterised by a single temperature.

2.D.6 Convolution iSHELL to JWST-MIRI resolution

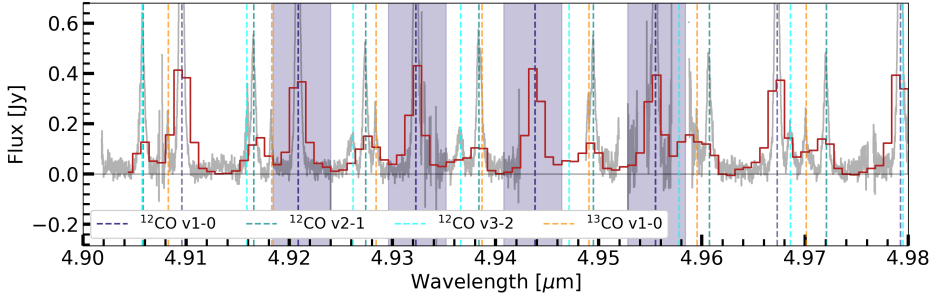


Figure 2.D.5: Xoom-in of Figure 2.3 on the JWST-MIRI data (red) within the wavelength region 4.90-4.98 μm . The iSHELL observations are shown here in grey. The different transitions in this wavelength region of the ^{12}CO $v=1-0$ (dark blue), $v=2-1$ (teal), $v=3-2$ (cyan), and the ^{13}CO $v=1-0$ (orange) transitions are shown to identify the different lines and highlight corresponding line overlaps. The dark blue shaded areas indicate the (relatively) isolated ^{12}CO $v=1-0$ transitions that have been used to determine the pseudo-Voigt line profile of the JWST-MIRI data.

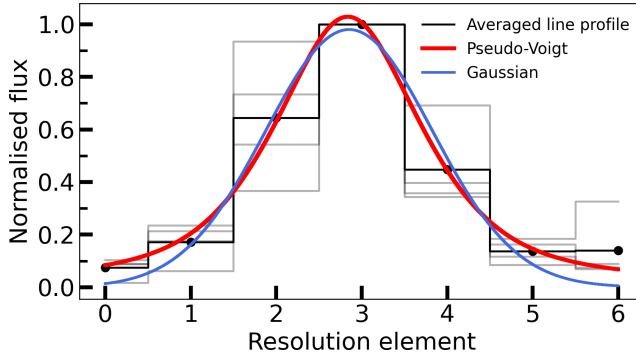


Figure 2.D.6: Averaged, normalised line profile of the four selected, unblended ^{12}CO $v=1-0$ transitions observed with JWST-MIRI (see also Figure 2.D.5). The faint grey lines indicate the individual, normalised lines, whereas the red and blue lines display, respectively, the fitted pseudo-Voigt and Gaussian profiles.

2.D.6.1 Gaussian line profile

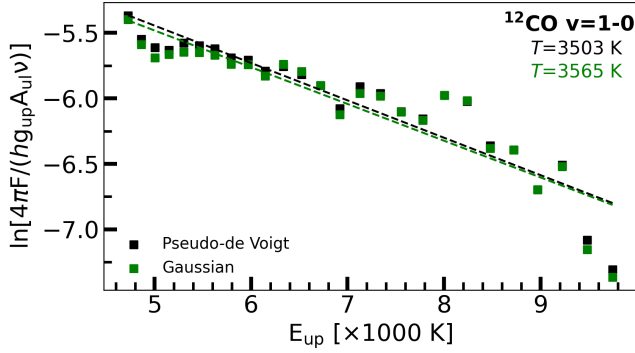


Figure 2.D.7: Simple rotational diagrams of the JWST-MIRI integrated fluxes when considering a pseudo-Voigt (black) or a Gaussian (green) line profile. Straight line fits suggest excitation temperatures of $T=3503 \text{ K}$ when considering the pseudo-Voigt profile and $T=3565$ when using a Gaussian.

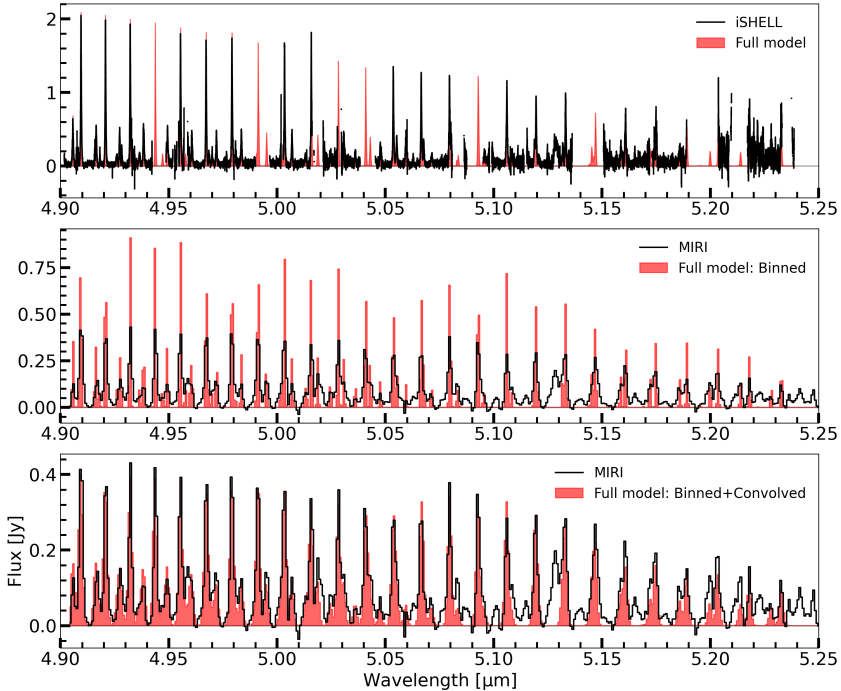


Figure 2.D.8: Same as Figure 2.11, but for the Gaussian line profile.

Chapter 3

MINDS: The DR Tau disk

II. Probing the hot and cold H₂O reservoirs in the JWST-MIRI spectrum

M. Temmink, E. F. van Dishoeck, S. L. Grant, B. Tabone, M. Güdel,
T. Henning, D. Barrado, A. Caratti o Garatti, A. M. Glauser, I.
Kamp, A. M. Arabhavi, H. Jang, N. T. Kurtovic, G. Perotti, K.
Schwarz, M. Vlasblom

A&A, 689, A330 (2024)

Abstract

Context. The Medium Resolution Spectrometer (MRS) of the Mid-InfraRed Instrument (MIRI) on the *James Webb* Space Telescope (JWST) gives insights into the chemical richness and complexity of the inner regions of planet-forming disks. Several disks that are compact in the millimetre dust emission have been found by Spitzer to be particularly bright in H₂O, which is thought to be caused by the inward drift of icy pebbles. Here, we analyse the H₂O-rich spectrum of the compact disk DR Tau using high-quality JWST-MIRI observations.

Aims. We infer the H₂O column densities (in cm⁻²) using methods presented in previous works, as well as introducing a new method to fully characterise the pure rotational spectrum. We aim to further characterise the abundances of H₂O in the inner regions of this disk and its abundance relative to CO. We also search for emission of other molecular species, such as CH₄, NH₃, CS, H₂, SO₂, and larger hydrocarbons; commonly detected species, such as CO, CO₂, HCN, and C₂H₂, have been investigated in our previous paper.

Methods. We first use 0D local thermodynamic equilibrium (LTE) slab models to investigate the excitation properties observed in different wavelength regions across the entire spectrum, probing both the ro-vibrational and rotational transitions. To further analyse the pure rotational spectrum ($\geq 10 \mu\text{m}$), we use the spectrum of a large, structured disk (CI Tau) as a template to search for differences with our compact disk. Finally, we fit multiple components to characterise the radial (and vertical) temperature gradient(s) present in the spectrum of DR Tau.

Results. The 0D slab models indicate a radial gradient in the disk, as the excitation temperature (emitting radius) decreases (increases) with increasing wavelength, which is confirmed by the analysis involving the large disk template. To explain the derived emitting radii, we need a larger inclination for the inner disk ($i \sim 10\text{-}23^\circ$), agreeing with our previous analysis on CO. From our multi-component fit, we find that at least three temperature components ($T_1 \sim 800$ K, $T_2 \sim 470$ K, and $T_3 \sim 180$ K) are required to reproduce the observed rotational spectrum of H₂O arising from the inner $R_{\text{em}} \sim 0.3\text{-}8$ au. By comparing line ratios, we derived an upper limit on the column densities (in cm⁻²) for the first two components of $\log_{10}(N) \leq 18.4$ within ~ 1.2 au. We note that the models with a pure temperature gradient provide as robust results as the more complex models, which include spatial line shielding. No robust detection of the isotopologue H₂¹⁸O can be made and upper limits are provided for other molecular species.

Conclusions. Our analysis confirms the presence of a pure radial temperature gradient present in the inner disk of DR Tau, which can be described by at least three components. This gradient scales roughly as $\sim R_{\text{em}}^{-0.5}$ in the emitting layers, in the inner 2 au. As the observed H₂O is mainly optically thick, a lower limit on the abundance ratio of H₂O/CO ~ 0.17 is derived, suggesting a potential depletion of H₂O. Similarly to previous work, we detect a cold H₂O component ($T \sim 180$ K) originating from near the snowline, now with a multi-component analysis. Yet, we cannot conclude whether an enhancement of the H₂O reservoir is observed following radial drift. A consistent analysis of a larger sample is necessary to study the importance of drift in enhancing the H₂O abundances.

3.1 Introduction

H₂O is a key ingredient in making habitable planets. As the bulk of exoplanets form in the inner-most regions (<10 au; Morbidelli et al. 2012; Dawson & Johnson 2018) of planet-forming disks, their (atmospheric) composition is determined by the available elemental abundances. Therefore, it is of importance to characterise these regions in detail and, in particular, to analyse the H₂O emission present.

The recently launched *James Webb* Space Telescope (JWST; Rigby et al. 2023) and, in particular, the Medium Resolution Spectroscopy mode (MRS; Wells et al. 2015) of the Mid-Infrared Instrument (MIRI; Rieke et al. 2015; Wright et al. 2015), provides the best opportunity to study the chemical composition of these inner-most regions of planet-forming disks. The wide wavelength range of JWST-MIRI (4.9-27.9 μm) covers many transitions of H₂O. These include the ro-vibrational lines at the shorter wavelengths between ~ 5.0 and $8.0 \mu\text{m}$ and the rotational transitions longward of $10.0 \mu\text{m}$ (Meijerink et al. 2009). This forest of H₂O lines across the mid-infrared wavelength provides insights into the different parts of the inner disk: the lines at shorter wavelengths are thought to probe the innermost gas, whereas those at longer wavelengths probe colder gas located at larger radial distances (e.g. Blevins et al. 2016; Banzatti et al. 2017, 2023b, and Gasman et al. 2023). Observations suggest that H₂O vapour is prevalent in the spectra of T-Tauri disks, even in those with inner, dust-depleted cavities, albeit with lower line strengths (Perotti et al. 2023; Schwarz et al. 2024).

Furthermore, Banzatti et al. (2020) have found a correlation between the flux of strong H₂O lines measured with the *Spitzer* Space Telescope and the radial dust disk size (R_{dust}) as measured with ALMA. The proposed explanation for the correlation is driven by the H₂O abundances expected for three types of disks: compact disks ($R_{\text{dust}} \lesssim 60$ au) with efficient radial drift; large disks ($60 \lesssim R_{\text{dust}} \lesssim 300$ au) with substructures; and large disks with substructures and an inner cavity. Substructures are able to trap icy pebbles in the outer disk, preventing them from drifting inside the H₂O snowline and enhancing the H₂O column density in the inner disk. Subsequently, these large disks are thought to have low H₂O column densities in the inner disk, which are expected to be further depleted in the presence of an inner cavity. For the compact dust disks, where radial drift is thought to be very efficient (e.g., Facchini et al. 2019) and substructures are found to be less common (Long et al. 2019), the H₂O column density is thought to be enhanced through the sublimation of H₂O-ice. However, not all compact disks show strong H₂O emission, such as DN Tau, for example (Pontoppidan et al. 2010; Salyk et al. 2011b; Banzatti et al. 2020).

In this work we analyse the H₂O emission in the JWST-MIRI spectrum of DR Tau, a compact T-Tauri (K6) disk (< 60 au, Long et al. 2019) located at a distance of ~ 195 pc (Gaia Collaboration et al. 2018) in the Taurus star-forming region. DR Tau has a mass of $M=0.93 M_{\odot}$, an effective temperature of $T_{\text{eff}}=4205$ K, and a luminosity of $L=0.63 L_{\odot}$ (Long et al. 2019). Observations with *Spitzer* have shown that DR Tau has one of the highest line-to-continuum ratios and contains a rich H₂O reservoir (e.g., Salyk et al. 2011b and Banzatti et al. 2020). Using ground-based observatories, various previous studies have analysed some of the

bright H₂O lines at much higher spectral resolution at both near- and mid-infrared wavelengths (Salyk et al. 2008; Najita et al. 2018; Salyk et al. 2019; Banzatti et al. 2023b). High-resolution, ground-based ro-vibrational CO observations at $\sim 4.6\text{--}5.3\ \mu\text{m}$ are also available for this disk, which have been analysed in Bast et al. (2011); Brown et al. (2013); Banzatti et al. (2022) and Temmink et al. (2024b).

Temmink et al. (2024b) used rotational diagrams to investigate the excitation properties of the various CO isotopologues: ¹²CO, ¹³CO, and C¹⁸O. For the optically thin isotopologue C¹⁸O an excitation temperature of $T \sim 975\ \text{K}$, a column density of $N \sim 2.0 \times 10^{16}\ \text{cm}^{-2}$, and an emitting radius of $R_{\text{CO}} \sim 0.23\ \text{au}$ were derived. Using these parameters and accounting for the involved isotopologue ratio, a total number of molecules of $\mathcal{N}_{\text{CO}} \sim 4.1 \times 10^{44}$ was found for CO. The physical parameters derived from the high spectral resolution CO observations were shown to also provide an explanation for the CO emission observed with JWST-MIRI. In addition, Temmink et al. (2024b) investigated the emission of CO₂, HCN, and C₂H₂. Left unanalysed, however, was the plethora of H₂O lines present in the spectrum. Due to the strength of the H₂O lines, the high line-to-continuum ratio, and the disk having the most ground-based, ro-vibrational and rotational H₂O transitions observed to date (see, for example, Najita et al. 2018; Salyk et al. 2019; Banzatti et al. 2023b), DR Tau is one of the best candidates for an extensive analysis of the H₂O emission and to make a detailed comparison with the physical structure and abundance of CO, under the assumption that these molecules are at least partially co-spatial. In addition, due to its compactness, DR Tau is also a good candidate to study the effects of radial drift on the observable H₂O abundance.

In this paper, we provide a deep analysis of the H₂O-rich spectrum using three different methods: we analyse various wavelength regions in the spectrum using 0D local thermal equilibrium (LTE) slab models. Additionally, we investigate the difference between the spectrum of a compact disk with that of a large, structured disk. Finally, we introduce a multi-component, radial and vertical gradient slab model fitting technique, effectively providing a 1D LTE slab model, to derive the temperature and column density gradients of the emitting layers in the inner disk.

This paper is structured as follows: in Section 7.2 we describe the JWST-MIRI observations of DR Tau. Section 3.3 provides the used analysis methods and the accompanying results, which are further discussed in Section 7.4. Finally, our conclusions are summarised in Section 4.6.

3.2 Observations

DR Tau has been observed with JWST-MIRI as part of the JWST Guaranteed Time Observations Program MIRI mid-INfrared Disk Survey (MINDS, PID: 1282, PI: T. Henning; Henning et al. 2024). The details of the observations are described in Temmink et al. (2024b). For the analysis in this work, we have re-reduced the observations using a standard pipeline reduction (Version 1.12.3, Bushouse et al. 2023b) and the photom updates released in November 2023, which significantly improve the reduction of Channel 4. This reduction uses the residual fringe cor-

rection implemented in the pipeline, uses an annulus background subtraction, and the spectrum is extracted using an aperture with a size of $2\times$ the full width at half maximum (FWHM). We note that the photom updates do not have a significant impact on the other channels, indicating that the results listed in Temmink et al. (2024b) still hold.

We have used the continuum subtraction method as described in Temmink et al. (2024b), which includes Channel 4 now as well. This continuum subtraction method first filters out downwards spikes before estimating the baseline with the ‘Iterative Reweighted Spline Quantile Regression’ (IRSQR) method included in the python-package PYBASELINES (Erb 2022). The estimated continuum is also visible in Figure 3.1.

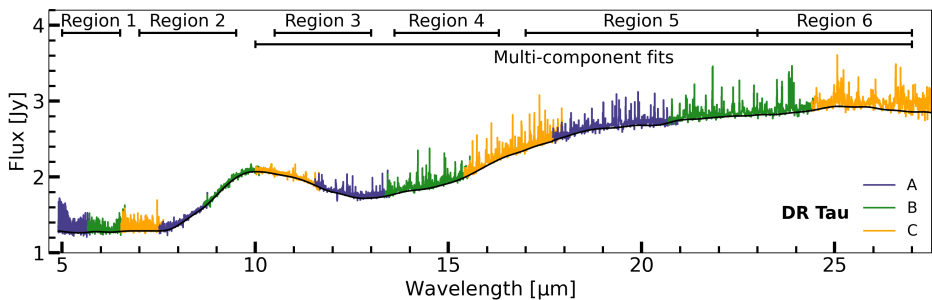


Figure 3.1: Full JWST-MIRI spectrum ($4.9\text{--}27.5\ \mu\text{m}$) of DR Tau. The different wavelength ranges (subbands) of each MIRI/MRS channel are shown in blue (‘A’), green (‘B’), and orange (‘C’), respectively. The wavelength regions over which H_2O will be analysed are indicated by the horizontal bars. The continuum fit is indicated by the black line.

Our results, the multi-component slab model fits (see Section 3.3.3) and the potential (non-)detection of H_2^{18}O (see Section 3.3.5) may be partially influenced by the wavelength calibration of JWST-MIRI/MRS. The wavelength accuracy, as shown by Argyriou et al. (2023) and Pontoppidan et al. (2024), can be off by $40\text{--}90\ \text{km s}^{-1}$ and the offset is the largest in Channel 4 as clearly shown in Figure 5 of Pontoppidan et al. (2024). As Channel 4 covers a large range of important H_2O transitions, as well as the strongest H_2^{18}O transitions observable with JWST-MIRI, the velocity shifts can significantly impact the slab models and/or ones ability of detecting H_2^{18}O .

To account for the wavelength correction, we have used, similar to Pontoppidan et al. (2024), a plethora of CO and H_2O lines to estimate the offset between the spectrum and an initial model through a cross-correlation technique. In our estimates, we have accounted for the heliocentric velocity of DR Tau ($v_{\text{hel}} \sim 27.6\ \text{km s}^{-1}$; Ardila et al. 2002). In total, we have used 483 (blended) transitions, yielding corrections between $\sim 100\ \text{km s}^{-1}$ and $\sim 120\ \text{km s}^{-1}$ with the largest offsets found in Channel 4. As the silicate feature is dominated by noise and no strong H_2O transitions are found between ~ 8 and $\sim 10\ \mu\text{m}$, we have not determined the offsets for any possible transitions present in this region. In addition, as the offsets for

the shortest wavelengths are mostly concentrated around zero, we have also not applied corrections for these regions. The corrections are thus only applied for the longer wavelengths ($>10 \mu\text{m}$), where the offsets are found to be the largest. Figure 3.2 displays our offsets found for the different CO and H₂O transitions.

To properly determine the wavelength corrections across the spectrum of DR Tau, we have fitted polynomials of degree 3 through the found offsets for each JWST-MIRI subband. These polynomials, indicated by the red lines in Figure 3.2, have been used to correct the spectrum. We note that the corrections of Pontoppidan et al. (2024) have been implemented for the longest wavelengths in a newer version of the JWST reduction pipeline than used in this work (priv. comm.).

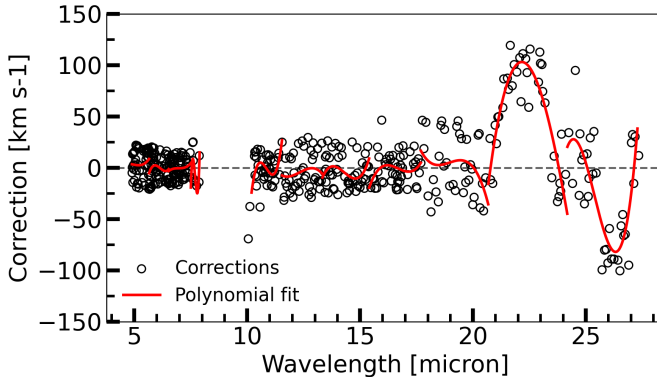


Figure 3.2: Estimated wavelength corrections (black circles) for the selected lines. The red lines are the polynomials of degree 3 fitted for each JWST-MIRI subband and are used in correcting the wavelength calibration.

3.3 Analysis and results

We analysed the H₂O emission in DR Tau using four different methods: first, in Section 3.3.1, similar to Gasman et al. (2023), we investigated the H₂O emission across separate regions in the spectrum using 0D local-thermal equilibrium (LTE) slab models (see Section 3.3.1). The slab model fitting procedure is described in detail in Temmink et al. (2024b) (see also Grant et al. 2023b and Tabone et al. 2023). As the new reduction yields slightly different fluxes, especially in Channel 4, we report in Table 3.A.1 new values for the median flux, the signal-to-noise ratio (S/N) as given by the JWST Exposure Time Calculator (ETC)¹, which accounts for the degrading transmission² of JWST-MIRI/MRS, and for the estimated noise on the continuum used in our fitting procedure. For the H₂O slab models, we used grids where the column density (N in cm^{-2}) was allowed to vary between 12 and 22 in \log_{10} -spacing using a of $\Delta N=0.1$. We note that these column densities probe

¹ETC: <https://jwst.etc.stsci.edu/>

²For more information on the degrading transmission, see: <https://www.stsci.edu/contents/news/jwst/2023/miri-mrs-reduced-count-rate-update>

the upper layers of the disk, above the height where the dust becomes optically thick, or, in the case of optically thick lines, above the height where the emission lines become optically thick (Bruderer et al. 2015; Woitke et al. 2018). The temperature (T) was allowed to vary between 150 and 2500 K in steps of $\Delta T=25$ K, whereas the emitting radius (R_{em}) was allowed to take on values between 0.01 and 10 au, using step sizes of $\Delta R=0.02$ au. The emitting radius is used as a parametrisation of the emitting area, assuming $A = \pi R_{\text{em}}^2$. We note that the emitting area does not have to be a circle, it can have any shape (i.e. an annulus) at any radial distance from the star. In addition to regions listed in Gasman et al. (2023) (5.0-6.5, 13.6-16.3, 17.0-23.0, and 23.0-27.0 μm), we also investigate the H_2O emission in the regions between 7.0-9.5 and 10.5-13.0 μm . The different wavelength regions are also indicated in Figure 3.1.

Second (see Section 3.3.2), we followed the method described in Banzatti et al. (2023a), where a continuum-subtracted spectrum of a large disk (CI Tau) was used to investigate a second, colder H_2O component in a compact disk (GK Tau), after scaling for the differences in distances and luminosity of the H_2O lines with highest upper energy levels (6000-8000 K). They expect this second component to trace the enrichment of the H_2O gas near the snowline, following the sublimation of icy mantles of drifting grains. As DR Tau is a compact disk, we expect pebble drift to be efficient and, subsequently, we expect such a second H_2O component should also be visible. Here, we also used the spectrum of CI Tau as the template spectrum to investigate the presence of an excess, cold second component in DR Tau (see Section 3.3.2.2). For consistency, the CI Tau observations have been reduced in the same way as done for DR Tau (see Section 7.2).

As a third method (Section 3.3.3), we investigate how well 0D LTE slab models can reproduce the observed spectrum when implementing radial and vertical temperature gradients.

Finally, we obtained limits on the H_2O column density (in cm^{-2}) by comparing the ratios of the Einstein-A coefficients and the line fluxes of H_2O line pairs with the same upper energy level (Section 3.3.4, see also Gasman et al. 2023). We also searched for emission of the rare isotopologue $\text{H}_2\text{}^{18}\text{O}$ in Section 3.3.5, using the isolated lines listed in Calahan et al. (2022).

Additionally, in Section 3.3.6, we fitted an LTE slab model to the OH emission over the wavelength region between 10.0 and 27.5 μm and investigated the presence of other molecular species, such as CH_4 , NH_3 , and larger hydrocarbons. We compare their emission properties with those of H_2O , CO_2 , HCN, and C_2H_2 , of which the final three are presented in Temmink et al. (2024b).

3.3.1 Single H_2O LTE slab models

The JWST-MIRI observations of DR Tau show a plethora of both ro-vibrational (<10 μm) and rotational (>10 μm) transitions of H_2O . Following Gasman et al. (2023), we investigated the excitation properties of H_2O across different wavelength regions, covering both ro-vibrational and rotational transitions, using 0D-LTE slab models. We have used slab models without and with line overlap, i.e. mutual shielding of H_2O lines (i.e. no shielding by other molecules, see Tabone et al. 2023

for a full description). Table 3.1 lists the best fitting slab model parameters for both the models without line overlap (top half) and with line overlap (bottom half). The best fitting slab models are also displayed in Figures 3.B.1 and 3.B.2 for those without and with line overlap, respectively.

Table 3.1: Best fit parameters of the H₂O slab models without (top) and with line overlap (bottom).

Region [μm]	$\log_{10}(N)^\alpha$	T [K]	R [au]	\mathcal{N}
Without line overlap				
5.0-6.5	$18.4^{+0.2}_{-0.1}$	1000^{+250}_{-50}	$0.21^{+0.02}_{-0.04}$	7.79×10^{43}
7.0-9.5	$18.3^{+0.1}_{-0.1}$	1000^{+50}_{-100}	$0.21^{+0.02}_{-0.00}$	6.19×10^{43}
10.5-13.0	$18.1^{+0.3}_{-1.8}$	850^{+50}_{-50}	$0.87^{+5.18}_{-0.20}$	6.70×10^{44}
13.6-16.3	$18.4^{+0.0}_{-0.0}$	675^{+0}_{-0}	$0.93^{+0.00}_{-0.00}$	1.53×10^{45}
17.0-23.0	$18.9^{+0.6}_{-0.3}$	450^{+25}_{-50}	$1.31^{+0.14}_{-0.12}$	9.58×10^{45}
23.0-27.0	$20.1^{+2.0}_{-2.1}$	375^{+350}_{-175}	$1.55^{+1.92}_{-0.64}$	2.13×10^{47}
With line overlap				
5.0-6.5	$18.5^{+0.1}_{-0.0}$	1150^{+100}_{-75}	$0.17^{+0.00}_{-0.00}$	6.43×10^{43}
7.0-9.5	$18.5^{+0.2}_{-0.1}$	850^{+75}_{-75}	$0.25^{+0.02}_{-0.02}$	1.39×10^{44}
10.5-13.0	$18.0^{+0.4}_{-1.3}$	850^{+50}_{-50}	$0.95^{+2.86}_{-0.30}$	6.35×10^{44}
13.6-16.3	$18.5^{+0.0}_{-0.0}$	675^{+25}_{-0}	$0.89^{+0.00}_{-0.06}$	1.76×10^{45}
17.0-23.0	$18.5^{+0.3}_{-0.2}$	500^{+25}_{-50}	$1.35^{+0.14}_{-0.08}$	4.05×10^{45}
23.0-27.0	$19.5^{+2.6}_{-1.8}$	400^{+350}_{-200}	$1.69^{+2.36}_{-0.68}$	6.35×10^{46}

Notes. $^\alpha$: N is given in units of cm^{-2} .

The best fitting models were determined using a reduced χ^2 -minimisation method, following, for example, Grant et al. (2023b), Tabone et al. (2023), and Temmink et al. (2024b). The reduced χ^2 is determined using the following equation:

$$\chi_{\text{red}}^2 = \frac{1}{N_{\text{obs}}} \sum_{i=1}^{N_{\text{obs}}} \frac{(F_{\text{obs},i} - F_{\text{mod},i})^2}{\sigma^2}. \quad (3.1)$$

Here, N_{obs} is the number of spectral resolution elements, covering isolated H₂O transitions, used in the fitting, F_{obs} and F_{mod} are the corresponding observed and model flux, respectively, and σ denotes the uncertainty on the flux (see Table 3.A.1). The uncertainties on the best-fit parameters are taken from the confidence intervals, which are determined for, respectively, 1σ , 2σ , and 3σ as $\chi_{\text{red,min}}^2 + 2.3$, $\chi_{\text{red,min}}^2 + 6.2$ and $\chi_{\text{red,min}}^2 + 11.8$ (Avni 1976; Press et al. 1992).

In accordance with previous works (e.g. Blevins et al. 2016; Banzatti et al. 2023a; Gasman et al. 2023), the slab models probe the inner, hotter regions at the shortest wavelengths, whereas the outer, colder regions are traced by the longer wavelengths. The trends hold for both the models with and without line overlap.

Figure 3.3 visualises the decreasing (increasing) trend of temperature (emitting radius) with wavelength for the models without overlap (squares) and those with line overlap (circles). We find that the temperatures decrease from 1000 K to 400 K over a span of 0.2 to 2.0 au, if R_{em} corresponds to the actual radius of the emitting area. Additionally, we show the temperature as a function of radius in the right panel of Figure 3.3. This panel also includes the results from our three component fit (using method 3, see Section 3.3.3) and the 1σ uncertainties.

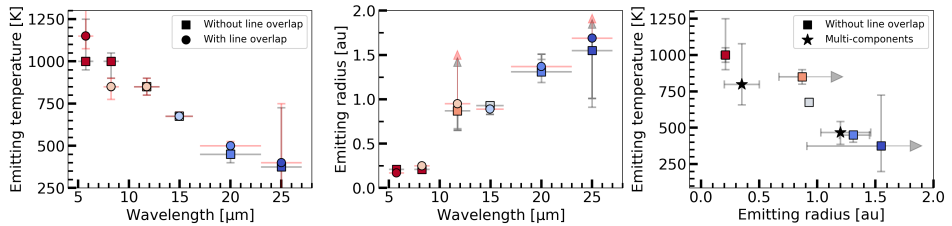


Figure 3.3: Inferred gas temperature (left) and emitting radii (middle) for the different wavelength regions, and the emitting temperature as a function of the emitting radius (right). We show the results for the slab model fits without (squares) and with (circles) line overlap. The colours indicate the varying gas temperatures, whereas the horizontal bars denote the wavelength ranges of the regions. Errorbars are shown for the derived quantities, where those for the models without line overlap are shown in black and those for the models with line overlap are shown in red. In addition, we show for comparison the results (black stars) of the three component fit (approach 3, see Section 3.3.3.3) in the right panel.

All fits yield generally well constrained values for the column densities, excitation temperatures and emitting areas, parameterised by the emitting radius R_{em} . The uncertainties, which are mostly within ± 0.5 for the logarithm of the column density (in cm^{-2}), ± 100 K for the excitation temperature, and ± 0.20 au for the emitting radius, are the largest for the fits in region 6 (23.0–27.0 μm), likely the effect of this wavelength region having the lowest sensitivity. In addition, the upper uncertainty on the emitting radius for the third region is found to be higher compared to the other uncertainties. This is likely the result of this region having fewer bright, optically thick lines. Using the results for the inner two regions, those traced by the ro-vibrational H_2O transitions, we can make a comparison with those for CO as analysed in Temmink et al. (2024b), since those arise from a similar region of ~ 0.2 au. This comparison is made in Section 3.4.4.

We find that our slab models to the JWST-MIRI spectrum of DR Tau yield very similar results for the excitation temperatures and emitting radii for both the vibrational and rotational transitions of H_2O compared to the previously mentioned ground-based, high spectral resolution observations (Najita et al. 2018; Salyk et al. 2019; Banzatti et al. 2023b). Furthermore, Banzatti et al. (2023b) provides linewidths for the vibrational H_2O lines at 5.0 μm ($FWHM \sim 22 \text{ km s}^{-1}$) and the rotational transitions at 12.4 μm ($FWHM \sim 16 \text{ km s}^{-1}$), so we can estimate the emitting radii from these line profiles using Kepler’s law: $R = GM_*(\sin(i)/\Delta v)^2$,

where i is the inclination of the disk ($i \sim 5.4$, as derived from ALMA observations; Long et al. 2019) and Δv is the linewidth, here taken equal to half the width at half maximum (HWHM). We derive emitting radii of $R_{\text{em}} \sim 0.06$ au and ~ 0.11 au for the 5.0 and 12.4 μm high-resolution transitions, respectively. Both of these are significantly smaller than the derived emitting radii from our JWST observations and the slab models fitted to the ground-based, high-resolution observations. A similar discrepancy was found in our previous work, analysing the high spectral resolution CO observations (Temmink et al. 2024b). There we found that the emitting radii derived from the slab models and those using the linewidths for CO agree if the (inner) disk inclinations are increased to $i_{\text{inner}} \sim 10\text{-}23^\circ$. Notably, observations of the VLTI-GRAVITY instrument suggest at similar inclinations for the inner disk ($i_{\text{inner}} \sim 18_{-18}^{+10^\circ}$; GRAVITY Collaboration et al. 2021). Using these inclinations, we derive emitting radii in the ranges of $R_{\text{em}} \sim 0.21\text{-}0.96$ au for vibrational transitions at 5 μm and $R_{\text{em}} \sim 0.39\text{-}1.81$ au, which do agree with the emitting radii derived from the slab models. As mentioned in Temmink et al. (2024b), these derivations hold for the assumption that the emitting radii correspond to a circular region enclosing the host star and may suggest a misalignment between the inner and outer disk of DR Tau.

3.3.2 Cold and warm H₂O reservoirs: large disk template

3.3.2.1 Identifying unblended lines

Evidence for the presence of multiple rotational H₂O components in the JWST-MIRI spectra was introduced by Banzatti et al. (2023a) and Gasman et al. (2023). In a similar fashion to Banzatti et al. (2023a), we first identified the unblended, high-energy ($6000 \leq E_{\text{up}} \leq 8000$ K) H₂O lines, which all happen to have Einstein-A coefficients $A_{\text{ul}} > 10 \text{ s}^{-1}$. Figure 3.C.1 shows A_{ul} as a function of E_{up} (left panel) and wavelength (right panel), where only the lines with $A_{\text{ul}} \geq 10^{-2} \text{ s}^{-1}$ and wavelengths above 10 μm are shown. Figure 3.C.2, on the other hand, shows all lines available for our analysis without a lower limit imposed on A_{ul} . The lines highlighted by the black circles have been used for the scaling of CI Tau. As our analysis includes many more H₂O lines compared to Banzatti et al. (2023a), we have identified fewer isolated lines. This is mainly due to the inclusion of transitions with low Einstein-A coefficients ($< 10^{-2} \text{ s}^{-1}$). These low Einstein-A coefficient transitions are expected to have a negligible contribution to the spectrum, unless the transitions with high Einstein-A values have high optical depths of $\tau > 100$.

To identify unblended, high-energy lines or high-energy lines that are blended together, we cross-listed these lines with all the transitions available (including Einstein-A coefficients $< 10^{-2} \text{ s}^{-1}$) for the molecules detected in DR Tau. As mentioned above, the transitions with low Einstein-A coefficients may have a significant contribution to the spectra if the transitions with higher Einstein-A values have high optical depths. Consequently, we also considered using these transitions when identifying the unblended lines. In this process, we only included these lines in the wavelength regions in which molecules have been detected. For C₂H₂, CO₂,

and HCN this means that we cross-listed with all the available transitions in the region between 13.6 and 16.3 μm , whereas for OH we cross-listed with all transitions at wavelengths $>13.6 \mu\text{m}$. In addition, we cross-listed with all the low-energy ($<6000 \text{ K}$) H_2O transitions. If no transitions of any of the molecules are located within five resolution elements enclosing a high-energy H_2O transition, we considered the transition to be useful for this analysis. Our cross-listing yielded a total of 24 potentially useful transitions, of which 11 are, upon visual inspection, strongly detected in both DR Tau and CI Tau. Of those 11 lines, six are blended together in three pairs and are, subsequently, treated as one.

3.3.2.2 Large disk template: CI Tau

We scaled the spectrum of CI Tau to match the flux level of the hot H_2O transitions in DR Tau by accounting for the different distances and scaling by the averaged H_2O line luminosity of the unblended lines of $L_{\text{H}_2\text{O,DR Tau}}/L_{\text{H}_2\text{O,CI Tau}} \simeq 4.88$. Figure 3.4 displays the (scaled) spectra of DR Tau (grey) and CI Tau (black) placed at a small flux offset with respect to the residuals in red over a large portion of the 10.0-27.5 μm wavelength region. Similar to Banzatti et al. (2023a), various cold H_2O lines have excess flux present in the residuals, suggestive of a second, colder H_2O emission component, likely the result of efficient radial drift. By fitting a simple LTE slab model to the residuals, which is also displayed in Figure 3.4, we find that the second component has an excitation temperature of $T=375 \text{ K}$, traces a column density of $N=2.0 \times 10^{19} \text{ cm}^{-2}$, and has an emitting radius of $R_{\text{em}}=0.91 \text{ au}$.

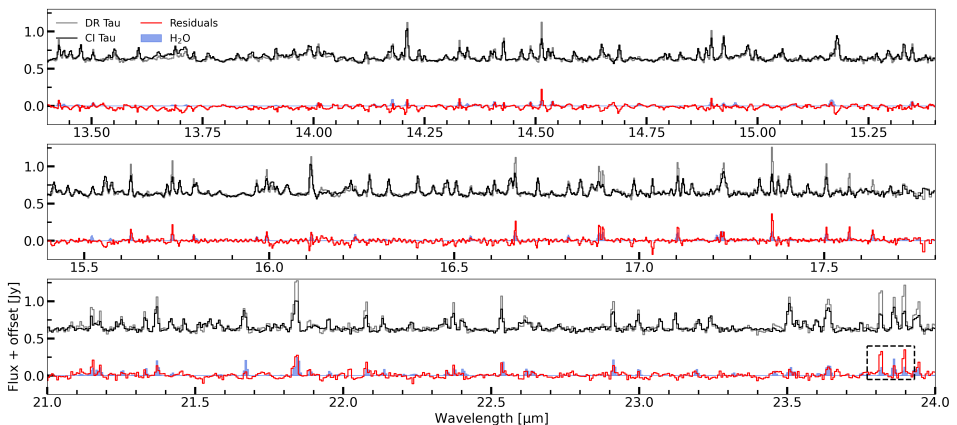


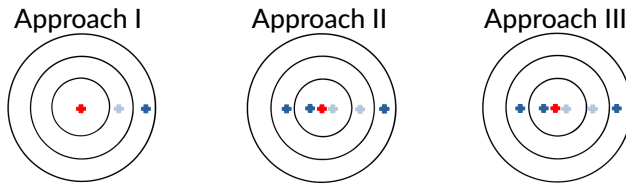
Figure 3.4: Spectra (across 13.4-24.0 μm) of DR Tau (grey) and CI Tau (black, scaled; see Section 3.3.2.2) shown together with the residual spectrum (in red) of DR Tau after subtraction of the scaled spectrum of CI Tau. The best fitting H_2O slab model ($T=375 \text{ K}$) to the residuals is shown in blue. The black dashed box just shortward of $\sim 24.0 \mu\text{m}$ indicates the pair of lines identified by Banzatti et al. (2023a), hinting at a third component ($\sim 170 \text{ K}$) needed to fully explain the observed H_2O reservoir.

Two lines just short of $\sim 24 \mu\text{m}$, indicated by the black, dashed rectangle in Figure 3.4, are not well fitted by the residual slab model. These lines are also visible in the work of Banzatti et al. (2023a), who found that these are best fitted by an even colder component at $T \sim 170 \text{ K}$, which most prominently emits at even larger wavelengths, $\geq 30 \mu\text{m}$ (Zhang et al. 2013; Blevins et al. 2016; Banzatti et al. 2023a).

3.3.3 Cold and warm H_2O reservoirs: multi-component slab models

As shown in Section 3.3.2.2, the pure rotational H_2O spectrum ($\geq 10 \mu\text{m}$) of DR Tau is best described by multiple, at least three, temperature components. In addition, following Section 3.3.1, the hotter (colder) components are thought to trace emission at shorter (longer) wavelengths with smaller (larger) emitting areas. A next step in the analysis of H_2O would be to combine these notions: i.e., we fitted multiple slab models to the spectrum, consisting of components with decreasing temperatures and increasing emitting areas. The fitting is carried out using the Monte-Carlo Markov Chain implementation EMCEE (Foreman-Mackey et al. 2013), using 250 walkers and 150,000 iterations. We test three different approaches for fitting multiple components, see also Figure 3.5.

Top-down view



Edge-on view

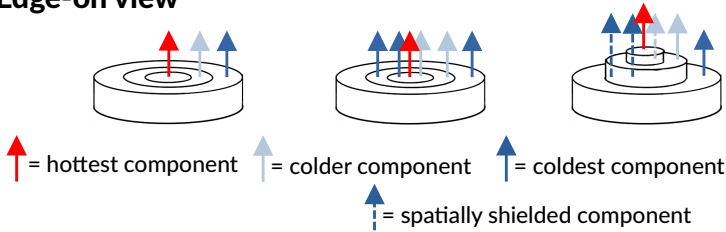


Figure 3.5: Cartoon visualising the different radial and vertical temperature gradients tested in this work. A top down version is shown in the top half of the figure, whereas as an edge-on view is shown in the bottom half. The coloured arrows indicate the emission from the different components, with red showing the emission from the hottest component, light blue for the component with the intermediate temperature, and dark blue for the coldest component. The dashed arrows indicate emission originating from spatially shielded regions.

In the first approach (I) we assumed that the temperature only varies radially, accounting for the decreasing temperature gradient found in planet-forming disks. We consider that each component has a separate emitting region, with hotter components emitting from the smallest regions, closest to the host star. A simple radial temperature gradient is introduced by considering a weighted sum of the components, where the weights correspond to the emitting area (A), $F_{\text{total}} = \sum_i F_i A_i$. The flux of each component, F_i , is determined by a temperature T_i (in K) and a column density N_i (in cm^{-2}), whereas the emitting area is parameterised by an emitting radius R_i (in au). For our three components, this yields the following total flux:

$$F_{\text{total}} = F_1 \pi \left(\frac{R_1}{1 \text{ au}} \right)^2 + F_2 \pi \left[\left(\frac{R_2}{1 \text{ au}} \right)^2 - \left(\frac{R_1}{1 \text{ au}} \right)^2 \right] + F_3 \pi \left[\left(\frac{R_3}{1 \text{ au}} \right)^2 - \left(\frac{R_2}{1 \text{ au}} \right)^2 \right]. \quad (3.2)$$

As planet-forming disks also have a vertical temperature gradient, we allowed the colder components in the second approach (II) to also emit from the overlapping regions with the hotter components. If we are not taking shielding into account and assume that the various components have overlapping emitting areas, the total flux simply becomes:

$$F_{\text{total}} = F_1 \pi \left(\frac{R_1}{1 \text{ au}} \right)^2 + F_2 \pi \left(\frac{R_2}{1 \text{ au}} \right)^2 + F_3 \pi \left(\frac{R_3}{1 \text{ au}} \right)^2. \quad (3.3)$$

In the final approach (III), we accounted for shielding of the colder, deeper components by the optical depth of the hotter components. In the case of shielding, the flux is attenuated by a factor of $\exp(-\sum_i \tau_i)$, where the sum is taken over the optical depths of all the components with a higher temperature. The optical depth is taken to be wavelength-dependent determined for all transitions combined using the corresponding excitation temperature and column density. As shown in Sections 3.3.1 and 3.4.1, and in Table 3.1, the mutual line shielding by neighbouring H_2O transitions does not have a significant impact on the slab models and, hence, we only account for the spatial shielding of colder components by the hotter ones (see Figure 3.5). The total flux of the this approach, in which we account for spatial line shielding of the colder components by the hotter one, becomes:

$$F_{\text{total}} = F_1 \pi \left(\frac{R_1}{1 \text{ au}} \right)^2 + F_2 \pi \left(\frac{R_1}{1 \text{ au}} \right)^2 \exp(-\tau_1) + F_2 \pi \left[\left(\frac{R_2}{1 \text{ au}} \right)^2 - \left(\frac{R_1}{1 \text{ au}} \right)^2 \right] + F_3 \pi \left(\frac{R_1}{1 \text{ au}} \right)^2 \exp(-(\tau_1 + \tau_2)) + F_3 \pi \left[\left(\frac{R_2}{1 \text{ au}} \right)^2 - \left(\frac{R_1}{1 \text{ au}} \right)^2 \right] \exp(-\tau_2) + F_3 \pi \left[\left(\frac{R_3}{1 \text{ au}} \right)^2 - \left(\frac{R_2}{1 \text{ au}} \right)^2 \right]. \quad (3.4)$$

For the two component version, all terms including F_3 can be neglected.

For all three approaches, we considered three components and imposed the following constraints: the temperature must decrease with each component, whereas the emitting radius must increase. We kept the column density as a completely free parameter. In addition, we also show a model with two components for the third method, which allows for a thorough comparison between the models. The results for the different approaches are presented in the following subsections.

Table 3.2: Best-fit parameters for the multiple component slab model fits, including radial and vertical temperature gradients.

Component	T [K]	$\log_{10}(N)^\alpha$	R_{em} [au]	\mathcal{N}
Approach I				
1	806^{+289}_{-154}	$19.2^{+1.5}_{-0.5}$	0.35 ± 0.15	1.40×10^{45}
2	468^{+79}_{-85}	$18.5^{+0.9}_{-0.4}$	$1.18^{+0.27}_{-0.18}$	3.03×10^{45}
3	181^{+36}_{-43}	$17.9^{+2.2}_{-0.7}$	$6.45^{+2.26}_{-2.64}$	2.30×10^{46}
Approach II				
1	796^{+268}_{-141}	$19.2^{+1.4}_{-0.5}$	$0.36^{+0.14}_{-0.15}$	1.50×10^{45}
2	466^{+77}_{-84}	$18.5^{+0.9}_{-0.4}$	$1.14^{+0.24}_{-0.17}$	2.78×10^{45}
3	184^{+29}_{-42}	$17.6^{+2.2}_{-0.7}$	$7.98^{+4.49}_{-3.52}$	1.68×10^{46}
Approach III				
1	798^{+281}_{-141}	$19.2^{+1.5}_{-0.5}$	0.35 ± 0.15	1.50×10^{45}
2	467^{+76}_{-81}	$18.5^{+0.9}_{-0.4}$	$1.20^{+0.26}_{-0.17}$	3.03×10^{45}
3	184^{+30}_{-43}	$17.6^{+2.2}_{-0.7}$	$8.08^{+4.43}_{-3.42}$	1.70×10^{46}
Approach III - two components				
1	712^{+130}_{-100}	$19.1^{+0.8}_{-0.3}$	$0.50^{+0.14}_{-0.12}$	2.02×10^{45}
2	341^{+74}_{-78}	$18.5^{+1.0}_{-0.4}$	$1.83^{+0.54}_{-0.32}$	7.97×10^{45}

Notes. $^\alpha$: N is given in units of cm^{-2} .

3.3.3.1 Radial temperature gradient

The top part of Table 3.2 contains median values yielded by the MCMC for the first approach. The uncertainties are given, respectively, by the 16th and 84th percentiles. For this first approach, we retrieve temperatures of 806^{+289}_{-154} K, 468^{+79}_{-85} K, and 181^{+36}_{-43} K for the different components. In addition, we obtain combinations for the column density ($\log_{10}(N)$, with N in units of cm^{-2}) and emitting radius of, respectively, $19.2^{+1.5}_{-0.5}$ and 0.35 ± 0.15 au, $18.5^{+0.9}_{-0.4}$ and $1.18^{+0.27}_{-0.18}$ au, and $17.9^{+2.2}_{-0.7}$ and $6.45^{+2.26}_{-2.64}$ au. The best fitting model is displayed in the top panel of Figure 3.6, while the corner plots are shown in Figure 3.E.1.

3.3.3.2 Radial and vertical temperature gradient: no shielding

The resulting values for the second approach are shown in the second part of Table 3.2. Compared with approach I, assuming only a radial gradient with no spatial overlap, our best fit parameters do not significantly change. In particular, the main

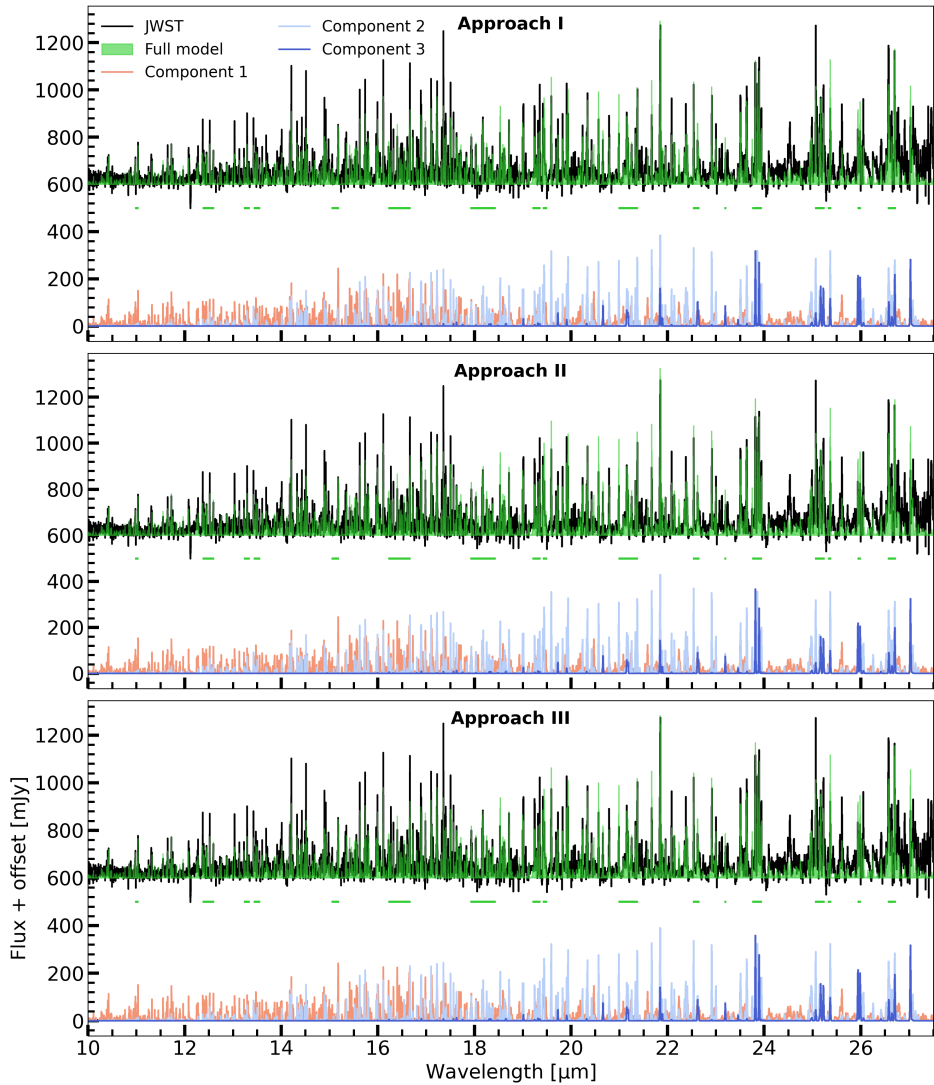


Figure 3.6: Multi-component slab model fits for the different methods of radial gradients: method 1 (radial temperature gradient, without overlapping regions) is shown in the top panel, whereas the methods 2 (radial gradients with overlapping regions, but no line shielding) and 3 (radial and vertical temperature gradients) are displayed in the middle and bottom panels, respectively. The full model is in each panel shown in green, whereas the components are coloured depending on the corresponding temperatures. Red indicates the hottest component, followed by the light blue and dark blue ones. The green horizontal bars indicate the regions used in the χ^2_{red} -fits.

difference can be found in the emitting radius of the third, coldest component.

However, the values still agree within the given uncertainties and show a clear gradient. The final model is shown in the middle panel of Figure 3.6 and their corresponding corner plots are shown in Figure 3.E.2.

3.3.3.3 Radial and vertical temperature gradient: accounting for spatial shielding

The results for the three component and two component fits, using the third approach, are shown in respectively the third and bottom parts of Table 3.2. For the three component fit (also visible in the bottom panel of Figure 3.6), we find that the best fit parameters are similar to those of the second approach. That means that the main difference can once more be found in the emitting radius of the third component. It must be noted that the values for all three approaches agree with one another within the given uncertainties. In accordance with Pontoppidan et al. (2024), we find that the results for this approach can be well described by the power-law $T(R_{\text{em}}) \sim 500 \left(\frac{R_{\text{em}}}{1 \text{ [au]}} \right)^{-0.5}$ K for the emitting layer. For the two component fit, we see that the temperature of the first (hottest) component and the second component are lower by $\gtrsim 100$ K. It is clear that the coldest component, $T \sim 180$ K, is not considered by the two component fit. The lack of this component is also visible in Figure 3.D.1, where the lines just short of $24 \mu\text{m}$ are not well fitted by the model. The column density and the emitting radius of the first component have, respectively, slightly decreased and increased with respect to the three component fit. On the other hand, only the emitting radius of the second component increased from ~ 1.20 au to ~ 1.83 au. The corner plots for the three component and two component fits are shown in Figures 3.E.3 and 3.E.4, respectively.

We find that all models underproduce the flux for a range of H_2O transitions between $\sim 14 \mu\text{m}$ and $\sim 18 \mu\text{m}$. This region is dominated by both the first (hottest) and second (warm) component, suggesting that either one or both components do not properly describe this region and slightly different values for the parameters would yield a better fit. Nonetheless, the fit provides an overall good description of the observed rotational spectrum of H_2O in DR Tau.

Finally, Figure 6.9 displays a cartoon of the disk, indicating the expected emission locations from our multi-component fit. We have also included the expected locations from CO, CO_2 , HCN, C_2H_2 as found in Temmink et al. (2024b) (see also their Figure 12), based on their excitation temperatures and emitting areas.

3.3.4 Line pair ratios

The inferred column density of the slab models can be tested and further constrained by comparing the peak fluxes of H_2O line pairs which have the same value for E_{up} , but different values for A_{ul} (Gasman et al. 2023). As the strength of these lines and, therefore, their ratio depends primarily on the line opacity, they can be used to approximate as independent constraints on the column density and provide a sanity check for the column densities retrieved with the slab models. If

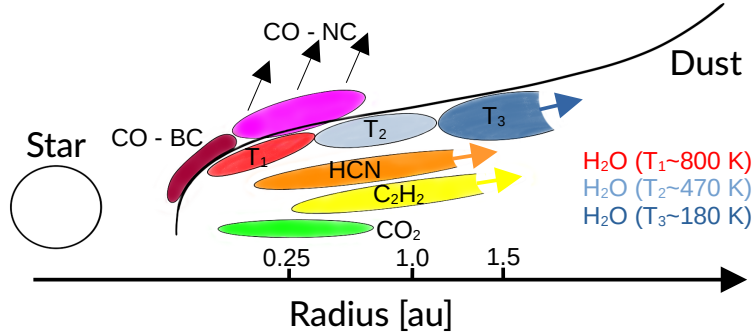


Figure 3.7: Cartoon visualising the expected emission regions, based on the derived excitation temperatures, emitting radii, and optical depths, of the multiple components of H_2O . Shown are also the expected emission locations of CO, CO_2 , HCN, and C_2H_2 adopted from Temmink et al. (2024b). The CO is decomposed in two components: one broad component (BC) tracing the Keplerian rotation of the disk, and a narrow component (NC) tracing a disk wind.

both lines are optically thin, the flux ratio is expected to converge to the ratio of the respective values for A_{ul} , whereas the flux ratio will deviate from the A_{ul} ratio if one of the lines becomes optically thick. We use the same, pure rotational line pairs as Gasman et al. (2023) (see their Table 2) to investigate the H_2O column density. Some of the lines are part of line clusters and are, subsequently, blended, which means that it cannot be concluded from the flux ratio alone which of the lines are optically thick, if the flux ratio deviates from that of A_{ul} .

Figure 3.8 shows the model line ratios for different temperatures (300, 500, and 900 K) and column densities ($14 \leq \log_{10}(N) \leq 22$, with N in units of cm^{-2}). The ratios become constant for column densities of $\lesssim 10^{17} \text{ cm}^{-2}$. For these column densities we can expect both lines to be optically thin and, subsequently, their ratios to be equal to the values for A_{ul} . At larger column densities (at least) one of the lines becomes optically thick and the ratio deviates from that for A_{ul} . For even larger column densities ($\geq 10^{20} \text{ cm}^{-2}$) the ratio becomes constant again, the effect of both lines being fully saturated.

The black horizontal line shown in Figure 3.8 is the line ratio obtained from the JWST-MIRI spectrum. The coloured, dotted vertical lines are the intercepts between the black horizontal line and the model ratio curves. Based on the intercept, we can expect the actual H_2O column density to take on values of $\leq 10^{19.4} \text{ cm}^{-2}$, $\leq 10^{18.4} \text{ cm}^{-2}$, and/or $\leq 10^{18.0} \text{ cm}^{-2}$ for the different temperatures ($T=300$, 500, and 900 K), respectively. Using the results from the multi-component fits, we can infer the contributions from each component to the lines used for both line pairs. For the bottom pair ($11_{5,6}-10_{4,7}/11_{5,6}-10_{2,9}$), both transitions consist of contributions from the hotter two components, so the $T \sim 300$ K models can be ignored. For both transitions, the lower temperature ($T \sim 475$ K) has a slightly larger contribution to the flux. Based on this line pair and the temperature from

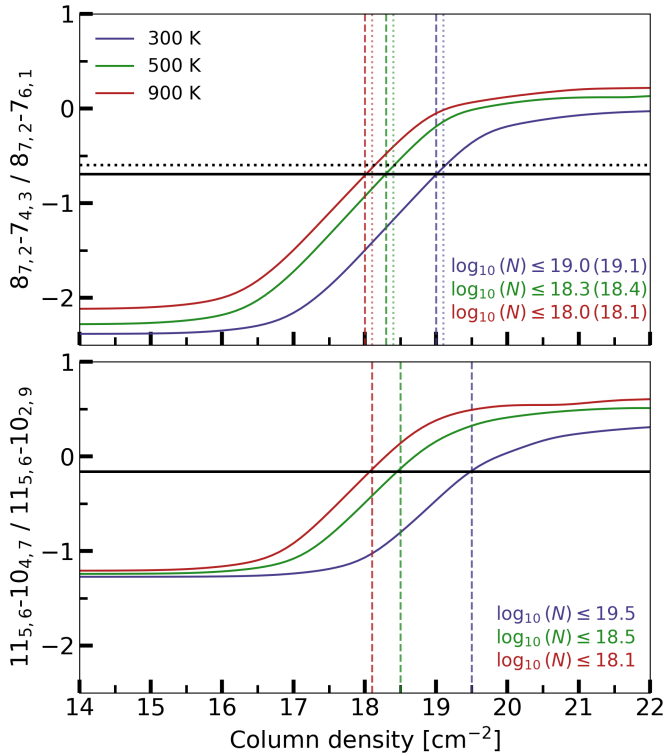


Figure 3.8: Logarithm of the line flux ratios as a function of the logarithm of the column densities (in cm^{-2}) for the line pairs with similar upper level energies. The ratios for the slab models with $T = 300$ K are shown in blue, whereas those for $T = 500$ K and $T = 900$ K are shown in green and red, respectively. The horizontal black line indicates the line ratio taken from the continuum-subtracted spectrum of DR Tau. The dashed, vertical lines indicate where the different model ratios equal the observed line ratio. In addition, the dotted lines and the column densities listed in parenthesis indicate the results for the top line pair after subtracting off the contribution of the component with the lowest temperature (see Section 3.3.3).

both contributing components ($T \sim 830$ K and $T \sim 475$ K), we infer that the column density of the combination of these two H_2O components must be $\log_{10}(N) \leq 18.5$ within ~ 1.2 au. For the top pair ($8_{7,2}-7_{4,3}/8_{7,2}-7_{6,1}$), however, the lowest temperature component ($T \sim 185$ K) also has a significant contribution to the line flux of one of the lines. As only one of these lines has a contribution from the lowest temperature component, this pair does not provide strong constraints. After subtracting off the model corresponding to this temperature, we do infer a slightly more stringent constraint on the H_2O column density (in cm^{-2}) of $\log_{10}(N) \leq 18.4$ for the first two components combined, compared to value derived for the other line pair. Even though H_2O is optically thick, these line pair ratios provide good constraints on the column densities for the first two components. We note that

the derived limit agrees well with those obtained for the second, warm component, whereas it falls just outside the uncertainties for the hottest, most optically thick component.

3.3.5 Searching for H_2^{18}O

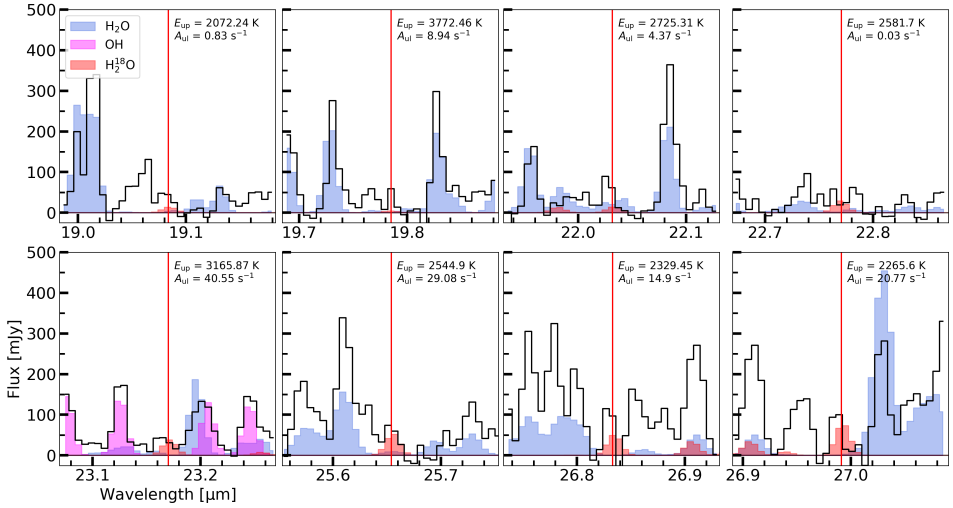


Figure 3.9: Zoom-ins on the isolated H_2^{18}O lines, highlighted by the red vertical line. A simple H_2^{18}O slab model ($T=350$ K, $\log_{10}(N)=17.66$, and $R_{\text{em}}=1.0$ au) is shown in red, whereas the best models of H_2O (three component fit accounting for both the radial and vertical temperature gradient) and OH are shown in blue and magenta, respectively. For each transition, we have listed the upper level energies and Einstein-A coefficients.

We are inconclusive about the detection of H_2^{18}O in DR Tau. Some of the transitions, in particular those at 25.65, 26.83, and 26.99 μm , look promising (see Figure 3.9). Accounting for the large error in subband 4C (see Table 3.A.1), the peak fluxes suggest maximum detection levels of $\lesssim 4\sigma$ and should be statistically significant for the confirmation of a detection. However, the lack of flux seen for the transitions at ~ 22.03 μm and ~ 23.17 μm provide the strongest argument against a detection of H_2^{18}O in DR Tau. Re-observing DR Tau with JWST-MIRI with the aim of achieving higher signal-to-noise ratios across Channel 4 may improve our chances of detecting H_2^{18}O .

Using our three component models, we find that the majority of the H_2O emission features are optically thick. While transitions with low Einstein-A values may be optically thin and can be used to derive better constraints on the total H_2O vapour reservoir present in the inner disk, we note that these lines are very scarce in the spectrum of DR Tau. In total, we identify four clean emission features (between 12.496-12.506, 14.377-14.392, 16.362-16.375, and 19.370-19.392 μm) that are optically thin ($\tau < 1$) according to our models and not blended with other (unidentified) emission features. All these transitions trace mainly the hottest

component. Subsequently, a fit to these transitions only may provide a better constraint on the column density for the hottest component and observations of the optically thin isotopologues, such as H_2^{18}O , could help to infer a better estimate of the column density and the total number of H_2O molecules present in the inner disk.

Calahan et al. (2022) list eight lines in the 19.0-27.0 μm wavelength range that may be used for the detection of H_2^{18}O in JWST-MIRI spectra (see their Table 1). We, however, note that the line at 20.01 μm is blended with OH and can likely not be used for the detection of H_2^{18}O in many T-Tauri disks. On the other hand, through slab model exploration we discovered a blended pair of H_2^{18}O lines that can be used instead. The line pair ($8_{8,0}-7_{7,1}$ and $8_{8,1}-7_{7,0}$) is located at 25.65 μm and have the same upper level energies ($E_{\text{up}} \sim 2544.9$ K) and Einstein-A coefficients ($A_{\text{ul}} \sim 29.08$ s $^{-1}$), suggesting that both lines contribute half of the observed line flux. The individual lines are displayed in Figure 3.9. The H_2^{18}O emission is highlighted by a simple H_2^{18}O slab model ($T=350$ K, $\log_{10}(N)=17.36$, and $R_{\text{em}}=1.0$ au), where we have accounted for the isotopologue ratio in the local interstellar medium (ISM) of $^{16}\text{O}/^{18}\text{O} \sim 550$ (Wilson 1999) in the column density, i.e. we have divided the found column density of H_2O in the wavelength region of 23.0-27.0 μm ($\log(N) \sim 20.1$, see Table 3.1) by 550. We show our best fitting H_2^{16}O and OH slab models (see Table 3.1 and Section 3.3.6.1) for further identification. We show the full 17.0-27.5 μm wavelength region, including the aforementioned H_2^{16}O , H_2^{18}O , and OH slab models in Figure 3.F.1.

Even though we are inconclusive about the detection of H_2^{18}O , the used slab model yields underproduced fluxes for the most promising peaks. This may suggest that, for the used temperature, the input column density is not high enough. As the column density was set to account for the isotopologue ratio ($^{16}\text{O}/^{18}\text{O} \sim 550$), this indicates optically thick H_2O emission, which is in agreement with our models. We note that an underestimate of the column density for H_2^{18}O may also point to a deviation of the isotopologue from the ISM value. As discussed in Calahan et al. (2022), the gas may be enriched in H_2^{18}O in the disk layers where CO becomes optically thick and self-shielding against photodissociation becomes important. As the main isotopologue, C^{16}O , is more abundant than C^{18}O , there will be a layer where C^{16}O will be self-shielded, whereas C^{18}O is still being dissociated. The gas in this layer will in that case be enriched in ^{18}O atoms, which may end up in H_2O -molecules, enhancing the H_2^{18}O column. Additionally, UV-shielding by the main isotopologue, H_2^{16}O , can also enhance the H_2^{18}O abundance.

3.3.6 Other emission features

Besides emission from H_2O , the spectrum of DR Tau is rather molecule rich. CO, CO_2 , HCN, and C_2H_2 have been thoroughly discussed in Temmink et al. (2024b), so the upcoming subsections discuss the other molecular features potentially present in the spectrum, including OH and the larger hydrocarbons that have been observed in the disks around very low-mass stars (e.g. Tabone et al. 2023).

3.3.6.1 OH

Since we do not detect any OH lines at wavelengths $<13 \mu\text{m}$, similar to Gasman et al. (2023), we do not expect prompt emission, following H_2O photodissociation (Najita et al. 2010), to play a role in the observed OH emission in DR Tau. We fit the OH emission, using a reduced χ^2 -minimisation (see also Section 3.3.1), over the entire wavelength range of $10 \mu\text{m}$ to $27.5 \mu\text{m}$. We have used the same grid for T , $\log_{10}(N)$, and R_{em} as in Section 3.3, except we extended the grid for the excitation temperature up to 4000 K. The emission was fit to the residual spectrum after subtracting the resulting H_2O model spectrum taking both a radial and vertical temperature gradient into account (see Section 3.3.3.3). For OH, we retrieve a temperature of $T=1875^{+775}_{-725}$ K, a column density (in cm^{-2}) of $\log(N)=13.5^{+3.3}_{-0.3}$, and emitting radius of $R_{\text{em}}=9.49^{+0.52}_{-9.06}$ au. As the emission is optically thin ($\tau \leq 0.005$) for this combination of excitation temperature and column density, the emitting radius is not well constrained, as indicated by the large lower uncertainty. We note that the upper uncertainty of the emitting radius and, therefore, the lower constraints on the column density are set by the limits of our grids. For these parameters, we derive that the number of OH molecules present in the inner disk of DR Tau is $\mathcal{N} \sim 2.0 \times 10^{42}$. Parts of the best fitting spectrum, including the wavelength regions used in the fitting, are displayed in the bottom part of Figure 3.B.1. Similar to Gasman et al. (2023), the OH lines probe larger gas temperatures compared to H_2O , but lower column densities. As the excitation of the OH lines includes prompt emission (Tabone et al. 2021, 2024) and collisional excitation or chemical pumping (Zannese et al. 2024) through the $\text{O}+\text{H}_2 \rightarrow \text{OH}+\text{H}$ reaction, it is unlikely that the observed transitions follow a single excitation temperature. Therefore, the inferred temperature from the slab model is not related to a kinetic temperature. While they cannot infer a kinetic temperature, we note that slab models are a powerful tool for the identification of OH transitions in the JWST-MIRI/MRS spectra of disks. Detailed models, including the different excitation pathways, can be used to further explore the excitation properties and to infer other key disk parameters (see, for example, Tabone et al. 2024).

3.3.6.2 Atomic and molecular hydrogen

We list the detection of three atomic hydrogen (H) transitions (10-6, 6-5, and 8-6) and the potential detection of four molecular hydrogen (H_2) transitions: 0,0 S(1), S(2), S(3), and S(4). As the H_2 lines are either blended with H_2O or potentially blended with unidentified features, their detections are not fully secure. Higher transitions (e.g. S(5), S(6), S(7), and S(8)) may also be present, however, their detections are even less certain due to stronger blending with H_2O and CO emission features. Figures 3.G.1 and 3.G.2 display the (potentially) observed transitions of H and H_2 (S(1), S(2), S(3), and S(4)), respectively. We also see no evidence of extended H_2 emission coming from the DR Tau disk in the form of a disk wind or an outflow, however, we do observe extended H_2 emission (most prominent in the S(1) transition) from the cloud surrounding DR Tau, as was previously observed by Thi et al. (2001) in millimetre single dish CO $J=3-2$ transitions offset by $\sim 2 \text{ km s}^{-1}$. The emission coming from the background is visualised in Figure 3.G.3.

Visual inspection of the spectral cube shows that the flux of the cloud emission ($F_{S(1)} \sim 2 \times 10^2$ MJy sr $^{-1}$) is a factor ~ 100 lower than the flux at the position of DR Tau ($F_{S(1)} \sim 2 \times 10^4$ MJy sr $^{-1}$). As we approximate our background using an annulus, the H $_2$ emission from the cloud will be captured in that annulus. However, as the flux is significantly lower than the source flux, the background subtraction does not impact our detections.

Using the residual flux, after subtracting the corresponding H $_2$ O slab model fit, we determined an upper limit on the column density of H $_2$ based on the 0,0 S(4) transition ($E_{\text{up}}=3474.5$ K). Assuming that H $_2$ comes from the inner most region, we adopt a temperature of $T=1000$ K and an emitting radius of $R_{\text{em}}=0.20$ au, as this also allows us to make direct comparisons with the total number of molecules of both CO and H $_2$ O (as obtained in regions 1 and 2 for the ro-vibrational transitions, see Section 3.3.1) derived in these innermost regions. To calculate the column density under the assumption of optically thin emission, we follow the description given in Goldsmith & Langer (1999):

$$\frac{4\pi F}{hc\nu\Omega g_{\text{up}}A_{\text{ul}}} = \frac{N_{\text{tot}}}{Q(T)} \exp\left(-\frac{E_{\text{up}}}{k_B T}\right), \quad (3.5)$$

where F is the integrated flux (in erg s $^{-1}$ cm $^{-2}$), ν the frequency (in cm $^{-1}$), g_{up} the upper level degeneracy, $Q(T)$ the partition function at a temperature T , and E_{up} the upper level energy (in K). Using the resolution element at the location of the S(4) transition and the two resolution elements directly next to it, we derive $F=3.9 \times 10^{-15}$ erg s $^{-1}$ cm $^{-2}$. As mentioned above, the H $_2$ flux might be slightly affected by the annulus background subtraction due to cloud emission. However, as the background emission is significantly lower than the on-source emission, we expect the derived flux to be minimally impacted. This yields a column density of $N_{\text{tot}} \sim 7.6 \times 10^{25}$ cm $^{-2}$ and a total number of molecules, assuming an emitting radius of 0.20 au, of $\mathcal{N}_{\text{H}_2} \sim 2.1 \times 10^{51}$. We note once more that these derived column densities and total number of molecules hold for the upper layers of the disk, above the region where the dust emission becomes optically thick, or, in the case of optically thick lines, above the height where the emission lines become optically thick (see for example Bosman et al. 2022a).

3.3.6.3 Non-detections

In an attempt to identify as many molecular features as possible, we have also looked for emission signatures of various other molecules and isotopologues. These species are comprised of $^{13}\text{CO}_2$, CH $_4$, NH $_3$, CS, H $_2$ S, SO $_2$, and various larger hydrocarbons, including $^{13}\text{CCH}_2$. We have obtained the required spectroscopic data for these species through the HITRAN database (Gordon et al. 2022). Table 3.3 summarises the parameters (assuming an emitting radius of $R_{\text{em}}=1.0$ au) of simple LTE slab models with fixed temperature and column density that have been used to search for these species. In addition, the table lists the best fit parameters for CO $_2$, HCN, and C $_2$ H $_2$, as found in Temmink et al. (2024b). The slab models are also displayed in Figures 3.G.4 and 3.G.5.

We are not able to confidently detect any of the listed molecular species.

Table 3.3: Slab models parameters of the various detected (CO_2 , HCN , C_2H_2 ; Temmink et al. 2024b) and non-detected species, using $R_{\text{em}}=1$ au.

Mol.	Region [μm]	T [K]	$\log_{10}(N)^\alpha$	\mathcal{N}
$^{12}\text{CO}_2^\beta$	13.60-16.30	325_{-100}^{+50}	$17.4_{-0.2}^{+0.7}$	4.96×10^{43}
HCN^β	13.60-16.30	900_{-50}^{+50}	$14.7_{-0.6}^{+2.1}$	8.22×10^{42}
$\text{C}_2\text{H}_2^\beta$	13.60-16.30	775_{-625}^{+150}	$15.0_{-1.7}^{+5.6}$	1.48×10^{42}
$^{13}\text{CO}_2$	15.30-15.50	300	15.57	$\leq 2.6 \times 10^{42}$
CH_4	7.60-7.75	700	15.75	$\leq 4.0 \times 10^{42}$
NH_3	8.50-9.50	500	15.50	$\leq 2.2 \times 10^{42}$
CS	7.50-8.30	500	15.50	$\leq 2.2 \times 10^{42}$
H_2S	7.00-8.00	500	18.00	$\leq 7.0 \times 10^{44}$
SO_2	7.10-7.62	500	15.50	$\leq 2.2 \times 10^{42}$
$^{13}\text{CCH}_2$	13.60-13.85	750	15.00	$\leq 7.0 \times 10^{41}$
C_2H_4	10.50-10.60	700	16.00	$\leq 7.0 \times 10^{42}$
C_2H_6	12.00-12.34	700	17.00	$\leq 7.0 \times 10^{43}$
C_4H_2	15.80-16.00	700	15.50	$\leq 2.2 \times 10^{42}$
C_6H_6	14.70-15.00	700	11.25	$\leq 1.3 \times 10^{38}$

Notes. $^\alpha$: N is given in units of cm^{-2} .

$^\beta$: The listed values for CO_2 , HCN , and C_2H_2 are taken from Temmink et al. (2024b) and are shown here for completion.

The non-detection of some the molecules, for example, $^{13}\text{CO}_2$, CH_4 , SO_2 , and the larger hydrocarbons, becomes apparent from the slab models, mostly due to the lack of a molecular continuum. For the other molecules, NH_3 , CS , H_2S , and $^{13}\text{CCH}_2$, a (non-)detection cannot be confirmed, largely due to leftover broad features (especially visible at the location of the silicate feature at $\sim 10 \mu\text{m}$), which are potentially of molecular nature, in the spectrum. We also do not detect the larger hydrocarbons, mostly due to the lack of molecular continua. While the slab model of C_6H_6 looks promising in the last panel of Figure 3.G.5, the presence of C_6H_6 cannot be confirmed in the spectrum of DR Tau, as the lack of emission observed for the other hydrocarbons makes the presence of C_6H_6 less likely.

For most of the non-detected molecules, the upper limit on the total number of molecules is on the order of $\mathcal{N} \sim 10^{42}$ - 10^{43} . Only the upper limit for H_2S is larger ($\mathcal{N} \sim 7.0 \times 10^{44}$), whereas that for C_6H_6 is significantly lower ($\mathcal{N} \sim 1.3 \times 10^{38}$). Using the number of molecules from our three component H_2O fits ($\mathcal{N} \sim 10^{45}$ - 10^{46}), most of the non-detected molecules are a factor $\geq 10^2$ - 10^4 less abundant than H_2O . H_2S and C_6H_6 are factors of, respectively, ≥ 10 - 100 and $\geq 10^7$ - 10^8 less abundant. On the other hand, the upper limits are of a similar level compared to the total number of molecules derived for CO_2 , HCN , and C_2H_2 . Once again, the upper limit for H_2S is slightly larger, whereas that of C_6H_6 is a few orders of magnitude lower. For comparison, the abundance of CO_2 is found to be a factor ~ 60 lower than the second, warm component of H_2O .

3.4 Discussion

3.4.1 The need for H₂O line overlap

For slab model fits of molecules with a well defined Q -branch (see Tabone et al. 2023), line overlap (i.e. mutual shielding of lines) is often included to properly fit the spectra. The spectrum of H₂O, on the other hand, consists of well defined, separate/isolated transitions. In the disk of AS 209, Romero-Mirza et al. (2024b) also tested the need for line overlap of multiple molecular species. They conclude that a proper treatment of the line overlap is necessary when analysing the observed molecular species together.

In Section 3.3.1, we test the need for mutual shielding by the H₂O transitions alone. We test this by creating slab models without and with mutual line shielding. As can be seen in Table 3.1, the differences between the slab models without (top part of the table) and those with (bottom part) mutual line overlap are negligible when fitting H₂O alone. The largest differences are found for temperatures derived for the regions spanning the ro-vibrational transitions, which is likely due to the lines being more densely packed in this part of the spectrum compared to those in the pure rotational part. We note that the residuals for the models without and with mutual line shielding are quite similar. We find that one model will provide a better fit for some transitions, whereas other transitions are better fitted by the other model. Therefore, we conclude that the inclusion of mutual shielding of neighbouring H₂O lines is not of particular importance for the pure rotational transitions of H₂O, when fitting them alone, and that the slab models without mutual line shielding can be used to infer constraints on the excitation conditions. As our slab models yield different results for the rovibrational part of the spectrum, the inclusion of mutual shielding may be more important for these more densely packed transitions. Mutual line shielding is of particular importance for molecules with a well defined Q -branch, such as CO₂, HCN, and C₂H₂.

3.4.2 The need for a radial temperature gradient

As expected, the various methods all indicate a radial temperature gradient visible in the spectrum. Fitting, however, the H₂O spectrum across multiple, independent wavelength regions does not yield any information on the low temperature ($T \sim 170$ -200 K, see Table 3.1) component, even though the fitted regions include the lines best suitable for finding this component. Subsequently, to properly investigate the various components, one could use the large disk template method implemented by Banzatti et al. (2023a) or the multi-component slab model method introduced here.

Rather surprisingly, the current approaches of the multi-component slab model fits yield the same results for all three methods: temperatures of ~ 800 K, ~ 470 K, and ~ 180 K, column densities of $\sim 10^{19.2}$ cm⁻², $\sim 10^{18.5}$ cm⁻², and $\sim 10^{17.4}$ cm⁻², and emitting radii of ~ 0.3 au, ~ 1.2 au, and ~ 6.5 -8.1 au. For comparison, the mid-plane H₂O snowline in DR Tau can be estimated from a simple power law (Chiang & Goldreich 1997; Dullemond et al. 2001; van der Marel et al. 2021b) involving

the total luminosity ($L_{\text{tot}}=L_*+L_{\text{acc}} \simeq 0.63 + 0.58 L_{\odot}$; Long et al. 2019; Banzatti et al. 2020), providing a radius $R_{\text{H}_2\text{O}} \sim 0.75$ au. The calculations of Mulders et al. (2015) (see their Figure 1) suggest that the snowline is located at a radial distance of ~ 1 -2 au. Radiative transfer modelling of the dust disks may provide further constraints on the location of the H_2O snowline. As the third component at ~ 180 K is at larger distances than the midplane snow surface, this suggests a curved rather than vertical snow surface. We find that the decreasing temperature profile can be well described by the powerlaw $T(R_{\text{em}}) \sim 500 \left(\frac{R_{\text{em}}}{1 \text{ [au]}} \right)^{-0.5}$ K. Only the emitting radius for the final component differs between approach 1 and approaches 2 and 3, but still agrees well within the given uncertainties. The resulting temperatures agree with those given by the large scale template method, in particular the third component ($T \sim 180$ K) corresponds well with the one ($T \sim 170$ K) that Banzatti et al. (2023a) needed to explain the lines just shortward of $24 \mu\text{m}$. To extend upon this notion, Figure 3.D.1 shows a comparison between the multi-component fits including three and two components. The main difference is most clearly visible in the region of 23.50 - $24.25 \mu\text{m}$, which includes the aforementioned cold lines. The two component model is not able to properly fit this line cluster, whereas the three component model can.

Compared to results from fitting H_2O across the different wavelength regions (see Section 3.3.1), we note that the derived column densities for these methods do not show the same behaviour. For the multi-component fit, the column densities decrease with lower temperatures, whereas they increase with temperature for the different regions. The difference in behaviour may have arisen from combining the contribution of every component in the multi-component fits, whereas contributions of other components and/or wavelength regions have not been accounted for in the fits to the different wavelength regions.

A multi-component fit could, instead of a large disk model, also be used to investigate the enhanced reservoir of cold H_2O through radial drift. We expect that a two component fit is sufficient to fit the spectra without enhancement of cold H_2O through radial drift, whereas three component fits are required to properly fit those with the enhancement. Further work examining a large sample of disks, small and large, structured and smooth, is necessary to fully explore this thought.

The reason why all three models yield the same results is due to line optical depths. These optical depths are too high (reaching values up to $\tau \sim 3000$ for the innermost region and $\tau \sim 350$ for the first annulus for the brightest lines) for any of the shielded regions to make a significant contribution to the total model. In other words, considering only the innermost region, the optical depth of the hottest components is so high that the contributions (i.e. those with an exponential in Equation 3.4) of the lower temperature components are negligible. As discussed in Section 3.3.4, the column density (in cm^{-2}) of the warmer two components (components 1 and 2) can be expected to be on the order of $\log(N) \sim 18.4$.

When using simple LTE slab models to describe the full rotational spectrum of H_2O , it is clear that a vertical temperature gradient does not need to be included. Due to the negligible contributions from the overlapping region, a simple radial gradient (using two or three components) alone should be sufficient to represent

the emitting layer in the upper region of the disk. For more sophisticated thermochemical modelling methods, more realistic column densities may be probed and the inclusion of vertical temperature gradients may become of significant importance.

3.4.3 The importance of radial drift

We find that our introduced multi-component models, with various levels of complexity, are able to yield similar results as those obtained with the method of Banzatti et al. (2023a). We note that at least three components are required to fully describe the pure rotational H₂O of DR Tau (see also Section 3.4.2). In particular, these three components, including a cold component of $T \sim 180$ K, are necessary to describe the quartet of H₂O lines just shortward of $\sim 24 \mu\text{m}$. This cold component has been suggested by Banzatti et al. (2023a) to trace an additional H₂O reservoir near the snowline, following the inward drift of icy pebbles, the subsequent sublimation, and the diffusion of H₂O vapour. Modelling works (e.g. Bosman et al. 2018; Kalyaan et al. 2021) have shown that the inward drift of solids can increase the H₂O abundance (or vapour mass) inside the snowline up to an order of magnitude during the first few million years. As our models require this cold component and the disk around DR Tau is compact in the millimetre dust ($\lesssim 60$ au), our multi-component analysis can be used to further study the importance of radial drift in setting the potentially enhanced observable H₂O reservoirs in the inner regions of planet-forming disks. An upcoming paper will utilise this method on a larger sample of compact disks.

3.4.4 CO versus H₂O

With both CO (see Temmink et al. 2024b) and ro-vibrational H₂O (Regions 1 and 2 in Table 3.1) analysed, we can compare their respective total number of molecules, assuming the two molecules are co-spatial down to the layer where the $\sim 6 \mu\text{m}$ dust continuum becomes optically thick. The assumption that the two molecules may be co-spatial is supported by the high spectral resolution study of Banzatti et al. (2023b), where the similar line profiles suggest that the ro-vibrational H₂O lines may originate from the same region as the broad component of CO, which is thought to trace the Keplerian rotation of the disk. Using the optically thin C¹⁸O emission seen in the VLT-CRIRES observations of DR Tau, Temmink et al. (2024b) derived a total number of molecules of $\mathcal{N}_{\text{CO}} = 4.1 \times 10^{44}$. For the C¹⁸O, they retrieved an excitation temperature of $T \sim 975$ K and an emitting radius of $R_{\text{em}} = 0.23$ au, which agree well with the best fit parameters found for the ro-vibrational H₂O transitions at the shortest wavelengths ($5.0\text{--}6.5 \mu\text{m}$, see Table 3.1), suggesting that the probed emission may indeed come from the same region in the disk. For this wavelength range ($5.0\text{--}6.5 \mu\text{m}$), we retrieve a total number of molecules of $\mathcal{N}_{\text{H}_2\text{O}} \sim 7 \times 10^{43}$. These values yield a ratio of $\mathcal{N}_{\text{H}_2\text{O}}/\mathcal{N}_{\text{CO}} \sim 0.17$.

Taking typical ISM abundances of $[\text{O}] = 5.8 \times 10^{-4}$ and $[\text{C}] = 3.0 \times 10^{-4}$, and taking into account the amounts of oxygen and carbon that are locked up in solid form, the maximum H₂O/CO ratio is $\sim 1.4\text{--}2.0$, if all volatile oxygen not locked

up in CO is driven into H₂O (van Dishoeck et al. 2021). This ratio is significantly higher than we retrieve for DR Tau, suggesting that the total number of H₂O molecules may be low, instead of enhanced as expected for compact disks, in the inner disk. However, as discussed at previous points throughout this work (see Sections 3.3.5 and 3.4.2), many of the observed H₂O transitions are optically thick. Subsequently, our derived ratio of $\mathcal{N}_{\text{H}_2\text{O}}/\mathcal{N}_{\text{CO}} \sim 0.16$ acts as a lower limit. A factor ~ 10 is required to meet the aforementioned expected ratio of H₂O/CO ~ 1.4 – 2.0 . Perhaps the H₂O emission becomes optically thick well above the layer where the dust becomes optically thick, suggesting that we may probe less deep into disk compared to both CO (probed with the optically thin C¹⁸O emission) and H₂. Additionally, H₂O may self-shield against the photodissociating UV-photons before C¹⁸O (Calahan et al. 2022), leaving a thin emitting layer where both molecules are co-located. Higher signal-to-noise detections of one of the rarer H₂O isotopologue (e.g. H₂¹⁸O) or detections of the optically thin, low Einstein-A H₂¹⁶O transitions (see Section 3.3.5), which probe deeper into the disk (Bosman et al. 2022a), are needed to further explore the abundance ratio of CO and H₂O.

We note that the total number of molecules for both H₂O and CO appear to be low with respect to that of molecular hydrogen, H₂. For CO the ISM abundance is of the order of CO/H₂ $\sim 10^{-4}$ (Bergin & Williams 2017; Lacy et al. 2017), whereas that of H₂O is H₂O/H₂ $\sim 4 \times 10^{-4}$ (van Dishoeck et al. 2021), if most volatile oxygen is used in the formation of H₂O. Assuming a temperature of $T \sim 1000$ K and an emitting radius of $R_{\text{em}} = 0.20$ au, we derive an upper limit on the total number of molecules of $\mathcal{N}_{\text{H}_2} \leq 2.1 \times 10^{51}$. This number is a factor of, respectively, 5.1×10^6 and 3.0×10^7 higher than the total number of molecules derived for CO and H₂O, under the assumption that all molecules probe the same region of the disk. However, caution is warranted as H₂ is not strongly detected and we emphasise that derived number of molecules must be treated as an lower limit.

3.5 Conclusions and summary

In this work, we thoroughly analysed the H₂O excitation temperatures and column densities in the inner region of the planet-forming disk of DR Tau, as seen with JWST-MIRI/MRS. We have used techniques presented in previous works, as well as tried, for the first time, a multi-component approach to fully describe the rotational H₂O spectrum ($\geq 10 \mu\text{m}$). In addition, to the H₂O analysis, we have also analysed the OH, atomic and molecular hydrogen emission, and looked for other molecular species. We summarise our conclusions as follows:

- By analysing the H₂O over various wavelength regions, we find that the excitation temperature decreases with wavelength, whereas the emitting radius increases. This is a clear sign of a radial temperature gradient visible in the spectrum. The need for a temperature gradient, or multiple components, is further confirmed by using the spectrum of a large disk (CI Tau) as comparison template for the spectrum of our compact disk. Various cold emission lines are not reproduced by this large disk template and are explained by slab models with low temperatures of $T \sim 400$ K and $T \sim 200$ K.

- To further test the need for multiple components, we used an MCMC approach to fit two and three components at the same time. Our methods include a simple radial gradient, a radial gradient with spatial overlap, and a radial and vertical gradient. The different methods yield no significant differences in the excitation properties (temperatures, column densities, and emitting radii) of the different components, likely due to the high optical depth of the hotter components in the overlapping regions. Consequently, we can state that simple models (i.e. models only considering a radial temperature gradient) are able to provide a proper description of the rotational H₂O spectrum and are supported by the more complex models (i.e. those including a vertical gradient). Only for disks where the hotter components are not optically thick, the results will differ and a more complex model must be used.
- We find that the temperature for the third approach can be described roughly as $T(R_{\text{em}}) \sim 500 \left(\frac{R_{\text{em}}}{1 \text{ [au]}} \right)^{-0.5}$ K. For DR Tau, we emphasise the need for a minimum of three components ($T_1 \sim 800$ K, $T_2 \sim 470$ K, and $T_3 \sim 180$ K), as the two component model is unable to fit the transitions at the longest wavelengths, especially those around $\sim 24 \mu\text{m}$. While the need for the third component around the H₂O snowline is in agreement with previous works, it is not yet possible to conclude whether the H₂O abundance is enhanced due to radial drift. A future study focusing on a consistent analysis of a larger sample of compact disks will provide more insights in the importance of radial drift.
- While OH and various atomic and molecular hydrogen transitions are detected, we are inconclusive about the detection of the isotopologue H₂¹⁸O, mostly due to the (current) large uncertainties at the longest wavelengths. We also do not report the detections of various other species, including: CH₄, NH₃, CS, H₂, SO₂, and larger hydrocarbons. The derived upper limits on the column densities of these non-detected species are almost all significantly lower, by factors $\sim 10^2$ - 10^4 , than those found for H₂O in the different wavelength regions (see Section 3.3.1).
- Finally, we have compared the derived number of H₂O molecules with that of CO, derived from the optically thin C¹⁸O emission. The comparison yields a low ratio of ~ 0.17 , which, for the hot H₂O component $T \sim 1000$ K, may point to H₂O having a relative low total number of molecules in the layer that we are able to trace. However, the strongest H₂O lines are found to be optically thick, suggesting that we may be probing less deep into the disk compared to C¹⁸O, and so this ratio must be treated as a lower limit. A detection of one of the rarer isotopologues (e.g. H₂¹⁸O) is required to better constrain their relative number of molecules down to the layer where the dust continuum becomes optically thick.

This work has shown the need of fitting multiple components to explain the rotational spectrum of H₂O. Future works focusing on the multiple-component anal-

ysis of H_2O in larger samples of disks can help us further understand the H_2O reservoir present in the inner regions of disks. In addition, this method may shed more light on the importance of radial drift in setting the inner disk H_2O reservoir by comparing small disks, where radial drift is expected to be very efficient, with large disks, in which drift is expected to be halted by substructures.

Abstract

The authors would like to thank Andrea Banzatti for many very useful discussions. We also thank the referee for many thoughtful, constructive comments that helped improve the manuscript.

This work is based on observations made with the NASA/ESA/CSA James Webb Space Telescope. The data were obtained from the Mikulski Archive for Space Telescopes at the Space Telescope Science Institute, which is operated by the Association of Universities for Research in Astronomy, Inc., under NASA contract NAS 5-03127 for JWST. These observations are associated with program #1282. The following National and International Funding Agencies funded and supported the MIRI development: NASA; ESA; Belgian Science Policy Office (BELSPO); Centre Nationale d’Etudes Spatiales (CNES); Danish National Space Centre; Deutsches Zentrum für Luft- und Raumfahrt (DLR); Enterprise Ireland; Ministerio De Economía y Competividad; Netherlands Research School for Astronomy (NOVA); Netherlands Organisation for Scientific Research (NWO); Science and Technology Facilities Council; Swiss Space Office; Swedish National Space Agency; and UK Space Agency.

The authors acknowledge the GO #1640 team for developing their observing program with a zero-exclusive-access period, which includes CI Tau.

M.T., E.v.D., and M.V. acknowledge support from the ERC grant 101019751 MOLDISK. E.v.D. acknowledges support from the Danish National Research Foundation through the Center of Excellence “InterCat” (DNRF150). E.v.D., I.K., and A.M.A., acknowledge support from grant TOP-1 614.001.751 from the Dutch Research Council (NWO). D.G. thank the Belgian Federal Science Policy Office (BELSPO) for the provision of financial support in the framework of the PRODEX Programme of the European Space Agency (ESA). B.T. is a Laureate of the Paris Region fellowship program, which is supported by the Ile-de-France Region and has received funding under the Horizon 2020 innovation framework program and Marie Skłodowska-Curie grant agreement No. 945298. T.H. and K.S. acknowledge support from the European Research Council under the Horizon 2020 Framework Program via the ERC Advanced Grant Origins 83 24 28. D.B. has been funded by Spanish MCIN/AEI/10.13039/501100011033 grants PID2019-107061GB-C61 and No. MDM-2017-0737. A.C.G. acknowledges from PRIN-MUR 2022 20228JPA3A “The path to star and planet formation in the JWST era (PATH)” funded by NextGeneration EU and by INAF-GoG 2022 “NIR-dark Accretion Outbursts in Massive Young stellar objects (NAOMY)” and Large Grant INAF 2022 “YSOs Outflows, Disks and Accretion: towards a global framework for the evolution of planet forming systems (YODA)”. I.K. acknowledge funding from H2020-MSCA-

ITN-2019, grant no. 860470 (CHAMELEON). G.P. gratefully acknowledges support from the Max Planck Society.

This work also has made use of the following software packages that have not been mentioned in the main text: NumPy, SciPy, Astropy, Matplotlib, pandas, IPython, Jupyter (Harris et al. 2020; Virtanen et al. 2020; Astropy Collaboration et al. 2013, 2018, 2022; Hunter 2007; pandas development team 2020; Pérez & Granger 2007; Kluyver et al. 2016).

Appendix

3.A Uncertainties for the JWST-MIRI subbands

Table 3.A.1: Median continuum flux, estimated S/N from the ETC, and the obtained uncertainty σ for each subband.

Subband ($[\mu\text{m}]$)	Median flux [Jy]	ETC S/N	σ [mJy]
1A (4.90-5.74)	1.31	533.5	2.5
1B (5.66-6.63)	1.31	613.5	2.1
1C (7.51-8.77)	1.32	743.9	1.8
2A (7.51-8.77)	1.43	745.2	1.9
2B (8.67-10.13)	1.98	962.6	2.1
2C (10.02-11.70)	2.03	1014.2	2.0
3A (11.55-13.47)	1.79	956.5	2.0
3B (13.34-15.57)	1.89	991.57	1.9
3C (15.41-17.98)	2.35	1143.0	2.1
4A (17.70-20.95)	2.69	497.3	5.4
4B (20.69-24.48)	2.85	271.7	10.5
4C (24.19-27.90)	2.97	75.5	39.4

3.B H₂O slab models across the wavelength regions

3.B.1 Without line overlap

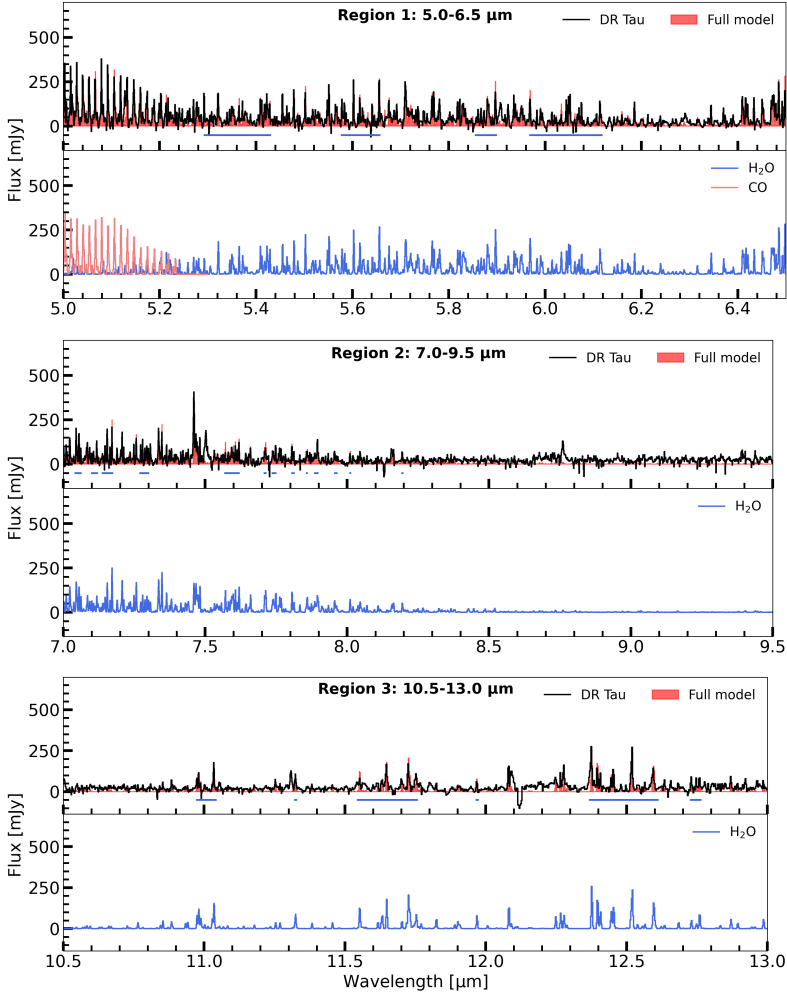


Figure 3.B.1: Best fitting slab models (without line overlap) for the different regions. In each subfigure, the top panel displays the continuum subtracted JWST spectrum in a specific region, while the full model spectrum is shown in red. The bottom panels show the models for the individually detected molecules. In addition, we show the CO model in pink from Temmink et al. (2024b). The horizontal bar in each top panel indicate the line regions used in the χ^2 -fits.

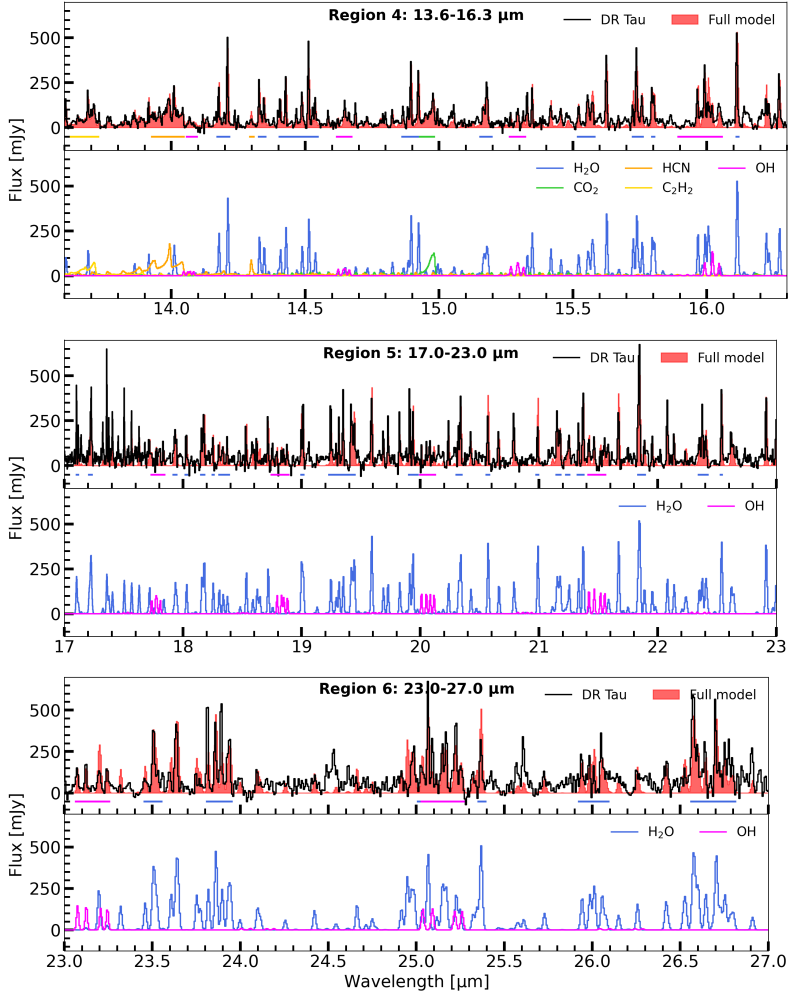


Figure 3.B.1: Continuation of Figure 3.B.1. The best fit to the OH emission is shown in magenta. In addition, we show the best fitting slab models, adopted from Temmink et al. (2024b), for CO₂ (green), HCN (orange), and C₂H₂ (yellow) in the wavelength region of 13.6-16.3 μm .

3.B.2 With line overlap

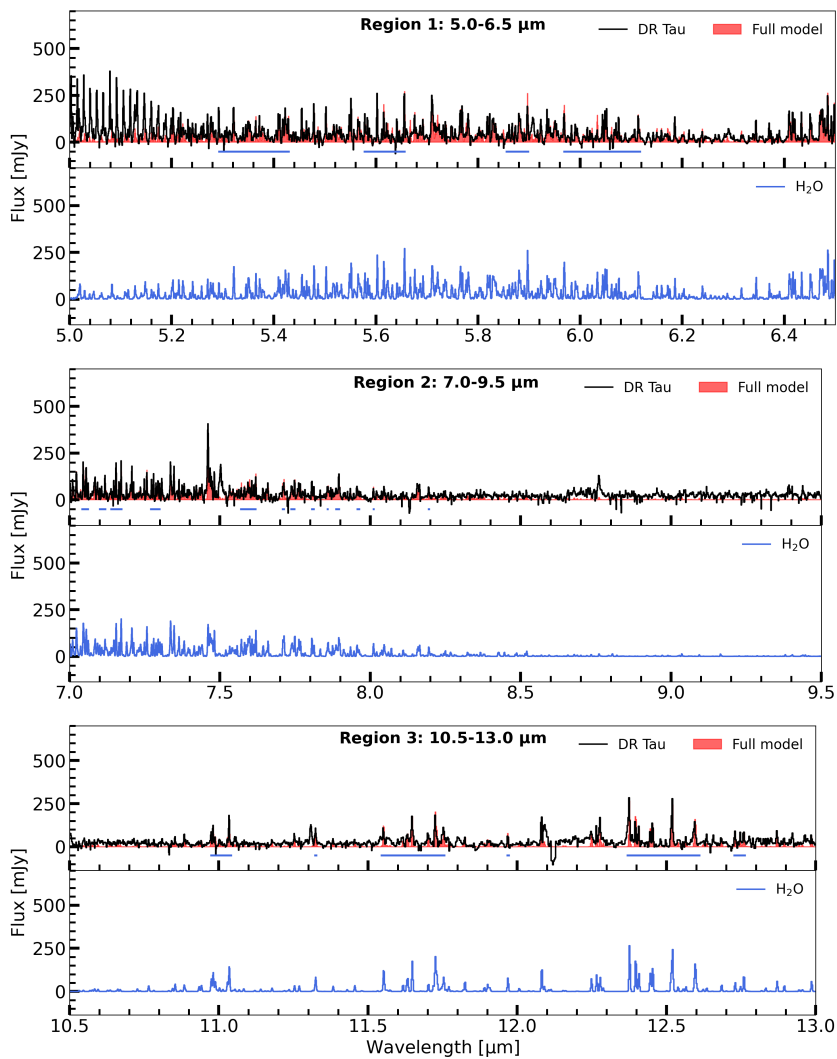


Figure 3.B.2: The same as Figure 3.B.1, but only showing the fitted H₂O slab models with mutual line overlap.

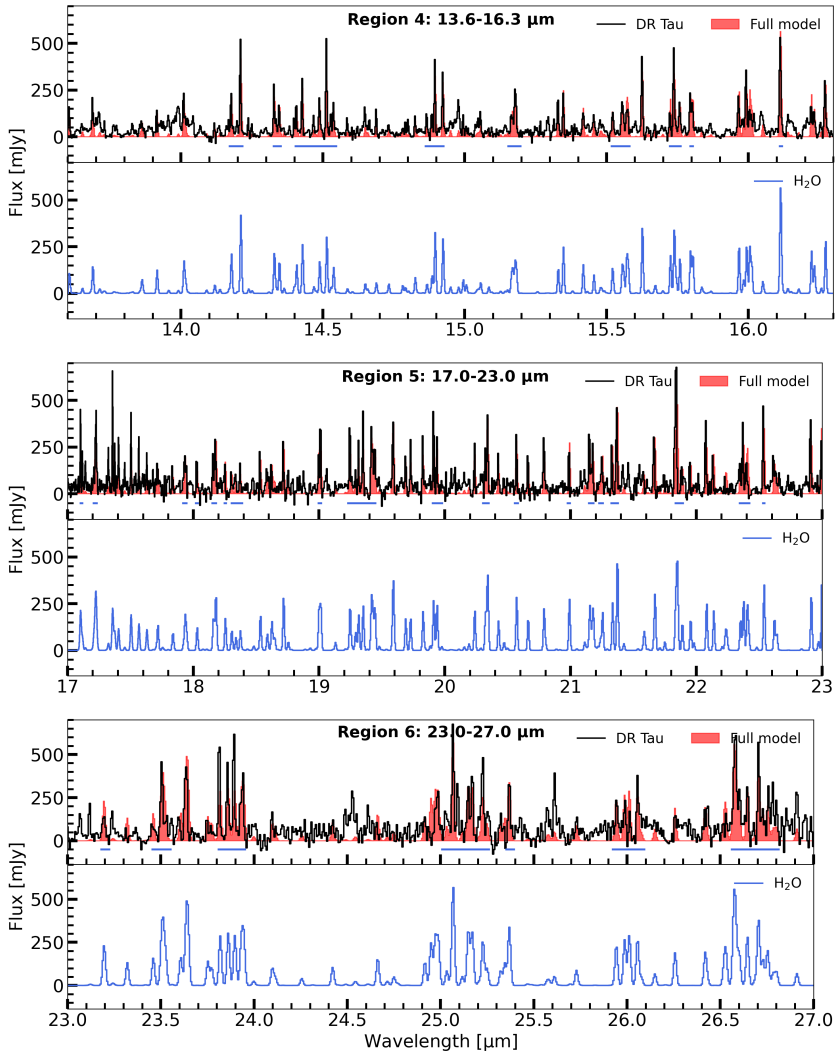


Figure 3.B.2: Continuation of Figure 3.B.2.

3.C Selected, isolated H₂O transitions

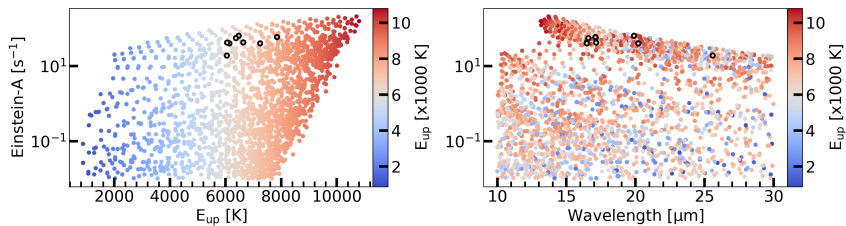


Figure 3.C.1: All the H₂O transitions with $A_{ul} \geq 10^{-2} \text{ s}^{-1}$ used in our analysis. The 6 hot ($6000 \leq E_{\text{up}} \leq 8000 \text{ K}$), unblended transitions are indicated by the black circles. The colour-scale indicates the upper level energies.

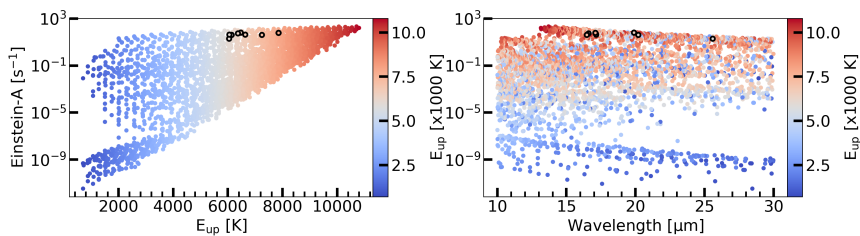


Figure 3.C.2: The same as Figure 3.C.1, but without a lower limit imposed on the values for A_{ul} .

3.D Two versus three component fits

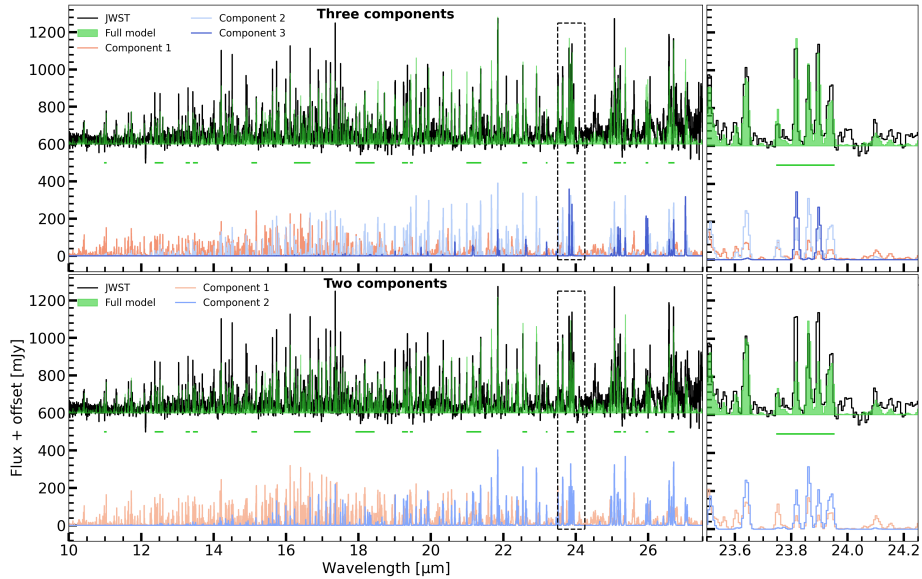


Figure 3.D.1: Fits of the three (top panels) and two (bottom panels) component slab models. The full models are shown in green, whereas the different components are shown in various shades of red and blue. The green horizontal bars indicate the regions used in the χ^2 -fits. The panels on the right-side of the figure show a zoom-in on the 23.5-24.25 μm region, which is also indicated by the dashed lines in the left panels. Table 3.2 (see ‘Method 3’) lists the parameters of each component; the coldest component (i.e. component 3) is not accounted for in the two-component fit.

3.E Multi-component corner plots

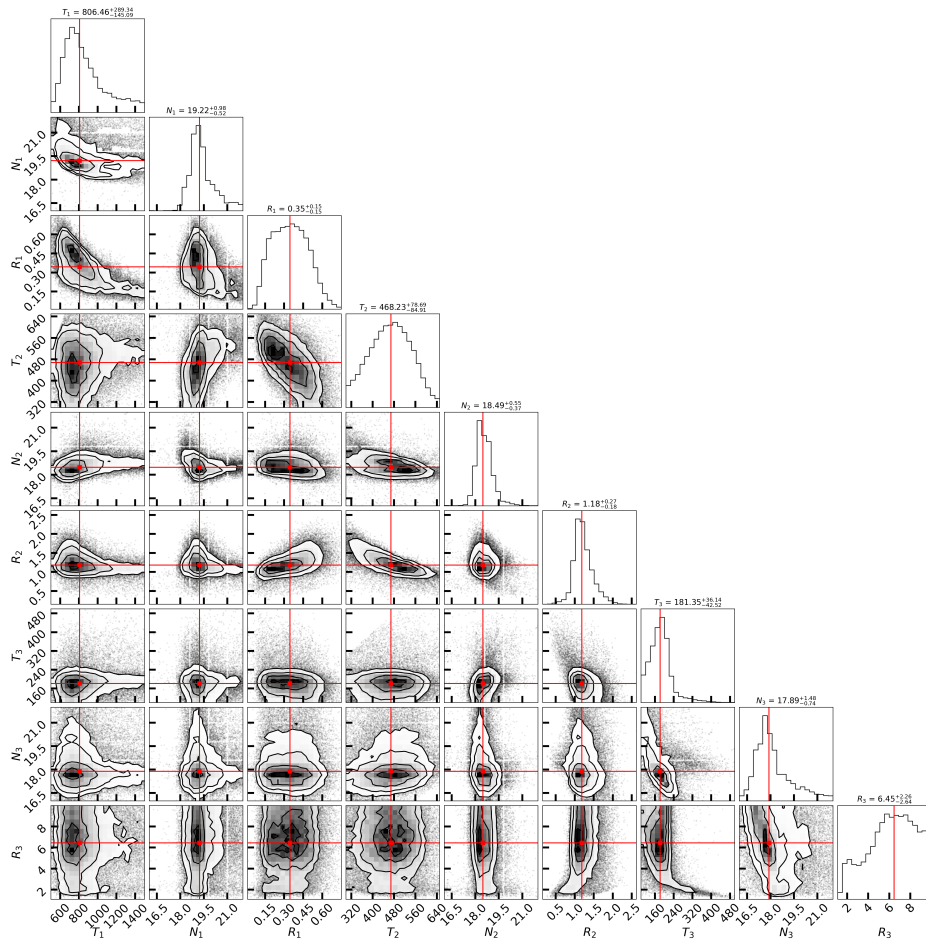


Figure 3.E.1: Corner plots for our three component model fits including only a radial temperature gradient (approach I). T_i , N_i , and R_i denote the excitation temperature (in K), the column density (given in \log_{10} -space, where N is given in units of cm^{-2}), and the emitting radius (in au) of component i , respectively.

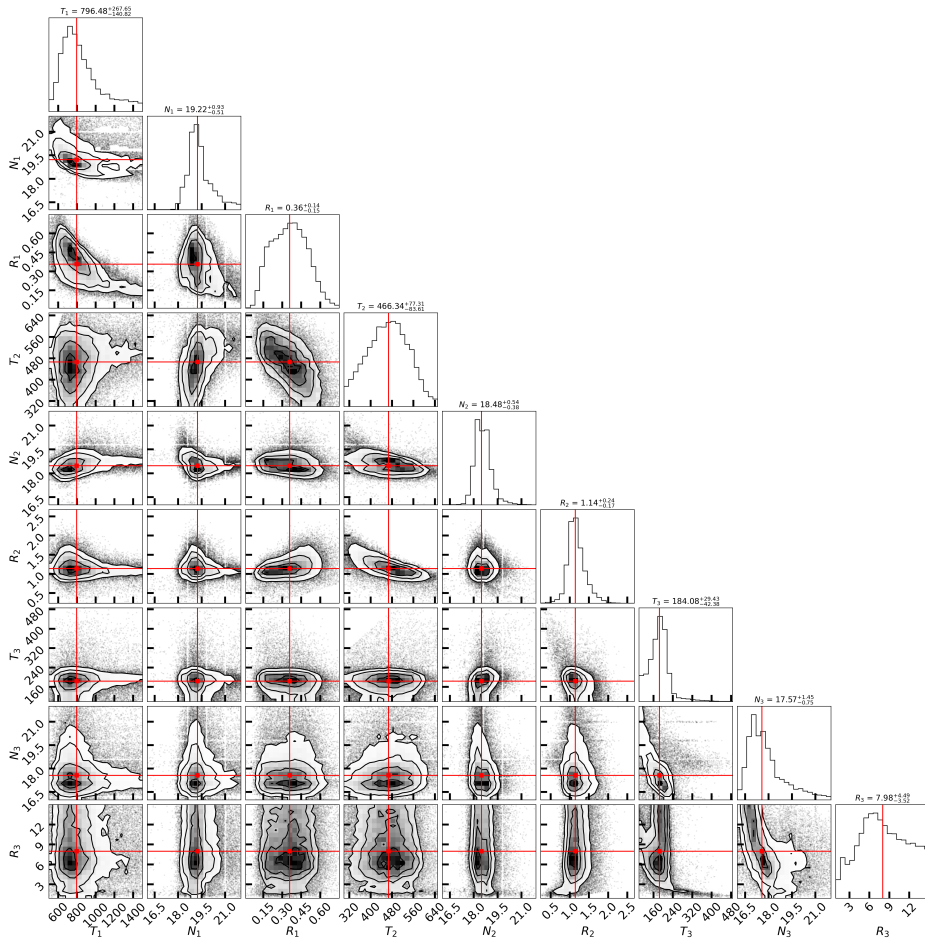


Figure 3.E.2: Similar as Figure 3.E.1, but for the models with spatial overlap (approach II).

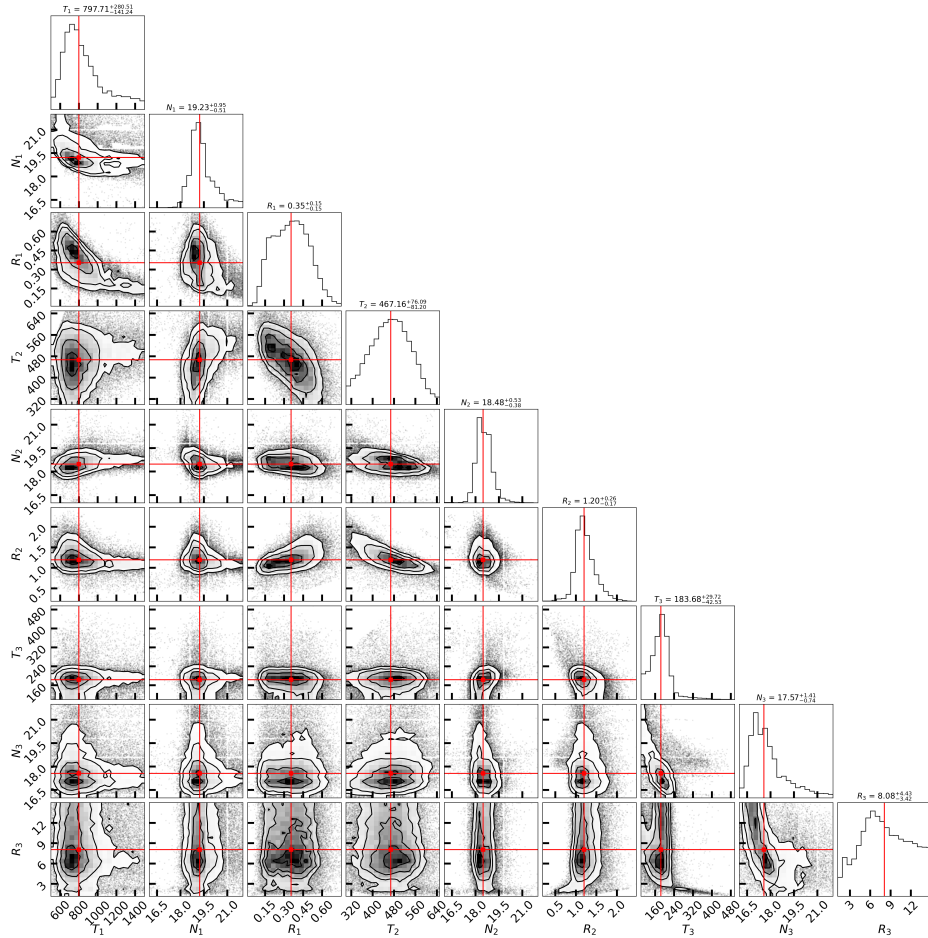


Figure 3.E.3: Similar as Figure 3.E.1, but for the models with also a vertical temperature gradient and allowing for spatial line shielding (approach III).

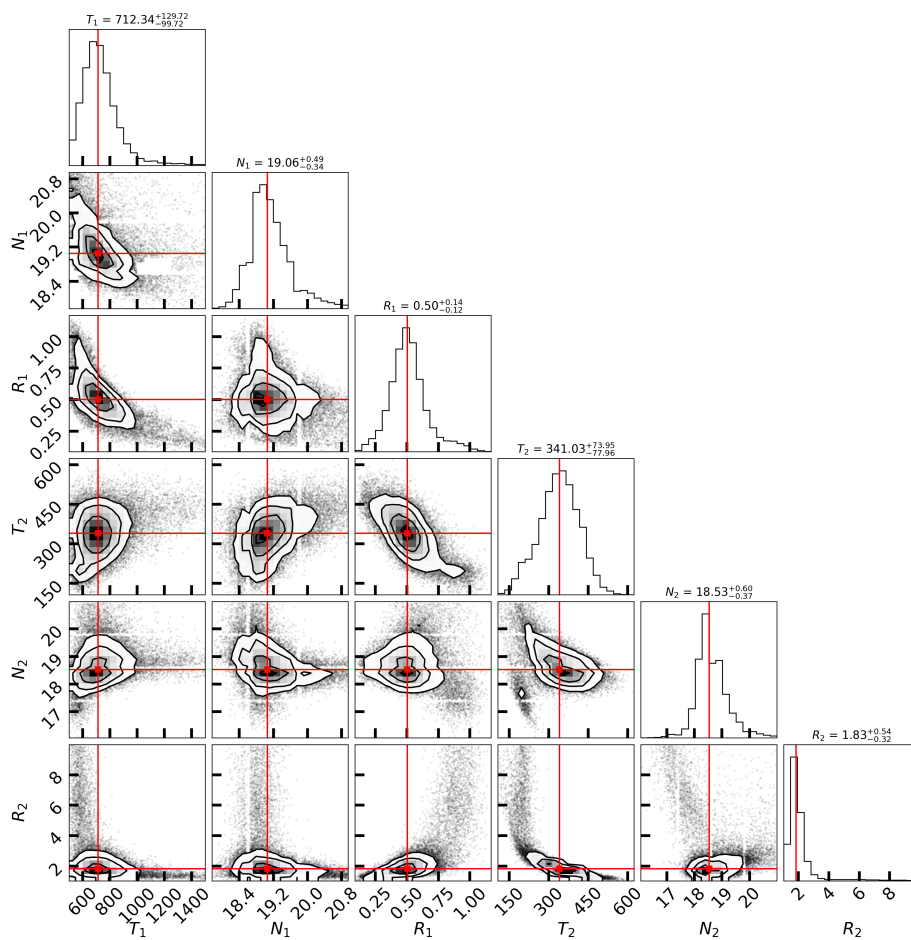


Figure 3.E.4: Similar as Figure 3.E.3, but for the models with only two components.

3.F H_2^{18}O over 17.0-27.5 μm

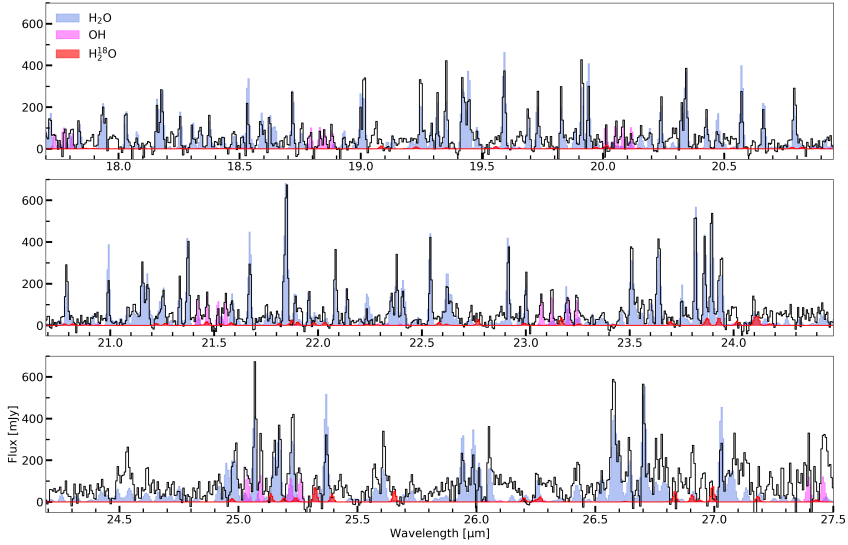


Figure 3.F.1: The spectra from subbands 4A to 4C from DR Tau are shown from top to bottom. A H_2^{18}O slab model is shown in red, to indicate the locations of the various transitions. The best fitting slab models of H_2O and OH are shown in, respectively, blue and magenta.

3.G Searching for other molecular species

3.G.1 Atomic and molecular hydrogen

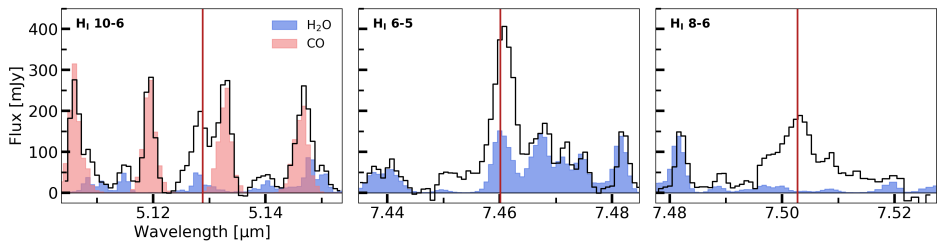


Figure 3.G.1: The identified atomic hydrogen transitions in DR Tau. From left to right we report the detections of the H_I 10-6, 6-5, and 8-6 transitions, respectively. The CO (see Temmink et al. 2024b) and H_2O slab models are shown for completeness and to show potential blending effects.

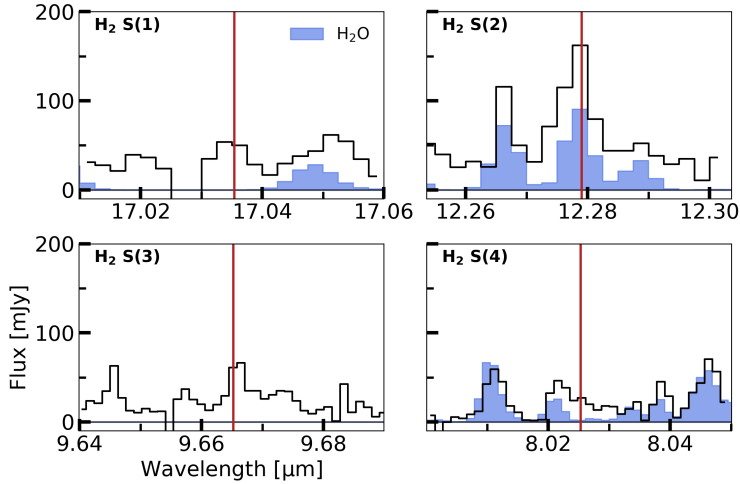


Figure 3.G.2: The potential detected H₂ transitions. The S(1), S(2), S(3), and S(4) transitions are displayed in, respectively, the top left, top right, bottom left, and bottom right panels. The H₂O slab models are shown for completeness and to show potential blending effects.

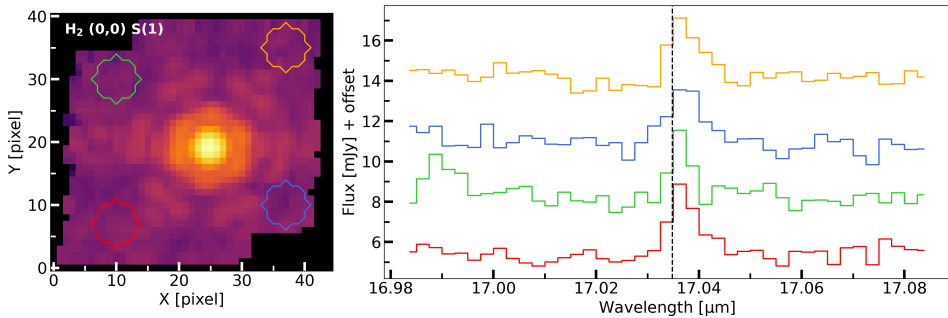


Figure 3.G.3: The spectra (right panel) of four off-source locations (as indicated in the left panel), showing the H₂ S(1) emission of the background cloud. The black dotted, horizontal line indicates the rest frequency of the transition.

3.G.2 Simple molecules

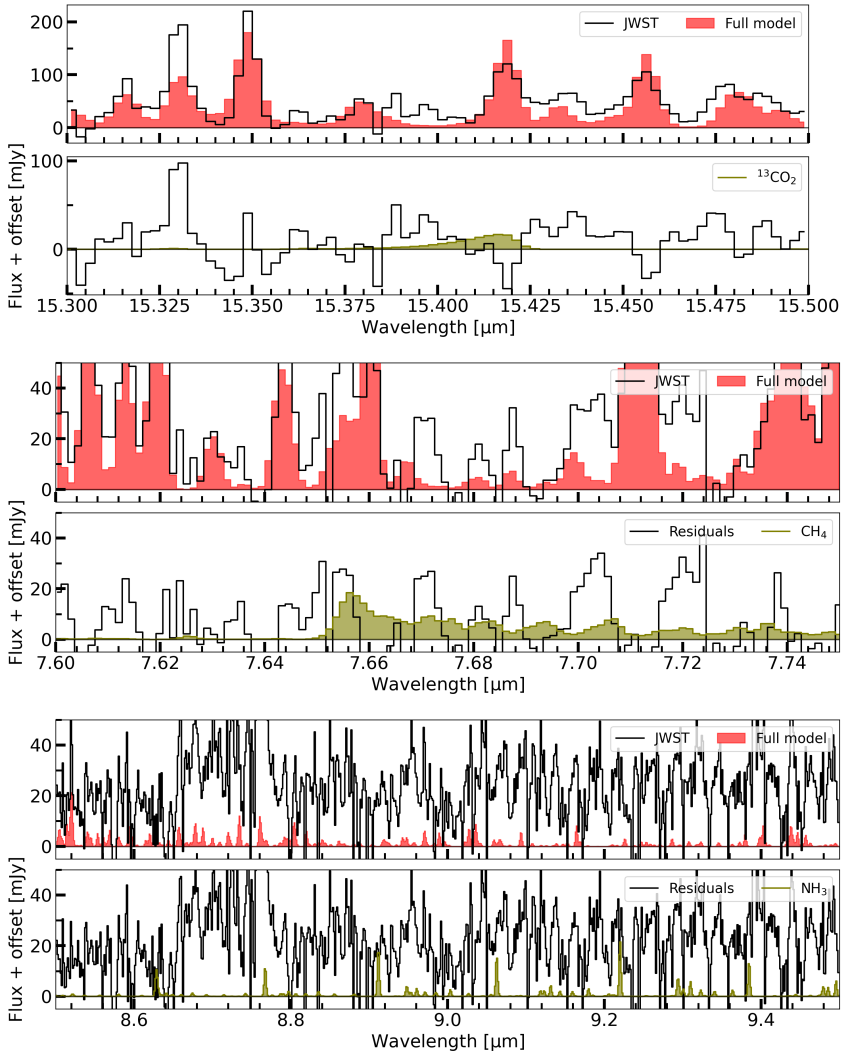


Figure 3.G.4: Slab models to investigate the maximum contribution of $^{13}\text{CO}_2$ (top figure), CH_4 (middle figure), and NH_3 (bottom panel) to the spectrum of DR Tau. We include all confidently detected species to investigate potential blending effects. This include CO_2 , HCN , and C_2H_2 , which all have been discussed in Temmink et al. (2024b). The top panel shows the spectrum and the full model consisting of all observed species, while the bottom panel shows the residual spectrum (after subtracting off the full model) and slab models of the targeted species.

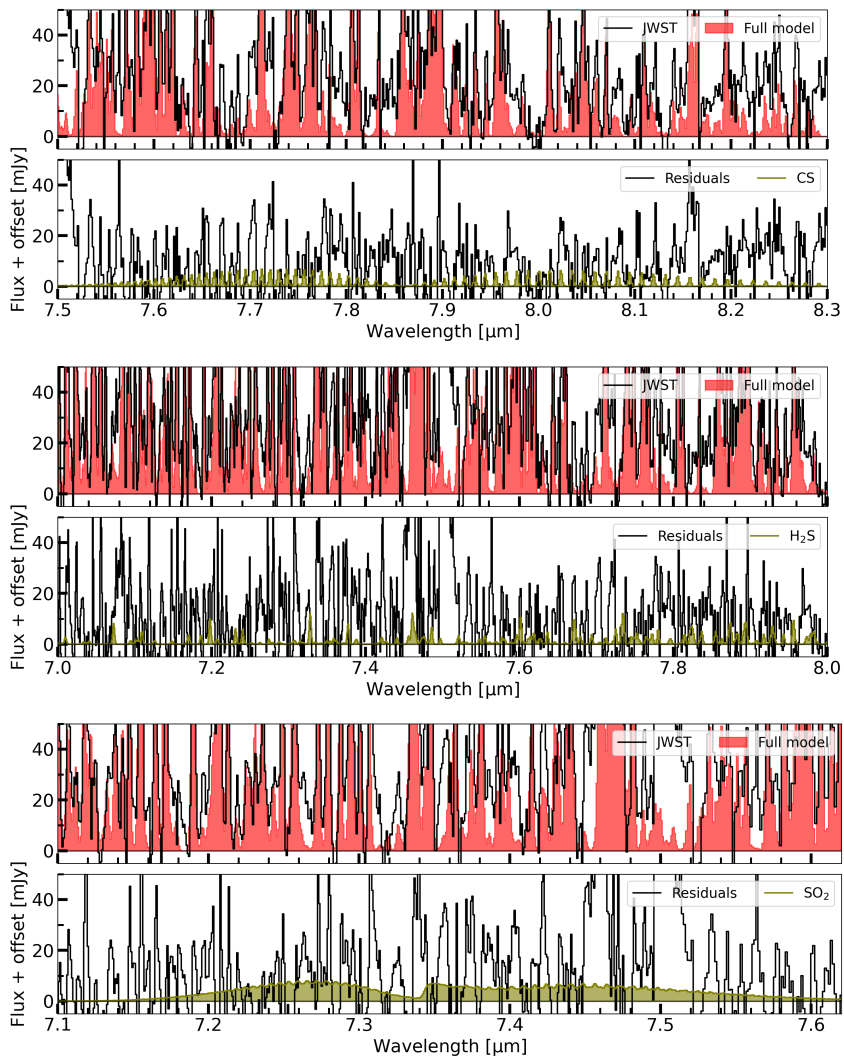


Figure 3.G.4: Continuation of Figure 3.G.4. The molecules shown here in green are CS (top panel), H₂S (middle panel), and SO₂ (bottom panel).

3.G.3 Hydrocarbons

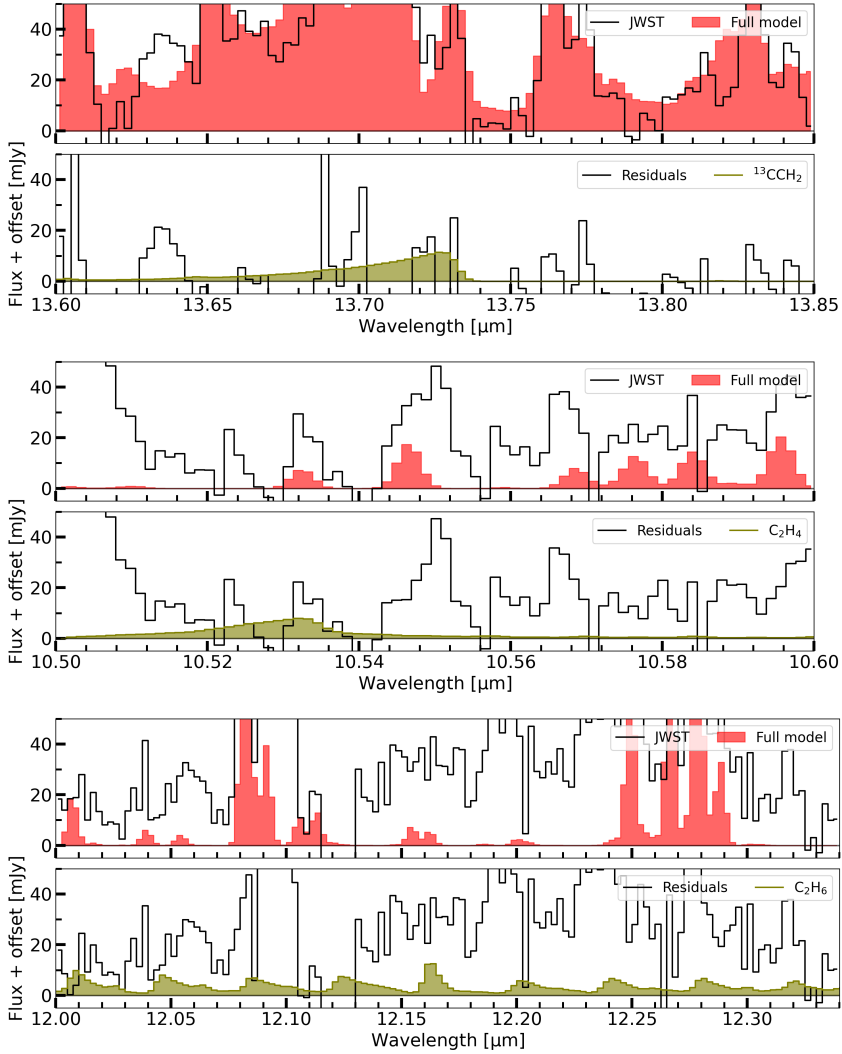


Figure 3.G.5: Slab models to investigate the detection of $^{13}\text{CCH}_2$ (top figure), C_2H_4 (middle figure), and C_2H_6 (bottom panel). We include all confidently detected species to investigate potential blending effects. This includes CO_2 , HCN , and C_2H_2 , which all have been discussed in Temmink et al. (2024b). The top panel shows the spectrum and the full model consisting of all observed species, while the bottom panel shows the residual spectrum (after subtracting off the full model) and slab models of the targeted species.

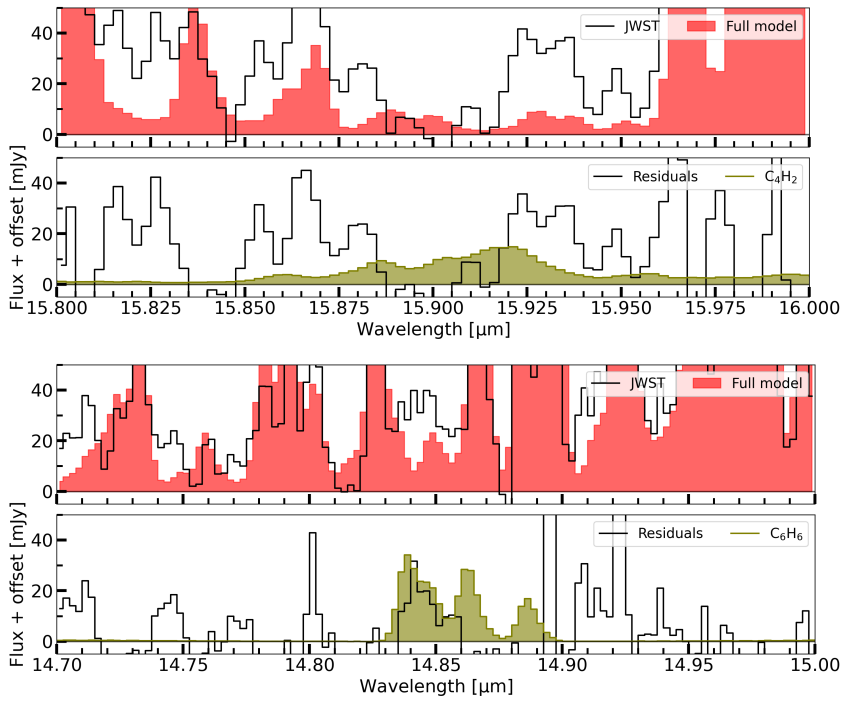


Figure 3.G.5: Continuation of Figure 3.G.5. The molecules shown here are C_4H_2 (top panel) and C_6H_6 (bottom panel).

MINDS: Water reservoirs of compact planet-forming dust disks

A diversity of H₂O distribution

M. Temmink, A. D. Sellek, D. Gasman, E. F. van Dishoeck, M. Vlasblom, A. Pranger, M. Güdel, T. Henning, P.-O. Lagage, A. Caratti o Garatti, I. Kamp, G. Olofsson, A. M. Arabhavi, S. L. Grant, T. Kaeufer, N. T. Kurtovic, G. Perotti, M. Samland, K. Schwarz, B. Tabone

A&A, 699, A134 (2025)

Abstract

Context. Millimetre-compact dust disks are thought to have efficient radial drift of icy dust pebbles. It has been hypothesised that this drift could produce an enhanced cold ($T < 400$ K) H_2O reservoir in their inner disks. Mid-infrared spectral surveys, now including the *James Webb* Space Telescope (JWST), pave the way to explore this hypothesis. In this work, we test this theory for eight compact disks ($R_{\text{dust}} < 60$ au) with JWST-MIRI/MRS observations.

Aims. To explore the H_2O distribution in the inner disks and consider whether these disks are enhanced in cold H_2O emission, we analyse the different reservoirs that can be probed with the pure rotational lines ($> 10 \mu\text{m}$) by JWST: hot ($T > 800$ K), intermediate ($400 < T < 800$ K), and cold ($T < 400$ K).

Methods. We probed the H_2O reservoirs with JWST-MIRI observations for a sample of eight compact disks through parametric column density profiles (power laws, jump abundances, and parabolas), multiple-component (two or three) slab models, and line flux ratios.

Results. We find that not all compact disks show strong enhancements of the cold H_2O reservoir; instead, we propose three different classes of inner disk H_2O distributions. Four of our disks (BP Tau, CY Tau, DR Tau, and RNO 90; i.e. type N or ‘normal’ disks) appear to have similar H_2O distributions to many of the large and structured disks, as indicated by the slab model fitting and the line flux ratios. These disks have a small cold reservoir, suggesting the inward drift of dust, but it is not as efficient as hypothesised before. Only two disks (FT Tau and XX Cha; type E or cold H_2O enhanced disks) do show a strong enhancement of the cold H_2O emission, in agreement with the original hypothesis. The two remaining disks (CX Tau and DN Tau; type P or H_2O -poor disks) are found to be very H_2O -poor, yet they show emission from either the hot or immediate reservoirs (depending on the fit) in addition to emission from the cold one. For the three types, we find that different parametrisation schemes are able to provide a good description of the observed H_2O spectra. Overall, a jump abundance at a free temperature is amongst the preferred profiles for all three types, suggesting that this profile can provide a good description of the observed reservoirs for most disks. The multiple-component analysis yields similar results to those of the parametric models. However, in some cases, a power law can give an entirely different distribution compared to the other parametric models. Finally, we also report the detection of other molecules in these disks, including a tentative detection of CH_4 in CY Tau.

Conclusions. Not all compact disks follow the hypothesis that their cold H_2O reservoir is enhanced following efficient radial drift. Therefore, we introduced a classification based on the observed H_2O reservoirs, which should hold for all (isolated) disks: type N, type E, and type P. Type N disks are considered to behave as many other (large and structured) disks, with all three reservoirs present; yet the cold emission is not enhanced. The type E disks show strong enhancements of the cold H_2O emission, while the type P disks are generally H_2O -poor.

4.1 Introduction

The inner regions (<10 au) of planet-forming disks are active sites of planet formation (Morbidelli et al. 2012; Dawson & Johnson 2018). The chemical composition of these forming planets is set by the elemental and molecular composition of the nascent disk. One of the key ingredients for habitable worlds is H_2O and, therefore, studying the available H_2O vapour reservoirs in disks is of great importance.

Based on H_2O vapour observations with the *Spitzer* Space Telescope and spatially resolved continuum images with the Atacama Large Millimeter/submillimeter Array, Banzatti et al. (2020) proposed scenarios for the expected H_2O reservoirs given the sizes of the dust disks. Disks that are observed to be compact in their millimetre emission ($R_{\text{dust}} < 60$ au) are thought to have efficient radial drift, leading to enriched H_2O reservoirs ($N \sim 10^{18}\text{-}10^{21}$ cm^{-2}) in the innermost regions ($<$ few au) of these disks. The larger, structured disks ($60 < R_{\text{dust}} < 300$ au) are expected to not show these enriched H_2O abundances ($\leq 10^{17.5}$ cm^{-2}), since sub-structures (i.e. gaps and rings) could trap the icy dust grains in the outer regions, halting them from reaching the inner disk and from crossing the H_2O snowline. Furthermore, for disks with large cavities, the situation is expected to be even more extreme, with the inner disks expected to be depleted of H_2O .

Recent modelling studies have explored the notion of both unimpeded enhancement due to radial drift and the opposite case of sub-structures halting the inward drift of pebbles. In particular, Kalyaan et al. (2023) investigated the influence of gaps on the gaseous enhancement in the inner disk. They noted that the enhancement, at least for the H_2O vapour reservoir, is of limited duration (up to a few million years) before the material gets accreted onto the host star. It is only when the gaps do not block the dust entirely, but some of the grains are still able to pass through (Pinilla et al. 2024; Mah et al. 2024) that the lifetime of this enhanced reservoir be prolonged. However, the inward drift of the dust particles not only enhances the gaseous reservoir, but it also increases the opacity of the dust itself. Recent models by Sellek et al. (2025) suggest that the increased opacity of the dust elevates the $\tau=1$ layer of the continuum, which could hide a larger gas reservoir that lies deeper in the disk. The observable column densities may thus not reflect the enhanced reservoirs. Further works by Houge et al. (2025) support this idea, while also investigating the competition between photodissociation and vertical mixing on the available reservoir. Finally, Kalyaan et al. (2023), Sellek et al. (2025), and Easterwood et al. (2024) noted the importance of the gap locations and the time at which they form for the drifting pebbles. Gaps located at smaller radial distances, and which formed early on, are more effective at limiting the gaseous enhancement, as more dust grains are blocked outside the snowline. However, they may leak more for a given gap depth or grain size. For gaps located at larger radial distances, the enhancement is stronger, as a smaller icy dust reservoir is blocked. Furthermore, the way the gap opens may also be of importance. Lienert et al. (2024) have shown that gaps opened due to internal photoevaporation are able to block both the pebble and gas flow, strongly influencing the inner disk composition. In contrast, the models from Greenwood et al. (2019) have shown that in the absence of gaps, the dust opacity decreases as the

disk evolves with time and this leads to an increase in the H₂O flux. Current observations of mid-infrared spectra of large and structured disks with the *James Webb* Space Telescope (JWST), including those with large cavities, already show that inner regions of such disks are not completely devoid of H₂O (Perotti et al. 2023; Schwarz et al. 2024). Furthermore, in some cases, they may have strong emission from the cold reservoir (<400 K; Gasman et al. 2023, 2025).

The *James Webb* Space Telescope (Rigby et al. 2023) provides the best opportunity to fully explore the available H₂O reservoirs in the inner regions of planet-forming disks, using the increased sensitivity and resolution of the Medium Resolution Spectrometer (MRS; Wells et al. 2015; Argyriou et al. 2023) of the Mid-InfraRed Instrument (MIRI; Wright et al. 2015; Rieke et al. 2015; Wright et al. 2023) with respect to the *Spitzer* Space Telescope. Since its launch, multiple works have studied the available reservoirs, including the analysis of H₂O emission across the entire JWST-MIRI wavelength range (Gasman et al. 2023) using 0D local thermal equilibrium (LTE) slab models. This analysis directly proved the existence of an expected radial temperature gradient, where the longer wavelengths probe larger radii and, thus, colder temperatures (Blevins et al. 2016; Banzatti et al. 2017, 2023b, 2025b). Banzatti et al. (2023a) identified the emergence of a cold H₂O reservoir ($T < 240$ K), which is expected to be the effect of radial dust drift. Subsequently, multiple slab models were fitted to the pure rotational H₂O spectra ($> 10 \mu\text{m}$) identifying the available reservoirs (Pontoppidan et al. 2024; Temmink et al. 2024a). A third cold component, in addition to hot (> 800 K) and warm ($400 < T < 800$ K) components, was found to be necessary to describe the same cold H₂O reservoir of $T < 240$ K. The three-component analysis of Temmink et al. (2024a) also provided another confirmation of the radial temperature gradient, where the multiple-component analysis of DR Tau could be approximated with a temperature profile of $T(R) \sim 500 (R/1\text{au})^{-0.5}$ K. More recently, efforts have been made to increase the complexity by moving away from using multiple components and to describe the temperature and column density profiles by parametric functions (Kaeufer et al. 2024; Romero-Mirza et al. 2024a). These profiles, including simple and exponentially tapered power laws, show that the pure rotational H₂O transitions can be explained by such parametric models; however, this has only been tested for a limited sample of disks with different disk characteristics, such as their radial sizes and structures. We also note the effort by Woitke et al. (2024), who used a full 2D thermochemical code to model, for the first time, the observed molecular emission in the outbursting source of EX Lup.

In this work, we aim to analyse the pure rotational H₂O emission in 8 millimetre-compact disks (dust radii of $R_{\text{dust},95\%} \sim 25\text{--}60$ au; Long et al. 2019; Facchini et al. 2019), using both the parametric and multiple component techniques highlighted above. Our criterion for a dust disk to be compact follows the classification of Banzatti et al. (2020), namely, assuming compact disks have dust radii of $\lesssim 60$ au. All sources have been observed with JWST/MIRI-MRS as part of the JWST Guaranteed Time Observations Program MIRI mid-INfrared Disk Survey (MINDS, PID:1282, PI: T. Henning; Kamp et al. 2023; Henning et al. 2024). Throughout our analysis, we aim to investigate the strengths of the different H₂O reservoirs, indicated throughout the paper as hot (> 800 K), intermediate (400-800 K), and

cold (<400 K, see also Banzatti et al. 2023a). We use this to explore the H_2O reservoirs and column density profiles. In addition, we also infer whether these compact disks show an enhancement in the cold H_2O reservoir, as suggested by Banzatti et al. (2020), or whether the situation is more complex than this scenario.

The paper is structured as follows. Section 7.2 describes the sample and the observations, while Section 4.3 contains a description of the used methodology. The results are represented in Section 4.4 and interpreted in Section 7.4. Aside from the interpretation, Section 7.4 also discusses the role of sub-structures in setting the H_2O reservoirs and offers a comparison with existing models. Finally, Section 4.6 contains our conclusions and a short summary.

4.2 Sample and observations

4.2.1 Sample

Table 4.1: Stellar properties and observational details of the sample of compact disks studied in this work.

Source	M_* [M_\odot]	L_* [L_\odot]	Dist. [pc]	v_{hel} [km s^{-1}]	Inclination [$^\circ$]	R_{in} [au]	$R_{\text{dust},95\%}$ [au]	Obs. date dd/mm/yyyy	Int. time [min]	References $M_*/L_*/v_{\text{hel}}/i/R_{\text{dust}}$
BP Tau	0.52	0.40	129	16.76	23.6	0.04	41	20/02/2023	29.0	<i>m1, l1, v1, i1, d1</i>
CX Tau	0.37	0.26	128	19.30	55.1	0.04	38	20/02/2023	60.0	<i>m2, l2, v2, i2, d2</i>
CY Tau	0.31	0.26	128	15.10	32.0	0.04	<64	20/02/2023	60.0	<i>m2, l2, v2, i3, d3</i>
DN Tau	0.52	0.70	128	18.80	35.2	0.06	61	28/09/2023	60.0	<i>m1, l1, v2, i4, d1</i>
DR Tau	0.93	0.63	195	27.60	5.4	0.06	54	04/03/2023	27.8	<i>m1, l1, v3, i4, d1</i>
FT Tau	0.34	0.15	127	17.24	35.5	0.03	45	20/02/2023	30.0	<i>m1, l1, v4, i4, d1</i>
RNO 90	1.50	2.14	117	-10.10	37.0	0.10	<47	25/08/2023	33.4	<i>m3, l3, v5, i5, d3</i>
XX Cha	0.36	0.29	190	16.26	39.7	0.04	<25	31/08/2023	60.0	<i>m4, l4, v6, i6, d3</i>

Notes. All distances have been acquired from GAIA (Gaia Collaboration et al. 2018). References (mass, luminosity, heliocentric velocity, inclination, dust radii): *m1*-Long et al. (2019), *m2*-Simon et al. (2017), *m3*-Banzatti et al. (2022), *m4*-Manara et al. (2016), *l1*-Long et al. (2019), *l2*-Herczeg & Hillenbrand (2014), *l3*-Banzatti et al. (2022), *l4*-Manara et al. (2016), *v1*-Fang et al. (2018), *v2*-Banzatti et al. (2019), *v3*-Ardila et al. (2002), *v4*-Roccatagliata et al. (2020), *v5*-Banzatti et al. (2022), *v6*-Nguyen et al. (2012), *i1*-Gasman et al. (2025), *i2*-Facchini et al. (2017), *i3*-Simon et al. (2017), *i4*-Long et al. (2019), *i5*-Bosman & Bergin (2021), *i6*-This work, *d1*-Long et al. (2019), *d2*-Facchini et al. (2019), *d3*-Estimated in this work

Our sample of compact planet-forming disks consists of eight sources: BP Tau, CX Tau, CY Tau, DN Tau, DR Tau, FT Tau, RNO 90, and XX Cha, for which stellar properties are summarised in Table 5.1. Dedicated papers, exploring the observed molecular emission, exist for two of the sources: CX Tau (Vlasblom et al. 2025a) and DR Tau (Temmink et al. 2024b,a).

Although the disks in our sample are known to be rather compact in the millimetre continuum emission ($R_{\text{dust}} \lesssim 60$ au), there is limited information available about their gas disk sizes (R_{gas}). Trapman et al. (2019) proposed that a gas-to-dust size ratio of $R_{\text{gas}}/R_{\text{dust}} > 4$ is a clear sign of radial drift. For our sources, only one disk has literature values for both R_{dust} and R_{gas} : CX Tau (Facchini et al. 2019). These values suggest a ratio of $R_{\text{gas}}/R_{\text{dust}} > 5$, hinting at strong radial drift

being the potential cause of this disk’s compactness. For the other disks, the gas radius has not been determined and, in some cases, high-resolution observations of the continuum emission do not (yet) exist. Consequently, the gas-to-dust size ratio is still to be determined in a consistent manner and it is unclear whether the compactness of these disks can be attributed to an evolution dominated by radial drift or simply to their initial conditions. For these reasons, we have chosen our sample to follow the criteria of Banzatti et al. (2020) and we considered disks with millimetre continuum emission radii of $R_{\text{dust}} \lesssim 60$ au as compact.

As can be seen from Table 5.1, our sample is rather homogeneous in terms of masses, luminosities, and inclinations. There are a few outliers: for instance, DR Tau and RNO 90 have higher stellar masses compared to the others, while DR Tau also has the lowest inclination ($i \sim 5.4^\circ$, Long et al. 2019). CX Tau, on the other hand, has the highest inclination ($\sim 55.1^\circ$). Furthermore, as six out of eight disks are located in the Taurus star-forming region, we can expect them to be of similar ages ($\sim 1\text{-}3$ Myr, Krolikowski et al. 2021; Luhman 2023). In contrast, RNO 90 is located in Ophiuchus and may, therefore, be on the younger side. These small differences suggest that our sample is overall rather homogeneous and differences must therefore be due to either their initial conditions or differences in their (potentially drift-dominated) evolution. A larger sample will be analysed in Temmink et al. (in prep.), which may provide more insights into the differences related to the stellar properties.

4.2.2 Observations and data reduction

The JWST-MIRI/MRS details (date of observation and integration time) are also included in Table 5.1. All MRS spectra have been taken in the FASTR1 read-out mode with a four-point dither pattern using all three grating settings (A, B, and C). All data have been reduced using a standard pipeline reduction (version 1.16.1; Bushouse et al. 2024) and pmap 1315. The spectra have been extracted through aperture photometry, where the aperture has a size of $2 \times$ the full width at half maximum (FWHM). Additionally, we have corrected for residual fringes using the implementation of the default pipeline, as most of the observations (except XX Cha) were taken without target acquisition. The resulting spectra were continuum subtracted using an updated version of the method by Temmink et al. (2024b), which makes use of the ‘iterative reweighted spline quantile regression’ method included in the PYBASELINES package (Erb 2022). Before estimating the continuum, downward spikes were masked using the same method as in Temmink et al. (2024b), but now they were masked per MIRI sub-band as opposed to over the whole spectrum. We used a quantile regression value of 0.1 and placed the knots of the cubic splines every 75 data points, except for Channel 4 and the silicate feature ($\sim 8.25\text{-}11.25 \mu\text{m}$), where the knots were placed every 25 points to better estimate the varying continuum. For CX Tau and DN Tau, a knot spacing of 25 data points was used for the entire spectrum, due to their strongly varying continuum. Given the large uncertainty of the observations at the location of the silicate feature, the quantile regression value was set to 0.5 for all disks, which places the baseline through the median of the observations. Additionally,

we changed the continuum estimate for the Q -branches of CO_2 , HCN , and C_2H_2 . The typical fit could overestimate the continuum of these Q -branches, effectively taking away molecular flux in the subtraction. To avoid this over-subtraction, we used a cubic interpolation of the estimated baseline just before and after the Q -branch to better fit the continuum level underneath the Q -branch. In particular, we masked the 13.45-14.20 μm wavelength region that captures the HCN and C_2H_2 Q -branches, and the 14.88-15.01 μm region for that of CO_2 . The reduced spectra and continuum estimates are displayed in Figure 4.1.

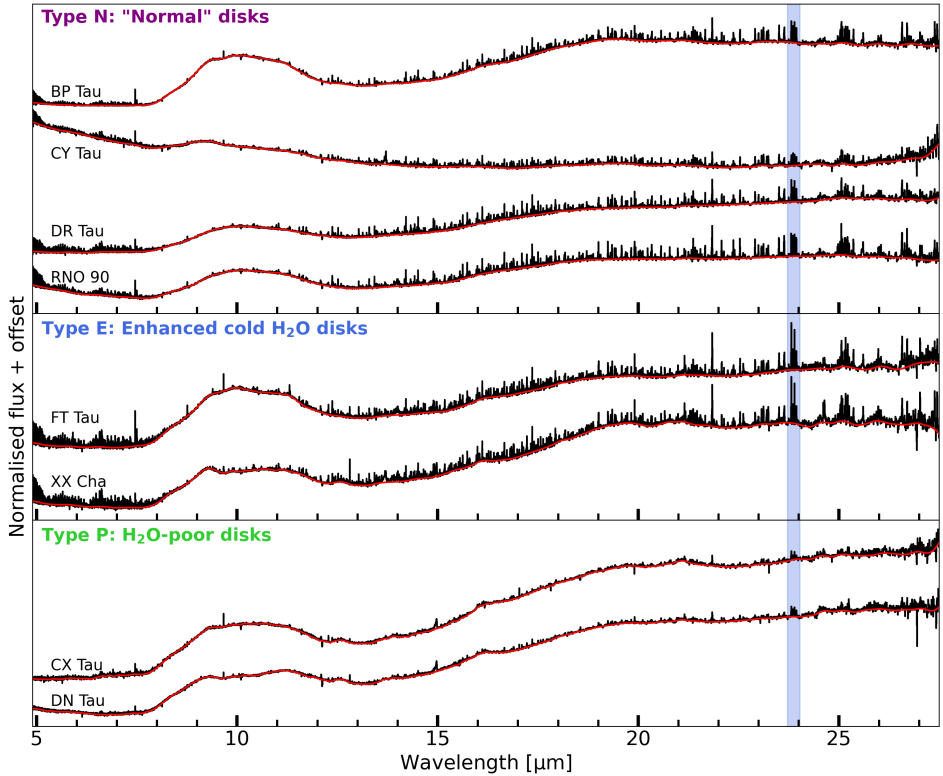


Figure 4.1: Normalised-to-peak-flux spectra of our sample of millimetre-compact disks. The red line indicates the estimated continuum. The indicated types and their meaning are discussed in Section 4.5.1. In blue, we highlight the 23.72-24.03 μm wavelength region, where two transitions are located that are most important for obtaining information about the cold H_2O reservoir.

Figure 4.1 shows that the shape of the spectra overall looks similar and in some cases nearly indistinguishable. All sources have a silicate feature at ~ 10 μm and contain emission features from a variety of molecular species. The only outlier is CY Tau, which has stronger emission at the shortest wavelengths. This is likely due to an inner (puffy) rim self-shadowing the outer disk and, subsequently,

lowering the mid- and far-infrared flux (see, for example, Dullemond & Dominik 2004; Woitke et al. 2019). We leave the analysis of the dust continua to a future work.

4.3 Methodology

To analyse the pure rotational H₂O emission in the JWST-MIRI/MRS spectra of our sample of compact disks, we used slab models under the assumption of local thermal equilibrium (see Grant et al. 2023b; Tabone et al. 2023 for more details on the slab model generation). Following Banzatti et al. (2025b), we included mutual line shielding in the H₂O slab models to account for the shielding of ortho- and para-line pairs. Additionally, we took the mean spectral resolution, calculated using the results of Pontoppidan et al. (2024) and the updates by Banzatti et al. (2025b), of each MIRI sub-band to properly sample the wavelength grid of the slabs over the entire spectrum. We used two different line widths for our models: a constant value of $\Delta V=4.71 \text{ km s}^{-1}$, which is the line width of H₂ at a temperature of 700 K (Salyk et al. 2011a), as well as a similar approach to Romero-Mirza et al. (2024a), where the line width is taken as the sum in quadrature (hereafter, simply called the quadrature line width) of the turbulent line width (ΔV_{turb} fixed to 1.0 km s^{-1}) and the thermal line width ($\Delta V_{\text{therm}} = \sqrt{2kT/m}$, with T the temperature of the slab model and m the mass of an H₂O molecule). The two line widths were used to make a comparison between the practices applied in the recent literature. While earlier works (e.g. Tabone et al. 2023; Grant et al. 2023b; Gasman et al. 2023) have used a constant value of 4.71 km s^{-1} , Romero-Mirza et al. (2024a) recently used the sum in quadrature. To investigate which of these approaches offers a better fit to our spectra, we tested both options in our fits and make a comparison (see Section 4.5.4). The Python package SPECTRES (Carnall 2017) was subsequently used to resample the slab models onto the wavelength grid of MIRI. However, before the resampling, we applied a wavelength shift to the slab models (see also Pontoppidan et al. 2024), based on the heliocentric velocity of the sources (see Table 5.1). Figure 4.A.1, using the spectrum of DR Tau as an example, shows that these wavelength shifts, although subtle, are required to properly recreate the observed line profiles and will subsequently improve the fit results.

We fit our spectra using two different approaches: similarly to Temmink et al. (2024a), we used a multi-component analysis where three or two distinct components (with decreasing temperatures and increasing emitting areas) were fitted to the entire rotational spectrum. Furthermore, we use and extended the methods implemented by Romero-Mirza et al. (2024a), who used (exponentially tapered) power law profiles for the temperature and column density. We denoted these models as multi-component and parametric models; in the latter case, we explored more options than (exponentially tapered) power laws. By using both these methods, we have been able to explore the strengths of the different H₂O reservoirs and investigate the robustness of what kind of profile for the column density is preferred in the inner region. By using both techniques, we can also gain more insights into the changing excitation conditions with radius in the inner regions of these disks.

4.3.1 Rotational H₂O spectrum: Parametric analysis

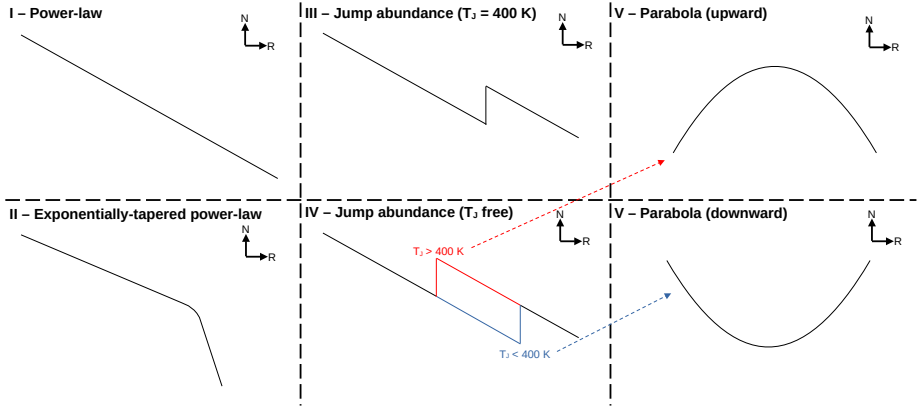


Figure 4.2: Schematic highlighting the different parametric models used for the column density profiles. Both the horizontal (radius) and vertical (column density) axes are taken in \log_{10} -space.

In an attempt to parametrically describe the observed H₂O emission, we followed the approach from Romero-Mirza et al. (2024a), whereby 50 slab models are used to sample profiles in both temperature and column density as a function of the emitting radius. As opposed to Romero-Mirza et al. (2024a), we chose to first determine the radius as a function of temperature,

$$R(T) = R_{\text{in}} \left(\frac{T}{1500 \text{ K}} \right)^{-1/q}. \quad (4.1)$$

This relation ensures that the inner radius (R_{in} (in au), as listed in Table 5.1) of our slab models is located at the estimated dust sublimation radius at 1500 K. Using this equation, we sampled the annular emitting regions of our 50 slab models for temperatures between 1500 K (the dust sublimation radius; Barvainis 1987) and 150 K (the condensation temperature of H₂O; Collings et al. 2004) in \log_{10} -space. The dust sublimation radius was calculated following the approach of Dullemond et al. (2001), $R_{\text{in}} \sim 0.07 \sqrt{(L_*/L_{\odot})}$. Both the calculated inner radii and adopted stellar luminosities can be found in Table 5.1. By simply rewriting Equation 4.1, we obtain a relation for the temperature as a function of the radius,

$$T(R) = 1500 \text{ K} \left(\frac{R}{R_{\text{in}}} \right)^{-q}. \quad (4.2)$$

For the column density, we used the same profiles as Romero-Mirza et al. (2024a): a power law (profile I, Equation 4.3) and an exponentially tapered power law (profile II, Equation 4.4). In addition, we also tried different profiles. Figure 4.2 provides a schematic overview of the different profiles and their potential behaviours. In particular, we assumed a constant number of molecules (\mathcal{N}_{mol}) with

radius, whereby each annulus contains the same number of molecules, which automatically resembles a power law with a power of -2 (the emitting area, A , is proportional to the square of the radius). We then allowed this number of molecules to experience a jump; namely, the number of molecules would get enhanced (or depleted) by a factor, F_{scale} , at temperatures below a given jump temperature, T_{jump} (see Equation 4.5). We tried profiles with a fixed jump temperature, at 400 K (profile III) and we kept T_{jump} as a free parameter (profile IV). The value of 400 K approximately resembles the boundary temperature between the sublimated (colder temperatures) and gas-phase-formed (hotter temperatures) H_2O vapour reservoirs (see also Romero-Mirza et al. 2024a). The jump temperature can move to higher temperatures, indicating a potential depletion of the hot H_2O reservoir, or to colder temperatures, representing a potential enhancement of the cold H_2O reservoirs. A parabola provides a smoother description of this behaviour: the jump moving to higher temperatures is captured by an upward parabola (the parabola has a maximum), while a downward parabola (the parabola has a minimum) captures the behaviour of the jump moving to lower temperatures (see also Figure 4.2). Therefore, we fitted a parabola in log space (profile V, Equation 4.6). The equations describing the column density profiles of each of these cases are:

$$N_{\text{I}}(R) = N_0 \left(\frac{R}{1\text{au}} \right)^{-p}, \quad (4.3)$$

$$N_{\text{II}}(R) = N_0 \left(\frac{R}{1\text{au}} \right)^{-p} \exp \left[- \left(\frac{R}{R_c} \right)^\phi \right], \quad (4.4)$$

$$N_{\text{III,IV}}(R) \propto \begin{cases} \frac{N_{\text{mol}}}{A} & \text{if } T > T_{\text{jump}}, \\ \frac{N_{\text{mol}} \times F_{\text{scale}}}{A} & \text{if } T \leq T_{\text{jump}}, \end{cases} \quad (4.5)$$

$$N_{\text{V}}(R) = N_0 \left(\frac{R}{1\text{au}} \right)^{\alpha + \beta \ln(R/1\text{au})}. \quad (4.6)$$

The emitting area of each slab model is accounted for in the exact same manner as reported in Romero-Mirza et al. (2024a). The area is multiplied by the cosine of the disk's inclination (i , reported in Table 5.1), $A = \pi (R_2^2 - R_1^2) \times \cos(i)$, where R_1 and R_2 are, respectively, the inner and outer radii of each annulus (see also Equation 4.1).

We fit the profiles, sampled by the 50 slab models, using a Markov chain Monte Carlo (MCMC) approach, implemented through the EMCEE python-package (Foreman-Mackey et al. 2013). From the posterior distribution of the MCMC, we take the median values as the best-fit values for the fitted parameter. Additionally, the 18th and 84th percentiles are taken as the lower and upper 1σ uncertainties. We use a reduced- χ^2 as the likelihood function of the MCMC, in order to compare the full model (the sum of the 50 slab models) with the observations. The likelihood has, therefore, takes the following form:

$$\chi_{\text{red}}^2 = \frac{1}{N_{\text{data}}} \sum_i \frac{w_i (F_{\text{obs},i} - F_{\text{model},i})^2}{\sigma_i^2}, \quad (4.7)$$

where F_{obs} is the observed spectrum and N_{data} is the number of data points within the used fit regions. Then, σ denotes the noise of the observations, determined in a similar manner as in Temmink et al. (2024b), where the *James Webb Exposure Time Calculator*¹ has been used to obtain the continuum signal-to-noise (S/N) at the midpoint of each sub-band given the observational setup. The S/N values are given in Table 4.B.1. As the noise is significantly higher in Channel 4 and many important H₂O lines can be found at these wavelengths, we slightly offset the large noise by introducing weights in the χ^2 -formula, w_i . All fit regions beyond 20 μm have been given a higher weight of 5, while select regions with important transitions probing the cold reservoir have been given a weight of 10 or 15 (for the strongest transitions). While the values are arbitrary, these weights ensure that we are able to properly fit the full rotational spectrum, without favouring the hot reservoir, as the transitions at smaller wavelengths have lower flux uncertainties. Fits without any weights favour the hot reservoir. Therefore, the chosen weights ensure that our models properly fit all reservoirs, including the cold one that is best probed by the longer wavelengths that are more noisy given the lower sensitivity of JWST/MIRI’s Channel 4. While the choice for the weights is arbitrary, using lower weights will still favour the hotter reservoirs and result in a worse fit for the colder reservoir, whereas higher weights may start overrepresenting the cold reservoir and result in worse fits for the hot one.

Table 4.2: Priors used for the profiles listed in Section 4.3.1.

Profile	Parameter	Priors
Temperature-radius	q	$\mathcal{U}(0, 5)$
Power law (I)	$\log_{10}(N_0)$	$\mathcal{U}(12, 30)$
	p	$\mathcal{U}(-10, 10)$
Exponential taper (II)	$\log_{10}(R_c)$	$\mathcal{U}(\log_{10}(R_{\text{in}}), 1)$
	ϕ	$\mathcal{U}(0.5, 5)$
Jump abundance (III)	$\log_{10}(\mathcal{N}_{\text{mol}})$	$\mathcal{U}(30, 50)$
	$\log_{10}(F_{\text{scale}})$	$\mathcal{U}(-3, 5)$
Free temperature (IV)	T_{jump}	$\mathcal{U}(150, 1500)$
Parabola (V)	$\log_{10}(N_0)$	$\mathcal{U}(12, 30)$
	α	$\mathcal{U}(-100, 100)$
	β	$\mathcal{U}(-50, 50)$

In the MCMC, we used 20 walkers per free parameter and allowed the MCMC to explore the prior space for 50,000 iterations. Table 4.2 lists the prior spaces for each profile. Common priors that are kept the same in each fit are only listed once, for example, the number of molecules, \mathcal{N}_{mol} , in the jump abundances. For some sources, we ran a second fit with a more limited prior space. In these cases, a second, less favourable solution was often found and a number of walkers got stuck in this local minimum, not allowing the fit to converge. The updated prior space was subsequently chosen to exclude these local minima. All fits use selected isolated

¹Exposure Time Calculator: <https://jwst.etc.stsci.edu/>

H₂O lines and ortho-para line pairs, which all have been taken from Banzatti et al. (2025b) (see their Figure 3 and Tables 5 and 6). The applied fit regions, which were also shifted by the heliocentric velocity, are listed in Table 4.C.1. We used fewer regions for CX Tau and DN Tau, as the CO₂ *P*- and *R*- branches strongly contribute to their observed emission.

4.3.2 Rotational H₂O spectrum: Multiple components

As a comparison, we also followed Temmink et al. (2024a) to investigate the pure rotational H₂O spectrum using two (in the case of CX Tau and DN Tau) or three slab model components. Through trial and error (i.e. by fitting three or two components), we found that only two components were needed to fully describe the rotational H₂O spectra of CX Tau and DN Tau. This is very likely due to the H₂O emission being much weaker compared to the other sources (see Figure 4.1). We did not use all three approaches presented in Temmink et al. (2024a), but only the simplest one, approach I, which assumes a simple radial gradient. The line optical depths are sufficiently high that the vertical gradient in approach III does not matter and the results resemble those of approach I.

To agree with the parametric analyses discussed in Section 4.3.1, we slightly adapted approach I: instead of having a circular area surrounded by two annuli, we use three annuli with the inner radius of the first set to the dust sublimation radius, R_{in} . The other two or three radii are kept free, together with their respective temperatures and column densities. Therefore, Equation 2 of Temmink et al. (2024a) becomes:

$$\begin{aligned}
 F_{\text{total}} = & F_1 \pi \left[\left(\frac{R_1}{1\text{au}} \right)^2 - \left(\frac{R_{\text{in}}}{1\text{au}} \right)^2 \right] \cos(i) \\
 & + F_2 \pi \left[\left(\frac{R_2}{1\text{au}} \right)^2 - \left(\frac{R_1}{1\text{au}} \right)^2 \right] \cos(i) \\
 & + F_3 \pi \left[\left(\frac{R_3}{1\text{au}} \right)^2 - \left(\frac{R_2}{1\text{au}} \right)^2 \right] \cos(i). \tag{4.8}
 \end{aligned}$$

For the sources for which we only fit two components, the third term in the above equation can be ignored.

The fits were done using the same MCMC setup, with the same reduced- χ^2 formula taken as the likelihood (see Equation 4.7), as in Section 4.3.1. The same fit regions are used for the most optimal comparison between the results.

4.3.3 Line flux ratios

Aside from analysing the spectrum through slab models, we followed Banzatti et al. (2025b) and analysed their suggested line flux ratios: $F_{1500\text{K}/3600\text{K}}$ and $F_{3600\text{K}/6000\text{K}}$ (see also the right-most panel in their Figure 10). In particular, these line ratios will provide information on, respectively, the cold and hot H₂O vapour reservoirs. The temperatures indicate the approximate upper level energy. The

1500 K flux is comprised of two isolated H₂O transitions, with upper level energies of, respectively, 1448 K (at $\lambda=23.81676 \mu\text{m}$) and 1615 K (at $\lambda=23.89518 \mu\text{m}$), while the 3600 K and 6000 K fluxes are taken to be the isolated lines at $17.50436 \mu\text{m}$ and $17.32395 \mu\text{m}$. Given their upper level energies, these lines probe the strength of the different temperature reservoirs and the ratios provide insights into the potential enhancement of the cold reservoir. Following Banzatti et al. (2025b), we take the sum from the line fluxes of the 1448 K and 1615 K transitions as the total value for $F_{1500\text{K}}$. To determine the line fluxes, we followed the approach of Banzatti et al. (2012) and Temmink et al. (2024b), based on the techniques provided by Pascucci et al. (2008), Najita et al. (2010), and Pontoppidan et al. (2010): we obtained a Gaussian distribution of measured line flux, using 1000 iterations of adding normally distributed noise (following the S/N values in Table 4.B.1), by fitting Gaussians (using the python-package LMFIT, Newville et al. 2014) to the lines. From these distributions, we took the median value as the line flux and the full FWHM as the uncertainty.

4.4 Results

In the following section, we highlight the results from our different fitting methods. In Section 4.4.1, we present the parametric results for the different fit profiles, while the results of the multiple-component analysis are shown in Section 4.4.2. The calculated line fluxes for the different line tracers are displayed in Section 4.4.3.

4.4.1 Parametric analysis

Figure 4.3 displays all fitted profiles for our sample of compact disks with a line width of 4.71 km s^{-1} . Those for the quadrature line widths are given in Figure 4.D.1. Given the profiles, we find three groups of disks: BP Tau, CY Tau, DR Tau, and RNO 90 all behave very similarly, which is most notable in the exponentially tapered power laws (second column), the jump abundances with T_{jump} at higher temperatures ($T_{\text{jump}} \gtrsim 650 \text{ K}$, fourth column), and the resulting upward parabolas (fifth column). The resulting profiles for FT Tau and XX Cha are also nearly identical, but differ from the other four sources. The jump abundance occurs at a low temperature of $T_{\text{jump}} \leq 250 \text{ K}$ for these disks, while their power laws are very slowly declining and their downward parabolas are very shallow. Finally, aside from their very similar spectra (see Figure 4.1), the parametrisations of CX Tau and DN Tau also behave very similarly to each other, but are different from the other disks. Their jump abundance occurs at the intermediate temperatures $T_{\text{jump}} \sim 500\text{-}600 \text{ K}$, while their power laws are monotonically increasing with radius and their parabolas are turned downwards.

The χ_{red}^2 values are listed in Table 4.D.1, where we have highlighted the parametrisations with the lowest χ_{red}^2 -value in boldface. Figures 4.D.2-4.D.9 compare these best-fitting models with the observations and the fitting parameters are also listed in Tables 4.D.2 and 4.D.3. These tables also include uncertainty

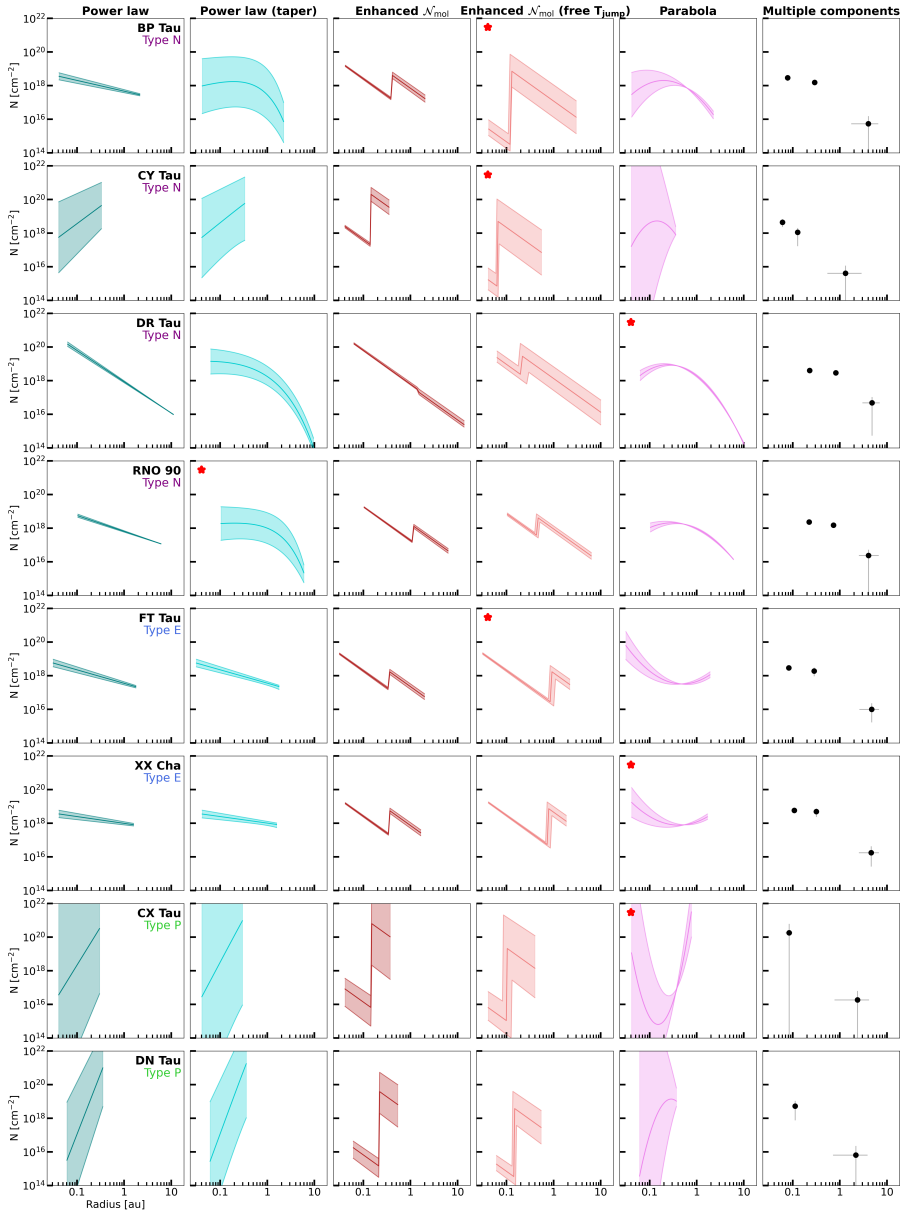


Figure 4.3: Profiles and multiple components (right-most panel) fitted for our sample of compact disks using a line width of 4.71 km s^{-1} . The shaded area is the 1σ -confidence interval, given the uncertainties listed in Tables 4.D.2. The red stars in the top-left corner indicate the best fitting profiles for each disk (see Table 4.D.1). We note that the best-fitting profile for DN Tau is highlighted in Figure 4.D.1.

values on the retrieved fitting parameters. Those uncertainties are taken as the 16th and 84th percentiles of the posterior distributions and, therefore, represent the 1σ upper and lower limits, respectively. From the χ_{red}^2 values, it is clear that not one single parametrisation provides the best description of all observations. Instead, a combination of the different profiles is preferred. We also note that the χ_{red}^2 values of the different parametrisations are overall very similar.

Finally, we briefly highlight the resulting temperature slopes (values for q , see Equations 4.1 and 4.2) according to our retrieved profiles. From Tables 4.D.2 and 4.D.3 it is clear that our retrieved values of q are between 0.35 and 1.30. Overall, we find the lower values for BP Tau, DR Tau, FT Tau, RNO 90, and XX Cha, while the higher values are found for CX Tau, CY Tau, and DN Tau. The average of the best-fitting parametrisations for all disks suggests a power law slope of $q \sim 0.57$ for the temperature, which is somewhat lower than the value found by Romero-Mirza et al. (2024a) of $q \sim 0.69$ and the value suggested by thermochemical modelling of $q \sim 0.7$ in the surface layers of disks (Bosman et al. 2022a; Vlasblom et al. 2025b). Our average value would be even lower if we had only accounted for the results from the quadrature line widths.

4.4.2 Multiple component analysis

Overall, we find rather good agreement between the best-fitting profiles and the multiple components (three or two), as can be seen in Figures 4.3 and 4.D.1, where the discrete data points indicate the results of such fits. The resulting values are given in Table 4.D.4, while the χ_{red}^2 values are also listed in Table 4.D.1. We note that the radial locations shown in Figures 4.3 and 4.D.1 are not the values for R_1 , R_2 , and R_3 , the outer edge of each emitting area, but these are the central values of each emitting area. The resulting spectra for the best-fitting models are also included in Figures 4.D.2-4.D.9 (red profiles).

The results for the multiple-component analysis are rather similar between the different disks with either three or two components fitted: for the three-component fits, we find that the temperatures for the first component all fall in the 765-970 K range, while those for the second and third components fall in the respective ranges of 355-530 K and 200-300 K. We note that the temperatures of the second and third components for FT Tau and XX Cha ($T_2 \sim 385$ and $T_3 < 215$) are lower than those for BP Tau, CY Tau, DR Tau, and RNO 90, further suggesting a difference in behaviour as seen for the parametric analysis in Section 4.4.1. The temperatures for CX Tau and DN Tau, where only two components were fitted, are also very similar. The first component has a temperature between ~ 400 -500 K for both sources, with slightly higher temperatures for DN Tau, while the second component has a temperature in the range of 190-240 K.

Similarly, the column densities follow the same structure, where generally the first component has the highest column density, followed by the second and the third (where applicable). We note, however, that the retrieved column densities cannot be assumed to lie on a simple power law: as can be seen in Figure 4.3 and 4.D.1, the other parametrisations provide better agreement with the multiple-component fits. For example, the downward parabola structure of CX Tau and

DN Tau cannot be captured by a power law through the individual components. Finally, the high values for the emitting areas of the third component very likely indicate optically thin emission (see also Temmink et al. 2024a).

4.4.3 Line flux ratios

The values for the derived line fluxes are given in Table 4.F.1, while the ratios are displayed in Figure 4.4, which has been adapted from Banzatti et al. (2025b) (see their Figure 10, right panel) to include our sample of compact disks (the coloured data points). The grey data points are those from Banzatti et al. (2025b), using the values listed in their Table 3. We find that BP Tau, CY Tau, DR Tau, and RNO 90 show similar line flux ratios as the sample of Banzatti et al. (2025b), while the line fluxes of the cold lines ($F_{1500\text{ K}}$) are much stronger in FT Tau and XX Cha. CX Tau and DN Tau also appear to have higher cold line fluxes, but we note that their hot H_2O line fluxes ($F_{6000\text{ K}}$) are significantly lower. The implications of the locations of the different disks in Figure 4.4 are further discussed in Section 4.5.1.

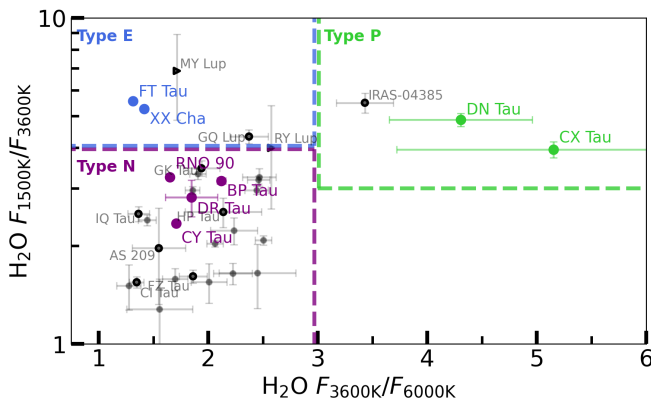


Figure 4.4: Ratios of the 3600 K/6000 K and 1500 K/3600 K line fluxes, used to investigate the respective strength of each H_2O reservoir. The grey data points are adapted from Banzatti et al. (2025b) (see their Table 3), where we have highlighted those analysed by Romero-Mirza et al. (2024a) and potential type P sources (i.e. MY Lup, RY Lup and IRAS-04385). The coloured data points indicate the line ratios of our sample of compact disks. See Section 4.5.1 for a discussion on the different types.

4.5 Discussion

In the following sections, we discuss and interpret our results. From our analysis, it immediately becomes clear that these disks, even though they are all classified as compact, show different behaviours given their H_2O spectra and inferred H_2O distributions. Not all of these disks show a strong, enhanced cold H_2O reservoir,

suggesting that additional factors are at play within these systems. Within our sample of compact disks, many of them may behave just like large and structured disks, while only a limited number actually show cold H₂O emission to be strongly enhanced, likely due to radial drift.

4.5.1 Profile types and H₂O reservoirs

Given the different observed behaviours (see Section 4.4.1) and the observed line fluxes, we propose to categorise planet-forming disks in at least three different types, based on their H₂O reservoirs: type N, type E, and type P (as already highlighted in Figures 4.1 and 4.4). Type N includes the ‘normal’ disks, which show all three H₂O reservoirs (hot with $T > 800$ K, intermediate with $400 < T < 800$ K, and cold with $T < 400$ K). The cold reservoir is present following the temperature gradient, expected to be present in all disks, but not strongly enhanced suggesting that radial drift is not efficiently replenishing the inner disk with icy pebbles. These disks can be found in the lower-left corner of Figure 4.4, where both ratios ($F_{1500\text{K}}/F_{3600\text{K}}$ and $F_{3600\text{K}}/F_{6000\text{K}}$) have low values. We expect many of the large and structured disks to be part of this category.

The type E disks include those with very strong cold H₂O gas reservoirs, which appear to be significantly enhanced, suggesting efficient radial drift. These disks can be found in the top left corner of Figure 4.4, indicating their large cold H₂O reservoirs by large values for $F_{1500\text{K}}/F_{3600\text{K}}$, while their values for $F_{3600\text{K}}/F_{6000\text{K}}$ are similar to the type N disks.

Finally, type P indicates the H₂O-poor (or CO₂-rich; Pontoppidan et al. 2010; Vlasblom et al. 2025a) disks, whose spectra are generally devoid of H₂O, but still show strong emission from the cold reservoir. Emission from the other two components is often found to be weak and the emission present can be fitted with either a hot or an intermediate temperature. The lack of H₂O emission from both components (i.e. strong emission from both hot and intermediate) could potentially be due to a small inner cavity depleting the reservoirs in these components (Grant et al. 2023b; Vlasblom et al. 2024). The cold component could still be prevalent due to radial drift, especially since snowlines are pushed further out in disks with cavities, holding for both the inner and outer regions (Temminck et al. 2023; Vlasblom et al. 2024). These H₂O-poor disks can be found in the top right corner of Figure 4.4, with high values for both $F_{1500\text{K}}/F_{3600\text{K}}$ and $F_{3600\text{K}}/F_{6000\text{K}}$. We note that the boundaries for the different types in Figure 4.4 are arbitrary. To empirically determine the boundaries between the different types, a larger number of disks needs to be consistently analysed. We leave this for future work (Temminck et al. in prep.).

Based on our analysis of the 8 compact disks in the MINDS sample, we suggest that BP Tau, CY Tau, DR Tau, and RNO 90 can all be considered as type N disks, while FT Tau and XX Cha are the only two compact disks with very strong cold H₂O reservoirs: we consider them to be type E disks. CX Tau and DN Tau are considered to be type P disks. Using this categorisation we suggest that the type N disks can best be described (that is, lowest χ^2_{red} -values) by profiles with jump abundances at higher temperatures or upward parabola, which also

resembles the power law profile with a strong exponential taper. The type E disks are the ones with a jump abundance occurring at low temperatures ($T < 250$ K), have slow monotonically decreasing power laws, and may be described by a shallow downward parabola. On the other hand, the type P disks likely have rising power law profiles or jump abundances occurring at intermediate temperatures. Furthermore, their parabolas have a strong minimum.

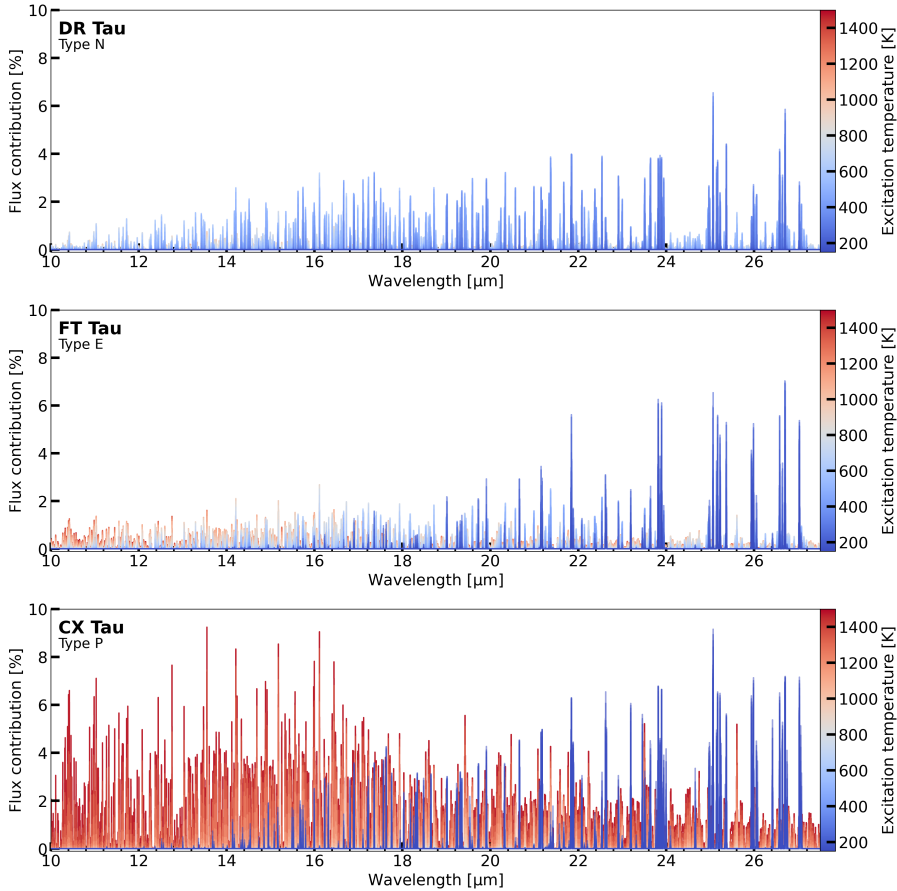


Figure 4.5: Contributions of each individual slab model with the colour representing the excitation temperature of the respective slab. The contributions are shown for the best fitting parametric models of DR Tau (type N), FT Tau (type E), and CX Tau (type P). The contributions are taken as the percentage with respect to the maximum line flux in the full model. We note that the maximum line flux of CX Tau is at least a factor of 5 lower than that of the other two types.

The distinction between the different groups also becomes visible when investigating the contribution (with respect to the maximum flux in the observed spectrum) of the 50 individual slab models within the different profiles. As we are

fitting 50 different slab models, if they all contributed equally, they would each reach a maximum contribution of 2% at every wavelength. Figure 4.5 displays the flux contribution of the slab models for DR Tau (top panel: type N), FT Tau (middle panel: type E), and CX Tau (bottom panel: type P). The contributions for DR Tau show that the hot component is the weakest ($\leq 1.5\%$), as expected from the upward parabola, while the intermediate and cold reservoirs are of similar strength ($\sim 3\text{-}4\%$) given the increasing emitting areas with decreasing temperature. For FT Tau, the hot and intermediate reservoirs are of similar strength ($\sim 2\%$), while the cold reservoir has the strongest contribution ($\leq 6\%$). The contributions for CX Tau show similar strengths in the hot and cold H₂O reservoirs ($\leq 8\%$), but a negligible intermediate component, as expected from the downward parabola. While slab models probing the hot and cold reservoirs may have similar maximum contributions, fewer hot H₂O slabs contribute this much to the spectrum and the spectrum is dominated by the cold reservoir overall. Additionally, we want to emphasise that the best-fitting profile dictates the outcome of Figure 4.5: while the contributions for CX Tau, because of the parabola, have a strong contribution of the hot component, those of DN Tau (both type P disks) will lack the hot component and have significant contributions from the intermediate component as the spectrum is best-fitted by a jump abundance at a temperature of $T_{\text{jump}} \sim 600$ K. Finally, we note that the line-to-continuum ratio of CX Tau is much lower (factor of ≥ 5) than for the other two sources, highlighting that even the higher percental contributions may not be as noticeable as for the other sources.

4.5.2 Role of sub-structures

With our sample of compact disks now categorised, we highlight that the analysis of the ALMA visibilities of some of our sources has suggested that these rather compact disks may harbour sub-structures. In particular, gaps and rings have been proposed for the outer regions (>15 au) of BP Tau (Jennings et al. 2022b; Zhang et al. 2023; Gasman et al. 2025), DN Tau (Long et al. 2018; Zhang et al. 2023), DR Tau (Jennings et al. 2022b; Zhang et al. 2023; Gasman et al. 2025), and FT Tau (Long et al. 2018; Jennings et al. 2022b; Zhang et al. 2023). With sub-structures hypothesised in disks across all three types, it is clear that the role of sub-structures in setting the inner disk H₂O reservoirs is not yet well understood (see also Gasman et al. 2025). Furthermore, as modelling works have shown that the influence depends on the gap location, the time at which the structure formed, and how leaky the traps are, this implies that sub-structures may play a very diverse role in setting the inner disk reservoirs (Kalyaan et al. 2023; Sellek et al. 2025; Easterwood et al. 2024). Age may also play a role (Mah et al. 2023), but we note that the majority of our sample consists of sources from the Taurus star-forming region and it can, therefore, be assumed that these disks all have a similar age. Therefore, our sample may be rather homogeneous and a larger sample, consisting of sources from a variety of different star-forming regions and with different ages, is needed to not only investigate the role of the structure formation time, but also the drift timescale (Mah et al. 2023, 2024).

Our introduced types may, therefore, be comprised of a wide variety of disks.

Higher-resolution ALMA observations (spatial resolution of $<0.1''$, but preferably as high as possible) and observations with infrared observatories are needed to confirm and further study these sub-structures and their potential roles in setting the inner disk abundances, as well as hunt for sub-structures at smaller scales.

4.5.3 Profile implications

The following section discusses the differences in more detail. In particular, we further highlight the behaviours of the profiles and what this implies. In Section 4.G, we also discuss how well the different profiles fit each type.

For the type N disks, we find that all disks prefer a jump abundance at higher temperatures of generally $T_{\text{jump}} \gtrsim 700$ K or a downward parabola (maxima generally at temperatures above 600 K). This behaviour suggests a potential depletion of the hotter component with respect to the stronger intermediate and cold components. This ‘depletion’ could simply mean that the hot H_2O reservoir is not as abundant as the intermediate and cold ones and, therefore, does not follow a simple power law profile, but it may also have a more physical explanation. As suggested by theoretical models (Sellek et al. 2025; Houge et al. 2025), the inward drift of icy pebbles not only increases the molecular reservoirs when crossing the snowlines, but also increases the continuum optical depth (τ) and, therefore, the continuum $\tau=1$ layer may be moved to higher layers and obscure the underlying H_2O reservoirs.

On the other hand, the optical depth of the H_2O lines themselves may play an important role, which could reach values of $\tau \sim 3000$ (Temmink et al. 2024a). Therefore, it is possible that only the very top region of the emitting layer can be probed, well above the dust continuum $\tau=1$ layer, while the remainder of the reservoir remains invisible given the high optical depths. As the line optical depth is found to be higher for the hottest component compared to the cooler components (Temmink et al. 2024a), this may play an important role in setting the observable column density for H_2O in the innermost region.

Finally, the destruction of H_2O could also play a role in depleting the inner regions. One of the main destruction routes in these high atmospheric layers of disks is photodissociation. The photodissociation must, however, occur on timescales faster than the gas-phase formation, which is efficient at > 300 K (Bosman & Bergin 2021), to effectively destroy H_2O . Additionally, H_2O can be destroyed in these layers through collisions with C^+ , Si^+ , and H^+ (Kamp et al. 2013). There is no consensus on which explanation for the flattening of the profiles in the inner regions is correct, as it may be a combination of all three: dust obscuration, optical depth, and destruction. We expect that it is more than likely that different combinations are preferred by different disks and the importance of each explanation will also differ.

The type E disks, FT Tau and XX Cha, have most notably the jump abundance at low temperature ($T_{\text{jump}} < 250$ K) or a shallow downward parabola. As drift can be expected to play to a certain extent a role in all disks, both smooth and structured, where the leakiness of the sub-structures determines the inward flow of material (Mah et al. 2023, 2024; Gasman et al. 2025), the cold component

should be present in most if not all disks. The strength of the cold component in FT Tau and XX Cha, and therefore the jump in abundance at $T_{\text{jump}} \sim 250$ K and the slowly decreasing power law, can be explained by an extreme or very efficient inward flux of the icy pebbles, enhancing the abundance of this cold component near the H₂O snowline with respect to the other disks.

We note that not all disks in the type E category may undergo efficient radial drift. Instead, an accretion outburst that significantly heats up the disk and, therefore, enlarges the emitting area of the cold component may also result in disks falling into this category. In particular, it has been found that XX Cha is highly variable in its accretion (Claes et al. 2022). Even though its variability timescales have not yet been constrained, the observed variation with the X-shooter instrument is on a scale of almost 2 dex (i.e. a factor of 100). Therefore, the strong cold component of XX Cha may be due to its strong variable accretion instead of efficient drift. Furthermore, recent work attributed the strong cold H₂O reservoir observed in the disk of EX Lup to an accretion outburst and the subsequent sublimation of H₂O ice, given the snowline being pushed outwards (Smith et al. 2025). For FT Tau, the other disk identified as a type E disk in our sample, there are currently no claims of accretion outburst or a strongly variable accretion rate. The reported accretion rate for FT Tau gives values between $\log_{10}(\dot{M}_{\text{acc}}) \sim -7.5$ and -8.9 (Garufi et al. 2014; Gangi et al. 2022) (with \dot{M}_{acc} given in $M_{\odot} \text{ year}^{-1}$), but have not been monitored closely over time. To confirm the role of accretion outbursts and variability in setting the inner disk chemical reservoirs, the accretion rates need to be monitored over an extended period of time to also infer the variability timescales. Also, if present, a larger sample of these sources needs to be observed with JWST-MIRI/MRS and analysed in a consistent manner.

The preferred parametrisations of CX Tau and DN Tau, the type P disks, include a monotonically increasing power law, a jump abundance at the intermediate temperatures, and a downward parabola. These profiles all imply a depletion of the hot or intermediate H₂O component with respect to the colder reservoir, which is clearly the strongest. This may suggest a potential dust and gas cavity (see, for example, Salyk et al. 2025), where the cold H₂O is most prominent due to sublimation of H₂O ice near the cavity edge (see also Vlasblom et al. 2024).

Finally, we note that Banzatti et al. (2023a) described two compact disks (GK Tau and HP Tau) having an ‘excess’ in their cold H₂O reservoir with respect to a large and structured disk (CI Tau). Here, we find that similar line flux ratios, as for their two compact disks and for our type N disks, do not necessarily imply an enhancement of the cold H₂O reservoir, but rather a smooth distribution from hot and/or warm to cold. A true enhancement, as found for our type E disks, produces an even stronger excess in the cold H₂O lines with respect to their warmer or hotter counterparts. This may also imply that CI Tau is actually depleted in the cold H₂O and, therefore, falls to the lower left corner of Figure 4.4. Therefore, the type E compact disks of FT Tau and XX Cha most closely conform with the hypothesis posed by Banzatti et al. (2020) and the overall situation appears to be more complex.

Overall, we find that the jump abundance with the jump temperature (T_{jump})

kept free is amongst the favoured fit for all three types. Therefore, we suggest that this profile can be fitted to investigate the H₂O reservoirs in all disks. Furthermore, the location of the jump, as discussed for each type above, may suggest which type the disk belongs to.

4.5.4 Line width comparison

One aspect that has not yet been addressed relates to the choices made for the different line widths, namely, between a fixed value of 4.71 km s⁻¹ or the sum in quadrature of a fixed turbulent line width and the thermal line width, given the temperature of the slab model. Intuitively, the quadrature line profiles may be preferred, as the line width changes accordingly with the temperature. One downside is that the strength of turbulence is not known in the inner regions of these disks, therefore, the turbulent component of the line width (fixed to 1 km s⁻¹) may be stronger or weaker. Thus far, a few studies have measured the turbulence in the outer regions of large disks using ALMA, resulting in values of < 0.2 km s⁻¹ (Paneque-Carreño et al. 2024) or up to ~35% of the sound speed (<0.35c_s; Flaherty et al. 2015, 2017, 2020). We find that seven out of eight of our disks prefer the fixed value of 4.71 km s⁻¹. This may suggest that the inner regions of these disks are more turbulent and higher values need to be assumed for the turbulent component ($\Delta V_{\text{turb}} > 1.0 \text{ km s}^{-1}$).

The preferred larger line width may be related to the change in the optical depth of the lines, which decreases with larger line widths ($\tau \sim N/\Delta V$, with ΔV the line width). As the quadrature line widths are generally smaller (see also Romero-Mirza et al. 2024a), these models will have larger optical depths. Furthermore, it becomes apparent from the contribution plots (Figures 4.G.1-4.G.2) that the quadrature line profiles have stronger fluxes in certain lines of the cold component (see, for example, transitions around 25.05 or 26.70 μm). Given the added weights to the lines fitted at the longest wavelengths (>20 μm), we expect the fitting method to find the best profile describing the observed spectrum, regardless of the lower sensitivity of the larger wavelengths observed with JWST-MIRI. Therefore, it is possible that the cold component of the majority of our sample is less optically thick compared to the other disks.

Finally, we notice that our profiles show no qualitative differences between the different line widths (see Figures 4.3 and 4.D.1), except for the parabola of DN Tau, which changes between upward and downward. Therefore, we conclude that the choice of line width does not really matter for the profiles, but note that the optical depth of the reservoirs, as discussed above, does depend on the chosen line width.

4.5.5 Comparisons with previous analyses

In this section, we compare our analysis with the works of Romero-Mirza et al. (2024a) and Gasman et al. (2025), who, respectively, fitted (tapered) power-laws to seven other disks and analysed the H₂O emission in ten structured disks. Additionally, we compare our results with the interpretation of the models by Houge

et al. (2025).

Romero-Mirza et al. (2024a) only used power law and tapered power law profiles (our profiles I and II) to fit the column density distributions of four compact disks (FZ Tau, GK Tau, GQ Tau, and HP Tau) and three larger disks (AS 209, CI Tau, and IQ Tau). They find that all these disks can be well described by a simple power law, while both CI Tau and FZ Tau prefer the exponentially tapered power law, potentially suggesting a ring-like distribution of the H₂O reservoir. All disks are also captured in the analysis of Banzatti et al. (2025b) and are, therefore, displayed in Figure 4.4, in which we have highlighted their respective positions. All of them, except for maybe GQ Lup, fall within our selection of type N disks. GQ Lup may also be a type N disk, given that it is located towards the lower right of Figure 4.4 with respect to FT Tau and XX Cha and has, therefore, a stronger intermediate component. As stated before, the current definition of the types on Figure 4.4 is somewhat arbitrary and refining the boundaries for each disk type requires a larger sample of sources, which will be addressed in future work (Temminck et al. in prep.). We also cannot exclude the possibility that other behaviours and types may exist outside the parameter space covered by the eight disks in our sample. As all disks analysed by Romero-Mirza et al. (2024a) may be type N disks, their profiles can indeed be described by power laws (similar to CY Tau), but may also be represented by jump abundances at higher temperatures or upward parabolas.

Gasman et al. (2025) compared a sample of 10 structured disks and put their H₂O emission in context with respect to DR Tau. They note that the H₂O reservoirs are complicated for these structured disks and that the H₂O reservoirs strongly depend on the age of the system, the mechanisms that open a gap in the outer disk, and the leakiness of such sub-structures (see also Mah et al. 2024). We note that BP Tau and DR Tau are the two disks overlapping between their sample and ours, highlighting that compact disks may be structured as well. Relative to DR Tau, there is a distinct group of large, structured disks (CI Tau, DL Tau, GW Lup, and V1094 Sco) that have a weaker cold H₂O reservoir, which may end up in the lower left corner of Figure 4.4, where the position of CI Tau is already highlighted. Another group of structured disks (SY Cha and Sz 98) shows, on the other hand, a very strong cold component (stronger than DR Tau) and may, therefore, end up in the upper left corner of Figure 4.4 near FT Tau and XX Cha. This suggests that the H₂O reservoirs of planet-forming disks are much more complicated and one cannot simply separate them into different types based on their size and/or dust structures, as already discussed in Section 4.5.3.

Finally, we compare our best-fitting profiles to the predicted model column density profiles by Houge et al. (2025) (for a star with $L_* = 4 L_\odot$, see Figure 4.6). Their column density profiles are given for the observable H₂O reservoir above the $\tau=1$ layer at 20 μm . Their predictions are given for a fixed ratio between the chemical and mixing timescales ($t_{\text{chem}}/t_{\text{mix}}=0.01$) or for a fixed chemical timescale ($t_{\text{chem}}=10$ years) with a radially varying mixing timescale. Furthermore, their models include three types of dust models: fragile ($v_{\text{frag}}=1 \text{ m s}^{-1}$), composition-dependent ($v_{\text{frag}}=1-10 \text{ m s}^{-1}$), and resistant ($v_{\text{frag}}=10 \text{ m s}^{-1}$). They find that for sufficient fragile dust (i.e. in the fragile or composition-dependent cases) the

column density is set by the vapour-to-dust mass ratio and the dust opacity, as the profiles for those models do not strongly depend on any disk properties and, therefore, do not evolve over time (see also Sellek et al. 2025). While a direct comparison with the models of Houge et al. (2025) cannot be made given the stellar parameters used in their models, we compare the overall shape of the models with our best-fitting column density profiles in Figure 4.6. In particular, we make the comparisons with the models with a fixed chemical timescale and radially varying vertical mixing for the different dust types at a time of 1 Myr, an appropriate assumed age for the majority of our sources (see, for example, Krolikowski et al. 2021; Luhman 2023).

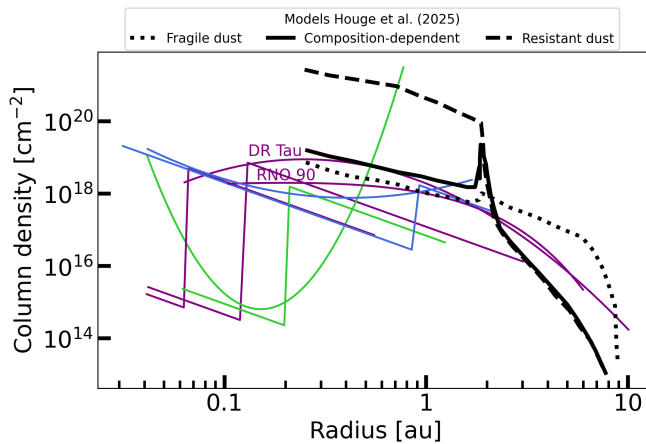


Figure 4.6: Comparisons between our parametric models with the lowest χ_{red}^2 -values and the prediction from the radially varying vertical models from Houge et al. (2025) for all three tested dust types: fragile (dotted), composition-dependent (solid), and resistant (dashed). The profiles of our disks identified to be type N are shown in purple, while those of the type E and type P disks are displayed in, respectively, blue and green.

Qualitatively, the models and observations agree in the sense that the column density profiles decrease towards larger radii. However, our profiles decrease or flatten off towards the inner regions (see, for example, DR Tau and RNO 90). This could be due to the fact that the expression used by Houge et al. (2025) to derive the abundance of water in the surface layers assumes that the chemical timescale (i.e. the destruction timescale) is always much shorter than the mixing timescale. Under their assumptions, the abundance should saturate inside 0.16 au at a level equal to that of the midplane, resulting in the profile flattening off. This level, namely the limit of $N \sim 10^{20} \text{ cm}^{-2}$ explored by Sellek et al. (2025), would be equivalent to negligible destruction under the assumption that the H₂O and dust particles behave the same and on similar timescales (that is, as long as the dust is not depleted on faster timescales than the H₂O). Our best-fitting profiles, except for the outer regions of CX Tau, do not exceed a column density of $N \sim 10^{20} \text{ cm}^{-2}$, which is in agreement with the limit proposed by Sellek et al. (2025).

Quantitatively, the retrieved column densities fall below all the model profiles for many of our sources, even for the most conservative model predictions with the fragile dust. On the one hand, while their expected column density profiles are based on the increased dust obscuration following radial drift, the importance of the optical depth of the H₂O lines themselves is not explored, which may be important (as discussed in Section 4.5.3). Alternatively, this may suggest that for our sample of disks, the ratio of the chemical and mixing timescales is smaller than their assumptions. This may result from shorter photodissociation timescales, which are typically expected to be <1 year in the upper most layers of the disk (Bosman & Bergin 2021; Vlasblom et al. 2025b) and depend source-by-source on the stellar properties (i.e. the UV irradiation field). This may suggest that a chemical timescale of $t_{\text{chem}}=10$ yr may be too long. Future 2D models should further investigate the physical and chemical processing of H₂O in the inner regions and explore how effective the combination of increased dust obscuration following radial drift and line optical depth is.

4.5.6 Other molecular species

While our analysis focuses solely on the H₂O emission, the spectra of these compact disks contain more molecular species. In this section, we only highlight the other molecular species detected and leave the analysis of this emission for future work. We start by noting that CX Tau (Vlasblom et al. 2025a) and DR Tau (Temink et al. 2024b,a) have dedicated papers analysing their molecular emission and we, therefore, refer the reader to these papers. For the other disks in our sample, the commonly observed species (OH, CO₂, HCN, and C₂H₂) are detected in nearly all disks. For some disks, we also report the (potential) detection of CH₄ in CY Tau and that of some of the isotopologues, such as ¹³CCH₂ in CY Tau and both ¹³CO₂ and CO¹⁸O in DN Tau, which is very similar to CX Tau (Vlasblom et al. 2025a). The different species detected in each disk are summarised in Table 4.3, while Appendix 4.E contains a more elaborate discussion of the detected species.

Table 4.3: Summary of the other molecules detected in our sample of disks.

Source	Type	OH	CO ₂	¹³ CO ₂	CO ¹⁸ O	HCN	C ₂ H ₂	¹³ CCH ₂	CH ₄
BP Tau	N	✓	✓	×	×	✓	×	×	×
CX Tau ^α	P	✓	✓	✓	✓(?)	✓	✓	×	×
CY Tau	N	✓	✓	×	×	✓	✓	✓	✓(?)
DN Tau	P	✓	✓	✓	✓(?)	×	×	×	×
DR Tau ^α	N	✓	✓	×	×	✓	✓	×	×
FT Tau	E	✓	✓	×	×	✓	✓	×	×
RNO 90	N	✓	✓	×	×	✓	✓	×	×
XX Cha	E	✓	✓	×	×	✓	✓	×	×

Notes. ^α: see Vlasblom et al. (2025a) for the molecules detected in CX Tau and Temink et al. (2024b,a) for those in DR Tau.

4.6 Conclusions and summary

In this work, we analyse the pure rotational H₂O JWST-MIRI/MRS spectra of 8 millimetre-compact dust disks. We expand upon existing techniques to provide detailed parametric profiles of the column densities beyond (exponentially tapered) power laws. This leads us to infer the best-fitting radial profiles and investigate whether these compact disks show signatures of enhanced reservoirs due to radial drift or whether the overall situation is more complex. Our main conclusions are summarised as follows:

- The pure rotational H₂O spectra of compact dust disks are very different from each other. Half of the disks show similar strengths for the different H₂O reservoirs, conforming with what is seen among large and structured disks, while others show clear signs of an enhanced cold reservoir, even beyond that found in previous comparisons of compact and large disks.
- Different combinations of parametrisations can be used to describe the observed reservoirs in different disks, leading to the conclusion that planet-forming disks can be grouped into at least three different types (N, E, and P), based on their mid-infrared H₂O spectra.
- The parametrisation that assumes a constant of number of molecules with radius (i.e. the column density is proportional to negative the square of the radius) and has a jump (either an enhancement or depletion) in the abundance at a free temperature is able to provide a good fit for the column density profiles for all disks. The temperature of the jump varies per disk but is found to be similar within each of the different types (N, E, or P).
- We find that the column density profiles and, therefore, the distribution of the H₂O reservoirs are generally best fitted with a fixed line width of $\Delta V = 4.71 \text{ km s}^{-1}$. As the quadrature sum is intuitively and physically more correct, this may suggest that the turbulence is stronger in the inner disk and, therefore, a larger value for the turbulent component needs to be assumed ($\Delta V_{\text{turb}} > 1 \text{ km s}^{-1}$).
- Overall, a good agreement is found between the column densities retrieved through a multiple-component analysis and the profiles obtained through the parametric models. The parametric models show that one cannot assume a simple power law through the column densities derived from a multiple-component fit, but it is recommended to fit one of the other parametric models used throughout this work.

This work has shown that not all millimetre-compact disks have signatures of strongly enhanced cold H₂O reservoirs following radial drift. Instead, half of our sample behaves similarly to larger, more structured disks. Therefore, we have introduced a new categorisation, given the behaviour of the H₂O reservoirs seen for our disks: type N, type E, and type P disks. Here, N stands for ‘normal’ disks, whose spectra have contributions from all the components (hot, intermediate, and

cold). Type P disks are the H₂O-poor disks, whose spectra are dominated by other molecular species, yet have a strong contribution from the cold reservoir. Finally, the type E disks are the ones that show enhanced cold H₂O, which may be the result of the strong inward drift of icy pebbles or, perhaps, the product of an accretion outburst that pushes out the H₂O and increases the emitting area of the cold H₂O reservoir. Only two of our eight compact disks fit into this final category, further highlighting that not all compact disks have enhanced cold H₂O reservoirs. These three types provide a new classification of disks, purely based on their rotational H₂O emission and may be used to further explore trends involving system properties. Higher resolution ALMA observations and/or observations with infrared interferometers are required to further study the occurrence of substructures in these disks, on small and large scales, and how they may affect the observable reservoirs.

Acknowledgements

The authors would like to thank the referee for many thoughtful, constructive comments that helped improve the manuscript.

This work is based on observations made with the NASA/ESA/CSA James Webb Space Telescope. The data were obtained from the Mikulski Archive for Space Telescopes at the Space Telescope Science Institute, which is operated by the Association of Universities for Research in Astronomy, Inc., under NASA contract NAS 5-03127 for JWST. These observations are associated with program #1282. The following National and International Funding Agencies funded and supported the MIRI development: NASA; ESA; Belgian Science Policy Office (BELSPO); Centre Nationale d’Etudes Spatiales (CNES); Danish National Space Centre; Deutsches Zentrum für Luft- und Raumfahrt (DLR); Enterprise Ireland; Ministerio De Economía y Competividad; Netherlands Research School for Astronomy (NOVA); Netherlands Organisation for Scientific Research (NWO); Science and Technology Facilities Council; Swiss Space Office; Swedish National Space Agency; and UK Space Agency. The data described here may be obtained from 10.17909/t6gq-q023.

M.T., A.D.S., E.F.v.D., and M.V. all acknowledge support from the ERC grant 101019751 MOLDISK. D.G. thanks the Belgian Federal Science Policy Office (BELSPO) for the provision of financial support in the framework of the PRODEX Programme of the European Space Agency (ESA). E.F.v.D. also acknowledges support from the Danish National Research Foundation through the Center of Excellence “InterCat” (DNRF150). E.F.v.D., I.K., and A.M.A. acknowledge support from grant TOP-1 614.001.751 from the Dutch Research Council (NWO). T.H., K.S. and M.S. acknowledge support from the European Research Council under the Horizon 2020 Framework Program via the ERC Advanced Grant Origins 83 24 28. A.C.G. acknowledges support from PRIN-MUR 2022 20228JPA3A “The path to star and planet formation in the JWST era (PATH)” funded by NextGeneration EU and by INAF-GoG 2022 “NIR-dark Accretion Outbursts in Massive Young stellar objects (NAOMY)” and Large Grant INAF 2022 “YSOs

Outflows, Disks and Accretion: towards a global framework for the evolution of planet forming systems (YODA)”. G.P. gratefully acknowledges support from the Carlsberg Foundation, grant CF23-0481 and from the Max Planck Society. B.T. is a Laureate of the Paris Region fellowship program, which is supported by the Ile-de-France Region and has received funding under the Horizon 2020 innovation framework program and Marie Skłodowska-Curie grant agreement No. 945298.

This work also has made use of the following software packages that have not been mentioned in the main text: NumPy, SciPy, Astropy, Matplotlib, pandas, IPython, Jupyter (Harris et al. 2020; Virtanen et al. 2020; Astropy Collaboration et al. 2013, 2018, 2022; Hunter 2007; pandas development team 2020; Pérez & Granger 2007; Kluyver et al. 2016)

Appendix

4.A Velocity shifted slab models

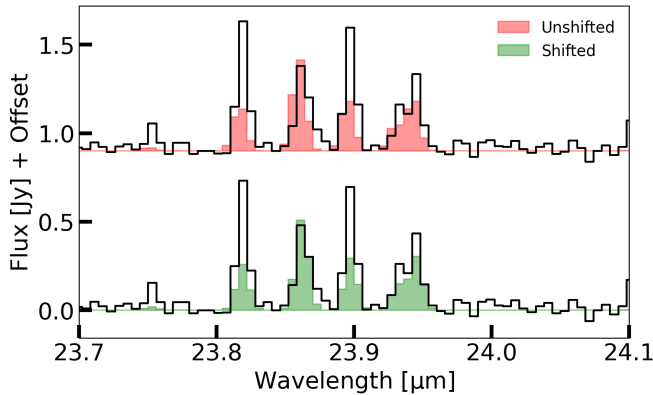


Figure 4.A.1: Comparison, using DR Tau as a test case, between an unshifted slab model (red) and one shifted by the heliocentric velocity.

4.B S/N on the continuum and uncertainties for the observations

Table 4.B.1: S/N values for each sub-band obtained from the *Exposure Time Calculator*.

Source	ETC S/N values in each sub-band											
	1A	1B	1C	2A	2B	2C	3A	3B	3C	4A	4B	4C
BP Tau	383.46	428.72	519.87	570.45	900.21	996.66	799.42	827.84	992.3	519.48	301.15	73.06
CX Tau	368.49	422.36	529.29	575.06	794.03	892.06	783.2	835.26	984.43	518.9	339.39	103.01
CY Tau	497.79	557.57	647.37	619.63	736.81	782.54	685.5	666.27	671.04	288.82	155.6	41.29
DN Tau	511.39	584.19	700.23	723.75	921.2	1046.72	961.64	1014.51	1143.0	622.85	427.47	137.28
DR Tau	558.15	624.65	755.79	767.27	994.22	1098.16	968.84	1006.86	1133.53	493.85	265.88	60.77
FT Tau	373.63	414.88	504.52	553.14	769.13	857.08	724.21	754.76	843.66	405.9	245.9	66.0
RNO 90	668.11	719.03	835.31	833.83	1075.98	1194.92	910.9	922.45	1057.8	435.4	219.53	45.73
XX Cha	383.02	423.56	506.03	538.19	740.69	822.55	720.9	753.22	862.37	457.42	283.29	78.24

4.C Slab model fit regions

Table 4.C.1: Fit regions used for the fitting of H₂O transitions.

Molecule	Sources	Fit regions ^a
H ₂ O	BP Tau, CY Tau, DR Tau, FT Tau, RNO 90, XX Cha	11.717-11.735, 12.56-12.57, 13.128-13.138, 13.2875-13.318, 13.495-13.513, 14.202-14.218, 14.34-14.355, 14.42-14.438, 14.505-14.523, 14.68-14.695, 14.857-14.872, 14.888-14.905, 15.17-15.19, 15.41-15.425, 15.447-15.463, 15.567-15.583, 15.615-15.635, 15.717-15.732, 15.75-15.767, 15.958-15.975, 16.10-16.125, 16.263-16.28, 16.313-16.332, 16.535-16.553, 16.715-16.735, 16.975-16.993, 17.093-17.111, 17.135-17.15, 17.318-17.333, 17.348-17.366, 17.367-17.38, 17.397-17.415, 17.493-17.515, 17.558-17.575, 17.910-17.955, 18.240-18.270, 18.702-18.732, 19.230-19.266, 19.338-19.368, 19.572-19.608, 19.674-19.704, 19.925-19.95, 20.556-20.586 (5), 20.646-20.676 (15), 20.972-21.008 (5), 21.313-21.35 (5), 21.356-21.386 (5), 21.65-21.686 (5), 22.064-22.10 (5), 22.118-22.154 (5), 22.358-22.388 (5), 22.52-22.556 (5), 22.898-22.928 (5), 22.982-23.018 (5), 23.798-23.834 (15), 23.84-23.876 (5), 23.882-23.912 (15), 25.042-25.084 (10), 25.131-25.157 (5), 25.342-25.39 (5), 26.038-26.068 (5), 26.242-26.272 (5), 26.626-26.656 (5), 26.69-26.72 (10), 27.01-27.046 (15)
	CX Tau, DN Tau	11.717-11.735, 12.56-12.57, 13.128-13.138, 13.2875-13.318, 13.495-13.513, 15.958-15.975, 16.10-16.125, 16.263-16.28, 16.313-16.332, 16.535-16.553, 16.715-16.735, 16.975-16.993, 17.093-17.111, 17.135-17.15, 17.318-17.333, 17.348-17.366, 17.367-17.38, 17.397-17.415, 17.493-17.515, 17.558-17.575, 17.910-17.955, 18.240-18.270, 18.702-18.732, 19.230-19.266, 19.338-19.368, 19.572-19.608, 19.674-19.704, 19.925-19.95, 20.556-20.586 (5), 20.646-20.676 (15), 20.972-21.008 (5), 21.313-21.35 (5), 21.356-21.386 (5), 21.65-21.686 (5), 22.064-22.10 (5), 22.118-22.154 (5), 22.358-22.388 (5), 22.52-22.556 (5), 22.898-22.928 (5), 22.982-23.018 (5), 23.798-23.834 (15), 23.84-23.876 (5), 23.882-23.912 (15), 25.042-25.084 (10), 25.131-25.157 (5), 25.342-25.39 (5), 26.038-26.068 (5), 26.242-26.272 (5), 26.626-26.656 (5), 26.69-26.72 (10), 27.01-27.046 (15)

Notes. ^a: values listed in parenthesis in the fit regions denote the chosen weight, w , in Equation 4.7. If no value is listed, the weight is set to unity.

4.D Fit results

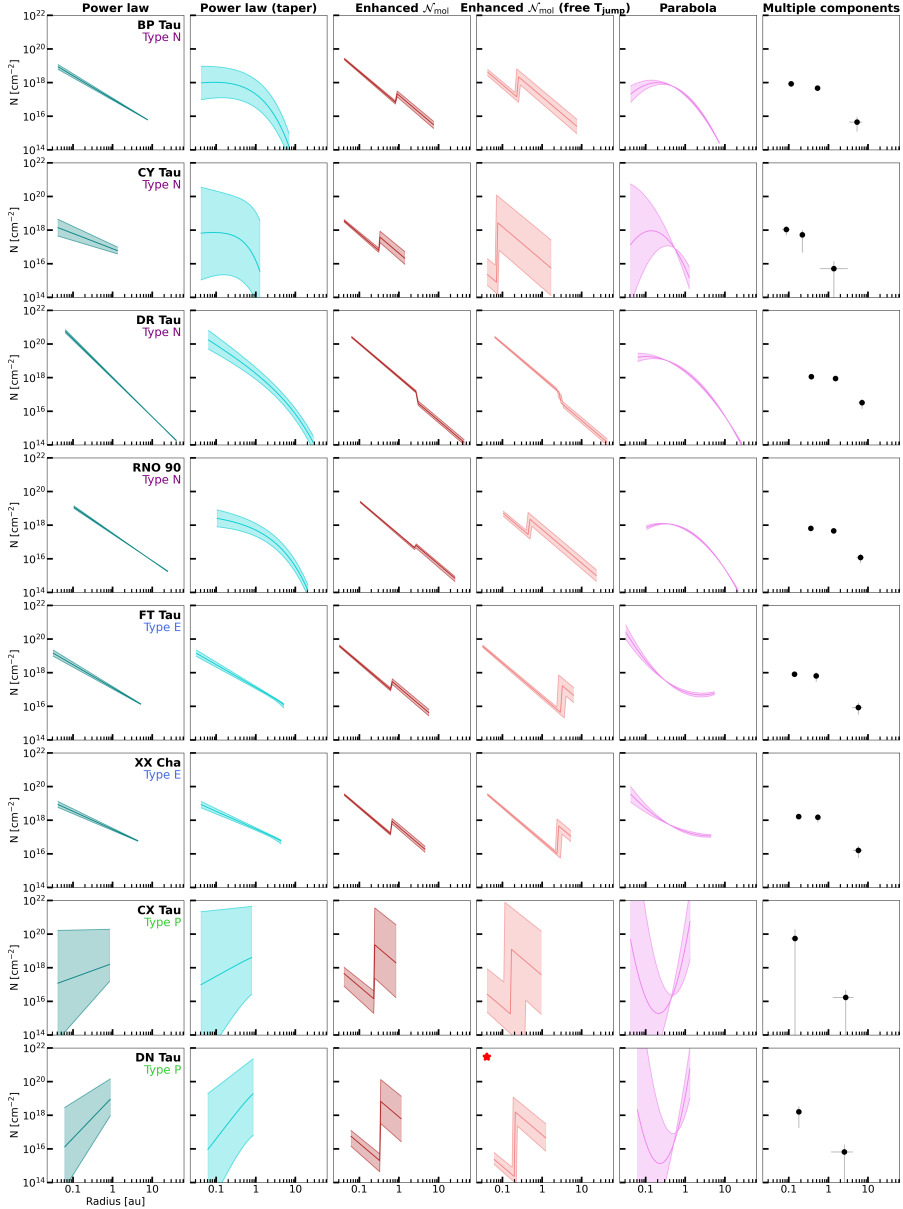


Figure 4.D.1: Similar to Figure 4.3, but for the quadrature line widths. The shaded area is the 1σ -confidence interval, given the uncertainties listed in Tables 4.D.3.

Table 4.D.1: Summary of the results: χ_{red}^2 values.

Source	I		II		III		IV		V		MC	
	4.71	Quad.	4.71	Quad.	4.71	Quad.	4.71	Quad.	4.71	Quad.	4.71	Quad.
BP Tau	157.58	173.89	140.25	145.55	187.20	198.48	128.52	143.63	139.37	142.61	117.23	133.22
CX Tau	32.37	29.59	33.01	29.81	29.27	27.95	27.45	27.35	24.08	24.74	25.04	21.51
CY Tau	70.80	69.94	72.58	67.00	67.15	78.36	55.48	62.22	70.79	64.82	55.39	60.22
DN Tau	45.48	42.03	46.70	43.11	40.43	39.38	33.39	32.98	43.14	43.26	27.13	27.88
DR Tau	277.59	327.08	240.21	314.62	279.71	293.29	251.75	293.77	232.89	298.08	222.74	243.85
FT Tau	125.18	138.15	125.68	138.39	127.23	144.95	102.26	116.22	104.21	123.19	88.35	97.56
RNO 90	286.99	331.84	265.07	296.33	341.82	359.50	265.30	291.75	265.45	284.71	254.25	272.68
XX Cha	200.57	197.65	200.45	198.50	211.05	218.82	191.71	191.13	189.78	193.44	149.05	161.40

Notes. The Roman numbers have the following meanings: I - Power law fit, II - Power law with exponential taper, III - Jump abundance ($T_{\text{jump}}=400$ K), IV - Jump abundance (free T_{jump}), V - Parabola in log-space. MC stands for the multiple-component analysis. The bold-faced entries highlight the fitted profile with the lowest value for χ_{red}^2 .

Table 4.D.2: Fit values for the profiles with a line width of 4.71 km s⁻¹.

Source	Power law			Power law with exponential taper				
	q	$\log_{10}(N_0)$	p	q	$\log_{10}(N_0)$	p	$\log_{10}(R_c)$	ϕ
BP Tau	0.57±0.01	17.67±0.09	0.64 ^{+0.08} _{-0.09}	0.57±0.01	19.27 ^{+0.81} _{-0.68}	-0.86 ^{+0.52} _{-0.56}	-0.70 ^{+0.39} _{-0.45}	0.89 ^{+0.43} _{-0.21}
CX Tau	1.13 ^{+0.10} _{-0.11}	22.87 ^{+2.55} _{-2.74}	-4.54 ^{+2.26} _{-2.18}	1.14±0.10	23.79 ^{+2.49} _{-3.10}	-5.28 ^{+2.57} _{-2.13}	-0.09 ^{+0.74} _{-0.69}	2.51 ^{+1.66} _{-1.37}
CY Tau	1.08±0.04	20.64±0.99	-2.08 ^{+0.81} _{-0.80}	1.08±0.04	20.87 ^{+1.13} _{-1.07}	-2.25 ^{+0.86} _{-0.91}	-0.01 ^{+0.69} _{-0.67}	2.52 ^{+1.65} _{-1.41}
DN Tau	1.29±0.08	24.25 ^{+1.47} _{-1.62}	-7.20 ^{+1.63} _{-1.52}	1.28±0.08	24.73 ^{+1.45} _{-1.71}	-7.65 ^{+1.72} _{-1.47}	-0.16 ^{+0.78} _{-0.57}	2.54 ^{+1.60} _{-1.36}
DR Tau	0.44±0.01	17.94±0.06	1.86±0.06	0.45±0.01	19.97 ^{+0.26} _{-0.36}	-0.39 ^{+0.30} _{-0.27}	-1.04 ^{+0.24} _{-0.13}	0.57 ^{+0.06} _{-0.03}
FT Tau	0.56±0.01	17.55±0.09	0.80±0.09	0.56±0.01	17.56±0.09	0.79±0.09	0.76 ^{+0.17} _{-0.22}	3.52 ^{+1.03} _{-1.38}
RNO 90	0.56±0.01	17.81±0.04	0.94 ^{+0.06} _{-0.05}	0.56±0.01	18.67 ^{+0.56} _{-0.36}	-0.32 ^{+0.38} _{-0.46}	-0.20 ^{+0.30} _{-0.46}	0.94 ^{+0.38} _{-0.25}
XX Cha	0.62±0.01	17.99 ^{+0.10} _{-0.09}	0.40±0.09	0.62±0.01	18.01 ^{+0.09} _{-0.10}	0.39 ^{+0.09} _{-0.10}	0.74 ^{+0.18} _{-0.23}	3.39 ^{+1.12} _{-1.51}
Source	Jump abundance ($T_{\text{jump}}=400$ K)			Jump abundance (T_{jump} free)				
	q	$\log_{10}(N_{\text{mol}})$	$\log_{10}(F_{\text{scale}})$	q	T_{jump}	$\log_{10}(N_{\text{mol}})$	$\log_{10}(F_{\text{scale}})$	
BP Tau	0.58±0.01	42.42±0.03	1.44 ^{+0.12} _{-0.11}	0.53±0.01	843±28	38.71 ^{+0.54} _{-0.38}	4.42 ^{+0.38} _{-0.54}	
CX Tau	1.02±0.07	39.70 ^{+0.60} _{-1.00}	5.02 ^{+1.25} _{-1.36}	0.99 ^{+0.08} _{-0.07}	599 ⁺¹⁰⁹ ₋₁₂₇	38.60 ^{+0.91} _{-0.72}	4.32 ^{+0.84} _{-0.84}	
CY Tau	1.05±0.03	41.33±0.06	3.02 ^{+0.31} _{-0.30}	0.87 ^{+0.03} _{-0.02}	989 ⁺⁴¹ ₋₄₂	38.25 ^{+0.69} _{-0.58}	3.88 ^{+0.58} _{-0.68}	
DN Tau	1.04±0.05	39.53 ^{+0.37} _{-0.60}	4.45 ^{+0.71} _{-0.61}	1.03 ^{+0.06} _{-0.05}	593 ⁺⁵² ₋₅₃	38.55 ^{+0.49} _{-0.37}	4.08 ^{+0.40} _{-0.49}	
DR Tau	0.42±0.01	43.98 ^{+0.05} _{-0.02}	-0.13±0.08	0.45±0.01	854 ⁺⁶² ₋₉₈	43.13 ^{+0.39} _{-0.26}	1.16 ^{+0.27} _{-0.38}	
FT Tau	0.54±0.01	42.27±0.04	1.06±0.08	0.53±0.01	247±18	42.30±0.04	1.84 ^{+0.21} _{-0.18}	
RNO 90	0.55±0.01	43.25±0.02	0.98±0.06	0.55±0.01	655 ⁺²⁹ ₋₂₈	42.83 ^{+0.07} _{-0.08}	1.09±0.08	
XX Cha	0.61±0.01	42.33±0.04	1.45±0.09	0.59±0.01	258 ⁺¹⁷ ₋₁₆	42.39±0.03	2.19 ^{+0.26} _{-0.20}	
Source	Parabola							
	q	$\log_{10}(N_0)$	α	β				
BP Tau	0.57±0.01	17.40 ^{+0.11} _{-0.12}	-2.56 ^{+0.43} _{-0.49}	0.79 ^{+0.19} _{-0.17}				
CX Tau	0.77 ^{+0.05} _{-0.04}	23.80 ^{+1.72} _{-1.97}	21.93 ^{+2.89} _{-4.05}	-5.80 ^{+0.94} _{-0.72}				
CY Tau	1.04 ^{+0.05} _{-0.04}	15.07 ^{+3.48} _{-2.71}	-8.65 ^{+6.81} _{-4.55}	2.22 ^{+1.00} _{-1.43}				
DN Tau	1.25±0.08	16.15 ^{+2.11} _{-2.61}	-11.01 ^{+5.33} _{-5.91}	4.41 ^{+1.43} _{-1.97}				
DR Tau	0.45±0.01	18.28±0.06	-2.21±0.08	0.79±0.08				
FT Tau	0.55±0.01	17.65±0.11	0.97 ^{+0.28} _{-0.27}	-0.69±0.10				
RNO 90	0.56±0.01	17.97 ^{+0.04} _{-0.05}	-1.34 ^{+0.10} _{-0.11}	0.56 ^{+0.10} _{-0.09}				
XX Cha	0.61±0.01	18.08 ^{+0.11} _{-0.10}	1.03 ^{+0.33} _{-0.31}	0.59±0.12				

Table 4.D.3: Fit values for the profiles with the quadrature line widths.

Source	Power law			Power law with exponential taper				
	q	$\log_{10}(N_0)$	p	q	$\log_{10}(N_0)$	p	$\log_{10}(R_c)$	ϕ
BP Tau	0.44 ± 0.01	17.02 ± 0.06	$1.39^{+0.05}_{-0.06}$	0.44 ± 0.01	$19.10^{+0.38}_{-0.49}$	$-0.60^{+0.35}_{-0.29}$	$-1.08^{+0.35}_{-0.22}$	$0.57^{+0.09}_{-0.04}$
CX Tau	$0.75^{+0.08}_{-0.03}$	$18.26^{+2.03}_{-0.87}$	$-0.85^{+0.80}_{-1.81}$	0.77 ± 0.08	$18.80^{+2.87}_{-1.18}$	$-1.31^{+1.06}_{-2.61}$	$0.26^{+0.50}_{-0.62}$	$2.42^{+1.71}_{-1.42}$
CY Tau	0.65 ± 0.02	$16.89^{+0.23}_{-0.22}$	$0.91^{+0.19}_{-0.20}$	0.66 ± 0.02	$18.39^{+1.36}_{-1.14}$	$-0.37^{+0.94}_{-1.04}$	$-0.63^{+0.53}_{-0.49}$	$1.12^{+0.93}_{-0.33}$
DN Tau	0.85 ± 0.05	$19.10^{+1.15}_{-0.91}$	$-2.46^{+0.98}_{-1.28}$	0.86 ± 0.05	$19.67^{+1.81}_{-1.15}$	$-3.06^{+1.25}_{-1.97}$	$0.11^{+0.61}_{-0.69}$	$2.09^{+1.87}_{-1.11}$
DR Tau	0.35 ± 0.01	$17.99^{+0.05}_{-0.04}$	2.32 ± 0.04	0.37 ± 0.01	$18.67^{+0.21}_{-0.19}$	1.40 ± 0.26	$0.02^{+0.31}_{-0.26}$	$0.53^{+0.05}_{-0.02}$
FT Tau	0.44 ± 0.01	17.11 ± 0.07	1.37 ± 0.07	0.45 ± 0.01	$17.12^{+0.08}_{-0.07}$	1.36 ± 0.08	$0.90^{+0.07}_{-0.10}$	$3.84^{+0.82}_{-1.24}$
RNO 90	0.41 ± 0.01	$17.50^{+0.03}_{-0.04}$	1.61 ± 0.04	0.43 ± 0.01	$18.58^{+0.21}_{-0.22}$	0.09 ± 0.23	$-0.57^{+0.24}_{-0.16}$	$0.53^{+0.05}_{-0.02}$
XX Cha	0.49 ± 0.01	17.46 ± 0.07	$1.07^{+0.08}_{-0.07}$	0.49 ± 0.01	$17.48^{+0.08}_{-0.07}$	1.05 ± 0.08	$0.90^{+0.07}_{-0.11}$	$3.72^{+0.91}_{-1.53}$
Source	Jump abundance ($T_{\text{jump}}=400$ K)			Jump abundance (T_{jump} free)				
	q	$\log_{10}(N_{\text{mol}})$	$\log_{10}(F_{\text{scale}})$	q	T_{jump}	$\log_{10}(N_{\text{mol}})$	$\log_{10}(F_{\text{scale}})$	
BP Tau	0.44 ± 0.01	42.78 ± 0.04	0.60 ± 0.08	0.44 ± 0.01	694^{+39}_{-36}	$42.01^{+0.15}_{-0.20}$	$1.28^{+0.20}_{-0.16}$	
CX Tau	0.75 ± 0.05	$40.58^{+0.34}_{-0.72}$	$3.26^{+1.11}_{-1.73}$	0.72 ± 0.05	549^{+165}_{-255}	$39.36^{+1.48}_{-1.04}$	$3.89^{+0.89}_{-1.07}$	
CY Tau	0.64 ± 0.02	41.72 ± 0.05	$0.83^{+0.22}_{-0.19}$	0.61 ± 0.02	1044^{+53}_{-61}	$38.55^{+0.93}_{-0.63}$	$3.60^{+0.93}_{-0.91}$	
DN Tau	0.78 ± 0.03	$40.16^{+0.57}_{-0.57}$	$3.57^{+0.89}_{-0.65}$	0.75 ± 0.03	602^{+97}_{-61}	$38.80^{+0.39}_{-0.27}$	$3.88^{+0.41}_{-0.40}$	
DR Tau	0.35 ± 0.01	$44.29^{+0.04}_{-0.03}$	-0.57 ± 0.06	0.35 ± 0.01	393^{+19}_{-19}	44.29 ± 0.04	-0.57 ± 0.07	
FT Tau	0.44 ± 0.01	42.66 ± 0.05	0.55 ± 0.07	0.43 ± 0.01	205^{+29}_{-17}	42.66 ± 0.06	$1.67^{+0.32}_{-0.28}$	
RNO 90	0.41 ± 0.01	$43.54^{+0.01}_{-0.05}$	$0.23^{+0.06}_{-0.05}$	0.42 ± 0.01	779^{+42}_{-40}	$42.83^{+0.13}_{-0.17}$	$1.00^{+0.16}_{-0.14}$	
XX Cha	0.48 ± 0.01	42.77 ± 0.04	0.83 ± 0.08	0.47 ± 0.01	214^{+16}_{-14}	$42.79^{+0.05}_{-0.04}$	$1.73^{+0.24}_{-0.21}$	
Source	Parabola							
	q	$\log_{10}(N_0)$	α	β				
BP Tau	0.44 ± 0.01	17.28 ± 0.06	$-2.06^{+0.13}_{-0.12}$	0.64 ± 0.09	-	-	-	-
CX Tau	$0.65^{+0.05}_{-0.04}$	$19.22^{+1.57}_{-1.72}$	$11.71^{+3.18}_{-4.74}$	$-3.78^{+1.30}_{-0.90}$	-	-	-	-
CY Tau	0.66 ± 0.02	$15.75^{+0.50}_{-0.49}$	$-5.19^{+0.47}_{-1.56}$	$1.32^{+0.44}_{-0.44}$	-	-	-	-
DN Tau	$0.74^{+0.07}_{-0.03}$	$19.14^{+1.13}_{-1.13}$	$12.57^{+2.29}_{-4.42}$	$-4.28^{+2.09}_{-0.78}$	-	-	-	-
DR Tau	0.37 ± 0.01	$18.38^{+0.08}_{-0.07}$	-1.77 ± 0.09	$0.39^{+0.07}_{-0.06}$	-	-	-	-
FT Tau	0.44 ± 0.01	$16.85^{+0.11}_{-0.10}$	-0.84 ± 0.11	-0.44 ± 0.07	-	-	-	-
RNO 90	0.42 ± 0.01	$17.77^{+0.04}_{-0.05}$	-1.22 ± 0.06	$0.50^{+0.04}_{-0.05}$	-	-	-	-
XX Cha	0.48 ± 0.01	17.33 ± 0.08	-0.79 ± 0.12	-0.26 ± 0.09	-	-	-	-

Table 4.D.4: Fit values for the multiple-component fits.

Fixed 4.71 line width								
	BP Tau	CX Tau	CY Tau	DN Tau	DR Tau	FT Tau	RNO 90	XX Cha
T_1	933^{+136}_{-101}	425^{+114}_{-77}	821^{+150}_{-86}	486^{+53}_{-52}	906^{+64}_{-55}	920^{+56}_{-47}	953^{+66}_{-54}	765^{+43}_{-35}
$\log_{10}(N_1)$	18.5 ± 0.2	20.3 ± 1.1	18.7 ± 0.2	$18.7^{+0.5}_{-0.4}$	18.6 ± 0.1	18.5 ± 0.1	18.4 ± 0.1	18.8 ± 0.1
R_1	0.12 ± 0.02	0.13 ± 0.03	$0.08^{+0.02}_{-0.1}$	0.16 ± 0.02	0.39 ± 0.04	0.13 ± 0.01	0.34 ± 0.03	$0.18^{+0.01}_{-0.02}$
T_2	516^{+15}_{-17}	196^{+42}_{-31}	535^{+43}_{-56}	239^{+30}_{-31}	487^{+15}_{-16}	364^{+49}_{-33}	513 ± 13	357^{+55}_{-38}
$\log_{10}(N_2)$	18.2 ± 0.1	$16.3^{+1.1}_{-0.7}$	18.1 ± 0.4	$15.8^{+1.1}_{-0.6}$	18.5 ± 0.1	$18.3^{+0.3}_{-0.2}$	18.2 ± 0.1	18.7 ± 0.2
R_2	0.46 ± 0.02	$4.60^{+3.54}_{-3.19}$	$0.17^{+0.03}_{-0.02}$	$4.21^{+3.37}_{-2.94}$	1.24 ± 0.04	0.44 ± 0.08	1.12 ± 0.05	$0.5^{+0.08}_{-0.07}$
T_3	259^{+18}_{-19}	-	268^{+67}_{-79}	-	247^{+22}_{-23}	217^{+14}_{-15}	295 ± 18	207 ± 12
$\log_{10}(N_3)$	$15.7^{+0.8}_{-0.4}$	-	$15.6^{+0.8}_{-0.5}$	-	$16.7^{+0.5}_{-0.4}$	$16.0^{+0.6}_{-0.4}$	16.4 ± 0.5	$16.3^{+0.6}_{-0.4}$
R_3	$7.59^{+4.98}_{-4.57}$	-	$2.45^{+3.13}_{-1.55}$	-	$8.39^{+4.41}_{-3.65}$	$9.00^{+4.08}_{-4.28}$	$6.97^{+5.22}_{-3.03}$	$8.79^{+2.21}_{-4.19}$
Quadrature line widths								
	BP Tau	CX Tau	CY Tau	DN Tau	DR Tau	FT Tau	RNO 90	XX Cha
T_1	959^{+150}_{-107}	415^{+75}_{-75}	836^{+169}_{-100}	481^{+96}_{-52}	921^{+57}_{-43}	903^{+60}_{-48}	940^{+59}_{-48}	767^{+49}_{-38}
$\log_{10}(N_1)$	17.9 ± 0.2	19.7 ± 1.1	$18.0^{+0.3}_{-0.2}$	$18.2^{+0.5}_{-0.4}$	18.1 ± 0.1	17.9 ± 0.1	17.8 ± 0.1	18.2 ± 0.1
R_1	$0.19^{+0.05}_{-0.04}$	0.25 ± 0.06	0.13 ± 0.04	0.30 ± 0.04	$0.68^{+0.05}_{-0.06}$	0.25 ± 0.02	0.62 ± 0.06	$0.31^{+0.03}_{-0.04}$
T_2	517^{+17}_{-17}	192^{+41}_{-28}	530^{+50}_{-65}	231^{+31}_{-32}	491 ± 15	382^{+60}_{-48}	511^{+13}_{-14}	389^{+49}_{-54}
$\log_{10}(N_2)$	17.2 ± 0.1	$16.2^{+0.8}_{-0.6}$	17.7 ± 0.4	$15.8^{+0.8}_{-0.5}$	18.0 ± 0.1	$17.8^{+0.3}_{-0.2}$	17.7 ± 0.1	18.2 ± 0.2
R_2	0.87 ± 0.03	$5.19^{+3.15}_{-2.87}$	$0.30^{+0.04}_{-0.03}$	$4.75^{+3.20}_{-2.72}$	2.34 ± 0.08	$0.74^{+0.17}_{-0.13}$	2.10 ± 0.08	$0.76^{+0.15}_{-0.09}$
T_3	250^{+17}_{-18}	-	278^{+66}_{-82}	-	242^{+19}_{-20}	215^{+13}_{-14}	289^{+17}_{-17}	202 ± 11
$\log_{10}(N_3)$	$15.7^{+0.5}_{-0.3}$	-	$15.7^{+0.8}_{-0.5}$	-	16.5 ± 0.3	$15.9^{+0.4}_{-0.3}$	$16.1^{+0.3}_{-0.2}$	$16.2^{+0.4}_{-0.3}$
R_3	$9.67^{+3.64}_{-3.93}$	-	$2.42^{+3.40}_{-1.50}$	-	$11.8^{+2.21}_{-2.62}$	$10.62^{+3.01}_{-3.48}$	$10.84^{+2.80}_{-2.76}$	$10.60^{+2.98}_{-3.03}$

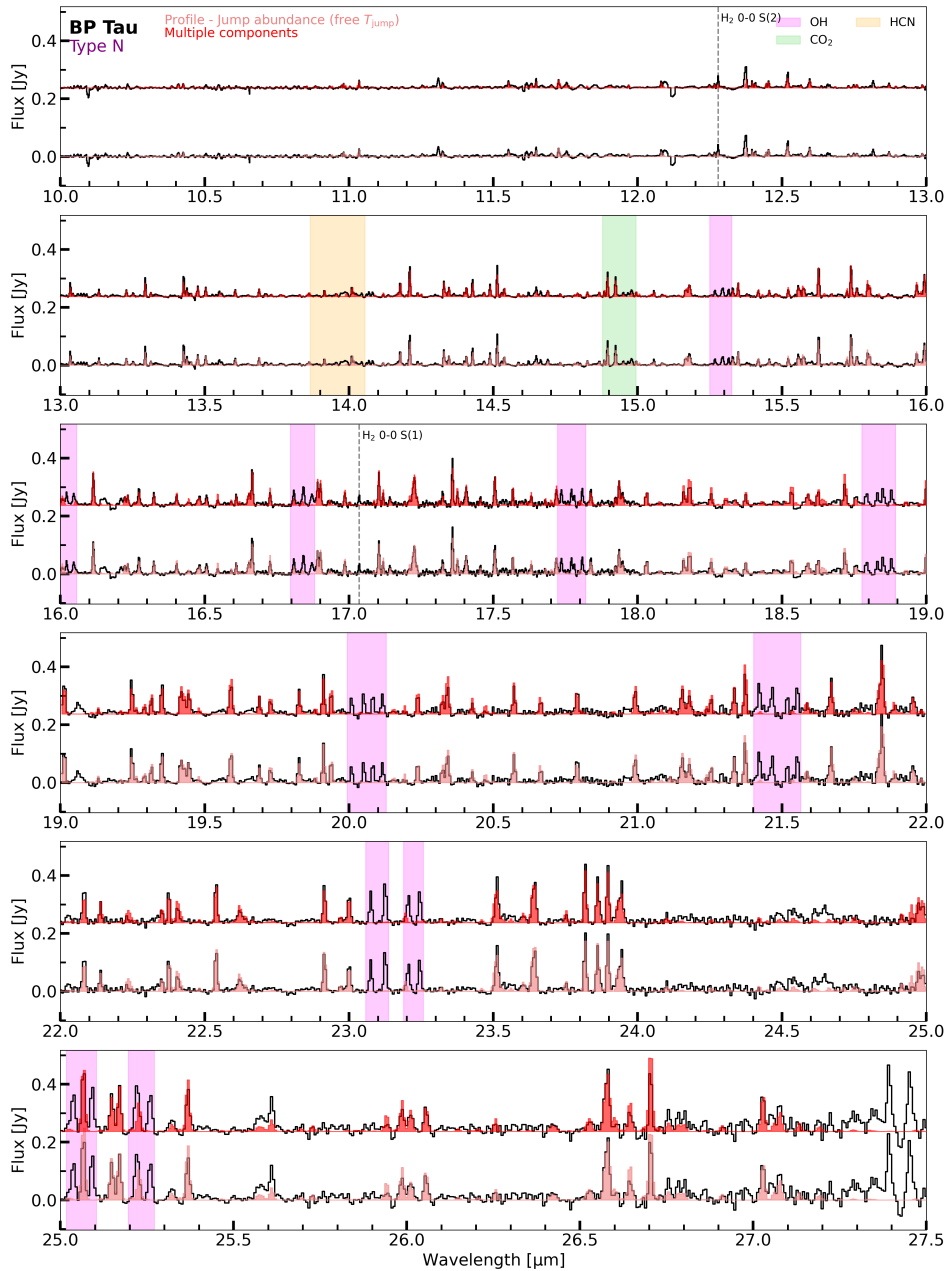


Figure 4.D.2: Comparison between the full models of the best-fitting parametric model (bottom fit) and of the multiple components (red, top fit) for BP Tau. The colour of the best-fitting profile matches that of Figure 4.3. Indicated are also the molecular features from OH (magenta), CO₂ (green), and HCN (orange). The vertical lines indicate the S(1) and S(2) transitions of H₂.

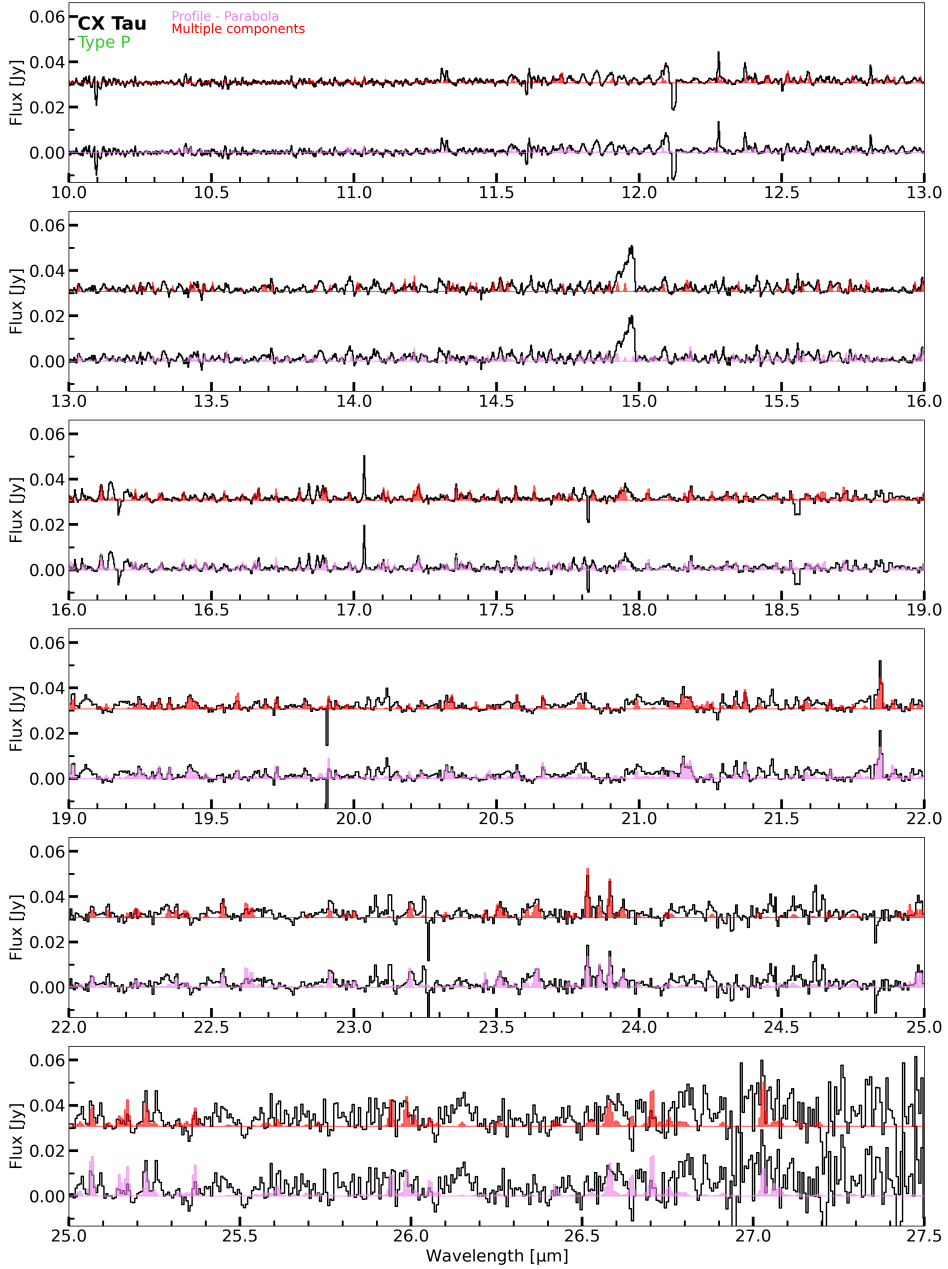


Figure 4.D.3: Similar as Figure 4.D.2, but for CX Tau. We refer the reader to Vlasblom et al. (2025a) for the other molecular emission features.

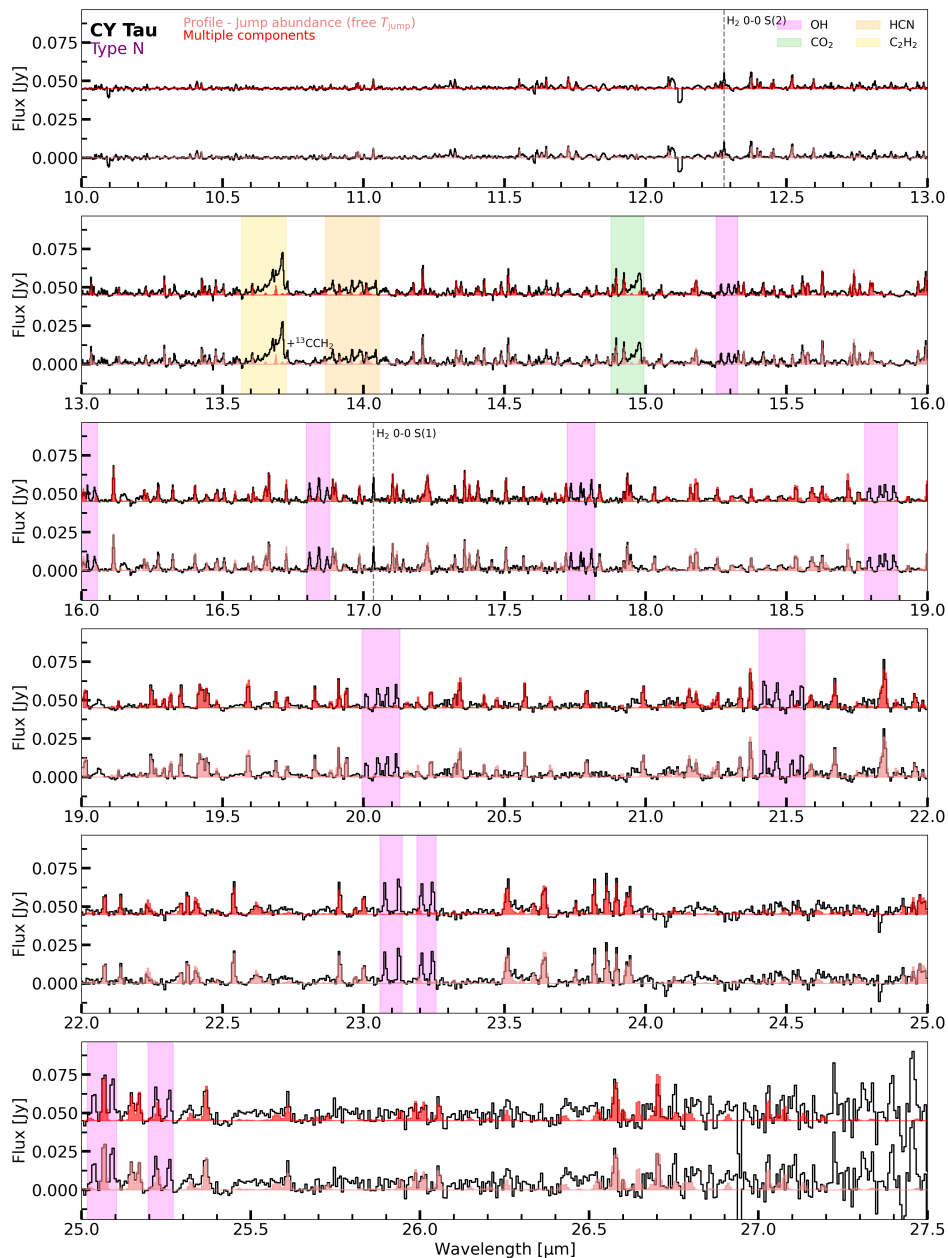


Figure 4.D.4: Similar as Figure 4.D.2, but for CY Tau. Highlighted in yellow is the C_2H_2 emission feature, while the approximate location of $^{13}\text{CCH}_2$ is also shown.

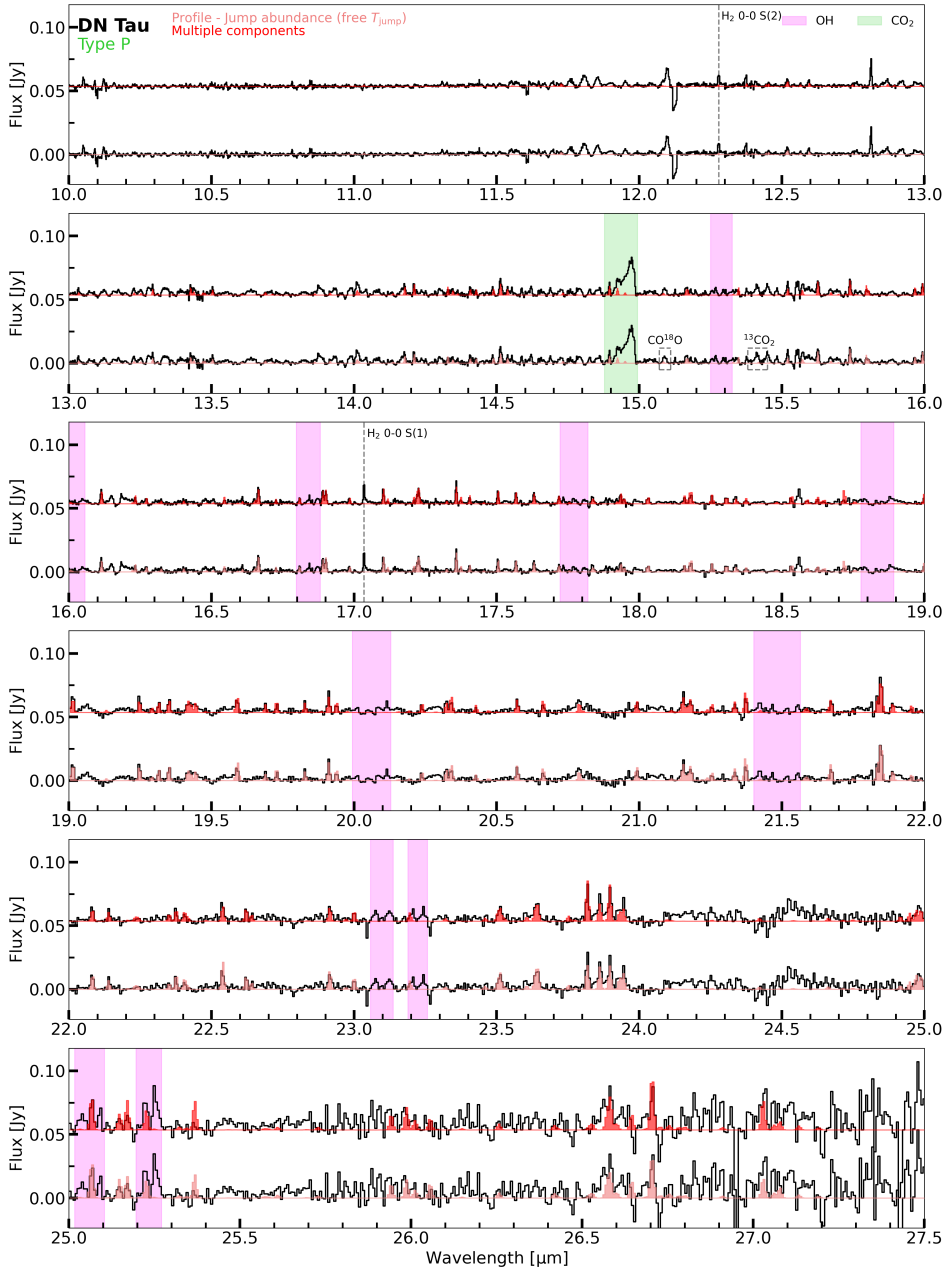


Figure 4.D.5: Similar as Figure 4.D.2, but for DN Tau. The boxes indicate the detection of $^{13}\text{CO}_2$ and the potential detection of CO^{18}O .

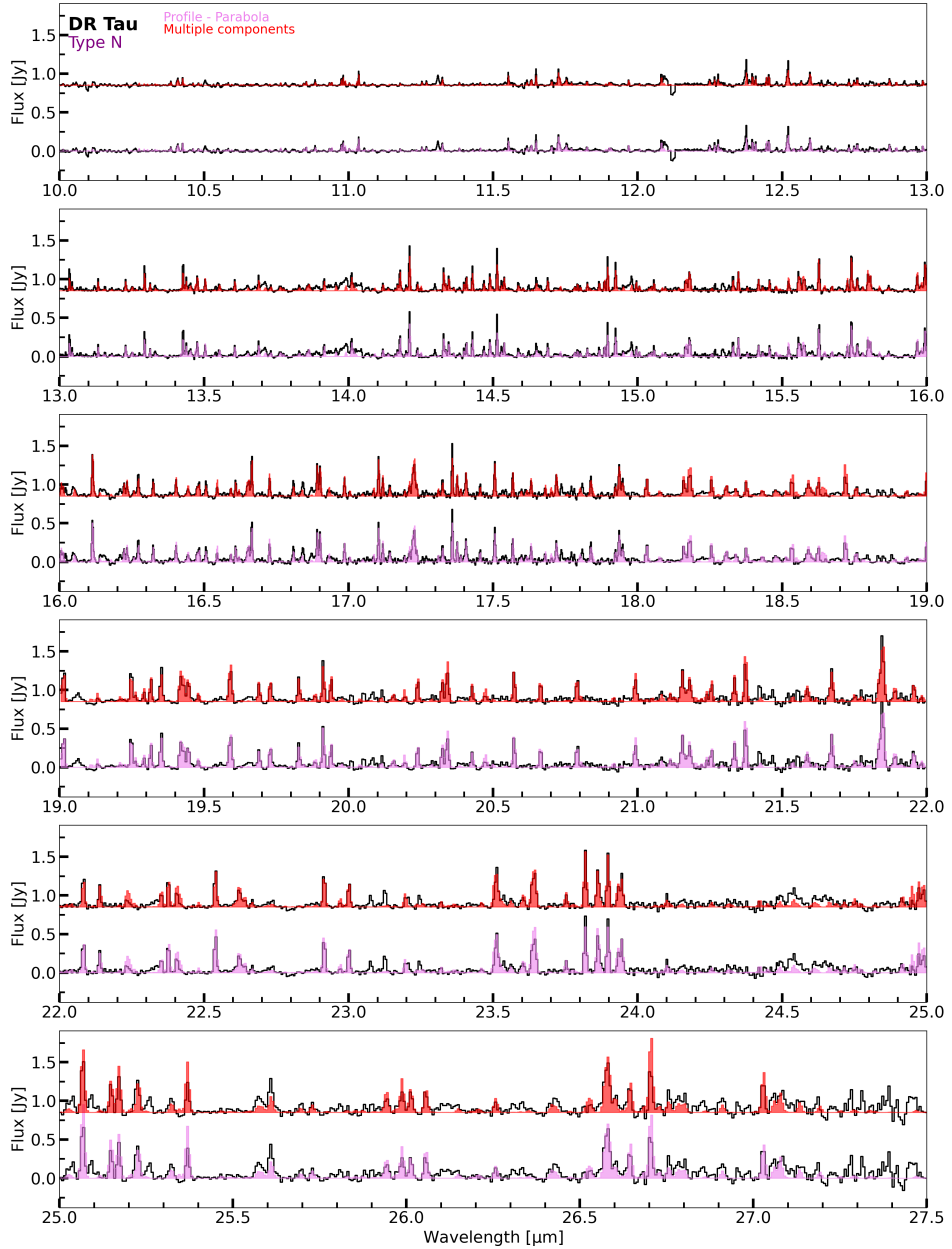


Figure 4.D.6: Similar as Figure 4.D.2, but for DR Tau. We refer the reader to Temmink et al. (2024b) and Temmink et al. (2024a) for the other molecular emission features.

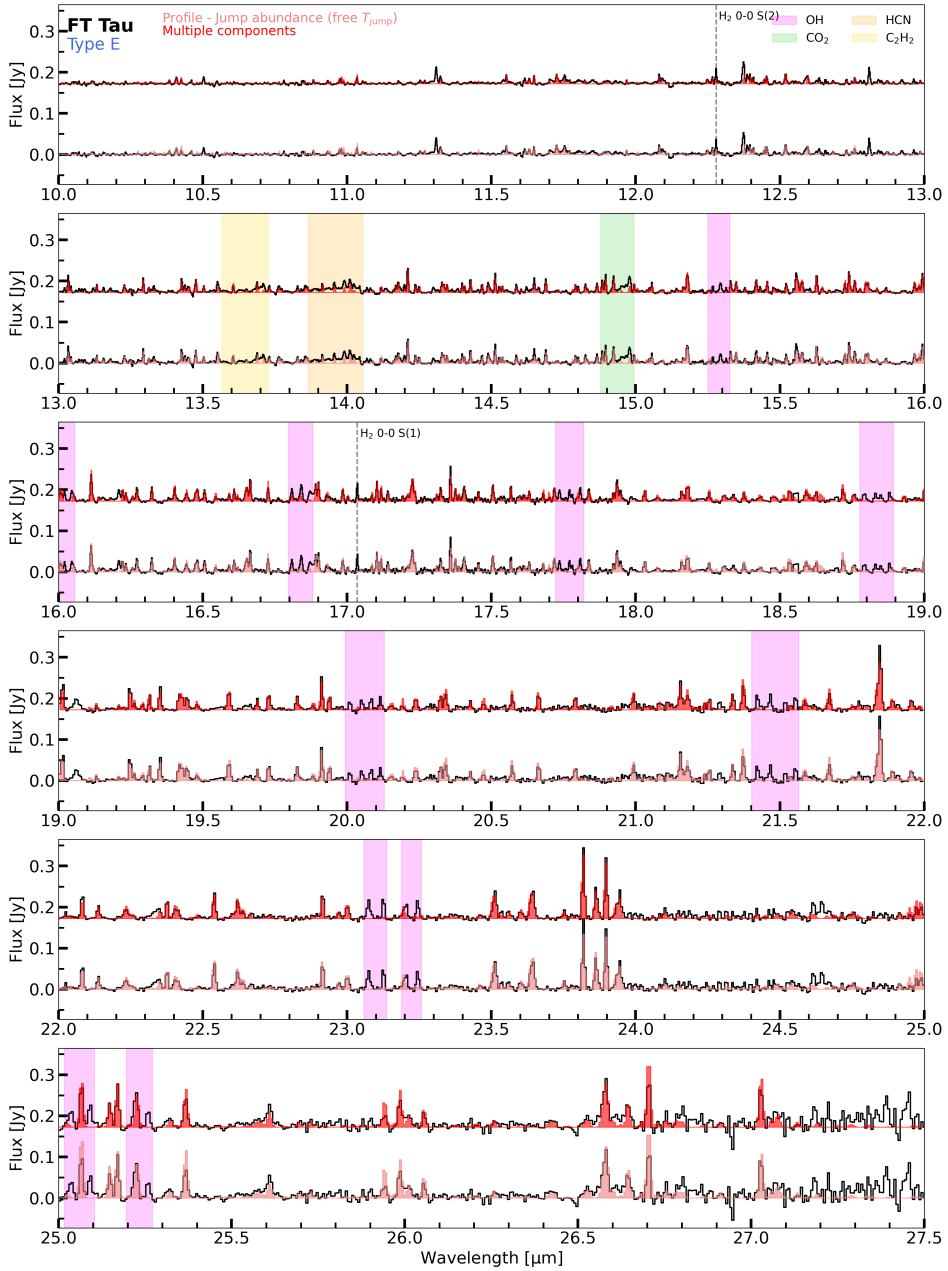


Figure 4.D.7: Similar as Figure 4.D.2, but for FT Tau. Highlighted in yellow is the C₂H₂ emission feature.

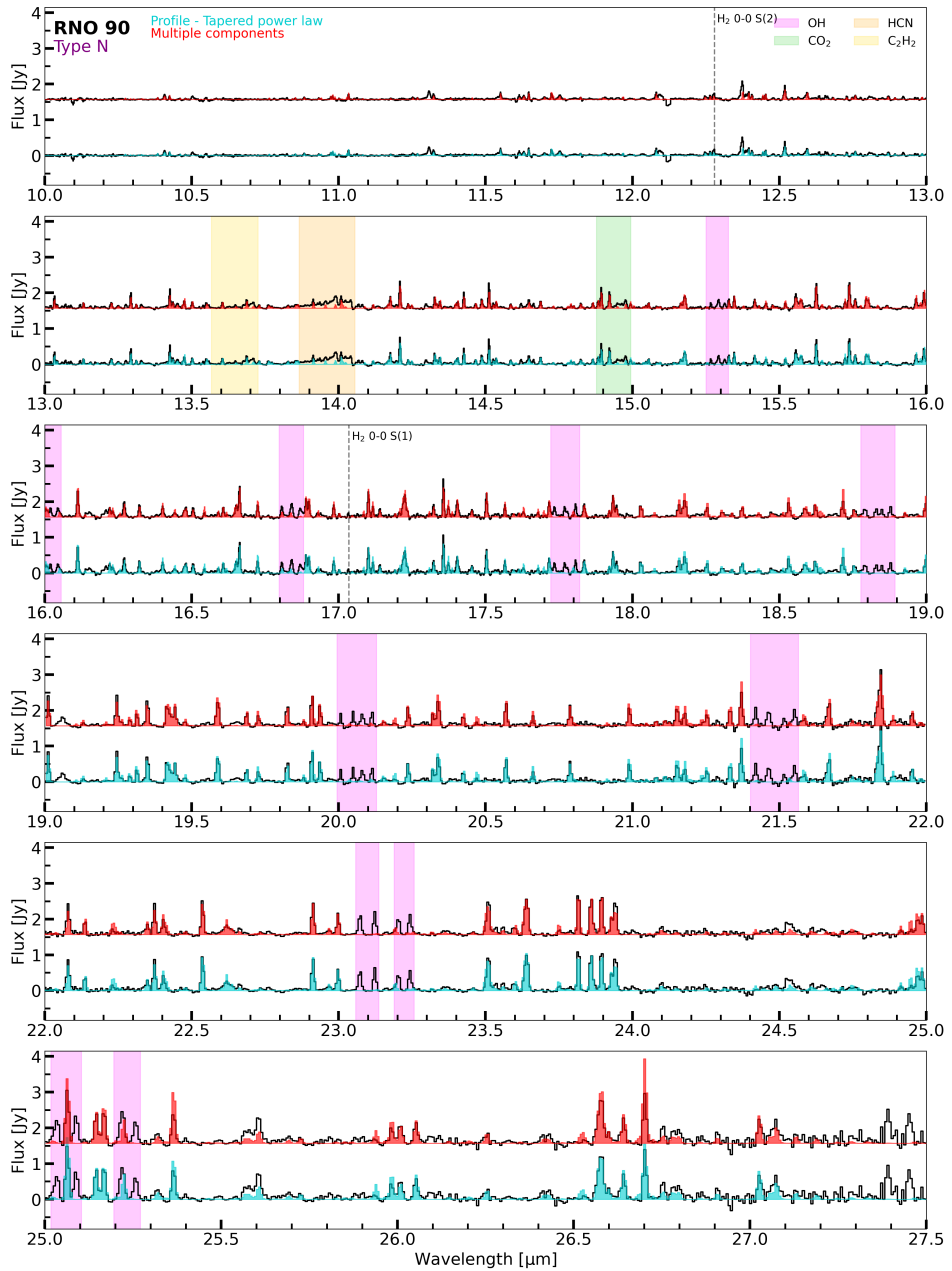


Figure 4.D.8: Similar as Figure 4.D.2, but for RNO 90. Highlighted in yellow is the C₂H₂ emission feature.

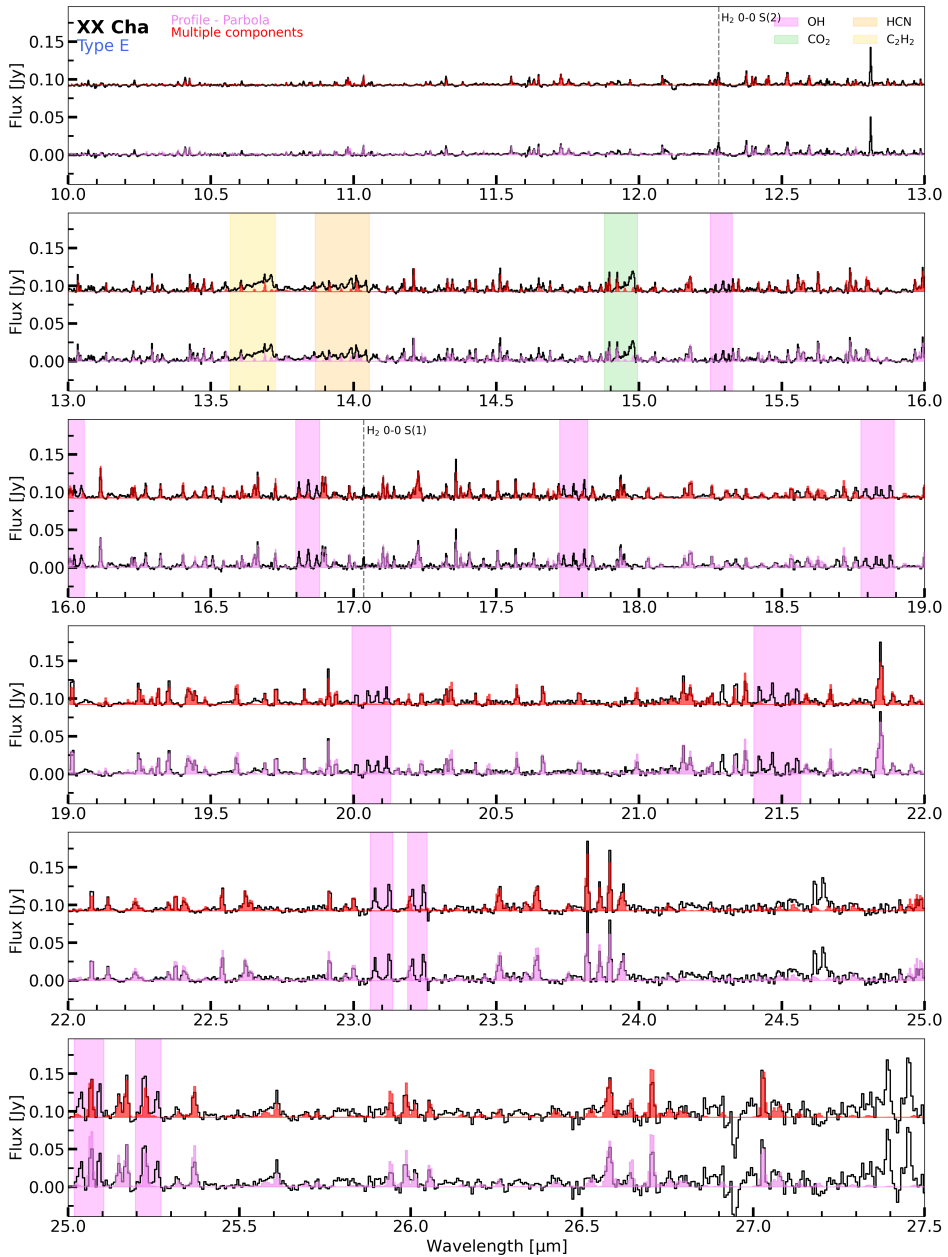


Figure 4.D.9: Similar as Figure 4.D.2, but for XX Cha. Highlighted in yellow is the C_2H_2 emission feature.

4.E Other molecular species

In this following section, we discuss the observed molecular species, aside from H_2O , in each disk (Section 4.E.1) and we discuss the tentative detection of CH_4 in CY Tau (Section 4.E.2). These features are also highlighted in Figures 4.D.2-4.D.9.

4.E.1 Molecules per source

BP Tau: Aside from the pure rotational H_2O lines, the spectrum of BP Tau also contains strong emission of the ro-vibrational transitions and CO emission at the shortest wavelengths (4.9-5.3 μm). Other molecular species, such as CO_2 and HCN, are only weakly detected, while OH transitions are strongly detected above $>15 \mu\text{m}$. Both the H_2 0-0 S(1) (at 17.30484 μm) and S(2) (at 12.27861 μm) are detected. The detected molecular species at $>10 \mu\text{m}$ are also highlighted in Figure 4.D.2.

CY Tau: The strongest molecular feature in the spectrum of CY Tau belongs to C_2H_2 , also visible in Figure 4.1. Its isotopologue, $^{13}\text{CCH}_2$ is also well detected. Other molecular species include CO, the ro-vibrational lines of H_2O , OH, HCN, and CO_2 . Both the H_2 S(1) and S(2) transitions are also detected. Additionally, we present a potential detection of CH_4 in this disk. The tentative detection is further highlighted in Section 4.E.2. The molecular species are highlighted in Figure 4.D.4.

DN Tau: DN Tau has previously been classified, just as CX Tau, as a CO_2 -rich source (Pontoppidan et al. 2010). Aside from the strong emission of CO_2 , we report the detection of its isotopologue $^{13}\text{CO}_2$ and the potential detection of CO^{18}O . Other molecular species, such as HCN and C_2H_2 are not confidently detected, while OH is. At the shortest wavelengths, CO is only tentatively detected, while emission from the ro-vibrational H_2O transitions is clearly detected. As for the other sources, both the H_2 S(1) and S(2) transitions are also detected. Figure 4.D.5 highlights the detected molecular species.

FT Tau: Aside from the strong pure rotational H_2O emission, the spectrum of FT Tau also contains emission from the ro-vibrational lines and from CO. At the longer wavelengths, we clearly detect OH, CO_2 , HCN, and C_2H_2 . The H_2 S(1) and S(2) transitions are also detected. The emission of these species is also highlighted in Figure 4.D.7.

RNO 90: Besides the rotational H_2O transitions, the spectrum of RNO 90 also contains emission from CO, the ro-vibrational H_2O transitions, OH, CO_2 , HCN, and C_2H_2 . Both the S(1) and S(2) transitions of H_2 are also detected. The molecular emission is highlighted in Figure 4.D.8.

XX Cha: Although the spectrum of XX Cha is very similar to that of FT Tau, the emission from both CO_2 and C_2H_2 is stronger. Emission from CO, the ro-vibrational H_2O lines, OH, and HCN are also clearly detected. As for all the other sources, both the H_2 S(1) and S(2) transitions are also detected. Figure 4.D.9 highlights the molecular emission of the other species in the spectrum of XX Cha.

4.E.2 Tentative detection of CH₄ in CY Tau

We report a tentative detection of CH₄ in the spectrum of CY Tau, whose Q-branch is located at $\sim 7.66 \mu\text{m}$. In Figure 4.E.1, we display the 7.60–8.00 μm wavelength region, containing molecular emission from ro-vibrational H₂O transitions and potential weak features from C₂H₂ and the potential detection of CH₄. For the slab models (H₂O, C₂H₂, and CH₄) we have used excitation temperatures of 975 K, 500 K, and 500 K, column densities ($\log_{10}(N)$ with N in cm^{-2}) of 18.4, 17.0, and 16.8, and emitting radii of 0.03 au, 0.10 au, and 0.10 au, respectively. The parameters for H₂O and C₂H₂ were obtained using a χ^2_{red} -approach similar to that described in Section 4.3.1 but using grids instead of an MCMC exploration (see also, for example, Grant et al. 2023b). The model for CH₄ has been obtained by visually fitting the residuals. These slab models thus suggest a column density ratio of $N_{\text{C}_2\text{H}_2}/N_{\text{CH}_4} \gtrsim 1.5$, under the assumption that the species are co-existing. The potential presence of CH₄, in addition to the detection of ¹³CCH₂, suggests that CY Tau may be the most carbon-rich disk in our sample. This disk may be similar to the much larger disk of DoAr 33, where Colmenares et al. (2024) reported, alongside other hydrocarbons, a tentative detection of CH₄. They compared their spectra to thermochemical models and argued for an overall carbon-to-oxygen ratio (C/O) larger than unity.

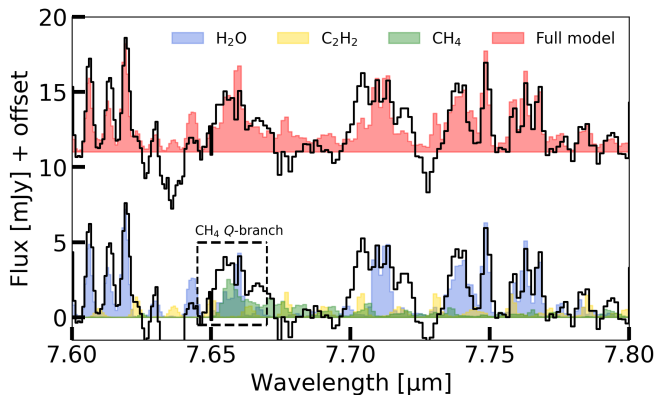


Figure 4.E.1: Zoom-in on the 7.60–8.00 μm region of CY Tau, showing the potential detection of CH₄ (green). Also shown are approximate contributions from H₂O (blue) and C₂H₂ (yellow) slab models. The full model is shown in red with a small offset applied to the flux.

4.F Integrated line fluxes

Table 4.F.1: Integrated fluxes for the lines tracing the cold, intermediate, and hot H₂O reservoirs.

Source	$F_{1448\text{K}}$	$F_{1615\text{K}}$	$F_{3646\text{K}}$	$F_{6052\text{K}}$	$F_{1500\text{K}}^\alpha$
BP Tau	10.67±0.07	10.43±0.04	6.68±0.05	3.15±0.05	21.09±0.08
CX Tau	0.99±0.02	0.93±0.02	0.49±0.03	0.09±0.03	1.91±0.03
CY Tau	1.17±0.01	1.22±0.01	1.02±0.01	0.60±0.01	2.40±0.01
DN Tau	1.29±0.03	1.49±0.05	0.57±0.02	0.13±0.02	2.78±0.06
DR Tau	36.38±0.20	33.89±0.16	24.94±3.17	13.49±0.26	70.27±0.26
FT Tau	8.60±0.03	6.99±0.03	2.81±0.03	2.13±0.03	15.59±0.05
RNO 90	66.03±0.26	66.65±0.22	40.82±0.19	24.72±0.27	132.68±0.34
XX Cha	4.23±0.01	3.88±0.02	1.54±0.01	1.09±0.01	8.11±0.02

Notes. The fluxes are given in $\times 10^{-15}$ erg s⁻¹ cm⁻².

^α: The $F_{1500\text{K}}$ flux is the summation of the fluxes of the 1448 K and 1615 K lines, following Banzatti et al. (2025b).

4.G Profile comparison

In Figures 4.G.1, 4.G.2, and 4.G.3, we show the flux contributions of the 50 slab models for the profiles fitted for DR Tau, CX Tau, and FT Tau, respectively. These disks are each part of one of the different types and comparing their contribution plots provides information on how well the different profiles fit for their types.

DR Tau (type N): The type N disks (BP Tau, CY Tau, DR Tau, and RNO 90) are overall best described by the exponentially tapered power laws, the jump abundances with the jump occurring at high temperatures, and upward parabola (see also Table 4.D.1). As can be seen in Figure 4.G.1, those profiles all yield very similar contributions. The main differences between those profiles and the ones with the simple power law or the jump abundance with the jump fixed at $T_{\text{jump}}=400$ K is the flux at the shortest wavelengths (<15.0 μm), best probed by the hottest component, where the power law and the fixed temperature jump abundance have stronger contributions of the hotter components (most notable in the left panels of Figure 4.G.1). These stronger contributions results in overfitting the observed flux in those inner regions, whereas the preferred profiles have a decrease in column density in the innermost and, therefore, do not overfit these inner regions.

FT Tau (Type E): FT Tau and XX Cha, the Type E disks, are best described by a jump abundance at low temperatures or parabola with a small upturn (see also Table 4.D.1). As can be seen in Figure 4.G.2 for FT Tau, the jump abundance with a jump at $T_{\text{jump}} \lesssim 250$ K is really able to capture the strength of the cold component. The power law is not able to capture this cold component as strongly, but the contributions are clearly still there. The parabola, while being able to yield

a similar contribution to the cold component as the power law, has a much stronger contribution at the shortest wavelengths ($<15.0 \mu\text{m}$) following its upward turn. This stronger contribution actually overfits the observed flux at these wavelengths, disfavours the parabola as the best fit.

CX Tau (type P): The type P disks (CX Tau and DN Tau) mainly prefer the downward parabola and jump abundance profiles (see also Table 4.D.1). As can be seen in Figure 4.G.3, those profiles have the strongest contributions from either the hot or intermediate and cold components, while the (tapered) power law profiles are not able to capture the strength of all three components (hot, intermediate, and cold). The preference for these profiles shows that the P type disks do have contributions from at least two of the components.

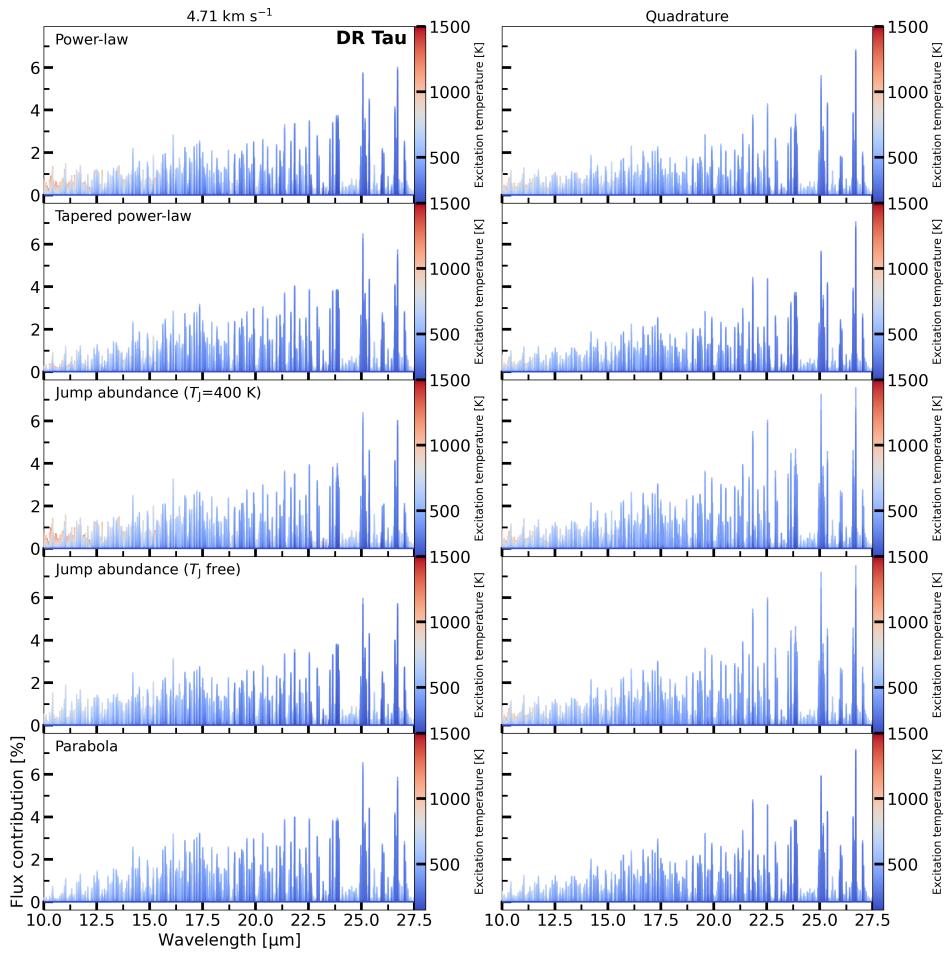


Figure 4.G.1: Contributions from all parametric fits for DR Tau, representing the type N disks.

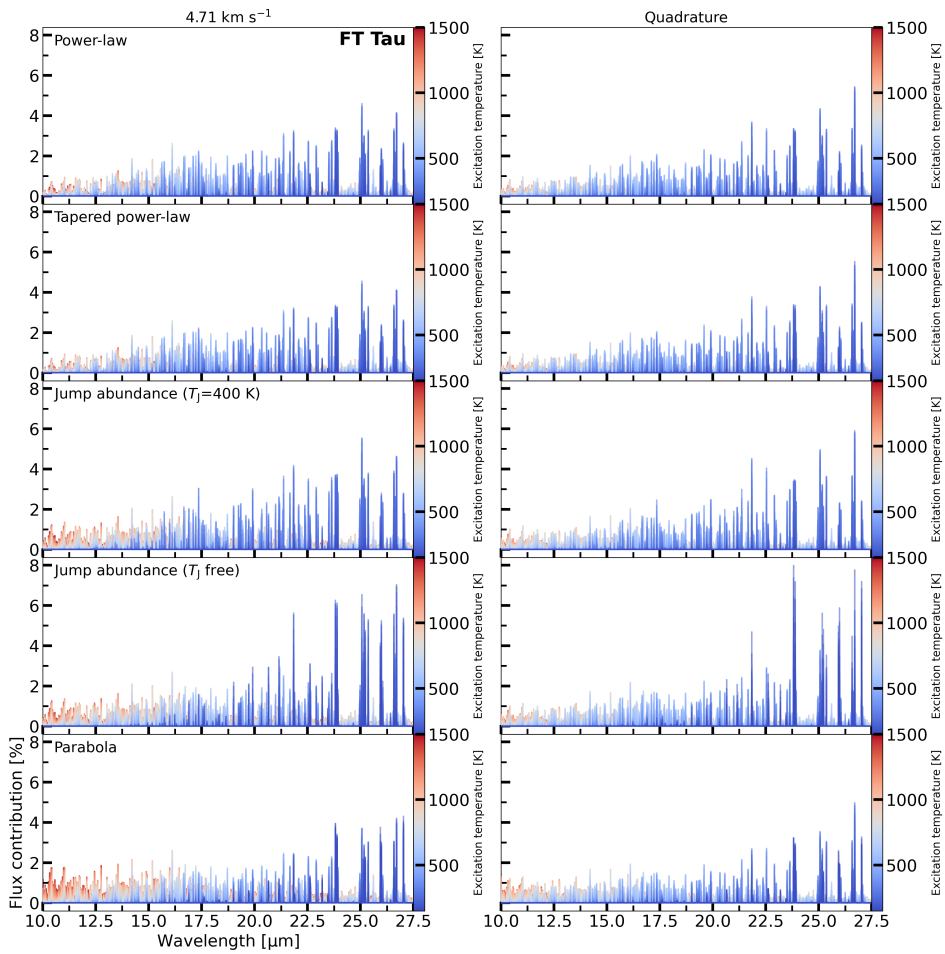


Figure 4.G.2: Similar as Figure 4.G.1, but for FT Tau, representing the type E disks.

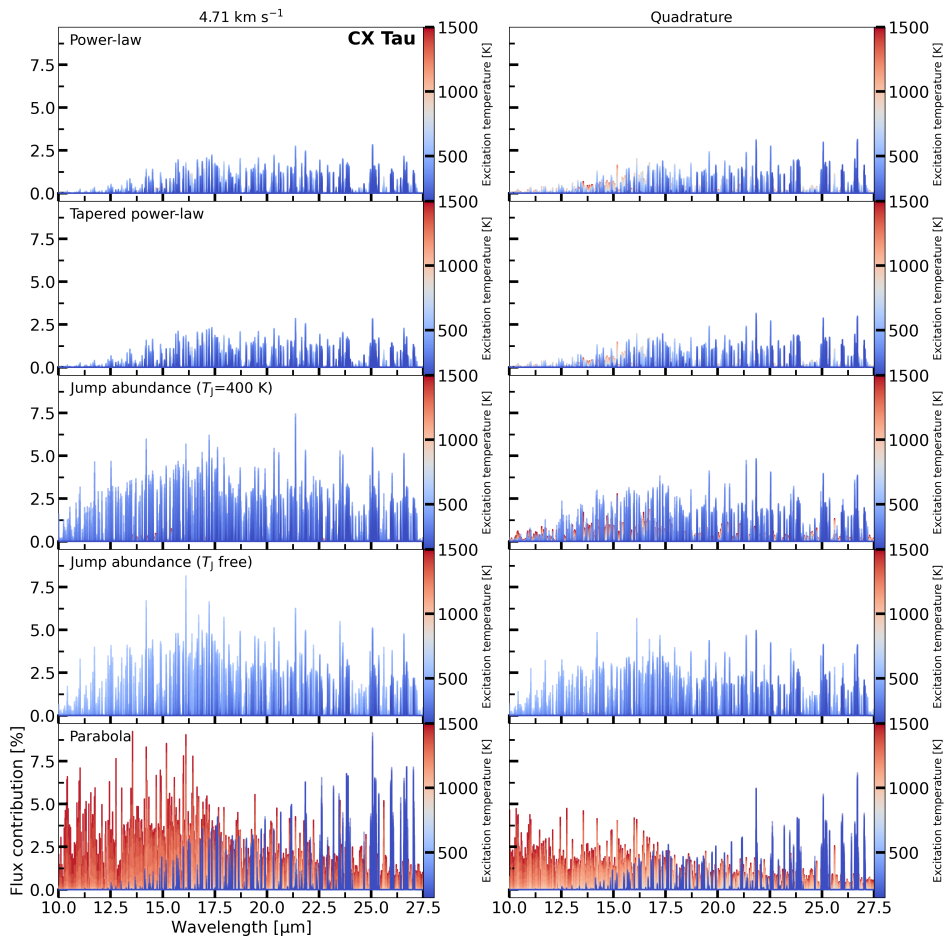


Figure 4.G.3: Similar as Figure 4.G.1, but for CX Tau, representing the type P disks.

PART II

Substructures in the outer disk

MINDS: The influence of outer dust disk structure on the volatile delivery to the inner disk

Shortened version focused on the ALMA analysis of

D. Gasman, M. Temmink, E. F. van Dishoeck, N. T. Kurtovic, S. L. Grant, A. D. Sellek, B. Tabone, T. Henning, I. Kamp, M. Güdel, D. Barrado, A. Caratti o Garatti, A. M. Glauser, L. B. F. M. Waters, A. M. Arabhavi, H. Jang, J. Kanwar, J. L. Lienert, G. Perotti, K. Schwarz, M. Vlasblom

A&A, 694, A147 (2025)

Abstract

Context. Substructures, such as gaps and rings, have been proposed to play a unique role in setting the chemical reservoirs in the inner regions of planet-forming disks. In particular, radial drift has been proposed to enhance the inner disk (cold) H₂O reservoir. To investigate the influence of these substructures on the chemistry in the inner disk as seen with JWST-MIRI, detailed information on their location, width, and depth is required.

Aims. This work aims to find and characterise substructures at small radii (<20 au) in a sample of 8 disks that have existing high-resolution ALMA continuum, indicative of gaps and rings at larger radii, and JWST-MIRI/MRS observations.

Methods. The ALMA visibilities were fitted in the visibility plane. The modelled brightness profile was used to identify rings (local maxima) and gaps (local minima), and to determine the width and depth of the gaps. A curve-of-growth technique was used to constrain the dust disk size.

Results. Substructures were identified in all 8 disks, matching in many cases with the results of previous works at larger radii and finding new ones at smaller radii. Crucially, we have identified a small inner cavity (a width of ~ 9 au) in the disk of BP Tau and a deep inner gap in the disk of Sz 98 (at $R_{\text{gap}} \sim 8.6$ au). Upon visual inspection of the inferred radial profiles, additional plateaus were identified in the inner regions of the DR Tau, GW Lup, and IQ Tau disks, suggesting that even more substructures may be revealed with higher-resolution observations.

Conclusions. Since rings and gaps or plateaus are found within the inner 20 au of all modelled sources, substructures at radial distances of $\lesssim 15$ au may be a common occurrence in disks. The role of the identified structures in setting the inner disk chemistry is, however, unclear. The strongest (cold) H₂O reservoir is seen for Sz 98, a disk with a deep gap located close to the host star, suggesting that the leakiness of the gaps is a crucial factor in setting the composition of the inner regions of planet-forming disks.

5.1 Introduction

This Chapter is part of the work by Gasman et al. (2025), which aimed to observationally assess the role of substructures in setting the inner disk’s molecular reservoirs. In particular, the strength of the H₂O reservoir is thought to depend on the radial drift of icy pebbles. Banzatti et al. (2020) proposed a scenario in which small disks ($R_{\text{dust}} \leq 60$ au) show an enhanced (cold, $T \leq 400$ K) H₂O reservoir near its snowline due to efficient drift. Large and structured disks ($R_{\text{dust}} \geq 60$ au) should, on the other hand, not show such an enhancement, as the drifting icy pebbles should be captured in the pressure traps. To test this scenario and to determine the role of pressure traps setting the inner disk composition, precise information on the location, width, and depth of the gaps - in particular, that of the gap closest to the host star - needs to be inferred from ALMA observations. Therefore, we employed visibility fitting techniques to obtain superresolution information on substructures that otherwise cannot be obtained from the resolution-limited images.

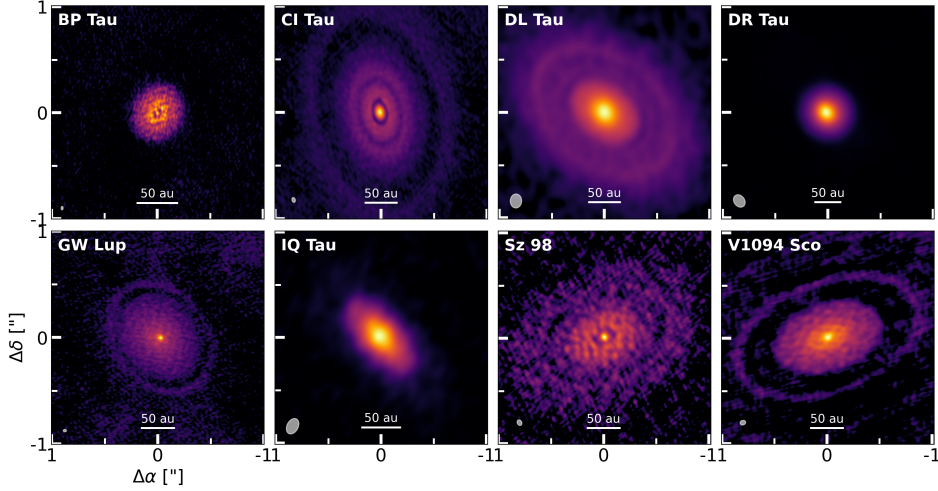
5.2 ALMA observations

In 2024, a sample of 8 disks was selected from all disks with existing JWST-MIRI/MRS observations, stellar masses of $M_{\odot} \geq 0.45 M_{\odot}$, and previously confirmed gaps in the millimetre dust continuum (see Gasman et al. 2025 for full details on the sample selection). Binary systems, sources with spiral features in the millimetre continuum emission, and highly inclined disks ($i \geq 70^{\circ}$) were excluded. The majority of the selected disks are part of the JWST Miri mid-INfrared Disk Survey (MINDS; Kamp et al. 2023; Henning et al. 2024) collaboration.

To study the presence of rings and gaps at small radii, we have retrieved the highest available spatial resolution ALMA observations publicly available for our sources. We list the distances, inclinations, position angles, and some of the observational properties in Table 5.1. Since for many of the sources, except BP Tau, the inclination and the position angle are well constrained, so we use the literature values while fitting the visibilities. For BP Tau, we estimated updated values using the CASA-task IMFIT by fitting an elliptical Gaussian. Additionally, we used IMFIT to estimate the phase offsets ($\Delta\alpha$ and $\Delta\delta$, both in arcsec) for each source and corrected for these offsets using the CASA-task FIXVIS. For some sources (CI Tau and GW Lup), additional shifts were determined from the image plane, ensuring that the peak flux in the model falls on the same position as the peak flux in the image. For only three of our sources (CI Tau, DR Tau, and IQ Tau), self-calibration yielded an increased signal-to-noise ratios (S/N). Therefore, we performed two rounds of phase-only self-calibration (solution intervals of ‘inf’ and ‘30s’) for these sources. We have imaged (down to a threshold of $1.5 \times$ the root-mean square) the dust continuum of all our sources using the ‘Briggs’ weighting scheme with a robust parameter of +0.5. Figure 5.1 displays the continuum images and the resolving beams are highlighted in Table 5.1.

Table 5.1: Source properties and band 6 ALMA observations of the eight T Tauri disks.

Source	Inc. [°]	PA [°]	ALMA PID (PI)	Frequency [GHz]	Reference frequency [GHz]	Reference wavelength [mm]	Beam [″ × ″ (°)]	Ref.
BP Tau	23.6	163.9	2019.1.00607.S (F. Long)	215-234	230.7	1.3	0.034 × 0.020 (-2.5)	This work
CI Tau	50.0	11.2	2016.1.01370.S (C. Clarke)	223-243	224.0	1.3	0.046 × 0.032 (15.9)	Long et al. (2018)
DL Tau	45.0	52.1	2016.1.01164.S (G. Herczeg)	217-234	218.0	1.4	0.133 × 0.108 (-2.3)	Long et al. (2018)
DR Tau	5.4	3.4	2016.1.01164.S (G. Herczeg)	217-234	218.0	1.4	0.128 × 0.100 (38.3)	Long et al. (2019)
GW Lup	38.7	37.7	2016.1.00484.L (S. Andrews)	230-248	232.6	1.3	0.030 × 0.023 (-89.2)	Huang et al. (2018a)
IQ Tau	62.1	42.4	2016.1.01164.S (G. Herczeg)	217-234	218.0	1.4	0.157 × 0.106 (-28.0)	Long et al. (2018)
Sz 98	47.1	111.6	2018.1.01458.S (Yen, H-W)	217-234	233.0	1.3	0.056 × 0.043 (27.3)	Tazzari et al. (2017)
V1094 Sco	53.0	109.0	2017.1.01167.S (S. Perez)	229-248	232.5	1.3	0.054 × 0.043 (-73.9)	van Terwisga et al. (2018)

**Figure 5.1:** ALMA continuum images of the various sources. The images of CI Tau, DL Tau, GW Lup, Sz 98, and V1094 Sco have been imaged with a square-root scaling to reveal the weaker rings in the outer regions. The resolving beams are displayed in the lower left corner and the horizontal bars indicate scales of 50 au.

5.3 Visibility fitting

Given the non-uniformity of the ALMA sample, we have fitted the visibilities to infer potentially ‘hidden’ substructures in the disks that cannot be retrieved from the cleaned images. We have followed the approach by Zhang et al. (2016), where a Hankel transform acts as the link between the deprojected uv -distance and the radial brightness distribution ($I(\theta)$; Pearson 1999:

$$u' = (u \cos(\phi) - v \sin(\phi)) \times \cos(i), \quad (5.1)$$

$$v' = u \sin(\phi) + v \cos(\phi), \quad (5.2)$$

$$V(\rho) = 2\pi \int_0^\infty I_\nu(\theta) \theta J_0(2\pi\theta\rho) d\theta. \quad (5.3)$$

Here, i and ϕ are the disk’s inclination and position, $\rho = \sqrt{u'^2 + v'^2}$ denotes the deprojected uv -distance (given in units of λ , and θ is the radial angular scale as

seen from the disk's centre. Finally, J_0 denotes the zeroth-order Bessel function of the first kind. The model brightness distribution consists of a set of Gaussian functions, inspired by the peaks seen in the visibilities and modulated by a sinusoidal function that has a spatial frequency of ρ_i ,

$$I(\theta) = \frac{a_0}{\sqrt{2\pi}\sigma_0} \exp\left(\frac{\theta^2}{-2\sigma_0^2}\right) + \sum_i \cos(2\pi\theta\rho_i) \times \frac{a_i}{\sqrt{2\pi}\sigma_i} \exp\left(-\frac{\theta^2}{2\sigma_i^2}\right). \quad (5.4)$$

This function yields the $\{a_0, \sigma_0, a_i, \sigma_i, \rho_i\}$ as the set of free parameters. For our sample, we report the minimum of additional Gaussian functions that results in a good fit to all the visible features in the visibilities.

We have deprojected the visibilities using the inclinations and position angles listed in Table 5.1. To ensure that we are able to fit the visibilities properly, we have visually compared the visibilities of all spectral windows (line and continuum) with those of the continuum spectral windows alone. For the line spectral windows, we masked visible lines, ensuring that they only contain continuum emission. In the cases of DR Tau, GW Lup, and Sz 98, we found that the uncertainties of the visibilities of the continuum spectral windows were significantly lower than those when including all spectral windows. Therefore, we only used the continuum spectral windows for those three sources. In addition, we only use the continuum spectral windows for DL Tau, as the measurement set was obtained through private communication. For the four other sources we have used all spectral windows.

We bin the visibilities to speed up the fitting process, using the implementation of the FRANKENSTEIN-code (Jennings et al. 2020), and we avoid fitting the visibilities with large scatter, generally occurring at larger values of $k\lambda$. For BP Tau, DL Tau, DR Tau, Sz 98, and V1094 Sco we limit the visibilities to $\leq 2000 k\lambda$, whereas we limit the visibilities of CI Tau and GW Lup to $\leq 3000 k\lambda$. Finally, the visibilities of IQ Tau are limited to $\leq 1500 k\lambda$. In addition, the visibilities are binned to widths of $1.2 \times 10^4 \lambda$. We fit the visibilities using the Markov Chain Monte Carlo (MCMC) implementation of the EMCEE-package (Foreman-Mackey et al. 2013). The fitting was performed two-fold, similarly to the approach carried out by Long et al. (2018): in the first round, we used 2500 iterations to explore the prior space, identifying the best-fit parameters. In the second round, we used 10,000 iterations to explore a confined parameter space around these best-fit parameters. From this second round, we use a final 5000 iterations to identify the median values of the posterior distributions. The lower and upper uncertainties are, respectively, taken to be the 16th and 84th percentiles. Our fitting results are listed in Table 5.2 and the fits to the visibilities are presented in Figure 5.2.

Table 5.2: Median values from the fitting posterior distributions and the corresponding uncertainties.

Source	a_i	σ_i	ρ_i
	[a.u.]	["]	[k λ]
BP Tau	104^{+5}_{-10}	$0.17^{+0.04}_{-0.02}$	-
	17^{+39}_{-14}	$0.28^{+0.07}_{-0.04}$	251^{+35}_{-37}
	2 ± 6	0.48 ± 0.07	818^{+58}_{-66}
	13^{+7}_{-6}	$0.21^{+0.06}_{-0.05}$	904^{+62}_{-38}
	-17^{+6}_{-7}	0.07 ± 0.03	719^{+62}_{-67}
CI Tau	186^{+20}_{-15}	0.46 ± 0.02	-
	135^{+35}_{-26}	0.43 ± 0.04	161^{+8}_{-9}
	45^{+21}_{-14}	0.45 ± 0.06	388 ± 14
	120^{+24}_{-29}	$0.08^{+0.03}_{-0.01}$	516^{+66}_{-61}
	28^{+22}_{-16}	$0.29^{+0.07}_{-0.05}$	544^{+42}_{-43}
	111^{+23}_{-26}	0.17 ± 0.03	1018^{+26}_{-25}
	63^{+16}_{-29}	$0.16^{+0.07}_{-0.04}$	1401^{+63}_{-53}
DL Tau	27^{+18}_{-15}	$0.22^{+0.05}_{-0.04}$	1714^{+53}_{-55}
	251 ± 10	0.39 ± 0.01	-
	208^{+28}_{-20}	0.33 ± 0.01	215 ± 3
	172 ± 4	$0.11^{+0.02}_{-0.01}$	527^{+11}_{-13}
	48^{+19}_{-11}	$0.39^{+0.06}_{-0.05}$	853 ± 6
	92 ± 9	0.30 ± 0.03	1194^{+10}_{-12}
DR Tau	77^{+7}_{-9}	$0.49^{+0.03}_{-0.02}$	1371 ± 4
	99 ± 5	0.22 ± 0.01	1731^{+7}_{-5}
	461^{+17}_{-21}	0.16 ± 0.01	-
	179^{+60}_{-65}	$0.21^{+0.02}_{-0.01}$	329^{+21}_{-20}
GW Lup	210 ± 8	0.09 ± 0.01	807^{+28}_{-30}
	99 ± 7	$0.16^{+0.01}_{-0.02}$	1692 ± 16
	100^{+30}_{-22}	0.31 ± 0.02	-
	106^{+11}_{-14}	$0.18^{+0.04}_{-0.05}$	208^{+36}_{-56}
	62^{+8}_{-9}	$0.14^{+0.04}_{-0.03}$	688^{+49}_{-58}
IQ Tau	26 ± 8	$0.36^{+0.06}_{-0.05}$	1113 ± 22
	25 ± 6	0.17 ± 0.04	1414^{+47}_{-49}
	12 ± 5	$0.42^{+0.07}_{-0.06}$	1819^{+31}_{-32}
	69^{+28}_{-20}	0.36 ± 0.03	-
Sz 98	64^{+15}_{-18}	$0.26^{+0.06}_{-0.03}$	135^{+54}_{-31}
	23 ± 4	0.34 ± 0.06	528^{+17}_{-16}
	11^{+5}_{-4}	$0.33^{+0.07}_{-0.06}$	1013^{+38}_{-45}
	10 ± 4	0.92 ± 0.07	1200^{+13}_{-16}
	143^{+7}_{-4}	0.40 ± 0.01	-
V1094 Sco	81^{+9}_{-8}	$0.42^{+0.02}_{-0.03}$	216^{+3}_{-4}
	31^{+17}_{-7}	$0.16^{+0.04}_{-0.03}$	661^{+30}_{-29}
	16 ± 4	$0.55^{+0.07}_{-0.05}$	994^{+12}_{-13}
	29^{+4}_{-3}	$0.45^{+0.05}_{-0.04}$	1258^{+9}_{-8}
	104^{+12}_{-15}	0.04 ± 0.01	1449^{+65}_{-54}
	131^{+11}_{-16}	$0.66^{+0.04}_{-0.03}$	-
	166 ± 6	$0.48^{+0.04}_{-0.05}$	124 ± 5
	61^{+8}_{-7}	$0.68^{+0.04}_{-0.05}$	261 ± 4
	57^{+6}_{-11}	0.38 ± 0.03	430 ± 5
	33 ± 4	0.19 ± 0.07	709^{+31}_{-35}
V1094 Sco	31 ± 8	0.46 ± 0.05	943^{+9}_{-8}
	41^{+4}_{-5}	$0.51^{+0.05}_{-0.06}$	1173 ± 7
	29 ± 4	0.41 ± 0.06	1368 ± 12
	16 ± 3	0.36 ± 0.06	1619^{+17}_{-18}

Notes. Gaussian function fit parameters a_i , σ_i , and ρ_i , describing the intensity, width, and spatial frequency, respectively (see Eq. 5.4).

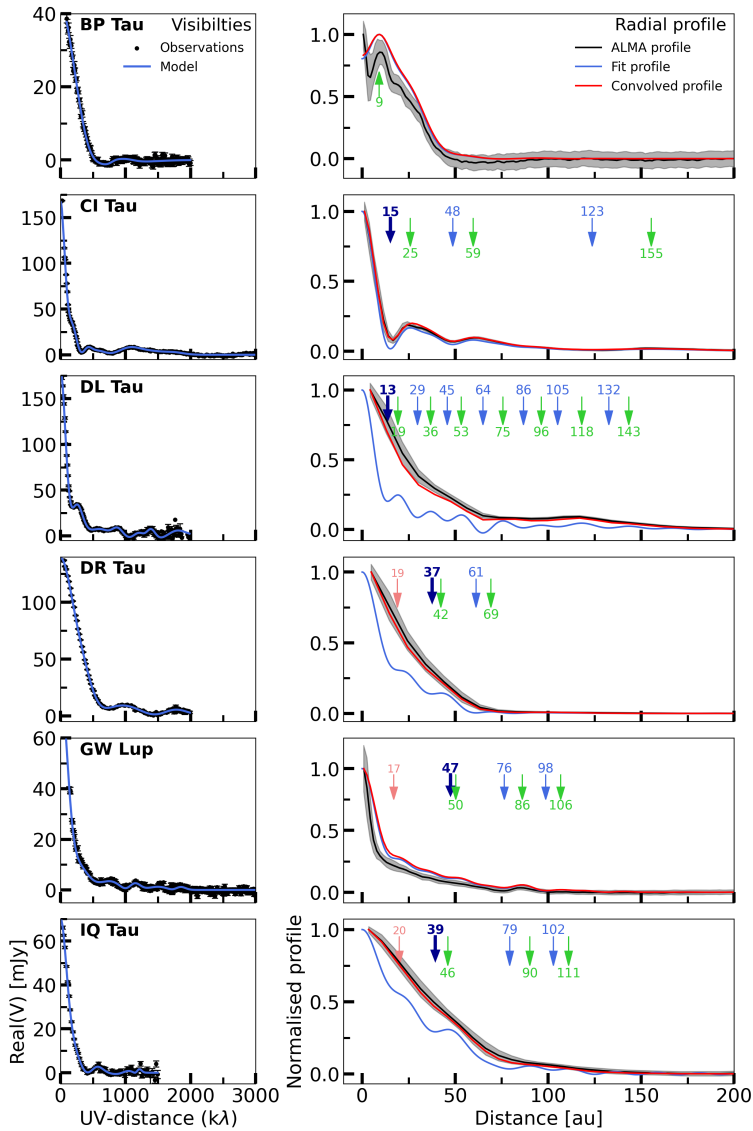


Figure 5.2: Fit to the visibilities (blue line in the left panels for each source) and the various radial profiles (right panels): one from the ALMA image (black line), the model radial profile (blue line), and the radial profile from the model convolved with a Gaussian kernel tailored after the resolving beam (red line). The gaps and rings (or local minima and maxima) and plateaus/shoulders are indicated by, respectively, the blue, green, and red arrows, where the values indicate their integer radial positions. The location of the innermost gap is emphasised by the dark blue arrows. The shaded grey area indicates the standard deviation in each radial bin of the ALMA profile.

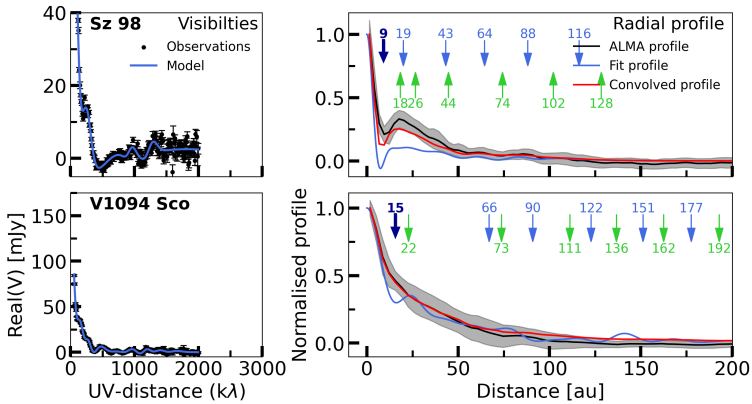


Figure 5.2: Continuation of Figure 5.2.

5.4 Characterising the millimetre continuum emission

Using the radial brightness distribution from median values of the posterior distributions, we infer the radial locations of substructures. The locations of rings (r_r) and gaps (r_g) are identified through, respectively, the local maxima and minima present in the radial profiles. Other structures, such as ‘shoulders’ or ‘plateaus’, visible in the radial profiles are visually identified. To characterise the depth and widths of the identified gaps, we follow the approach of Huang et al. (2018a). Here, the gap depth is defined as the ratio of the gap intensity (I_g) and that of the neighbouring ring with the smallest flux contrast (I_r), $\Delta I_g = I_g/I_r$. Given the ratio, the gaps with the smallest value reported for the depth are the deepest ones. The width of the gap is determined as the radial width between the inner and outer edges of the gaps ($r_{g,i}$ and $r_{g,o}$), which are the radial locations where the intensity equals $I_{\text{mean}} = 0.5 (I_g + I_r)$. Therefore, the width is given by $\Delta r_g = r_{g,o} - r_{g,i}$.

We also determine the continuum disk radius (R_{disk}) using a curve-of-growth method (see also Ansdell et al. 2016 and/or Stapper et al. 2022 for more information) for radii containing 68%, 90%, and 95% of the flux density. The values for the disk radii are listed in Table 5.3. In short, we use aperture photometry to investigate at what radius the flux density within the apertures flattens off. We increase the apertures by the pixel size and limit our range to where we see no significant substructures in the ALMA radial profiles, as we are only using high-resolution observations, and therefore we may lack the resolving power for weak outer disk features.

The model radial profiles, together with the identified gaps and rings, are presented in Figure 5.2. In particular, we have highlighted the gap that is located closest to the host star. Here, we also show the ALMA continuum image and the model radial profile convolved with a Gaussian kernel tailored after the ALMA resolving beam. The convolved radial profiles clearly show that the beam is respon-

Table 5.3: Identified substructures and dust continuum sizes for the sources.

Source	r_g	r_r	Δr_g	ΔI_g	R_{disk} (Model/ALMA) ^(a)		
	[au]	[au]	[au]		68% [au]	90% [au]	95% [au]
BP Tau	-	9	-	-	30.0/29.0	40.6/38.1	46.7/44.7
CI Tau	15.2	25.9	7.8	0.10	105.3/114.2	172.5/180.3	189.3/199.4
	48.7	59.7	9.4	0.59			
	123.7	155.5	27.2	0.59			
DL Tau	13.8	19.2	4.5	0.81	112.0/115.2	147.2/156.8	163.2/176.0
	29.9	37.0	5.9	0.65			
	45.9	53.3	7.0	0.59			
	65.0	75.9	9.6	-0.44			
	86.7	96.2	7.7	0.38			
	105.0	117.9	8.2	0.66			
DR Tau	37.7	42.3	3.9	0.96	39.0/42.9	54.6/66.3	89.7/97.5
	<i>61.2</i>	<i>69.2</i>	6.0	0.33			
GW Lup	47.5	<i>50.4</i>	2.4	0.99	67.4/65.1	102.3/110.8	115.5/134.1
	76.5	86.1	11.0	0.56			
	98.7	106.8	6.5	0.54			
IQ Tau	39.3	46.1	5.7	0.95	58.0/68.6	103.0/118.8	118.8/145.2
	<i>79.3</i>	<i>90.2</i>	10.2	0.62			
	<i>102.8</i>	<i>111.0</i>	7.5	0.73			
Sz 98	8.6	<i>16.4</i>	4.6	-0.72	109.8/107.3	147.3/146.0	159.7/162.2
	<i>19.3</i>	<i>27.3</i>	3.1	0.97			
	<i>42.8</i>	<i>45.3</i>	2.1	1.00			
	<i>64.3</i>	<i>74.3</i>	8.9	0.63			
	<i>88.1</i>	<i>102.0</i>	13.3	0.21			
	<i>116.0</i>	<i>128.0</i>	10.5	0.61			
V1094 Sco	15.6	<i>22.8</i>	5.8	0.85	162.4/131.4	239.3/238.1	255.4/256.7
	<i>67.0</i>	<i>73.7</i>	6.4	0.92			
	90.8	111.2	14.3	0.40			
	<i>122.8</i>	<i>136.7</i>	9.8	0.22			
	<i>151.2</i>	<i>162.5</i>	9.5	0.37			
	177.6	193.0	12.0	0.37			
	<i>200.2</i>	<i>217.2</i>	6.8	0.95			

Notes. ^(a)We list the values for the outer dust disk radii retrieved from both the model image and from the ALMA image. The value before the slash is obtained from the model images, whereas the value after the slash is obtained from the ALMA image. r_g , r_r , Δr_g , and ΔI_g are the gap location, ring location, gap width and depth, respectively. The values used as R_{gap} in the analysis of the JWST/MIRI-MRS data are highlighted in boldface. The values listed in italics are newly identified substructures in this work.

sible for smoothing out weak structures in the ALMA images and, subsequently, that these features cannot be distinguished from analysis in the image plane. All the retrieved locations of the gaps and the rings, and the gap widths and depths are listed in Table 5.3. Additionally, in Figure 5.3 we display a comparison between

the ALMA continuum image, the model image, the model image convolved with a Gaussian kernel, and the residuals. The residuals are obtained by subtracting the convolved model image off the ALMA image. Similarly to what is seen for the radial profiles, the convolution with the Gaussian kernel smooths out the various weak substructures visible in the model and therefore become unidentifiable in the images.

Besides the various gaps and rings, we also visually identified a few plateaus, which may hint at additional substructures. These plateaus are indicated by the red arrows in Figure 5.2. To summarise, we identify three plateaus: in DR Tau at ~ 19 au, in GW Lup at ~ 17 au, and in IQ Tau at ~ 20 au.

Overall we find that the convolved images represent the ALMA images quite well, but there are some residuals that require attention. The residuals of BP Tau are mostly negative, indicating larger flux in the model image following the identified cavity in the models. The central, unresolved spot in the ALMA image may be attributed to free-free emission or emission from the host star itself (see e.g. Rota et al. 2024). For CI Tau, the residuals show that clear asymmetric structures are found in the ALMA image. These residuals show that the outer edges of the gap are not perfectly oval shaped as they are in the model. DL Tau, DR Tau, and IQ Tau all three show clear residuals in the central positions. These asymmetries likely arise from sub-pixel offsets between the peaks of the ALMA images and the model images. We note that the observations for these sources have the lowest spatial resolution ($\sim 0.11''$), which provides a potential explanation why these residuals are the largest. Higher resolution observations will likely provide better fits and cleaner residuals. The residuals of GW Lup are dominated by the model overfitting the width of the inner region, as can also be seen from the radial profiles (see Figure 5.2). Additionally, there may be a sub-pixel offset for the location of the maximum flux in the ALMA image, which causes the asymmetric feature to appear in the residuals. For both Sz 98 and V1094 Sco, we see that the residuals are rather patchy, which may be caused by the use of only the highest resolution observations available. Combining these observations with those of lower resolution, which are better at resolving the largest scales, may improve the residuals.

5.5 Comparison with previous works

Nearly all disks, except Sz 98, have been modelled before, so we compare the inferred substructures:

BP Tau: BP Tau has previously been fitted by Zhang et al. (2023), but no fits have been carried out for the high-resolution observations used in this work. We note that the models of Zhang et al. (2023) already point towards a small cavity in this disk, which now seems confirmed by our results.

CI Tau: The high-resolution CI Tau observations used in this work have previously been modelled by Clarke et al. (2018) and Rosotti et al. (2021). They find radial locations for the gaps of ~ 12 , ~ 45 , and ~ 114 au, and radii of ~ 23 , ~ 54 , and ~ 114 au for the rings. Generally, these values are close to our values, except

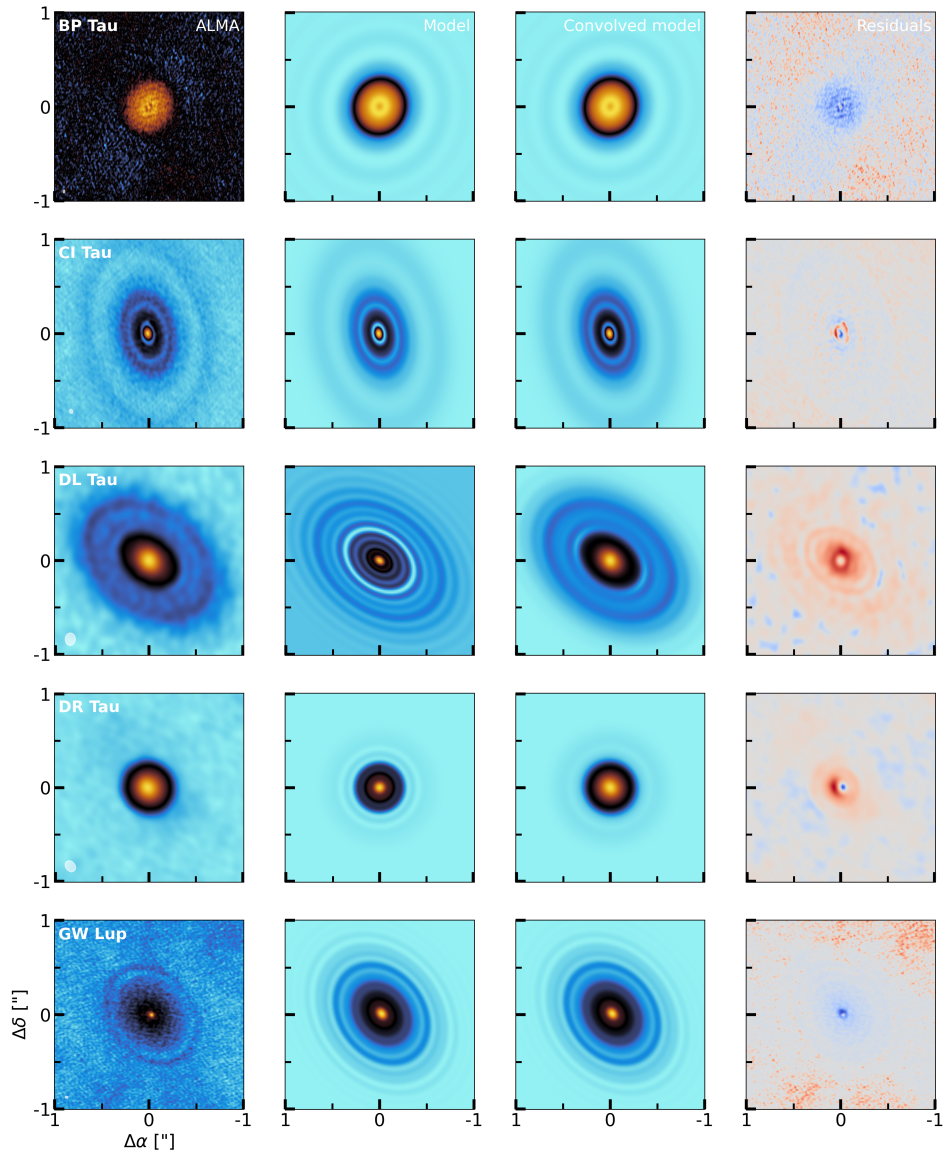


Figure 5.3: Comparison between the ALMA image (first column), the model image (second column), the convolved model (third column), and the residuals (final column). All images, except the residuals, are shown with an arcsinh-stretch colourmap. The residuals are taken by subtracting the convolved model image off the ALMA image. Here, red residuals indicate more flux in the ALMA image, whereas blue residuals indicate more flux in the convolved model image.

for the outer most ring, for which we find a larger value of ~ 155 au.

DL Tau: DL Tau has been modelled by Zhang et al. (2023) using the same tech-

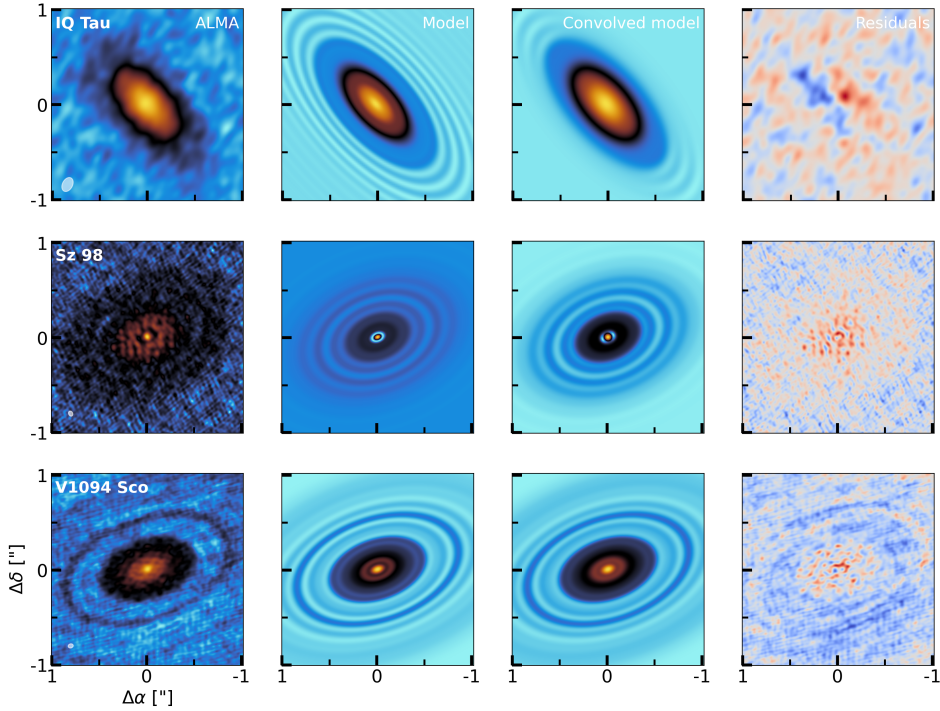


Figure 5.3: Continuation of Figure 5.3.

nique, but also has been given an extensive treatment by Jennings et al. (2022b). Both works yield similar radial brightness profiles. In addition, Zhang et al. (2023) lists gap locations of ~ 15 , ~ 31 , ~ 47 , ~ 66 , ~ 95 , and ~ 129 au, which all fall within 10 au of our listed values. The fit by Zhang et al. (2023) suggests deeper gaps. As is seen in Figure 5.2 our convolved profile does not fully match the ALMA profile, suggesting that our modelled rings are not as strong as those of Zhang et al. (2023), yielding smaller gap depths.

DR Tau: Similar to DL Tau, DR Tau has been modelled by Jennings et al. (2022b) and Zhang et al. (2023). Again, our respective brightness profiles are rather similar, except we find an additional potential substructure gap-ring combination at, respectively, 61.2 and 69.2 au. The other gaps are found at similar locations, although the first gap identified by Zhang et al. (2023) (~ 18 au) appears as a plateau in our profile.

GW Lup: GW Lup was modelled by Jennings et al. (2022a), who finds a similar looking brightness profile, with a plateau in the inner regions ($< 0.1''$). Overall, we find a few more potential substructures in addition to the well-known ring at 86 au.

IQ Tau: IQ Tau has also been modelled by Zhang et al. (2023). We find the same location for the gap-ring combination around ~ 40 au. However, the outer two rings identified in our work are not found in their work. Higher spatial res-

olution and sensitivity observations may prove the validity if these substructures do indeed exist or not.

V1094 Sco: These higher resolution observations of V1094 Sco have not been modelled before, but van Terwisga et al. (2018) modelled lower resolution ($\sim 0.18''$) data. They only provided locations for gaps located at 100 and 170 au. Our fit to the higher resolution observations thus provide hints for potentially more substructures, with the most notable gap at ~ 16 au.

5.6 Identified structures, snowlines, and proposed scenarios

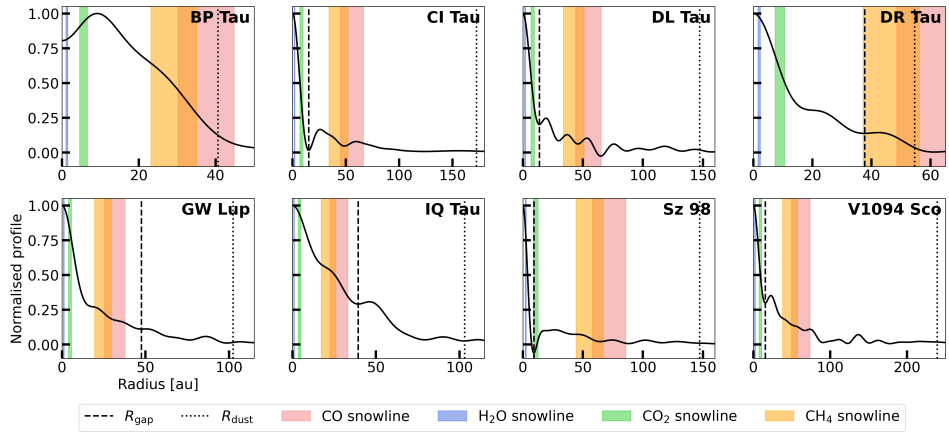


Figure 5.4: Normalised, modelled radial profiles of the ALMA observations. The blue, green, orange, and red shaded areas indicate estimated locations of, respectively, the H₂O, CO₂, CH₄, and CO snowlines (Gasman et al. 2025). The dashed line displays the position of the closet-in identified gap, while the dotted line indicates the 90% dust disk radius (see Table 5.3).

To investigate the role of the innermost gap, its location was compared with the estimated locations of the H₂O, CO₂, CH₄, and CO snowlines in Gasman et al. (2025) (see also Figure 5.4). For all disks, the H₂O snowline was found to be located inwards of the innermost gap. This also holds mostly for the CO₂ snowline, except for Sz 98, where the snowline is located towards the outer edge of the gap. Conversely, the CH₄ and CO appear to be mostly located beyond the first gap, except in the cases of GW Lup and IQ Tau.

Based on the locations of the gaps and the snowlines, the strengths of the different molecular reservoirs (H₂O, CO₂, HCN, and C₂H₂) seen in the JWST-MIRI/MRS spectra were compared with different scenarios put forward by existing models (Kalyaan et al. 2021, 2023; Mah et al. 2024; Lienert et al. 2024; Sellek et al. 2025). These scenarios explore the change of the inner disk composition from oxygen-rich (or H₂O-rich) to carbon-rich over the disk’s lifetime, considering

gaps at different locations and three levels of leakiness to drifting pebbles: leaky, moderately leaky, and not leaky. The transition from an oxygen-rich to carbon-rich is expected to occur naturally during the evolution of a disk, however, the age at which this happens is related to the location and leakiness of the innermost gap. Given the uncertainties in the ages, multiple scenarios were deemed likely for each disks. Therefore, the exact scenario and role of substructures in setting the inner disk composition could not be pinpointed.

Most notably, Sz 98 is a large disk ($R_{\text{dust}} \gg 100$ au) with a deep gap located very close to the host star ($r_g \sim 8.6$ au). Intuitively, this disk should have not have an enhanced cold H₂O reservoir following the scheme proposed by Banzatti et al. (2020). Yet, this disk has the strongest cold H₂O reservoir of the entire sample. Therefore, the small dust grains and the gas may not be impeded by the gap from radially moving inwards, and the leakiness of the gaps is very likely crucial in setting the inner disk reservoirs. More details and searches for correlations with the observed JWST-MIRI line fluxes are presented in Gasman et al. (2025).

5.7 Concluding remarks

Visibility fitting techniques are a powerful tool to identify and characterise substructures in planet-forming disks. Gaps and rings are found in all 8 analysed disks, including the confirmation of a small cavity in the disk of BP Tau and a deep gap at ~ 8.6 au in the disk of Sz 98. Many of the found substructures match those proposed in other works, yet additional gaps are proposed in the disks of GW Lup, IQ Tau, and V1094 Sco. Furthermore, visual inspection leads to the identification of plateaus - potentially further substructures - in the inner regions (~ 17 -20 au) of the disks of DR Tau, GW Lup, and IQ Tau. As all disks show substructures or plateaus within the inner 20 au, we propose that substructures at radial distances of $\lesssim 15$ au may be a common occurrence in planet-forming disks.

Given large uncertainties in the ages of the systems, the role of substructures in setting the inner disk composition with time could not be established. The case of Sz 98 is of particular interest, as this large and structured disk shows particularly strong emission from the cold H₂O reservoir. A deep gap was identified close to the host star, yet it may be leaky to small dust grains and the gas, still replenishing the inner regions with fresh material. Therefore, it is thought that the leakiness of the gaps plays a crucial role in setting the inner disk composition of planet-forming disks.

PART III

Outer disk chemistry

Chapter 6

Characterising the molecular line emission in the asymmetric Oph-IRS 48

Temperatures, timescales, and sub-thermal excitation

M. Temmink, A. S. Booth, M. Leemker, N. van der Marel, E. F. van Dishoeck, L. Evans, L. Keyte, C. J. Law, S. Notsu, K. Öberg, C. Walsh

A&A, 693, A101 (2025)

Abstract

Context. The ongoing physical and chemical processes in planet-forming disks set the stage for planet (and comet) formation. The asymmetric disk around the young star Oph-IRS 48 has one of the most well-characterised chemical inventories, showing molecular emission from a wide variety of species at the dust trap: from simple molecules, such as CO, SO, SO₂, and H₂CO, to large complex organics, such as CH₃OH, CH₃OCHO, and CH₃OCH₃. One of the explanations for the asymmetric structure in the disk is dust trapping by a perturbation-induced vortex.

Aims. We aimed to constrain the excitation properties of the molecular species SO₂, CH₃OH, and H₂CO, for which we have used 13, 22, and 7 transitions of each species, respectively. We further characterised the extent of the molecular emission, which differs among molecules, through the determination of important physical and chemical timescales at the location of the dust trap. We also investigated whether the anticyclonic motion of the potential vortex influences the observable temperature structure of the gas.

Methods. Through a pixel-by-pixel rotational diagram analysis, we created maps of the rotational temperatures and column densities of SO₂ and CH₃OH. To determine the temperature structure of H₂CO, we have used line ratios of the various transitions in combination with non-local thermal equilibrium (LTE) RADEX calculations. The timescales for freeze-out, desorption, photodissociation, and turbulent mixing at the location of the dust trap were determined using an existing thermochemical model.

Results. Our rotational diagram analysis yields temperatures of $T=54.8\pm 1.4$ K (SO₂) and $T=125.5^{+3.7}_{-3.5}$ K (CH₃OH) at the emission peak positions of the respective lines. As the SO₂ rotational diagram is well characterised and points towards thermalised emission, the emission must originate from a layer close to the midplane where the gas densities are high enough. The rotational diagram of CH₃OH is, in contrast, dominated by scatter and subsequent non-LTE RADEX calculations suggest that both CH₃OH and H₂CO must be sub-thermally excited higher up in the disk ($z/r \sim 0.17-0.25$). For H₂CO, the derived line ratios suggest temperatures in the range of $T \sim 150-350$ K. The SO₂ temperature map hints at a potential radial temperature gradient, whereas that of CH₃OH is nearly uniform and that of H₂CO peaks in the central regions. We, however, do not find any hints of the vortex influencing the temperature structure across the dust trap. The longer turbulent mixing timescale, compared to that of photodissociation, does provide an explanation for the expected vertical emitting heights of the observed molecules. On the other hand, the short photodissociation timescales are able to explain the wider azimuthal molecular extent of SO₂ compared to CH₃OH. The short timescales are, however, not able to explain the wider azimuthal extent of the H₂CO emission. Instead, it can be explained by a secondary reservoir that is produced through the gas-phase formation routes, which are sustained by the photodissociation products of, for example, CH₃OH and H₂O.

Conclusions. Based on our derived temperatures, we expect SO₂ to originate from deep inside the disk, whereas CO comes from a higher layer and both CH₃OH

and H_2CO emit from the highest emitting layer. The sub-thermal excitation of CH_3OH and H_2CO suggests that our derived (rotational) temperatures underestimate the kinetic temperature. Given the non-thermal excitation of important species, such as H_2CO and CH_3OH , it is important to use non-LTE approaches when characterising low-mass disks, such as that of IRS 48. Furthermore, for the H_2CO emission to be optically thick, as expected from an earlier derived isotopic ratio, we suggest that the emission must originate from a small radial ‘sliver’ with a width of ~ 10 au, located at the inner edge of the dust trap.

6.1 Introduction

Planets form in the disks surrounding newly formed stars. Their atmospheric composition, as well as the composition of comets, is determined by the chemical makeup of these planet-forming disks, which itself is the result of the combination of ongoing chemical processes and the inheritance of molecular species from the earlier star formation stages (e.g. Öberg & Bergin 2021; Öberg et al. 2023). The Atacama Large Millimeter/submillimeter Array (ALMA) allows us to characterise the chemical inventory of planet-forming disks with an unprecedented sensitivity. The sensitivity enables us to detect multiple transitions of the same species that span a range of excitation conditions, even those with weaker line strengths. Detecting multiple transitions allows one, under the assumption of local thermal equilibrium (LTE), to directly infer both the gas thermal and excitation properties through a rotational diagram analysis (e.g. Goldsmith & Langer 1999). The use of multiple lines of the same molecule in order to constrain the physical structure of disks has a long history (see, e.g., van Zadelhoff et al. 2001; Dartois et al. 2003; Leemker et al. 2022). Such studies have also highlighted the potential importance of non-LTE excitation in the upper layers of the disks (e.g., van Zadelhoff et al. 2003; Thi et al. 2004; Woitke et al. 2009). Loomis et al. (2018) presented a rotational diagram analysis for a protoplanetary disk with the detection of CH₃CN in the TW Hya disk, and rotational diagrams have also been used for a variety of molecules in other disks (e.g. Bergner et al. 2018; Guzmán et al. 2018; Pegues et al. 2020; Le Gal et al. 2019, 2021; Cleeves et al. 2021; Romero-Mirza et al. 2023; Temmink et al. 2023; Rampinelli et al. 2024). Using the derived excitation properties, unresolved observations can be linked to the radial extent and vertical height of the molecular emission in the disk and, therefore, the chemical origin of the species may be inferred (e.g. Carney et al. 2017; Salinas et al. 2017; Carney et al. 2018; Ilee et al. 2021; Terwisscha van Scheltinga et al. 2021; Romero-Mirza et al. 2023; Hernández-Vera et al. 2024).

One of the disks with the best-studied chemical inventory is that of Oph-IRS 48 (IRS 48 hereafter), a Herbig A0 star ($M \sim 2.0 M_{\odot}$ and $L \sim 17.8 L_{\odot}$; Brown et al. 2012; Francis & van der Marel 2020) located in the Ophiuchus star-forming region (at a distance of 135 pc; Gaia Collaboration et al. 2018) with many simple and complex organic molecules (COMs) having been detected (van der Marel et al. 2014, 2021a; Booth et al. 2021a; Brunken et al. 2022; Leemker et al. 2023; Booth et al. 2024b), with the latter defined as molecules with ≥ 6 atoms of which at least one is carbon (Herbst & van Dishoeck 2009). IRS 48 is well known for its asymmetric dust trap, in which the large, millimetre-sized dust grains have been captured mostly on the southern side of the disk (van der Marel et al. 2013; Yang et al. 2023). The molecular emission originates from approximately the same location as the asymmetric dust trap, suggesting that the sublimation of the icy mantles of pebbles plays an important role in setting the observable gas content. The dust asymmetry is potentially the result of a vortex, introduced due to an instability in the disk. The Rossby wave instability (RWI), for which the theoretical groundwork in disks was first described by Lovelace et al. (1999) and Li et al. (2000), is often thought to be the cause of the vortex. Various studies (see, for example,

Lyra et al. 2009; Crnkovic-Rubsamen et al. 2015; Owen & Kollmeier 2017; Raettig et al. 2021; Regály et al. 2021) have shown that these vortices can trap significant amounts of dust if it has an anticyclonic rotation, can have large dust-to-gas ratios, and, therefore, can act as the formation sites of planetary and/or cometary bodies.

One curious matter of these asymmetric dust traps is the temperature structure of the gas. Normally, the temperature of disks decreases radially outwards, that is, the further away from the host star the lower the temperature, and vertically downwards, that is, lower temperatures are reached at the midplane of the disk, unless there is significant heating due to viscous accretion in the midplane (e.g. D’Alessio et al. 1998, Woitke et al. 2009, and Harsono et al. 2015). Intuitively, the vortex may add additional complexity to the temperature structure, as its motions may transfer hot gas out of view of the host star, towards larger radii, and cold gas into view. Additionally, direct UV irradiation can heat the gas at cavity edges (Bruderer 2013; Bruderer et al. 2014; Leemker et al. 2023). Consequently, the temperature may not decrease radially in these kinds of disks. In this paper, we study the temperature structure of the gas, as well as the origins and distribution of different chemical species in the IRS 48 disk using the plethora of observed SO_2 , CH_3OH , and H_2CO transitions, which were first reported by van der Marel et al. (2021a), Booth et al. (2021a), and Booth et al. (2024b). We use complementary observations of the optically thick ^{13}CO isotopologue (van der Marel et al. 2016b; Leemker et al. 2023) to further characterise the temperature and the vertical distribution of the molecular species.

This paper is structured as follows: in Section 6.2 we describe our target and the used data, while our analysis is explained in Section 6.3. Our results can be found in Section 6.4, which are further discussed in Section 6.5. Section 6.6 contains an analysis of important physical and chemical timescales that aid in the explanation of the observed molecular signatures. Finally, our conclusions are summarised in Section 6.7.

6.2 Data

Throughout this work, we use Band 7 ALMA data of IRS 48 observed in Cycle 8 (2021.1.00738.S, PI: A. S. Booth). We refer to Booth et al. (2024b) for a description of the data reduction, self-calibration, and continuum subtraction. The observations consist of 8 spectral windows, covering transitions at frequencies between ~ 336.9 and ~ 356.9 GHz at a spectral resolution of ~ 0.84 km s $^{-1}$. We detect 13 and 22 clean (i.e. not blended with other molecules) transitions of SO_2 and CH_3OH , respectively. Through a pixel-by-pixel rotational diagram analysis (pixel sizes of $0.04''$, beam sizes of $0.34'' \times 0.26''$), we investigate the temperature of the IRS 48 disk, as probed by these molecules. Throughout our analysis, we used all pixels within a radius of $1.5''$ of the host star as seen within the disk coordinates (i.e., accounting for the disk’s inclination, $i=50^\circ$, and position angle, $PA=100^\circ$). In addition, we use the lower angular resolution ($\sim 0.46''$), Cycle 5 Band 7 observations of H_2CO presented in van der Marel et al. (2021a).

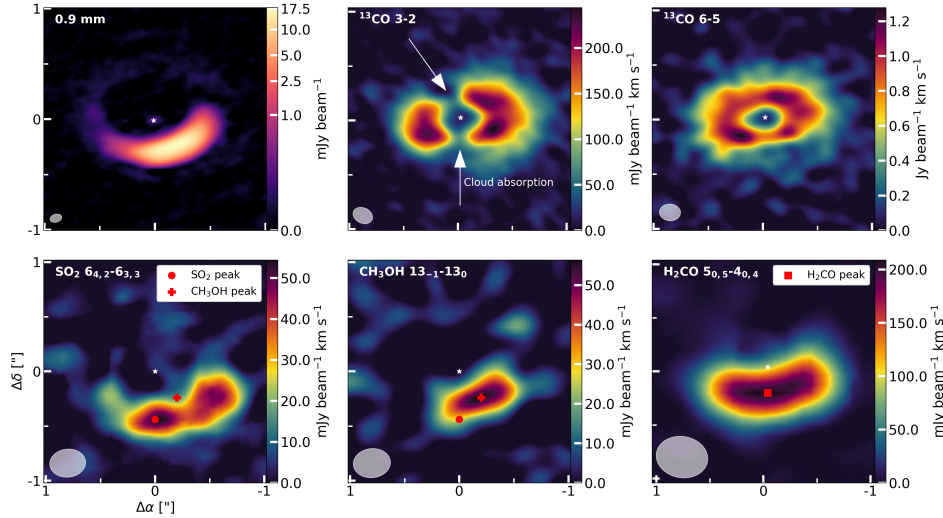


Figure 6.1: Dust continuum (top left; Yang et al. 2023) and moment-0 maps of the ^{13}CO $J=3-2$ (top centre; Leemker et al. 2023) and $J=6-5$ (top right; van der Marel et al. 2016b), and the SO_2 $J=6_{4,2}-6_{3,3}$ (bottom left), CH_3OH $J=13_{-1}-13_0$ (bottom centre), and H_2CO $J=5_{0,5}-4_{0,4}$ (bottom right) transitions. The white star in the centre indicates the approximate location of the host star, whereas the resolving beam is indicated in the lower left. The red circle and cross provide, respectively, the peak flux position of the SO_2 and CH_3OH transitions in the bottom left and centre plots, whereas the red square denotes the peak flux position of the H_2CO transition in the bottom right plot. In addition, the arrows in the ^{13}CO $J=3-2$ transition indicate where the emission is affected by the cloud absorption.

The integrated flux, or moment-0, maps of the SO_2 $6_{4,2}-6_{3,3}$, CH_3OH $13_{-1}-13_0$, and H_2CO $5_{0,5}-4_{0,4}$ transitions are displayed in Figure 6.1, together with high-resolution, 0.9 mm dust observations (Yang et al. 2023) and the ^{13}CO $J=3-2$ (Leemker et al. 2023) and $J=6-5$ (van der Marel et al. 2016b) transitions. These transitions of SO_2 , CH_3OH , and H_2CO are among the brightest ones observed in the disk and, therefore, their peak position provide good insights into the excitation conditions at the positions in the disk where these molecules are strongly detected. Immediately clear from the moment-0 maps are the differences in the azimuthal extent of the molecular species: the CH_3OH is very compact at the location of the dust trap, whereas the emission of both SO_2 and H_2CO is spread out over a larger azimuthal extent, up to approximately quarter of an orbit. The ^{13}CO transitions, in particular the $J=3-2$ one, are affected by cloud absorption. Within the images, we have indicated the pixel position of the peak flux and throughout this paper we show examples for these peak pixel positions.

6.3 Methods

6.3.1 Identifying detected transitions

The various SO₂, CH₃OH, and H₂CO transitions are, for each separate pixel, identified using the ‘Leiden Atomic and Molecular Database’ (LAMDA; Müller et al. 2001; Schöier et al. 2005; Wiesenfeld & Faure 2013; Rabli & Flower 2010; Balança et al. 2016). We limit our search to transitions with Einstein-A coefficients of $A_{ul} \geq 10^{-6} \text{ s}^{-1}$ and upper level energies of $E_{\text{up}} \leq 500 \text{ K}$, as lines with lower Einstein-A coefficients and higher upper level energies are not detected. For each pixel and spectral window, we obtain the corresponding spectrum in units of Jy beam^{-1} . The spectra extracted for the pixel where the moment-0 maps peak (highlighted in Figure 6.1) are shown in Figures 6.B.1, 6.B.2, and 6.B.3 for SO₂, CH₃OH, and H₂CO, respectively. Within each spectrum, we consider all transitions with peak fluxes above three times the root mean square (RMS) as detections. As we retrieve spectra for each pixel and all spectral windows, we determine the RMS in each spectrum using an automated approach consisting of various steps: first, the residual variation in the continuum-subtracted baseline is determined using an iterative, 2σ -outlier masking process and a Savitzky-Golay filter (Savitzky & Golay 1964). The Savitzky-Golay filter allows one to smooth the data using a low-order polynomial over a subset of the data, without altering the underlying shape of the spectrum. We filtered the data using third-order polynomials that smoothed the data every 100 data points. Secondly, the standard deviation (SD) of the residuals, after subtracting the final Savitzky-Golay filter from the 2σ -outlier masked spectrum, is obtained. Finally, we identify and mask all emission lines from the full spectrum, by removing all emission lines that have fluxes above $3\times$ the aforementioned SD. The RMS is, subsequently, obtained from the resulting line-free spectrum. Overall, we find RMS values of $\sim 1 \text{ mJy beam}^{-1}$ for the Cycle 8 observations, very similar to the values listed in Table 6 of Booth et al. (2024b). The RMS varies between ~ 1.0 - $1.5 \text{ mJy beam}^{-1}$ for the Cycle 5 observations, in agreement with the value listed in van der Marel et al. (2021a) of $\sim 1.2 \text{ mJy beam}^{-1}$.

From our list of detected transitions, we have removed transitions which are blended with other transitions of the same molecule with different excitation conditions and/or blended with transitions of other molecules. However, we have kept the transitions that are blended with the transitions of the same molecule that have the same Einstein-A coefficient and upper level energy. This allowed us to include two pairs of CH₃OH transitions. As both transitions have the same excitation conditions and, therefore, are expected to contribute equally to the observed line, we assume that half of the observed line flux can be attributed to each of the transitions. Furthermore, through trial and error and visual inspection of the image cubes and line profiles, we have removed additional SO₂ transitions for which we could not confidently distinguish between emission and 3σ noise spikes, i.e. features that appear only locally and do not follow the emission morphologies (i.e. do not follow the same pattern, such as Keplerian rotation, or display different line profiles) seen for stronger transitions. All detected transitions are listed

in Table 6.A.1, whereas the blended transitions or those dominated by noise are listed in Table 6.A.2.

6.3.2 Integrated intensity and rotational diagram analysis

We infer the excitation conditions (rotational temperature and column density) using a rotational diagram analysis. We obtain integrated fluxes by fitting Gaussian line profiles. As the flux from individual pixels is not independent, we consider the beam area to be the emitting area in our calculations. In addition, we follow the method described by, for example, Banzatti et al. (2012) to create model intensities, which, subsequently, are fitted to inferred values. In the calculation of the optical depth, we have used a line width of $\Delta V_{\text{line}} = \sqrt{\Delta V_{\text{thermal}}^2 + \Delta V_{\text{turbulence}}^2} = 0.2 \text{ km s}^{-1}$. This line width is a combination of the thermal line width (expected to be of the order of $\sim 0.15 \text{ km s}^{-1}$) and the intrinsic width due to local turbulence, which can also reach values of $\sim 0.1 \text{ km s}^{-1}$ (see, e.g. Paneque-Carreño et al. 2024). Additionally, we have calculated 3σ upper limits, following the description of Carney et al. (2019), for the pixels for which we have not created a rotational diagram.

6.4 Results

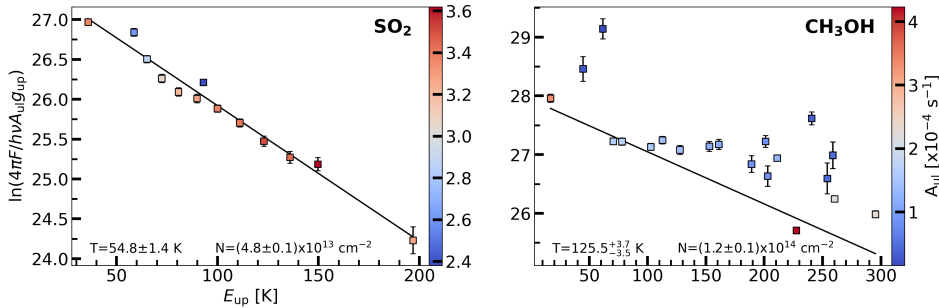


Figure 6.2: Rotational diagrams for SO₂ (left) and CH₃OH (right) at the peak flux positions of their 6_{4,2}-6_{3,3} and 13₋₁-13₀ transitions, respectively. The colour bar indicates the value for A_{ul} ($\times 10^{-4}$) of the transitions.

In Figure 6.2, we present the rotational diagrams for SO₂ and CH₃OH. In addition, we show the resulting temperature, column density, and optical depth maps (Figures 6.3 and 6.4 and line profiles (Figures 6.B.1, 6.B.2, and 6.B.3) retrieved for the molecules at the peak position of their $J=6_{4,2}$ -6_{3,3}, $J=13_{-1}$ -13₀, and $J=5_{0,5}$ -4_{0,4} transitions, respectively. These peak positions are highlighted in Figure 6.1. Our analysis assumes that the molecular emission is optically thin, for a discussion on the potential effects of optically thick emission, see Section 6.5.3.

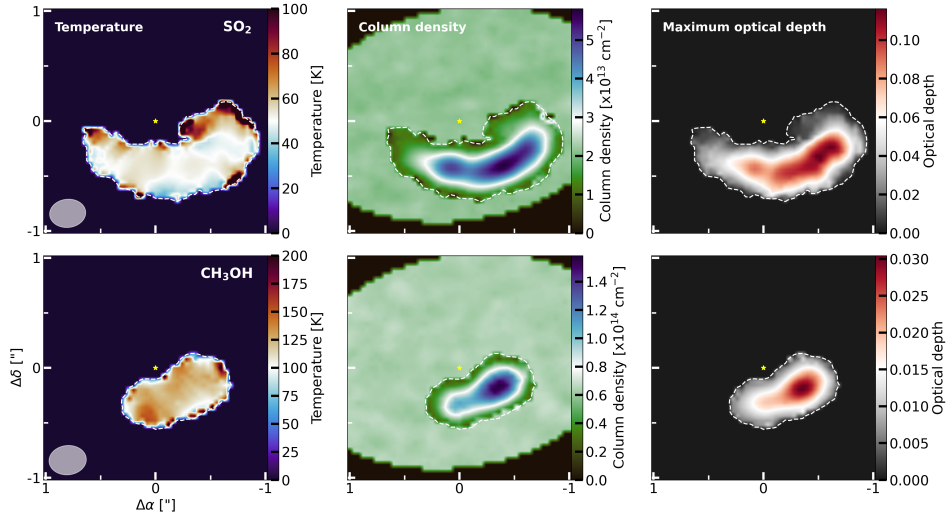


Figure 6.3: Temperature (left column), column density (middle column), and maximum optical depth (right column) maps for SO₂ (top) and CH₃OH (bottom).

6.4.1 SO₂

At the peak position of the integrated intensity map of the $J=6_{4,2}-6_{3,3}$ transitions of SO₂, we detect 13 isolated transitions (see also Table 6.A.1). The rotational diagram for this position is displayed in the left panel of Figure 6.2, while the line profiles are shown in Figure 6.B.1. The left-side of Figure 6.D.1 displays the intensity ratios between the observations and the modelled intensities. We find a well-constrained rotational diagram and derive a rotational temperature of $T=54.8\pm 1.4$ K and a peak total column density of $N=(4.8\pm 0.1)\times 10^{13}$ cm⁻². The upper limits on the column density, for pixels with an insufficient number of detected transitions, range between $\sim 2.0\times 10^{13}$ and $\sim 2.4\times 10^{13}$ cm⁻², which are a factor of ~ 2 lower than found at the peak position. We also find, for all pixel positions, a maximum optical depth of $\tau\sim 0.1$, suggesting that the SO₂ emission is optically thin. The optical depth is further discussed in Section 6.5.3. The final maps (temperature, column density, and optical depth) are displayed in the left panel of Figure 6.3. Given the low inferred uncertainties on the temperatures (of the order of a few Kelvin, see Figure 6.D.2), the hotter temperature (~ 70 K) at the inner edge is significantly higher than that at the outer edge (~ 40 K). The higher temperatures inferred at some of the edge pixels are likely due to fewer transitions detected and weaker line fluxes, and are, therefore, more uncertain (see also Figure 6.D.2).

The well-behaved rotational diagram of SO₂ points towards thermalised emission. As the gas densities necessary for the SO₂ emission to become thermalised are only found in a layer just above the midplane, we suggest that the emission must originate from this layer deep inside the disk (see also Section 6.5.2.2), which is also consistent with the derived rotational temperature.

6.4.2 CH₃OH

For CH₃OH, we observe 22 transitions at the peak position of the integrated intensity map of the $J=13_{-1}-13_0$ transition that are either unblended or blended with other CH₃OH lines with similar parameters (see also Table 6.A.1). The rotational diagram and the ratios between the observations and modelled intensities are shown in the right panels of Figures 6.2 and 6.D.1, the line profiles are displayed in Figure 6.B.2, and the final maps are shown in the lower row of Figure 6.3. Using these transitions, we derive a rotational temperature of $T=125.5^{+3.7}_{-3.5}$ K and a total column density of $N=(1.2\pm 0.1)\times 10^{14}$ cm⁻² at the peak position. The upper limits on the column density are of the order of $\sim 5.8\times 10^{13}$ cm⁻² to $\sim 6.9\times 10^{13}$ cm⁻², a factor of ~ 2 lower than the peak value. We find a maximum optical depth of $\tau \sim 0.03$, suggesting that the CH₃OH emission is optically thin. In contrast with that of SO₂, the rotational diagram of CH₃OH shows a large scatter between the data points, this is further discussed in Section 6.5.1.

6.4.3 H₂CO

The pixel-by-pixel rotational diagram analysis for the 7 observed H₂CO transitions in Cycle 5 (van der Marel et al. 2021a) proved to be more difficult and we were not able to retrieve reliable values for the rotational temperature and column density, likely due to a combination of the optical depth (discussed later in this section), a mixture of the ortho- and para-transitions, and sub-thermal excitation (see Section 6.5.1). In order to obtain a pixel-by-pixel temperature map, we derived the temperatures using various line ratios. Similar to van der Marel et al. (2021a), we use RADEX to obtain line ratios for various values of the kinetic temperature (T_{kin} in K) and the gas density (n_{H_2} in cm⁻³). Following van der Marel et al. (2021a) we used a column density of $N_{\text{H}_2\text{CO}}=10^{14}$ cm⁻² in the calculations, at which the emission should be optically thin. Additionally, we have used the default line width of 1 km s⁻¹ within the RADEX calculations. More details on the calculations can be found in Section 6.5.1. We determine the temperature, using a simple minimisation of the ratios obtained through RADEX with the inferred ratios from the observations, for gas densities of $n_{\text{H}_2}=10^7$ cm⁻³ and 10^8 cm⁻³, which, respectively, correspond to the disk's atmosphere and the midplane.

We have determined the line ratios for one pair of ortho-transitions ($5_{3,3}-4_{3,2}/5_{1,5}-4_{1,4}$) and three pairs of para-transitions ($5_{2,4}-4_{2,3}/5_{0,5}-4_{0,4}$, $5_{4,2}-4_{4,1}/5_{0,5}-4_{0,4}$, and $5_{4,2}-4_{4,1}/5_{2,4}-4_{2,3}$). The second and third pairs of the para-transitions allow us to investigate how the ratios change for transitions with different upper level energies, as the line excitation and, therefore, the observed flux and ratios are temperature sensitive. The ratios and inferred temperature maps are displayed in Figure 6.4. We highlight our findings for each line pair separately in Section 6.C of the Appendix.

Overall, we can infer from the ratios that the temperatures of H₂CO across the dust trap can be expected to be of the order of $T \sim 150-350$ K, with the highest temperatures found in the centre of the dust trap. As discussed above, this is generally similar to, albeit slightly higher than, the ratios derived from the disk-integrated values of van der Marel et al. (2021a). Such high temperatures are not

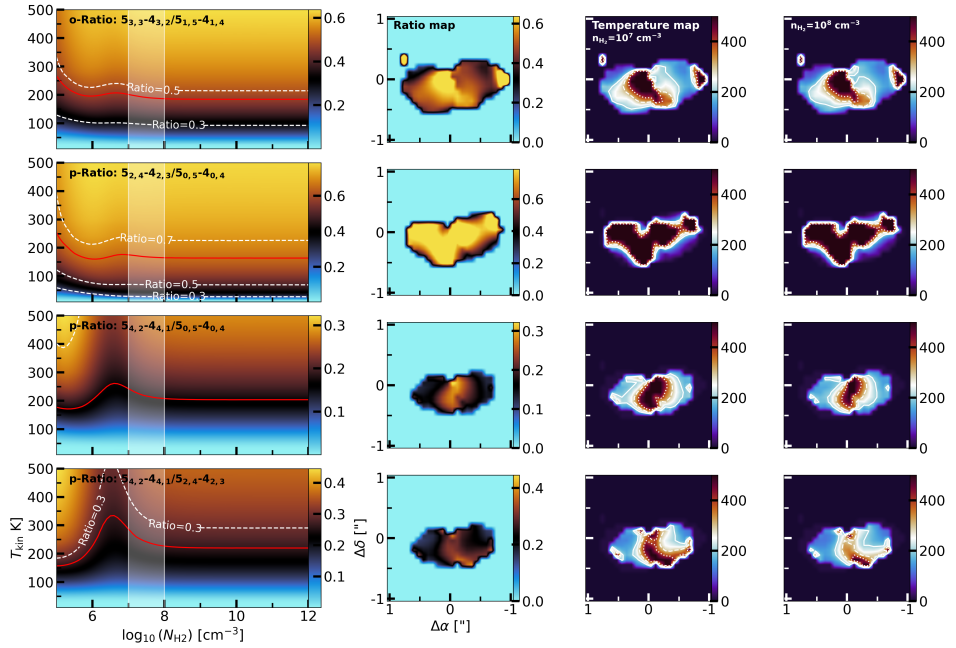


Figure 6.4: Line ratios for the different pairs of H_2CO transitions. The left panels show the RADEX calculations, with the colour map indicating the various ratios. The white contours indicate the values of 0.3, 0.5, and 0.7, whereas the red contour indicates the disk integrated ratio from van der Marel et al. (2021a). The panels in the second column indicate the ratios derived for the pixels where both transitions are detected, using the colour scheme as for the left panels. The final two columns display the derived temperatures for gas densities of $n_{\text{H}_2}=10^7 \text{ cm}^{-3}$ (representative of the disk’s atmosphere, $z/r \gtrsim 0.2$) and 10^8 cm^{-3} (representative of the disk’s midplane). The white solid, dashed, and dotted contours indicate temperatures of 200 K, 300 K, and 400 K, respectively.

unexpected given the high upper level energies of some of the H_2CO transitions detected in the disk of IRS 48 (i.e. the $J=5_{4,2}-5_{4,1}$ and $J=5_{4,1}-5_{4,0}$ transitions with $E_{\text{up}}=240.7 \text{ K}$ or the warm transition of $J=9_{1,8}-8_{1,7}$ with $E_{\text{up}}=174 \text{ K}$ detected in van der Marel et al. 2014). Compared to the other molecules, SO_2 and CH_3OH , we find that the temperatures are significantly higher than those of SO_2 , but are similar to and/or higher than those of CH_3OH . These high temperatures indicate that the emission must come from high up in the disk, as suggested before by van der Marel et al. (2021a). Therefore, the temperatures derived assuming a gas density of $n_{\text{H}_2}=10^7 \text{ cm}^{-3}$ should provide the best constraints. These are, however, also more limited by the ratios and the involved temperature sensitivity of the transitions. For the remainder of this work, we assume that the temperature derived for H_2CO is at least $\sim 150 \text{ K}$.

For a temperature of $T=150 \text{ K}$, a column density of $N=10^{15} \text{ cm}^{-2}$, and a gas density of $n_{\text{H}_2}=10^7 \text{ cm}^{-3}$, the RADEX calculations yield a maximum optical depth of $\tau \sim 1.9$, suggesting that some of the transitions may be (moderately)

optically thick in the outer edges of the dust trap (i.e. the regions where probe temperatures of $T_{\text{rot}} \sim 150$ K, see Figure 6.4). For the same conditions, but a temperature of $T=350$ K, we infer a maximum optical depth of $\tau \sim 0.6$, suggesting that the emission in the central regions are more optically thin.

6.5 Discussion

In the following sections, we discuss our results. We start by discussing the well-behaved rotational diagram of SO_2 , which is in contrast with that for CH_3OH which is dominated by large scatter. This points towards SO_2 being thermally excited, while CH_3OH is sub-thermally excited (Section 6.5.1). In Section 6.5.2, we discuss the temperature and resulting vertical structures of the disk, whereas the optical depth and radial structure are discussed in Section 6.5.3. Finally, we highlight potential follow-up observations in Section 6.5.4, which are needed to fully resolve the molecular emission and to infer more information on the column densities.

6.5.1 Sub-thermal excitation

Given the well-behaved rotational diagram of SO_2 , characterised by very limited scatter, we expect the emission to be (close to) thermalised. In stark contrast with this, is the large scatter observed in the rotational diagram of CH_3OH , which is likely due to the effects of sub-thermal excitation. As shown in Figure 6 of Johnstone et al. (2003), higher energy lines of CH_3OH have higher critical densities and are, subsequently, not thermalised at relatively low densities (i.e. $n=10^7$ cm^{-3}). A rotational diagram can still yield a single excitation temperature using a rotational diagram, but this value is much lower than the kinetic one, because the levels are not thermalised. By increasing the density (to, for example, $n=10^9$ cm^{-3}) in their RADEX calculations, Johnstone et al. (2003) found that the lines became thermalised tended towards the physical input conditions. In particular, the derived rotational temperature started to represent the input kinetic temperature.

We have used RADEX (van der Tak et al. 2007) to investigate at what gas densities the SO_2 , CH_3OH , and H_2CO emission thermalises. We have run the calculations for each molecular species, including all transitions with frequencies <1000 GHz, but limiting the transitions to those with $E_{\text{up}} \leq 300$ K and $A_{\text{ul}} \geq 10^{-6}$ s^{-1} to cover similar properties as our observed transitions, as only using the detected transitions did not yield sensible results. The number of transitions is too sparse to derive meaningful rotational temperatures for the entire grid. We ran the calculations separately for the A- and E-transitions of CH_3OH and for the ortho- and para-transitions of H_2CO . The calculations are run over grids of T_{kin} (10 K to 200 K in steps of 10 K) and $\log_{10}(n_{\text{H}_2})$ (5 to 12 in steps of 0.1, with n_{H_2} in units of cm^{-3}). In our calculations, we have kept the column density at a fixed value of $N=10^{12}$ cm^{-2} , which ensures optically thin emission and we used, similarly as in Section 6.4.3, the default line width of ~ 1 km s^{-1} . For each calculation, we

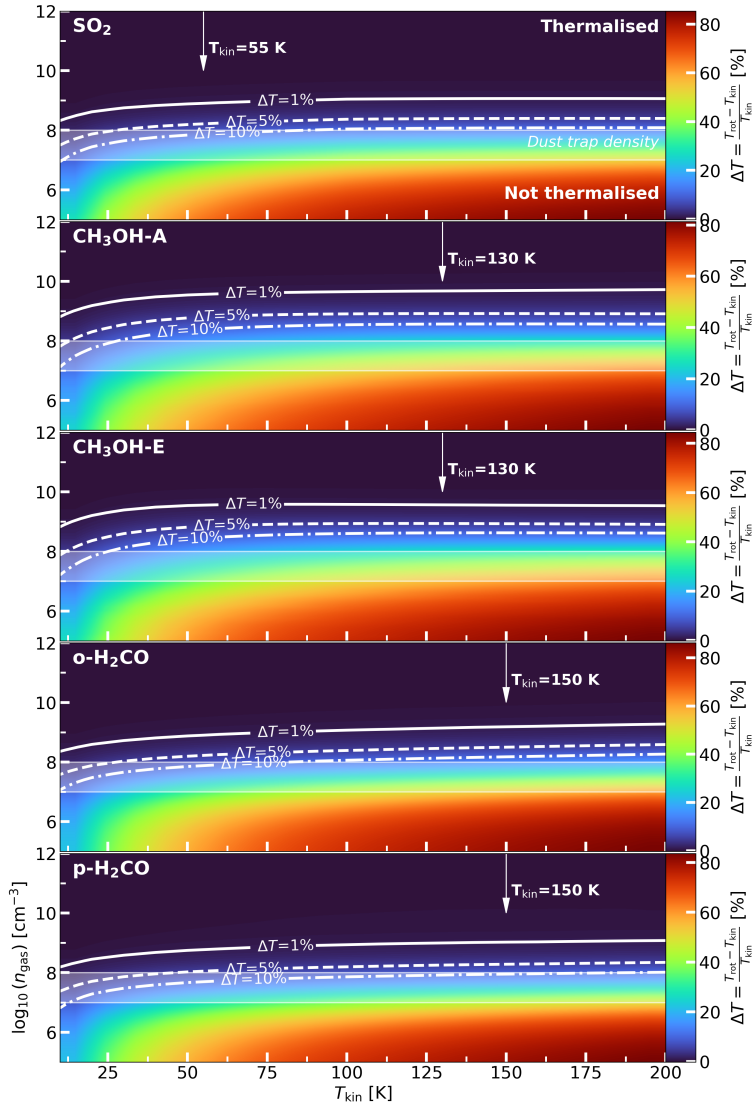


Figure 6.5: RADEX grids for SO₂ (top panel), A- and E-type CH₃OH (second and third panels), and ortho- and para-H₂CO (bottom two panels) showing the percentile difference between the kinetic and rotational temperature (ΔT), as a measure of thermalised transitions. The contours (solid, dashed, and dashed-dotted) in each panel indicates when $\Delta T=1\%$, 5% , and 10% , respectively. Above these contours the lines will be thermalised. The white shaded area indicates the gas density of the dust trap according to the DALI model (Leemker et al. 2023). Finally, the arrows indicate the derived excitation temperatures of $T \sim 55$ K for SO₂ and $T \sim 130$ K for CH₃OH. For H₂CO we show the rotational temperature of 150 K, the lower value of the inferred temperature range.

infer the rotational temperature by fitting a straight line ($y = ax + b$) through all the retrieved RADEX integrated fluxes, where the rotation temperature is given by the slope, $a = -1/T_{\text{rot}}$. Figure 6.5 displays the percentile difference between the input kinetic temperature and the derived rotational temperature (ΔT) from the RADEX calculations. For smaller percentages, the lines are thermalised. The contours (solid, dashed, and dashed-dotted) indicate where the differences are, respectively, $\Delta T=1\%$, 5% , and 10% . Above these contours (i.e. for higher densities), the difference becomes smaller and the emission is thermalised, whereas below these contours the differences become larger and the lines are not thermalised. Figure 6.5 also indicates the gas density, up to a height of 20 au, at the location of the IRS 48 dust trap, following the DALI model of Leemker et al. (2023) (see also Figure 6.10), and the derived excitation conditions from the rotational diagrams: $T \sim 55$ K for SO_2 , $T \sim 130$ K for CH_3OH , and the lower end of the derived temperature range ($T \sim 150$ K) for H_2CO .

We find that SO_2 thermalises at densities of $n_{\text{H}_2} \sim 10^8 \text{ cm}^{-3}$ and higher. As the rotational temperature of SO_2 is well-constrained at $T \sim 55$ K, this requires that the SO_2 emission should be thermalised. However, densities of $n_{\text{H}_2} \sim 10^8 \text{ cm}^{-3}$ are only achieved near the midplane of the disk at heights of ~ 5 au ($z/r < 0.1$, see also Figure 6.10), suggesting that the SO_2 may originate from deep inside the disk. The emitting height of SO_2 is further discussed in Section 6.5.2.

For H_2CO we find that the emission thermalises at similar densities as SO_2 , however, the derived temperatures are significantly higher, suggesting that the H_2CO emission does not originate from the same layer as SO_2 . CH_3OH requires, on the other hand, even higher densities of $n_{\text{H}_2} > 10^9 \text{ cm}^{-3}$. Combining these dust trap densities with the derived rotational temperatures, we infer that the emission of both CH_3OH and H_2CO may be sub-thermally excited. Therefore, the presented rotational temperatures are considered to underestimate the kinetic temperature and non-LTE approaches should be used to correctly derive the excitation conditions. As CH_3OH requires higher gas densities to be thermalised compared to H_2CO (i.e. the differences, ΔT , are larger), we expect that the underestimation of the kinetic temperature is larger for CH_3OH than for H_2CO (as indicated in Figure 6.5). Therefore, we expect that the CH_3OH and H_2CO may actually probe very similar temperatures and, as suggested by van der Marel et al. (2021a), that the species may originate from the same high layer inside the disk.

We reiterate that the IRS 48 disk has exceptionally low gas and dust masses. For disks with higher masses and, therefore, higher densities, the molecular emission is more likely to be thermally excited. Therefore, observations (or surveys) of massive disks, covering multiple (≥ 3 or at least 2, if the upper level energies are significantly different) transitions of the same molecular species, could be used to infer the (gas) temperature and chemical structure from their molecular line emission. For these less massive disks, a non-LTE analysis is a necessary and powerful tool to infer the excitation conditions.

6.5.2 Temperature and vertical structure

In the following section, we discuss the resulting temperature (Section 6.5.2.1) and vertical structure (Section 6.5.2.2) of the disk, as interpreted from our results.

6.5.2.1 Temperature structure

Using our temperature maps (top row in Figure 6.3), we assess how the temperature may vary across the IRS 48 dust trap. In Figure 6.D.2, we display the derived lower and upper uncertainties for the temperature maps of SO_2 and CH_3OH . The uncertainties are found to be the highest for pixels near the edge, for which often also the highest temperatures are found. This is very likely due to the fact that fewer transitions are detected and the line emission is not as strong as for pixels closer to the centre (see also Figure 6.F.1). The temperature map for CH_3OH does not show a clear temperature structure but is rather constant across the entire disk with temperatures of $T \gtrsim 125$ K. The SO_2 map, on the other hand, shows hints of a potential radial temperature gradient, which is generally expected to be present in disks. The temperature closer to the host star is hotter ($T \sim 70$ K) compared to the temperature at the outer edge ($T \sim 40$ K).

Overall, we find that the uncertainties for SO_2 and CH_3OH are nearly uniform ($\sigma_T \lesssim 5$ K) across the molecular emission extent. Additionally, Figure 6.D.3 show the uncertainties for the column density maps. We find that the uncertainties on the column density are uniform across the maps of all three molecular species, of the order of $\lesssim 10\%$. As our temperature uncertainties are of the order of $\sigma_T \lesssim 5$ K, we expect this radial temperature gradient in the SO_2 map to be real. The observed radial decrease in the temperature is of the order of 10 K to 30 K when considering the uncertainties. The DALI model suggests, on the other hand, that the temperature for the expected emitting layer of SO_2 (see Section 6.5.2.2), remains fairly constant between 40 and 70 K.

As the asymmetric dust trap of IRS 48 may be the result of a vortex present in the disk, this vortex could also influence the observable temperature structure. As discussed by Lovelace & Romanova (2014), if the vortex is the result of the RWI, the vortex must be anticyclonic (i.e. rotate clockwise) for it to generate a pressure maximum that can trap the dust. Most of the recent work on vortices has gone into their existence, evolution, and stability (e.g. Lovelace et al. 1999; Meheut et al. 2012b,a; Lovelace & Hohlfield 2013; Meheut et al. 2013), or into their relationship with forming planets (e.g. Hammer et al. 2017, 2019, 2021; Hammer & Lin 2023). Little work (see, for example, Huang et al. 2018b; Leemker et al. 2023) has focused on how the gas and chemistry may be affected by the vortices. Vortices perturb the motion of the gas, so intuitively, such a perturbation may also be visible in the temperature structure. If the gas perturbation follows the anticyclonic rotation of the vortex, gas with slightly higher temperature would be rotating away from the host star, whereas cooler gas would move towards the host star. This is also visualised in Figure 6.6. The strength of this effect would depend on the rotational timescale of the vortex, which itself is set by the vorticity (Meheut et al. 2013): the faster the vortex rotates, the stronger the effect will be. As vortices predominantly arise in the midplane, their effect on the dust and gas should be most notable for

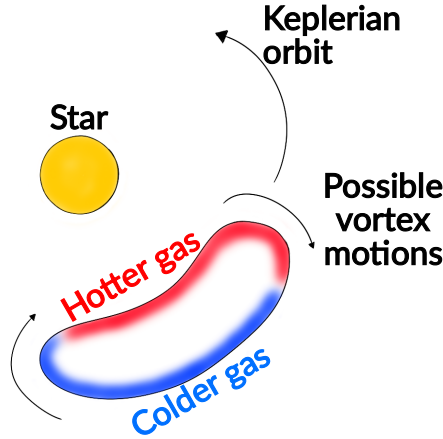


Figure 6.6: Cartoon visualising the expected effect of the vortex on the temperature structure. Hotter gas, due to UV heating, will be counteracted by colder gas being brought in due to the potential vortex motions, which primarily acts in the midplane. This effect is not observed in the IRS 48 disk, unless the temperatures variations are very small.

molecular emission originating from close to the midplane, but may be negligible in elevated layers, where UV heating dominates. As we expect SO_2 to emit from close to the midplane and we do not see an azimuthal variation that could be induced by a potential vortex, the temperature variation induced by such a vortex can only be of the order of ~ 2 K, given the small uncertainties. CH_3OH is, on the other hand, together with H_2CO expected to emit from an elevated layer ~ 10 - 15 au ($z/r \sim 0.17$ - 0.25) above the midplane (van der Marel et al. 2021a). Therefore, we expect not to see any variation in the temperature related to a potential vortex. Only if vertical mixing, which is expected to play a role in liberating the molecular species from the icy dust mantles in the IRS 48 disk, can transmit the effect from a vortex to elevated regions, a different temperature structure may be found in the molecular emitting layers. Detailed models that constrain the vorticity and include vertical mixing can be used to investigate the interplay between the dust and gas in vortices and, subsequently, are necessary to investigate the potential influences of vortices on the temperature structures of disks.

6.5.2.2 Vertical structure

In addition to the temperature maps, we have measured the temperature using the brightness temperature (T_b) of optically thick emission, i.e. from the dust continuum or from one of the CO isotopologues. Using Planck’s law, we have calculated the brightness temperature of the high-resolution, optically thick 0.9 mm continuum emission (Yang et al. 2023) and of the ^{13}CO $J=3-2$ (Leemker et al. 2023) and $J=6-5$ (van der Marel et al. 2016b) transitions. The brightness temper-

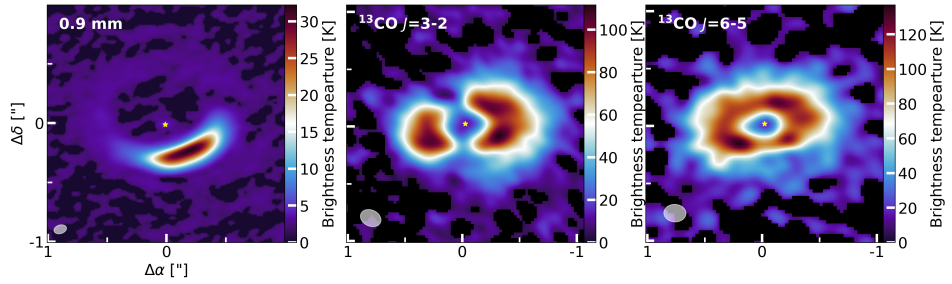


Figure 6.7: Brightness temperature maps of the dust continuum (left) and the ^{13}CO $J=3-2$ (middle panel) and ^{13}CO $J=6-5$ (right panel) transitions. The yellow stars in the centre indicate the approximate location of the host star, while the resolving beams are indicated by the white ellipses.

ature maps are displayed in Figure 6.7. We find a peak brightness temperature of $T_b \sim 32$ K for the dust continuum, which is only slightly higher ($\Delta T_b \sim 5$ K) than that found in van der Marel et al. (2021a), likely due to the difference in the beam sizes. The higher brightness temperature determined here confirms the notion that the temperature of the dust in the disk’s midplane is too high for CO freeze-out and in situ COM formation through the hydrogenation of CO (Watanabe & Kouchi 2002; Fuchs et al. 2009; Santos et al. 2022). However, CO may still react with solid-state OH to form CO_2 , even though the temperatures are above its sublimation temperature (Terwisscha van Scheltinga et al. 2022).

As the CO emission is affected by foreground cloud absorption (Bruderer et al. 2014), the temperature can only be estimated for select emission channels. We find peak brightness temperatures of $T_{b,3-2} \sim 110$ K and $T_{b,6-5} \sim 135$ K, from the absorption-free channels of the optically thick ^{13}CO $J=3-2$ and $J=6-5$ transitions, respectively. Based on these derived temperatures, and those derived for SO_2 , CH_3OH and H_2CO , we can infer the vertical emission structure of the disk. We expect CH_3OH and H_2CO to trace the highest temperatures, given their derived temperatures and the notion that the emission is sub-thermally excited, and, therefore, they should arise from a higher emitting layer. The ^{13}CO , probing a slightly colder temperature, should originate from a slightly deeper layer in the disk, under the assumption that the emission is fully resolved (Leemker et al. 2022), while the SO_2 should originate from the deepest vertical layer. The notion that SO_2 originates from deep inside the disk, based on the temperature, is supported by our RADEX calculations (see Section 6.5.1), which show that SO_2 becomes thermalised at densities of $n_{\text{gas}} \sim 10^8 \text{ cm}^{-3}$. These densities are only reached in the layers close to the midplane, with heights of $\lesssim 5$ au (or $z/r < 0.1$, see also Figure 6.10). Therefore, under the assumption of thermalised emission, the SO_2 emission must originate from this layer just above the midplane. We also consider the radial locations of the emission to support our vertical structure posed above. We note that the SO_2 emission peaks at larger distances, by ~ 10 au, than both CH_3OH and H_2CO (see Booth et al. 2024b).

6.5.3 Optical depth and emission structure

Below, we discuss the optical depth of the various molecules (Section 6.5.3.1). In addition, we also discuss the required radial extent of the emission to become optically thick.

6.5.3.1 Optical depth

For the chosen turbulent line width ($\Delta V_{\text{line}}=0.2 \text{ km s}^{-1}$) our analysis points towards potentially optically thin emission. However, it is still possible that the molecular emission, in particular that of H_2CO , is optically thick. Considering a previously derived isotopologue ratio, $\text{H}_2\text{CO}/\text{H}_2^{13}\text{CO}\sim 4$ (Booth et al. 2024b), it is very likely that its emission is optically thick. As the spatial resolution of the used observations is low, one likely explanation for our analysis pointing towards optically thin emission is that the actual emitting areas are smaller than currently can be probed. As can be seen in Figure 6.1, the radial extent is of a similar size as that of the beam. The azimuthal extent of both SO_2 and H_2CO is, on the other hand, larger than a single beam. Therefore, we conclude that the azimuthal extent is resolved, whereas the radial one is not.

To test for what emitting areas, parameterised by the beam radius (assuming a circular beam), and values for the local (turbulent) line widths we can ensure optically thick emission, we have explored grids over both parameters. We have run the grids for the same transitions as used throughout our analysis: SO_2 $J=6_{4,2}-6_{3,3}$, CH_3OH $J=13_{-1}-13_0$, and H_2CO $J=5_{1,5}-4_{1,4}$. For H_2CO , we have used a higher resolution (both spatial and spectral) transition that has been presented in Booth et al. (2024b) (see also Figure 6.E.1), which is of the same spectral and spatial resolution as the SO_2 and CH_3OH transitions. In our calculations of the optical depth, we have used fixed rotational temperatures of $T_{\text{rot}}=55 \text{ K}$ for SO_2 , $T_{\text{rot}}=150 \text{ K}$ for CH_3OH , and $T_{\text{rot}}=150 \text{ K}$ and $T_{\text{rot}}=350 \text{ K}$ for H_2CO to represent the range of temperatures found. Our grid of the line width extends up to 1.0 km s^{-1} . If the line profiles are only thermally broadened, they will be of the order of $\sim 0.15 \text{ km s}^{-1}$, but local turbulence can additionally broaden the lines by $\sim 0.1 \text{ km s}^{-1}$ (see, e.g. Flaherty et al. 2020, 2024; Paneque-Carreño et al. 2024).

The inferred optical depths for our grids of turbulent line widths and beam radii are displayed in Figure 6.8. As can be seen, we require beam radii of $\lesssim 8 \text{ au}$ for the H_2CO emission to become optically thick at a temperature of $T_{\text{rot}} \sim 350 \text{ K}$. For the lower temperature of $T_{\text{rot}} \sim 150 \text{ K}$, a larger beam area of $\lesssim 16 \text{ au}$ is sufficient for optically thick emission. These lower temperatures should hold for the outer edges of the dust trap, whereas the warmer temperature accounts for the central region (see also Section 6.4.3). The SO_2 emission also becomes optically thick for an emitting radius of $\lesssim 8 \text{ au}$, whereas the CH_3OH emission requires slightly smaller radii. For smaller line widths ($\Delta V_{\text{line}} < 0.2 \text{ km s}^{-1}$), we find that the emission becomes optically thick for larger beam areas.

We, thus, propose a scenario in which the emission (in particular that of H_2CO) originates from a small radial ‘sliver’ with an approximate width of $\lesssim 10 \text{ au}$. This ‘sliver’ must be located at the inner edge of the dust trap for CH_3OH and H_2CO to conform with the current hypothesis that the observed molecules

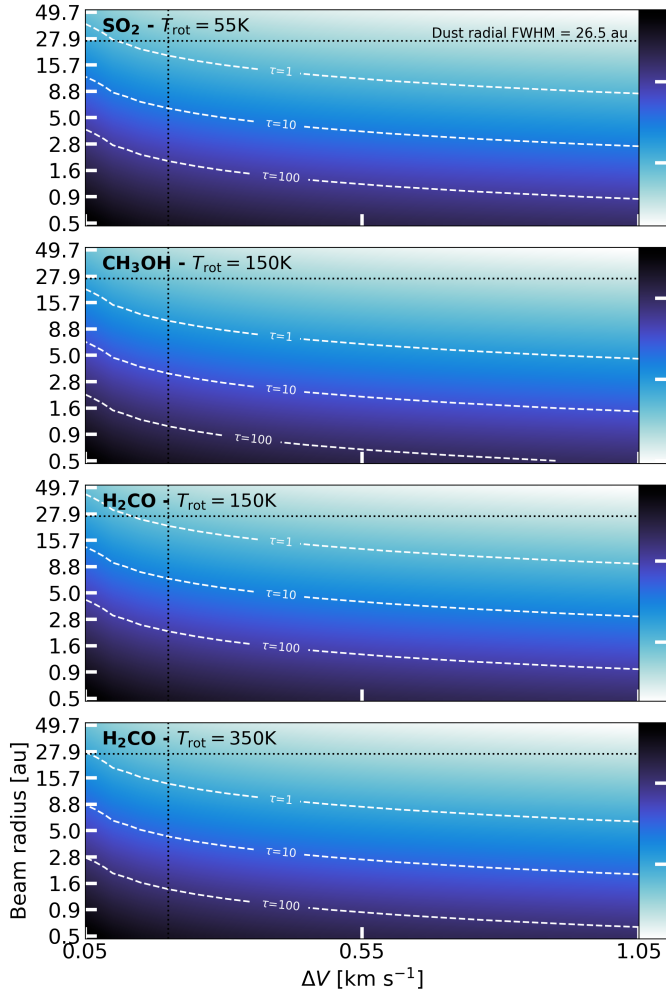


Figure 6.8: Optical depth (given in \log_{10} -space) grids for a range of beam radii (assuming circular beams) and turbulent line widths (ΔV) for SO_2 $J=6_{4,2}-6_{3,3}$ (at $T_{\text{rot}}=55$ K), CH_3OH $J=13_{-1}-13_0$ (at $T_{\text{rot}}=150$ K, accounting for the underestimation of the temperature due to sub-thermal excitation), and H_2CO $J=5_{1,5}-4_{1,4}$ (at $T_{\text{rot}}=150$ K and $T_{\text{rot}}=350$ K). The contour lines indicate values of $\tau=1, 10,$ and 100 . The dotted black line indicates the radial FWHM of the dust trap ($\text{FWHM}_{\text{dust}} \simeq 26.5$ au), found using the high-resolution observations of Yang et al. (2023). The vertical dashed line indicates a turbulent line width of $\Delta V_{\text{line}}=0.2$ km s^{-1} , the lower value used in our analysis.

are in the gas phase following thermal sublimation (see, e.g., van der Marel et al. 2021a; Booth et al. 2021a, 2024b). While SO_2 emission is known to originate from a larger radial distance (Booth et al. 2024b), it is still possible that the emission originates from a similar ‘sliver’, only placed at a larger radial distance, coming from close to the midplane, and is located closer to the outer edge of the dust trap.

For comparison, we have estimated, from the high-resolution dust observations (Yang et al. 2023), that the dust trap has a width of ~ 26.5 au (see also Figure 6.8). Interestingly, from imaging of the H_2CO $J=5_{1,5}-4_{1,4}$ transition with superuniform weighting (see right panel of Figure 6.E.1), a smaller width of the emission is inferred. We note that the radial extent is still unresolved with this weighting scheme. The resulting beam ($0.22'' \times 0.18''$) has a width of ~ 25 au, which is bigger than the proposed width of the ‘sliver’. Finally, we note that one of the models presented by van der Marel et al. (2021a) also suggests this sliver theory for the H_2CO theory. In particular, their full model, where the large grain population is increased throughout the entire dust column instead of settled to the midplane, with a surface density of $\Sigma_d=5.0 \text{ g cm}^{-2}$ at 60 au, has the H_2CO distributed over the entire vertical extent, but radially only between 60 and 70 au (see their Figure C.2). We have visualised our proposed emission scheme in Figure 6.9, based on the temperatures as discussed in Section 6.5.2 and the potential radial extent of the molecules as discussed here.

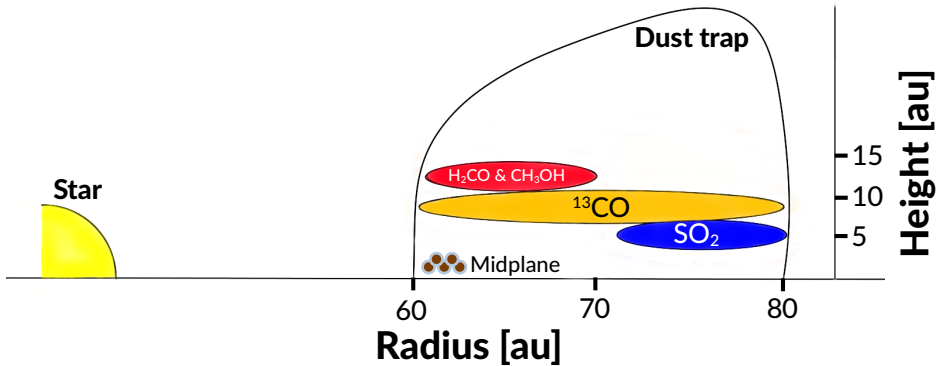


Figure 6.9: Cartoon visualising our proposed radial vertical emission scheme, containing SO_2 (blue), ^{13}CO (orange), and H_2CO and CH_3OH (red). The radial and vertical emission locations are based on the derived temperatures, the proposed sliver theory, and the assumption that the ^{13}CO emission is spatially resolved.

The discussion above suggests that the emitting areas of the molecules are radially unresolved and, subsequently, the emission is beam diluted. This has previously already been discussed in Brunken et al. (2022) and Booth et al. (2024b). Beam dilution results in an underestimation of the inferred column densities. Higher-resolution observations with spatial resolutions of $<0.1''$ (translating to a resolution of <13.5 au for the distance of IRS 48) are needed to obtain better constraints on the column densities. Using the following equation,

$$\text{DF}^{-1} = \frac{\Omega_{\text{source}}^2}{\Omega_{\text{beam}}^2 + \Omega_{\text{source}}^2},$$

we provide an estimate on the dilution factor for the molecular emission, assuming the emission comes from a circular region with a total width of 10 au, as proposed above with our ‘sliver’ theory. As determined by the column densities on a pixel-by-pixel basis, we take the Ω_{beam}^2 to be equal to the beam size of the current observations, whereas we set Ω_{source}^2 equal to the area of the circular region. This yields $\text{DF}^{-1} \sim 0.002$ or, in other words, an underestimation of the column density by a factor of ~ 500 .

For our derived column densities (see Section 6.4) and given the uncertain optical depths, we derive lower limits on the fractional abundances, with respect to H_2 ($\Sigma_g = 0.25 \text{ g cm}^{-2}$ or $N_{\text{H}_2} \sim 7 \times 10^{22} \text{ cm}^{-3}$; van der Marel et al. 2016b; Leemker et al. 2023), of $N_{\text{SO}_2}/N_{\text{H}_2} \sim 7 \times 10^{-10}$ - 3×10^{-9} and $N_{\text{CH}_3\text{OH}}/N_{\text{H}_2} \sim (1-8) \times 10^{-9}$. Assuming that we underestimate the column densities by a factor of ~ 500 , these fractional abundances become $N_{\text{SO}_2}/N_{\text{H}_2} \sim 3 \times 10^{-7}$ - 2×10^{-6} and $N_{\text{CH}_3\text{OH}}/N_{\text{H}_2} \sim 7 \times 10^{-7}$ - 4×10^{-6} . Compared to two other Herbig stars, HD 100546 and HD 169142, we find that our derived column densities for CH_3OH are of the same order of magnitude (Booth et al. 2023 and Evans et al. in prep.). However, we note that our column densities may be underestimated by this factor of ~ 500 .

6.5.3.2 Continuum affecting the line emission

One additional concern for our derived excitation properties is the potential effect of the dust continuum on the observed molecular emission, in particular, that of CH_3OH and H_2CO . The continuum emission can impact the line emission in two ways (Boehler et al. 2017; Weaver et al. 2018; Isella et al. 2018; Rab et al. 2020; Bosman et al. 2021; Rosotti et al. 2021; Nazari et al. 2023): (1) if the lines themselves are optically thick, the continuum subtraction procedure may overestimate the contribution of the continuum at the line centre. The subtraction would, subsequently, result in an oversubtraction of the continuum. This effect maximises once the continuum also becomes optically thick. (2) On the other hand, if the line is optically thin and the continuum is optically thick, up to half of the total emission, originating from the backside of the disk, may be blocked by the continuum.

As it is expected that the H_2CO emission is optically thick and polarisation observations of the IRS 48 continuum and accompanying modelling works by Ohashi et al. (2020) suggest that the dust continuum at 0.86 mm ($\sim 348.6 \text{ GHz}$) is optically thick ($\tau_{\text{dust}} \sim 7.3$), it is not immediately clear which effect is at play. Nonetheless, the channel maps of the $\text{CH}_3\text{OH } J=13_{-1}-13_0$ and $\text{H}_2\text{CO } J=5_{1,5}-4_{1,4}$ transitions show that the observed emission is affected by the continuum, see Figure 6.G.1. The channel maps for CH_3OH and H_2CO show a decrease, most notable in the 4.8-6.6 km s^{-1} velocity range for CH_3OH and 3.9-7.5 km s^{-1} range for H_2CO , in the line emission near the peak location of the dust continuum, which is not visible in those of the $\text{SO}_2 J=6_{4,2}-6_{3,3}$ transition. Therefore, we expect that we are not probing the full line flux of these molecules, either due to continuum oversubtraction or the continuum blocking emission originating from the backside of the disk. Given that the effect is most notable in the channel maps of CH_3OH and H_2CO , and not in those of SO_2 , we propose that continuum oversubtraction

is the likely effect. Especially considering that the SO_2 originates from near the midplane, where the secondary effect (dust blocking the emission) could be even stronger than for the elevated layers, i.e. more than half of the emission could be blocked. This suggests that CH_3OH , in addition to H_2CO , should be optically thick. Therefore, we propose that the ‘sliver’ theory mentioned above should also hold for CH_3OH . This, in addition to the beam dilution, results in an underestimation of the column density by as much as a factor of 500.

6.5.4 Future observations

Any conclusions on the chemistry are currently limited by the spatial and spectral resolution of the observations. Therefore, to be able to infer more information on the chemistry (i.e. column densities), we need higher resolution (both spatially and spectrally) observations that are able to test our ‘sliver’ theory proposed in Section 6.5.3 for H_2CO and potentially CH_3OH . At the distance of IRS 48 ($d \sim 135$ pc), an angular resolution of $\sim 0.1''$ is needed to retrieve the necessary beam radius of ~ 8 au. In addition, these observations may provide more insights into the varying temperature structure, potentially related to the influence of a vortex.

Furthermore, a spectral resolution of $\sim 0.1 \text{ km s}^{-1}$ will ensure resolved line profiles for line widths of $\gtrsim 0.5 \text{ km s}^{-1}$. This spectral resolution will allow one to infer the vertical emission heights from the channel maps, as recently has been done for a multitude of other inclined disks (Law et al. 2021; Paneque-Carreño et al. 2023; Law et al. 2023b,a, 2024; Urbina et al. 2024). A vertical decomposition of the emission layers could also confirm our notion that the CH_3OH and the H_2CO must come from higher emitting layers compared to ^{13}CO , while the SO_2 must originate from deep inside the disk. Additionally, the proposed resolutions will be sufficient to study kinematical signatures that deviate from Keplerian emission at the location of the dust trap, as was performed for the asymmetric HD 142527 disk using CO isotopologues (Boehler et al. 2021).

Finally, as seen in Figure 6.4, many of the line ratios are limited by the temperature sensitivity of the transitions. In order to better constrain the temperature through these ratios, transitions with higher upper level energies need to be observed. These lines, in addition to the higher-resolution observations, will ensure proper constraints on the temperature, not influenced by effects such as beam dilution.

6.6 Timescales: Vertical mixing, desorption, and photodissociation

6.6.1 Methodology

To further determine what sets the observable molecular abundance in the IRS 48 disk, we have calculated multiple timescales at the location of the dust trap: the vertical turbulence mixing timescale, the desorption and freeze-out timescales of SO_2 , CH_3OH , and H_2CO , and their photodissociation timescales. Interestingly,

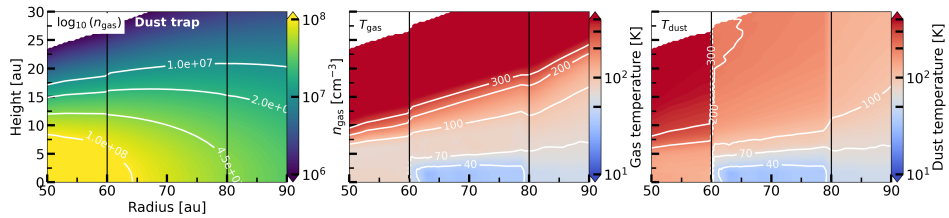


Figure 6.10: Zoom-in of the model structure of the dust trap region of the IRS 48 disk of the gas density (n_{gas} in cm^{-3} , left panel) and gas and dust temperature (both in Kelvin, left and right panels, respectively). The vertical bars indicate the location of the dust trap, extending from 60 to 80 au, while the white contours in the left most panel indicate gas densities between 10^7 and 10^8 cm^{-3} . The images have been adapted from Leemker et al. (2023).

the disk of IRS 48 has very low gas and dust masses, with a gas mass of the order of $M_{\text{gas}} \sim 1.4 \times 10^{-4} M_{\odot}$ (Bruderer et al. 2014), obtained through modelling the observed C^{17}O $J=6-5$ flux and found to be consistent with the mass derived from the C^{18}O observations (van der Marel et al. 2016b), and a dust mass of $M_{\text{dust}} \sim (6.2 \pm 0.6) \times 10^{-5} M_{\odot}$ (Temmink et al. 2023). These masses are lower compared to other Herbig stars, which have disk masses of the order of $\sim 10^{-2} M_{\odot}$ (e.g. Stapper et al. 2024). Therefore, the gas densities in the IRS 48 dust trap, even near the midplane, are only of the order of 10^8 cm^{-3} and drop to 10^6 cm^{-3} in the surface layers. We have used the inferred properties (i.e. n_{gas} , T_{gas} , and T_{dust}) of the IRS 48 disk as modelled by Leemker et al. (2023) using the thermochemical code DALI (Bruderer et al. 2012; Bruderer 2013). This DALI model is built upon an existing model from Bruderer et al. (2014), van der Marel et al. (2016b), and van der Marel et al. (2021a), and is described by a radial surface density profile that uses the self-similar solution for a viscously evolving disk (Lynden-Bell & Pringle 1974; Hartmann et al. 1998). It consists of deep dust and gas cavities between 1 and 60 au, while the dust trap is placed at 60 to 80 au. The model is separated into two different models: one representing the dust-trap side (where the dust density distribution has been altered under the assumption that the small grains have grown to larger sizes) and one tailored to the other side of the disk. This model is able to reproduce the continuum emission (at 0.44 mm and 0.89 mm) and the emission of various CO isotopologues. The gas temperature is also well constrained within the model, as it is able to reproduce emission of the CO $J=6-5$ transition. We refer the reader to Leemker et al. (2023) for all details on the model (see their Appendix B). Figure 6.10 displays the gas density (in cm^{-3}) and the gas and dust temperature of the DALI model in the region of the dust trap. Below, we discuss how the timescales are calculated, whereas their implications on the emission are further discussed in Section 6.6.2.

We determine the turbulent vertical mixing timescale following the description provided by Xie et al. (1995) and Semenov et al. (2006), where the vertical mixing is set by the turbulent diffusion. The mixing timescale can be approximated as $t_{\text{mix}} \sim H^2/D_{\text{turb}}$, where H is the scale height (taken as $H = c_s/\Omega_K$)

and $D_{\text{turb}} = \alpha c_s^2 / \Omega_K$ is the turbulent diffusion coefficient (in $\text{cm}^{-2} \text{s}^{-1}$). Here, c_s and Ω_K denote the sound speed (taken to be isothermal) and the Keplerian angular frequency, respectively, while α parametrises the viscosity strength. We have determined the vertical mixing timescales for three commonly used values of α : 10^{-4} , 10^{-3} , 10^{-2} . For comparison, Yang et al. (2024) find turbulent α parameters, using the scale height ratio prescription of Youdin & Lithwick (2007) and assuming a grain size of $140 \mu\text{m}$ and a dust surface density of $\Sigma_d = 1 \text{ g cm}^{-2}$, ranging from 10^{-4} to 5×10^{-3} for gas-to-dust mass ratios of 3-100 in the IRS 48 disk. As the gas-to-dust mass ratio is expected to be much lower in the dust trap $\sim 0.009\text{-}0.04$ (Ohashi et al. 2020; van der Marel et al. 2016b; Leemker et al. 2023), the α parameter could be even higher. Therefore, our range of α values encapsulates the expected range well. We note that a higher α parameter, for example $\alpha = 0.1$, only changes our results by a factor of 10, i.e. the turbulent diffusion coefficient would increase by this factor, whereas the mixing timescale would decrease by this factor.

The desorption (k_d) and freeze-out (k_f) rates (in s^{-1}) are determined for each molecular species i following the equations given in Tielens & Allamandola (1987) (see also Walsh et al. 2010 and Leemker et al. 2021):

$$\begin{aligned} k_{d,i} &= v_0(i) \exp\left(-\frac{E_{b,i}}{k_B T_{\text{dust}}}\right) \\ &= \sqrt{\frac{2n_s E_{b,i}}{\pi^2 m_i}} \exp\left(-\frac{E_{b,i}}{k_B T_{\text{dust}}}\right) \end{aligned} \quad (6.1)$$

$$k_{f,i} = \sqrt{\frac{k_B T_{\text{gas}}}{m_i}} \pi a_{\text{grain}}^2 n(\text{grain}) S. \quad (6.2)$$

Here, T_{gas} and T_{dust} represent, respectively, the gas and dust temperature. $E_{b,i}$ denotes the binding energy (in K), while m_i is molecular mass. $v_0(i)$ is the characteristic vibrational frequency of species i , which has been approximated with the harmonic oscillator relation (Hasegawa et al. 1992). n_s is the number density of surface sites ($n_s = 1.5 \times 10^{15} \text{ cm}^{-2}$) and $n(\text{grain})$ is the grain number density of the DALI model. Additionally, a_{grain} is the grain size, which we have taken to be the average grain size in the DALI model (see Equation 14 of Facchini et al. 2017), and S is the sticking coefficient, assumed to be unity for temperatures below the desorption temperature. For our molecular species, we have taken binding energies of $E_{b,\text{SO}_2} = 3254 \text{ K}$ (Perrero et al. 2022), $E_{b,\text{CH}_3\text{OH}} = 4930 \text{ K}$ (Brown & Bolina 2007), and $E_{b,\text{H}_2\text{CO}} = 3260 \text{ K}$ (Noble et al. 2012; Penteado et al. 2017). We note that generally both the freeze-out and desorption of a molecular species cannot be described by a single binding energy, but that a range of values is more realistic, as the binding energy may depend, for example, on the composition of the ice (see, e.g., Minissale et al. 2022; Furuya 2024). However, we use the listed values to obtain the approximate timescales for our target species, as we expect these values to provide reasonable timescales with respect to one another. The timescales for both desorption and freeze-out were estimated by taking the inverse of their respective rates.

Finally, the photodissociation timescales are determined using the following

equation,

$$t_{\text{pd}} = \frac{1}{kG_0}. \quad (6.3)$$

Here, k is the photodissociation rate, which is taken to be the rate for a blackbody with a temperature of $T = 10,000$ K when scaled to have the same integrated intensity between 912 and 2000 Å as the interstellar radiation field (IRSF) and G_0 is the integrated intensity in the FUV band, normalised to the Draine field, as calculated within DALI (see, e.g. Figures C.1 and C.2 in van der Marel et al. 2021a). We have used the following values for k , $k_{\text{SO}_2} = 1.6 \times 10^{-9} \text{ s}^{-1}$, $k_{\text{CH}_3\text{OH}} = 5.3 \times 10^{-10} \text{ s}^{-1}$, $k_{\text{H}_2\text{CO}} = 9.6 \times 10^{-10} \text{ s}^{-1}$ (Heays et al. 2017).

6.6.2 Timescale comparisons

The determined timescales are shown in Figures 6.H.1, 6.H.2, and 6.H.3, respectively. As shown in these figures, we find (for all three molecules, SO_2 , CH_3OH , and H_2CO) $t_{\text{desorption}} < t_{\text{photodissociation}} < t_{\text{mixing}}$ in the higher emitting layers, whereas we see $t_{\text{photodissociation}} < t_{\text{mixing}} < t_{\text{desorption}}$ in the midplane.

As can be seen in the top panels of Figure 6.H.2, desorption occurs nearly instantaneous for emitting heights of >5 au ($z/r > 0.08$) for both SO_2 and H_2CO , where the temperature is higher than the freeze-out temperature. As the binding energy of CH_3OH is higher, these ices will desorb at higher temperatures (given the T in the exponential in Equation 6.1) and, therefore, at larger heights in the disk ($\gtrsim 10$ au, or $z/r \gtrsim 0.17$). As soon as the ices are brought up to this layer, the molecules will be liberated from the ices. On the other hand, the bottom panels show that re-freezing (i.e. due to downward vertical mixing, Kama et al. 2016) occurs on very long timescales ($>10^3$ years) in the emitting layers, but occurs, as expected, very fast (<100 years) in the midplane of the dust trap. The vertical mixing timescale, based on turbulent diffusion, is dependent on the chosen value of α . In Figure 6.H.1, we show the diffusion coefficients and corresponding timescales for values of $\alpha = 10^{-4}$, 10^{-3} , and 10^{-2} . At the location of the dust trap, these values yield mixing timescales of, respectively, $t_{\text{mixing}} \sim (5-8) \times 10^5$ years, $\sim (5-8) \times 10^4$ years, and $\sim (5-8) \times 10^3$ years. In addition, we find diffusion coefficients (see also the top panels in Figure 6.H.1) in the emitting layer of $D_{\text{turbulence}} \gtrsim 10^{15} \text{ cm}^2 \text{ s}^{-1}$ for the different values for α , which is consistent with the typical value of $D_{\text{turbulence}} \sim 10^{17} \text{ cm}^2 \text{ s}^{-1}$ for disks at distances of 100 au (Semenov et al. 2006).

Finally, Figure 6.H.3 shows the photodissociation timescales (top panels) and the distances the molecules can travel, under the assumption of a Keplerian orbit, before they are photodissociated (bottom panels). We find that the timescales are similar for all three molecules. For vertical heights of 10 to 15 au ($z/r \sim 0.17-0.25$), the layer from which CH_3OH and H_2CO are expected to emit, the timescales are less than a year. Closer to the midplane, however, the timescales become a year and longer. These photodissociation timescales are significantly shorter than the vertical mixing timescales. Given the expected icy origin of the molecular emission, it is, therefore, unlikely that turbulent diffusion is the correct explanation for vertical mixing, unless the turbulence in the dust trap is really high and larger values for the α -parameter ($\alpha > 0.01$) should have been adopted. Other mechanisms,

resulting favourably in faster timescales, need to be explored to further investigate the importance of vertical mixing and its dominant cause. One potential explanation is the vertical shear instability (VSI). The VSI is thought to more strongly mix the grains vertically than radially and should even be able to mix the grains into the warm molecular layers before molecules photodissociate (Flock et al. 2017, 2020).

As the photodissociation timescales are very short in the emitting layers (≤ 1 year), the molecules are not able to travel large distances before they are destroyed. However, for SO_2 , which lies deeper in the disk, there is a small layer above the midplane for the radial outer half of the dust trap, where the photodissociation timescales are long enough (> 1 year) that molecules can travel distances of > 10 au to half an orbit (red line in the bottom panels of Figure 6.H.3). This small layer of the dust trap agrees with our proposed emitting height based on the temperatures and the radial location as derived from the images. The larger distances the SO_2 molecules can travel in this layer may explain the azimuthal extent of the observed SO_2 transitions. For the higher proposed emitting layers of CH_3OH and H_2CO , the photodissociation timescales are too fast for the molecules to travel a significant distance. This can explain the azimuthally compact extent of the CH_3OH emission, but not that of H_2CO .

Instead, we propose that the azimuthal extent of H_2CO can be explained due to a significant contribution of gas-phase formation, which is efficient for H_2CO but not for CH_3OH . Gas-phase formation of H_2CO is efficient in regions with efficient (ice) desorption and photodissociation (Aikawa et al. 2002; Loomis et al. 2015; Carney et al. 2017), where atomic oxygen and radicals, such as CH_3 , CH_2 , and OH , are present. The formation occurs through the reactions of $\text{CH}_3 + \text{O} \rightarrow \text{H}_2\text{CO} + \text{H}$ and $\text{CH}_2 + \text{OH} \rightarrow \text{H}_2\text{CO} + \text{H}$ (Fockenberg & Preses 2002; Atkinson et al. 2006). Interestingly, both CH_3 and OH are photodissociation products of CH_3OH (Kayanuma et al. 2019), therefore, the gas-phase formation of H_2CO can be sustained by the photodissociation of, for example, CH_3OH , H_2O (which produces both OH and O), and CH_4 (which produces both CH_3 and CH_2). In relation to our derived temperatures, we infer higher temperatures ($T > 300$ K) for the centre of the dust trap and lower temperatures for the leading and trailing sides. This temperature difference may be explained by the ice-sublimated reservoir having a larger contribution in the centre, whereas the gas-phase formation reservoir may dominate more towards the sides of the dust trap. (Thermo-)chemical modelling efforts are required to further explore this scenario.

6.7 Conclusions and summary

With this work, we investigated the gas temperature of the asymmetric IRS 48 dust trap using the 13, 22, and 7 observed transitions of SO_2 , CH_3OH , and H_2CO through pixel-by-pixel analyses, respectively. In addition, we provided new insights into the potential emitting locations of these species and determined their major timescales: vertical mixing, desorption, freeze-out, and photodissociation. Our conclusions are summarised as follows:

- Our rotational diagram analysis resulted in temperatures of $T=54.8\pm 1.4$ K and $T=125.5^{+3.7}_{-3.5}$ K at the peak positions of the SO_2 $J=6_{4,2}-6_{3,3}$ and CH_3OH $J=13_{-1}-13_0$ transitions, respectively. In addition, our ratio maps for H_2CO yield temperatures in the range of $T_{\text{rot}}=150$ K to $T_{\text{rot}}=350$ K.
- The well-constrained rotational diagram of SO_2 suggests that the emission is thermalised, which occurs at gas densities of $n_{\text{gas}} > 10^8 \text{ cm}^{-3}$. These densities and temperatures can only be found in the deepest layers of the disk, near the midplane (heights of < 5 au or $z/r < 0.1$), suggesting that the SO_2 emission originates from this layer. In contrast, the rotational diagram of CH_3OH is characterised by a large scatter, which suggests sub-thermal excitation. Using non-LTE RADEX calculations we have shown that the gas densities for the derived temperatures at the locations of the dust trap are too low for the CH_3OH and H_2CO transitions to be thermalised. Therefore, our derived rotational temperatures underestimate the kinetic temperature.
- The resulting temperature map of SO_2 hints at a potential radial gradient, where the temperature decreases with increasing radial distance. The map of CH_3OH is, on the other hand, nearly uniform. We do not infer any hint of any possible vortex influencing the temperature structure of the dust trap. Given the rather low uncertainties of the derived temperatures, this influence, if present, is very small, that is, of the order of a few Kelvin. The maps for H_2CO show that the temperatures peak in the centre of the dust trap, while it decreases towards the leading and trailing edges.
- An additional analysis of the brightness temperature of the optically thick ^{13}CO $J=3-2$ and $J=6-5$ transitions, under the assumption that the emission is fully resolved, yield temperatures of $T_{\text{b},3-2} \sim 110$ K and $T_{\text{b},6-5} \sim 135$ K. Combining these temperatures with the inferred rotational temperatures of SO_2 , CH_3OH , and H_2CO , we propose that the CH_3OH and H_2CO emission must originate from the highest elevated layer, also accounting for the rotational temperatures underestimating the kinetic ones. The lower brightness temperature of the ^{13}CO suggests that this molecule originates from deeper in the disk, whereas SO_2 likely emits from deep inside the disk near the midplane.
- Our pixel-by-pixel analysis suggests that some of the transitions of H_2CO may be moderately optically thick at most, depending on the used temperature. In contrast, the previously low derived isotopic ratio observed for H_2CO (H_2 $^{12}\text{CO}/\text{H}_2$ $^{13}\text{CO} \sim 4$) suggests the emission must be highly optically thick. For this, it must originate from an emitting area parametrised by a beam radius of ~ 8 au. Such a small beam radius suggests that the H_2CO emission must originate from a small radial sliver at the inner edge of the dust trap. As the current observations do not radially resolve the emission, higher-resolution observations are required to fully constrain the optical depth of H_2CO .

- Finally, we have determined the turbulent vertical mixing, desorption, freeze-out, and photodissociation timescales at the location of the dust trap. The photodissociation timescales are too fast compared with the turbulent mixing timescales; therefore turbulent diffusion cannot explain the observed molecular emission. Other vertical mixing mechanisms should be explored to investigate its influence on the observable chemistry.
- The photodissociation timescale of SO_2 and the corresponding azimuthal distance the molecules can travel before they are destroyed, under the assumption of a Keplerian orbit, can explain the observed azimuthal extent (up to approximately a quarter of an orbit) of the molecular emission. The compact azimuthal extent of the CH_3OH is, on the other hand, consistent with the short photodissociation timescales in the expected emitting layer, higher up in the disk.
- Photodissociation occurs too fast to explain the azimuthal extent of H_2CO . Instead, we propose that the extent can be explained by an additional reservoir that follows from gas-phase reactions, which may be sustained by the photodissociation of CH_3OH and H_2O . The large inferred temperature range, $T_{\text{rot}} \sim 150\text{-}350$ K, can also be explained by these two reservoirs: the gas-phase reservoir dominates in the cold outer regions of the dust trap, whereas the reservoir resulting from the sublimation of ices mainly contributes to the hot central region.

Our findings highlight the power of line surveys and the need for multiple transitions of the same molecule for the characterisation of the emission in disks and an empirical determination of the gas temperature across and within the disk. Our analysis of the IRS 48 disk shows that the properties of the molecular emission are more complex than originally thought, with both the CH_3OH and H_2CO being sub-thermally excited and that the low isotopologue ratio for H_2CO can only be explained if optically thick emission originates from a small radial sliver. Higher spatial and spectral resolution observations are required to further investigate the emitting regions of each molecular species and, therefore, gain more insights into the radial width over which sublimation is important in the dust traps of transition disks.

Acknowledgements

The authors thank Haifeng Yang for sharing the high-resolution continuum observations of IRS 48. The authors acknowledge assistance from Allegro, the European ALMA Regional Center node in the Netherlands.

This paper makes use of the following ALMA data: 2013.1.00100.S, 2017.1.00834.S, 2019.1.01059.S, 2021.1.00738.S. ALMA is a partnership of ESO (representing its member states), NSF (USA) and NINS (Japan), together with NRC (Canada), NSTC and ASIAA (Taiwan), and KASI (Republic of Korea), in cooperation with the Republic of Chile. The Joint ALMA Observatory is operated by ESO, AUI/NRAO and NAOJ.

M.T. and E.F.v.D. acknowledge support from the ERC grant 101019751 MOLD-ISK. A.S.B is supported by a Clay Postdoctoral Fellowship from the Smithsonian Astrophysical Observatory. M.L. is funded by the European Union (ERC, UNVEIL, 101076613). Views and opinions expressed are however those of the author(s) only and do not necessarily reflect those of the European Union or the European Research Council. Neither the European Union nor the granting authority can be held responsible for them. E.F.v.D. acknowledges support from the Danish National Research Foundation through the Center of Excellence “InterCat” (DNRF150). L.E. acknowledges financial support from the Science and Technology Facilities Council (grant number ST/X001016/1). L.K. is funded by UKRI guaranteed funding for a Horizon Europe ERC consolidator grant (EP/Y024710/1). Support for C.J.L. was provided by NASA through the NASA Hubble Fellowship grant No. HST-HF2-51535.001-A awarded by the Space Telescope Science Institute, which is operated by the Association of Universities for Research in Astronomy, Inc., for NASA, under contract NAS5-26555. S.N. is grateful for support from Grants-in-Aid for JSPS (Japan Society for the Promotion of Science) Fellows Grant Number JP23KJ0329, and MEXT/JSPS Grants-in-Aid for Scientific Research (KAKENHI) Grant Numbers JP20H05845, JP20H05847, JP23K13155, and JP24K00674. C.W. acknowledges financial support from the Science and Technology Facilities Council and UK Research and Innovation (grant numbers ST/X001016/1 and MR/T040726/1).

The project leading to this publication has received support from ORP, that is funded by the European Union’s Horizon 2020 research and innovation programme under grant agreement No 101004719 [ORP].

This work also has made use of the following software packages that have not been mentioned in the main text: NumPy, SciPy, Astropy, Matplotlib, pandas, IPython, Jupyter (Harris et al. 2020; Virtanen et al. 2020; Astropy Collaboration et al. 2013, 2018, 2022; Hunter 2007; pandas development team 2020; Pérez & Granger 2007; Kluyver et al. 2016).

Appendix

6.A SO₂, CH₃OH, and H₂CO transitions

Table 6.A.1: Detected transitions of SO₂ (top part), CH₃OH (middle part), and H₂CO (bottom part).

Molecule	Transition ^(a)	Frequency [GHz]	E _{low} [K]	E _{up} [K]	A _{ul} [s ⁻¹]	g _{low}	g _{up}	Int. flux [mJy beam ⁻¹ km s ⁻¹]	
SO ₂ ^(b)	18 _{4,14} -18 _{3,15}	338.3059931	180.6	196.8	3.3×10^{-4}	37	37	16.1±2.7	
	13 _{2,12} -12 _{1,11}	345.3385377	76.4	93.0	2.4×10^{-4}	25	27	58.9±2.0	
	5 _{3,3} -4 _{2,2}	351.2572233	19.0	35.9	3.4×10^{-4}	9	11	70.5±2.6	
	14 _{4,10} -14 _{3,11}	351.8738732	119.0	135.9	3.4×10^{-4}	29	29	34.9±2.6	
	12 _{4,8} -12 _{3,9}	355.0455169	94.0	111.0	3.4×10^{-4}	25	25	44.7±2.2	
	10 _{4,6} -10 _{3,7}	356.7551899	72.7	89.8	3.3×10^{-4}	21	21	49.1±2.7	
	13 _{4,10} -13 _{3,11}	357.1653904	105.8	123.0	3.5×10^{-4}	27	27	39.6±2.5	
	15 _{4,12} -15 _{3,13}	357.2411932	132.5	149.7	3.6×10^{-4}	31	31	35.0±2.9	
	11 _{4,8} -11 _{3,9}	357.3875795	82.8	100.0	3.4×10^{-4}	23	23	48.8±2.3	
	8 _{4,4} -8 _{3,5}	357.5814486	55.2	72.4	3.1×10^{-4}	17	17	47.6±2.5	
	9 _{4,6} -9 _{3,7}	357.6718206	63.5	80.6	3.2×10^{-4}	19	19	46.9±2.5	
	7 _{4,4} -7 _{3,5}	357.8924422	47.8	65.0	2.9×10^{-4}	15	15	50.3±2.3	
	6 _{4,2} -6 _{3,3}	357.9258478	41.4	58.6	2.6×10^{-4}	13	13	55.3±2.7	
	CH ₃ OH ^(b)	3 ₃ -4 ₂ (E)	337.135853	45.5	61.6	1.6×10^{-5}	9	7	20.0±3.4
		7 ₀ -6 ₀ (E)	338.124488	61.9	78.1	1.7×10^{-4}	13	15	67.5±4.1
7 ₋₁ -6 ₋₁ (E)		338.344588	54.3	70.6	1.7×10^{-4}	13	15	66.7±3.8	
7 ₋₆ -6 ₋₆ (E)		338.430975	237.7	253.9	4.5×10^{-5}	13	15	9.7±2.5	
7 ₋₆ -6 ₋₆ (A)		338.442367	242.5	258.7	4.5×10^{-5}	13	15	14.3±3.2	
7 ₆ -6 ₆ (E)		338.442367	242.5	258.7	4.5×10^{-5}	13	15	14.3±3.2	
7 ₋₅ -6 ₋₅ (E)		338.456536	172.8	189.0	8.3×10^{-5}	13	15	22.6±3.2	
7 ₅ -6 ₅ (E)		338.475226	184.8	201.1	8.4×10^{-5}	13	15	33.4±3.4	
7 ₅ -6 ₅ (A)		338.486322	186.6	202.9	8.4×10^{-5}	13	15	18.6±3.1	
7 ₋₅ -6 ₋₅ (A)		338.486322	186.6	202.9	8.4×10^{-5}	13	15	18.6±3.1	
7 ₋₄ -6 ₋₄ (E)		338.504065	136.6	152.9	1.1×10^{-4}	13	15	42.1±3.6	
7 ₄ -6 ₄ (E)		338.530257	144.7	161.0	1.2×10^{-4}	13	15	43.8±3.8	
7 ₋₃ -6 ₋₃ (E)		338.559963	111.5	127.7	1.4×10^{-4}	13	15	48.4±3.6	
7 ₃ -6 ₃ (E)		338.583216	96.5	112.7	1.4×10^{-4}	13	15	56.9±3.8	
7 ₂ -6 ₂ (A)		338.639802	86.5	102.7	1.6×10^{-4}	13	15	57.3±3.4	
2 ₂ -3 ₁ (A)		340.141143	28.3	44.7	2.8×10^{-5}	7	5	13.2±2.8	
13 ₋₁ -13 ₀ (A)		342.729796	211.0	227.5	4.2×10^{-4}	27	27	64.0±3.0	
14 ₋₁ -14 ₀ (A)		349.106997	243.4	260.2	2.2×10^{-4}	29	29	58.7±3.0	
1 ₁ -0 ₀ (A)		350.905100	0.0	16.8	3.3×10^{-4}	1	3	51.2±3.5	
9 ₅ -10 ₄ (E)		351.236479	223.6	240.5	3.6×10^{-5}	21	19	25.3±2.8	
13 ₀ -12 ₁ (A)	355.602945	194.0	211.0	1.3×10^{-4}	25	27	61.9±3.3		
15 ₋₁ -15 ₀ (A)	356.007235	278.2	295.3	2.3×10^{-4}	31	31	49.6±3.0		
H ₂ CO ^(b)	5 _{1,5} -4 _{1,4} (o)	351.768645	45.6	62.5	12.0×10^{-4}	27	33	265.7±5.8	
	5 _{0,5} -4 _{0,4} (p)	362.736048	34.9	52.3	13.7×10^{-4}	9	11	188.9±7.1	
	5 _{2,4} -4 _{2,3} (p)	363.945894	82.1	99.5	11.6×10^{-4}	9	11	167.4±8.1	
	5 _{4,2} -4 _{4,1} (p)	364.103249	223.3	240.7	5.0×10^{-4}	9	11	53.6±8.1	
	5 _{4,1} -4 _{4,0} (p)	364.103249	223.3	240.7	5.0×10^{-4}	9	11	53.6±8.1	
	5 _{3,3} -4 _{3,2} (o)	364.275141	140.9	158.4	8.9×10^{-4}	27	33	169.9±7.6	
	5 _{3,2} -4 _{3,1} (o)	364.288884	140.9	158.4	8.9×10^{-4}	27	33	175.8±8.5	

Notes. ^(a): The listed transitions consist of the quantum configuration as given in the LAMDA files: J_{K_a, K_c} for SO₂, J_K for CH₃OH, and J_{K_p, K_o} for H₂CO.

^(b): The beam sizes for the SO₂ and CH₃OH transitions are on the order of 0.33"×0.26", whereas those for H₂CO are on the order of 0.48"×0.38".

Table 6.A.2: All removed transitions due to blending and/or noise.

Molecule	Transition ^(a)	Frequency [GHz]	E _{up} [K]	A _{ul} [s ⁻¹]	Reason
SO ₂	20 _{1,19} -19 _{2,18}	338.6118103	198.9	2.9×10 ⁻⁴	Blend
	28 _{2,16} -28 _{1,27}	340.3164059	391.8	2.6×10 ⁻⁴	Noise
	29 _{3,27} -30 _{0,30}	342.634969	421.4	2.5×10 ⁻⁶	Noise
	5 _{5,1} -6 _{4,2}	345.1489708	75.1	9.8×10 ⁻⁶	Noise
	10 _{6,4} -11 _{5,7}	350.862756	138.8	4.4×10 ⁻⁵	Noise
	17 _{4,14} -18 _{1,17}	355.1864962	180.1	2.6×10 ⁻⁶	Noise
	15 _{7,9} -16 _{6,10}	356.0406442	230.4	6.4×10 ⁻⁵	Noise
CH ₃ OH	7 ₆ -6 ₆ (E)	338.40461	243.8	4.5×10 ⁻⁵	Blend
	7 ₀ -6 ₀ (A)	338.408698	65.0	1.7×10 ⁻⁴	Blend
	7 ₁ -6 ₁ (E)	338.614936	86.1	1.7×10 ⁻⁴	Blend
	7 ₂ -6 ₂ (E)	338.721693	87.3	1.6×10 ⁻⁴	Blend
	7 ₋₂ -6 ₋₂ (E)	338.722898	90.9	1.6×10 ⁻⁴	Blend
	7 ₋₄ -6 ₋₄ (A)	338.512632	145.3	1.1×10 ⁻⁴	Blend
	7 ₄ -6 ₄ (A)	338.512644	145.3	1.1×10 ⁻⁴	Blend
	7 ₋₂ -6 ₋₂ (A)	338.512853	102.7	1.6×10 ⁻⁴	Blend
	7 ₃ -6 ₃ (A)	338.540826	114.8	1.4×10 ⁻⁴	Blend
	7 ₋₃ -6 ₋₃ (A)	338.543152	114.8	1.4×10 ⁻⁴	Blend
4 ₀ -3 ₋₁ (E)	350.687662	36.3	8.7×10 ⁻⁵	Blend	

Notes. ^(a): The listed transitions consist of the quantum configuration as given in the LAMDA files: J_{K_a, K_c} for SO₂ and J_K for CH₃OH.

6.B Line profiles

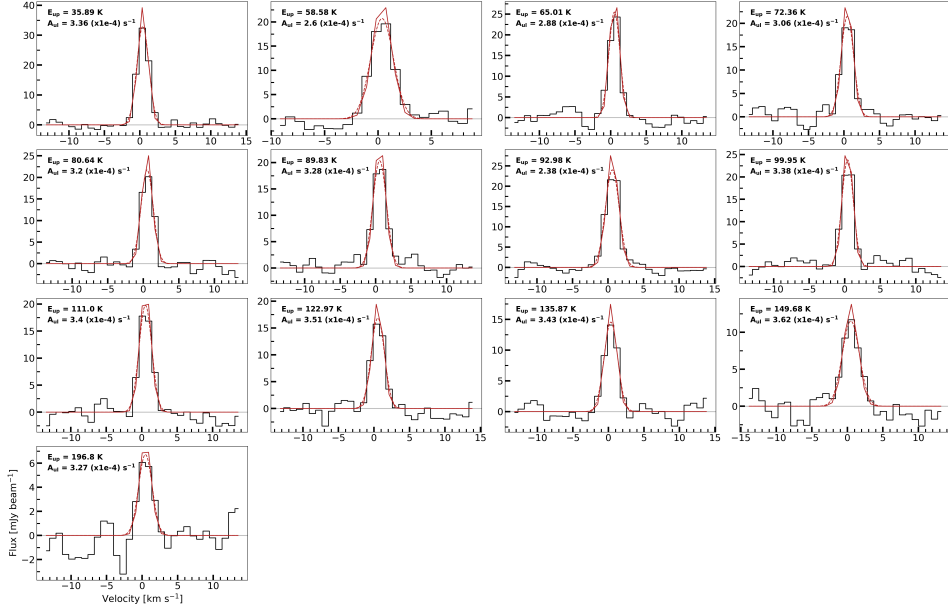


Figure 6.B.1: Line profiles of the detected SO₂ transitions at the peak flux location of the 6_{4,2}-6_{3,3} transition. The red line displays the fitted Gaussian line profile at the resolution of the spectrum (0.9 km s⁻¹), whereas the red dashed line shows the Gaussian line profile at a higher resolution. The lines are ordered based on their upper level energies (E_{up}).

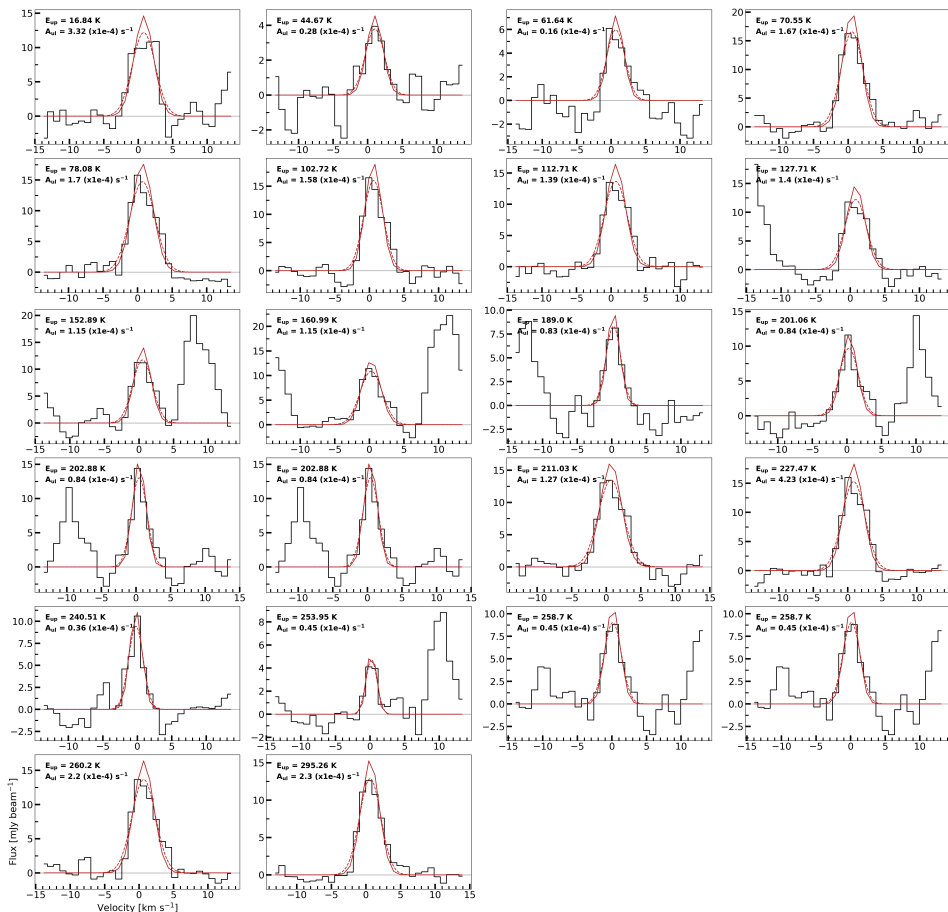


Figure 6.B.2: Similar as Figure 6.B.1, but for the detected CH₃OH transitions at the peak flux position of the 13₋₁-13₀ transition.

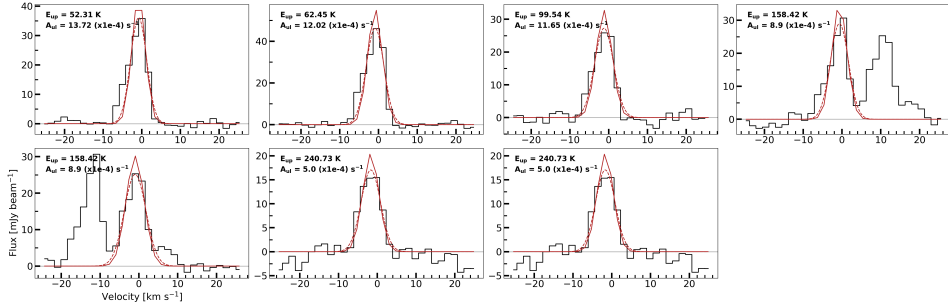


Figure 6.B.3: Similar as Figure 6.B.1, but for the detected H₂CO transitions at the peak flux position of the 5_{0,5}-4_{0,4} transition.

6.C H₂CO line ratios

$5_{3,3-4_{3,2}}/5_{1,5-4_{1,4}}$: for the ortho-transition line pair, we see a clear spot (bright yellow) in the ratio map, where the ratios exceed those from the RADEX calculations. Therefore, the temperature derived for these pixels is limited by the upper range of 500 K. Ratios involving transitions with higher upper level energies are, therefore, needed to infer the temperature for these pixels. For the pixels for which the ratio does not exceed those from the calculations, we generally find temperatures, for both gas densities (and, therefore, across the vertical height of the disk), of the order of ~ 150 -300 K. These are similar to and slightly higher than the derived temperatures for the disk-integrated fluxes of ~ 200 K inferred by van der Marel et al. (2021a) (red line in the left panels). The peak pixel of the 5_{0,5}-4_{0,4} transition is contained within the region of pixels that exceed the ratios from the RADEX calculations and the temperature is, therefore, not well constrained.

$5_{2,4-4_{2,3}}/5_{0,5-4_{0,4}}$: for this first para-transition line pair we find that the inferred ratios from the observations exceed the ratios obtained from the RADEX calculations. This is likely the result of the low upper level energies of the transitions involved, 100 K and 52 K, respectively, which are not sensitive to the higher temperatures ~ 150 -350 K as probed by the ortho line pair.

$5_{4,2-4_{4,1}}/5_{0,5-4_{0,4}}$: for the second line pair, we find very similar results to the single ortho line pair. We find a spot in the centre of the maps that is limited by the temperature sensitivity of the lines. In addition, we find temperatures, for the other pixels, of the order of 150 K to 300 K for both gas densities. Those temperatures are, again, similar to those inferred for the disk-integrated fluxes by van der Marel et al. (2021a). Once more, the peak position of the 5_{0,5}-4_{0,4} transition falls within the range for which the temperature is not well constrained.

$5_{4,2-4_{4,1}}/5_{2,4-4_{2,3}}$: for this final line pair, which involves the ratio of the transitions with the highest upper level energies (241 K and 100 K, respectively), we find similar results as for the ratio ($5_{4,2-4_{4,1}}/5_{0,5-4_{0,4}}$) above, although we are able to provide better constraints on the temperature for a larger number of pixels. The temperature across the disk, especially when considering the gas den-

sity of $n_{\text{H}_2}=10^8 \text{ cm}^{-3}$, is of the order of 150 K to 350 K. Again, this is similar to or slightly higher than the disk-integrated one.

6.D Observations-to-model ratios and uncertainty maps

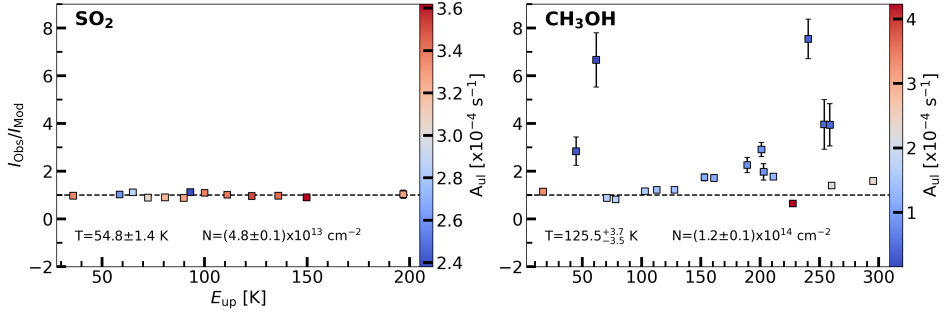


Figure 6.D.1: Intensity ratios between the observations and the model for SO_2 (left) and CH_3OH (right). The horizontal bar indicates a value of unity. The colour bar indicates the value for A_{ul} of the transitions.

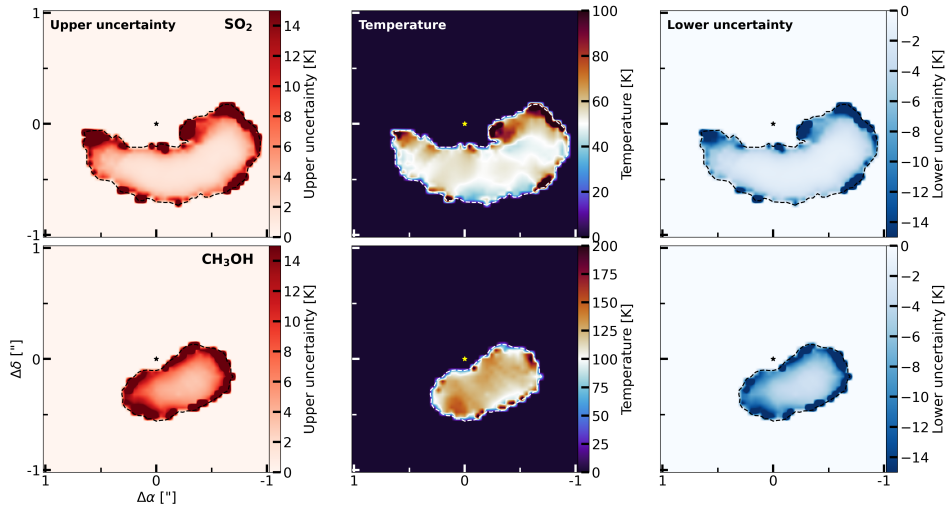


Figure 6.D.2: Uncertainty maps for the derived rotational temperatures. The left panels displays the upper uncertainties, while the right panels show the lower uncertainties. The derived temperature maps themselves are shown in the middle panels. The top row corresponds to SO_2 , whereas the bottom row displays those for CH_3OH .

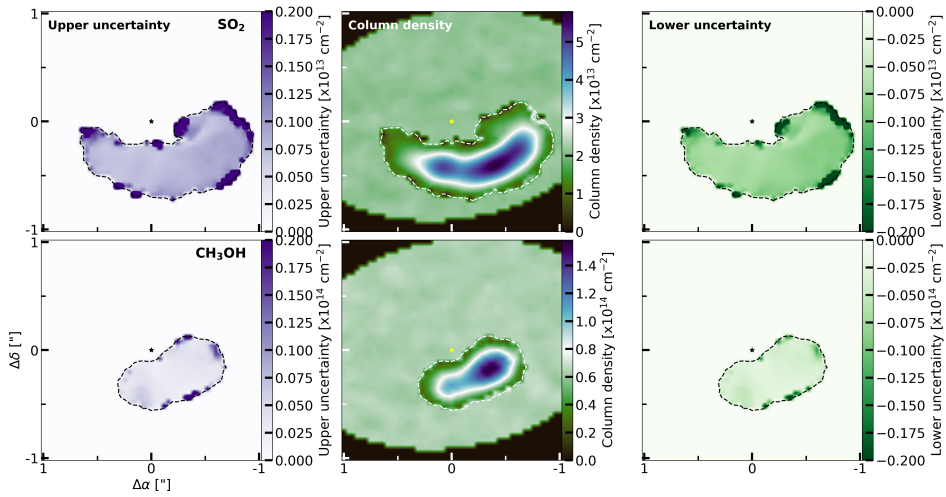


Figure 6.D.3: Similar as Figure 6.D.2, but for the column density maps.

6.E H₂CO moment-0 maps

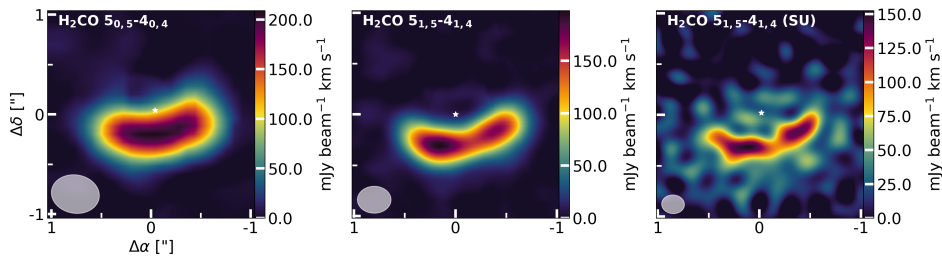


Figure 6.E.1: Moment-0 maps of the H₂CO $J=5_{0,5}-4_{0,4}$ transition from the low resolution observations of van der Marel et al. (2021a) (left) and the $J=5_{1,5}-4_{1,4}$ transition from the higher resolution observations of Booth et al. (2024b), imaged both with Briggs weighting (robust of 0.5, middle panel) and superuniform weighting (right). The white star indicates the approximate location of the host star, while the resolving beam is shown in the lower left corner.

6.F Observed transitions per pixel

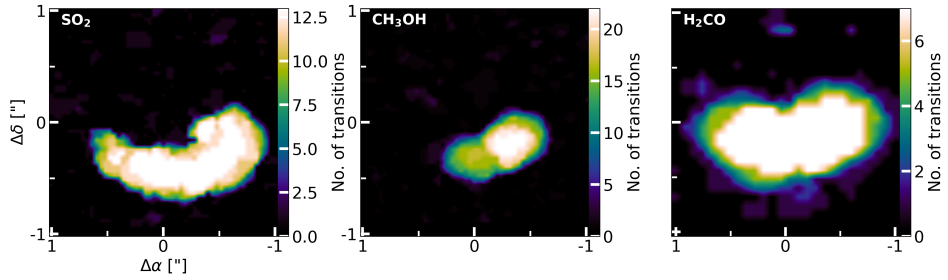


Figure 6.F.1: Number of detected transitions for SO₂ (left), CH₃OH (middle), and H₂CO (right) across the dust trap.

6.G Channel maps

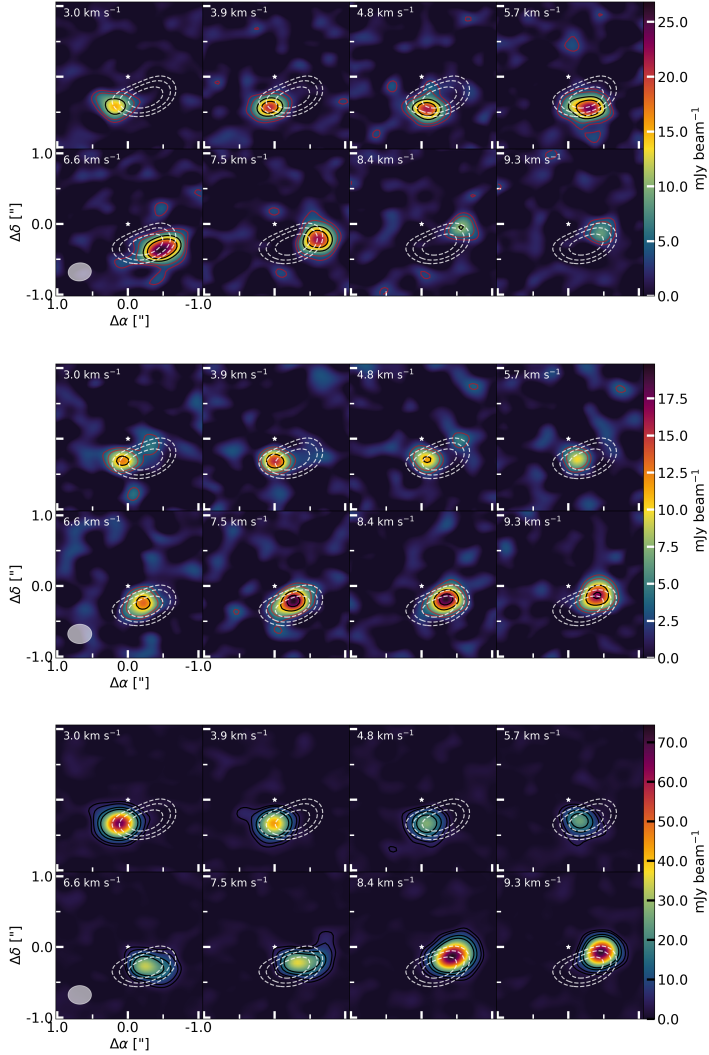


Figure 6.G.1: Channel maps of SO_2 (top row), CH_3OH (middle row), and H_2CO (bottom row) over the 3.0-9.3 km s^{-1} range. The solid contours indicate the 3 \times and 5 \times (both in red) and the 10 \times and 15 \times (both in black) RMS levels of the emission, whereas the white dashed contours indicate the location of the continuum emission. The white star indicates the location of the host star, whereas the grey ellipse denotes the resolving beam.

6.H Timescale figures

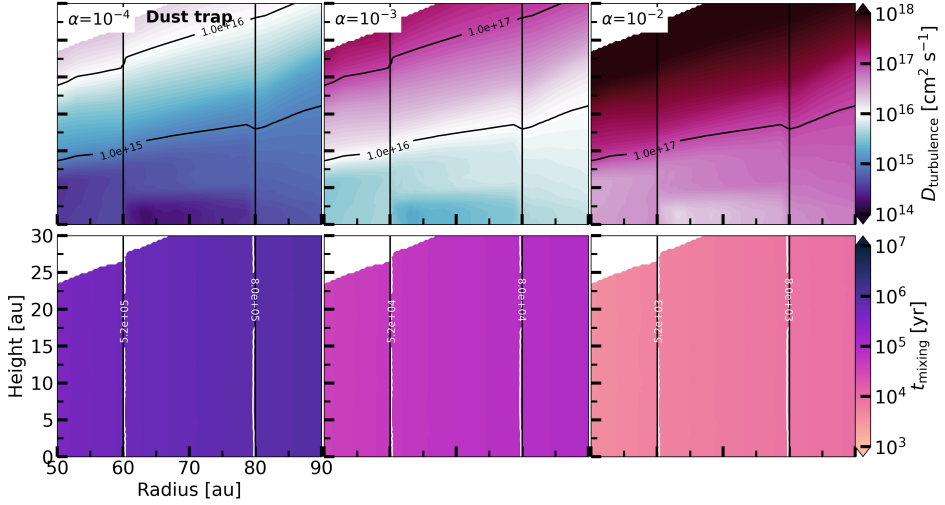


Figure 6.H.1: The turbulent diffusion coefficient (in $\text{cm}^2 \text{s}^{-1}$, top panel) and the vertical mixing timescale (bottom panel) according to the DALI model of Leemker et al. (2023). The coefficient and timescale have been calculated for α values of 10^{-4} (left panels), 10^{-3} (middle panels), and 10^{-2} (right panels).

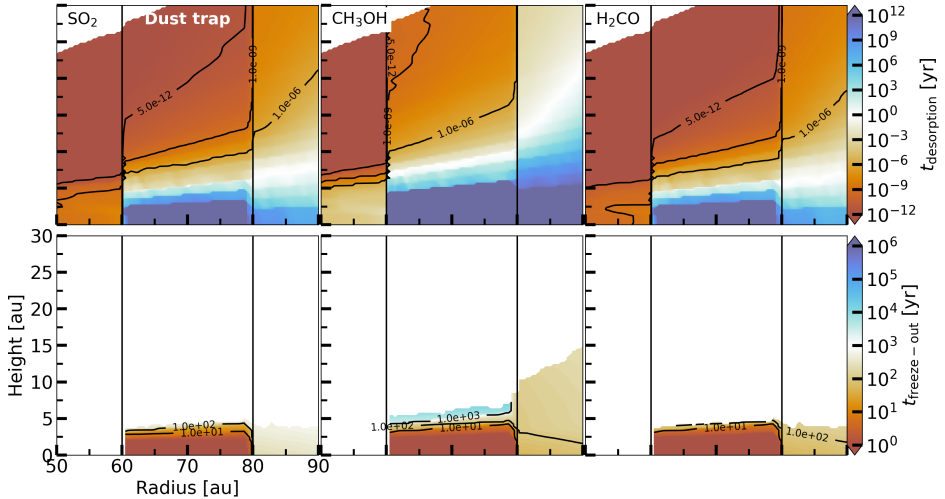


Figure 6.H.2: The desorption (top panels) and freeze-out (bottom panels, only showing $t_{\text{freeze-out}} < t_{\text{desorption}}$) timescales for SO_2 (left panels), CH_3OH (middle panels), and H_2CO (right panels) following the DALI model of Leemker et al. (2023).

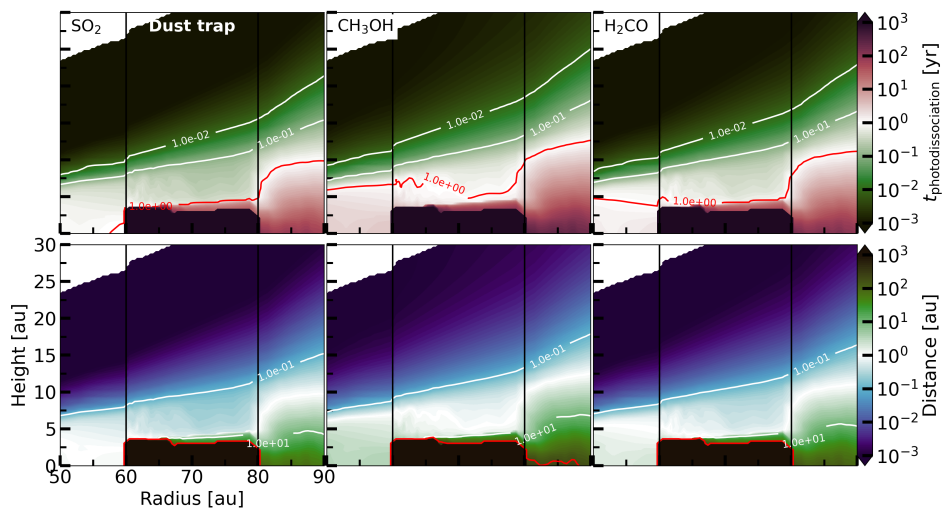


Figure 6.H.3: The photodissociation timescales (top panels) and the azimuthal distances (by Keplerian motion) the molecules can travel before they get dissociated (bottom panels) based on the DALI model of Leemker et al. (2023). From left to right, the timescales and distances are shown for SO₂, CH₃OH, and H₂CO, respectively.

The asymmetric carbon-rich
chemistry of the
planet-forming disk of
HD 142527 triggered by late
infall

M. Temmink, E. F. van Dishoeck, A. S. Booth, N. van der Marel, M.
Benisty, M. R. Hogerheijde

Submitted to A&A

Abstract

The planet-forming disk of HD 142527 is known for its azimuthally asymmetric dust trap, shadows, and spiral arms. In this work, we use new observations of the Atacama Large Millimeter/submillimeter Array to investigate the molecular composition and to determine the ongoing chemical processes and the origin of its asymmetric chemistry, and to infer possible effects of dust continuum obscuration. The observations cover a wide variety of molecular species over a large frequency range, enlarging the known molecular inventory of this system. Strikingly, the emission of H_2CO , CN , and C_2H is dominated by spiral-like features peaking in the southern region of the disk, opposite to the large dust trap, while no relation is found between the observed asymmetries and the shadows seen in the scattered light due to the misaligned inner disk. We attribute these features to late infalling, atomic carbon-rich material that locally enhances the C/O-ratio and, subsequently, facilitates the gas-phase formation of these species. Azimuthal offsets between the peak emission of H_2CO and that of CN and C_2H are possibly due to a delay of a few hundred years in the gas-phase formation of H_2CO . As opposed to the emission of H_2CO , CN , and C_2H , the emission of C^{17}O and the $\text{HCO}^+ J=1-0$ transition is aligned with the large dust trap, likely due to an enhancement in the surface density. Differences between the two observed C^{17}O transitions may be due to freeze-out and dust obscuration effects. The latter effect is not expected to affect molecular emission at 3 millimetres, given the lower optical depth of the dust trap. The four observed transitions of CS display different azimuthal extents and strengths, with the lines with lower upper level energies appearing more ring-like. An analysis of the ^{13}CO brightness temperature yields no significant temperature variations across the disk's azimuth. Therefore, we propose that the observed CS transitions trace two different reservoirs. A cold reservoir that resides on a Keplerian orbit and a second, hotter reservoir of CS that is facilitated by the infalling material and resides in a higher atmospheric layer of the disk. A single weak transition of SO is observed, which may be explained by weak shocks induced by the spirals observed in the scattered light that liberate sulphur. Future higher-resolution, multi-line observations of species such as H_2CO , CS, CN, and C_2H are needed to investigate the role and importance of late infalling material in setting the chemical composition of planet-forming disks.

7.1 Introduction

As giant planets accrete their atmospheres from the gaseous reservoirs of planet-forming disks, understanding the molecular composition and, in particular, the processes that set this composition is of great importance for our understanding of planet formation. The Atacama Large Millimeter/submillimeter Array (ALMA) yields unique insights to study the chemistry in the cold outer disks with unprecedented sensitivity and resolution. Recent programs have unveiled the chemical inventories in both individual disks (see, for example Qi et al. 2013; Öberg et al. 2015; Bergin et al. 2016; Walsh et al. 2016; Cleeves et al. 2018; Kastner et al. 2018; Loomis et al. 2018; Semenov et al. 2018; Facchini et al. 2021; Booth et al. 2024a,b, 2025; Rampinelli et al. 2024) and larger samples (see, for example, Le Gal et al. 2019; Öberg et al. 2021; Booth et al. 2026). However, the dominant processes that set the observable chemistry are still far from being fully understood.

One disk that can improve our understanding of the dominant processes in planet-forming disks is that around the young star HD 142527. This system is located at a distance of 159.26 pc (Gaia Collaboration et al. 2023) and consists of a young F6 star (Fairlamb et al. 2015), an M-dwarf companion (Biller et al. 2012; Lacour et al. 2016; Balmer et al. 2022; Stolker et al. 2024), and a massive planet-forming disk ($M_{\text{gas}} = (1.6 \pm 0.6) \times 10^{-2} M_{\odot}$; Temmink et al. 2023). The mass of the host star is, however, uncertain, as recent papers yield a range of stellar masses from 1.69 M_{\odot} to 2.40 M_{\odot} (Fukagawa et al. 2006; Verhoeff et al. 2011; Arun et al. 2019; Francis & van der Marel 2020). In this work, we assume the recent value from Vioque et al. (2026) ($M_{*} \sim 2.24 M_{\odot}$) as their astrometry results also yield a mass of the M-dwarf companion ($\sim 158 M_{\text{Jup}}$ or $\sim 0.15 M_{\odot}$) that is dependent on the mass of the host star. The importance of this moderately inclined ($i \sim 28^{\circ}$) disk stems from the various key features it hosts (see Figure 7.1): an asymmetric dust trap (Fujiwara et al. 2006; Ohashi 2008; Casassus et al. 2013), spiral arms in both the scattered light and the ^{12}CO molecular emission (Avenhaus et al. 2014; Christiaens et al. 2014; Garg et al. 2021), and shadows due to a misaligned inner disk (Marino et al. 2015b; Bohn et al. 2022). The hydrodynamical models of Price et al. (2018) show that all these features can be attributed to the M-dwarf companion. A thorough investigation of the molecular emission may reveal unique insights into the importance of these features in setting the observable chemistry.

Disks with asymmetries, both in the dust and in the gas, are unique laboratories to study the role of the dust in setting the observable chemistry. This has become most apparent in the case of Oph-IRS 48 (A0-type star), the most asymmetric system known to date (van der Marel et al. 2013), where the molecular emission, except CO, is approximately co-spatial with the dust continuum emission located at ~ 60 au (van der Marel et al. 2021a; Booth et al. 2021a; Brunken et al. 2022; Leemker et al. 2023; Booth et al. 2024b). As the emission of both simple and more complex species is co-spatial with the continuum, the dust trap has been proposed to be an ice trap, where radial and vertical transport leads to the sublimation of the icy mantles coating the dust grains. In addition, a more recent work also discusses the role of photodissociation and the subsequent gas-phase reactions involving the dissociation products in setting the observable molecular

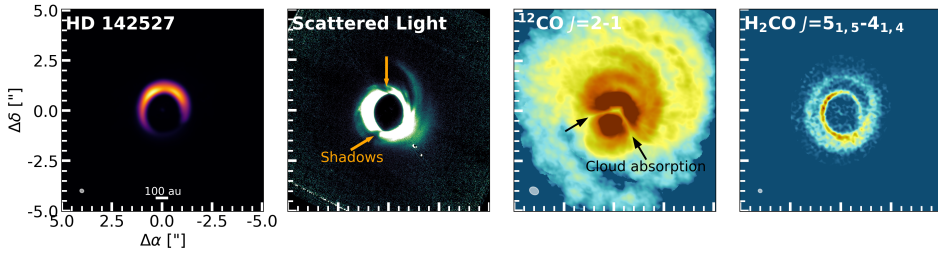


Figure 7.1: Continuum emission (left), scattered light (left central; H -band with SPHERE/IRDIS, Hunziker et al. 2021), peak intensity map of the $^{12}\text{CO } J=2-1$ transition (right central; see also Christiaens et al. 2014; Garg et al. 2021), and integrated intensity map of the $\text{H}_2\text{CO } J=5_{1,5}-4_{1,4}$ transition (right) within the disk of HD 142527. The ^{12}CO map has been imaged using a square-root scaling scheme for the colour map. Additionally, the scattered light image has been scaled using the radial-distance squared, accounting for the drop off in stellar flux. We note that a few imaging artefacts are visible in the scattered light image. The arrows point, respectively, to the shadows observed in the scattered light and the dark emission lanes due to cloud absorption in the ^{12}CO image.

composition (Temmink et al. 2025a).

Aside from dust traps, asymmetries may also be related to decoupled dust dynamics surrounding a binary-carved cavity (Price et al. 2018), azimuthal variations in the gas density, the temperature, and the incident ultraviolet (UV) radiation. A change in the temperature and UV radiation follows most likely from shadowing effects, which are often observed in the scattered light (see Benisty et al. 2023 for a recent review) and are attributed to misaligned inner disks and/or warps (Marino et al. 2015b; Bohn et al. 2022). Recent modelling work has shown that an azimuthally varying temperature structure yields asymmetric column densities (Young et al. 2021). Extended structures, such as spirals and streamers, may also influence the observable chemistry and locally enhance the emission, for example, through shocks. Recently, two studies suggest a potential connection between observed SO emission and the spiral arms in the disks of AB Aur (Speedie et al. 2025) and MWC 758 (Zagaria et al. 2025). Additionally, Ilee et al. (2017) studied the influence of gravitational instabilities on the chemistry in protoplanetary fragments, finding that certain molecular species (e.g., H_2O , H_2S , SO) are abundant in the fragments, while others (such as CO, CH_4 , CN, CS, and H_2CO) are more abundant in spiral shocks. Streamers (or late infalling material), on the other hand, may replenish the disk with fresh material that locally alters the elemental and molecular abundances, leading to molecular asymmetries.

In this work, we use new ALMA observations to study the molecular emission of HD 142527 and to expand upon the known molecular inventory (Casassus et al. 2013; van der Plas et al. 2014; Temmink et al. 2023). Using these observations, we propose various scenarios that may explain the observed molecular morphologies and try to answer the question of what sets the asymmetric molecular emission in the disk of HD 142527.

This paper is structured as follows: the observations and self-calibration process are described in Section 7.2, while we report our (weak) detected molecular species and non-detections in Section 7.3. Section 7.4 contains the analysis and discussion of the observed molecular species, including various scenarios to explain the origins of the emission. Finally, we summarise our findings and conclusions in Section 7.5.

7.2 Observations and self-calibration

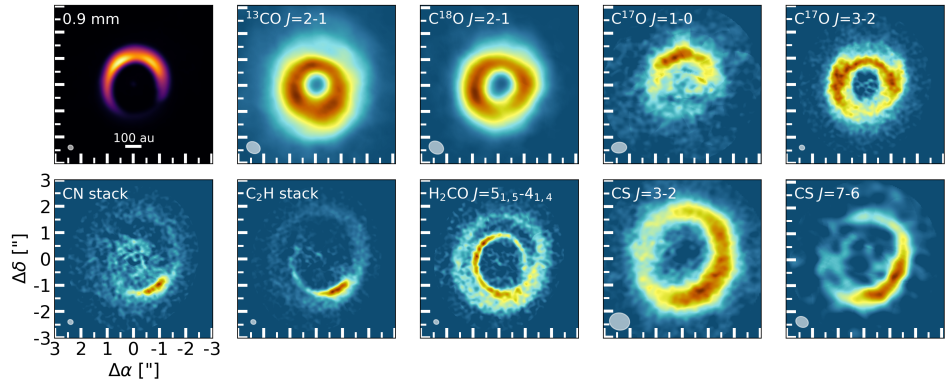


Figure 7.2: Integrated intensity maps of the dust continuum at 1.3 mm and key molecular species detected in the disk of HD 142527. To increase the S/N -ratio of the respective integrated intensity maps, the images of the $C^{17}O$ $J=1-0$, C_2H and CN were created by stacking the detected transitions (two, four, and three transitions, respectively). Additionally, the displayed images of $C^{17}O$ $J=1-0$ and CS $J=2-1$ transitions were created using a robust value of 2.0. The resolving beams are shown in the lower-left corner of each image.

The disk of HD 142527 was observed in two separate Cycle 10 and 11 ALMA programs, 2023.1.00628.S and 2024.1.00446.S (PI: M. Temmink). The first program covers two spectral settings in Band 3 and one spectral setting in Band 4, while the second program consists of one spectral setting in Band 7. Both programs have been taken in the C3 and C6 configurations, allowing for high spatial resolution observations of ~ 0.15 - $0.20''$. The spectral windows in Band 3 have resolutions of 70.56 kHz and 564.45 kHz, resulting in velocity resolutions of, respectively, ~ 0.22 km s $^{-1}$ (at 97.98 GHz) and ~ 1.96 km s $^{-1}$ (at 86.43 GHz). Those in Band 4 have spectral resolutions of 141.113 kHz (~ 0.29 km s $^{-1}$ at 146.95 GHz) and 564.453 kHz (~ 1.17 km s $^{-1}$ at 144.52 GHz). Finally, the Band 7 spectral windows have resolutions of 141.113 kHz and 1.129 MHz, yielding velocity resolutions of ~ 0.12 km s $^{-1}$ at 349.36 GHz and ~ 0.96 km s $^{-1}$ at 351.55 GHz, respectively. The observations were reduced with the provided pipeline scripts using the specified Common Astronomy Software Applications (CASA; McMullin et al. 2007; CASA Team et al. 2022). Self-calibration and imaging have, on the other hand,

been carried out with CASA versions 6.4.1.12 and 6.5.4. Further details on the observations can be found in Table 7.A.1. Furthermore, we make use of the following archival programs: 2011.1.00318.S (PI: M. Fukagawa), 2011.0.00465.S (PI: S. Casassus), 2012.1.00631.S (PI: M. Fukagawa), 2013.1.00305.S (PI: S. Casassus), 2015.1.00805.S (PI: S. Casassus), and 2015.1.01137.S (PI: T. Tsukagoshi).

To increase the signal-to-noise ratio (S/N -ratio) of the observations, we employ similar self-calibration techniques as used in various successful ALMA programs (Andrews et al. 2018; Czekala et al. 2021; Loomis et al. 2025; Leemker et al. 2025). To summarise, we performed the self-calibration routine on the short-baseline observations before combining the short- and long-baseline observations and performing the routine on the combined dataset. If an observation consists of multiple execution blocks, a single round of phase-only self-calibration was performed on each execution block before the execution blocks were aligned (if needed) and combined. The self-calibration routine consists of multiple rounds of phase-only self-calibration, using solution intervals given in the weblog of the observations, followed by a single round of phase-amplitude self-calibration (`SOLINT='inf'`). During the rounds of phase-only self-calibrations, the models used in the self-calibration process were created by cleaning the emission down to a conservative 6σ noise level. For the phase-amplitude round, the model was created by cleaning down to a 1σ noise level to include as much flux as possible in the model for the amplitude calibration. All rounds of self-calibration (phase-only and phase-amplitude) were performed for the short-baseline observations of all spectral settings and the combined data of the Band 7 observations. For the combined datasets, no self-calibration was performed for the Band 3 spectral settings, as many solutions were flagged. Following the same reasoning, self-calibration of the combined Band 4 observations was stopped after three rounds of phase-only self-calibration. Table 7.B.1 lists the starting and final S/N -ratio of the continuum emission in all spectral settings.

We used the CASA task `TCLEAN` to extract spectra and search for molecular emission of known transitions in the Cologne Database for Molecular Spectroscopy (CDMS; Müller et al. 2001, 2005). Before imaging, we performed a continuum subtraction using the `UVCONTSUB`-task of CASA, selecting line-free regions and using a fit-order of unity. The images were created using the ‘Briggs’ weighting scheme and robust parameters of $+0.5$ in the case of strong detections, and $+2.0$ in the case of weak detections. As the velocity resolution changes between the different spectral settings and programs, the molecular transitions were imaged with resolutions of 0.30 km s^{-1} in Bands 3 and 4, and 0.15 km s^{-1} in Band 7. For transitions located in continuum spectral windows, which were observed in the ‘Frequency Domain Mode’, we used velocity resolutions of 2.0 km s^{-1} , 1.20 km s^{-1} , and 1.00 km s^{-1} .

7.3 Molecular emission

In case of a detected molecular species, we used a Keplerian mask (see Teague 2020) to clean the emission down to a level of $3\times$ the noise in the dirty image. The Keplerian mask, using an outer radius of $2.5''$ for the molecular emission, was defined using a central mass of $2.39 M_{\odot}$ (host star plus companion mass; Vioque et al. 2026), a distance of 159.26 pc, and a disk inclination and position angle of, respectively, 28.3° and 162.5° (see Section 7.4.1 for more details). Furthermore, we used the Python package GOFISH (Teague 2019b) to confirm the detection of weak molecular emission. By accounting for the Keplerian rotation of the disk, GOFISH can improve the S/N -ratio for lines by aligning and stacking spectra taken from different sides of the disk (see also Yen et al. 2016). Weakly detected species and non-detections are discussed in Section 7.C.1.

7.3.1 Detected molecular species and azimuthal distributions

Figure 7.2 displays the key detected molecular species for our analysis, while 7.C.1 contains the expanded molecular inventory of the disk around HD 142527. Using the new ALMA observations, we report strong detections of 6 molecular species: two transitions of $C^{17}O$, two additional transitions of CS, one transition of SO, three transitions of CN, four transitions of C_2H , and one additional transition of H_2CO . Molecular transitions of $C^{17}O$, SO, CN, and C_2H are detected for the first time in the disk of HD 142527. Furthermore, we report the detection of one additional transition of HCO^+ ($J=1-0$) that was found in archival Band 3 observations. The integrated intensity (or moment-0) maps of these transitions are shown, together with previously observed molecular species (Casassus et al. 2013; van der Plas et al. 2014; Temmink et al. 2023), in Figure 7.C.1. Further information on the observed transitions, their line properties (all taken from CDMS), and peak fluxes are listed in Table 7.C.1.

As can be seen in both Figure 7.2 and Figure 7.C.1, the molecular emission, except for the more abundant CO isotopologues, is dominated by asymmetric features. However, these molecular asymmetries are distributed differently throughout the disk. While the emission of $C^{17}O$ and the HCO^+ $J=1-0$ transition is co-spatial with the continuum emission, the emission of CS is most prominent in the south-western side of the disk. Even though the emission of H_2CO , CN, and C_2H peaks in a similar region as the CS transitions, their morphology displays a spiral-like feature. We discuss these different asymmetric features and their potential origins in Section 7.4.3.

While the molecular emission is dominated by asymmetries, we highlight that many molecular transitions display evidence for Keplerian motion. Although weak, these rings are visible in the molecular emission of the CS transitions (except for the $J=10-9$ transition), the stacked images of CN and C_2H transitions, and that of the H_2CO $J=5_{1,5}-4_{1,4}$ transition. This suggests that, even though the asymmetries dominate the emission, the molecules are fully distributed along the disk's azimuth and are (partially) captured on Keplerian orbits.

7.4 Analysis and discussion

7.4.1 Inclination and position angle

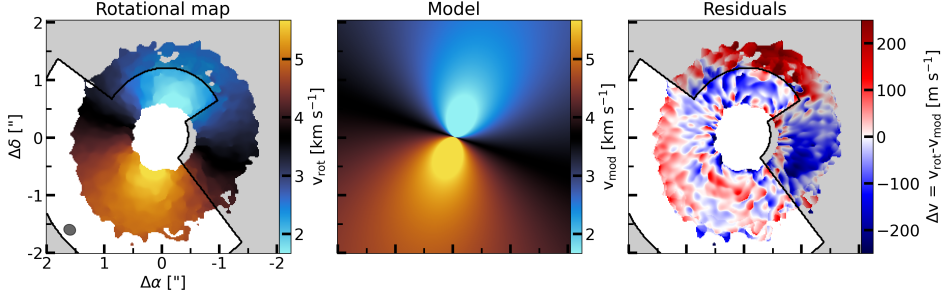


Figure 7.3: Rotational velocity map, resulting model, and residuals of the $\text{C}^{17}\text{O } J=3-2$ transition. The used mask is shown in black. The greyed-out regions have not been used in the fitting process.

Using the $\text{C}^{17}\text{O } J=3-2$ transition, we reanalyse the inclination, position angle, and system velocity (v_{lsr}) for the disk of HD 142527. As the C^{17}O is a rare isotope, this transition has the benefit of the emission originating from close to the disk’s midplane. Therefore, we fit the rotational velocity maps, created with the BETTERMOMENTS code (clipping all $<5\sigma$ data; Teague & Foreman-Mackey 2018), using the thin disk model implemented in eddy (Teague 2019a). As the inclination and stellar mass are degenerate, we fix the stellar mass to the total summed mass of the host star and the companion ($M_{\text{tot}}=2.39 M_{\odot}$).

While fitting the rotational velocities, we noticed strong super-Keplerian residuals in the northern side of the disk. The western side of the disk was, on the other hand, dominated by sub-Keplerian residuals (see the right panel of Figure 7.3). To ensure these regions did not impact the Keplerian models, we excluded them, through trial and error, when creating the rotational velocity maps. Figure 7.3 shows the full rotational map, model and residuals for completion. This fit yields an inclination of $i=28.3^{\circ}$, a position angle of $PA=162.5^{\circ}$, and a velocity of $v_{\text{lsr}}=3.67 \text{ km s}^{-1}$. Uncertainties are found to be very small, well below $<1\%$, for all parameters. The derived value for the inclination closely represents that found by Fukagawa et al. (2013) ($i \sim 27^{\circ}$ and $PA \sim 160^{\circ}$), yet it is significantly lower compared to that derived by Bohn et al. (2022), following from their lower assumed stellar mass of $1.75 M_{\odot}$.

7.4.2 Brightness temperature

One potential explanation for the different observed molecular distributions could be azimuthal variations in the temperature. We investigate the brightness temperature of the $^{13}\text{CO } J=2-1$ transition. Since the ^{12}CO emission is dominated by the various spirals and affected by the continuum absorption (Christiaens et al. 2014;

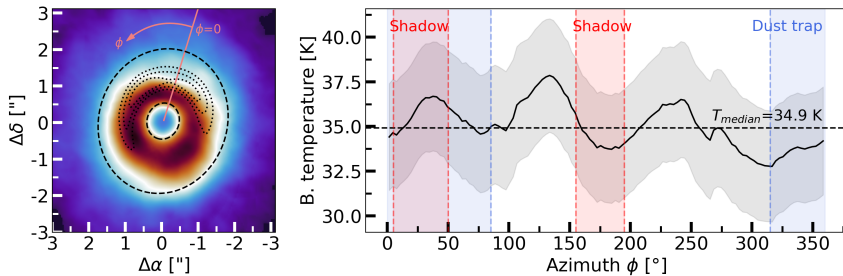


Figure 7.4: Brightness temperature map of the ^{13}CO $J=2-1$ transition (left panel) and the azimuthal peak temperature profile between 0.5" and 2.0" (right panel). The location of the shadows is indicated by the red shaded areas, whereas the location of the strongest emission of the dust continuum is indicated by the blue shaded areas.

Garg et al. 2021), and the C^{18}O emission was found to be moderately optically thick ($\tau_{\text{C}^{18}\text{O}} \sim 0.7$; Temmink et al. 2023), the optically thick ^{13}CO emission yields the best opportunity to directly study the gas temperature across the disk's radial and azimuthal extent.

The left panel of Figure 7.4 shows the brightness temperature map, while the azimuthal peak temperature profile, taken between radial distances of 0.5" and 2.0" with azimuthal increments of $\delta\phi=3^\circ$, is shown in the right panel. Uncertainties on the integrated intensity map have been estimated following the method described in Leemker et al. (2022). The red shaded areas indicate approximately the location of the shadows seen in the scattered light, while the blue shaded areas indicate the azimuthal increment in which the continuum is the strongest. We find that the temperature of the ^{13}CO emission is fairly constant, with maximum differences of ~ 5 K, and we obtain a median peak brightness temperature of $T_{\text{med},^{13}\text{CO}} \sim 34.9$ K.

7.4.3 Molecular asymmetries and structures

In the following sections, we discuss the various asymmetries and substructures seen in the molecular emission. We tackle different subsets of molecular species and propose scenarios that may explain the origins of these morphologies.

7.4.3.1 Enhanced surface density: C^{17}O and HCO^+

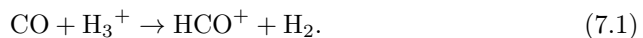
The emission of both C^{17}O transitions is strikingly coincidental with the dust trap, which is in contrast with that of the main isotopologues of CO, which are distributed throughout the disk's full azimuth. As opposed to the (moderately) optically thick emission from the main isotopologues, the C^{17}O emission is very likely optically thin, assuming that the isotopic ratio of $^{18}\text{O}/^{17}\text{O} \sim 3.6$ for the local interstellar medium (Wilson 1999) holds locally in the disk. While optically thick emission traces the gas temperature (see Section 7.4.2), the optically thin C^{17}O emission will trace the surface density of the gas. As the emission is coincidental

with the continuum emission, this suggests that there could be an enhancement in the surface density at the location of the dust trap.

There is one striking difference between the emission of the $\text{C}^{17}\text{O } J = 1 - 0$ and $J=3-2$ transitions. While the overall weaker $J=1-0$ transition is only located at the exact location of the dust trap, the stronger $J=3-2$ is more azimuthally extended and, crucially, lacks emission in the northern side of the disk. Two potential explanations for this decrement could be considered: continuum oversubtraction effects or freeze-out. Continuum oversubtraction effects can arise in two different ways (Boehler et al. 2017; Weaver et al. 2018; Nazari et al. 2023). First, in the case of optically thick line emission, the molecules block the thermal continuum emission originating from the disk's midplane. In this case, continuum oversubtraction techniques remove line emission instead of continuum emission. Second, in the case of optically thin line emission but optically thick continuum emission, the optically thick continuum will block emission originating from the disk's backside. This second scenario can effectively remove up to half the line flux. As the disk has a relatively low inclination ($i=28.3^\circ$), the decrement in emission may be the result of this second scenario. The lack of a such a decrement in the $J=1-0$ transition may be due to a difference in optical depth between the Band 3 (3 millimetre) and Band 7 (0.9 millimetre) continuum observations. Guidi et al. (2022) showed that the continuum emission of the disk around HD 163296 is still optically thin ($\tau < 1$) in the Band 3 observations, while it became optically thick ($\tau > 1$) in Band 7. Detailed modelling of the dust optical depth at both 3 mm and 0.9 mm is required to confirm this notion.

Freeze-out, on the other hand, is possible in the cold outer regions of the disk, where the dust temperature has dropped down to approximately 20 K or lower, the freeze-out temperature of CO. Temmink et al. (2023) have proposed that the CO snowline is located at the outer edge of the dust trap ($R_{\text{outer}} > 200$ au or $> 1.25''$) following the weak detection of the $\text{DCO}^+ J=4-3$ and a RADMC-3D model. Higher-resolution and sensitivity observations of DCO^+ and, ideally, N_2H^+ are needed to further confirm this notion. We further note that the brightness temperature of the band 7 continuum observations peaks at $T_{\text{b},0.9\text{mm}} \sim 29$ K (see Figure 7.D.1), which is consistent with a temperature of 20 K being located at the outer edge of the dust trap. Therefore, we propose that both scenarios - continuum optical depth at higher frequencies and freeze-out - or a combination of the two, can be viable explanations for the observed decrement in the emission of the $\text{C}^{17}\text{O } J=3-2$ transition.

Similar to the C^{17}O emission, the $\text{HCO}^+ J=1-0$ transition is co-spatial with the dust continuum. A simple explanation can be found in the main gas-phase formation reaction governing the HCO^+ abundances in disks (Herbst & Klemperer 1973; Leemker et al. 2021):



This reaction involves gas-phase CO and, therefore, the same enhanced surface density as seen for the C^{17}O transitions may be the cause of the $\text{HCO}^+ J=1-0$ transition being co-spatial with the dust continuum.

One clear difference between the $\text{HCO}^+ J=1-0$ and $J=4-3$ transitions is that

the former is dominated by emission that peaks co-spatially at the location of the dust trap, while the latter reveals emission along the disk’s full azimuth. However, the $J=4-3$ transition is dominated by a bright central spot, which was also seen for the $J=8-7$ transition (Temmink et al. 2023). Casassus et al. (2013) proposed that this bright spot is connected to the outer disk and must be the result of inflowing material. It is, however, also possible that the emission connecting the bright inner spot with the outer disk is due to beam smearing effects. Furthermore, HCO^+ emission from the central regions can potentially be affected by X-ray flares, where gas-phase cations (including HCO^+) are most strongly affected, and their abundance can be temporarily enhanced (Waggoner & Cleeves 2022; Waggoner et al. 2023). To confirm the role of a potential X-ray flare in temporarily increasing the HCO^+ abundance, the molecular emission may need to be investigated per observation scan and/or re-observing the $J=4-3$ transition may reveal the lasting emission of this bright spot.

7.4.3.2 Spirals or late infall: H_2CO , C_2H , and CN

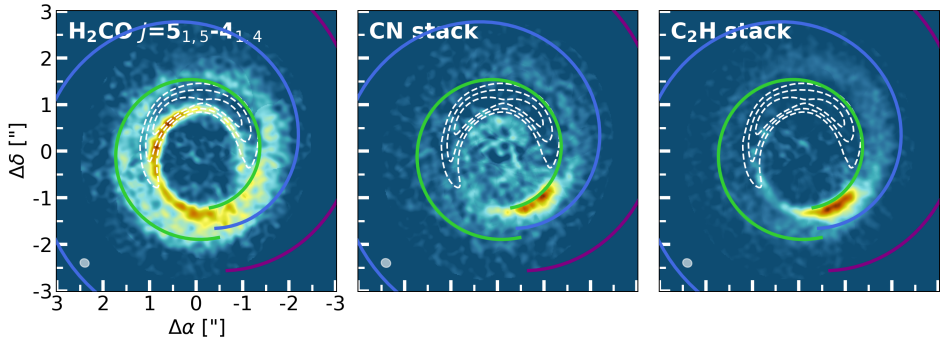


Figure 7.5: Integrated intensity maps of the $\text{H}_2\text{CO } J=5_{1,5}-4_{1,4}$ transition and the stacked CN and C_2H transitions. Overlaid are the traced spiral features from the ^{12}CO brightness temperature channel maps (see Appendix 7.F). The white, dashed contours indicate the continuum emission at flux levels of 25%, 50%, and 75%.

We now turn to the distribution of H_2CO , C_2H , and CN, all of which peak opposite to the dust trap. Since temperature and surface density variations are excluded, another process must be at work. A possible explanation lies in the presence of spiral arms, of which large-scale structures have already been identified in the emission of ^{12}CO and ^{13}CO (Christiaens et al. 2014; Garg et al. 2021; Wölfer et al. 2023). However, similar structures were not seen in the emission of other molecular species, with, for example, van der Plas et al. (2014) reporting that no counterpart of these spiral structures was seen in the CS $J=7-6$ and HCN $J=4-3$ transitions. Our new ALMA observations create a new perspective, as spiral-like features are clearly visible in the emission of the $\text{H}_2\text{CO } J=5_{1,5}-4_{1,4}$ transition, the stacked transitions of C_2H and CN (see Figure 7.5), and even the selected channel maps of the stacked $\text{c-C}_3\text{H}_2$ transitions (see bottom row of Figure 7.C.3). Figure

7.E.1 displays the channel maps of the $\text{H}_2\text{CO } J=5_{1,5}-4_{1,4}$ transition together with overlaying contours of the dust continuum. These channels reveal that the spiral-like features are real and not an artefact due to, for example, the optically thick continuum. Additionally, we have distinguished between the contribution from the disk and that of the spiral-like feature. Using these new observations as guidance, we report that weak hints for similar structures can also be seen in the CS $J=7-6$ and the HCN and $\text{HCO}^+ J=4-3$ transitions (see Figure 7.C.1).

The first question to address is whether the observed spiral-like features in the emission of the H_2CO , CN, and C_2H transitions align with the known spiral arms observed in the $^{12}\text{CO } J=2-1$ transition. To test the alignment, we have traced the spiral arms in the ^{12}CO (see Section 7.F for more details) and overlaid the resulting spirals on top of the integrated intensity maps of H_2CO , CN, and C_2H (see Figure 7.5). The traced spirals appear to align rather well with those seen in the other molecular species. Offsets between the observations may be due to the lower spatial resolution of the ^{12}CO emission.

As the molecular emission now appears to be directly intertwined with the presence of these spiral features, another question must be posed: how are these structures influencing the observable chemistry in the disk of HD 142527? Both CN and C_2H are linked to UV-chemistry, following the need for atomic carbon in their gas-phase formation pathways. Similarly, CN is also known to be the photodissociation product of HCN (Sternberg & Dalgarno 1995). A direct role of UV-driven chemistry in setting the observable emission morphologies is, however, not evident. As the molecular emission is found at a large distance (>150 au) with respect to the host star, and small dust grains are present along the disk's entire azimuth (see Figure 7.1), we consider it unlikely that UV radiation dominates the observable chemistry at one specific location outside of the shadows.

Aside from UV-chemistry, a locally varying carbon-to-oxygen ratio (C/O-ratio) can also affect the formation efficiency of C_2H , CN, and $\text{c-C}_3\text{H}_2$. Models have shown that a strong reservoir of hydrocarbons, such as C_2H , requires a C/O-ratio larger than unity (Bergin et al. 2016; Kama et al. 2016; Miotello et al. 2019). The emission of CN is similarly impacted by an increasing C/O-ratio. However, the effects are weaker compared to C_2H : when increasing the C/O-ratio from 0.3 to 1.5, the C_2H abundance was shown to increase up to an order of magnitude, while that of CN only increases by a factor of two (Cazzoletti et al. 2018; Miotello et al. 2019). As our observed peak fluxes of C_2H are stronger than those of CN (see Table 7.C.1), a locally enhanced C/O-ratio may be the cause of the observed emission.

We propose that the observed spiral-like features are the result of late infall material or streamers replenishing the disk with fresh atomic carbon. Lesur et al. (2015) has shown that infalling material can yield long-lived spiral arms in planet-forming disks, and can result in efficient radial transport of angular momentum. Another scenario could be a locally depleted oxygen abundance following the freeze-out of oxygen-bearing species. This latter scenario is less likely, as the majority of the millimetre-sized dust grains are trapped on the opposite side of the disk. It must be noted that the southern side of the disk is not completely void of large dust grains and that the small dust grains are distributed along the

disk's full azimuth. Therefore, freeze-out cannot be fully ruled out, but it is alone unlikely to explain the observed C₂H and CN emission peaking at a specific azimuthal location.

The detection of H₂O-ice confirms that freeze-out takes place in the disk of HD 142527 (Honda et al. 2009; Min et al. 2016; Tazaki et al. 2021). Furthermore, Min et al. (2016) used observations of the *Herschel* Photodetector Array Camera and Spectrometer (PACS) instrument to conclude that 80% of the available oxygen atoms must be locked up in the H₂O-ice. Since the RADMC-3D model of Temmink et al. (2023) yields dust temperatures of 40-50 K at the location of the dust trap, it is not surprising that oxygen-bearing species such as H₂CO (binding energy of $E_{\text{bind}} > 3300$ K; Penteado et al. 2017; Minissale et al. 2022) and H₂O and CH₃OH (both have binding energies of $E_{\text{bind}} \gtrsim 5600$ K; Fraser et al. 2001; Penteado et al. 2017; Minissale et al. 2022) will be frozen out. The presence of a spiral-like feature in the H₂CO emission is, in that case, surprising, unless the infalling material or streamer is able to release ices through a weak shock. While a shock may explain the presence of H₂CO, it does not explain the emission morphology of another known shock-tracer, SO (van Gelder et al. 2021), which has a lower binding energy of $E_{\text{bind}} \gtrsim 2800$ K (Penteado et al. 2017) and, therefore, should also be released from the grains. The SO emission is further discussed in Section 7.4.3.5.

We note that H₂CO, unlike CH₃OH, can also form efficiently in the gas. The reactions involve atomic oxygen, OH, and the radical hydrocarbons CH₃ and CH₂ (Fockenberg & Preses 2002; Atkinson et al. 2006):



Since both formation routes involve a hydrocarbon, a locally increased C/O-ratio will enhance the CH₃ and CH₂ abundances and may, therefore, boost the gas-phase formation of H₂CO. Since the spiral-like features are strongest in the emission of H₂CO, CN, and C₂H, while weak signatures can be found in the emission of the other carbon-bearing species HCN and CS, we consider the local enhancement of the C/O-ratio, following from infalling material replenishing the disk with fresh atomic carbon and potentially other carbon-rich material, as a viable scenario for the observed emission morphology of these molecular species.

To summarise this section, we see spiral-like features in the emission of H₂CO, CN, C₂H, and c-C₃H₂, and we propose that similar features are weakly visible in those of the previously detected CS $J=7-6$ and HCN and HCO⁺ $J=4-3$ transitions. We consider it most likely that these features are due to an influx of fresh atomic carbon, syphoned onto the disk by late infalling material or streamers along the spiral arms seen in the ¹²CO emission. This influx of carbonaceous material locally increases the C/O-ratio and facilitates the gas-phase formation of hydrocarbons, CN, and even that of H₂CO. We consider an increasing C/O-ratio following a depleted oxygen abundance to be less likely, as this would suggest that the H₂CO emission may trace sublimation due to the infalling material creating a weak shock at its impact location on the disk.

To further support the scenario of infalling, atomic carbon-rich material, we

highlight that (atomic) carbon-rich streamers may not be uncommon in young stellar objects (YSOs). For example, carbon-bearing molecules, such as C_2H , $\text{c-C}_3\text{H}_2$, and HC_3N , have been detected in the streamers of the Class 0 YSO Per-emb-2 (Taniguchi et al. 2024) and the Class 1 YSO L1489 IRS (Tanious et al. 2024, 2025).

7.4.3.3 H_2CO formation timescale delay

As shown in Figure 7.5, the $\text{H}_2\text{CO } J=5_{1,5}-4_{1,4}$ is azimuthally offset from the peak location of the CN and C_2H emission. We propose that this may be due to a delay in the gas-phase formation of H_2CO through Equations 7.2 and 7.3. To investigate the potential delay timescale, Figure 7.G.1 displays the deprojected integrated intensity maps of the stacked C_2H and $\text{H}_2\text{CO } J=5_{1,5}-4_{1,4}$ emission. In both images, we have visually indicated the peak location of the C_2H emission, which has a radial extent between 215 and 275 au and an azimuthal extent of 210° to 255° or $1/8^{\text{th}}$ of the disk's azimuth. We further note that H_2CO emission is stronger outside this defined box. At these radial locations, the Keplerian orbital timescales of the disk are $\tau_{215\text{au}}=2041$ and $\tau_{275\text{au}}=2952$ years. By taking the average of $1/8^{\text{th}}$ of these timescales - thus, accounting for the azimuthal extent of the C_2H - the peak H_2CO emission is delayed by $\tau_{\text{H}_2\text{CO, delay}}=312$ years.

To investigate whether this difference is due to a delay in the gas-phase formation of H_2CO , we have calculated the formation timescale of Reactions 7.2 and 7.3 for different gas densities ($n(\text{H}_2)$) and fractional abundances ($X(\text{CH}_x/\text{H}_2)$) of CH_3 and CH_2 , the expected limiting reactants. Using the Kinetic Database for Astrochemistry (KIDA; Wakelam et al. 2012), we retrieve an average reaction rate coefficient of $1.1 \times 10^{-10} \text{ cm}^3 \text{ s}^{-1}$ (at a temperature of $T=298 \text{ K}$) for Equation 7.2 and a reaction rate coefficient of $3.0 \times 10^{-10} \text{ cm}^3 \text{ s}^{-1}$ (at temperatures of $T=10\text{--}280 \text{ K}$) for Equation 7.3. Since the temperature dependence of these radial-atom reactions is expected to be weak, we expect that these rate coefficients hold for the disk. Furthermore, we explore the reaction rates for gas densities of 10^6 to 10^9 cm^{-3} , as the gas density of the disk depends on the vertical emitting layer of the disk. Similarly, we use strongly enhanced values of 10^{-6} to an expected value of 10^{-10} for the fractional abundance. A thermochemical model of a massive disk, such as HD 142527, suggests that fractional abundance of $\sim 10^{-8}$ and $\sim 10^{-10}$ can be reached for, respectively, CH_2 and CH_3 in their respective emitting layers (M. Leemker, priv. comm.). A formation timescale of the same order of magnitude as the above derived $\tau_{\text{H}_2\text{CO, delay}}=312$ years can be reached for any combination of $n(\text{H}_2)=10^Y \text{ cm}^{-3}$ and $X(\text{CH}_x/\text{H}_2)=10^{-Y}$, where Y is the same number.

Since lower densities are expected for emitting layers higher up in the disk, this suggests that enhanced fractional abundances are needed for these layers. As the above suggested scenario of infalling material is a local effect, it is possible that the fractional abundances, similarly to the C/O-ratio, are locally enhanced. Therefore, we deem it likely that the azimuthal differences between the $\text{H}_2\text{CO } J=5_{1,5}-4_{1,4}$ peak emission and the stacked CN and C_2H can be due to a lag in the H_2CO gas-phase formation timescales. Furthermore, the lag may also be introduced by the slow formation rate of the precursors CH_2 and CH_3 . In particular, CH_3 forms

through the, in comparison with the formation routes of C_2H and CN , slow radiative association of $\text{CH}_3^+ + \text{H}_2$ that forms CH_5^+ and the subsequent dissociative recombination into neutral hydrocarbons (Millar & Nejad 1985). This analysis shows that time-dependent chemistry can play an important role in setting the observable molecular composition in planet-forming disks and that systems with (molecular) asymmetries and/or signatures of infalling material yield the unique opportunity to study these processes.

7.4.3.4 Azimuthal or vertical variations: CS

Including the new Cycle 10 and 11 observations, four molecular transitions of CS have been detected in the disk of HD 142527 (compared to van der Plas et al. 2014 and Temmink et al. 2023): $J=2-1$ ($E_{\text{up}} \sim 7$ K), $J=3-2$ ($E_{\text{up}} \sim 14$ K), $J=7-6$ ($E_{\text{up}} \sim 66$ K), and $J=10-9$ ($E_{\text{up}} \sim 129$ K). As shown in the second row of Figure 7.C.1, the emission morphology changes between the transitions. While all four transitions exhibit the strongest emission in the western side of the disk, the $J=2-1$ and $J=3-2$ are much more ring-like. The $J=7-6$ transition shows weak hints of the spiral-like feature that is also seen in the emission of H_2CO , C_2H , and CN , and the $J=10-9$ transition is potentially co-spatial with the bright emission spot seen for C_2H and CN .

Models by Fedele & Favre (2020) suggest that the main CS emitting layer is located below that of ^{13}CO . As the brightness temperature of ^{13}CO was found to be fairly constant along the disk's azimuth, with maximum variations of ~ 5 K (see Figure 7.4), we do not expect the differences between the CS transitions to be due to azimuthal temperature variations.

As the $J=7-6$ transition appears to exhibit weak signatures of the spiral-like feature, and the $J=10-9$ transition may be co-spatial with the bright emission spot seen in the C_2H and CN transitions, we propose that we are observing two vertically distinct CS reservoirs. The first reservoir comes from deep inside the disk, closer to the midplane and below the ^{13}CO emitting layer, where the emission follows a Keplerian orbit. The emission of the $J=2-1$ and $J=3-2$ transitions, and part of the $J=7-6$ transition, originates from this reservoir. The second, hotter reservoir resides higher up in the disk and is facilitated by the infalling material or streamer. Gas-phase formation reactions, such as the neutral-neutral reactions $\text{CH} + \text{S} \rightarrow \text{CS} + \text{H}$ or $\text{HS} + \text{C} \rightarrow \text{CS} + \text{H}$ (Vidal et al. 2017), may play a role in forming this second reservoir. Additional formation routes include the gas-phase reactions of S^+ with hydrocarbons of the form CH_x and C_yH (where $x=1-4$ and $y=2-3$), which produce HCS^+ , CS^+ , HC_3S^+ , and C_2S^+ , which may form neutral S-bearing species, such as CS and H_2CS , after recombination reactions with electrons (Le Gal et al. 2019). These reactions all require the presence of S^+ , S , HS , and atomic carbon or hydrocarbons. While the abundances of the former three have not been established for the disk of HD 142527, the presence of atomic carbon and hydrocarbons can be due to infalling material or a streamer that replenishes the disk with fresh atomic carbon-rich material, following the same reasoning as in Section 7.4.3.2.

This scenario may also explain the observed H_2CS $J=10_{1,10}-9_{1,9}$ transition. As

can be seen in the middle panel of Figure 7.C.3, the H_2CS transition peaks in a similar region to those of C_2H and CN , and we expect that the observed emission is facilitated by the gas-phase reactions discussed in the previous paragraph. Furthermore, as both the $\text{CS } J=10-9$ and the $\text{H}_2\text{CS } J=10_{1,10}-9_{1,9}$ have high upper level energies of, respectively, $E_{\text{up}}=129.3$ K and $E_{\text{up}}=102.4$ K, it is likely that the emission comes from a high atmospheric layer of the disk, especially as disks have steep temperature gradients (see, for example, Paneque-Carreño et al. 2023).

Finally, we note that the $\text{C}^{34}\text{S } J=7-6$ transition also appears to be co-spatial with the C_2H and CN transitions (see top panel of Figure 7.C.3). Being a rarer isotopologue of CS , this may further agree with a second, strong reservoir of CS formed by infalling atomic carbon-rich material.

7.4.3.5 A potential shock: SO

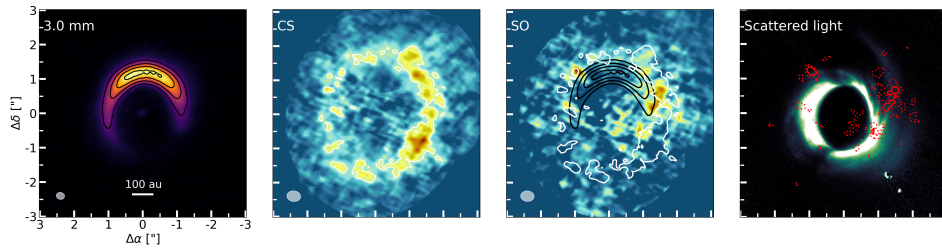


Figure 7.6: Continuum emission (left panel), integrated intensity maps of the $\text{CS } J=2-1$ and $\text{SO } J=3-2_1$ transitions (middle panels), and the scattered light image (rightmost panel). The black contours indicate the continuum emission at 25%, 50%, 75%, and 95% the peak flux, whereas the white contours indicate the 3σ CM emission. In the scattered light image, the red contours indicate the SO emission at 2σ (dotted) and 3σ (solid) levels.

While a clear scenario can be put forward to explain the observed emission of H_2CO , CS , C_2H , and CN , this is not the case for SO . We report the detection of a single, intrinsically weak ($\log_{10}(A_{ij}) \sim -4.94$) SO transition, $J=3-2_1$, that was observed in both spectral settings of the Band 3 observations. One was observed with high spectral resolution, while the other was placed in a continuum spectral window. Using the high spectral resolution observation, we note that the SO emission originates from a radial distance between the continuum emission and the CS emission (see Figure 7.6). Furthermore, the SO emission is not azimuthally co-spatial with other observed molecular species.

As previously mentioned, SO is a known shock tracer (see, for example, van Gelder et al. 2021). The observed emission of SO in the disks of AB Aur and MWC 480 has previously been linked to observed gaseous spiral arms (Speedie et al. 2025; Zagaria et al. 2025). In the case of HD 142527 this may be most evident once the SO observations are compared with those in the scattered light. As shown in the right panel of Figure 7.6, there may be a connection between the observed spirals and the SO emission. However, as the molecular emission is weak with respect to

other molecular species, this can, however, not be directly confirmed. Observations of stronger SO transitions, such as the $J=7_8-6_7$ ($E_{\text{up}}=81.2$, $\log_{10}(A_{\text{ul}})=-3.3023$) and $J=8_8-7_7$ ($E_{\text{up}}=87.5$, $\log_{10}(A_{\text{ul}})=-3.2852$) transitions in Band 7, are needed to confirm this scenario or to explore others.

7.4.4 Origins of the spirals and dust trap

Spirals are thought to form through disk interactions with heavy, embedded companions (see, for example, Kley 1999; Dong et al. 2015; Zhu et al. 2015; Bae & Zhu 2018), gravitational instability (see, for example, Cossins et al. 2009; Speedie et al. 2024), and even shadows (see, for example, Montesinos et al. 2016; Su & Bai 2024; Zhang et al. 2025). As the system of HD 142527 has a known stellar companion and shadows due to a misaligned inner disk, neither of these mechanisms can immediately be ruled out.

An additional explanation for the asymmetry and spiral features (see also Lesur et al. 2015) observed in HD 142527 can be found in the works of Bae et al. (2015) and Kuznetsova et al. (2022). Their models suggest that protostellar or anisotropic infall may generate a Rossby Wave Instability (RWI; Lovelace et al. 1999; Li et al. 2000). The RWI, in turn, can give rise to vortices, which may trap the large dust grains (Lyra et al. 2009; Crnkovic-Rubsamen et al. 2015; Owen & Kollmeier 2017; Raettig et al. 2021; Regály et al. 2021) and lead to the large asymmetric structures seen in the continuum emission, as may be the case for the disks of Oph-IRS 48 and HD 142527. This may, therefore, have given rise to enhanced surface density proposed for the emission of, for example, the C^{17}O transitions, which is consistent with the dust trap. As the spirals observed in the molecular emission, most prominently in that of H_2CO , trace the inner edge of the dust trap (see Figure 7.5 and Figure 7.E.1), we propose that the dust trap of HD 142527 may be the result of a vortex caused by the late infalling material. Stadler et al. (2026) also recently proposed that infalling material may be the cause of the asymmetric dust feature seen in the disk of HD 34700A.

7.4.5 Future work and studies

The disk of HD 142527 yields unique insights into the chemistry of disks and a potential connection to infalling material, but not all molecular species tell a clear story. As mentioned in Section 7.4.3.5, observations of stronger transitions of SO are needed to investigate the shocks induced by the spiral arms. Furthermore, given the low resolution, sensitivity, and image fidelity of the old Cycle 0 observations due to the smaller number of ALMA antennas, re-observing the CS $J=7-6$, HCN, and HCO^+ $J=4-3$ transitions will be crucial for investigating the role of this infalling material in setting the morphology of these species. Additionally, re-observing the HCO^+ $J=4-3$ transitions may reveal insights into the origins of the observed central bright spot and whether it was caused by an X-ray flare. Similarly, higher spatial resolution observations of the CS $J=10-9$ transition, or even targeting any other CS transition with high upper level energies, will reveal whether this transition is fully co-spatial with the observed C_2H and CN emission

and will, therefore, confirm whether the origins of these species are all related to the potentially infalling material.

HD 142527 is not the only disk with spiral arms seen in CO gas emission (see, for example, Rosotti et al. 2020; Casassus et al. 2021; Teague et al. 2021; Wölfer et al. 2021, 2023). To investigate how important and widespread our proposed scenario is for planet-forming disks, a larger sample of disks with spiral arms needs to be studied with high-resolution and high-sensitivity ALMA observations. These studies should target species that have been key in our analysis, such as H_2CO , C_2H (as an important C/O-ratio tracer), CN, and CS, but also SO and CH_3OH to investigate (and potentially rule out) the role of shocks. Thus far, C_2H has been observed in only a few of the Herbig disks studied by Stapper et al. (2022) and Stapper et al. (2024), leaving a large sample open for follow-up studies.

7.5 Summary

In this work, we have investigated the peculiar carbon-rich chemistry of the disk around the young star HD 142527 using new ALMA observations. Our main conclusions can be summarised as follows:

- We have greatly expanded the known molecular inventory of the HD 142527 disk by detecting, for the first time, transitions of the key species C_2H , CN, and $\text{c-C}_3\text{H}_2$. Furthermore, we detected additional transitions of CS, H_2CO , multiple isotopologues of HCO^+ and more. The non-detection of CH_3OH suggests that the dust trap is too cold for sublimation of the icy mantles to occur.
- We found that the brightness temperature of ^{13}CO is fairly constant along the disk's azimuth, suggesting that there are no thermal variations along the disk's surface.
- The emission of the optically thin $\text{C}^{17}\text{O } J=1-0$ and $J=3-2$, and $\text{HCO}^+ J=1-0$ transitions is co-spatial with the asymmetric dust trap, suggesting that the gas surface density has an enhancement at the location of the dust trap. The decrement observed in the northern region of the $\text{C}^{17}\text{O } J=3-2$ transition may be due to the dust being more optically thick at higher frequencies, blocking emission from the disk's backside, or due to freeze-out at the outer edge of the dust trap.
- We propose that the spiral-like features seen in the molecular emission of H_2CO , CN, and C_2H transitions follow from infalling atomic carbon-rich material. This material locally increases the C/O-ratio and, therefore, facilitates the gas-phase formation of these molecular species.
- An azimuthal offset between the peak emission of the H_2CO and that of CN and C_2H can be explained by a delay of a few hundred years in the gas-phase formation timescales of H_2CO . According to simple calculations, such a time-scale would require enhanced fractional abundances of the hydrocarbons CH_3 and CH_2 in the lower density surface layers. Disks with

(molecular) asymmetries yield, therefore, unique opportunities to study the role of time-dependent chemistry in setting the observable molecular composition.

- Four transitions of CS have now been detected in the disk of HD 142527, and we propose that they trace two different reservoirs: a cold reservoir that follows a Keplerian orbit and a hotter reservoir, residing higher up in the disk, that is the result of the infalling atomic carbon-rich material. This is supported by the CS $J=10-9$ and H₂CS $J=10_{1,10}-9_{1,9}$ having a similar emission morphology as the CN and C₂H, and the high temperatures needed to excite these higher upper level energy transitions ($E_{\text{up}} > 100$ K).
- A single weak transition of SO is detected that is radially and azimuthally offset from both the dust continuum and the CS emission. We propose that this transition may potentially trace a shock caused by the spirals observed in the scattered light impacting the disk, but additional observations of other SO transitions are needed to confirm this notion.

This work has shown that the azimuthally asymmetric disk of HD 142527 provides a unique laboratory to study the impact of the environment and, in particular, late infalling material on the observable chemistry. We advocate the need for a large study investigating the role and importance of spirals and/or potentially infalling material in setting the chemical composition of planet-forming disks. To conduct such a study, high-resolution and sensitivity observations, targeting molecular species such as H₂CO, CS, CN, and C₂H, are needed in many more disks with asymmetries and/or spiral features.

Acknowledgements

The authors acknowledge assistance from Allegro, the European ALMA Regional Center node in the Netherlands.

This paper makes use of the following ALMA data: 2011.1.00318.S, 2011.0.00465.S, 2012.1.00631.S, 2013.1.00305.S, 2015.1.00805.S, 2015.1.01137.S, 2023.1.00628.S, and 2024.1.00446.S. ALMA is a partnership of ESO (representing its member states), NSF (USA) and NINS (Japan), together with NRC (Canada), NSTC and ASIAA (Taiwan), and KASI (Republic of Korea), in cooperation with the Republic of Chile. The Joint ALMA Observatory is operated by ESO, auI/NRAO and NAOJ.

M.T. and E.v.D. acknowledge support from the ERC grant 101019751 MOLD-ISK. E.v.D. also acknowledges support the Danish National Research Foundation through the Center of Excellence “InterCat” (DNRF150) and the grant TOP-1 614.001.751 from the Dutch Research Council (NWO). M.B. has received funding from the European Research Council (ERC) under the European Union’s Horizon 2020 research and innovation programme (PROTOPLANETS, grant agreement No. 101002188).

The project leading to this publication has received support from ORP, that is funded by the European Union’s Horizon 2020 research and innovation programme

under grant agreement No 101004719 [ORP].

This work also has made use of the following software packages that have not been mentioned in the main text: NumPy, SciPy, Astropy, Matplotlib, pandas, IPython, Jupyter (Harris et al. 2020; Virtanen et al. 2020; Astropy Collaboration et al. 2013, 2018, 2022; Hunter 2007; pandas development team 2020; Pérez & Granger 2007; Kluyver et al. 2016)

Appendix

7.A Observational details

Table 7.A.1: Observational details of the Cycle 10 and 11 ALMA observations.

Band	Date (DD/MM/YYYY)	No. antennas	On source time [min]	Freq. coverage [GHz]	Baselines [m]	Mean PWV [mm]	MRS ["]	Phase cal.	Flux/Bandpass cal.
3 (#1)	06/01/2024	42	21.25	86.0-101.5	15.1-783.5	3.7	15.4	J1604-4441	J1427-4206
	07/11/2023	48	42.37	-	30.9-6582.7	4.8	3.2	J1604-4441	J1924-2914
	09/11/2023	48	42.32	-	30.9-5185.6	5.1	3.1	J1604-4441	J1427-4206
3 (#2)	27/12/2023	41	36.43	99.2-113.5	15.1-783.5	6.5	11.7	J1604-4441	J1517-2422
	06/01/2024	42	36.45	-	15.1-783.5	4.1	12.0	J1604-4441	J1427-4206
	07/11/2023	46	44.85	-	30.9-6582.7	4.9	2.5	J1604-4441	J1427-4206
	07/11/2023	47	44.82	-	30.9-6582.7	4.9	2.7	J1604-4441	J1427-4206
	08/11/2023	46	44.88	-	30.9-5185.6	5.1	2.8	J1604-4441	J1427-4206
4	06/01/2024	28	16.20	144.0-157.3	15.1-783.5	3.4	9.4	J1604-4441	J1427-4206
	13/01/2024	45	16.20	-	15.1-500.2	2.8	12.7	J1604-4441	J1427-4206
	03/12/2023	33	30.72	-	41.5-3083.2	0.9	3.1	J1604-4441	J1427-4206
7	05/12/2023	43	30.73	-	15.1-2516.8	1.5	4.2	J1604-4441	J1427-4206
	26/12/2024	43	48.92	337.0-352.5	15.0-499.8	0.7	4.9	J1604-4441	J1517-2422
	17/04/2025	47	39.27	-	15.1-1397.8	0.6	2.6	J1604-4441	J1924-2914
	18/04/2025	48	39.33	-	15.1-1397.8	0.7	2.6	J1604-4441	J1256-0547
	19/04/2025	47	39.32	-	15.1-1604.4	1.0	2.4	J1604-4441	J1256-0547

7.B Self-calibration: S/N -ratios

Table 7.B.1: S/N -ratios before and after self-calibration.

	Band 3 - Setting 1		Band 3 - Setting 2		Band 4		Band 7	
	SB	Combined	SB	Combined	SB	Combined	SB	Combined
Start S/N	147.5	106	250	147	184	192	90	170
End S/N	552	-	919	-	1808	514	483	672

7.C Molecular species: detections and non-detections

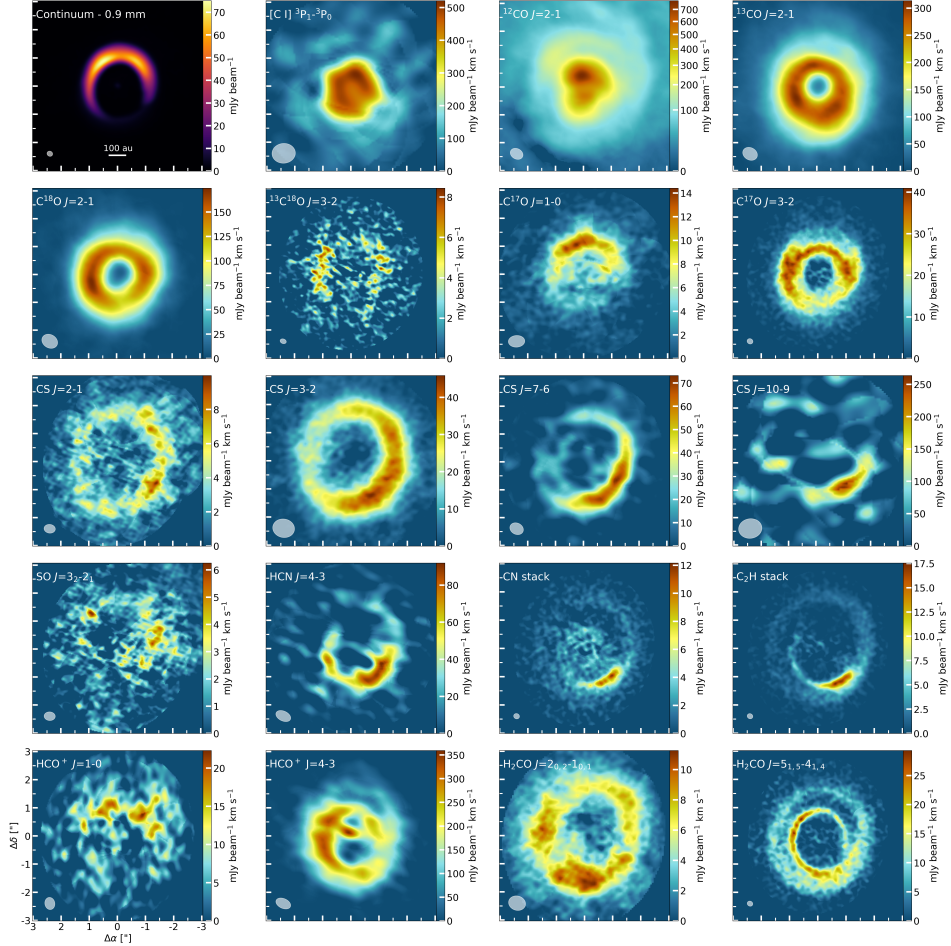


Figure 7.C.1: Integrated intensity maps of the dust continuum at 1.3 mm and the strongest detected molecular species in the disk of HD 142527. To increase the S/N -ratio of the respective integrated intensity maps, the images of the $\text{C}^{17}\text{O } J=1-0$, C_2H and CN were created by stacking the detected transitions (two, four, and three transitions, respectively). The image of $^{12}\text{CO } J=2-1$ was created with a different colour scaling to better highlight the weak extended emission. For the $\text{HCO}^+ J=4-3$ transition, we focused on imaging the Keplerian ring instead of the bright central spot. Subsequently, the integrated flux of the central spot may be lower than shown in Temmink et al. (2023). Additionally, the displayed images of $\text{C}^{17}\text{O } J=1-0$, $^{13}\text{C}^{18}\text{O } J=3-2$, $\text{CS } J=2-1$ and $J=3-2$, and $\text{H}_2\text{CO } J=2_{0,2}-1_{0,1}$ were created using a robust value of 2.0. The resolving beams are shown in the lower-left corner of each image.

Table 7.C.1: Strongly detected molecular transitions in the disk of HD 142527.

Molecule	Transition	Freq. [GHz]	$\log(A_{ij})$ [s ⁻¹]	E_{up} [K]	Robust	Beam [" \times " (°)]	Peak flux [mJy beam ⁻¹]	RMS	δv [km s ⁻¹]
C ¹⁷ O	$J=1-0, F=7/2-5/2$	112.358982	-7.17	5.4	0.5	0.28 \times 0.24 (-85.9)	11.1	1.8	0.30
	$J=1-0, F=5/2-5/2$	112.360007	-7.17	5.4	0.5	0.28 \times 0.24 (-85.9)	13.2	1.8	0.30
	$J=3-2, F=9/2-7/2$	337.060988	-5.63	32.4	0.5	0.21 \times 0.18 (65.8)	56.8	2.6	0.15
CS	$J=2-1$	97.980953	-4.78	7.1	0.5	0.25 \times 0.20 (77.2)	10.0	1.7	0.30
	-	-	-	-	2.0	0.40 \times 0.31 (83.1)	14.6	1.5	0.30
	$J=3-2$	146.969029	-4.22	14.1	0.5	0.39 \times 0.32 (88.0)	32.1	3.0	0.30
SO	-	-	-	-	2.0	0.78 \times 0.66 (79.4)	63.8	2.2	0.30
	$J=3_2-2_1$	99.299870	-4.95	9.2	2.0	0.40 \times 0.31 (85.8)	9.1	1.5	0.30
	-	-	-	-	2.0	0.66 \times 0.47 (-85.4)	2.4	0.4	2.00
CN	$N=3-2, J=5/2-3/2, F=7/2-5/2$	340.031549	-3.42	32.6	0.5	0.21 \times 0.18 (67.6)	17.9	2.0	0.15
	$N=3-2, J=5/3-3/2, F=3/2-1/2$	340.035408	-3.49	32.6	0.5	0.21 \times 0.18 (67.6)	20.9	2.0	0.15
	$N=3-2, J=7/2-5/2, F=7/2-5/2$	340.247770	-3.38	32.7	0.5	0.21 \times 0.18 (64.7)	28.7	2.0	0.15
C ₂ H	$N=4-3, J=9/2-7/2, F=5-4$	349.337707	-3.88	41.9	0.5	0.20 \times 0.18 (64.5)	49.3	2.2	0.15
	$N=4-3, J=9/2-7/2, F=4-3$	349.339067	-3.89	41.9	0.5	0.20 \times 0.18 (64.5)	40.0	2.2	0.15
	$N=4-3, J=7/2-5/2, F=4-3$	349.399374	-3.90	41.9	0.5	0.20 \times 0.18 (64.5)	42.9	2.2	0.15
	$N=4-3, J=7/2-5/2, F=3-2$	349.400669	-3.92	41.9	0.5	0.20 \times 0.18 (64.5)	31.9	2.2	0.15
HCO ⁺	$J=1-0$	89.188525	-4.38	4.3	0.5	0.43 \times 0.35 (10.6)	25.4	3.9	0.25
H ₂ CO	$J=2_{0,2}-1_{0,1}$	145.602949	-4.11	10.5	0.5	0.32 \times 0.27 (-85.3)	9.5	1.2	0.30
	-	-	-	-	2.0	0.61 \times 0.51 (73.6)	17.5	1.0	0.30
	$J=5_{1,5}-4_{1,4}$	351.768645	-2.92	62.5	0.5	0.20 \times 0.18 (63.4)	19.6	0.9	1.00

7.C.1 Weak and/or tentative detections

With the aid of GOFISH and subsequent visual inspection of the image cubes, we also report weak and/or tentative detections of C³⁴S (two transitions), CN, HCN, C₂H, H¹³CO⁺, HC¹⁸O⁺, DCO⁺, H₂CS, c-C₃H₂, and HC₃N. The detections of CN, HCN, C₂H, and c-C₃H₂ required the stacking of, respectively, three, three, three, and five separate transitions. The normalised integrated spectra obtained with GOFISH are shown in Figure 7.C.2, while the bottom part of Table 7.C.2 contains information on the transitions. The additional peaks visible in the GOFISH spectrum of HCN (top panel in Figure 7.C.2) are the result of stacking hyperfine transitions that lie closely together in frequency space. Finally, as the Band 7 transitions have stronger flux levels, Figure 7.C.3 shows selected channel maps - in particular, channels containing the strongest flux levels - of the C³⁴S $J=7-6$, H₂CS $J=10_{1,10}-9_{1,9}$, and stacked c-C₃H₂ transitions to reveal the emission morphology of these species.

The integrated GOFISH spectra of the C³³S $J=7-6$ transition and the H₂¹³CO $J=2_{1,1}-1_{1,0}$ also hint at weak detections of these transitions. However, emission signatures could not be confirmed upon visual inspection of the image cubes. Therefore, we deem these two transitions to be non-detections.

7.C.2 Non-detections

We also report non-detections of transitions of a wide variety of species: C³³S, SO, SiO, CCS, SO₂, H¹³CN, HC¹⁵N, DCN, H₂CO, H₂¹³CO, H₂CS, HC₃N, CH₃OH, and CH₃CN. All information on the non-detected transitions, including the RMS of the observations, can be found in Table 7.C.3.

The most notable non-detection is that of CH₃OH, even upon stacking 10 transitions. This is surprising since the molecule is now commonly observed in Herbig disks (van der Marel et al. 2021a; Booth et al. 2024a,b, 2025, 2026). However, the stacked transitions have lower Einstein-A values compared to detected transitions

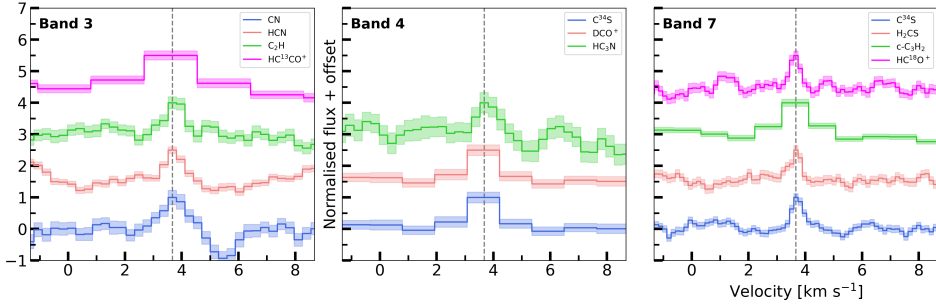


Figure 7.C.2: Normalised integrated spectra of the weak and tentative transitions detected with GoFISH. The transitions found in Bands 3, 4, and 7 are, respectively, shown in the top, middle and bottom panels.

Table 7.C.2: Weakly or tentatively detected molecular transitions in the disk of HD 142527.

Molecule	Transition	Freq. [GHz]	$\log(A_{ij})$ [s ⁻¹]	E_{up} [K]	Robust	Beam [" × " (°)]	Peak flux [mJy beam ⁻¹]	RMS	δV [km s ⁻¹]
C ³⁴ S	$J=3-2$	144.617101	-4.24	13.9	2.0	0.63×0.51 (68.6)	2.6	0.5	0.30
	$J=7-6$	337.396459	-3.12	64.8	2.0	0.31×0.25 (65.7)	14.6	1.9	0.15
CN ^(α)	$N=1-0, J=3/2-1/2, F=3/2-1/2$	113.4881202	-5.17	5.4	2.0	0.57×0.41 (-86.2)	4.4	1.0	0.30
	$N=1-0, J=3/2-1/2, F=5/2-3/2$	113.4909702	-4.92	5.4	2.0	-	-	-	0.30
	$N=1-0, J=3/2-1/2, F=1/2-1/2$	113.4996443	-4.97	5.4	2.0	-	-	-	0.30
HCN ^(α)	$J=1-0, F=1-1$	88.630416	-4.62	4.3	2.0	0.45×0.36 (81.4)	4.4	0.8	0.30
	$J=1-0, F=2-1$	88.631848	-4.62	4.3	2.0	-	-	-	0.30
	$J=1-0, F=0-1$	88.633936	-4.62	4.3	2.0	-	-	-	0.30
C ₂ H ^(α)	$N=1-0, J=3/2-1/2, F=1-1$	87.284156	-6.59	4.2	2.0	0.46×0.36 (83.1)	3.5	0.8	0.30
	$N=1-0, J=3/2-1/2, F=2-1$	87.316898	-5.82	4.2	2.0	-	-	-	0.30
	$N=1-0, J=3/2-1/2, F=1-0$	87.328585	-5.90	4.2	2.0	-	-	-	0.30
H ¹³ CO ⁺	$J=1-0$	86.7542884	-4.41	4.2	2.0	0.47×0.36 (82.6)	2.2	0.5	0.30
HC ¹⁸ O ⁺	$J=4-3$	340.6306916	-2.51	40.9	2.0	0.3×0.26 (69.5)	9.3	2.1	1.15
DCO ⁺	$J=2-1$	144.077289	-3.18	10.4	2.0	0.63×0.51 (68.6)	2.6	0.5	1.20
H ₂ CS	$J=10_{1,10}-9_{1,9}$	338.083195	-3.24	102.4	2.0	0.31×0.25 (65.7)	12.5	1.9	1.15
c-C ₃ H ₂ ^(α)	$J=7_{3,4}-6_{4,3}$	351.523317	-2.91	77.2	2.0	0.30×0.24 (64.9)	2.6	0.4	1.00
	$J=10_{0,10}-9_{1,9}$	351.781578	-2.61	96.5	2.0	-	-	-	1.00
	$J=9_{1,8}-8_{2,7}$	351.965969	-2.67	93.3	2.0	-	-	-	1.00
	$J=8_{2,6}-7_{3,5}$	352.185542	-2.76	86.9	2.0	-	-	-	1.00
	$J=8_{3,6}-7_{2,5}$	352.193656	-2.76	86.9	2.0	-	-	-	1.00
HC ₃ N	$J=16-15$	145.5609596	-3.62	59.4	2.0	0.61×0.51 (73.6)	5.5	1.0	0.30

Notes. ^(α): Only one value is listed for the beam, the peak flux, and the RMS for the transitions of CN, HCN, C₂H, and c-C₃H₂ because we stacked the displayed transitions to ensure a detection.

(Booth et al. 2024b, 2026; Temmink et al. 2023), but note that individual stronger transitions have not led to a detection (see, for example, Temmink et al. 2023). Observations of CH₃OH have often been linked to the sublimation of inherited molecular ices at cavity walls, as the disks are generally too warm for in-situ formation (see, for example, (van der Marel et al. 2021a; Booth et al. 2025, 2026)). Since CH₃OH does not have efficient gas-phase formation routes, the hydrogenation of frozen-out CO molecules is considered to be the most common formation pathway (Watanabe & Kouchi 2002; Fuchs et al. 2009; Santos et al. 2022). The RADMC-3D model of Temmink et al. (2023) suggests that CO can only be frozen out at the outer edge of the dust trap. Therefore, the in-situ formation of CH₃OH

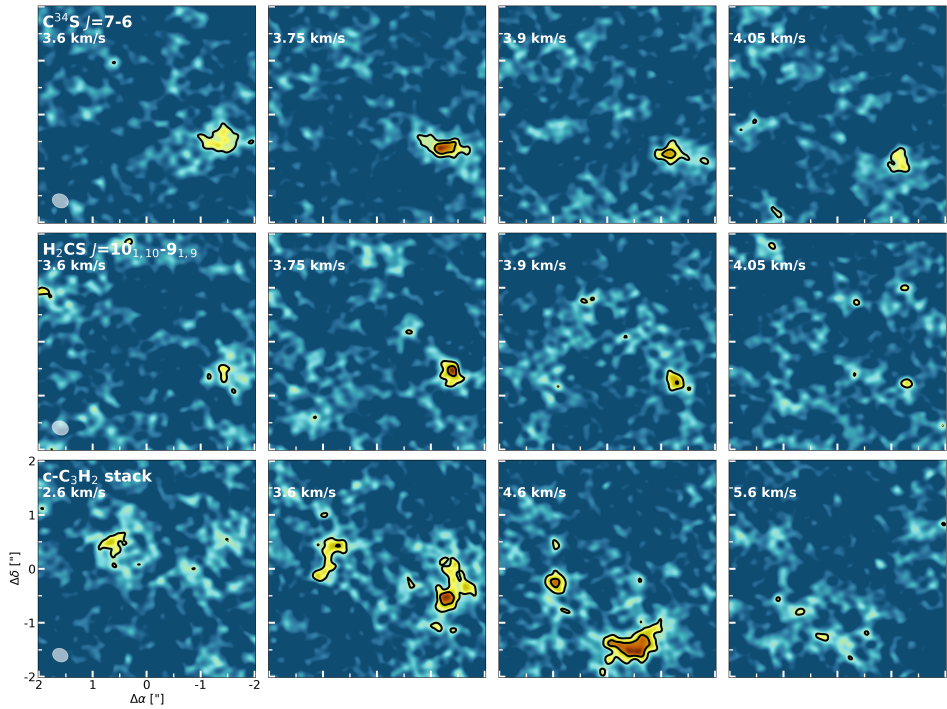


Figure 7.C.3: Selected channels of the weakly detected C^{34}S $J=7-6$, H_2CS $J=10_{1,10}-9_{1,9}$, and stacked $\text{c-C}_3\text{H}_2$ transitions. The black contours indicate the 3σ and 5σ noise levels.

in the disk of HD 142527 is unlikely, and any CH_3OH present in the disk should also be the result of inheritance. Our non-detection of CH_3OH , suggests that the dust trap is located too far from the host star to be significantly heated for CH_3OH -ice to sublime. Additionally, the vertical turbulence may be too weak for the icy dust grains to be lifted to the higher elevated layers where sublimation may occur.

Table 7.C.3: Non-detected molecular transitions in the disk of HD 142527.

Molecule	Transition	Freq. [GHz]	$\log(A_{ij})$ [s ⁻¹]	E_{up} [K]	Robust	Beam [" \times " (°)]	RMS [mJy beam ⁻¹]	δV [km s ⁻¹]
C ³³ S	$J=7-6$	340.0525755	-3.10765	65.3	2.0	0.31 \times 0.26 (68.8)	1.8	0.15
SO	$J=2_2-1_1$	86.093950	-5.27985	19.3	2.0	0.47 \times 0.37 (82.5)	0.5	2.0
SiO	$J=2-1$	86.846985	-4.5334	6.3	2.0	0.47 \times 0.36 (82.6)	0.5	2.0
CCS $^{\alpha}$	$N=7-6, J=6-5$	86.181391	-4.55632	23.3	2.0	0.47 \times 0.37 (82.6)	0.5	2.0
	$N=8-7, J=7-6$	99.866521	-4.3562	28.1	2.0	0.65 \times 0.46 (-85.8)	0.4	2.0
	$N=9-8, J=8-7$	113.410186	-4.18482	33.6	2.0	-	-	2.0
SO $_2^{\alpha}$	$J=10_{6,4}-11_{5,7}$	350.862756	-4.35623	138.8	2.0	0.30 \times 0.24 (64.9)	0.5	1.0
	$J=5_{3,3}-4_{2,2}$	351.2572233	-3.47398	35.9	2.0	-	-	1.0
	$J=14_{4,10}-14_{3,11}$	351.8738732	-3.46440	135.9	2.0	-	-	1.0
H ¹³ CN	$J=1-0$	86.3399214	-4.65260	4.1	2.0	0.47 \times 0.37 (82.6)	0.5	2.0
HC ¹⁵ N	$J=1-0$	86.0549664	-4.65693	4.1	2.0	0.47 \times 0.37 (82.5)	0.5	2.0
DCN	$J=2-1$	144.8280015	-3.89786	10.4	2.0	0.63 \times 0.51 (68.8)	0.5	1.2
H ₂ CO	$J=6_{1,5}-6_{1,6}$	101.332991	-5.80378	87.6	2.0	0.39 \times 0.30 (84.9)	1.6	0.3
	-	-	-	-	2.0	0.67 \times 0.47 (-85.5)	0.4	2.0
H ₂ ¹³ CO	$J=2_{1,1}-1_{1,0}$	146.6356717	-4.22279	22.4	2.0	0.61 \times 0.51 (74.5)	1.1	0.3
H ₂ CS	$J=3_{1,3}-2_{1,2}$	101.4778095	-4.89960	22.9	2.0	0.39 \times 0.30 (85.0)	1.6	0.3
HC ₃ N	$J=11-10$	100.076392	-4.10963	28.8	2.0	0.65 \times 0.46 (-85.6)	0.4	2.0
CH ₃ OH $^{\alpha}$	$J=3_{-0,3}-2_{-0,2}$	145.093754	-4.91	27.1	2.0	0.59 \times 0.49 (71.3)	0.5	1.2
	$J=3_{0,3}-2_{0,2}$	145.103185	-4.91	13.9	2.0	-	-	1.2
	$J=3_{2,2}-2_{2,1}$	145.124332	-5.16	51.6	2.0	-	-	1.2
	$J=3_{-1,2}-2_{-1,1}$	145.131864	-4.95	35.0	2.0	-	-	1.2
	$J=6_{2,4}-7_{1,7}$	156.127544	-5.18	86.5	2.0	-	-	1.2
	$J=8_{-0,8}-8_{1,8}$	156.488902	-4.75	96.6	2.0	-	-	1.2
	$J=7_{-0,7}-7_{1,7}$	156.828517	-4.73	78.1	2.0	-	-	1.2
	$J=5_{-0,5}-5_{1,5}$	157.178987	-4.69	47.9	2.0	-	-	1.2
	$J=4_{-0,4}-4_{1,4}$	157.246062	-4.68	36.3	2.0	-	-	1.2
	$J=1_{-0,1}-1_{1,1}$	157.270832	-4.66	15.4	2.0	-	-	1.2
	$J=4_{-0,4}-3_{1,3}$	350.687662	-4.06	36.3	2.0	0.30 \times 0.24 (64.9)	0.5	1.0
	$J=1_{1,1}-0_{0,0}$	350.905100	-3.48	16.8	2.0	-	-	1.0
CH ₃ CN $^{\alpha}$	$J=19_3-18_{-3}$	349.3932973	-2.44	232.0	2.0	0.30 \times 0.24 (65.6)	0.5	1.0
	$J=19_2-18_2$	349.4268499	-2.43	196.3	2.0	-	-	1.0
	$J=19_1-18_1$	349.4469869	-2.43	174.9	2.0	-	-	1.0
	$J=19_0-18_0$	349.4537001	-2.43	167.7	2.0	-	-	1.0

Notes. ($^{\alpha}$): In an attempt to detect the molecular emission, we stacked the various transitions of CCS, SO₂, and CH₃OH. Therefore, only one value is listed for the beam and the RMS.

7.D Continuum brightness temperature

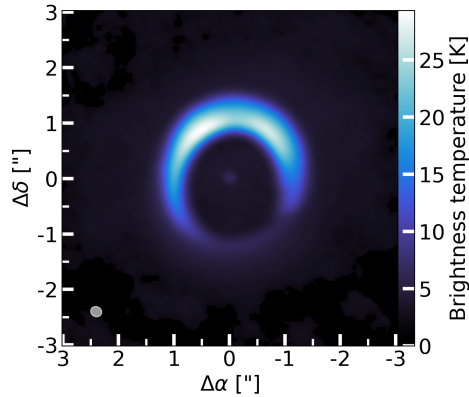


Figure 7.D.1: Brightness temperature of the dust continuum at 0.9 mm. The resolving beam is shown in the lower left corner.

7.E H₂CO channel maps

The H₂CO channel maps (Figure 7.E.1) reveal that the observed spiral-like feature is real and not the cause of continuum oversubtraction effects.

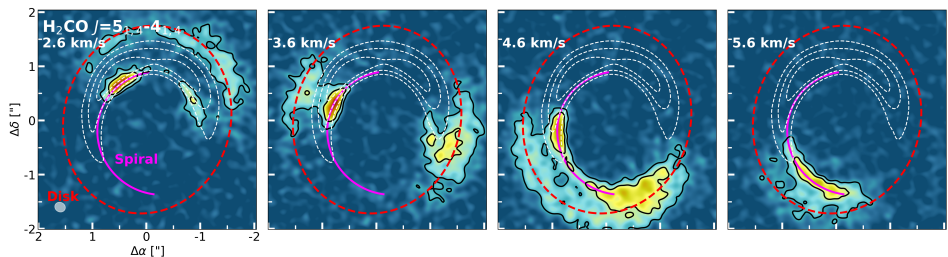


Figure 7.E.1: Selected channels of the H₂CO $J=5_{1,5}-4_{1,4}$ transition. We have labeled the different contributions from the spiral (pink) and the disk (red). The black contours indicate the 5σ and 10σ noise levels, while the white, dashed contours indicate the continuum emission at flux levels of 25%, 50%, and 75%.

7.F Tracing the ¹²CO spiral arms

To trace the spiral arms seen in the ¹²CO $J=2-1$ line emission, we combine previously used techniques (Teague et al. 2019; Garg et al. 2021; Wölfer et al. 2021).

In particular, we investigate the spiral arms in the brightness temperature channel maps after subtracting off the averaged brightness temperature map in each channel. Using azimuthal increments of 3° , we subsequently identify radial peaks whose flux exceeds at least $3\times$ the channel RMS and whose residual brightness temperature exceeds at least half the median flux of the averaged bright temperature map. Furthermore, we require the peaks to be spaced at least 10 pixels apart. Through visual inspection of the channels, we assign the identified peaks to a spiral or leave them unassigned. The left panel of Figure 7.F.1 shows the peak intensity map of the ^{12}CO emission, where the coloured dots (blue, green, or purple) are assigned to a spiral (three in total) and the white ones have been left unassigned. We note that a set of identified peaks, potentially connected to the blue and/or green spirals, has been left unassigned, due to the potential conjunction of these spirals, making it nearly impossible to assign the peaks to either one of the spirals. To avoid assigning data points to the wrong spiral, we have left these data points unassigned.

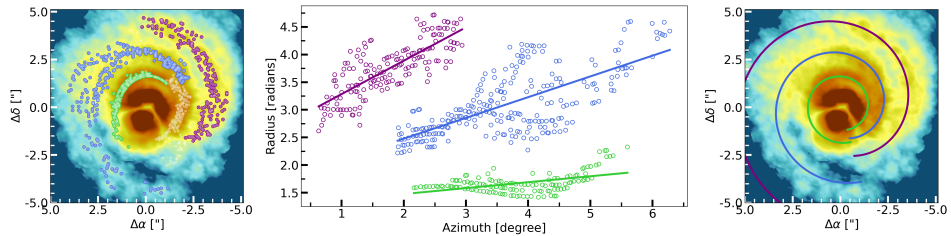


Figure 7.F.1: Left: Peak intensity map of the ^{12}CO $J=2-1$ transition with the identified peaks in the residual brightness channel maps (left panel). The coloured data points (blue, green, or purple) are the data points we have assigned to a spiral feature. Middle: Archimedean linear spiral fits (solid lines) to the identified spirals. Right: Fitted spiral plotted on top of the ^{12}CO peak intensity map.

To further investigate the spirals, we converted the Cartesian (pixel) coordinates of the peaks to cylindrical coordinates (r, ϕ) , not taking the disk’s inclination and position angle into account, and we have fitted an Archimedean linear spiral to these coordinates:

$$r = a + b\phi. \quad (7.4)$$

We note that the cylindrical coordinates were rotated by 105° to ensure that the spirals were not broken up along the ϕ -coordinate. The resulting fits are shown in the middle panel of Figure 7.F.1, and the fitted spirals, converted back to the Cartesian coordinates, are also shown on top of the ^{12}CO in the right panel of Figure 7.F.1. Furthermore, the fit values for a and b for each of the three spirals are listed in Table 7.F.1.

Our identified spirals match those of Garg et al. (2021). In particular, our blue spiral is a combination of their spirals 1 and 3 (S1 and S3), of which they

Table 7.F.1: Best-fitting parameters for the Archimedean linear spirals.

Spiral	a ["]	b ["] rad^{-1}]
Blue	1.73	0.38
Purple	2.68	0.60
Green	1.26	0.11

noted that they could be connected. Our purple spiral matches their spiral 2 (S2), while our green spiral matches their spiral 4 (S4). Furthermore, Garg et al. (2021) discussed that their S1 and S4 (or our blue and green) may also be connected. This is also hinted at by our traced spirals, but this cannot be confirmed due to the molecular emission being absorbed by the foreground cloud.

Following the procedure given by Wölfer et al. (2021), we also calculate the

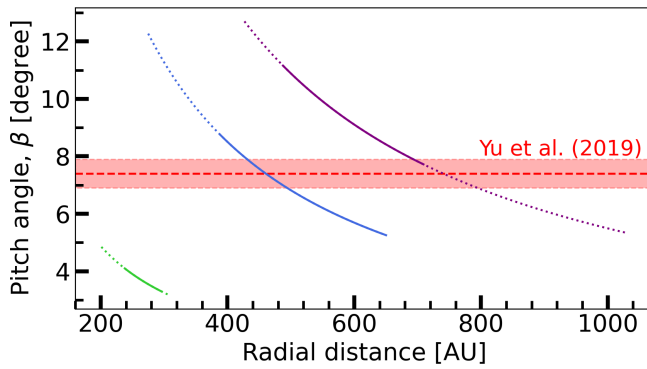


Figure 7.F.2: Pitch angles of the identified spiral arms. The horizontal red line indicates the value found by Yu et al. (2019) for the spiral arm observed in the scattered light.

pitch angle (β) for the linear fits. The pitch angle is given by the following formula:

$$\tan(\beta) = \left| \frac{dr}{d\phi} \right| \cdot \frac{1}{r}. \quad (7.5)$$

The pitch angles are calculated for all three identified spirals, and the results are shown in Figure 7.F.2. As a comparison, Yu et al. (2019) derived a pitch angle of $\beta=7.4\pm 0.5$ for the spiral arm observed in the scattered light image. This matches fairly well with the pitch angles derived for our spirals.

7.G Deprojected maps: C₂H and H₂CO

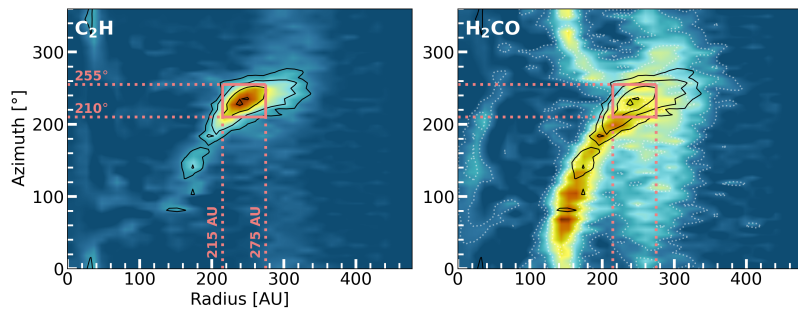


Figure 7.G.1: Deprojected versions of the integrated intensity maps of the stacked C₂H and H₂CO $J=5_{1,5}-4_{1,4}$ transitions. The pink lines indicate the visually approximated extent of the C₂H peak emission. Furthermore, the solid black contours indicate the 3σ , 5σ , 10σ , and 15σ C₂H emission, whereas the white dotted contours represent those of the H₂CO emission.

Bibliography

- Abgrall, H., Le Bourlot, J., Pineau Des Forets, G., et al. 1992, *A&A*, 253, 525
- Aikawa, Y., van Zadelhoff, G. J., van Dishoeck, E. F., & Herbst, E. 2002, *A&A*, 386, 622
- Akiyama, E., Vorobyov, E. I., Liu, H. B., et al. 2019, *AJ*, 157, 165
- Alexander, R. D., Clarke, C. J., & Pringle, J. E. 2006a, *MNRAS*, 369, 216
- Alexander, R. D., Clarke, C. J., & Pringle, J. E. 2006b, *MNRAS*, 369, 229
- ALMA Partnership, Brogan, C. L., Pérez, L. M., et al. 2015, *ApJ*, 808, L3
- Andrews, S. M. 2020, *ARA&A*, 58, 483
- Andrews, S. M., Huang, J., Pérez, L. M., et al. 2018, *ApJ*, 869, L41
- Ansdell, M., Williams, J. P., van der Marel, N., et al. 2016, *ApJ*, 828, 46
- Arabhavi, A. M., Kamp, I., Henning, T., et al. 2024, *Science*, 384, 1086
- Ardila, D. R., Basri, G., Walter, F. M., Valenti, J. A., & Johns-Krull, C. M. 2002, *ApJ*, 567, 1013
- Argyriou, I., Glasse, A., Law, D. R., et al. 2023, *A&A*, 675, A111
- Armitage, P. J. 2015, arXiv e-prints, arXiv:1509.06382
- Arulanantham, N., McClure, M. K., Pontoppidan, K., et al. 2024, *ApJ*, 965, L13
- Arun, R., Mathew, B., Manoj, P., et al. 2019, *AJ*, 157, 159
- Aspin, C., Reipurth, B., Herczeg, G. J., & Capak, P. 2010, *ApJ*, 719, L50
- Astropy Collaboration, Price-Whelan, A. M., Lim, P. L., et al. 2022, *ApJ*, 935, 167
- Astropy Collaboration, Price-Whelan, A. M., Sipőcz, B. M., et al. 2018, *AJ*, 156, 123

- Astropy Collaboration, Robitaille, T. P., Tollerud, E. J., et al. 2013, *A&A*, 558, A33
- Ataiee, S., Baruteau, C., Alibert, Y., & Benz, W. 2018, *A&A*, 615, A110
- Atkinson, R., Baulch, D. L., Cox, R. A., et al. 2006, *Atmospheric Chemistry & Physics*, 6, 3625
- Avenhaus, H., Quanz, S. P., Schmid, H. M., et al. 2014, *ApJ*, 781, 87
- Avni, Y. 1976, *ApJ*, 210, 642
- Bae, J., Hartmann, L., & Zhu, Z. 2015, *ApJ*, 805, 15
- Bae, J., Isella, A., Zhu, Z., et al. 2023, in *Astronomical Society of the Pacific Conference Series*, Vol. 534, *Protostars and Planets VII*, ed. S. Inutsuka, Y. Aikawa, T. Muto, K. Tomida, & M. Tamura, 423
- Bae, J. & Zhu, Z. 2018, *ApJ*, 859, 118
- Bae, J., Zhu, Z., & Hartmann, L. 2017, *ApJ*, 850, 201
- Balança, C., Spielfiedel, A., & Feautrier, N. 2016, *MNRAS*, 460, 3766
- Balmer, W. O., Follette, K. B., Close, L. M., et al. 2022, *AJ*, 164, 29
- Banzatti, A., Abernathy, K. M., Brittain, S., et al. 2022, *AJ*, 163, 174
- Banzatti, A., Ballering, N., Gasman, D., et al. 2025a, in *PRIMA General Observer Science Book Volume 2*, ed. A. Moullet, D. Burgarella, T. Kataria, H. Beuther, C. Battersby, M. Cheng, T. Essinger-Hileman, H. Inami, E. Mills, T. Nagao, & S. Unwin, Vol. 2, 314–318
- Banzatti, A., Meyer, M. R., Bruderer, S., et al. 2012, *ApJ*, 745, 90
- Banzatti, A., Pascucci, I., Bosman, A. D., et al. 2020, *ApJ*, 903, 124
- Banzatti, A., Pascucci, I., Edwards, S., et al. 2019, *ApJ*, 870, 76
- Banzatti, A. & Pontoppidan, K. M. 2015, *ApJ*, 809, 167
- Banzatti, A., Pontoppidan, K. M., Carr, J. S., et al. 2023a, *ApJ*, 957, L22
- Banzatti, A., Pontoppidan, K. M., Péré Chávez, J., et al. 2023b, *AJ*, 165, 72
- Banzatti, A., Pontoppidan, K. M., Salyk, C., et al. 2017, *ApJ*, 834, 152
- Banzatti, A., Salyk, C., Pontoppidan, K. M., et al. 2025b, *AJ*, 169, 165
- Barvainis, R. 1987, *ApJ*, 320, 537
- Bast, J. E., Brown, J. M., Herczeg, G. J., van Dishoeck, E. F., & Pontoppidan, K. M. 2011, *A&A*, 527, A119

- Benisty, M., Dominik, C., Follette, K., et al. 2023, in *Astronomical Society of the Pacific Conference Series*, Vol. 534, *Protostars and Planets VII*, ed. S. Inutsuka, Y. Aikawa, T. Muto, K. Tomida, & M. Tamura, 605
- Benisty, M., Juhász, A., Facchini, S., et al. 2018, *A&A*, 619, A171
- Bergin, E. A., Aikawa, Y., Blake, G. A., & van Dishoeck, E. F. 2007, in *Protostars and Planets V*, ed. B. Reipurth, D. Jewitt, & K. Keil, 751
- Bergin, E. A., Cleeves, L. I., Gorti, U., et al. 2013, *Nature*, 493, 644
- Bergin, E. A., Du, F., Cleeves, L. I., et al. 2016, *ApJ*, 831, 101
- Bergin, E. A. & Tafalla, M. 2007, *ARA&A*, 45, 339
- Bergin, E. A. & Williams, J. P. 2017, in *Astrophysics and Space Science Library*, Vol. 445, *Formation, Evolution, and Dynamics of Young Solar Systems*, ed. M. Pessah & O. Gressel, 1
- Bergner, J. B., Guzmán, V. G., Öberg, K. I., Loomis, R. A., & Pegues, J. 2018, *ApJ*, 857, 69
- Béthune, W., Lesur, G., & Ferreira, J. 2017, *A&A*, 600, A75
- Biller, B., Lacour, S., Juhász, A., et al. 2012, *ApJ*, 753, L38
- Birnstiel, T. 2024, *ARA&A*, 62, 157
- Birnstiel, T., Dullemond, C. P., & Brauer, F. 2010, *A&A*, 513, A79
- Bisschop, S. E., Fraser, H. J., Öberg, K. I., van Dishoeck, E. F., & Schlemmer, S. 2006, *A&A*, 449, 1297
- Bitsch, B., Morbidelli, A., Johansen, A., et al. 2018, *A&A*, 612, A30
- Blandford, R. D. & Payne, D. G. 1982, *MNRAS*, 199, 883
- Blevins, S. M., Pontoppidan, K. M., Banzatti, A., et al. 2016, *ApJ*, 818, 22
- Blum, J. & Wurm, G. 2008, *ARA&A*, 46, 21
- Boehler, Y., Ménard, F., Robert, C. M. T., et al. 2021, *A&A*, 650, A59
- Boehler, Y., Weaver, E., Isella, A., et al. 2017, *ApJ*, 840, 60
- Bohn, A. J., Benisty, M., Perraut, K., et al. 2022, *A&A*, 658, A183
- Boogert, A. C. A., Gerakines, P. A., & Whittet, D. C. B. 2015, *ARA&A*, 53, 541
- Booth, A. S., Calahan, J., Temmink, M., et al. 2026, *AJ*, 171, 128
- Booth, A. S., Ilee, J. D., Walsh, C., et al. 2023, *A&A*, 669, A53
- Booth, A. S., Leemker, M., van Dishoeck, E. F., et al. 2024a, *AJ*, 167, 164

- Booth, A. S., Temmink, M., van Dishoeck, E. F., et al. 2024b, *AJ*, 167, 165
- Booth, A. S., van der Marel, N., Leemker, M., van Dishoeck, E. F., & Ohashi, S. 2021a, *A&A*, 651, L6
- Booth, A. S., Walsh, C., Terwisscha van Scheltinga, J., et al. 2021b, *Nature Astronomy*, 5, 684
- Booth, A. S., Wölfer, L., Temmink, M., et al. 2025, *ApJ*, 986, L9
- Bosman, A. D. & Bergin, E. A. 2021, *ApJ*, 918, L10
- Bosman, A. D., Bergin, E. A., Calahan, J., & Duval, S. E. 2022a, *ApJ*, 930, L26
- Bosman, A. D., Bergin, E. A., Calahan, J. K., & Duval, S. E. 2022b, *ApJ*, 933, L40
- Bosman, A. D., Bergin, E. A., Loomis, R. A., et al. 2021, *ApJS*, 257, 15
- Bosman, A. D., Bruderer, S., & van Dishoeck, E. F. 2017, *A&A*, 601, A36
- Bosman, A. D., Tielens, A. G. G. M., & van Dishoeck, E. F. 2018, *A&A*, 611, A80
- Bouwman, J., Meeus, G., de Koter, A., et al. 2001, *A&A*, 375, 950
- Brandl, B., Bettonvil, F., van Boekel, R., et al. 2021, *The Messenger*, 182, 22
- Brauer, F., Dullemond, C. P., & Henning, T. 2008, *A&A*, 480, 859
- Braun, T. A. M., Yen, H.-W., Koch, P. M., et al. 2021, *ApJ*, 908, 46
- Brittain, S. D., Kamp, I., Meeus, G., Oudmaijer, R. D., & Waters, L. B. F. M. 2023, *Space Sci. Rev.*, 219, 7
- Brittain, S. D., Najita, J. R., & Carr, J. S. 2009, *ApJ*, 702, 85
- Brittain, S. D., Simon, T., Najita, J. R., & Rettig, T. W. 2007, *ApJ*, 659, 685
- Brown, J. M., Herczeg, G. J., Pontoppidan, K. M., & van Dishoeck, E. F. 2012, *ApJ*, 744, 116
- Brown, J. M., Pontoppidan, K. M., van Dishoeck, E. F., et al. 2013, *ApJ*, 770, 94
- Brown, W. A. & Bolina, A. S. 2007, *MNRAS*, 374, 1006
- Bruderer, S. 2013, *A&A*, 559, A46
- Bruderer, S., Harsono, D., & van Dishoeck, E. F. 2015, *A&A*, 575, A94
- Bruderer, S., van der Marel, N., van Dishoeck, E. F., & van Kempen, T. A. 2014, *A&A*, 562, A26
- Bruderer, S., van Dishoeck, E. F., Doty, S. D., & Herczeg, G. J. 2012, *A&A*, 541, A91

- Brunken, N. G. C., Booth, A. S., Leemker, M., et al. 2022, *A&A*, 659, A29
- Bushouse, H., Eisenhamer, J., Dencheva, N., et al. 2023a, JWST Calibration Pipeline, Zenodo
- Bushouse, H., Eisenhamer, J., Dencheva, N., et al. 2023b, JWST Calibration Pipeline
- Bushouse, H., Eisenhamer, J., Dencheva, N., et al. 2024, JWST Calibration Pipeline
- Calahan, J. K., Bergin, E., Zhang, K., et al. 2021, *ApJ*, 908, 8
- Calahan, J. K., Bergin, E. A., & Bosman, A. D. 2022, *ApJ*, 934, L14
- Calahan, J. K., Bergin, E. A., van't Hoff, M., et al. 2024, *ApJ*, 975, 170
- Carnall, A. C. 2017, arXiv e-prints, arXiv:1705.05165
- Carney, M. T., Fedele, D., Hogerheijde, M. R., et al. 2018, *A&A*, 614, A106
- Carney, M. T., Hogerheijde, M. R., Guzmán, V. V., et al. 2019, *A&A*, 623, A124
- Carney, M. T., Hogerheijde, M. R., Loomis, R. A., et al. 2017, *A&A*, 605, A21
- Carpenter, J., Brogan, C., Iono, D., & Mroczkowski, T. 2023, in *Physics and Chemistry of Star Formation: The Dynamical ISM Across Time and Spatial Scales*, ed. V. Ossenkopf-Okada, R. Schaaf, I. Breloy, & J. Stutzki, 304
- Carr, J. S. & Najita, J. R. 2011, *ApJ*, 733, 102
- Carr, J. S. & Najita, J. R. 2014, *ApJ*, 788, 66
- CASA Team, Bean, B., Bhatnagar, S., et al. 2022, *PASP*, 134, 114501
- Casassus, S., Christiaens, V., Cárcamo, M., et al. 2021, *MNRAS*, 507, 3789
- Casassus, S., van der Plas, G. M., Perez, S., et al. 2013, *Nature*, 493, 191
- Cassen, P. & Moosman, A. 1981, *ICARUS*, 48, 353
- Cazzoletti, P., van Dishoeck, E. F., Visser, R., Facchini, S., & Bruderer, S. 2018, *A&A*, 609, A93
- Charnley, S. B. 1997, *ApJ*, 481, 396
- Chiang, E. I. & Goldreich, P. 1997, *ApJ*, 490, 368
- Christiaens, V., Casassus, S., Perez, S., van der Plas, G., & Ménard, F. 2014, *ApJ*, 785, L12
- Christiaens, V., Gonzalez, C., Farkas, R., et al. 2023, *The Journal of Open Source Software*, 8, 4774

- Claes, R. A. B., Manara, C. F., Garcia-Lopez, R., et al. 2022, *A&A*, 664, L7
- Clarke, C. J., Tazzari, M., Juhasz, A., et al. 2018, *ApJ*, 866, L6
- Cleeves, L. I., Bergin, E. A., Qi, C., Adams, F. C., & Öberg, K. I. 2015, *ApJ*, 799, 204
- Cleeves, L. I., Loomis, R. A., Teague, R., et al. 2021, *ApJ*, 911, 29
- Cleeves, L. I., Öberg, K. I., Wilner, D. J., et al. 2018, *ApJ*, 865, 155
- Colangeli, L., Henning, T., Brucato, J. R., et al. 2003, *A&A Rev.*, 11, 97
- Collings, M. P., Anderson, M. A., Chen, R., et al. 2004, *MNRAS*, 354, 1133
- Colmenares, M. J., Bergin, E. A., Salyk, C., et al. 2024, *ApJ*, 977, 173
- Cossins, P., Lodato, G., & Clarke, C. J. 2009, *MNRAS*, 393, 1157
- Crnkovic-Rubsamen, I., Zhu, Z., & Stone, J. M. 2015, *MNRAS*, 450, 4285
- Cuppen, H. M., Linnartz, H., & Ioppolo, S. 2024, *ARA&A*, 62, 243
- Cutri, R. M., Wright, E. L., Conrow, T., et al. 2013, Explanatory Supplement to the AllWISE Data Release Products, Explanatory Supplement to the AllWISE Data Release Products, by R. M. Cutri et al.
- Cuzzi, J. N. & Zahnle, K. J. 2004, *ApJ*, 614, 490
- Czekala, I., Loomis, R. A., Teague, R., et al. 2021, *ApJS*, 257, 2
- D'Alessio, P., Cantö, J., Calvet, N., & Lizano, S. 1998, *ApJ*, 500, 411
- Dartois, E., Dutrey, A., & Guilloteau, S. 2003, *A&A*, 399, 773
- Dawson, R. I. & Johnson, J. A. 2018, *ARA&A*, 56, 175
- Dong, R., Li, S., Chiang, E., & Li, H. 2017, *ApJ*, 843, 127
- Dong, R., Zhu, Z., Rafikov, R. R., & Stone, J. M. 2015, *ApJ*, 809, L5
- Dorn, R. J., Anglada-Escude, G., Baade, D., et al. 2014, *The Messenger*, 156, 7
- Dorn, R. J., Bristow, P., Smoker, J. V., et al. 2023, *A&A*, 671, A24
- Draine, B. T. 2003, *ARA&A*, 41, 241
- Drażkowska, J., Alibert, Y., & Moore, B. 2016, *A&A*, 594, A105
- Drażkowska, J., Bitsch, B., Lambrechts, M., et al. 2023, in *Astronomical Society of the Pacific Conference Series*, Vol. 534, Protostars and Planets VII, ed. S. Inutsuka, Y. Aikawa, T. Muto, K. Tomida, & M. Tamura, 717
- Dubrulle, B., Morfill, G., & Sterzik, M. 1995, *ICARUS*, 114, 237

- Duchêne, G., Ménard, F., Stapelfeldt, K., & Duvert, G. 2003, *A&A*, 400, 559
- Dullemond, C. P. & Dominik, C. 2004, *A&A*, 417, 159
- Dullemond, C. P., Dominik, C., & Natta, A. 2001, *ApJ*, 560, 957
- Easterwood, W., Kalyaan, A., & Banzatti, A. 2024, *ApJ*, 977, 21
- Ehrenfreund, P., Boogert, A. C. A., Gerakines, P. A., Tielens, A. G. G. M., & van Dishoeck, E. F. 1997, *A&A*, 328, 649
- Eistrup, C., Walsh, C., & van Dishoeck, E. F. 2016, *A&A*, 595, A83
- Erb, D. 2022, pybaselines: A Python library of algorithms for the baseline correction of experimental data, Zenodo
- Ercolano, B. & Pascucci, I. 2017, *Royal Society Open Science*, 4, 170114
- Espaillet, C., Muzerolle, J., Najita, J., et al. 2014, in *Protostars and Planets VI*, ed. H. Beuther, R. S. Klessen, C. P. Dullemond, & T. Henning, 497–520
- Fabian, D., Jäger, C., Henning, T., Dorschner, J., & Mutschke, H. 2000, *A&A*, 364, 282
- Facchini, S., Birnstiel, T., Bruderer, S., & van Dishoeck, E. F. 2017, *A&A*, 605, A16
- Facchini, S., Teague, R., Bae, J., et al. 2021, *AJ*, 162, 99
- Facchini, S., van Dishoeck, E. F., Manara, C. F., et al. 2019, *A&A*, 626, L2
- Fairlamb, J. R., Oudmaijer, R. D., Mendigutía, I., Ilee, J. D., & van den Ancker, M. E. 2015, *MNRAS*, 453, 976
- Fang, M., Pascucci, I., Edwards, S., et al. 2018, *ApJ*, 868, 28
- Fedele, D. & Favre, C. 2020, *A&A*, 638, A110
- Fischer, W. J., Hillenbrand, L. A., Herczeg, G. J., et al. 2023, in *Astronomical Society of the Pacific Conference Series*, Vol. 534, *Protostars and Planets VII*, ed. S. Inutsuka, Y. Aikawa, T. Muto, K. Tomida, & M. Tamura, 355
- Flaherty, K., Hughes, A. M., Simon, J. B., et al. 2020, *ApJ*, 895, 109
- Flaherty, K., Hughes, A. M., Simon, J. B., et al. 2024, *MNRAS*, 532, 363
- Flaherty, K. M., Hughes, A. M., Rose, S. C., et al. 2017, *ApJ*, 843, 150
- Flaherty, K. M., Hughes, A. M., Rosenfeld, K. A., et al. 2015, *ApJ*, 813, 99
- Flock, M., Nelson, R. P., Turner, N. J., et al. 2017, *ApJ*, 850, 131
- Flock, M., Turner, N. J., Nelson, R. P., et al. 2020, *ApJ*, 897, 155

- Fockenbergh, C. & Preses, J. M. 2002, *Journal of Physical Chemistry A*, 106, 2924
- Foreman-Mackey, D., Hogg, D. W., Lang, D., & Goodman, J. 2013, *PASP*, 125, 306
- Francis, L. & van der Marel, N. 2020, *ApJ*, 892, 111
- Francis, L., van Gelder, M. L., van Dishoeck, E. F., et al. 2024, arXiv e-prints, arXiv:2401.06880
- Fraser, H. J., Collings, M. P., McCoustra, M. R. S., & Williams, D. A. 2001, *MNRAS*, 327, 1165
- Fuchs, G. W., Cuppen, H. M., Ioppolo, S., et al. 2009, *A&A*, 505, 629
- Fujiwara, H., Honda, M., Kataza, H., et al. 2006, *ApJ*, 644, L133
- Fukagawa, M., Tamura, M., Itoh, Y., et al. 2006, *ApJ*, 636, L153
- Fukagawa, M., Tsukagoshi, T., Momose, M., et al. 2013, *PASJ*, 65, L14
- Furuya, K. 2024, arXiv e-prints, arXiv:2408.02958
- Furuya, K., Tsukagoshi, T., Qi, C., et al. 2022, *ApJ*, 926, 148
- Gaia Collaboration, Brown, A. G. A., Vallenari, A., et al. 2018, *A&A*, 616, A1
- Gaia Collaboration, Vallenari, A., Brown, A. G. A., et al. 2023, *A&A*, 674, A1
- Gammie, C. F. 1996, *ApJ*, 457, 355
- Gangi, M., Antonucci, S., Biazzo, K., et al. 2022, *A&A*, 667, A124
- Garg, H., Pinte, C., Christiaens, V., et al. 2021, *MNRAS*, 504, 782
- Garufi, A., Podio, L., Codella, C., et al. 2022, *A&A*, 658, A104
- Garufi, A., Podio, L., Kamp, I., et al. 2014, *A&A*, 567, A141
- Gasman, D., Temmink, M., van Dishoeck, E. F., et al. 2025, *A&A*, 694, A147
- Gasman, D., van Dishoeck, E. F., Grant, S. L., et al. 2023, *A&A*, 679, A117
- Gerakines, P. A., Whittet, D. C. B., Ehrenfreund, P., et al. 1999, *ApJ*, 522, 357
- Ginski, C., Facchini, S., Huang, J., et al. 2021, *ApJ*, 908, L25
- Glass, I. S. 1999, *Handbook of Infrared Astronomy*
- Glassgold, A. E., Najita, J., & Igea, J. 1997, *ApJ*, 480, 344
- Glenn, J., Meixner, M., Bradford, C. M., et al. 2025, *Journal of Astronomical Telescopes, Instruments, and Systems*, 11, 031628
- Godon, P. & Livio, M. 1999, *ApJ*, 523, 350

- Goldsmith, P. F. & Langer, W. D. 1999, *ApJ*, 517, 209
- Gomez Gonzalez, C. A., Wertz, O., Absil, O., et al. 2017, *AJ*, 154, 7
- Gordon, I. E., Rothman, L. S., Hargreaves, R. J., et al. 2022, *J. Quant. Spectr. Rad. Transf.*, 277, 107949
- Gould, R. J. & Salpeter, E. E. 1963, *ApJ*, 138, 393
- Grant, S. L., Bettoni, G., Banzatti, A., et al. 2023a, arXiv e-prints, arXiv:2309.03888
- Grant, S. L., Temmink, M., van Dishoeck, E. F., et al. 2025, *A&A*, 702, A126
- Grant, S. L., van Dishoeck, E. F., Tabone, B., et al. 2023b, *ApJ*, 947, L6
- GRAVITY Collaboration, Perraut, K., Labadie, L., et al. 2021, *A&A*, 655, A73
- Greenwood, A. J., Kamp, I., Waters, L. B. F. M., Woitke, P., & Thi, W. F. 2019, *A&A*, 626, A6
- Guidi, G., Isella, A., Testi, L., et al. 2022, *A&A*, 664, A137
- Guillot, T., Ida, S., & Ormel, C. W. 2014, *A&A*, 572, A72
- Guzmán, V. V., Öberg, K. I., Carpenter, J., et al. 2018, *ApJ*, 864, 170
- Haffert, S. Y., Bohn, A. J., de Boer, J., et al. 2019, *Nature Astronomy*, 3, 749
- Hammer, M., Kratter, K. M., & Lin, M.-K. 2017, *MNRAS*, 466, 3533
- Hammer, M. & Lin, M.-K. 2023, *MNRAS*, 525, 123
- Hammer, M., Lin, M.-K., Kratter, K. M., & Pinilla, P. 2021, *MNRAS*, 504, 3963
- Hammer, M., Pinilla, P., Kratter, K. M., & Lin, M.-K. 2019, *MNRAS*, 482, 3609
- Harris, C. R., Millman, K. J., van der Walt, S. J., et al. 2020, *Nature*, 585, 357
- Harsono, D., Bjerkele, P., van der Wiel, M. H. D., et al. 2018, *Nature Astronomy*, 2, 646
- Harsono, D., Bruderer, S., & van Dishoeck, E. F. 2015, *A&A*, 582, A41
- Hartmann, L., Calvet, N., Gullbring, E., & D'Alessio, P. 1998, *ApJ*, 495, 385
- Hasegawa, T. I., Herbst, E., & Leung, C. M. 1992, *ApJS*, 82, 167
- Hawley, J. F. 2001, *ApJ*, 554, 534
- Heays, A. N., Bosman, A. D., & van Dishoeck, E. F. 2017, *A&A*, 602, A105
- Henning, T. 2010, *ARA&A*, 48, 21
- Henning, T., Kamp, I., Samland, M., et al. 2024, *PASP*, 136, 054302

- Herbig, G. H. 1960, *ApJS*, 4, 337
- Herbst, E. & Klemperer, W. 1973, *ApJ*, 185, 505
- Herbst, E. & van Dishoeck, E. F. 2009, *ARA&A*, 47, 427
- Herczeg, G. J., Brown, J. M., van Dishoeck, E. F., & Pontoppidan, K. M. 2011, *A&A*, 533, A112
- Herczeg, G. J. & Hillenbrand, L. A. 2014, *ApJ*, 786, 97
- Hernández-Vera, C., Guzmán, V. V., Artur de la Villarmois, E., et al. 2024, *ApJ*, 967, 68
- Ho, P. T. P., Moran, J. M., & Lo, K. Y. 2004, *ApJ*, 616, L1
- Hollenbach, D., Johnstone, D., Lizano, S., & Shu, F. 1994, *ApJ*, 428, 654
- Honda, M., Inoue, A. K., Fukagawa, M., et al. 2009, *ApJ*, 690, L110
- Houck, J. R., Roellig, T. L., van Cleve, J., et al. 2004, *ApJS*, 154, 18
- Houge, A., Krijt, S., Banzatti, A., et al. 2025, *MNRAS*, 537, 691
- Huang, J., Andrews, S. M., Pérez, L. M., et al. 2018a, *ApJ*, 869, L43
- Huang, J., Bergin, E. A., Öberg, K. I., et al. 2021, *ApJS*, 257, 19
- Huang, P., Isella, A., Li, H., Li, S., & Ji, J. 2018b, *ApJ*, 867, 3
- Hunter, J. D. 2007, *Computing in Science & Engineering*, 9, 90
- Hunziker, S., Schmid, H. M., Ma, J., et al. 2021, *A&A*, 648, A110
- Ikoma, M. & Kobayashi, H. 2025, *ARA&A*, 63, 217
- Ilee, J. D., Forgan, D. H., Evans, M. G., et al. 2017, *MNRAS*, 472, 189
- Ilee, J. D., Walsh, C., Booth, A. S., et al. 2021, *ApJS*, 257, 9
- Ilee, J. D., Walsh, C., & Calahan, J. K. 2026, *AJ*, 171, 3
- Isella, A., Huang, J., Andrews, S. M., et al. 2018, *ApJ*, 869, L49
- Itoh, Y., Oasa, Y., Kudo, T., et al. 2014, *Research in Astronomy and Astrophysics*, 14, 1438
- Izquierdo, A. F., Facchini, S., Rosotti, G. P., van Dishoeck, E. F., & Testi, L. 2022, *ApJ*, 928, 2
- Jakobsen, P., Ferruit, P., Alves de Oliveira, C., et al. 2022, *A&A*, 661, A80
- Jang, H., Waters, R., Kaeufer, T., et al. 2024, *A&A*, 691, A148

- Jansen, D. J., Spaans, M., Hogerheijde, M. R., & van Dishoeck, E. F. 1995, *A&A*, 303, 541
- Jennings, J., Booth, R. A., Tazzari, M., Clarke, C. J., & Rosotti, G. P. 2022a, *MNRAS*, 509, 2780
- Jennings, J., Booth, R. A., Tazzari, M., Rosotti, G. P., & Clarke, C. J. 2020, *MNRAS*, 495, 3209
- Jennings, J., Tazzari, M., Clarke, C. J., Booth, R. A., & Rosotti, G. P. 2022b, *MNRAS*, 514, 6053
- Johansen, A. & Lacerda, P. 2010, *MNRAS*, 404, 475
- Johansen, A. & Lambrechts, M. 2017, *Annual Review of Earth and Planetary Sciences*, 45, 359
- Johansen, A., Youdin, A., & Klahr, H. 2009, *ApJ*, 697, 1269
- Johnstone, D., Boonman, A. M. S., & van Dishoeck, E. F. 2003, *A&A*, 412, 157
- Juhász, A., Bouwman, J., Henning, T., et al. 2010, *ApJ*, 721, 431
- Kaeufer, T., Min, M., Woitke, P., Kamp, I., & Arabhavi, A. M. 2024, *A&A*, 687, A209
- Kaeuffl, H.-U., Ballester, P., Biereichel, P., et al. 2004, in *Society of Photo-Optical Instrumentation Engineers (SPIE) Conference Series*, Vol. 5492, *Ground-based Instrumentation for Astronomy*, ed. A. F. M. Moorwood & M. Iye, 1218–1227
- Kalyaan, A., Pinilla, P., Krijt, S., et al. 2023, *ApJ*, 954, 66
- Kalyaan, A., Pinilla, P., Krijt, S., Mulders, G. D., & Banzatti, A. 2021, *ApJ*, 921, 84
- Kama, M., Bruderer, S., van Dishoeck, E. F., et al. 2016, *A&A*, 592, A83
- Kama, M., Trapman, L., Fedele, D., et al. 2020, *A&A*, 634, A88
- Kamp, I., Henning, T., Arabhavi, A. M., et al. 2023, *Faraday Discussions*, 245, 112
- Kamp, I., Thi, W. F., Meeus, G., et al. 2013, *A&A*, 559, A24
- Kastner, J. H., Qi, C., Dickson-Vandervelde, D. A., et al. 2018, *ApJ*, 863, 106
- Kastner, J. H., Zuckerman, B., Weintraub, D. A., & Forveille, T. 1997, *Science*, 277, 67
- Kayanuma, M., Shoji, M., Furuya, K., et al. 2019, *Chemical Physics Letters*, 714, 137
- Kenyon, S. J., Dobrzycka, D., & Hartmann, L. 1994, *AJ*, 108, 1872

- Keppler, M., Benisty, M., Müller, A., et al. 2018, *A&A*, 617, A44
- Keppler, M., Penzlin, A., Benisty, M., et al. 2020, *A&A*, 639, A62
- Kessler, M. F., Steinz, J. A., Anderegg, M. E., et al. 1996, *A&A*, 315, L27
- Kley, W. 1999, *MNRAS*, 303, 696
- Kluyver, T., Ragan-Kelley, B., Pérez, F., et al. 2016, in *Positioning and Power in Academic Publishing: Players, Agents and Agendas*, ed. F. Loizides & B. Schmidt, IOS Press, 87 – 90
- Kokubo, E. & Ida, S. 1996, *ICARUS*, 123, 180
- Kokubo, E. & Ida, S. 2002, *ApJ*, 581, 666
- Kóspál, Á., Ábrahám, P., Diehl, L., et al. 2023, *ApJ*, 945, L7
- Kraus, S., Kreplin, A., Fukugawa, M., et al. 2017, *ApJ*, 848, L11
- Krist, J. E., Stapelfeldt, K. R., & Watson, A. M. 2002, *ApJ*, 570, 785
- Krolikowski, D. M., Kraus, A. L., & Rizzuto, A. C. 2021, *AJ*, 162, 110
- Kuznetsova, A., Bae, J., Hartmann, L., & Mac Low, M.-M. 2022, *ApJ*, 928, 92
- Labiano, A., Argyriou, I., Álvarez-Márquez, J., et al. 2021, *A&A*, 656, A57
- Lacour, S., Biller, B., Cheetham, A., et al. 2016, *A&A*, 590, A90
- Lacy, J. H., Sneden, C., Kim, H., & Jaffe, D. T. 2017, *ApJ*, 838, 66
- Lambrechts, M. & Johansen, A. 2012, *A&A*, 544, A32
- Lambrechts, M., Johansen, A., & Morbidelli, A. 2014, *A&A*, 572, A35
- Law, C. J., Alarcón, F., Cleaves, L. I., Öberg, K. I., & Paneque-Carreño, T. 2023a, *ApJ*, 959, L27
- Law, C. J., Benisty, M., Facchini, S., et al. 2024, *ApJ*, 964, 190
- Law, C. J., Teague, R., Loomis, R. A., et al. 2021, *ApJS*, 257, 4
- Law, C. J., Teague, R., Öberg, K. I., et al. 2023b, *ApJ*, 948, 60
- Le Gal, R., Öberg, K. I., Loomis, R. A., Pegues, J., & Bergner, J. B. 2019, *ApJ*, 876, 72
- Le Gal, R., Öberg, K. I., Teague, R., et al. 2021, *ApJS*, 257, 12
- Lee, J.-E., Lee, S., Baek, G., et al. 2019, *Nature Astronomy*, 3, 314
- Leemker, M., Booth, A. S., van Dishoeck, E. F., et al. 2022, *A&A*, 663, A23
- Leemker, M., Booth, A. S., van Dishoeck, E. F., et al. 2023, *A&A*, 673, A7

- Leemker, M., Tobin, J. J., Facchini, S., et al. 2025, *Nature Astronomy*, 9, 1486
- Leemker, M., van't Hoff, M. L. R., Trapman, L., et al. 2021, *A&A*, 646, A3
- Lesur, G., Ferreira, J., & Ogilvie, G. I. 2013, *A&A*, 550, A61
- Lesur, G., Flock, M., Ercolano, B., et al. 2023, in *Astronomical Society of the Pacific Conference Series*, Vol. 534, *Protostars and Planets VII*, ed. S. Inutsuka, Y. Aikawa, T. Muto, K. Tomida, & M. Tamura, 465
- Lesur, G., Hennebelle, P., & Fromang, S. 2015, *A&A*, 582, L9
- Li, H., Finn, J. M., Lovelace, R. V. E., & Colgate, S. A. 2000, *ApJ*, 533, 1023
- Lienert, J. L., Bitsch, B., & Henning, T. 2024, *A&A*, 691, A72
- Lissauer, J. J. 1993, *ARA&A*, 31, 129
- Long, F., Andrews, S. M., Zhang, S., et al. 2022, *ApJ*, 937, L1
- Long, F., Herczeg, G. J., Harsono, D., et al. 2019, *ApJ*, 882, 49
- Long, F., Pinilla, P., Herczeg, G. J., et al. 2018, *ApJ*, 869, 17
- Loomis, R. A., Cleeves, L. I., Öberg, K. I., et al. 2018, *ApJ*, 859, 131
- Loomis, R. A., Cleeves, L. I., Öberg, K. I., Guzman, V. V., & Andrews, S. M. 2015, *ApJ*, 809, L25
- Loomis, R. A., Facchini, S., Benisty, M., et al. 2025, *ApJ*, 984, L7
- Lovelace, R. V. E. & Hohlfield, R. G. 2013, *MNRAS*, 429, 529
- Lovelace, R. V. E., Li, H., Colgate, S. A., & Nelson, A. F. 1999, *ApJ*, 513, 805
- Lovelace, R. V. E. & Romanova, M. M. 2014, *Fluid Dynamics Research*, 46, 041401
- Luhman, K. L. 2012, *ARA&A*, 50, 65
- Luhman, K. L. 2023, *AJ*, 165, 37
- Lynden-Bell, D. & Pringle, J. E. 1974, *MNRAS*, 168, 603
- Lyra, W., Johansen, A., Zsom, A., Klahr, H., & Piskunov, N. 2009, *A&A*, 497, 869
- Mah, J., Bitsch, B., Pascucci, I., & Henning, T. 2023, *A&A*, 677, L7
- Mah, J., Savvidou, S., & Bitsch, B. 2024, *A&A*, 686, L17
- Malfait, K., Waelkens, C., Waters, L. B. F. M., et al. 1998, *A&A*, 332, L25
- Mallaney, P., Banzatti, A., Salyk, C., et al. 2026, *arXiv e-prints*, arXiv:2601.02344

- Mamajek, E. E. 2009, in *American Institute of Physics Conference Series*, Vol. 1158, *Exoplanets and Disks: Their Formation and Diversity*, ed. T. Usuda, M. Tamura, & M. Ishii (AIP), 3–10
- Manara, C. F., Ansdell, M., Rosotti, G. P., et al. 2023, in *Astronomical Society of the Pacific Conference Series*, Vol. 534, *Protostars and Planets VII*, ed. S. Inutsuka, Y. Aikawa, T. Muto, K. Tomida, & M. Tamura, 539
- Manara, C. F., Fedele, D., Herczeg, G. J., & Teixeira, P. S. 2016, *A&A*, 585, A136
- Mandell, A. M., Bast, J., van Dishoeck, E. F., et al. 2012, *ApJ*, 747, 92
- Marino, S., Casassus, S., Perez, S., et al. 2015a, *ApJ*, 813, 76
- Marino, S., Perez, S., & Casassus, S. 2015b, *ApJ*, 798, L44
- Mayama, S., Pérez, S., Kusakabe, N., et al. 2020, *AJ*, 159, 12
- McClure, M. K., Bergin, E. A., Cleeves, L. I., et al. 2016, *ApJ*, 831, 167
- McGuire, B. A. 2022, *ApJS*, 259, 30
- McKee, C. F. & Ostriker, E. C. 2007, *ARA&A*, 45, 565
- McLean, I. S., Becklin, E. E., Bendiksen, O., et al. 1998, in *Society of Photo-Optical Instrumentation Engineers (SPIE) Conference Series*, Vol. 3354, *Infrared Astronomical Instrumentation*, ed. A. M. Fowler, 566–578
- McMullin, J. P., Waters, B., Schiebel, D., Young, W., & Golap, K. 2007, in *Astronomical Society of the Pacific Conference Series*, Vol. 376, *Astronomical Data Analysis Software and Systems XVI*, ed. R. A. Shaw, F. Hill, & D. J. Bell, 127
- Meheut, H., Lovelace, R. V. E., & Lai, D. 2013, *MNRAS*, 430, 1988
- Meheut, H., Meliani, Z., Varniere, P., & Benz, W. 2012a, *A&A*, 545, A134
- Meheut, H., Yu, C., & Lai, D. 2012b, *MNRAS*, 422, 2399
- Meijerink, R., Pontoppidan, K. M., Blake, G. A., Poelman, D. R., & Dullemond, C. P. 2009, *ApJ*, 704, 1471
- Ménard, F., Cuello, N., Ginski, C., et al. 2020, *A&A*, 639, L1
- Milam, S. N., Savage, C., Brewster, M. A., Ziurys, L. M., & Wyckoff, S. 2005, *ApJ*, 634, 1126
- Millar, T. J. & Nejad, L. A. M. 1985, *MNRAS*, 217, 507
- Millar, T. J., Walsh, C., Cordiner, M. A., Ní Chuimín, R., & Herbst, E. 2007, *ApJ*, 662, L87
- Min, M., Bouwman, J., Dominik, C., et al. 2016, *A&A*, 593, A11

- Minissale, M., Aikawa, Y., Bergin, E., et al. 2022, *ACS Earth and Space Chemistry*, 6, 597
- Miotello, A., Facchini, S., van Dishoeck, E. F., et al. 2019, *A&A*, 631, A69
- Miotello, A., Kamp, I., Birnstiel, T., Cleeves, L. C., & Kataoka, A. 2023, in *Astronomical Society of the Pacific Conference Series*, Vol. 534, *Protostars and Planets VII*, ed. S. Inutsuka, Y. Aikawa, T. Muto, K. Tomida, & M. Tamura, 501
- Mollière, P., Molyarova, T., Bitsch, B., et al. 2022, *ApJ*, 934, 74
- Montesinos, M., Perez, S., Casassus, S., et al. 2016, *ApJ*, 823, L8
- Morbidelli, A., Lunine, J. I., O'Brien, D. P., Raymond, S. N., & Walsh, K. J. 2012, *Annual Review of Earth and Planetary Sciences*, 40, 251
- Mulders, G. D., Ciesla, F. J., Min, M., & Pascucci, I. 2015, *ApJ*, 807, 9
- Müller, A., Keppler, M., Henning, T., et al. 2018, *A&A*, 617, L2
- Müller, H. S. P., Schlöder, F., Stutzki, J., & Winnewisser, G. 2005, *Journal of Molecular Structure*, 742, 215
- Müller, H. S. P., Thorwirth, S., Roth, D. A., & Winnewisser, G. 2001, *A&A*, 370, L49
- Najita, J. R., Carr, J. S., Salyk, C., et al. 2018, *ApJ*, 862, 122
- Najita, J. R., Carr, J. S., Strom, S. E., et al. 2010, *ApJ*, 712, 274
- Najita, J. R., Strom, S. E., & Muzerolle, J. 2007, *MNRAS*, 378, 369
- Nazari, P., Tabone, B., & Rosotti, G. P. 2023, *A&A*, 671, A107
- Newville, M., Stensitzki, T., Allen, D. B., & Ingargiola, A. 2014, *LMFIT: Non-Linear Least-Square Minimization and Curve-Fitting for Python*
- Nguyen, D. C., Brandeker, A., van Kerkwijk, M. H., & Jayawardhana, R. 2012, *ApJ*, 745, 119
- Noble, J. A., Theule, P., Mispelaer, F., et al. 2012, *A&A*, 543, A5
- Öberg, K. I. & Bergin, E. A. 2021, *Phys. Rep.*, 893, 1
- Öberg, K. I., Facchini, S., & Anderson, D. E. 2023, *ARA&A*, 61, 287
- Öberg, K. I., Furuya, K., Loomis, R., et al. 2015, *ApJ*, 810, 112
- Öberg, K. I., Guzmán, V. V., Walsh, C., et al. 2021, *ApJS*, 257, 1
- Öberg, K. I., Qi, C., Fogel, J. K. J., et al. 2010, *ApJ*, 720, 480
- Öberg, K. I., Qi, C., Wilner, D. J., & Andrews, S. M. 2011, *ApJ*, 743, 152

- Ohashi, N. 2008, *AP&SS*, 313, 101
- Ohashi, S., Kataoka, A., van der Marel, N., et al. 2020, *ApJ*, 900, 81
- Olofsson, J., Augereau, J.-C., van Dishoeck, E. F., et al. 2009, *A&A*, 507, 327
- Ormel, C. W. & Klahr, H. H. 2010, *A&A*, 520, A43
- Owen, J. E. & Kollmeier, J. A. 2017, *MNRAS*, 467, 3379
- pandas development team, T. 2020, *pandas-dev/pandas*: Pandas
- Paneque-Carreño, T., Izquierdo, A. F., Teague, R., et al. 2024, *A&A*, 684, A174
- Paneque-Carreño, T., Miotello, A., van Dishoeck, E. F., et al. 2023, *A&A*, 669, A126
- Pascucci, I., Apai, D., Hardegree-Ullman, E. E., et al. 2008, *ApJ*, 673, 477
- Pascucci, I., Cabrit, S., Edwards, S., et al. 2023, in *Astronomical Society of the Pacific Conference Series*, Vol. 534, *Protostars and Planets VII*, ed. S. Inutsuka, Y. Aikawa, T. Muto, K. Tomida, & M. Tamura, 567
- Pearson, T. J. 1999, in *Astronomical Society of the Pacific Conference Series*, Vol. 180, *Synthesis Imaging in Radio Astronomy II*, ed. G. B. Taylor, C. L. Carilli, & R. A. Perley, 335
- Pegues, J., Öberg, K. I., Bergner, J. B., et al. 2020, *ApJ*, 890, 142
- Penteado, E. M., Walsh, C., & Cuppen, H. M. 2017, *ApJ*, 844, 71
- Pérez, F. & Granger, B. E. 2007, *Computing in Science and Engineering*, 9, 21
- Pérez, L. M., Isella, A., Carpenter, J. M., & Chandler, C. J. 2014, *ApJ*, 783, L13
- Perez, S., Dunhill, A., Casassus, S., et al. 2015, *ApJ*, 811, L5
- Perotti, G., Christiaens, V., Henning, T., et al. 2023, *Nature*, 620, 516
- Perrero, J., Enrique-Romero, J., Ferrero, S., et al. 2022, *ApJ*, 938, 158
- Pilbratt, G. L., Riedinger, J. R., Passvogel, T., et al. 2010, *A&A*, 518, L1
- Pinilla, P. 2022, *European Physical Journal Plus*, 137, 1206
- Pinilla, P., Benisty, M., & Birnstiel, T. 2012a, *A&A*, 545, A81
- Pinilla, P., Benisty, M., de Boer, J., et al. 2018, *ApJ*, 868, 85
- Pinilla, P., Benisty, M., Waters, R., Bae, J., & Facchini, S. 2024, *A&A*, 686, A135
- Pinilla, P., Birnstiel, T., Ricci, L., et al. 2012b, *A&A*, 538, A114
- Pinte, C., van der Plas, G., Ménard, F., et al. 2019, *Nature Astronomy*, 3, 1109

- Pollack, J. B., Hubickyj, O., Bodenheimer, P., et al. 1996, *ICARUS*, 124, 62
- Pontoppidan, K., Battersby, C., Kataria, T., et al. 2025, in *American Astronomical Society Meeting Abstracts*, Vol. 245, American Astronomical Society Meeting Abstracts #245, 209.07
- Pontoppidan, K. M., Blake, G. A., & Smette, A. 2011, *ApJ*, 733, 84
- Pontoppidan, K. M., Blake, G. A., van Dishoeck, E. F., et al. 2008a, *ApJ*, 684, 1323
- Pontoppidan, K. M., Boogert, A. C. A., Fraser, H. J., et al. 2008b, *ApJ*, 678, 1005
- Pontoppidan, K. M., Salyk, C., Banzatti, A., et al. 2024, *ApJ*, 963, 158
- Pontoppidan, K. M., Salyk, C., Bergin, E. A., et al. 2014, in *Protostars and Planets VI*, ed. H. Beuther, R. S. Klessen, C. P. Dullemond, & T. Henning, 363–385
- Pontoppidan, K. M., Salyk, C., Blake, G. A., et al. 2010, *ApJ*, 720, 887
- Press, W. H., Teukolsky, S. A., Vetterling, W. T., & Flannery, B. P. 1992, *Numerical recipes in C. The art of scientific computing*
- Price, D. J., Cuello, N., Pinte, C., et al. 2018, *MNRAS*, 477, 1270
- Pringle, J. E. 1981, *ARA&A*, 19, 137
- Qi, C., Öberg, K. I., & Wilner, D. J. 2013, *ApJ*, 765, 34
- Rab, C., Kamp, I., Dominik, C., et al. 2020, *A&A*, 642, A165
- Rabli, D. & Flower, D. R. 2010, *MNRAS*, 406, 95
- Raettig, N., Lyra, W., & Klahr, H. 2021, *ApJ*, 913, 92
- Rampinelli, L., Facchini, S., Leemker, M., et al. 2024, *A&A*, 689, A65
- Rayner, J., Tokunaga, A., Jaffe, D., et al. 2022, *PASP*, 134, 015002
- Rayner, J., Tokunaga, A., Jaffe, D., et al. 2016, in *Society of Photo-Optical Instrumentation Engineers (SPIE) Conference Series*, Vol. 9908, *Ground-based and Airborne Instrumentation for Astronomy VI*, ed. C. J. Evans, L. Simard, & H. Takami, 990884
- Regály, Z., Juhász, A., Sándor, Z., & Dullemond, C. P. 2012, *MNRAS*, 419, 1701
- Regály, Z., Kadam, K., & Dullemond, C. P. 2021, *MNRAS*, 506, 2685
- Rice, W. K. M., Lodato, G., Pringle, J. E., Armitage, P. J., & Bonnell, I. A. 2004, *MNRAS*, 355, 543
- Rich, E. A., Wisniewski, J. P., Currie, T., et al. 2019, *ApJ*, 875, 38
- Rieke, G. H., Wright, G. S., Böker, T., et al. 2015, *PASP*, 127, 584

- Rigby, J., Perrin, M., McElwain, M., et al. 2023, *PASP*, 135, 048001
- Roccatagliata, V., Franciosini, E., Sacco, G. G., Randich, S., & Sicilia-Aguilar, A. 2020, *A&A*, 638, A85
- Romero-Mirza, C. E., Banzatti, A., Öberg, K. I., et al. 2024a, *ApJ*, 975, 78
- Romero-Mirza, C. E., Öberg, K. I., Banzatti, A., et al. 2024b, *ApJ*, 964, 36
- Romero-Mirza, C. E., Öberg, K. I., Law, C. J., et al. 2023, *ApJ*, 943, 35
- Rometsch, T., Ziampras, A., Kley, W., & Béthune, W. 2021, *A&A*, 656, A130
- Rosotti, G. P., Benisty, M., Juhász, A., et al. 2020, *MNRAS*, 491, 1335
- Rosotti, G. P., Ilee, J. D., Facchini, S., et al. 2021, *MNRAS*, 501, 3427
- Rota, A. A., Meijerhof, J. D., van der Marel, N., et al. 2024, *A&A*, 684, A134
- Salinas, V. N., Hogerheijde, M. R., Mathews, G. S., et al. 2017, *A&A*, 606, A125
- Salyk, C., Blake, G. A., Boogert, A. C. A., & Brown, J. M. 2009, *ApJ*, 699, 330
- Salyk, C., Blake, G. A., Boogert, A. C. A., & Brown, J. M. 2011a, *ApJ*, 743, 112
- Salyk, C. & Gasman, D. 2025, in *PRIMA General Observer Science Book Volume 2*, ed. A. Moullet, D. Burgarella, T. Kataria, H. Beuther, C. Battersby, M. Cheng, T. Essinger-Hileman, H. Inami, E. Mills, T. Nagao, & S. Unwin, Vol. 2, 476–480
- Salyk, C., Lacy, J., Richter, M., et al. 2019, *ApJ*, 874, 24
- Salyk, C., Pontoppidan, K. M., Banzatti, A., et al. 2025, *AJ*, 169, 184
- Salyk, C., Pontoppidan, K. M., Blake, G. A., et al. 2008, *ApJ*, 676, L49
- Salyk, C., Pontoppidan, K. M., Blake, G. A., Najita, J. R., & Carr, J. S. 2011b, *ApJ*, 731, 130
- Santos, J. C., Chuang, K.-J., Lamberts, T., et al. 2022, *ApJ*, 931, L33
- Savitzky, A. & Golay, M. J. E. 1964, *Analytical Chemistry*, 36, 1627
- Schöier, F. L., van der Tak, F. F. S., van Dishoeck, E. F., & Black, J. H. 2005, *A&A*, 432, 369
- Schwarz, K. R., Henning, T., Christiaens, V., et al. 2024, *ApJ*, 962, 8
- Schwarz, K. R., Samland, M., Olofsson, G., et al. 2025, *ApJ*, 980, 148
- Sellek, A. D., Vlasblom, M., & van Dishoeck, E. F. 2025, *A&A*, 694, A79
- Semenov, D., Favre, C., Fedele, D., et al. 2018, *A&A*, 617, A28
- Semenov, D., Wiebe, D., & Henning, T. 2006, *ApJ*, 647, L57

- Shakura, N. I. & Sunyaev, R. A. 1973, *A&A*, 24, 337
- Shu, F. H., Adams, F. C., & Lizano, S. 1987, *ARA&A*, 25, 23
- Simon, M., Guilloteau, S., Di Folco, E., et al. 2017, *ApJ*, 844, 158
- Skrutskie, M. F., Dutkevitch, D., Strom, S. E., et al. 1990, *AJ*, 99, 1187
- Smith, S. A., Romero-Mirza, C. E., Banzatti, A., et al. 2025, *ApJ*, 984, L51
- Speedie, J., Dong, R., Hall, C., et al. 2024, *Nature*, 633, 58
- Speedie, J., Dong, R., Teague, R., et al. 2025, *ApJ*, 981, L30
- Stacey, G. & POEMM Science Team. 2025, in *American Astronomical Society Meeting Abstracts*, Vol. 245, *American Astronomical Society Meeting Abstracts #245*, 441.05
- Stadler, J., Benisty, M., Zagaria, F., et al. 2026, arXiv e-prints, arXiv:2601.15262
- Stapper, L. M., Hogerheijde, M. R., van Dishoeck, E. F., et al. 2024, *A&A*, 682, A149
- Stapper, L. M., Hogerheijde, M. R., van Dishoeck, E. F., & Mentel, R. 2022, *A&A*, 658, A112
- Stecher, T. P. & Williams, D. A. 1967, *ApJ*, 149, L29
- Sternberg, A. & Dalgarno, A. 1995, *ApJS*, 99, 565
- Stevenson, D. J. & Lunine, J. I. 1988, *ICARUS*, 75, 146
- Stolker, T., Kammerer, J., Benisty, M., et al. 2024, *A&A*, 682, A101
- Strom, K. M., Strom, S. E., Edwards, S., Cabrit, S., & Skrutskie, M. F. 1989, *AJ*, 97, 1451
- Sturm, J. A., McClure, M. K., Beck, T. L., et al. 2023a, *A&A*, 679, A138
- Sturm, J. A., McClure, M. K., Bergner, J. B., et al. 2023b, *A&A*, 677, A18
- Sturm, J. A., McClure, M. K., Law, C. J., et al. 2023c, *A&A*, 677, A17
- Su, Z. & Bai, X.-N. 2024, *ApJ*, 975, 126
- Tabone, B., Bettoni, G., van Dishoeck, E. F., et al. 2023, *Nature Astronomy*, 7, 805
- Tabone, B., Rosotti, G. P., Lodato, G., et al. 2022, *MNRAS*, 512, L74
- Tabone, B., van Dishoeck, E. F., & Black, J. H. 2024, *A&A*, 691, A11
- Tabone, B., van Hemert, M. C., van Dishoeck, E. F., & Black, J. H. 2021, *A&A*, 650, A192

- Taniguchi, K., Pineda, J. E., Caselli, P., et al. 2024, *ApJ*, 965, 162
- Tanious, M., Le Gal, R., Faure, A., et al. 2025, *A&A*, 703, A244
- Tanious, M., Le Gal, R., Neri, R., et al. 2024, *A&A*, 687, A92
- Tazaki, R., Murakawa, K., Muto, T., Honda, M., & Inoue, A. K. 2021, *ApJ*, 921, 173
- Tazzari, M., Testi, L., Ercolano, B., et al. 2016, *A&A*, 588, A53
- Tazzari, M., Testi, L., Natta, A., et al. 2017, *A&A*, 606, A88
- Teague, R. 2019a, *The Journal of Open Source Software*, 4, 1220
- Teague, R. 2019b, *The Journal of Open Source Software*, 4, 1632
- Teague, R. 2020, *richteague/keplerian_mask*: Initial Release
- Teague, R., Bae, J., Aikawa, Y., et al. 2021, *ApJS*, 257, 18
- Teague, R., Bae, J., Huang, J., & Bergin, E. A. 2019, *ApJ*, 884, L56
- Teague, R. & Foreman-Mackey, D. 2018, *Research Notes of the American Astronomical Society*, 2, 173
- Temmink, M., Booth, A. S., Leemker, M., et al. 2025a, *A&A*, 693, A101
- Temmink, M., Booth, A. S., van der Marel, N., & van Dishoeck, E. F. 2023, *A&A*, 675, A131
- Temmink, M., Sellek, A. D., Gasman, D., et al. 2025b, *A&A*, 699, A134
- Temmink, M., van Dishoeck, E. F., Gasman, D., et al. 2024a, *A&A*, 689, A330
- Temmink, M., van Dishoeck, E. F., Grant, S. L., et al. 2024b, *A&A*, 686, A117
- Tennyson, J. 2019, *Astronomical Spectroscopy. An Introduction to the Atomic and Molecular Physics of Astronomical Spectroscopy*
- Terwisscha van Scheltinga, J., Hogerheijde, M. R., Cleeves, L. I., et al. 2021, *ApJ*, 906, 111
- Terwisscha van Scheltinga, J., Ligterink, N. F. W., Bosman, A. D., Hogerheijde, M. R., & Linnartz, H. 2022, *A&A*, 666, A35
- Thi, W. F., Kamp, I., Woitke, P., et al. 2013, *A&A*, 551, A49
- Thi, W. F., van Dishoeck, E. F., Blake, G. A., et al. 2001, *ApJ*, 561, 1074
- Thi, W. F., van Zadelhoff, G. J., & van Dishoeck, E. F. 2004, *A&A*, 425, 955
- Tielens, A. 2021, *Molecular Astrophysics*
- Tielens, A. G. G. M. 2013, *Reviews of Modern Physics*, 85, 1021

- Tielens, A. G. G. M. & Allamandola, L. J. 1987, in *Interstellar Processes*, ed. D. J. Hollenbach & J. Thronson, Harley A., Vol. 134, 397
- Tielens, A. G. G. M. & Hagen, W. 1982, *A&A*, 114, 245
- Tielens, A. G. G. M. & Hollenbach, D. 1985, *ApJ*, 291, 747
- Tobin, J. J. & Sheehan, P. D. 2024, *ARA&A*, 62, 203
- Tobin, J. J., van't Hoff, M. L. R., Leemker, M., et al. 2023, *Nature*, 615, 227
- Trapman, L., Facchini, S., Hogerheijde, M. R., van Dishoeck, E. F., & Bruderer, S. 2019, *A&A*, 629, A79
- Trapman, L., Miotello, A., Kama, M., van Dishoeck, E. F., & Bruderer, S. 2017, *A&A*, 605, A69
- Trapman, L., Rosotti, G., Bosman, A. D., Hogerheijde, M. R., & van Dishoeck, E. F. 2020, *A&A*, 640, A5
- Trapman, L., Tabone, B., Rosotti, G., & Zhang, K. 2022a, *ApJ*, 926, 61
- Trapman, L., Zhang, K., van't Hoff, M. L. R., Hogerheijde, M. R., & Bergin, E. A. 2022b, *ApJ*, 926, L2
- Tychoniec, Ł., Manara, C. F., Rosotti, G. P., et al. 2020, *A&A*, 640, A19
- Tychoniec, Ł., van Gelder, M. L., van Dishoeck, E. F., et al. 2024, *A&A*, 687, A36
- Urbina, F., Miley, J., Kama, M., & Keyte, L. 2024, *A&A*, 686, A120
- Urpin, V. & Brandenburg, A. 1998, *MNRAS*, 294, 399
- Valenti, J. A., Johns-Krull, C. M., & Linsky, J. L. 2000, *ApJS*, 129, 399
- van Capelleveen, R. F., Ginski, C., Kenworthy, M. A., et al. 2025, *ApJ*, 990, L8
- van der Marel, N. 2023, *European Physical Journal Plus*, 138, 225
- van der Marel, N., Booth, A. S., Leemker, M., van Dishoeck, E. F., & Ohashi, S. 2021a, *A&A*, 651, L5
- van der Marel, N., Bosman, A. D., Krijt, S., Mulders, G. D., & Bergner, J. B. 2021b, *A&A*, 653, L9
- van der Marel, N., Cazzoletti, P., Pinilla, P., & Garufi, A. 2016a, *ApJ*, 832, 178
- van der Marel, N. & Pinilla, P. 2023, *arXiv e-prints*, arXiv:2310.09077
- van der Marel, N., van Dishoeck, E. F., Bruderer, S., et al. 2016b, *A&A*, 585, A58
- van der Marel, N., van Dishoeck, E. F., Bruderer, S., et al. 2013, *Science*, 340, 1199

- van der Marel, N., van Dishoeck, E. F., Bruderer, S., & van Kempen, T. A. 2014, *A&A*, 563, A113
- van der Plas, G., Casassus, S., Ménard, F., et al. 2014, *ApJ*, 792, L25
- van der Plas, G., van den Ancker, M. E., Waters, L. B. F. M., & Dominik, C. 2015, *A&A*, 574, A75
- van der Tak, F. F. S., Black, J. H., Schöier, F. L., Jansen, D. J., & van Dishoeck, E. F. 2007, *A&A*, 468, 627
- van Dishoeck, E. F. 2006, *Proceedings of the National Academy of Science*, 103, 12249
- van Dishoeck, E. F. 2014, *Faraday Discussions*, 168, 9
- van Dishoeck, E. F. & Black, J. H. 1988, *ApJ*, 334, 771
- van Dishoeck, E. F., Herbst, E., & Neufeld, D. A. 2013, *Chemical Reviews*, 113, 9043
- van Dishoeck, E. F., Kristensen, L. E., Mottram, J. C., et al. 2021, *A&A*, 648, A24
- van Gelder, M. L., Ressler, M. E., van Dishoeck, E. F., et al. 2024, *A&A*, 682, A78
- van Gelder, M. L., Tabone, B., van Dishoeck, E. F., & Godard, B. 2021, *A&A*, 653, A159
- van 't Hoff, M. L. R., Tobin, J. J., Trapman, L., et al. 2018, *ApJ*, 864, L23
- van 't Hoff, M. L. R., Walsh, C., Kama, M., Facchini, S., & van Dishoeck, E. F. 2017, *A&A*, 599, A101
- van Terwisga, S. E., van Dishoeck, E. F., Ansdell, M., et al. 2018, *A&A*, 616, A88
- van Zadelhoff, G. J., Aikawa, Y., Hogerheijde, M. R., & van Dishoeck, E. F. 2003, *A&A*, 397, 789
- van Zadelhoff, G. J., van Dishoeck, E. F., Thi, W. F., & Blake, G. A. 2001, *A&A*, 377, 566
- van't Hoff, M. L. R. & Bergner, J. B. 2026, in *Encyclopedia of Astrophysics*, Vol. 1, 210–232
- Verhoeff, A. P., Min, M., Pantin, E., et al. 2011, *A&A*, 528, A91
- Vidal, T. H. G., Loison, J.-C., Jaziri, A. Y., et al. 2017, *MNRAS*, 469, 435
- Villenave, M., Ménard, F., Dent, W. R. F., et al. 2020, *A&A*, 642, A164
- Vioque, M., Booth, R. A., Ragusa, E., et al. 2026, *A&A*, 705, A238
- Virtanen, P., Gommers, R., Oliphant, T. E., et al. 2020, *Nature Methods*, 17, 261

- Visser, R., van Dishoeck, E. F., Doty, S. D., & Dullemond, C. P. 2009, *A&A*, 495, 881
- Vlasblom, M., Temmink, M., Grant, S. L., et al. 2025a, *A&A*, 693, A278
- Vlasblom, M., Temmink, M., Sellek, A. D., & van Dishoeck, E. F. 2025b, *A&A*, 703, A52
- Vlasblom, M., van Dishoeck, E. F., Tabone, B., & Bruderer, S. 2024, *A&A*, 682, A91
- Waelkens, C., Waters, L. B. F. M., de Graauw, M. S., et al. 1996, *A&A*, 315, L245
- Wafflard-Fernandez, G. & Baruteau, C. 2020, *MNRAS*, 493, 5892
- Waggoner, A. R. & Cleeves, L. I. 2022, *ApJ*, 928, 46
- Waggoner, A. R., Cleeves, L. I., Loomis, R. A., et al. 2023, *ApJ*, 956, 103
- Wakelam, V., Bron, E., Cazaux, S., et al. 2017, *Molecular Astrophysics*, 9, 1
- Wakelam, V., Herbst, E., Loison, J.-C., et al. 2012, *ApJS*, 199, 21
- Walsh, C., Loomis, R. A., Öberg, K. I., et al. 2016, *ApJ*, 823, L10
- Walsh, C., Millar, T. J., & Nomura, H. 2010, *ApJ*, 722, 1607
- Walsh, C., Nomura, H., Millar, T. J., & Aikawa, Y. 2012, *ApJ*, 747, 114
- Walsh, C., Nomura, H., & van Dishoeck, E. 2015, *A&A*, 582, A88
- Watanabe, N. & Kouchi, A. 2002, *ApJ*, 571, L173
- Watson, D. M., Leisenring, J. M., Furlan, E., et al. 2009, *ApJS*, 180, 84
- Watson, W. D. 1976, *Reviews of Modern Physics*, 48, 513
- Weaver, E., Isella, A., & Boehler, Y. 2018, *ApJ*, 853, 113
- Wells, M., Pel, J. W., Glasse, A., et al. 2015, *PASP*, 127, 646
- Werner, M. W., Roellig, T. L., Low, F. J., et al. 2004, *ApJS*, 154, 1
- Wetherill, G. W. & Stewart, G. R. 1989, *ICARUS*, 77, 330
- Wheeler, C. H., Hinkel, N. R., & Banzatti, A. 2024, *PASP*, 136, 113002
- Wiesenfeld, L. & Faure, A. 2013, *MNRAS*, 432, 2573
- Williams, J. P. & Cieza, L. A. 2011, *ARA&A*, 49, 67
- Wilson, T. L. 1999, *Reports on Progress in Physics*, 62, 143
- Woitke, P., Kamp, I., Antonellini, S., et al. 2019, *PASP*, 131, 064301

- Woitke, P., Kamp, I., & Thi, W. F. 2009, *A&A*, 501, 383
- Woitke, P., Min, M., Thi, W. F., et al. 2018, *A&A*, 618, A57
- Woitke, P., Thi, W. F., Arabhavi, A. M., et al. 2024, *A&A*, 683, A219
- Wölfer, L., Facchini, S., Kurtovic, N. T., et al. 2021, *A&A*, 648, A19
- Wölfer, L., Facchini, S., van der Marel, N., et al. 2023, *A&A*, 670, A154
- Wootten, A. & Thompson, A. R. 2009, *IEEE Proceedings*, 97, 1463
- Wright, E. L., Eisenhardt, P. R. M., Mainzer, A. K., et al. 2010, *AJ*, 140, 1868
- Wright, G. S., Rieke, G. H., Glasse, A., et al. 2023, *PASP*, 135, 048003
- Wright, G. S., Wright, D., Goodson, G. B., et al. 2015, *PASP*, 127, 595
- Wyatt, M. C. 2018, in *Handbook of Exoplanets*, ed. H. J. Deeg & J. A. Belmonte, 146
- Xie, T., Allen, M., & Langer, W. D. 1995, *ApJ*, 440, 674
- Yamato, Y., Aikawa, Y., Guzmán, V. V., et al. 2024a, *ApJ*, 974, 83
- Yamato, Y., Notsu, S., Aikawa, Y., et al. 2024b, *AJ*, 167, 66
- Yang, H., Fernández-López, M., Li, Z.-Y., et al. 2023, *ApJ*, 948, L2
- Yang, H., Fernández-López, M., Li, Z.-Y., et al. 2024, *ApJ*, 963, 134
- Yen, H.-W., Koch, P. M., Liu, H. B., et al. 2016, *ApJ*, 832, 204
- Youdin, A. N. & Goodman, J. 2005, *ApJ*, 620, 459
- Youdin, A. N. & Lithwick, Y. 2007, *ICARUS*, 192, 588
- Young, A. K., Alexander, R., Walsh, C., et al. 2021, *MNRAS*, 505, 4821
- Yu, S.-Y., Ho, L. C., & Zhu, Z. 2019, *ApJ*, 877, 100
- Zagaria, F., Jiang, H., Cataldi, G., et al. 2025, *ApJ*, 989, 30
- Zannese, M., Tabone, B., Habart, E., et al. 2024, *Nature Astronomy* [[arXiv:2312.14056](https://arxiv.org/abs/2312.14056)]
- Zhang, K., Bergin, E. A., Blake, G. A., et al. 2016, *ApJ*, 818, L16
- Zhang, K., Booth, A. S., Law, C. J., et al. 2021, *ApJS*, 257, 5
- Zhang, K., Pontoppidan, K. M., Salyk, C., & Blake, G. A. 2013, *ApJ*, 766, 82
- Zhang, S., Kalscheur, M., Long, F., et al. 2023, *ApJ*, 952, 108
- Zhang, S., Zhu, Z., & Fairbairn, C. W. 2025, *ApJ*, 995, L33
- Zhu, Z., Dong, R., Stone, J. M., & Rafikov, R. R. 2015, *ApJ*, 813, 88
- Zhu, Z. & Stone, J. M. 2018, *ApJ*, 857, 34

Nederlandse samenvatting

Een belangrijke vraag die zowel astronomen als het algemene publiek bezig houdt is: "Bestaat buitenaards leven?" Met het ontelbare aantal sterrenstelsels en sterren dat het universum kent, is het bijna ondenkbaar dat buitenaards leven niet zou bestaan. Nog belangrijker, op dit moment zijn meer dan 6,000 exoplaneten - planeten in een baan rondom een andere ster dan onze zon - ontdekt. Statistisch gezien is de huidige verwachting dat elke ster tenminste omringd wordt door één planeet. De vraag zou daardoor niet moeten gaan over het bestaan van buitenaards leven, maar waar het zich bevindt en waar het kan ontstaan. Om dat te bepalen moeten we niet alleen kijken naar de exoplaneten zelf, maar ook de gebieden waarin deze planeten vormen: planeetvormende schijven.

Planeetvormende schijven zijn schijven bestaande uit stof en gas, die rondom een pasgeboren ster draaien. Waarnemingen hebben aangetoond dat planeten ontstaan in deze schijven tegelijkertijd met hun moederster. Om te achterhalen wat de ingrediënten zijn van een planeet en of die vatbaar is voor leven, is het van cruciaal belang dat de chemische samenstelling van planeetvormende schijven in detail onderzocht wordt. Om de samenstelling te bepalen zijn krachtige telescopen nodig. Momenteel wordt onze kennis dagelijks vergroot door waarnemingen van de *James Webb* Space Telescope (JWST) en de Atacama Large Millimeter Array (ALMA).

Dit proefschrift houdt zich bezig met het onderzoek naar de chemische samenstelling van het gas in planeetvormende schijven. Met behulp van JWST wordt de samenstelling onderzocht in de warme, binnenste 10 astronomische eenheden, d.w.z. binnen 10 keer de afstand tussen de zon en de aarde. Deze waarnemingen geven direct inzicht in de samenstelling van het gas in het gebied waar de aardachtige planeten vormen. Daarentegen worden ALMA waarnemingen gebruikt om de samenstelling van het gas in de koude, buitenste regionen van de schijf te onderzoeken.

Ster- en planeetvorming

Het proces van ster- en planeetvorming speelt zich af in verschillende fases, zoals afgebeeld in Figuur 1). Sterren ontstaan in grote moleculaire wolken (paneel a)

die grotendeels bestaan uit gas (99% in massa) en voor een klein gedeelte uit stof (1% in massa). Het gas in een wolk is niet egaal verdeeld en er zijn plekken waar de gasdichtheid groter is dan op andere plekken. Gebieden met een hoge gasdichtheid worden ook wel kernen genoemd. Als de zwaartekracht van zo'n kern te groot wordt, stort de kern ineen en ontstaat er een protoster (paneel b). Door materie van de wolk in zich op te nemen, groeit de jonge protoster in massa, maar een deel van het gas en stof wordt ook weggeblazen in sterke straalstromen (paneel c). Tegelijkertijd ontstaat er een schijf rondom de jonge ster, de planeetvormende schijf. Met tijd zal de jonge protoster het restant van zijn geboortewolk hebben weggeblazen en is de jonge protoster, samen met zijn planeetvormende schijf, zichtbaar voor het blote oog (paneel d). Door het samenklonteren van stofdeeltjes in de schijf ontstaan planeten, waarvan de samenstelling zal afhangen van de samenstelling van de schijven. Met tijd zal ook het gas en stof uit de schijf verdwijnen en blijft een volwassen ster met een planetenstelsel over (paneel e).

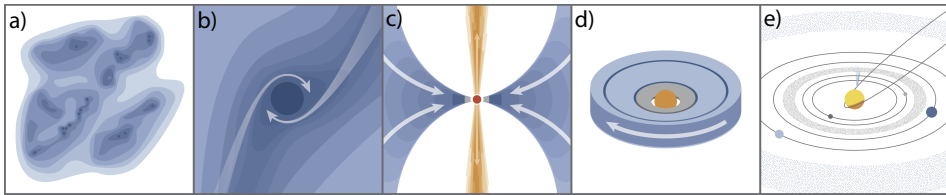


Figure 1: De verschillende fases van ster- en planeetvorming. Dit figuur is overgenomen van Öberg & Bergin (2021).

Planeetvormende schijven

Planeetvormende schijven zijn dynamische objecten die evolueren met de tijd. Het zijn objecten die, net als de moleculaire wolk waarin ze ontstaan, voor het grootste gedeelte bestaan uit gas en een klein beetje uit stof. Terwijl het gas door de hele schijf verdeeld is, hangt de locatie van het stof af van de grootte van de deeltjes. De kleine, micrometer stofdeeltjes bevinden zich vooral in de bovenlagen van de schijf, maar zodra deze groeien - naar millimeter en centimeter groottes, en uiteindelijk zelfs rotsblokken - zullen deze neerdalen in het middenvlak van de schijf. Terwijl de kleine stofdeeltjes zich voortbewegen met het gas, is er een snelheidsverschil tussen het gas en de grotere stofdeeltjes. Als gevolg van deze frictie verliezen de grote stofdeeltjes snelheid - dit is vergelijkbaar met het fietsen met tegenwind - en bewegen ze radieel naar de moederster toe. Deze radiële beweging leidt tot zowel een probleem voor planeetvorming als een verrijking van het gas in het binnenste gebied van de schijf.

Het probleem van deze beweging is de theoretische voorspelling dat de stofdeeltjes niet kunnen groeien voorbij groottes van ongeveer één meter voordat ze worden opgeslokt door hun moederster. Het bestaan van planeten, planetoïden en kometen spreekt deze verwachting natuurlijk tegen: er moet een manier zijn hoe de stofdeeltjes kunnen groeien tot enorme groottes. Een optie om de radiële

beweging van het stof te stoppen is met behulp van stofvallen, locaties in de schijf waar stof zich effectief kan ophopen. Binnenin deze stofvallen kan planeetvorming dan zijn weg vervolgen. Deze stofvallen kunnen direct worden waargenomen met ALMA via de warmtestraling van de stofdeeltjes. Totdusver dienen deze stofvallen zich voor in verschillende varianten: van ringen met bijbehorende gaten en holtes tot spiraalstructuren en grote asymmetrieën (zie Figuur 2).

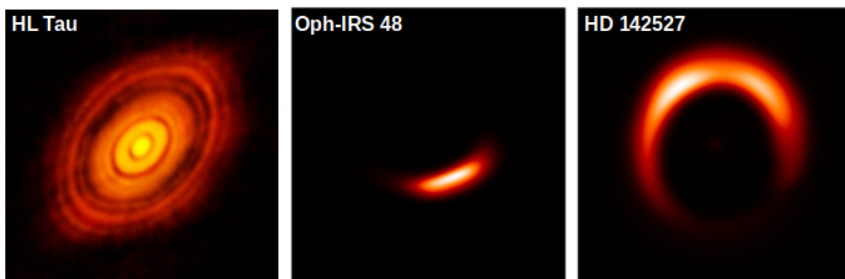


Figure 2: Warmtestraling van het stof in de planeetvormende schijven rondom de jonge sterren HL Tau (links), Oph-IRS 48 (midden) en HD 142527 (rechts). De stofschiif van HL Tau bestaat uit meerdere ringen en gaten (zwarte banden), terwijl die van Oph-IRS 48 en HD 142527 bestaan uit holtes en grote asymmetrieën. Dit figuur maakt gebruik van data gepubliceerd in ALMA Partnership et al. (2015) en Yang et al. (2023).

De verrijking van het gas gebeurt als een stofdeeltje een zogenoemde sneeuwlijn van een molecuul doorkruist. De sneeuwlijn is een scheidingslijn in de schijf die bepaalt in welke vorm (gasfase of ijsfase) een molecuul zich bevindt: binnen de sneeuwlijn is de temperatuur boven de sublimatietemperatuur van het molecuul en bevindt het zich in de gasfase. Buiten de sneeuwlijn is het te koud voor het molecuul en zal het gecondenseerd zijn op het stof – het vormt dan een laagje ijs rondom de stofdeeltjes. De radiële verplaatsing van het stof van buiten de sneeuwlijn naar binnen kan daardoor voor een verhoging van de abundantie van een molecuul zorgen. Het onderzoek naar deze verhoging is een actief onderzoeksveld binnen de astronomie.

Gas waarnemingen

Welk molecuul kan worden waargenomen met welke telescoop hangt af van de golflengte waarvoor de telescoop gevoelig is en de locatie van de sneeuwlijn van het molecuul. Een molecuul zoals water (H_2O) heeft bijvoorbeeld een sneeuwlijn locatie van een paar astronomische eenheden. Dit betekent dat emissielijnen van H_2O gas goed kunnen worden waargenomen met JWST. Waarnemingen van JWST, en in het bijzonder die van het MIRI instrument, bestaan uit een spectrum: de helderheid van het waargenomen licht als functie van golflengte. Naast H_2O wordt een MIRI spectrum van een schijf rondom een zonachtige ster gekarakteriseerd door signalen van moleculen zoals koolstofmonoxide (CO), koolstofdiox-

ide (CO_2), waterstofcyanide (HCN), acetyleen (C_2H_2) en het hydroxylradicaal (OH) (zie Figuur 3).

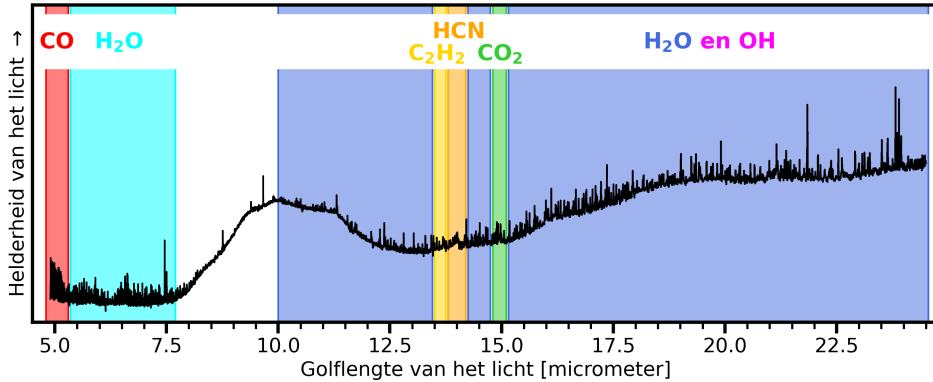


Figure 3: Het JWST-MIRI spectrum van de schijf rondom de jonge ster FT Tau. De gekleurde banden duiden aan welk molecuul zichtbaar is.

In tegenstelling tot de JWST waarnemingen, bestaan de ALMA waarnemingen niet alleen uit spectra, maar kan de emissie van moleculen ook worden vastgelegd in een 2D afbeelding. Hierdoor kan ook direct vastgesteld worden waar de moleculen zich bevinden in de schijf. Grote onderzoeken van meerdere moleculen in een schijf hebben aangetoond dat niet alle moleculen zich bevinden op dezelfde locatie, maar ook dat de emissie van moleculen verschillende structuren kan aannemen, net als het stof. ALMA waarnemingen van moleculen lopen uiteen van hele simpele moleculen, zoals CO, cyanide (CN), HCN, koolstofmonosulfide (CS) en zwavelmonoxide (SO), tot meer complexere moleculen, zoals formaldehyde (H_2CO), methanol (CH_3OH), methylformiaat (CH_3OCHO) en dimethylether (CH_3OCH_3). Figuur 4 toont ALMA waarnemingen van verschillende moleculen in een planeetvormende schijf.

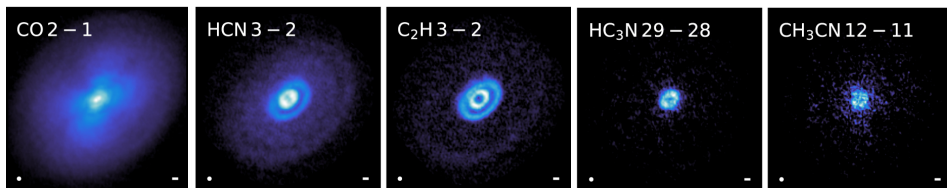


Figure 4: Een overzicht van een aantal moleculen waargenomen in de schijf rondom de jonge ster HD 163296 met ALMA. Dit figuur is aangepast overgenomen van Öberg et al. (2021).

Dit proefschrift

Zoals eerder benoemd houdt dit proefschrift zich bezig met de chemische samenstelling van planeetvormende schijven. Om deze samenstelling te onderzoeken wordt zowel gebruik gemaakt van JWST waarnemingen gericht op de binnenste regionen (Hoofdstukken 2-4) als ALMA waarnemingen van de buitenste delen van de schijven (Hoofdstukken 5-7). Nu volgt een korte samenvatting van elk hoofdstuk.

Hoofdstuk 2 richt zich op JWST waarnemingen van de schijf rondom de jongster DR Tau. De data toont de sterke emissie van de moleculen CO, H₂O (hoofdstuk 3), OH, CO₂, HCN, en C₂H₂. Om de emissie van CO goed te karakteriseren is extra gebruik gemaakt van waarnemingen van IRTF-iSHELL en VLT-CRIRES, instrumenten met een hogere spectrale resolutie dan JWST die zich op aarde bevinden. De analyse van de moleculen is gebruikt om de emissie structuur van de schijf bloot te leggen: de CO emissie komt van het binnenste gebied van de schijf, dichtbij de moederster, terwijl de banden van HCN en C₂H₂ komen uit een diepere laag van de schijf. De straling van CO₂ komt niet alleen dieper uit de schijf, maar ook van een grotere afstand ten opzichte van de moederster. De locaties van de moleculen zijn weergegeven in Figuur 5. Daarnaast suggereert de CO analyse dat de binnenste en buitenste delen van de schijf zich mogelijk niet op een lijn bevinden: het binnenste gedeelte zou zich in een ander vlak, gezien vanaf de evenaar van de moederster, bevinden ten opzichte van het buitenste gedeelte.

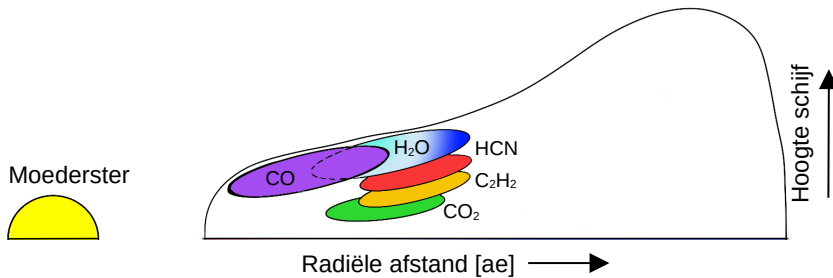


Figure 5: Schematische weergave van de verwachte locaties van CO, H₂O, CO₂, HCN en C₂H₂. Dit figuur is aangepast overgenomen van Temmink et al. (2024a,b).

Hoofdstuk 3 is gefocust op de H₂O emissie in de JWST waarnemingen van DR Tau. Het hoofdstuk maakt onderscheid tussen twee soorten emissielijnen: de ro-vibratoire lijnen, die ontstaan door een combinatie van de vibratie van de verschillende atomen in het molecuul met de rotatie van het hele molecuul, en de puur rotationele lijnen, die voortkomen uit pure rotatie. De ro-vibratoire lijnen van H₂O zijn zichtbaar op golflengtes kleiner dan 10 micrometer, terwijl de rotationele lijnen zich op grotere golflengtes bevinden. Deze verschillende soorten lijnen zijn

gebruikt om een radiële temperatuurgradiënt in de schijf bloot te leggen. Hierbij is gevonden dat de temperatuur omlaag gaat met de golflengte van de emissielijnen, terwijl ze worden uitgezonden op steeds grotere radiële locaties (zie Figuur 5). De puur rotationele lijnen kunnen worden onderverdeeld in drie verschillende reservoirs: een heet, een warm, en een koud reservoir. Er is gezocht naar aanwijzingen voor verrijking van het koude water door transport van de stofdeeltjes, maar dit kon niet worden vastgesteld voor deze schijf.

Hoofdstuk 4 vervolgt het onderzoek van Hoofdstuk 3 naar de verschillende rotationele H₂O reservoirs en de invloed van de radiële verplaatsing van het stof. In het bijzonder is gekeken naar de JWST waarnemingen van acht schijven die relatief compacte stof emissie tonen met ALMA, omdat het transport van ijsrijke stofdeeltjes in dit soort schijven als zeer effectief wordt beschouwd. Zes van de acht schijven tonen sterke emissie van alle drie de H₂O reservoirs, maar alleen twee van deze schijven tonen een mogelijke verrijking van het koude waterreservoir. Het kan niet worden vastgesteld of dit komt door radiële verplaatsing van de stofdeeltjes. De spectra van de laatste twee schijven worden niet gedomineerd door H₂O emissielijnen, maar door lijnen van andere moleculen, zoals CO₂.

Hoofdstuk 5 richt zich niet direct op de chemische samenstelling van planeetvormende schijven, maar onderzoekt de structuren die zichtbaar zijn in de warmtestraling van het stof en hoe deze de JWST waarnemingen kunnen beïnvloeden. In dit hoofdstuk worden hoge resolutie ALMA waarnemingen in detail onderzocht om de locaties en dieptes van de gaten in het stof van acht verschillende schijven vast te stellen. De gevonden structuren bestaan uit verschillende gaten en bijbehorende ringen, maar er is ook een zogenaamde "holte" - een centraal gat in het stof rondom de moederster - gevonden in de schijf rondom de jonge ster BP Tau. Een directe connectie tussen de gevonden structuren en de sterkte van de moleculaire emissie in de JWST waarnemingen kon niet worden vastgesteld.

Hoofdstuk 6 bestudeert de emissie van de zwaveldioxide (SO₂), formaldehyde H₂CO en methanol CH₃OH in de asymmetrische stofval van de Oph-IRS 48 schijf. De binnenrand van de stofval wordt opgewarmd door straling van de moederster wat er voor zorgt dat de ijslagen rondom het stof sublimeren en dat deze moleculen zichtbaar zijn in het gas. In dit hoofdstuk is vastgesteld dat zowel de straling van H₂CO als CH₃OH wordt uitgezonden vanuit een klein gebied rondom de binnenrand, terwijl de emissie van SO₂ van een grotere afstand binnen de stofval komt. Verder is geconstateerd dat de straling van de moederster de H₂CO en CH₃OH moleculen opbreekt in kleinere bestanddelen en daardoor hun abundanties verlaagt. Effectieve vorming van H₂CO door gasfase reacties, gebruikmakend van de opgebroken bestanddelen van CH₃OH en ook van H₂O en methaan (CH₄), verhogen daarentegen ook weer de abundantie. Dit creëert twee verschillende reservoirs van H₂CO: de één ontstaat door sublimatie aan de binnenrand van de stofval, de ander door volgt uit effectieve vorming in de gasfase.

Hoofdstuk 7 houdt zich bezig met de chemische samenstelling van de asym-

metrische schijf rondom de jonge ster HD 142527. Deze schijf is bijzonder omdat niet alleen het stof asymmetrisch is verdeeld, maar ook de moleculaire emissie van ethynyl (C_2H), CN, CS en H_2CO . De emissiekaarten van C_2H , CN en H_2CO vertonen zelfs kenmerken van een spiraalarm in de schijf. Dit hoofdstuk stelt voor dat vertraagd invallend materiaal, voortkomend uit het restant van de moederwolk waaruit de ster is gevormd, de asymmetrische emissie kan verklaren. In het bijzonder zorgt het invallende materiaal voor een lokaal verhoogde elementaire koolstof-tot-zuurstof verhouding in de schijf en kan het tevens de spiraalstructuur verklaren. Een verhoogde koolstof-tot-zuurstof verhouding leidt tot meer effectieve vorming van koolwaterstoffen (zoals C_2H), CN, CS en zelfs H_2CO .

Toekomstperspectief

Waarnemingen van JWST en ALMA geven ons de kans om de chemische samenstelling van planeetvormende schijven in hoog detail te bestuderen. Omdat beide telescopen gevoelig zijn voor de verschillende delen van de schijven, is het van groot belang voor ons begrip van de dominante fysische en chemische processen dat toekomstige studies zich richten op het combineren van deze waarnemingen. Naast deze bestaande krachtige telescopen, zijn meer telescopen in aanbouw (zoals de Extremely Large Telescope, ELT) of zijn deze in de ontwerpfase (zoals de ver-infrarood missies POEMM en PRIMA). Ook deze telescopen zijn weer gevoelig voor net iets andere golflengtes dan JWST en ALMA, waardoor ze andere moleculen of andere soorten emissielijnen van de reeds onderzochte moleculen kunnen waarnemen. De toekomst van het onderzoek naar de chemische samenstelling van planeetvormende schijven is rooskleurig: de mogelijke 20-jarige levensduur van JWST, de geplande verbeteringen van ALMA en deze nieuwe telescopen in aanbouw bieden ons de unieke kans en tijd om de waarnemingen te combineren, gedetailleerde onderzoeken uit te voeren en om onze kennis over planeetvormende schijven daardoor enorm te vergroten.

Publications

First-author publications

1. *MINDS: Water reservoirs of compact planet-forming dust discs: A diversity of H_2O distributions*
M. Temmink, A. D. Sellek, D. Gasman, E. F. van Dishoeck, M. Vlasblom, A. Pranger, M. Güdel, T. Henning, P.-O. Lagage, A. Caratti o Garatti, I. Kamp, G. Olofsson, A. M. Arabhavi, S. L. Grant, T. Kaeufer, N. T. Kurtovic, G. Perotti, M. Samland, K. Schwarz, and B. Tabone (2025), *Astronomy and Astrophysics*, 699, A134
2. *Characterising the molecular line emission in the asymmetric Oph-IRS 48 dust trap: Temperatures, timescales, and sub-thermal excitation*
M. Temmink, A. S. Booth, M. Leemker, N. van der Marel, E. F. van Dishoeck, L. Evans, L. Keyte, C. J. Law, S. Notsu, K. Öberg, and C. Walsh (2025), *Astronomy and Astrophysics*, 693, A101
3. *MINDS: The DR Tau disk: II. Probing the hot and cold H_2O reservoirs in the JWST-MIRI spectrum*
M. Temmink, E. F. van Dishoeck, D. Gasman, S. L. Grant, B. Tabone, M. Güdel, T. Henning, D. Barrado, A. Caratti o Garatti, A. M. Glauser, I. Kamp, A. M. Arabhavi, H. Jang, N. Kurtovic, G. Perotti, K. Schwarz, and M. Vlasblom (2024), *Astronomy and Astrophysics*, 689, A330
4. *MINDS: The DR Tau disk. I. Combining JWST-MIRI data with high-resolution CO spectra to characterise the hot gas*
M. Temmink, E. F. van Dishoeck, S. L. Grant, B. Tabone, D. Gasman, V. Christiaens, M. Samland, I. Argyriou, G. Perotti, M. Güdel, T. Henning, P.-O. Lagage, A. Abergel, O. Absil, D. Barrado, A. Caratti o Garatti, A. M. Glauser, I. Kamp, F. Lahuis, G. Olofsson, T. P. Ray, S. Scheithauer, B. Vandenbussche, L. B. F. M. Waters, A. M. Arabhavi, H. Jang, J. Kanwar, M. Morales-Calderón, D. Rodgers-Lee, J. Schreiber, K. Schwarz, and L. Colina (2024), *Astronomy and Astrophysics*, 686, A117

Submitted first-author publications

1. *The asymmetric carbon-rich chemistry of the planet-forming disk of HD 142527 triggered by late infall*
M. **Temmink**, E. F. van Dishoeck, A. S. Booth, N. van der Marel, M. Benisty, M. R. Hogerheijde, submitted to *Astronomy and Astrophysics*.

Co-author publications

1. *The chemical diversity of giant-planet nurseries as revealed by ALMA*
A. S. Booth, J. Calahan, M. **Temmink**, L. Wölfer, J. Pegues, C. J. Law, L. Evans, M. Leemker, S. Notsu, K. Öberg, C. Walsh, and E. F. van Dishoeck (2026), *The Astronomical Journal*, 171, 128
2. *MINDS: the molecule-rich disc of the Herbig star HD 35929 revealed with JWST/MIRI*
T. Kaeufer, R. Waters, D. Gasman, M. **Temmink**, H. Jang, E. F. van Dishoeck, M. Güdel, T. Henning, A. Caratti o Garatti, I. Kamp, A. M. Arabhavi, P. Esteve, S. L. Grant, J. Kanwar, N. T. Kurtovic, G. Perotti, K. Schwarz, L. M. Stapper, and B. Tabone (2026), *Monthly Notices of the Royal Astronomical Society*, 545, staf2056
3. *MINDS. Anatomy of a water-rich, inclined, brown dwarf disk: Lack of abundant hydrocarbons*
G. Perotti, N. T. Kurtovic, T. Henning, G. Olofsson, A. M. Arabhavi, K. Schwarz, J. Kanwar, R. van Boekel, I. Kamp, I. Pascucci, E. F. van Dishoeck, M. Güdel, P.-O. Lagage, D. Barrado, A. Caratti o Garatti, A. M. Glauser, F. Lahuis, V. Christiaens, R. Franceschi, D. Gasman, S. L. Grant, H. Jang, T. Kaeufer, M. Morales-Calderón, M. **Temmink**, and M. Vlasblom (2026), *The Astrophysical Journal*, 997, 281
4. *Observational evidence for a possible link between PAH emission and dust trap locations in protoplanetary disks*
N. van der Marel, N. F. W. Ligterink, R. van der Werf, M. **Temmink**, P. Pinilla, B. Jia, and Q. Bosschaart (2026), *Astronomy and Astrophysics*, 706, A214
5. *MINDS: Young binary systems with JWST/MIRI: Variable water-rich primaries and extended emission*
N. T. Kurtovic, S. L. Grant, M. **Temmink**, A. D. Sellek, E. F. van Dishoeck, T. Henning, I. Kamp, V. Christiaens, A. Banzatti, D. Gasman, T. Kaeufer, L. M. Stapper, R. Franceschi, M. Güdel, P.-O. Lagage, M. Vlasblom, G. Perotti, K. Schwarz, and A. Somigliana (2026), *Astronomy and Astrophysics*, 705, A97
6. *Understanding JWST water spectra: What can thermochemical models tell us about the (cold) water in protoplanetary disks?*

- M. Vlasblom, **M. Temmink**, A. D. Sellek, and E. F. van Dishoeck (2025), *Astronomy and Astrophysics*, 703, A52
7. *MINDS: Cha Ha 1, a brown dwarf with a hydrocarbon-rich disk*
M. Morales-Calderón, H. Jang, A. M. Arabhavi, V. Christiaens, D. Barrado, I. Kamp, E. F. van Dishoeck, T. Henning, L. B. F. M. Waters, **M. Temmink**, M. Güdel, P.-O. Lagage, A. Caratti o Garatti, A. M. Glauser, T. P. Ray, R. Franceschi, D. Gasman, S. L. Grant, T. Kaeufer, J. Kanwar, G. Perotti, M. Samland, K. Schwarz, M. Vlasblom, L. Colina, and G. Östlin (2025), *Astronomy and Astrophysics*, 703, A18
8. *MINDS: A transition from H₂O to C₂H₂ dominated disk spectra with decreasing stellar luminosity*
S. L. Grant, **M. Temmink**, E. F. van Dishoeck, D. Gasman, A. M. Arabhavi, B. Tabone, T. Henning, I. Kamp, A. Caratti o Garatti, V. Christiaens, P. Esteve, M. Güdel, H. Jang, T. Kaeufer, N. T. Kurtovic, M. Morales-Calderón, G. Perotti, K. Schwarz, A. D. Sellek, L. M. Stapper, M. Vlasblom, and L. B. F. M. Waters (2025), *Astronomy and Astrophysics*, 702, A126
9. *MINDS: Detection of an inner gas disk caused by evaporating bodies around HD 172555*
M. Samland, T. Henning, A. Caratti o Garatti, T. Giannini, J. Bouwman, B. Tabone, A. M. Arabhavi, G. Olofsson, M. Güdel, N. Pawellek, I. Kamp, L. B. F. M. Waters, D. Semenov, E. F. van Dishoeck, O. Absil, D. Barrado, A. Boccaletti, V. Christiaens, D. Gasman, S. L. Grant, H. Jang, T. Kaeufer, J. Kanwar, G. Perotti, K. Schwarz, and **M. Temmink** (2025), *The Astrophysical Journal*, 989, A132
10. *MINDS: The very low-mass star and brown dwarf sample: Detections and trends in the inner disk gas*
A. M. Arabhavi, I. Kamp, T. Henning, E. F. van Dishoeck, H. Jang, L. B. F. M. Waters, V. Christiaens, D. Gasman, I. Pascucci, G. Perotti, S. L. Grant, M. Güdel, P.-O. Lagage, D. Barrado, A. Caratti o Garatti, F. Lahuis, T. Kaeufer, J. Kanwar, M. Morales-Calderón, K. Schwarz, A. D. Sellek, B. Tabone, **M. Temmink**, M. Vlasblom, and P. Patapis (2025), *Astronomy and Astrophysics*, 699, A194
11. *Ice sublimation in the dynamic HD 100453 disk reveals a rich reservoir of inherited complex organics*
A. S. Booth, L. Wölfer, **M. Temmink**, J. Calahan, L. Evans, C. J. Law, M. Leemker, S. Notsu, K. Öberg, and C. Walsh (2025), *The Astrophysical Journal*, 986, L9
12. *MINDS: The very low-mass star and brown dwarf sample hidden water in carbon-dominated protoplanetary disks*
A. M. Arabhavi, I. Kamp, E. F. van Dishoeck, T. Henning, H. Jang, V. Christiaens, D. Gasman, I. Pascucci, G. Perotti, S. L. Grant, D. Barrado, M. Güdel, P.-O. Lagage, A. Caratti o Garatti, F. Lahuis, L. B. F. M. Waters,

- T. Kaeufer, J. Kanwar, M. Morales-Calderón, K. Schwarz, A. D. Sellek, B. Tabone, **M. Temmink**, and M. Vlasblom (2025), *The Astrophysical Journal*, 984, L62
13. *ALMA reveals thermal and nonthermal desorption of methanol ice in the HD 100546 protoplanetary disk*
L. Evans, A. S. Booth, C. Walsh, J. D. Ilee, L. Keyte, C. J. Law, M. Leemker, S. Notsu, K. Öberg, **M. Temmink**, and N. van der Marel (2025), *The Astrophysical Journal*, 982, 62
14. *MINDS. JWST-MIRI observations of a spatially resolved atomic jet and polychromatic molecular wind toward SY Cha*
K. R. Schwarz, M. Samland, G. Olofsson, T. Henning, A. Sellek, M. Güdel, B. Tabone, I. Kamp, P.-O. Lagage, E. F. van Dishoeck, A. Caratti o Garatti, A. M. Glauser, T. P. Ray, A. M. Arabhavi, V. Christiaens, R. Franceschi, D. Gasman, S. L. Grant, J. Kanwar, T. Kaeufer, N. T. Kurtovic, G. Perotti, **M. Temmink**, and M. Vlasblom (2025), *The Astrophysical Journal*, 980, 148
15. *MINDS: The influence of outer dust disc structure on the volatile delivery to the inner disc*
D. Gasman, **M. Temmink**, E. F. van Dishoeck, N. T. Kurtovic, S. L. Grant, A. Sellek, B. Tabone, T. Henning, I. Kamp, M. Güdel, D. Barrado, A. Caratti o Garatti, A. M. Glauser, L. B. F. M. Waters, A. M. Arabhavi, H. Jang, J. Kanwar, J. L. Lienert, G. Perotti, K. Schwarz, and M. Vlasblom (2025), *Astronomy and Astrophysics*, 694, A147
16. *MINDS. JWST-MIRI reveals a peculiar CO₂-rich chemistry in the drift-dominated disk CX Tau*
M. Vlasblom, **M. Temmink**, S. L. Grant, N. Kurtovic, A. D. Sellek, E. F. van Dishoeck, M. Güdel, T. Henning, P.-O. Lagage, D. Barrado, A. Caratti o Garatti, A. M. Glauser, I. Kamp, F. Lahuis, G. Olofsson, A. M. Arabhavi, V. Christiaens, D. Gasman, H. Jang, M. Morales-Calderón, G. Perotti, K. Schwarz, and B. Tabone (2025), *Astronomy and Astrophysics*, 693, A278
17. *Measuring the ³⁴S and ³³S isotopic ratios of volatile sulfur during planet formation*
A. S. Booth, M. N. Drozdovskaya, **M. Temmink**, H. Nomura, E. F. van Dishoeck, L. Keyte, C. J. Law, M. Leemker, N. van der Marel, S. Notsu, K. Öberg, and C. Walsh (2024), *The Astrophysical Journal*, 975, 72
18. *Dust mineralogy and variability of the inner PDS 70 disk: Insights from JWST/MIRI MRS and Spitzer IRS observations*
H. Jang, R. Waters, T. Kaeufer, A. Tamanai, G. Perotti, V. Christiaens, I. Kamp, T. Henning, M. Min, A. M. Arabhavi, D. Barrado, E. F. van Dishoeck, D. Gasman, S. L. Grant, M. Güdel, P.-O. Lagage, F. Lahuis, K. Schwarz, B. Tabone, and **M. Temmink** (2024), *Astronomy and Astrophysics*, 691, A148

19. *MINDS. Hydrocarbons detected by JWST/MIRI in the inner disk of Sz28 consistent with a high C/O gas-phase chemistry*
J. Kanwar, I. Kamp, H. Jang, L. B. F. M. Waters, E. F. van Dishoeck, V. Christiaens, A. M. Arabhavi, T. Henning, M. Güdel, P. Woitke, O. Absil, D. Barrado, A. Caratti o Garatti, A. M. Glauser, F. Lahuis, S. Scheithauer, B. Vandenbussche, D. Gasman, S. L. Grant, N. T. Kurtovic, G. Perotti, B. Tabone, and **M. Temmink** (2024), *Astronomy and Astrophysics*, 689, A231
20. *MINDS: A multi-instrument investigation into the molecule-rich JWST-MIRI spectrum of the DF Tau binary system*
S. L. Grant, N. T. Kurtovic, E. F. van Dishoeck, T. Henning, I. Kamp, H. Nowacki, K. Perraut, A. Banzatti, **M. Temmink**, V. Christiaens, M. Samland, D. Gasman, B. Tabone, M. Güdel, P.-O. Lagage, A. M. Arabhavi, D. Barrado, A. Caratti o Garatti, A. M. Glauser, H. Jang, J. Kanwar, F. Lahuis, M. Morales-Calderón, G. Olofsson, G. Perotti, K. Schwarz, M. Vlasblom, R. Garcia Lopez, and F. Long (2024), *Astronomy and Astrophysics*, 689, A85
21. *MINDS: Mid-infrared atomic and molecular hydrogen lines in the inner disk around a low-mass star*
R. Franceschi, T. Henning, B. Tabone, G. Perotti, A. Caratti o Garatti, G. Bettoni, E. F. van Dishoeck, I. Kamp, O. Absil, M. Güdel, G. Olofsson, L. B. F. M. Waters, A. M. Arabhavi, V. Christiaens, D. Gasman, S. L. Grant, H. Jang, D. Rodgers-Lee, M. Samland, K. Schwarz, **M. Temmink**, D. Barrado, A. Boccaletti, V. Geers, P.-O. Lagage, E. Pantin, T. P. Ray, S. Scheithauer, B. Vandenbussche, and G. Wright (2024), *Astronomy and Astrophysics*, 687, A96
22. *Abundant hydrocarbons in the disk around a very-low-mass star*
A. M. Arabhavi, I. Kamp, T. Henning, E. F. van Dishoeck, V. Christiaens, D. Gasman, A. Perrin, M. Güdel, B. Tabone, J. Kanwar, L. B. F. M. Waters, I. Pascucci, M. Samland, G. Perotti, G. Bettoni, S. L. Grant, P. O. Lagage, T. P. Ray, B. Vandenbussche, O. Absil, I. Argyriou, D. Barrado, A. Boccaletti, J. Bouwman, A. Caratti o Garatti, A. M. Glauser, F. Lahuis, M. Mueller, G. Olofsson, E. Pantin, S. Scheithauer, M. Morales-Calderón, R. Franceschi, H. Jang, N. Pawellek, D. Rodgers-Lee, J. Schreiber, K. Schwarz, **M. Temmink**, M. Vlasblom, G. Wright, L. Colina, and G. Östlin (2024), *Science*, 384, p.1086
23. *MINDS: The JWST MIRI Mid-INfrared Disk Survey*
T. Henning, I. Kamp, M. Samland, A. M. Arabhavi, J. Kanwar, E. F. van Dishoeck, M. Güdel, P.-O. Lagage, C. Waelkens, A. Abergel, O. Absil, D. Barrado, A. Boccaletti, J. Bouwman, A. Caratti o Garatti, V. Geers, A. M. Glauser, F. Lahuis, M. Mueller, C. Nehmé, G. Olofsson, E. Pantin, T. P. Ray, S. Scheithauer, B. Vandenbussche, L. B. F. M. Waters, G. Wright, I. Argyriou, V. Christiaens, R. Franceschi, D. Gasman, S. L. Grant, R. Guadarrama, H. Jang, M. Morales-Calderón, N. Pawellek, G. Perotti, D. Rodgers-Lee, J. Schreiber, K. Schwarz, B. Tabone, **M. Temmink**, M. Vlasblom, L.

- Colina, T. R. Greve, and G. Östlin (2024), Publications of the Astronomical Society of the Pacific, 136, 054302
24. *MINDS: JWST/NIRCam imaging of the protoplanetary disk PDS 70. A spiral accretion stream and a potential third protoplanet*
V. Christiaens, M. Samland, T. Henning, B. Portilla-Revelo, G. Perotti, E. Matthews, O. Absil, L. Decin, I. Kamp, A. Boccaletti, B. Tabone, G.-D. Marleau, E. F. van Dishoeck, M. Güdel, P.-O. Lagage, D. Barrado, A. Caratti o Garatti, A. M. Glauser, G. Olofsson, T. P. Ray, S. Scheithauer, B. Vandenbussche, L. B. F. M. Waters, A. M. Arabhavi, S. L. Grant, H. Jang, J. Kanwar, J. Schreiber, K. Schwarz, **M. Temmink**, and G. Östlin (2024), Astronomy and Astrophysics, 685, L1
25. *An ALMA molecular inventory of warm Herbig Ae disks. II. Abundant complex organics and volatile sulphur in the IRS 48 disk*
A. S. Booth, **M. Temmink**, E. F. van Dishoeck, L. Evans, J. D. Ilee, M. Kama, L. Keyte, C. J. Law, M. Leemker, N. van der Marel, H. Nomura, S. Notsu, K. Öberg, and C. Walsh (2024), The Astronomical Journal, 167, 165
26. *An ALMA molecular inventory of warm Herbig Ae Disks. I. Molecular rings, asymmetries, and complexity in the HD 100546 disk*
A. S. Booth, M. Leemker, E. F. van Dishoeck, L. Evans, J. D. Ilee, M. Kama, L. Keyte, C. J. Law, N. van der Marel, H. Nomura, S. Notsu, K. Öberg, **M. Temmink**, and C. Walsh (2024), The Astronomical Journal, 167, 164
27. *MINDS. JWST/MIRI reveals a dynamic gas-rich inner disk inside the cavity of SY Cha*
K. R. Schwarz, T. Henning, V. Christiaens, D. Gasman, M. Samland, G. Perotti, H. Jang, S. L. Grant, B. Tabone, M. Morales-Calderón, I. Kamp, E. F. van Dishoeck, M. Güdel, P.-O. Lagage, D. Barrado, A. Caratti o Garatti, A. M. Glauser, T. P. Ray, B. Vandenbussche, L. B. F. M. Waters, A. M. Arabhavi, J. Kanwar, G. Olofsson, D. Rodgers-Lee, J. Schreiber, and **M. Temmink** (2024), The Astrophysical Journal, 962, 8
28. *MINDS. Abundant water and varying C/O across the disk of Sz 98 as seen by JWST/MIRI*
D. Gasman, E. F. van Dishoeck, S. L. Grant, **M. Temmink**, B. Tabone, T. Henning, I. Kamp, M. Güdel, P.-O. Lagage, G. Perotti, V. Christiaens, M. Samland, A. M. Arabhavi, I. Argyriou, A. Abergel, O. Absil, D. Barrado, A. Boccaletti, J. Bouwman, A. Caratti o Garatti, V. Geers, A. M. Glauser, R. Guadarrama, H. Jang, J. Kanwar, F. Lahuis, M. Morales-Calderón, M. Mueller, C. Nehmé, G. Olofsson, É. Pantin, N. Pawellek, T. P. Ray, D. Rodgers-Lee, S. Scheithauer, J. Schreiber, K. Schwarz, B. Vandenbussche, M. Vlasblom, R. L. B. F. M. Waters, G. Wright, L. Colina, T. R. Greve, and G. Östlin (2023), Astronomy and Astrophysics, 679, A117
29. *Tracing snowlines and C/O ratio in a planet-hosting disk. ALMA molecular line observations towards the HD 169142 disk*

A. S. Booth, C. J. Law, **M. Temmink**, M. Leemker, and E. Macías (2023), *Astronomy and Astrophysics*, 678, A146

30. *The chemical inventory of the inner regions of planet-forming disks - the JWST/MINDS program*
I. Kamp, T. Henning, A. M. Arabhavi, G. Bettoni, V. Christiaens, D. Gasman, S. L. Grant, M. Morales-Calderón, B. Tabone, A. Abergel, O. Absil, I. Argyriou, D. Barrado, A. Boccaletti, J. Bouwman, A. Caratti o Garatti, E. F. van Dishoeck, V. Geers, A. M. Glauser, M. Güdel, R. Guadarrama, H. Jang, J. Kanwar, P.-O. Lagage, F. Lahuis, M. Mueller, C. Nehmé, G. Olofsson, E. Pantin, N. Pawellek, G. Perotti, T. P. Ray, D. Rodgers-Lee, M. Samland, S. Scheithauer, J. Schreiber, K. Schwarz, **M. Temmink**, B. Vandenbussche, M. Vlasblom, C. Waelkens, L. B. F. M. Waters, and G. Wright (2023), *Faraday Discussions*, 245, p.112
31. *MINDS. The detection of $^{13}\text{CO}_2$ with JWST-MIRI indicates abundant CO_2 in a protoplanetary disk*
S. L. Grant, E. F. van Dishoeck, B. Tabone, D. Gasman, T. Henning, I. Kamp, M. Güdel, P.-O. Lagage, G. Bettoni, G. Perotti, V. Christiaens, M. Samland, A. M. Arabhavi, I. Argyriou, A. Abergel, O. Absil, D. Barrado, A. Boccaletti, J. Bouwman, A. Caratti o Garatti, V. Geers, A. M. Glauser, R. Guadarrama, H. Jang, J. Kanwar, F. Lahuis, M. Morales-Calderón, M. Mueller, C. Nehmé, G. Olofsson, E. Pantin, N. Pawellek, T. P. Ray, D. Rodgers-Lee, S. Scheithauer, J. Schreiber, K. Schwarz, **M. Temmink**, B. Vandenbussche, M. Vlasblom, L. B. F. M. Waters, G. Wright, L. Colina, T. R. Greve, K. Justannont, and G. Östlin (2023), *The Astrophysical Journal*, 947, L6

Submitted co-author publications

1. *MINDS survey of silicates in T Tauri disks: correlation between dust and gas*
J. Varga, T. Henning, L. B. F. M. Waters, I. Kamp, Á. Kóspál, P. Ábrahám, O. Absil, A. M. Arabhavi, D. Gasman, S. L. Grant, M. Güdel, H. Jang, T. Kaeufer, J. Kanwar, N. T. Kurtovic, P.-O. Lagage, G. Perotti, A. Somigliana, L. M. Stapper, B. Tabone, **M. Temmink**, E. F. van Dishoeck, and M. Vlasblom, submitted to *Astronomy and Astrophysics*.
2. *MINDS. Disc diversity, ice features, and extended molecular emission in the binary system HK Tau*
A. Somigliana, G. Perotti, N. T. Kurtovic, T. Henning, M. Benisty, A. D. Sellek, M. K. McClure, Z. L. Smith, A. M. Arabhavi, A. Caratti o Garatti, V. Christiaens, E. F. van Dishoeck, D. Gasman, Sierra L. Grant, M. Güdel, T. Kaeufer, I. Kamp, L. Stapper, B. Tabone, **M. Temmink**, and M. Vlasblom, submitted to *Astronomy and Astrophysics*.

3. *MINDS: Intertwined evolution of dust and gas in large planet-forming disks. A diversity driven by halted pebble drift?*
B. Tabone, **M. Temmink**, L. B. F. M. Waters, E. F. van Dishoeck, A. D. Sellek, P. Esteve, N. T. Kurtovic, I. Kamp, T. Henning, D. Gasman, S. L. Grant, J. Varga, A. Guerras, D. Semenov, A. M. Arabhavi, A. Caratti o Garatti, A. Dutrey, E. Chapillon, S. Guilloteau, M. Güdel, H. Jang, T. Kaeufer, J. Kanwar, G. Olofsson, G. Perotti, V. Piétu, T. P. Ray, and M. Vlasblom, submitted to *Astronomy and Astrophysics*.
4. *Comparing the localization of complex organic molecules in the Oph-IRS 48 disk using ALMA data*
K. A. Kipfer, A. S. Booth, **M. Temmink**, N. van der Marel, and N. F. W. Ligterink, submitted to *Astronomy and Astrophysics*.

Curriculum Vitae

I was born on Thursday, the 6th of May, 1999, in a small village in the east of the Netherlands called Wesepe. I grew up with my parents and my two older brothers. My childhood mainly consisted of playing outside and, in particular, playing a lot of football. That did, however, not mean that my nose was not stuck in books quite often. I liked (and still do) reading a lot, and fantasy stories have always been my favourite. After all, what is more interesting than imagining a world different from our own, that is ruled by magic, and where everything is possible?

After finishing my education at our local primary school, I went to the "Carmel College Salland" in Raalte for my secondary education. During my studies, it became clear that the STEM courses, such as mathematics, physics, and chemistry, suited me best. Surprisingly, I struggled quite a bit with biology, but that did not deter me from choosing it as part of my curriculum. My love for fantasy stories also led to a large interest in Greek mythology and my choice to pursue ancient Greek as one of my courses. During my secondary education, playing video games became my main hobby, which did not always lead to me being as invested in my courses as I should have been...

Nearing the end of my secondary education, choosing a follow-up study was not hard. While I always thought that I would follow in my mom's footsteps and choose a healthcare-related study, one physics chapter on the topic of astrophysics during my final year of secondary education really caught my eye. While I always had a passing interest in space, its vastness, and the possibility of alien life, I never really considered that one could study astronomy. This chapter changed everything for me, and once I told my parents that I wanted to study astronomy, I visited both an open day and an orientation day at Leiden University. Partaking in these days only confirmed for me that I wanted to study astronomy.

While adapting to student life took a bit of time, I found my pace and what study methods worked best for me. I managed to pass all my courses in the first year of my bachelor's at Leiden University, and I was allowed to go to La Palma during the second year. This was an amazing experience and it also opened my eyes to astronomical research. My love for research only grew during the third year of my bachelors, when I completed my first research project - together with Sam de Regt - on the colour-magnitude diagrams of the Magellanic Clouds using the second data release of Gaia. I knew that I wanted to continue doing research,

and the choice to take on the general "Astronomy Research" master's at Leiden University was easily made. For my first master's research project, I wanted to do a topic related to exoplanets, and I ended up picking a project with prof. dr. Ignas Snellen to detect transiting exoplanets around red-giant stars.

This first research project already confirmed for me that I wanted to do a PhD after my Master's and to pursue an academic career. Discussing this with Ignas, he suggested to me that I ask prof. dr. Ewine van Dishoeck about potential research projects for my Master's thesis. Multiple projects were offered, but one caught my eye. This project aimed to study the chemical composition of azimuthally asymmetric planet-forming disks, following the recent discovery that the disk of Oph-IRS 48 hosts an ice trap. Under the supervision of Ewine, dr. Nienke van der Marel, and dr. Alice Booth, I learned how to work with ALMA observations of disks and I found the topic that inspired me most. Eventually, I had really found my footing, and my love for astronomy and astrochemistry only grew with time. I even managed to graduate Cum Laude for my master's studies.

Having made the prior choice to follow an academic career, I applied to PhD positions all over Europe. However, I realised that I was not yet ready to leave the Netherlands, and when Ewine offered me a PhD position at Leiden, I accepted it immediately. The topic of my PhD allowed me to continue my work on the chemistry of asymmetric disks, but it also took me in a completely new direction. During my master's thesis, a little bit over half a year before the start of my PhD, JWST launched. The launch was perfectly on time for my PhD and for me to become part of the MINDS collaboration, a team of international researchers that has access to over 100 hours of JWST time on the chemistry of planet-forming disks. Being part of this collaboration allowed me to work on the first observations of disks released with JWST, an opportunity for which I will forever be grateful.

During my PhD, I was not only always staring at my computer, processing either ALMA or JWST observations. I was a teaching assistant for different courses, ranging from the observations of molecular astrophysics in galaxies to stars. During my final year of the PhD, the University offered a new minor, "Our Universe" for non-astronomy students, and I became a teaching assistant for the course "The Habitable Universe". It was an eye-opening experience to teach these students about astronomy. I have also partaken in various outreach events, from providing tours and explanations at different JWST exhibitions to giving multiple public lectures. Each of these events has shown me how rewarding it is to make a difficult topic, such as astronomy, comprehensible to everyone. I also (co-)supervised multiple bachelor's (Philip and Olivier) and master's (Ryan, Bin, Angèl, and Victor) students during their research projects. Finally, I also had the great opportunity during my PhD to travel the world, participate in in-person meetings of the MINDS collaboration, attend conferences, and present my work. My travels have brought me to multiple places in Germany (Garching, Heidelberg, and Ringberg), Austria, France, Italy, Ireland, Spain, Sweden, and even twice to the USA.

However, everything has to come to an end. While I will finish my PhD this Summer, I am excited to continue my research as a Postdoctoral Fellow at the Planet-Formation & Exoplanets department at the Max-Planck Institute for Astronomy in Heidelberg, where I will work together with dr. Myriam Benisty.

Acknowledgements

Having spent 9 years at Leiden University, I have met many amazing people who have made this entire journey possible below. Here, I want to thank each and all of you for all your support, the fun discussions, and for making Leiden the beautiful place it is.

First of all, I want to thank Ewine for the past five years of teaching me science, how to be a researcher, how to write proposals and papers, and, finally, the importance of conveying science to the general public. Your excitement for science is infectious. I am grateful for everything you have taught me, and I feel like I learned something new every single day. I also want to express my gratitude to my other supervisors, Alice and Nienke. Both of you have been there since I started studying the chemistry of disks. Alice, even though our ways parted quickly as you moved to the USA, I am grateful for all your guidance on working with ALMA and your scientific insights and ideas over these past years. Nienke, I want to thank you for all our scientific discussions and for organising the Pangolin group meetings. I have learned a lot from you. I hope that a particular one-liter beer glass has proven useful to you. Michiel and Melissa, I also want to thank you both; our useful discussions and aid with proposals have proven to be invaluable.

One benefit of pursuing a PhD at Leiden is the ability to be part of a large scientific family, where you can learn from everyone around you and go through struggles together. I want to thank every one of you for all the discussions and, most importantly, all the joy: Alessia, Andrés, Andrew, Ardjan, Femke, Franciele, Ioannis, Jerry, Julia, Katie, Lisa, Logan, Lucas, Lukas, Łukasz, Margot, Mariana, Marissa, Martijn, Mulan, Nashanty, Nico, Osmar, Pooneh, Pranjal, Sierra, Teresa, Tobias, Will, Xinyu, Yuan, and Zak (also thank you for all the lunch walks, I am going to miss them!).

I also am grateful for everybody from the MINDS collaboration; these past few years have been really inspiring. In particular, I want to express my gratitude towards my MINDS partner in crime, Danny, and I am grateful for the friendship that we have built. I am looking forward to joining you in Heidelberg.

I also want to thank Sam and Victorine for all the fun times and discussions, from our time studying together to each doing our PhD at Leiden. Sam, I hope we can continue our somewhat bi-monthly dinners to catch up once we are both in Heidelberg.

And finally, but most certainly not least, I am grateful for my parents, my brothers Lars and Rik, and Charlie. Lieve mama en papa, ik denk niet dat ik ooit onder woorden kan brengen hoe belangrijk jullie voor mij zijn en hoe dankbaar ik ben voor alle steun van deze afgelopen jaren. Ik vond het heel fijn dat ik altijd even met jullie kan bellen als alles even te veel werd en dat ik met jullie over alles kan praten. Lars en Rik, ik beseft me dat ik het waarschijnlijk nooit verwoord, maar ik wil jullie ook bedanken voor jullie interesse en steun. Ik ben enorm dankbaar dat jullie mijn broers zijn. Charlie, ik ben enorm blij dat jij onderdeel bent van onze familie en jouw bestaan vrolijkt me elke dag op.